Ab-initio description of monopole resonances in light- and medium-mass nuclei

Andrea Porro

université PARIS-SACLAY

Ab initio description of monopole resonances in light- and medium-mass nuclei

Description des résonances monopolaires pour des noyaux de masse légère et moyenne par des méthodes ab initio

Thèse de doctorat de l'université Paris-Saclay

École doctorale n° 576, PHENIICS
Particules, Hadrons, Énergie, Noyau,
Instrumentation, Imagerie, Cosmos et Simulation
Spécialité de doctorat : Physique nucléaire
Graduate School : Physique. Référent : Faculté des sciences d'Orsay

Thèse préparée dans l'unité de recherche **Institut de recherche sur les lois Fondamentales de l'Univers (Université Paris-Saclay, CEA)**,
sous la direction de **Thomas DUGUET**, Ingénieur de recherche, Professeur,
le co-encadrement de **Vittorio SOMÀ**, Ingénieur de recherche

Thèse soutenue à Paris-Saclay, le 26 Septembre 2023, par

Andrea PORRO

Composition du jury

Membres du jury avec voix délibérative

Denis LACROIX Directeur de recherche, IJCLab - Université Paris-Saclay	Président
Luís ROBLEDO Professeur, Universidad Autónoma de Madrid	Rapporteur & Examinateur
Robert ROTH Professeur, Technische Universität Darmstadt	Rapporteur & Examinateur
Yorick BLUMENFELD Directeur de recherche, IJCLab - Université Paris-Saclay	Examinateur
Alessandro PASTORE Ingénieur de recherche, CEA DES - Université de Lyon	Examinateur
Sophie PÉRU Directeur de recherche, CEA DAM DIF - Université Paris-Saclay	Examinatrice

THESE DE DOCTORAT
NNT : 2023UPASP103

université PARIS-SACLAY

ÉCOLE DOCTORALE
Particules, hadrons, énergie et noyau : instrumentation, imagerie, cosmos et simulation (PHENIICS)

Titre : Description des résonances monopolaires pour des noyaux de masse légère et moyenne par des méthodes ab initio
Mots clés : Structure nucléaire théorique, résonances géantes, techniques à N corps

Résumé : Les Résonances Géantes (GRs) sont l'une des manifestations les plus évidentes des comportements collectifs au sein du noyau atomique. En utilisant une représentation inspirée du modèle de la goutte liquide, ce phénomène peut s'interpréter comme des vibrations de la surface nucléaire dans lesquelles prend part l'ensemble des nucléons. En particulier, la GR Monopolaire (GMR) est directement reliée à l'incompressibilité nucléaire, une quantité fondamentale dans l'équation d'état nucléaire.

La GMR a été largement étudiée sur le plan théorique grâce à la *Quasiparticle Random Phase Approximation* (QRPA) basée sur des fonctionnelles énergie de la densité. Dans ce cadre, des interactions phénoménologiques sont utilisées pour résoudre le problème à N corps nucléaire sous l'hypothèse que les états excités soient des vibrations harmoniques d'un état non corrélé, qui brise potentiellement les symétries de l'hamiltonien nucléaire.

A partir des années 2000, les méthodes dites *ab initio* se sont imposées pour l'étude des propriétés de l'état fondamental des noyaux. Elles se proposent de partir de la théorie sous-jacente, c'est à dire la chromodynamique quantique, pour obtenir des interactions réalistes. Des codes numériques QRPA *ab initio* ont récemment été développés et permettent aujourd'hui d'accéder aux GRs des systèmes à couches ouvertes.

Dans ce travail, la Méthode de la Coordonnée Génératrice (PGCM) a été utilisée pour la première fois afin d'étudier de manière *ab initio* la GMR des noyaux de masse légère et moyenne. Cette méthode permet de surmonter certaines limitations implicites aux calculs QRPA déformés, tout en permettant de traiter les effets inharmoniques. Notamment, la comparaison avec des calculs QRPA démontre que la PGCM *ab initio* est une méthode de choix pour l'étude des GRs.

Title : *Ab initio* description of monopole resonances in light- and medium-mass nuclei
Keywords : Theoretical nuclear structure, giant resonances, many-body methods

Abstract : Giant resonances (GRs) are the clearest manifestation of collective motions in the atomic nucleus. They can best be imagined in terms of vibrations of the nuclear surface in a liquid-drop picture, in which most if not all the nucleons take part to the process. The Giant Monopole Resonance (GMR), in particular, is also directly linked to the incompressibility of infinite nuclear matter, a key quantity entering the nuclear equation of state.

The GMR has largely been investigated, from a theoretical perspective, via the Quasiparticle Random Phase Approximations (QRPA) in the context of Energy Density Functional theories. In this frame, phenomenological interactions are used to solve the many-body Schrödinger equation under the assumption that excited states can be described as harmonic vibrations on an uncorrelated ground state, possibly breaking the symmetries of the nuclear Hamiltonian.

In the last twenty years the so-called *ab initio* methods parallelly became a reliable tool to access nuclear ground-state properties, starting from realistic interactions rooted into the underlying quantum chromodynamics via chiral Effective Field Theory. *Ab initio* QRPA solvers were also developed, nowadays allowing to address GRs in (doubly-)open-shell systems.

In this work the Projected Generator Coordinate Method (PGCM) is used in an *ab initio* context for the first time to investigate the GMR in light- and medium-mass nuclei. This method allows to overcome some drawbacks implicit in the formalisation of deformed QRPA, also allowing to treat the presence of anharmonic effects in an exact fashion. The comparison to consistent QRPA calculations is explicitly addressed, establishing *ab initio* PGCM as a trustful method to investigate the Physics of GRs.

Acknowledgements

With overflowing gratitude, I embark on writing the very last page of this manuscript. Three years within this remarkable community of people (actually four if we include my master's thesis) and almost five years in this incredible city. I must confess, nothing has been overlooked. While I might have omitted someone on this page, rest assured that no one has been forgotten in the unique path that has led me to this particularly special day.

First and foremost, in accordance with tradition, I would like to extend my heartfelt thanks to all the members of my PhD defence panel: Sophie Péru, Yorick Blumenfeld, Denis Lacroix, Alessandro Pastore, Luis Robledo, and Robert Roth. I very much enjoyed our discussion: thank you for the time and attention you devoted to me and my work, and for allowing me to share and present the culmination of these years of effort. I genuinely valued your constructive criticisms, which I believe will enhance the content of these pages, especially regarding the publications that will follow my PhD work.

> That which thy fathers have bequeathed to thee, earn it anew if thou wouldst possess it.
>
> Johann Wolfgang von Goethe, *Faust*, I, 682/3

My greatest thank naturally goes to my PhD supervisors Thomas Duguet and Vittorio Somà: it was an honour and a pleasure to work with you. I believe you both know how much I enjoyed this journey. Thomas, cela a été avant tout une aventure humaine. J'ai adoré nos discussion sur la Physique, le formalisme, la littérature scientifique. Mais cela ne s'arrête pas ici. Nos débats les plus divers (parfois assez animés), tes conseils littéraires, cinématographiques, ta disponibilité à te laisser déplacer. Merci pour ta curiosité humaine et pour ta quête. Merci pour me rappeler de muscler mon jeu et pour pousser toujours vers le mieux. Vittorio, merci pour ton attitude envers les autres: cela est une position que je désire pour moi et pour ma carrière. Merci pour nos discussions devant ta moka, pour avoir toujours pris le temps de m'expliquer une fois de plus les différents détails des interactions, pour ta présence constante. Peut-être que tu ne le sais pas, souvent je rentrais dans ton bureau un peu découragé par les faits les plus divers: sans besoin d'expliquer quoi que ce soit, le seul fait de parler avec toi remettait les choses dans la bonne perspective. À vous deux, merci pour ce beau chemin.

A special mention goes to the people I also had the chance to collaborate with. Thanks to Gianluca Colò for the continuous support and mentoring, and most importantly for having started all this: whatever will the outcome be, it was for the best. Thanks to Danilo Gambacurta for the nice project we have started together, to Jean-Paul Ebran for the great advices and Physics discussions.

Un grand merci à tous le collègues théoriciens du LENA. Merci Benjamin pour toujours dire les choses telles qu'elles sont et pour ta compagnie quotidienne, merci Mikael pour ton soutien constant pendant toute la thèse. À vous deux merci pour votre amitié sincère. Thanks to all the students and postdocs with whom I've shared these years, Alberto, Antoine, Gianluca, Lorenzo and Pepijn (you definitely are an honorary member of the group).

Merci à tous les *seniors* du DPhN, spécialement Alain, Anna, Barbara, Egle, Marine et Valérie. Merci pour votre disponibilité à me conseiller par rapport à la Physique expérimentale ou juste pour avoir partagé des moments de convivialité. Merci à Danielle et Isabelle pour être toujours disponibles et pour m'avoir aidé à m'en sortir avec les tâches administratives. Thanks a lot to all the PhD students and postdocs of DPhN: special mentions go to Andrea, Andrii, Michael, Paul and Pierre. Thanks for your sincere friendship and for having made the everyday life in the department definitely more interesting.

> People complain about the bad things that happen to em that they dont deserve but they seldom mention the good. About what they done to deserve them things. I dont recall that I ever give the good Lord all that much cause to smile on me. But he did.
>
> Cormac McCarthy, *No Country for Old Men*

Merci Héloïse pour l'espace de liberté dont tu me fais cadeau. Merci à ma famille pour être un port où je sais pouvoir toujours revenir. Merci aux amis qui ont rendu ces années inoubliables, bien au delà de toute humaine prévision. Sans ordre particulier: les parisiens Filippo, Clelia et Tommaso, Ceci et Pallu, Pietro et Laura, Luca et Marta, Hélo, Emma, Siggi, Léo, Murielle, Anna, Bore et Fede; agli amici di sempre: Sara e Colo, Fabio, Caterina, Ilaria; ai fisici milanesi Gio e Rache, Doge, Ila, Silvia, Francesca, Chiara S., Scott e Luci, Chiara B., Geck, Pietro, Tappo, Pota. Vous m'avez vu dans toute condition: hyperactif, paresseux, bourré, sobre, triste, heureux, à l'écoute, égoïste, sociable, solitaire. Et pourtant vous êtes toujours là: vous êtes la famille que j'ai choisie, qui ne me juge pas, qui partage me joies et qui me conforte quoi qu'il arrive. C'est en étant avec vous que j'apprends qui je suis, que je peux grandir, que je peux reconnaître mes erreurs: vous m'apprenez à pardonner et à être pardonné, toujours dans la certitude d'être aimé. Merci pour le don que vous êtes.

> Adriana: I can never decide whether Paris is more beautiful by day or by night. Gil: No, you can't, you couldn't pick one. I mean I can give you a checkmate argument for each side. You know, I sometimes think, how is anyone ever gonna come up with a book, or a painting, or a symphony, or a sculpture that can compete with a great city. You can't. Because you look around and every street, every boulevard, is its own special art form and when you think that in the cold, violent, meaningless universe that Paris exists, these lights, I mean come on, there's nothing happening on Jupiter or Neptune, but from way out in space you can see these lights, the cafés, people drinking and singing. For all we know, Paris is the hottest spot in the universe.
>
> Woody Allen, *Midnight in Paris*

Montrouge, 10 Octobre 2023

Contents

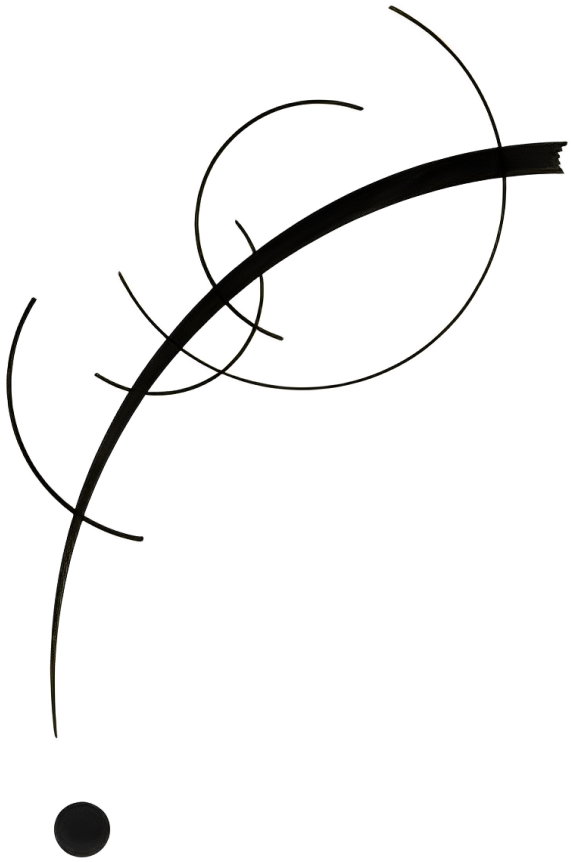

Introduction

During the twentieth century, the remarkable diversity of observable phenomena exhibited by nuclear systems at low-energy has compelled theorists to construct a diverse array of nuclear models. However, this multitude of models presents a challenge in unravelling the fundamental objectives of this research, as epistemological tools have predominantly been developed to accommodate a unified and stabilised theory rather than to grasp the plurality of models. Typically, the scientific value of a theory is assessed based on its predictive accuracy, applicability across a range of scenarios, and the comprehensibility of its principles [1]. In this sense, a theory is expected to be reductionist, unifying, and fundamentalist in nature. However, traditional models concerning inter-nucleon interactions, nuclear structure, and reactions, due to their inherent limitations in predictive precision, the difficulties in determining their applicability in advance, and their specific and disconnected nature, are inevitably deficient when subjected to standard epistemological interpretative frameworks. In this context, the concepts of emergence and effectiveness provide a valuable opportunity for a more relevant re-examination of the fundamental questions involved.

The concept of emergence, in particular, becomes relevant when properties observed at one scale cannot be explained or predicted based on a lower scale. In this way, it poses a challenge to our understanding and ability to describe the different levels of organisation within complex systems, like finite nuclei.

Employing an effective theory is justified when the reductionist perspective is within reach but unnecessarily complex for understanding the phenomena of interest. Emergence and effectiveness represent two contrasting departures from the conventional expectations set by reductionist, unifying, and fundamentalist theories. Emergence highlights the occurrence of phenomena that defy the aspiration to explain everything solely from a fundamental scale, while effectiveness suggests that it may be more advantageous to move away from such a requirement.

The development of effective theories, and their interconnected nature, represents a substantial transformation when compared to the situation characterised by the plethora of existing models. This transformation necessitates [2] (i) an *a priori* declaration of the theory's range of applicability and the specification of relevant degrees of freedom, along with the symmetries originating from the underlying scales (ii) a justification of an organisational framework (referred to as "power counting") for all permissible interaction operators determined by the symmetries and (iii) the determination of low-energy constants associated with unresolved physics, either deduced from the underlying effective theory or induced from experimental observations.

In the last two decades *ab initio* nuclear structure theory has greatly developed by describing experimentally observed quantities on the basis of chiral effective field theory (EFT) [3, 4, 5, 6], where quark degrees of freedom are integrated out and the strong force between nucleons as effective degrees of freedom is mediated via pions as Goldstone bosons of spontaneous chiral symmetry breaking, further supplemented by contact interactions. In this context, chiral EFT provides a link between nuclear properties and quantum chromodynamics (QCD), the underlying field theory of the strong interaction. Given the nuclear Hamiltonian H, *ab initio* nuclear structure calculations seek a solution of the A-body Schrödinger's eigenvalue

On previous page: *Free curve to the point - accompanying sound of geometric curves*, Wassily Kandinsky, 1925

problem

$$H|\Psi_\nu\rangle = E_\nu|\Psi_\nu\rangle\,. \tag{1}$$

The construction of the Hamiltonian from first principles combined with state-of-the-art many-body approaches offer a direction towards a universal theoretical framework to describe nuclear properties ranging from binding energies and charge radii to collective excitations.

Nuclear Hamiltonian

Effective field theories find their foundation in a systematic expansion in terms of a small perturbative parameter. In the case of nuclear physics, this parameter is typically related to the momentum transfer in nuclear processes. Consequently, a power counting is used to ascertain the importance of different terms in the Hamiltonian, based on their contributions at a given order in the expansion. Chiral perturbation theory (χPT) is an EFT framework for low-energy nuclear interactions based on the symmetries of QCD. χPT incorporates the approximate chiral symmetry of QCD, providing constraints on the form of the nuclear Hamiltonian.

The nuclear interactions are described in terms of effective fields and their associated couplings. In χPT, these fields correspond to nucleons and pions, which are the lightest hadrons in QCD. The interactions between these particles are encoded in an expansion of the Lagrangian, with each term contributing to a specific order in the power counting. A regulator function is typically employed to avoid infinities, consistently with the fact that χPT is a low-momentum expansion where the effects of higher-energy degrees of freedom are integrated out. High-energies contributions are accounted for by an iterative renormalisation process absorbing divergences that arise in loop diagrams.

Eventually, the determination of coupling and low-energy constants values appearing in the effective Lagrangian is achieved by matching EFT calculations to experimental data. This involves fitting the parameters to selected experimental observables, such as scattering cross-sections, binding energies, and excitation spectra. Eventually, the reproduction of a large variety of observables provides validation of the EFT. The construction of the Hamiltonian within EFTs provides, thus, a systematic and model-independent approach to describe nuclear interactions [7].

Many-body techniques

Once the nuclear Hamiltonian is constructed within the EFT framework, many-body techniques can be employed to solve the many-body Schrödinger equation. *Ab initio* methods play an important role in the description of strongly correlated quantum systems. In this context, the development and extensions of novel many-body techniques to solve the A-body Schrödinger equation is pivotal for a description of nuclear observables from first principles. Essentially exact solutions to the quantum many-body problem are provided by diagonalisation methods, such as the no-core shell model (NSCM) [8, 9, 10], or by quantum Monte Carlo techniques [11, 12]. However, due to their exponential scaling, these approaches are typically limited to light nuclei with mass number $A \lesssim 12$, although Importance Truncation (IT) techniques extend their reach up to Oxygen and Calcium isotopes [13, 14]. A breakthrough in the *ab initio* description of medium-mass nuclei was achieved via the (re)introduction of so-called expansion methods, where the action of a *wave-operator* acting on an unperturbed state captures the correlations missing in that suitably chosen initial state via a controlled expansion, which may happen to be either perturbative or non-perturbative. Truncating the expansion at a given order, all such methods share a polynomial scaling with respect to the size of the one-body Hilbert space. Therefore, nowadays a variety of observables is routinely accessible in nuclei with $A \lesssim 100$, and, in some specific cases, also for much heavier systems [15].

In general the specificities of the unperturbed state determine the domain of applicability of such techniques. First applications based on a symmetry-conserving single-reference Hartree-Fock (HF) Slater determinant enabled since 2005 to investigate nuclear properties of doubly-closed shell systems. Examples are Many-Body Perturbation Theory (MBPT) [16, 17], Coupled Cluster (CC) [18, 19, 20, 21], In-Medium Similarity Renormalisation Group (IM-SRG) [22, 23] and Dyson Self-Consistent Green's Function (SCGF) [24, 25, 26] theories.

Symmetry-conserving single-reference unperturbed states, however, are inadequate to describe open-shell systems due to the partial filling of the degenerate valence shell and the associated emergence of strong static correlations. In order to efficiently include static correlations, the use of more general unperturbed states is necessary. One possibility is to make use of an unperturbed state that spontaneously breaks one or several symmetries of the underlying Hamiltonian. Since 2011 particle-number broken Hartree-Fock-Bogoliubov (HFB) unperturbed states have been applied in the Gor'kov extension of SCGF for calculations along medium-mass semi-magic isotopic chains [27, 28, 29]. A similar option is available within a conceptually simpler and numerically cheaper Bogoliubov Many-Body Perturbation Theory (BMBPT) [30, 31, 32]. Furthermore, extensions of CC theory allowing for the breaking and restoration of $U(1)$ and $SU(2)$ symmetries have also been formulated and applied [33, 34, 35, 36], as well as $SU(2)$-breaking IMSRG [37] calculations. While the consistent restoration of $U(1)$ and $SU(2)$ has been worked out on a formal level in the CC scheme, the development of the corresponding framework in Gor'kov SCGF and IMSRG still poses a challenge which is yet unaddressed.

Symmetry-breaking states can also be used as an intermediate step in the definition of multi-reference symmetry-conserving states, used, in turn, as a reference state for more elaborated theories. This strategy has shown to be very successful in the context of the multi-reference extension of IM-SRG (MR-IMSRG) which allows for the calculation of ground-state energies of even open-shell nuclei [38, 39], as well as precise spectroscopy when combined with the Projected Generator Coordinate Method (PGCM) [40]. Recently, moreover, PGCM has been used as a (multi-) reference unperturbed state for an advanced version of many-body perturbation theory (PGCM-PT), delivering accurate predictions for both ground-state and collective (rotational and vibrational) excitations [41, 42, 43].

Access to excited states

Most of the many-body methods discussed above, despite the formidable task associated with their formal and numerical development, are limited as far as excited states properties are concerned. Thus, for what regards the access to excited states, the panorama is somehow seminal, even if already broad regarding the variety of techniques that have been employed in recent years.

A method addressing excited states in the context of IMSRG is its Valence Space extension (VS-IMSRG) [44, 45]. This method, however, displays an hybrid polynomial-exponential scaling due to the Configuration Interaction (CI) part of the calculation, such that its application is nowadays limited to sd- or pf-shell nuclei. In the same direction, equation-of-motion (EOM) techniques, where one starts from the correlated solution of a closed-shell nucleus and describes excited states as the result of the action of linear operators on the ground-state, have been extensively used in CC theory [46]. An EOM-extension of IM-SRG for the description of spectra of closed-shell nuclei has also been proposed [47]. Such methods access the low-lying spectroscopy of weakly collective excitations, i.e. excitations which are pre-eminently concentrated in few (many-)particle-(many-)holes excitations.

As for collective excitations, Lorentz Integral Transform techniques applied within a CC framework (CC-LIT) [48] allow one to access excitation strengths of various multipolarities in doubly-closed shell nuclei. However, this method suffers from numerical inversion issues and is reliable only when the response itself is concentrated in one or two broad peaks. Recently, these issues have been shown to be possibly overcome via the application of more sophisticated techniques like the Chebyshev expansion [49, 50].

Very recently, PGCM-PT has been successfully employed to provide an accurate *ab initio* description of both vibrational and rotational states, as shown in Refs. [41, 42, 43]. In particular, it was demonstrated [42, 43] that, while dynamical correlations are essential to access absolute energies, they largely cancel out in the description of collective excitations, thus justifying the use of the sole PGCM as a standalone method for *ab initio* spectroscopy.

In this spirit, many methods have been developed in the shadow of the many possible declinations of the (Quasiparticle) Random Phase Approximation ((Q)RPA) [51, 52, 53, 54, 55, 56, 57]. RPA calculations using dressed propagators from SCGF calculations have also been performed to investigate giant-dipole excitations in closed-shell systems [58, 59]. All these methods, however, are limited in their applications to spherical systems, greatly limiting their possible achievements. The recent development in the Saclay group of a Finite Amplitude Method (FAM) version of QRPA [60] has allowed to address singly- and doubly-open shell systems, either axially or triaxially intrinsically deformed.

Giant Resonances

Giant Resonances (GRs) are among the clearest manifestations of collective motion in finite nuclear systems. They correspond to collective excitations in which most, if not all, nucleons are involved in the process. GRs are categorised according to their multipolarity and isospin nature, and can be best pictured in terms of vibrations of the nuclear surface in a liquid-drop approach. The Giant Isoscalar Monopole Resonance (ISGMR, GMR for brevity in the following), which is addressed in this work, is also referred to as the *breathing mode*. Given its compression character, it is known to provide valuable information about the incompressibility of infinite nuclear matter [61, 62, 63, 64], a key quantity entering the nuclear equation of state (EoS).

Because they lie at energies of the order of the energy difference between major shells, GRs are embedded in a background of particle-hole (ph) excitations, into which they can, in principle, decay. The decay of collective vibrations into uncorrelated ph excitations is a well known phenomenon in solid state physics, referred to as Landau damping. Furthermore, giant resonances lie above the particle emission threshold: consequently, they may couple to particle decay in the continuum. Eventually, they can also be damped through coupling to the electromagnetic field leading to the emission of a photon [65, 66].

The theoretical description of GRs is a mature field. In particular, their coherent ph-excitation nature is at the heart of RPA and associated methods. The (Q)RPA implemented in the context of phenomenological Energy Density Functional (EDF) theories has proven extremely successful in the systematic description of GRs: deformed QRPA calculations have been performed over the nuclide chart [67, 68, 69, 70, 71, 72]. An overall good agreement with experimental data is observed, also ameliorating the understanding of the coupling between the GMR and the Giant Quadrupole Resonance (GQR). Beyond-RPA calculations have also revealed a noteworthy improvement in the understanding of non-trivial systems; selected examples are self-consistent-RPA (SCRPA) inspired theories (see Ref. [73] for a recent review), Second RPA (SRPA) [74, 75] and particle-vibration coupling (PVC) [66, 76].

Another class of theories relates to the time-dependent description of nuclear systems when an external multipolar perturbation is applied. If the time evolution is performed on Slater determinants (Bogoliubov vacua) it can be shown that such a theory is strictly equivalent to the traditional (Q)RPA in the small-amplitude limit (see Refs. [77, 78] for a systematic study of both spherical and deformed systems). The multi-reference extension of time-dependent theories, thus, represents an alternative method to go beyond canonical RPA; see Ref. [79] for a recent development.

Motivation of the present work

Among the multiple many-body methods addressing GRs, some interest was also shown for the GCM in different exploratory works [80, 81, 82, 83, 84, 85, 86, 87]. It was observed that anharmonic effects may have a non-negligible impact in the determination of nuclear incompressibility [88], which makes GCM a necessary tool in this respect. However, differently from (Q)RPA no extensive use of the GCM followed these seminal efforts to describe GRs.

Inspired by such existing works and sustained by the observation [43] that dynamical correlations essentially cancel out in the description of collective excitations, *ab initio* PGCM calculations are performed in the present work to access the GMR and, to some extent, the GQR in light- and medium-mass nuclei for the first time. This method opens to unprecedented possible applications. Indeed, closed- and (doubly-)open shell systems can be systematically addressed, investigating a new set of quantities and physical effects, such as a consistent treatment of pairing, deformation effects, the impact of shape coexistence and many other features. It will be shown that, at the price of a less systematic choice of the relevant degrees of freedom of the problem, PGCM comes with an exact treatment of anharmonic effects and a fully symmetry-conserving solution both for ground and excited states. These two aspects are addressed and compared separately to *ab initio* deformed QRPA calculations in a consistent setting.

The present manuscript is organised as follows. In Part I the formal bases of the many-body methods at use in this work are set: the PGCM is introduced in Chap. 1, together with basic elements of the Bogoliubov algebra. The kernels evaluation, which is at the heart of the PGCM, is addressed in Chap. 2 in an original formulation. The existing links between the GCM and QRPA are investigated from a novel perspective in Chap. 3. Formal aspects of the response function, which is key in the study of GRs, are presented in Chap. 4, with an extensive and original perspective to access the moments of the strength functions. Eventually, the fundamentals of angular momentum projection (AMP) are recalled in Chap. 5 and applied to symmetry-breaking multipole strengths. Numerical results of the present investigation are exposed in Part II: a systematic inquiry about the convergence properties of *ab initio* PGCM calculations is addressed in Chap. 6, followed in Chap. 7 by results of physical interest. The effects of AMP are extensively discussed in Chap. 8 and the comparison to *ab initio* QRPA calculations is presented in Chap. 9. A focus on the numerical performance of different strategies to evaluate the strength moments is given in Chap. 10. The unforeseen possibility of accessing multi-phonon states via the PGCM is discussed in Chap. 11. Finally, the effects of AMP on deformed RPA calculations are displayed in Chap. 12 in an EDF implementation. Some conclusions and perspectives close the main body of this document. Many appendices accompanying and reinforcing the theoretical sections of this work are provided in Part III.

Part I

Theoretical Frame

Chapter 1

Theoretical Setting

Contents

1.1 The Projected Generator Coordinate Method

The projected generator coordinate method (PGCM) is a popular and versatile many-body method based on the mixing of Bogoliubov vacua typically generated by solving constrained Hartree-Fock-Bogoliubov (HFB) mean-field equations [89]. The PGCM is traditionally employed with empirical effective interactions tailored to the full Hilbert space [90, 91, 92] or to a so-called valence space [93, 94, 95, 96, 97]. However, the PGCM has recently been extented to the context of ***ab initio*** calculations aiming at approximating exact solutions of Schrödinger's equation in the low-energy sector of the A-body Hilbert space starting from realistic nuclear Hamiltonians rooted into quantum chromodynamics.

Possibly combined with a pre-processing of the Hamiltonian via a multi-reference in-medium similarity renormalisation group transformation [98, 99, 43], the PGCM is either exploited as a stand-alone method for nuclear spectroscopy [42] or as a starting point of an expansion method towards the exact solution [41, 43]. Without a pre-processing of the nuclear Hamiltonian, the standard PGCM was shown to deliver an excellent first approximation to collective spectroscopy [43] thanks to the cancellation of dynamical correlations between ground and excited states.

1.1.1 The GCM and PGCM ansatz

The original GCM formulation is introduced first. The GCM wave-function ansatz [100, 101] is a general continuous superposition of so-called generating functions $|\Phi(q)\rangle$ reading

$$|\Psi_\nu\rangle = \int \mathrm{d}q\, f_\nu(q)|\Phi(q)\rangle\,, \tag{1.1}$$

where q is a set of collective variables called *generator coordinates*. The index ν refers to a principal quantum number and $f_\nu(q)$ is a weight function to be determined. The ensemble $\{|\Phi(q), q \in [q_0, q_1]\rangle\}$ denotes a set of non-orthogonal[1] Bogoliubov states labelled by the collective coordinate[2] q and typically obtained as solutions of constrained HFB calculations.

Constrained HFB solutions typically break symmetries of the Hamiltonian, so that restoring those symmetries is mandatory when questing a good approximation to the exact solution. Symmetry restoration is achieved by projecting the symmetry-breaking solution onto good symmetry quantum numbers. Doing so, Eq. (1.1) is modified as

$$|\Psi^\sigma_\nu\rangle = \int \mathrm{d}q\, f^\sigma_\nu(q) P^\sigma |\Phi(q)\rangle\,, \tag{1.2}$$

where P^σ is the projection operator associated with a symmetry group $\mathcal{G}$, which can be both continuous or discrete, in charge of selecting the components of $|\Phi(q)\rangle$ carrying the good symmetry quantum numbers σ. In the case of present interest $\sigma \equiv (JM\Pi NZ)$, i.e. the PGCM ansatz in Eq. (1.2) has good angular momentum J and its projection M, parity $\Pi = \pm 1$ as well as neutron N and proton Z numbers. The projector P^σ can be generically written as

$$P^\sigma = \int \mathrm{d}\varphi\, g^\sigma(\varphi) R(\varphi)\,, \tag{1.3}$$

where $g^\sigma(\varphi)$ represents irreducible representations of $\mathcal{G}$ and where $R(\varphi)$ is the unitary symmetry transformation operator changing the orientation of a state by the angle φ. The PGCM ansatz, thus, reads as

$$\begin{aligned} |\Psi^\sigma_\nu\rangle &= \int \mathrm{d}q\, f^\sigma_\nu(q) \int \mathrm{d}\varphi\, g^\sigma(\varphi) R(\varphi) |\Phi(q)\rangle \\ &\equiv \int \mathrm{d}q\, f^\sigma_\nu(q) \int \mathrm{d}\varphi\, g^\sigma(\varphi) |\Phi(q,\varphi)\rangle\,, \end{aligned} \tag{1.4}$$

where in the last equivalence the φ-rotated state $|\Phi(q,\varphi)\rangle \equiv R(\varphi)|\Phi(q)\rangle$ has been introduced[3].

1.1.2 Hill-Wheeler-Griffin equation

The unknown[4] coefficients $f^\sigma_\nu(q)$ are determined variationally on the basis of Ritz' variational principle, namely minimising the energy associated with $|\Psi^\sigma_\nu\rangle$

$$\delta \frac{\langle \Psi^\sigma_\nu | H | \Psi^\sigma_\nu \rangle}{\langle \Psi^\sigma_\nu | \Psi^\sigma_\nu \rangle} = 0. \tag{1.5}$$

The variation with respect to the weights $f^{\sigma *}_\nu(q)$ eventually leads to a generalised eigenvalue problem known as the *Hill-Wheeler-Griffin* secular equation [101], which can be formally written

$$\int \mathrm{d}q \Big[\mathcal{H}^\sigma(p,q) - E^\sigma_\nu \mathcal{N}^\sigma(p,q) \Big] f^\sigma_\nu(q) = 0\,, \tag{1.6}$$

[1] Some of the Bogoliubov states mixed in the GCM ansatz may be either manifestly or accidentally orthogonal. This situation can be dealt with at the price of a generalisation of the present work, where all pairs of Bogoliubov states entering Eq. (1.1) are considered to be non-orthogonal.

[2] The collective coordinate is multi dimensional and contains the variable(s) parameterising the transformations associated with the symmetry(ies) being restored via projection techniques.

[3] If $|\Phi(q)\rangle$ is a Bogoliubov product state, $|\Phi(q,\varphi)\rangle$ is also a Bogoliubov product state. Indeed, the transformation operator $R(\varphi)$ can be represented as $R(\varphi) = e^{i\varphi S}$, where S is a one-body operator and is referred to as the *generator of the group*. Thus, as a result of Thouless' theorem the rotated vacuum can also be written as a Bogoliubov vacuum with respect to the rotated quasiparticle annihilation operators.

[4] The part of the coefficients fixed by the structure of the symmetry group does not have to be determined variationally.

where the so-called symmetry-restored Hamiltonian and norm kernels are respectively defined as

$$\begin{aligned}\mathcal{H}^\sigma(p,q) &\equiv \langle\Phi(p)|P^\sigma H P^\sigma|\Phi(q)\rangle \\ &= \langle\Phi(p)|H P^\sigma|\Phi(q)\rangle \\ &= \int \mathrm{d}\varphi\, g^\sigma(\varphi)\langle\Phi(p)|H|\Phi(q,\varphi)\rangle\,, \end{aligned} \tag{1.7a}$$

$$\begin{aligned}\mathcal{N}^\sigma(p,q) &\equiv \langle\Phi(p)|P^\sigma|\Phi(q)\rangle \\ &= \int \mathrm{d}\varphi\, g^\sigma(\varphi)\langle\Phi(p)|\Phi(q,\varphi)\rangle\,. \end{aligned} \tag{1.7b}$$

Equation (1.6) can be then rewritten as

$$\int \mathrm{d}q \left[\frac{\mathcal{H}^\sigma(p,q)}{\mathcal{N}^\sigma(p,q)} - E^\sigma_\nu\right]\mathcal{N}^\sigma(p,q) f^\sigma_\nu(q) = 0\,, \tag{1.8}$$

or, in a discretised version of interest for actual implementations[5],

$$\sum_q \left[\frac{\mathcal{H}^\sigma(p,q)}{\mathcal{N}^\sigma(p,q)} - E^\sigma_\nu\right]\mathcal{N}^\sigma(p,q) f^\sigma_\nu(q) = 0\,. \tag{1.9}$$

As clearly visible from Eqs. (1.7), the key ingredients entering Eq. (1.9) and the computation of observables are the off-diagonal connected operator kernel and the norm kernel associated with two Bogoliubov states $\langle\Phi(p)|$ and $|\Phi(q,\varphi)\rangle$. For practical purposes the left and right Bogoliubov vacua are generically redefined as

$$\langle\Phi(p)| \equiv \langle\Phi(l)|\,, \tag{1.10a}$$

$$|\Phi(q,\varphi)\rangle \equiv |\Phi(r)\rangle\,. \tag{1.10b}$$

Given an arbitrary operator O, the operator and norm kernels in this notation read respectively

$$\mathcal{O}(l,r) \equiv \langle\Phi(l)|O|\Phi(r)\rangle\,, \tag{1.11a}$$

$$\mathcal{N}(l,r) \equiv \langle\Phi(l)|\Phi(r)\rangle\,, \tag{1.11b}$$

out of which the *connected* operator kernel [102, 103] is defined through

$$o(l,r) \equiv \frac{\mathcal{O}(l,r)}{\mathcal{N}(l,r)}\,. \tag{1.12}$$

The formal evaluation of the connected operator kernel and of the norm kernel is discussed in Chap. 2, where an original method is introduced and compared to existing techniques.

1.2 Basics of Bogoliubov algebra

The core of the present work involves three non-orthogonal Bogoliubov states[6] denoted as $|\Phi(l)\rangle$, $|\Phi(r)\rangle$ and $|\Phi\rangle$.

[5] The same procedure is readily obtained in the GCM, at the price of removing the projector and the associated symmetry quantum numbers wherever they appear.

[6] While a generalisation is possible, the reference state $|\Phi\rangle$ is supposed to be non-orthogonal to both $|\Phi(l)\rangle$ and $|\Phi(r)\rangle$.

1.2.1 Bogoliubov vacuum

Each of these three states is a vacuum for a set of associated quasi-particle operators. Taking $|\Phi\rangle$ as an example, this property reads as

$$\beta_k|\Phi\rangle = 0 \quad \forall k\,, \tag{1.13}$$

where the set of quasi-particle operators $\{\beta_k^\dagger, \beta_k\}$ is related to particle operators $\{c_a^\dagger, c_a\}$ associated with an arbitrary basis of the one-body Hilbert space $\mathcal{H}_1$ via a unitary Bogoliubov transformation of the form

$$\beta_k \equiv \sum_a \left(\mathcal{U}_{ak}^* c_a + \mathcal{V}_{ak}^* c_a^\dagger\right), \tag{1.14a}$$

$$\beta_k^\dagger \equiv \sum_a \left(\mathcal{U}_{ak} c_a^\dagger + \mathcal{V}_{ak} c_a\right). \tag{1.14b}$$

This transformation can be written more compactly via a matrix representation

$$\begin{pmatrix} \beta \\ \beta^\dagger \end{pmatrix} = \mathcal{W}^\dagger \begin{pmatrix} c \\ c^\dagger \end{pmatrix}, \tag{1.15}$$

where the Bogoliubov matrix

$$\mathcal{W} \equiv \begin{pmatrix} \mathcal{U} & \mathcal{V}^* \\ \mathcal{V} & \mathcal{U}^* \end{pmatrix} \tag{1.16}$$

is unitary, such that the following relations hold

$$\mathcal{W}\mathcal{W}^\dagger = \mathcal{W}^\dagger\mathcal{W} = 1\,. \tag{1.17}$$

This condition implies that the canonical fermionic anticommutation rules valid for the particle operators propagate to quasi-particle ones.

1.2.2 Thouless theorem

Starting from Bogoliubov transformations $\mathcal{W}(l)$, $\mathcal{W}(r)$ and $\mathcal{W}$ defining the three sets of quasi-particle operators $\{\beta_k^\dagger(l), \beta_k(l)\}$, $\{\beta_k^\dagger(r), \beta_k(r)\}$ and $\{\beta_k^\dagger, \beta_k\}$, respectively, Thouless' theorem [104] allows one to connect the three vacua $|\Phi(l)\rangle$, $|\Phi(r)\rangle$ and $|\Phi\rangle$.

First, $|\Phi(l)\rangle$ and $|\Phi(r)\rangle$ are expressed with respect to $|\Phi\rangle$. Taking $|\Phi(r)\rangle$ as an example, the transformation connecting the two sets of quasi-particle operators is given by (see Appendix E.3 of Ref. [89] for further details on the derivation)

$$\begin{aligned} \begin{pmatrix} \beta(r) \\ \beta^\dagger(r) \end{pmatrix} &= \mathcal{W}^\dagger(r)\mathcal{W} \begin{pmatrix} \beta \\ \beta^\dagger \end{pmatrix} \\ &\equiv \begin{pmatrix} U^\dagger(r) & V^\dagger(r) \\ V^T(r) & U^T(r) \end{pmatrix} \begin{pmatrix} \beta \\ \beta^\dagger \end{pmatrix}, \end{aligned} \tag{1.18}$$

with

$$U(r) \equiv \mathcal{V}^T\mathcal{U}(r) + \mathcal{U}^T\mathcal{V}(r), \tag{1.19a}$$

$$V(r) \equiv \mathcal{U}^\dagger\mathcal{U}(r) + \mathcal{V}^\dagger\mathcal{V}(r). \tag{1.19b}$$

Introducing the skew-symmetric matrix

$$\mathbf{z}(r) \equiv V^*(r)U^{*-1}(r), \tag{1.20}$$

Thouless' theorem allows one to write

$$|\Phi(r)\rangle = \langle\Phi|\Phi(r)\rangle e^{\mathbf{Z}^{20}(r)}|\Phi\rangle, \tag{1.21a}$$

where the one-body Thouless operator reads as

$$\mathbf{Z}^{20}(r) \equiv \frac{1}{2}\sum_{k_1k_2}\mathbf{z}^{k_1k_2}(r)\beta^\dagger_{k_1}\beta^\dagger_{k_2}. \tag{1.21b}$$

Similarly, the transformation

$$\begin{aligned}\begin{pmatrix}\beta(r)\\ \beta^\dagger(r)\end{pmatrix} &= W^\dagger(r)W(l)\begin{pmatrix}\beta(l)\\ \beta^\dagger(l)\end{pmatrix}\\ &\equiv W^\dagger(l,r)\begin{pmatrix}\beta(l)\\ \beta^\dagger(l)\end{pmatrix}\\ &\equiv \begin{pmatrix}B^\dagger(l,r) & A^\dagger(l,r)\\ A^T(l,r) & B^T(l,r)\end{pmatrix}\begin{pmatrix}\beta(l)\\ \beta^\dagger(l)\end{pmatrix},\end{aligned} \tag{1.22}$$

with

$$A(l,r) \equiv V^T(l)U(r) + U^T(l)V(r), \tag{1.23a}$$

$$B(l,r) \equiv U^\dagger(l)U(r) + V^\dagger(l)V(r), \tag{1.23b}$$

leads to defining the Thouless matrix

$$\mathbf{z}(l,r) \equiv A^*(l,r)B^{*-1}(l,r), \tag{1.24}$$

thanks to which $|\Phi(r)\rangle$ can be expressed with respect to $|\Phi(l)\rangle$ according to

$$|\Phi(r)\rangle = \langle\Phi(l)|\Phi(r)\rangle e^{\mathbf{Z}^{20}(l,r)}|\Phi(l)\rangle, \tag{1.25a}$$

where

$$\mathbf{Z}^{20}(l,r) \equiv \frac{1}{2}\sum_{k_1k_2}\mathbf{z}^{k_1k_2}(l,r)\beta^\dagger_{k_1}(l)\beta^\dagger_{k_2}(l). \tag{1.25b}$$

1.2.3 Elementary contractions

Given $|\Phi(l)\rangle$ and $|\Phi(r)\rangle$, the four one-body off-diagonal elementary contractions are defined in the quasi-particle basis of $|\Phi\rangle$ through

$$\begin{aligned}\mathbf{R}_{k_1k_2}(l,r) &\equiv \begin{pmatrix}\dfrac{\langle\Phi(l)|\beta^\dagger_{k_2}\beta_{k_1}|\Phi(r)\rangle}{\langle\Phi(l)|\Phi(r)\rangle} & \dfrac{\langle\Phi(l)|\beta_{k_2}\beta_{k_1}|\Phi(r)\rangle}{\langle\Phi(l)|\Phi(r)\rangle}\\ \dfrac{\langle\Phi(l)|\beta^\dagger_{k_2}\beta^\dagger_{k_1}|\Phi(r)\rangle}{\langle\Phi(l)|\Phi(r)\rangle} & \dfrac{\langle\Phi(l)|\beta_{k_2}\beta^\dagger_{k_1}|\Phi(r)\rangle}{\langle\Phi(l)|\Phi(r)\rangle}\end{pmatrix}\\ &\equiv \begin{pmatrix}+\rho_{k_1k_2}(l,r) & +\kappa_{k_1k_2}(l,r)\\ -\bar\kappa^*_{k_1k_2}(l,r) & -\sigma^*_{k_1k_2}(l,r)\end{pmatrix},\end{aligned} \tag{1.26}$$

and satisfy, due to anticommutation rules and complex conjugation,

$$\rho^*_{k_1k_2}(l,r) = +\rho_{k_2k_1}(r,l), \tag{1.27a}$$

$$\kappa_{k_1k_2}(l,r) = -\kappa_{k_2k_1}(l,r), \tag{1.27b}$$
$$\bar{\kappa}_{k_1k_2}(l,r) = +\kappa_{k_1k_2}(r,l), \tag{1.27c}$$
$$\sigma_{k_1k_2}(l,r) = +\rho_{k_1k_2}(r,l) - \delta_{ab}. \tag{1.27d}$$

Setting $|\Phi(l)\rangle = |\Phi(r)\rangle = |\Phi\rangle$, one can trivially obtain the diagonal contractions associated with $|\Phi\rangle$ as

$$\begin{aligned} \mathbf{R}_{k_1k_2} &= \begin{pmatrix} +\rho_{k_1k_2} & +\kappa_{k_1k_2} \\ -\bar{\kappa}^*_{k_1k_2} & -\sigma^*_{k_1k_2} \end{pmatrix} \\ &= \begin{pmatrix} 0 & 0 \\ 0 & \delta_{k_1k_2} \end{pmatrix}. \end{aligned} \tag{1.28}$$

From this most simplistic case, one can easily infer the diagonal contractions associated with $|\Phi(l)\rangle$ and $|\Phi(r)\rangle$ in the quasi-particle basis of $|\Phi\rangle$, e.g.

$$\mathbf{R}_{k_1k_2}(l,l) = \begin{pmatrix} (V^*(l)V^T(l))_{k_1k_2} & (V^*(l)U^T(l))_{k_1k_2} \\ (U^*(l)V^T(l))_{k_1k_2} & (U^*(l)U^T(l))_{k_1k_2} \end{pmatrix}. \tag{1.29}$$

Chapter 2

Kernels evaluation

Contents

The connected operator kernel from Eq. (1.12) can be efficiently computed via the off-diagonal Wick theorem (ODWT) of Balian and Brezin [105]. The evaluation of the norm kernel (1.11b) relies on the Onishi formula [106], on the Pfaffian formula by Robledo [107] or the integral formula by Bally and Duguet [103]. Traditionally, the derivation of these two categories of kernels relies on different formal schemes that do not seem to share a common ground. One exception relies on the use of fermion coherent states based on Grassmann variables allowing one to express both the connected operator kernel [108, 109] and the norm kernel [107] in terms of Pfaffians. The goal of the present chapter is to provide another consistent derivation of the connected operator kernel, i.e. of the ODWT, and of the norm kernel based on a common diagrammatic method. This newly-introduced formalism was published in Ref. [110].

The necessary elements of formalisms were introduced in Sec. 1.2. In Sec. 2.1, the diagrammatic method is used to derive both the ODWT for the connected operator kernel and the Onishi/Pfaffian formula for the norm kernel. Conclusions and perspectives are elaborated on in Sec. 2.2. Several appendices providing the necessary technical details accompany the main development, i.e. the normal-ordered representation of operators (App. A), the detailed diagrammatic rules (App. B) and the standard derivation of the ODWT for completeness and comparison (App. C).

2.1 Computation of the kernels

The traditional way to compute the connected operator kernel, i.e. to derive the off-diagonal Wick theorem [105], invokes an *asymmetric approach* that consists of expressing, e.g., $|\Phi(r)\rangle$ with respect to $|\Phi(l)\rangle$ via Eq. (1.25). This delivers the connected operator kernel under the asymmetric form

$$o(l,r) = \langle\Phi(l)|Oe^{\mathbf{Z}^{20}(l,r)}|\Phi(l)\rangle\,. \tag{2.1}$$

The proof of the off-diagonal Wick theorem [105] based on Eq. (2.1) is recalled for reference in App. C. This constitutes the simplest derivation of the ODWT because the power series associated with the exponential appearing on one side of the operator O in Eq. (2.1) naturally terminates after a finite number of terms.

The asymmetric approach cannot provide access to the norm kernel and thus only delivers half of the needed ingredients. Typically, accessing the norm kernel relies on a *symmetric approach*[1] where $|\Phi(l)\rangle$ and $|\Phi(r)\rangle$ are both expressed with respect to a common reference state $|\Phi\rangle$ according to Eq. (1.21).

In this context, it is of intellectual interest to consistently derive the connected operator kernel (i.e. the off-diagonal Wick theorem) and the norm kernel (i.e. the Onishi or Pfaffian formula) via a symmetric approach. While this was achieved starting from fermion coherent states based on Grassmann variables [108, 109], this is presently realised using standard diagrammatic techniques. The symmetric approach leads to expressing the operator and norm kernels as

$$\frac{\mathcal{O}(l,r)}{\langle\Phi(l)|\Phi\rangle\langle\Phi|\Phi(r)\rangle} \equiv \langle\Phi|e^{\mathbf{Z}^{20}(l)^\dagger} O e^{\mathbf{Z}^{20}(r)}|\Phi\rangle, \tag{2.2a}$$

$$\frac{\mathcal{N}(l,r)}{\langle\Phi(l)|\Phi\rangle\langle\Phi|\Phi(r)\rangle} \equiv \langle\Phi|e^{\mathbf{Z}^{20}(l)^\dagger} e^{\mathbf{Z}^{20}(r)}|\Phi\rangle, \tag{2.2b}$$

such that the connected operator kernel itself reads as

$$o(l,r) \equiv \frac{\langle\Phi|e^{\mathbf{Z}^{20}(l)^\dagger} O e^{\mathbf{Z}^{20}(r)}|\Phi\rangle}{\langle\Phi|e^{\mathbf{Z}^{20}(l)^\dagger} e^{\mathbf{Z}^{20}(r)}|\Phi\rangle}. \tag{2.3}$$

It is worth noting that the above expression resembles the expectation value at play in variational coupled cluster (vCC) theory [111, 112, 113]. On the one hand, it is more general because the two involved Thouless operators are not equal. On the other hand, it is more restricted given that the Thouless operators are one-body excitation operators, which essentially corresponds to the simplest vCC with singles (vCCS) approximation. Still, it is well known from vCC that, (i) while the norm overlap in the denominator can be exactly cancelled out in the numerator, (ii) the expansions of the two exponentials do not terminate and thus produce an infinite number of terms. It will thus have to be shown how the latter difficulty can be overcome to compute $\mathcal{N}(l,r)$ and $o(l,r)$ exactly.

2.1.1 Operator kernel

Employing the simplified notations

$$\mathbf{R} \equiv \mathbf{Z}^{20}(r) = \frac{1}{2}\sum_{k_1 k_2} \mathbf{z}^{k_1 k_2}(r)\beta^\dagger_{k_1}\beta^\dagger_{k_2}, \tag{2.4a}$$

$$\mathbf{L} \equiv \mathbf{Z}^{20}(l)^\dagger = \frac{1}{2}\sum_{k_1 k_2} \mathbf{z}^*_{k_1 k_2}(l)\beta_{k_2}\beta_{k_1}, \tag{2.4b}$$

for the Thouless operators fulfilling $\langle\Phi|\mathbf{R} = \mathbf{L}|\Phi\rangle = 0$, the operator kernel is expressed as

$$\begin{aligned}\frac{\mathcal{O}(l,r)}{\langle\Phi(l)|\Phi\rangle\langle\Phi|\Phi(r)\rangle} &\equiv \langle\Phi|e^{\mathbf{L}} O e^{\mathbf{R}}|\Phi\rangle \\ &= \sum_{n=0}^{N} \sum_{\substack{i,j=0 \\ i+j=2n}}^{2n} \sum_{s,t=0}^{\infty} \frac{1}{s!t!}\langle\Phi|\mathbf{L}^s \mathbf{O}^{ij} \mathbf{R}^t|\Phi\rangle \\ &\equiv \sum_{n=0}^{N} \sum_{\substack{i,j=0 \\ i+j=2n}}^{2n} \sum_{s,t=0}^{\infty} \langle_s|^i{}_j|^t\rangle,\end{aligned} \tag{2.5}$$

[1] An asymmetric approach to the normal kernel based on finding a *unitary* transformation between both states exists [103]. This however differs from the present discussion based on non-unitary Thouless transformations.

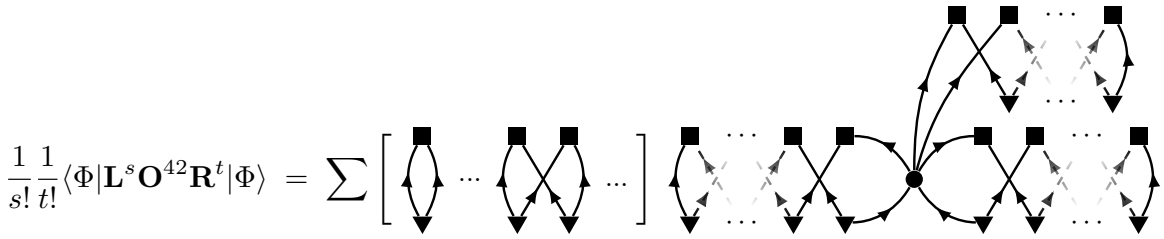

Figure 2.1: Diagrammatic representation of the matrix element $\langle_s|^4{}_2|^t\rangle$, where s and t are positive integers, contributing to the operator kernel $\langle\Phi(l)|\mathbf{O}^{42}|\Phi(r)\rangle$. Each square (triangle) vertex represents an operator $\mathbf{L}$ ($\mathbf{R}$), whereas the dot vertex denotes the operator $\mathbf{O}^{42}$. Whereas the vertex of $\mathbf{L}$ ($\mathbf{R}$) displays two lines entering (leaving) it, two lines enter the vertex representing $\mathbf{O}^{42}$ and four lines leave it. See App. B for relevant details regarding the diagrammatic representation.

where O has been decomposed into normal-ordered contributions $\{\mathbf{O}^{ij}\}$ with respect to $|\Phi\rangle$; see App. A for details[2]. The notation $\langle_s|^i{}_j|^t\rangle$ and the meaning of the integers (s,t,i,j) can be transparently understood by comparing the second and third lines of Eq. (2.5); see App. B for details.

The operator kernel thus takes the form of an infinite sum of expectation values in the Bogoliubov vacuum $|\Phi\rangle$ such that standard Wick's theorem with respect to it straightforwardly applies. As a result, diagrammatic rules can be worked out to efficiently compute the complete set of contributions to each matrix element $\langle_s|^i{}_j|^t\rangle$. The corresponding diagrammatic is introduced in details in App. B.

The operators $\mathbf{L}$, $\mathbf{R}$ and $\mathbf{O}^{ij}$ being expressed in the quasi-particle basis associated with $|\Phi\rangle$, the elementary contractions at play in the present application of Wick's theorem take the simple form given by Eq. (1.28). The operator $\mathbf{L}$ ($\mathbf{R}$) being a pure deexcitation (excitation) operator, no contraction may occur within itself or among its various occurrences. It makes mandatory for each $\mathbf{L}$ ($\mathbf{R}$) operator to contract with either the i creation (j annihilation) operators inside $\mathbf{O}^{ij}$ or with the available $\mathbf{R}$ ($\mathbf{L}$) operators.

Factorisation of the norm kernel

Focusing on a single normal-ordered component $\mathbf{O}^{ij}$, diagrams making up the operator kernel display characteristic topologies. Indeed, each contribution generated via the application of Wick's theorem is the product of *closed strings of contractions* (see, e.g., Ref. [114, 115]), each of which involves a subset of the $\mathbf{L}$ and $\mathbf{R}$ operators at play. Whenever $i+j \geq 4$, several strings involve quasi-particle operators belonging to $\mathbf{O}^{ij}$ thus forming an entity that is said to be *connected* to the operator $\mathbf{O}^{ij}$. Translated into diagrammatic language, each contribution to the operator kernel is thus made out of disjoint closed sub-diagrams, one of which is connected to $\mathbf{O}^{ij}$. This key feature is illustrated in Fig. 2.1 where the diagrammatic expansion of the matrix element $\langle_s|^4{}_2|^t\rangle$ contributing to the operator kernel $\langle\Phi(l)|\mathbf{O}^{42}|\Phi(r)\rangle$ is schematically displayed. Thus, each algebraic contribution to $\langle_s|^i{}_j|^t\rangle$ can be separated into two distinct factors associated with the two categories of strings. For a given s (t) value, s' (t') operators $\mathbf{L}$ ($\mathbf{R}$) belong to closed strings that are not connected, with s' (t') running from 0 to s (t). For a given s' (t') value, there are $\binom{s}{s'}$ ($\binom{t}{t'}$) ways to select the corresponding $\mathbf{L}$'s ($\mathbf{R}$'s). Eventually, the matrix elements entering the operator kernel can be written as

$$\langle\Phi|e^{\mathbf{L}}\mathbf{O}^{ij}e^{\mathbf{R}}|\Phi\rangle = \sum_{s,t=0}^{\infty}\frac{1}{s!t!}\langle\Phi|\underbrace{\mathbf{L}\cdot\mathbf{L}\cdot\ldots\cdot\mathbf{L}\cdot\mathbf{L}}_{s\text{ times}}\mathbf{O}^{ij}\underbrace{\mathbf{R}\cdot\mathbf{R}\cdot\ldots\cdot\mathbf{R}\cdot\mathbf{R}}_{t\text{ times}}|\Phi\rangle$$

[2]Given the chosen Bogoliubov reference state $|\Phi\rangle$, it is natural to normal order the operator O with respect to that state as is presently done. While this is already very general, one can easily go one step further and express the operator in normal order with respect to yet another product state, e.g. the particle vacuum. The connection between both situations is straightforward.

$$= \sum_{s,t=0}^{\infty} \frac{1}{s!t!} \sum_{s'=0}^{s} \sum_{t'=0}^{t} \binom{s}{s'} \binom{t}{t'} \langle\Phi| \underbrace{\mathbf{L}\cdot\ldots\cdot\mathbf{L}}_{(s-s')\text{ times}} \mathbf{O}^{ij} \underbrace{\mathbf{R}\cdot\ldots\cdot\mathbf{R}}_{(t-t')\text{ times}} |\Phi\rangle_c \langle\Phi| \underbrace{\mathbf{L}\cdot\ldots\cdot\mathbf{L}}_{s'\text{ times}} \underbrace{\mathbf{R}\cdot\ldots\cdot\mathbf{R}}_{t'\text{ times}} |\Phi\rangle, \quad (2.6)$$

where the index c stands for *connected terms*. Reshuffling the sums allows one to factorise in front of each connected contribution the infinite set of disjoint closed contributions making up the norm kernel according to

$$\begin{aligned}
\langle\Phi|e^{\mathbf{L}}\mathbf{O}^{ij}e^{\mathbf{R}}|\Phi\rangle &= \sum_{s',t'=0}^{\infty} \sum_{s=s'}^{\infty} \sum_{t=t'}^{\infty} \frac{1}{s'!(s-s')!} \frac{1}{t'!(t-t')!} \langle\Phi| \underbrace{\mathbf{L}\cdot\ldots\cdot\mathbf{L}}_{(s-s')\text{ times}} \mathbf{O}^{ij} \underbrace{\mathbf{R}\cdot\ldots\cdot\mathbf{R}}_{(t-t')\text{ times}} |\Phi\rangle_c \langle\Phi| \underbrace{\mathbf{L}\cdot\ldots\cdot\mathbf{L}}_{s'\text{ times}} \underbrace{\mathbf{R}\cdot\ldots\cdot\mathbf{R}}_{t'\text{ times}} |\Phi\rangle \\
&= \sum_{s,t=0}^{\infty} \frac{1}{s!t!} \langle\Phi| \underbrace{\mathbf{L}\cdot\ldots\cdot\mathbf{L}}_{s\text{ times}} \mathbf{O}^{ij} \underbrace{\mathbf{R}\cdot\ldots\cdot\mathbf{R}}_{t\text{ times}} |\Phi\rangle_c \sum_{s',t'=0}^{\infty} \frac{1}{s'!t'!} \langle\Phi| \underbrace{\mathbf{L}\cdot\ldots\cdot\mathbf{L}}_{s'\text{ times}} \underbrace{\mathbf{R}\cdot\ldots\cdot\mathbf{R}}_{t'\text{ times}} |\Phi\rangle \\
&= \langle\Phi|e^{\mathbf{L}}\mathbf{O}^{ij}e^{\mathbf{R}}|\Phi\rangle_c \langle\Phi|e^{\mathbf{L}}e^{\mathbf{R}}|\Phi\rangle. \quad (2.7)
\end{aligned}$$

The above equation demonstrates that the norm kernel exactly factorises in the operator kernel[3] such that the connected operator kernel is, hence the name, the sum of connected, necessarily joint, contributions

$$\begin{aligned}
o(l,r) &= \langle\Phi|e^{\mathbf{L}}Oe^{\mathbf{R}}|\Phi\rangle_c \\
&= \sum_{n=0}^{N} \sum_{\substack{i,j=0 \\ i+j=2n}}^{2n} \sum_{s,t=0}^{\infty} \langle_s|^i{}_j|^t\rangle_c, \quad (2.8)
\end{aligned}$$

where, for any $\mathbf{O}^{ij}$, the condition

$$s - t = \frac{i-j}{2} \quad (2.9)$$

is satisfied for each connected matrix element $\langle_s|^i{}_j|^t\rangle_c$ given that $\mathbf{L}$ ($\mathbf{R}$) contains two quasi-particle annihilation (creation) operators. In spite of the factorisation of the norm kernel, the symmetric approach does not lead to a natural termination of the infinite number of terms making up the connected operator kernel[4]. The operators $\mathbf{L}$ and $\mathbf{R}$ being presently of one-body character, the infinite series thus generated can however be shown to be factorisable in terms of off-diagonal elementary contractions such that the ODWT is recovered.

[3] Nothing in the proof depends on the character, e.g. rank, of the operators $\mathbf{R}$ and $\mathbf{L}$. Thus, the exact factorisation of the norm kernel out of the operator kernel constitutes a general result going beyond the scope of the present study that constraints $\mathbf{R}$ ($\mathbf{L}$) to be a one-body excitation (de-excitation) operator.

[4] The asymmetric approach to the connected operator kernel detailed in App. C, including the natural termination of the exponential at play, can be recovered from the results obtained below by setting $\mathbf{L} \equiv 0$ a posteriori.

Off-diagonal Wick's theorem

The connected operator kernel associated with the normal-order component $\mathbf{O}^{ij}$ of arbitrary rank $n \equiv (i+j)/2$ reads as

$$\begin{aligned}\langle\Phi|e^{\mathbf{L}}\mathbf{O}^{ij}e^{\mathbf{R}}|\Phi\rangle_c &= \sum_{s,t=0}^{\infty}\langle_s|^i{}_j|^t\rangle_c \\ &= \sum_{s,t=0}^{\infty}\frac{1}{s!t!}\frac{1}{i!j!}\sum_{\substack{k_1\ldots k_i\\ l_1\ldots l_j}}\mathbf{o}^{k_1\ldots k_i}_{l_1\ldots l_j}\langle\Phi|\underbrace{\mathbf{L}\cdot\ldots\cdot\mathbf{L}}_{s\text{ times}}\beta^\dagger_{k_1}\ldots\beta^\dagger_{k_i}\beta_{l_j}\ldots\beta_{l_1}\underbrace{\mathbf{R}\cdot\ldots\cdot\mathbf{R}}_{t\text{ times}}|\Phi\rangle_c\,,\end{aligned} \tag{2.10}$$

where Eq. (A.7) has been used to express $\mathbf{O}^{ij}$ in its second-quantised normal-ordered form.

The calculation of the connected operator kernel relies on the following considerations that are consistent with the diagrammatic rules detailed in App. B

1. Each contribution to $\langle_s|^i{}_j|^t\rangle_c$ is made out of strings of contractions connected to quasi-particle operators belonging to $\mathbf{O}^{ij}$. The characteristics of the operators $\mathbf{L}$ and $\mathbf{R}$ strongly constrains the topology of these connected strings

   (a) Starting from a quasi-particle operator belonging to $\mathbf{O}^{ij}$, a connected string of contractions goes alternatively through a set of $\mathbf{L}$ and $\mathbf{R}$ operators until it reaches other quasi-particle operators of $\mathbf{O}^{ij}$.

   (b) Two successive contractions involving an operator $\mathbf{L}$ ($\mathbf{R}$) exhaust the two quasi-particle operators it contains. Consequently, a string necessarily forms a single loop connecting two[5] quasi-particle operators of $\mathbf{O}^{ij}$.

   (c) There exist four types of closed loops joining two quasi-particle operators of $\mathbf{O}^{ij}$. A so-called *normal* string of contractions starting from an operator $\beta^\dagger$ and ending at an operator β is schematically indicated below by $[\beta^\dagger\beta]$ whenever the former operator is located to the left of the latter[6]. Similarly, an *anomalous* string starting from an operator $\beta(\beta^\dagger)$ and ending at another operator $\beta(\beta^\dagger)$ is denoted as $[\beta\beta]$ ($[\beta^\dagger\beta^\dagger]$).

2. The complete set of connected terms contributing to $\langle_s|^i{}_j|^t\rangle_c$ includes all possible combinations of n normal and anomalous connected loops. This topological characteristic is responsible for the validity of the off-diagonal Wick's theorem proven below, i.e. for the fact that the end result can be expressed in terms of products of off-diagonal elementary contractions[7]. Figure 2.2 displays one such contribution to $\langle_3|^4{}_2|^2\rangle_c$.

3. The combinatorial associated with each contribution to $\langle_s|^i{}_j|^t\rangle_c$ is obtained from the following considerations

[5] Would $\mathbf{L}$ and $\mathbf{R}$ be of higher rank, e.g. be two-body operators, this property would be lost. Indeed, an operator, e.g., $\mathbf{L}$ belonging to a loop going through an alternate succession of $\mathbf{L}$ and $\mathbf{R}$ operators connecting two quasi-particle operators of $\mathbf{O}^{ij}$ could further entertain a contraction with an operator $\mathbf{R}$ belonging to another closed loop, thus forming a more elaborate closed string eventually involving more than two quasi-particle operators of $\mathbf{O}^{ij}$.

[6] Given that $\mathbf{O}^{ij}$ is in normal-ordered form, no normal $[\beta\beta^\dagger]$ string may occur. This would however be the case if the present discussion were extended to the computation of the connected kernel associated with any *product*, e.g. $\mathbf{O}^{ij}\mathbf{O}^{kl}$, of normal-ordered operators. This happens for example when considering kernels involving elementary excitations of $\langle\Phi(l)|$ and/or $|\Phi(r)\rangle$ as in the multi-reference perturbation theory based on a PGCM unperturbed state [41]. Such an extension is straightforward.

[7] If $\mathbf{L}$ and/or $\mathbf{R}$ are of higher rank, i.e. if $|\Phi(l)\rangle$ and/or $|\Phi(r)\rangle$ do not belong to the manifold of Bogoliubov states, the validity of the off-diagonal Wick's theorem is lost.

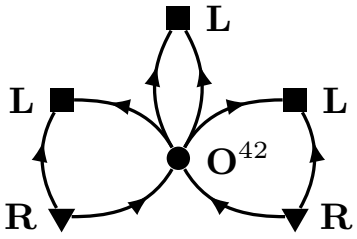

Figure 2.2: Example of diagram contributing to the connected operator matrix element $\langle_3|^4{}_2|^2\rangle_c$ and containing $n = (4+2)/2 = 3$ closed loops. In this diagram, one such string contains a single operator **L** connecting two quasi-particle creation operators of $\mathbf{O}^{42}$. The two other closed loops involve one operator **L** and one operator **R** each and connect one quasi-particle creation of $\mathbf{O}^{42}$ to one of its quasi-particle annihilation operator.

(a) Among the n strings, $k \leq \min(i,j)$ normal $[\beta^\dagger\beta]$ strings are formed, knowing that k is even whenever i and j are even[8] and odd otherwise[9]. Once k normal strings are formed, there remains an even number $i-k$ ($j-k$) of quasi-particle creation (annihilation) operators in $\mathbf{O}^{ij}$ giving rise to $(i-k)/2$ ($(j-k)/2$) anomalous $[\beta^\dagger\beta^\dagger]$ ($[\beta\beta]$) strings.

(b) There are $\binom{i}{k}$ different ways to pick k operators out of the i creation operators and, similarly, $\binom{j}{k}$ different ways to pick k operators out of the j annihilation operators. Once this done, there are $k!$ different ways to associate the k creators to the k annihilators to form the k normal strings. Next, there are $(i-k-1)!!$ ($(j-k-1)!!$) possible ways to form the $(i-k)/2$ ($(j-k)/2$) anomalous $[\beta^\dagger\beta^\dagger]$ ($[\beta\beta]$) strings.

(c) For a given k, all terms associated with the above combinatorial contribute identically[10] due to the anti-symmetric character of the operator matrix elements under the exchange of any pair of quasi-particle creation (i.e. upper) or annihilation (i.e. lower) indices; see Eq. (A.9).

(d) Combining the factor $(i!j!)^{-1}$ originating from the operator with the above combinatorial[11] one obtains the overall factor

$$c(i,j,k) \equiv \frac{1}{k!}\frac{1}{(i-k)!}\frac{1}{(j-k)!}(i-k-1)!!(j-k-1)!!$$

for the diagram associated to k normal strings $[\beta^\dagger\beta]$, $(i-k)/2$ anomalous strings $[\beta^\dagger\beta^\dagger]$ and $(j-k)/2$ anomalous strings $[\beta\beta]$.

[8] The integers i and j always carry the same parity.

[9] If this rule is not fulfilled, the operator cannot be fully contracted, thus providing a vanishing expectation value by virtue of its normal-ordered form.

[10] Instead of considering all possible strings, this is best seen by keeping the contraction pattern fixed and by exchanging the position of the quasi-particle operators within $\mathbf{O}^{ij}$ in all ways consistent with that contraction pattern and by employing the anti-symmetry of the operator matrix elements to recover the original algebraic contribution.

[11] Useful properties of the double factorial are

$$n! = n!!(n-1)!! \quad \forall n \tag{2.11a}$$

$$n!! = 2^k k! \qquad \text{for } n = 2k\,. \tag{2.11b}$$

4. So far, the focus has been on the nature and the number of closed strings that can be formed in Eq. (2.10) for a given operator $\mathbf{O}^{ij}$, while leaving the expansion of $\exp(\mathbf{L})$ ($\exp(\mathbf{R})$) in the abstract. Let us now consider the specific term of that expansion associated with the powers s (for $\mathbf{L}$) and t (for $\mathbf{R}$), i.e. $\langle_s|^i{}_j|^t\rangle_c$, and focus on the set of contributions characterised by $k \leq \min(i,j)$ normal strings. Below, an index $h \in [1,n]$ is artificially introduced to label each string for bookkeeping purposes.

   (a) Let us first concentrate on the k normal strings $[\beta^\dagger\beta]^{(h)}$. There are $s^{(1)}$ operators $\mathbf{L}$ out of s involved in the string $[\beta^\dagger\beta]^{(1)}$ and $\binom{s}{s^{(1)}}$ equivalent ways to choose them. Then, there are $s^{(2)}$ such operators out of $(s-s^{(1)})$ involved in $[\beta^\dagger\beta]^{(2)}$ and so on, up to selecting $s^{(k)}$ out of $(s-\sum_{h=1}^{k-1} s^{(h)})$ operators $\mathbf{L}$ involved in $[\beta^\dagger\beta]^{(k)}$, such that $s' \equiv \sum_{h=1}^{k} s^{(h)}$ operators out of s are eventually involved in the k normal strings. The overall associated combinatorial factor is given by

$$\begin{aligned}
&\binom{s}{s^{(1)}}\binom{s\text{-}s^{(1)}}{s^{(2)}}\binom{s\text{-}s^{(1)}\text{-}s^{(2)}}{s^{(3)}}\cdots\binom{s\text{-}s^{(1)}\text{-}s^{(2)}\text{-}\ldots\text{-}s^{(k-1)}}{s^{(k)}}\\
&= \frac{s!}{s^{(1)}!s^{(2)}!\ldots s^{(k)}!(s\text{-}s^{(1)}\text{-}s^{(2)}\ldots\text{-}s^{(k)})!}\\
&= \frac{s!}{s^{(1)}!s^{(2)}!\ldots s^{(k)}!(s\text{-}s')!},
\end{aligned} \tag{2.12}$$

   such that the initial $(s!)^{-1}$ factor is replaced by similar factors for each normal contraction and for the remaining $s-s'$ operators $\mathbf{L}$ involved in anomalous strings. The very same operation is considered for the t' operators $\mathbf{R}$ involved in the k normal strings, delivering the same combinatorial factor with s variables replaced by t ones. Because one is presently dealing with normal strings, the additional factor $\prod_{h=1}^{k}\delta_{s^{(h)}t^{(h)}}$ must be included given that as many $\mathbf{L}$ and $\mathbf{R}$ operators must be involved in each of them.

   (b) The same reasoning applies to both sets of anomalous strings, knowing that the operators $\mathbf{L}$ and $\mathbf{R}$ must be selected among the operators that have not been used yet and that the condition $\delta_{s^{(h)}-1,t^{(h)}}$ ($\delta_{s^{(h)},t^{(h)}-1}$) must be used for each string $[\beta^\dagger\beta^\dagger]^{(h)}$ ($[\beta\beta]^{(h)}$).

5. Eventually summing over all possible values of s and t, along with the subset of $s^{(h)}$ and $t^{(h)}$ values, taking into account the Kronecker deltas generated through the processes described above, each contribution to the operator kernel containing $k \leq \min(i,j)$ normal strings involves intricate sums with the generic structure

$$\sum_{a=0}^{\infty}\sum_{b=0}^{a}\sum_{c=0}^{a-b}\sum_{d=0}^{a-b-c}\cdots \tag{2.13}$$

   where, e.g. for normal strings, $a \equiv n = s = t$, $b \equiv s^{(1)} = t^{(1)}$, $c \equiv s^{(2)} = t^{(2)}$, etc. These intricate sums are easily shown to be equivalent to

$$\sum_{a'=0}^{\infty}\sum_{b=0}^{\infty}\sum_{c=0}^{\infty}\sum_{d=0}^{\infty}\cdots, \tag{2.14}$$

   with $a' = a-b-c-d-\ldots$. Each disentangled sum gathers an infinite set of contributions corresponding to closed strings connected to the same pair of quasi-particle operators and involving an increasing number of successive $\mathbf{L}$ and $\mathbf{R}$ operators. Weighted by the prefactor $(s^{(h)}!)^{-1}(t^{(h)}!)^{-1}$ originating from the successive appropriate applications of Eq. (2.12), this set of terms exactly makes up the

corresponding off-diagonal elementary contractions (Eq. (1.26)) according to the expansions[12]

$$\rho_{k_1k_2}(l,r) = \sum_{s,t=0}^{\infty} \frac{1}{s!t!} \langle \Phi | \mathbf{L}^s \beta_{k_2}^\dagger \beta_{k_1} \mathbf{R}^t | \Phi \rangle_c$$
$$\equiv \sum_{s,t=0}^{\infty} \langle s |^{k_2} | |_{k_1} | t \rangle_c \,, \tag{2.15a}$$

$$\kappa_{k_1k_2}(l,r) = \sum_{s,t=0}^{\infty} \frac{1}{s!t!} \langle \Phi | \mathbf{L}^s \beta_{k_2} \beta_{k_1} \mathbf{R}^t | \Phi \rangle_c$$
$$\equiv \sum_{s,t=0}^{\infty} \langle s |_{k_2} | |_{k_1} | t \rangle_c \tag{2.15b}$$

$$-\bar{\kappa}^*_{k_1k_2}(l,r) = \sum_{s,t=0}^{\infty} \frac{1}{s!t!} \langle \Phi | \mathbf{L}^s \beta_{k_2}^\dagger \beta_{k_1}^\dagger \mathbf{R}^t | \Phi \rangle_c$$
$$\equiv \sum_{s,t=0}^{\infty} \langle s |^{k_2} | |^{k_1} | t \rangle_c \,, \tag{2.15c}$$

$$-\sigma^*_{k_1k_2}(l,r) = \sum_{s,t=0}^{\infty} \frac{1}{s!t!} \langle \Phi | \mathbf{L}^s \beta_{k_2} \beta_{k_1}^\dagger \mathbf{R}^t | \Phi \rangle_c$$
$$\equiv \sum_{s,t=0}^{\infty} \langle s |_{k_2} | |^{k_1} | t \rangle_c \,, \tag{2.15d}$$

knowing that the diagrammatic rules applicable to the four connected[13] matrix elements introduced through Eq. (2.15) are laid out in App. B.

Taking into account all multiplicative factors pointed out above and summing over all allowed numbers k of normal strings/contractions[14], one eventually obtains Eq. (2.10) under the final form

$$\frac{\langle \Phi(l) | \mathbf{O}^{ij} | \Phi(r) \rangle}{\langle \Phi(l) | \Phi(r) \rangle} = \sum_{\substack{k=0 \\ \text{parity}}}^{\min(i,j)} c(i,j,k) \, \mathbf{o}_{l_1 \dots l_j}^{k_1 \dots k_i}$$
$$\times \rho_{l_1k_1}(l,r) \dots \rho_{l_kk_k}(l,r)$$
$$\times \bar{\kappa}^*_{k_{k+1}k_{k+2}}(l,r) \dots \bar{\kappa}^*_{k_{i-1}k_i}(l,r)$$
$$\times \kappa_{l_{k+1}l_{k+2}}(l,r) \dots \kappa_{l_{j-1}l_j}(l,r) \,, \tag{2.16}$$

which proves the off-diagonal Wick's theorem [105] by expressing the connected operator kernel in terms of off-diagonal elementary contractions. Applying Eq. (2.16) to the sum of $\mathbf{O}^{ij}$ operators characterised by $n \leq 3$, the expression of the connected operator kernel of a three-body operator ($N = 3$) is given in App. D.

While the ODWT has indeed been formally recovered, a full proof requires an explicit computation of the off-diagonal elementary contractions themselves via the symmetric approach. As clearly illustrated in

[12] The fourth contraction appearing in Eq. (2.15d) does not presently occur due to the normal-ordered character of $\mathbf{O}^{ij}$.

[13] The connected character of the presently introduced matrix elements is defined with respect to the two operators $\beta_{k_2}^{(\dagger)}$ and $\beta_{k_1}^{(\dagger)}$ that translate diagrammatically into two external lines; see App. B for details.

[14] The sum over k starts from 0 (1) and runs over even (odd) integers whenever i and j are even (odd).

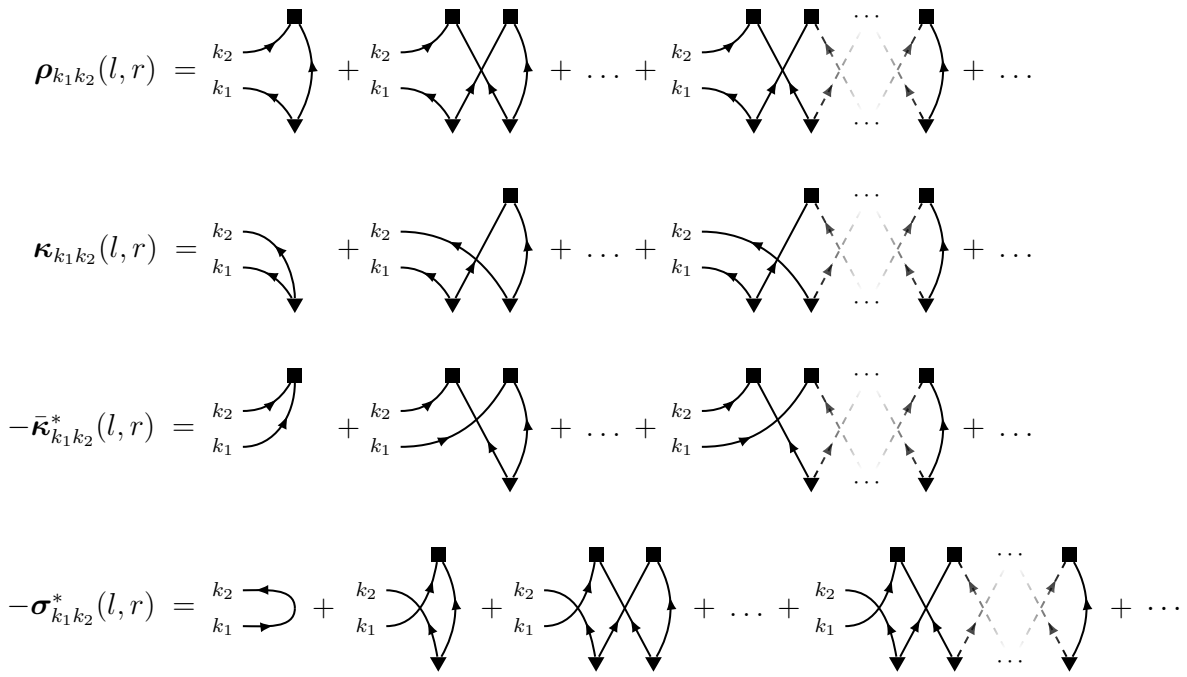

Figure 2.3: Diagrammatic expansions of the four off-diagonal elementary contractions.

Eq. (2.15), each of these contractions takes itself the form of an infinite, non-terminating, expansion. As demonstrated below, these expansions however happen to deliver known power series that are shown to be equal to the expressions obtained via the asymmetric approach in App. C.

Elementary contractions

The first elementary contraction $\rho_{k_1k_2}(l,r)$ (Eq. (2.15a)) sums the connected matrix elements $\langle_s|^{k_2}||_{k_1}|^t\rangle_c$ over all s and t values, knowing in fact that both integers are constrained to be equal, i.e. $s=t\equiv n$. The matrix element $\langle_n|^{k_2}||_{k_1}|^n\rangle_c$ is made out of a single unlabelled connected diagram with two external legs. Indeed, there is only one topologically distinct way to connect $\beta^\dagger_{k_2}$ to β_{k_1} via an alternate succession of n operators $\mathbf{L}$ and n operators $\mathbf{R}$. By virtue of Eq. (1.28), the term of order $n=0$ is zero in the present case.

The corresponding diagrammatic expansion of $\rho_{k_1k_2}(l,r)$ is provided in Fig. 2.3. Diagrammatic rules deliver the algebraic expressions for each order n, thus leading to

$$\begin{aligned}\rho_{k_1k_2}(l,r) &= +\sum_{n=1}^{\infty}\sum_{\substack{h_1h_2\\ \dots\\ h_{2n-1}}}\mathbf{z}^{k_1h_1}(r)\mathbf{z}^*_{h_1h_2}(l)\mathbf{z}^{h_2h_3}(r)\dots\\ &\quad\times\mathbf{z}^*_{h_{2n-3}h_{2n-2}}(l)\mathbf{z}^{h_{2n-2}h_{2n-1}}(r)\mathbf{z}^*_{k_2h_{2n-1}}(l)\\ &= -\sum_{n=0}^{\infty}\Big[\mathbf{z}(r)\Big(\mathbf{z}^*(l)\mathbf{z}(r)\Big)^n\mathbf{z}^*(l)\Big]_{k_1k_2}\\ &= -\left[\mathbf{z}(r)\frac{1}{1-\mathbf{z}^*(l)\mathbf{z}(r)}\mathbf{z}^*(l)\right]_{k_1k_2},\end{aligned}\tag{2.17}$$

where the Taylor series

$$\sum_{n=0}^{\infty} \varepsilon^n = \frac{1}{1-\varepsilon} \tag{2.18}$$

has been used to resum the infinite expansion.

The three other elementary contractions (Eqs. (2.15b- 2.15d)) can be calculated similarly. Their diagrammatic expansions are also displayed in Fig. 2.3, where one notices that the fourth contraction contains a non-zero term of order $n = 0$. The corresponding algebraic expressions are given by

$$\begin{aligned}
\kappa_{k_1k_2}(l,r) &= +\sum_{n=0}^{\infty}\Big[\mathbf{z}(r)\Big(\mathbf{z}^*(l)\mathbf{z}(r)\Big)^n\Big]_{k_1k_2} \\
&= +\left[\mathbf{z}(r)\frac{1}{1-\mathbf{z}^*(l)\mathbf{z}(r)}\right]_{k_1k_2}, && (2.19a)\\
-\bar{\kappa}^*_{k_1k_2}(l,r) &= -\sum_{n=0}^{\infty}\Big[\Big(\mathbf{z}^*(l)\mathbf{z}(r)\Big)^n\mathbf{z}^*(l)\Big]_{k_1k_2} \\
&= -\left[\frac{1}{1-\mathbf{z}^*(l)\mathbf{z}(r)}\mathbf{z}^*(l)\right]_{k_1k_2}, && (2.19b)\\
-\sigma^*_{k_1k_2}(l,r) &= +\sum_{n=0}^{\infty}\Big[\Big(\mathbf{z}^*(l)\mathbf{z}(r)\Big)^n\Big]_{k_1k_2} \\
&= +\left[\frac{1}{1-\mathbf{z}^*(l)\mathbf{z}(r)}\right]_{k_1k_2}. && (2.19c)
\end{aligned}$$

It is easy to check that the four properties listed in Eqs. (1.27) are indeed satisfied by the off-diagonal contractions.

Eventually, the off-diagonal contractions have been expressed as a known power series in the variable $\mathbf{z}^*(l)\mathbf{z}(r)$. While this result looks very different from the one obtained from the asymmetric approach where the off-diagonal contractions read as linear functions of the Thouless matrix $\mathbf{z}(l,r)$, it can be easily shown, as stipulated in App. C, that both sets of expressions are in fact identical.

2.1.2 Norm kernel

The norm kernel reads in the symmetric approach as

$$\begin{aligned}
\frac{\langle\Phi(l)|\Phi(r)\rangle}{\langle\Phi(l)|\Phi\rangle\langle\Phi|\Phi(r)\rangle} &= \sum_{s,t=0}^{\infty}\frac{1}{s!t!}\langle\Phi|\mathbf{L}^s\mathbf{R}^t|\Phi\rangle \\
&\equiv \sum_{s,t=0}^{\infty}\langle_s||^t\rangle, && (2.20)
\end{aligned}$$

where the condition $s = t \equiv n$ must be fulfilled.

Exponentiation of closed diagrams

As already discussed, and as detailed in App. B, diagrams contributing to $\langle_n||^n\rangle$ are composed of disjoint closed sub-diagrams. A closed[15] diagram involves an equal number of successively connected operators $\mathbf{L}$

[15] The trivial diagram obtained for $n = 0$ is $\langle_0||^0\rangle = \langle\Phi|\Phi\rangle = 1$. Since it contains neither vertices nor lines, it does not qualify as a closed diagram.

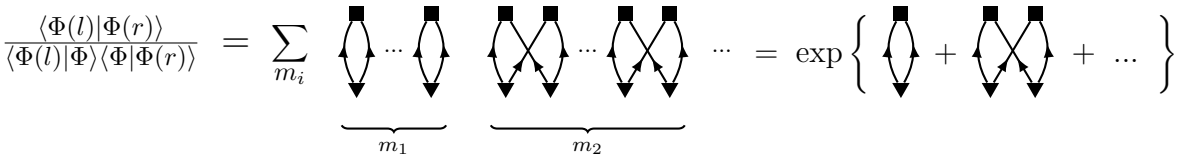

Figure 2.4: Representation of the norm kernel in terms of (repeated) disjoint closed diagrams and as the exponential of the sum of distinct closed diagrams.

and **R**. For a given $n_i \geq 1$, there exists in fact a single topologically distinct unlabelled closed diagram[16]

$$\Gamma_{cl}(n_i) \equiv \langle_{n_i}||^{n_i}\rangle_{cl}\,, \tag{2.21}$$

where the index cl stands for *closed*.

A generic diagram $\Gamma(n)$ contributing to $\langle_n||^n\rangle$ factorises into m_1 identical closed subdiagrams $\Gamma_{cl}(n_1)$, m_2 identical closed sub-diagrams $\Gamma_{cl}(n_2)$, and so on. Obviously, a closed diagram $\Gamma_{cl}(n_i)$ can only contribute whenever $n \geq n_i$. Using the convention that a closed diagram occurs with multiplicity $m_i = 0$ whenever $n < n_i$, a diagram contributing to $\langle_n||^n\rangle$ can be written as

$$\Gamma(n) = \frac{[\Gamma_{cl}(n_1)]^{m_1}}{m_1!}\frac{[\Gamma_{cl}(n_2)]^{m_2}}{m_2!}\cdots \tag{2.22}$$

where the product runs over all possible closed strings $\Gamma_{cl}(n_i)$ such that the condition

$$\sum_{n_i=1}^{\infty} m_i n_i = n\,, \tag{2.23}$$

is satisfied. According to the diagrammatic rules, the symmetry factor of $\Gamma(n)$ must be worked out. In addition to the symmetry factors associated with each closed subdiagram (included into $\Gamma_{cl}(n_i)$), the symmetry factor $S_{\Gamma(n)}$ incorporates the set of denominators in Eq. (2.22). Each such denominator $m_i!$ denotes the number of permutations of the equivalent groups of **L** and **R** operators belonging to the m_i identical closed sub-diagrams $\Gamma_{cl}(n_i)$.

Summing over all topologically distinct diagrams $\Gamma(n)$, with n running from 0 to ∞, each closed contribution $\Gamma_{cl}(n_i)$ eventually occur with all possible integer multiplicities m_i such that

$$\begin{aligned}\frac{\langle\Phi(l)|\Phi(r)\rangle}{\langle\Phi(l)|\Phi\rangle\langle\Phi|\Phi(r)\rangle} &= \sum_{n=0}^{\infty}\sum_{\Gamma(n)}\Gamma(n)\\ &= \sum_{m_1 m_2 \ldots=0}^{\infty}\frac{[\Gamma_{cl}(1)]^{m_1}}{m_1!}\frac{[\Gamma_{cl}(2)]^{m_2}}{m_2!}\cdots\\ &= \exp\left\{\sum_{n=1}^{\infty}\Gamma_{cl}(n)\right\},\end{aligned} \tag{2.24}$$

thus demonstrating the exponentiation of closed diagrams in the expansion of the norm kernel. The above rationale is illustrated diagrammatically in Fig. 2.4.

[16] In the present discussion $\Gamma_{cl}(n_i)$ equally represents the closed diagram and its algebraic contribution.

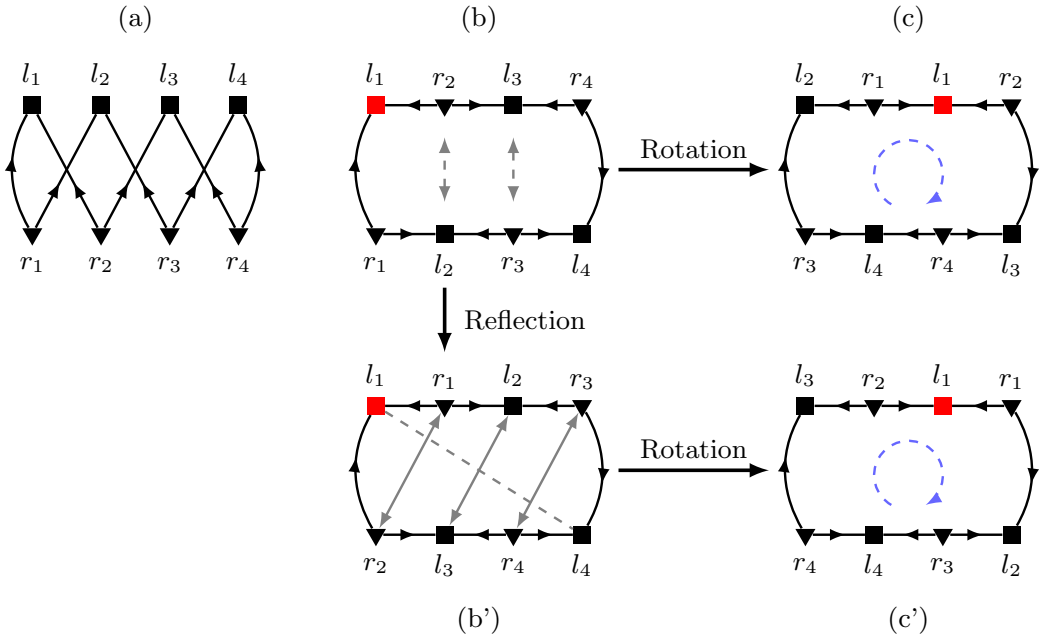

Figure 2.5: Permutations of the labelled diagram $\Gamma_{cl}(4)$ delivering topologically equivalent diagrams. (a): Labelled diagram in the original representation. (b): Same diagram but expanded in a way that makes permutations of the vertices more transparent. (b'): Labelled diagram obtained from (b) via a reflection with respect to the diagonal $l_1 - l_4$ inverting the clockwise ordering of the labelled vertices. (c) and (c'): one representative of the four clockwise circular permutations obtained from (b) and (b'), respectively. There is thus a total of $S_{\Gamma_{cl}(4)} = 2 \times 4$ permutations out of which the original labelled diagram can be recovered by a mere translation of the vertices in the plane.

Resummation of closed diagrams

One is now left with the computation of the exponent in Eq. (2.24). According to the diagrammatic rules, the algebraic expression of the single topologically distinct unlabelled closed diagram of order n reads as

$$\Gamma_{cl}(n) = -\frac{1}{2n}\mathrm{Tr}\Big\{\Big(\mathbf{z}^*(l)\mathbf{z}(r)\Big)^n\Big\}, \tag{2.25}$$

where the symmetry factor is $S_{\Gamma_{cl}(n)} = 2n$. As visible from Fig. 2.4, the 1/2 factor obtained for $n = 1$ relates to the existence of a pair of equivalent lines. For $n > 1$, the symmetry factor relates to the number of permutations of the **L** and **R** vertices in the *labelled* diagram $\Gamma_{cl}(n)$ delivering topologically equivalent labelled diagrams. As illustrated in Fig. 2.5 for $n = 4$, there are $S_{\Gamma_{cl}(n)} = 2n$ such permutations, made out of the convolution of

1. The identity plus 1 reflection inverting the clockwise ordering,
2. n clockwise circular permutations.

Summing over all closed diagrams, the final result is obtained as

$$\begin{aligned}\sum_{n=1}^{\infty}\Gamma_{cl}(n) &= -\frac{1}{2}\mathrm{Tr}\Big\{\sum_{n=1}^{\infty}\frac{1}{n}\Big(\mathbf{z}^*(l)\mathbf{z}(r)\Big)^n\Big\}\\ &= \frac{1}{2}\mathrm{Tr}\Big\{\ln\Big(1-\mathbf{z}^*(l)\mathbf{z}(r)\Big)\Big\},\end{aligned} \tag{2.26}$$

where the Taylor series

$$-\sum_{n=1}^{\infty}\frac{\varepsilon^n}{n} = \ln(1-\varepsilon), \tag{2.27}$$

has been used to resum the infinite expansion.

Onishi formula

Combining Eqs. (2.24) and (2.26), the norm kernel eventually reads as

$$\frac{\langle\Phi(l)|\Phi(r)\rangle}{\langle\Phi(l)|\Phi\rangle\langle\Phi|\Phi(r)\rangle} = \exp\Big[\frac{1}{2}\mathrm{Tr}\Big\{\ln\Big(1-\mathbf{z}^*(l)\mathbf{z}(r)\Big)\Big\}\Big], \tag{2.28}$$

which is nothing but the well-celebrated Onishi formula [106]. It has often been stated that the Onishi formula[17] is compromised by an undefined complex phase. In the derivation above based on the application of standard Wick's theorem, there is no algebraic manipulation that can be responsible for a loss of phase. Thus, the loss of phase due to the apparent necessity to compute the square root originating from the factor 1/2 in the exponent in Eq. (2.28) can only be fictitious. The same observation is at the heart of Ref. [116]. The key point relates to the fact that the eigenvalues of the matrix $\mathbf{z}^*(l)\mathbf{z}(r)$, which is the product of two skew-symmetric matrices, are doubly-degenerate [117, 118]. This double degeneracy necessarily compensates for the incriminated factor 1/2 in Eq. (2.28), thus demonstrating the fictitious character of the square root and of the apparent loss of phase [103, 116].

[17] Strickly speaking, the Onishi formula, as any formula based on the symmetric approach, can only deliver the phase of the overlap $\langle\Phi(l)|\Phi(r)\rangle$ modulo the knowledge of the phase associated with, i.e. initially fixed for, the overlaps $\langle\Phi(l)|\Phi\rangle$ and $\langle\Phi|\Phi(r)\rangle$ of the two involved states with respect to the reference Bogoliubov state $|\Phi\rangle$.

Pfaffian formula

The equivalence of the Onishi and Pfaffian [107] formulae for the norm kernel has been demonstrated in a pedestrian way in Ref. [116]. As a matter of fact, the two formulae can be directly connected by exploiting the generic identity [119]

$$\mathrm{pf}(A)\mathrm{pf}(B) = \exp\left[\frac{1}{2}\mathrm{Tr}\ln(A^{\mathrm{T}}B)\right], \tag{2.29}$$

where A and B are two skew-symmetric matrices such that $A^T B$ is itself a positive-definite matrix. Rewriting the argument of the logarithm in Eq. (2.28) as

$$1 - \mathbf{z}^*(l)\mathbf{z}(r) = \mathbf{z}^*(l)\Big(\mathbf{z}^*(l)^{-1} - \mathbf{z}(r)\Big), \tag{2.30}$$

Eq. (2.29) is applied for

$$A \equiv \mathbf{z}^{\dagger}(l) \tag{2.31a}$$

$$B \equiv \mathbf{z}^*(l)^{-1} - \mathbf{z}(r). \tag{2.31b}$$

This leads to expressing the norm overlap as

$$\begin{aligned}\frac{\langle\Phi(l)|\Phi(r)\rangle}{\langle\Phi(l)|\Phi\rangle\langle\Phi|\Phi(r)\rangle} &= \mathrm{pf}\Big(\mathbf{z}^{\dagger}(l)\Big)\mathrm{pf}\Big(\mathbf{z}^*(l)^{-1} - \mathbf{z}(r)\Big)\\ &= (-1)^{n_1/2}\mathrm{pf}\Big(\mathbf{z}^*(l)\Big)\mathrm{pf}\Big(\mathbf{z}^*(l)^{-1} + \mathbf{z}^{\mathrm{T}}(r)\Big),\end{aligned}$$

where the last equivalence makes use of the property

$$\mathrm{pf}(A^{\mathrm{T}}) = (-1)^n \mathrm{pf}(A), \tag{2.32}$$

with $2n$ the size of the matrix A, i.e. the (even) dimension n_1 of the (truncated) one-body Hilbert space $\mathcal{H}_1$ in the present context. The last useful identity for the pfaffian of a skew-symmetric matrix displaying the structure

$$S = \begin{pmatrix} M & Q \\ -Q^T & N \end{pmatrix}, \tag{2.33}$$

with M an invertible matrix, is given by [120]

$$\mathrm{pf}(S) = \mathrm{pf}(M)\mathrm{pf}(N + Q^{\mathrm{T}}M^{-1}Q). \tag{2.34}$$

Identifying

$$M \equiv \mathbf{z}^*(l), \tag{2.35a}$$

$$N \equiv \mathbf{z}^{\mathrm{T}}(r), \tag{2.35b}$$

$$Q \equiv 1, \tag{2.35c}$$

the pfaffian formulation of the norm overlap

$$\frac{\langle\Phi(l)|\Phi(r)\rangle}{\langle\Phi(l)|\Phi\rangle\langle\Phi|\Phi(r)\rangle} = (-1)^{n_1/2}\mathrm{pf}\left[\begin{pmatrix} \mathbf{z}^*(l) & 1 \\ -1 & \mathbf{z}^{\mathrm{T}}(r) \end{pmatrix}\right], \tag{2.36}$$

is eventually obtained from the Onishi formula, thus bypassing the intermediate apparent phase undetermination.

2.2 Discussion and conclusions

The interest of the present development is primarily formal and conceptual. The main goal has been to offer a novel perspective on the off-diagonal Wick theorem and the Onishi formula by consistently computing the off-diagonal operator and norm kernels at play in, e.g., the projected generator coordinate method via a single formal approach. The method expresses the two Bogoliubov states at play with respect to a third reference state $|\Phi\rangle$ via Thouless' theorem such that the kernels of interest read as

$$\frac{\langle\Phi(l)|O|\Phi(r)\rangle}{\langle\Phi(l)|\Phi(r)\rangle} = \frac{\langle\Phi|e^{\mathbf{Z}^{20}(l)^\dagger} O e^{\mathbf{Z}^{20}(r)}|\Phi\rangle}{\langle\Phi|e^{\mathbf{Z}^{20}(l)^\dagger} e^{\mathbf{Z}^{20}(r)}|\Phi\rangle}, \tag{2.37a}$$

$$\frac{\langle\Phi(l)|\Phi(r)\rangle}{\langle\Phi(l)|\Phi\rangle\langle\Phi|\Phi(r)\rangle} \equiv \langle\Phi|e^{\mathbf{Z}^{20}(l)^\dagger} e^{\mathbf{Z}^{20}(r)}|\Phi\rangle. \tag{2.37b}$$

While the exponentials of the Thouless one-body operators $\mathbf{Z}^{20}(l)^\dagger$ and $\mathbf{Z}^{20}(r)$ do not naturally terminate, a diagrammatic method was used to demonstrate that the infinite set of terms can be resummed exactly.

Interestingly, the diagrammatic technique and the associated infinite resummations leading to the exact computation of the above kernels can be used to design non-trivial approximations to more complex kernels of interest. As the simplest example, replacing the two Thouless one-body operators by a two-body cluster amplitude into Eq. (2.37a) leads to

$$E^{\text{vCCD}} = \frac{\langle\Phi|e^{T_2^\dagger} H e^{T_2}|\Phi\rangle}{\langle\Phi|e^{T_2^\dagger} e^{T_2}|\Phi\rangle} = \langle\Phi|e^{T_2^\dagger} H e^{T_2}|\Phi\rangle_c, \tag{2.38}$$

which is nothing but the energy at play in the variational coupled cluster with doubles method [111]. Because T_2 is now a two-body operator, the equivalent to the off-diagonal Wick theorem and the associated resummation of the infinite expansion of the exponentials do not hold. As a result, approximation schemes have to be set up [112, 113] such that designing more advanced truncation schemes than existing ones can be of interest. Because the diagrammatic does not require the operators in the two exponentials to be the same, addressing even more general kernels (including the corresponding norm kernels) than the one displayed in Eq. (2.38) can be envisioned.

Chapter 3

Derivation of the Quasiparticle Random Phase Approximation from the GCM

Contents

One of the main objectives of this work lies in the comparative description of the GMR in *ab initio* (P)GCM and QRPA. The numerical results relative to (P)GCM calculations are addressed in Chaps. 6, 7 and 8. They are later explicitly compared to QRPA calculations in Chap. 9, in order to appreciate the similarities and differences between the two methods. It is, thus, important to understand the formal connection between such two techniques.

In the present chapter the QRPA equations are derived from the GCM based on Bogoliubov states. This development follows in spirit the derivation from Ref. [121], generalising it to quasiparticle states and to n-body Hamiltonians[1].

3.1 Bogoliubov transformation for bosons

In Sec. 1.2.1 the unitary Bogoliubov transformation was introduced for fermionic operators. A similar transformation is now introduced for bosons, although differences arise from the use of commutation rather

[1] An alternative derivation of the RPA equation from the GCM can be obtained under the Gaussian overlap approximation, see [122]

than anti-commutation rules. This will be of interest in the following. A boson quasiparticle vacuum (denoted by round brackets, as opposed to the fermion vacuum, for which sharp brackets are used) is defined as

$$\gamma_i|\Phi) = 0 \quad \forall i\,, \tag{3.1}$$

where boson quasiparticle operators γ and $\gamma^\dagger$ are related to boson particle operators b and $b^\dagger$ via a Bogoliubov transformation

$$\begin{pmatrix}\gamma\\ \gamma^\dagger\end{pmatrix} = \mathcal{X}^{-1}\begin{pmatrix}b\\ b^\dagger\end{pmatrix}, \tag{3.2}$$

with

$$\mathcal{X} \equiv \begin{pmatrix}X & Y^*\\ Y & X^*\end{pmatrix}. \tag{3.3}$$

Similarly to the fermionic case, bosonic commutation rules

$$[b_k^\dagger, b_l] = \delta_{kl}\,, \tag{3.4a}$$
$$[b_k, b_l] = 0\,, \tag{3.4b}$$
$$[b_k^\dagger, b_l^\dagger] = 0\,, \tag{3.4c}$$

are re-written in more compact form for non-vanishing commutators as

$$\begin{pmatrix}b^\dagger & b\end{pmatrix}\eta\begin{pmatrix}b\\ b^\dagger\end{pmatrix} = \mathbb{1}\,, \tag{3.5}$$

where the metric tensor η reads as

$$\eta \equiv \begin{pmatrix}\mathbb{1} & \mathbb{0}\\ \mathbb{0} & -\mathbb{1}\end{pmatrix}. \tag{3.6}$$

The same relations are required to propagate to quasiparticle creation and annihilation operators, such that

$$\begin{aligned}\begin{pmatrix}\gamma^\dagger & \gamma\end{pmatrix}\eta\begin{pmatrix}\gamma\\ \gamma^\dagger\end{pmatrix} &= \begin{pmatrix}b^\dagger & b\end{pmatrix}\left(\mathcal{X}^\dagger\right)^{-1}\eta\left(\mathcal{X}\right)^{-1}\begin{pmatrix}b\\ b^\dagger\end{pmatrix}\\ &= \begin{pmatrix}b^\dagger & b\end{pmatrix}\eta\begin{pmatrix}b\\ b^\dagger\end{pmatrix},\end{aligned} \tag{3.7}$$

Consequently, the Bogoliubov transformation for bosons must be unitary with respect to the metric η, i.e.

$$\mathcal{X}^\dagger\eta\mathcal{X} = \eta\,, \tag{3.8}$$

or, alternatively,

$$\left(\mathcal{X}^\dagger\right)^{-1} = \eta\mathcal{X}\eta\,. \tag{3.9}$$

3.2 Bosonic mapping of fermion pairs

The description of an even many-body fermionic system can be fully achieved in terms of *fermionic pair operators* instead of canonical quasiparticle operators. These pair operators are naturally defined as

$$b_{kl}^\dagger \equiv \beta_k^\dagger\beta_l^\dagger\,, \tag{3.10a}$$
$$b_{kl} \equiv \beta_l\beta_k\,, \tag{3.10b}$$

$$a_{kl} \equiv \beta_l^\dagger \beta_k = a_{lk}^\dagger \,. \tag{3.10c}$$

The operators introduced in Eqs. (3.10) form a Lie algebra (belonging to the $SO(2M)$ group), whose commutation rules are provided by

$$[b_{k_1 l_1}, b_{k_2 l_2}] = [b^\dagger_{k_1 l_1}, b^\dagger_{k_2 l_2}] = 0 \,, \tag{3.11a}$$
$$[b_{k_1 l_1}, b^\dagger_{k_2 l_2}] = \delta_{k_1 k_2}\delta_{l_1 l_2} - \delta_{l_1 k_2}\delta_{k_1 l_2} + \delta_{k_1 l_2} a_{l_1 k_2} + \delta_{l_1 k_2} a_{k_1 l_2} - \delta_{l_1 l_2} a_{k_1 k_2} - \delta_{k_1 k_2} a_{l_1 l_2} \,, \tag{3.11b}$$
$$[b_{k_1 l_1}, a_{k_2 l_2}] = \delta_{l_1 l_2} b_{k_1 k_2} - \delta_{k_1 l_2} b_{l_1 k_2} \,, \tag{3.11c}$$
$$[a_{k_1 l_1}, a_{k_2 l_2}] = \delta_{k_1 l_2} a_{k_2 l_1} - \delta_{l_1 k_2} a_{k_1 l_2} \,. \tag{3.11d}$$

These exact relations encode the Fermi statistic of the original quasiparticle description, and should be strictly fulfilled in order for the Pauli principle to be respected and to prevent the emergence of spurious states. However, historically many authors have investigated the possibility to represent the original fermionic system in terms of pure boson operators B and $B^\dagger$ creation and annihilation operators fulfilling exact boson commutation relations

$$[B_{k_1 k_2}, B_{k_3 k_4}] = 0 \,, \tag{3.12a}$$
$$[B^\dagger_{k_1 k_2}, B^\dagger_{k_3 k_4}] = 0 \,, \tag{3.12b}$$
$$[B_{k_1 k_2}, B^\dagger_{k_3 k_4}] = \delta_{k_1 k_3}\delta_{k_2 k_4} - \delta_{k_1 k_4}\delta_{k_2 k_3} \,. \tag{3.12c}$$

The above relations simplify the algebraic properties of the problem and, thus, boson theories have been used as a more suitable representation for the phonon excitations traditionally invoked in the description of collective nuclear phenomena. An extensive review of such techniques is provided in Chapter 9 of Ref. [89] and some examples in close relation to GCM are presented in Sec. 3.6.

Quasi-boson approximation

The zeroth order expansion of fermion pairs in terms of boson operators is provided by the so-called *quasi-boson approximation* (QBA), in which the naive substitution

$$\beta_{k_2}\beta_{k_1} \longrightarrow B_{k_1 k_2} \,, \tag{3.13a}$$
$$\beta^\dagger_{k_1}\beta^\dagger_{k_2} \longrightarrow B^\dagger_{k_1 k_2} \,, \tag{3.13b}$$
$$\beta^\dagger_{k_1}\beta_{k_2} \longrightarrow \sum_j B^\dagger_{k_1 j} B_{k_2 j} \,, \tag{3.13c}$$

is performed. In this frame fermionic pairs are directly replaced with boson operators, thus violating the commutation rules from Eq. (3.11). Also, in such case, the boson and the fermion vacua are assumed to coincide, i.e.

$$B_{k_1 k_2}|\Phi\rangle = 0 \quad \forall\, k_1, k_2 \,. \tag{3.14}$$

The QBA is shown in the following to be at the heart of QRPA.

3.3 Commutator formulation of kernels

A formulation of the kernel evaluation problem alternative to the ones discussed in Chap. 2 is now given in terms of nested commutators. This technique does not provide an easy method to compute the exact solution of the problem but is useful in the derivation of the QRPA as a direct consequence of the QBA.

3.3.1 Operator kernel

Let us consider the quantity $\langle\Phi|e^{\mathbf{L}}Oe^{\mathbf{R}}|\Phi\rangle$ and write it as

$$\begin{aligned}\langle\Phi|e^{\mathbf{L}}Oe^{\mathbf{R}}|\Phi\rangle - O^{[0]} &= \sum_{l=1}^{\infty}\frac{1}{l!}\langle\Phi|\mathbf{L}^l O|\Phi\rangle + \sum_{r=1}^{\infty}\frac{1}{r!}\langle\Phi|O\mathbf{R}^r|\Phi\rangle + \sum_{l,r=1}^{\infty}\frac{1}{l!r!}\langle\Phi|\mathbf{L}^l O\mathbf{R}^r|\Phi\rangle \\ &\equiv S_l + S_r + S_{lr}\,. \end{aligned} \tag{3.15}$$

The notation for nested commutators

$$C_l(L,X) \equiv [\underbrace{L,[L,...[L,[L,X]]...]}_{l \text{ times}}], \tag{3.16a}$$

$$\tilde{C}_r(X,R) \equiv [[...[[X,\underbrace{R],R]...,R}_{r \text{ times}}],R], \tag{3.16b}$$

is then adopted, with

$$C_0(L,X) = \tilde{C}_0(X,R) \equiv X\,. \tag{3.17}$$

The two definitions in Eqs. (3.16) are linked by the property

$$\tilde{C}_m(X,Y) = (-1)^m C_m(Y,X), \tag{3.18}$$

and are useful when recurring to the formulas [123] for $l, r \geq 1$

$$[L^l, X] = \sum_{m=0}^{l-1}\binom{l}{m} C_{l-m}(L,X)L^m\,, \tag{3.19a}$$

$$[X, R^r] = \sum_{m=0}^{r-1}\binom{r}{m} R^m \tilde{C}_{r-m}(X,R). \tag{3.19b}$$

Let us now compute the three contributions on the right hand side of Eq. (3.15). The property $\mathbf{L}|\Phi\rangle = 0$ allows to rewrite S_l introducing a commutator. Hence, Eq. (3.19a) implies

$$\begin{aligned}\langle\Phi|\mathbf{L}^l O|\Phi\rangle &= \langle\Phi|[\mathbf{L}^l, O]|\Phi\rangle \\ &= \sum_{i=1}^{l}\binom{l}{l-i}\langle\Phi|C_i(\mathbf{L},O)\mathbf{L}^{l-i}|\Phi\rangle \\ &= \langle\Phi|C_l(\mathbf{L},O)|\Phi\rangle\,, \end{aligned} \tag{3.20}$$

since the only non-vanishing term is provided by $i = l$. Eventually,

$$S_l = \sum_{l=1}^{\infty}\frac{1}{l!}\langle\Phi|C_l(\mathbf{L},O)|\Phi\rangle\,. \tag{3.21}$$

Similarly, since $\langle\Phi|\mathbf{R} = 0$, let us introduce a commutator into S_r, allowing the application of Eq. (3.19b)

$$\begin{aligned}\langle\Phi|O\mathbf{R}^r|\Phi\rangle &= \langle\Phi|[O,\mathbf{R}^r]|\Phi\rangle \\ &= \sum_{i=1}^{r}\binom{r}{r-i}\langle\Phi|\mathbf{R}^{r-i}\tilde{C}_i(O,\mathbf{R})|\Phi\rangle \end{aligned}$$

$$= \langle \Phi | \tilde{C}_r(O, \mathbf{R}) | \Phi \rangle \,, \tag{3.22}$$

where the only non-vanishing term is provided by $i = r$. Eventually,

$$S_r = \sum_{r=1}^{\infty} \frac{1}{r!} \langle \Phi | \tilde{C}_r(O, \mathbf{R}) | \Phi \rangle \,. \tag{3.23}$$

Keeping in mind that $\langle \Phi | \mathbf{R} = \mathbf{L} | \Phi \rangle = 0$, the term S_{lr} can be written

$$\begin{aligned}
\sum_{l,r=1}^{\infty} \langle \Phi | \mathbf{L}^l O \mathbf{R}^r | \Phi \rangle &= \sum_{l,r=1}^{\infty} \langle \Phi | [\mathbf{L}^l O, \mathbf{R}^r] | \Phi \rangle \\
&= \sum_{l,r=1}^{\infty} \langle \Phi | \mathbf{L}^l [O, \mathbf{R}^r] | \Phi \rangle + \sum_{l,r=1}^{\infty} \langle \Phi | [\mathbf{L}^l, \mathbf{R}^r] O | \Phi \rangle \\
&= \sum_{l,r=1}^{\infty} \langle \Phi | [\mathbf{L}^l, [O, \mathbf{R}^r]] | \Phi \rangle + \sum_{l,r=1}^{\infty} \langle \Phi | [[\mathbf{L}^l, \mathbf{R}^r], O] | \Phi \rangle \\
&= \sum_{l,r=1}^{\infty} \langle \Phi | [[\mathbf{L}^l, O], \mathbf{R}^r]] | \Phi \rangle \,.
\end{aligned} \tag{3.24}$$

The third equivalence from Eq. (3.24) is a consequence of O being a normal-ordered operator, whereas the last equivalence follows from the Jacobi identity. The application of Eq. (3.19b) then implies

$$\begin{aligned}
\langle \Phi | [[\mathbf{L}^l, O] \mathbf{R}^r] | \Phi \rangle &= \sum_{k=0}^{r-1} \binom{r}{k} \langle \Phi | \mathbf{R}^k \tilde{C}_{r-k}([\mathbf{L}^l, O], \mathbf{R}) | \Phi \rangle \\
&= \langle \Phi | \tilde{C}_r([\mathbf{L}^l, O], \mathbf{R}) | \Phi \rangle \,,
\end{aligned} \tag{3.25}$$

since the only non-vanishing term is provided by $k = 0$. Equation (3.19a) then implies

$$\begin{aligned}
\langle \Phi | [[\mathbf{L}^l, O] \mathbf{R}^r] | \Phi \rangle &= \sum_{k=0}^{l-1} \binom{l}{k} \langle \Phi | \tilde{C}_r(C_{l-k}(\mathbf{L}, O) \mathbf{L}^k, \mathbf{R}) | \Phi \rangle \\
&= \sum_{k=0}^{l-1} \binom{l}{k} \sum_{j=0}^{r} \binom{r}{j} \langle \Phi | \tilde{C}_{r-j}(C_{l-k}(\mathbf{L}, O), \mathbf{R}) \tilde{C}_j(\mathbf{L}^k, \mathbf{R}) | \Phi \rangle \,,
\end{aligned} \tag{3.26}$$

where the last equality follows from the identity from Eq. (E.1). Eventually

$$S_{lr} = \sum_{l,r=1}^{\infty} \frac{1}{l!r!} \sum_{k=0}^{l-1} \binom{l}{k} \sum_{j=0}^{r} \binom{r}{j} \langle \Phi | \tilde{C}_{r-j}(C_{l-k}(\mathbf{L}, O), \mathbf{R}) \tilde{C}_j(\mathbf{L}^k, \mathbf{R}) | \Phi \rangle \,. \tag{3.27}$$

Summing the previously obtained contributions one gets

$$S_r + O^{[0]} = \sum_{r=0}^{\infty} \frac{1}{r!} \langle \Phi | \tilde{C}_r(O, \mathbf{R}) | \Phi \rangle \,, \tag{3.28a}$$

$$S_l + S_{lr} = \sum_{l=1}^{\infty} \sum_{k=0}^{l-1} \sum_{r=0}^{\infty} \sum_{j=0}^{r} \frac{1}{k!(l-k)!} \frac{1}{j!(r-j)!} \langle \Phi | \tilde{C}_{r-j}(C_{l-k}(\mathbf{L}, O), \mathbf{R}) \tilde{C}_j(\mathbf{L}^k, \mathbf{R}) | \Phi \rangle \,. \tag{3.28b}$$

The indices within Eq. (3.28b) are easily rearranged providing

$$S_l + S_{lr} = \sum_{l=1}^{\infty}\sum_{k=0}^{\infty}\sum_{r=0}^{\infty}\sum_{j=0}^{\infty}\frac{1}{k!l!}\frac{1}{j!r!}\langle\Phi|\tilde{C}_r(C_l(\mathbf{L},O),\mathbf{R})\tilde{C}_j(\mathbf{L}^k,\mathbf{R})|\Phi\rangle\,, \tag{3.29}$$

so that overall all the terms can be summed in a compact form reading

$$\begin{aligned}\langle\Phi|e^{\mathbf{L}}Oe^{\mathbf{R}}|\Phi\rangle &= O^{[0]} + S_l + S_r + S_{lr}\\ &= \sum_{l,r=0}^{\infty}\frac{1}{l!r!}\sum_{j,k=0}^{\infty}\frac{1}{j!k!}\langle\Phi|\tilde{C}_r(C_l(\mathbf{L},O),\mathbf{R})\tilde{C}_j(\mathbf{L}^k,\mathbf{R})|\Phi\rangle\,.\end{aligned} \tag{3.30}$$

Eventually, Eq. (E.4) is used to rewrite Eq. (3.30) in the form

$$\langle\Phi|e^{\mathbf{L}}Oe^{\mathbf{R}}|\Phi\rangle = \sum_{l,r=0}^{\infty}\frac{1}{l!r!}\langle\Phi|\tilde{C}_r(C_l(\mathbf{L},O),\mathbf{R})\exp\left\{\sum_{k=0}^{\infty}\frac{1}{k!}\tilde{C}_k(\mathbf{L},\mathbf{R})\right\}|\Phi\rangle\,, \tag{3.31}$$

which represents an exact expression of the operator kernel. Equation (3.31) actually provides a general expression to compute the average over a state $|\Phi\rangle$ of any operator O which is transformed using two different exponential maps (as opposed to similarity transformations) on the left and on the right, under the only assumption $\langle\Phi|\mathbf{R}=\mathbf{L}|\Phi\rangle = 0$. For $\mathbf{L}$ and $\mathbf{R}$ defined as in Eqs. (2.4), the series in the exponent happens to truncate for all $k > 2$, as it is shown in Eq. (E.7c). Thus, only taking into account the non-vanishing terms in the exponent, Eq. (3.31) reads[2]

$$\langle\Phi(l)|O|\Phi(r)\rangle = \langle\Phi(l)|\Phi\rangle\langle\Phi|\Phi(r)\rangle\sum_{l,r=0}^{\infty}\frac{1}{l!r!}\langle\Phi|\tilde{C}_r(C_l(\mathbf{L},O),\mathbf{R})\exp\left\{\mathbf{L}+[\mathbf{L},\mathbf{R}]+\frac{1}{2}[[\mathbf{L},\mathbf{R}],\mathbf{R}]\right\}|\Phi\rangle\,. \tag{3.32}$$

3.3.2 Norm kernel

In this notation the norm kernel is computed as a special case of Eq. (3.32) taking $O = \mathbb{1}$. In such case the only non-vanishing contribution is obtained for $l = 0$, such that

$$\frac{\langle\Phi(l)|\Phi(r)\rangle}{\langle\Phi(l)|\Phi\rangle\langle\Phi|\Phi(r)\rangle} = \langle\Phi|\exp\left\{\sum_{k=0}^{\infty}\frac{1}{k!}\tilde{C}_k(\mathbf{L},\mathbf{R})\right\}|\Phi\rangle\,. \tag{3.33}$$

3.4 Introduction of the QBA

In the derivation of Eqs. (3.32) and (3.33) no approximation was made, so that the commutator formulation may appear a cumbersome alternative to previously discussed expressions (see Chap. 2). However, this notation is of interest when introducing the QBA, which has been presented in Sec. 3.2.

Under this assumption, the $\mathbf{L}$ and $\mathbf{R}$ operators introduced in Eqs. (2.4) are rewritten in the quasi-boson picture, i.e. employing the replacement of Eqs. (3.13), providing

$$\mathbf{L} \approx \sum_{\lambda}\frac{1}{2}\mathbf{z}^*_{\lambda}(l)B_{\lambda}\,, \tag{3.34a}$$

$$\mathbf{R} \approx \sum_{\rho}\frac{1}{2}\mathbf{z}^{\rho}(r)B^{\dagger}_{\rho}\,. \tag{3.34b}$$

[2] No ambiguity should rise from the simultaneous use of l and r to refer both to the generator coordinates (of the left and right vacuum respectively) and to the dummy indices in the sums.

In the QBA, thus, the commutator $[\mathbf{L},\mathbf{R}]$ is a number

$$\begin{aligned}[\mathbf{L},\mathbf{R}] &= \frac{1}{4}\sum_{\lambda\rho}\mathbf{z}^{*}_{\lambda}(l)\mathbf{z}^{\rho}(r)[B_{\lambda},B^{\dagger}_{\rho}] \\ &= \frac{1}{4}\mathrm{Tr}\Big\{\mathbf{z}^{\dagger}(l)\mathbf{z}(r)\Big\} \\ &\equiv \mathbf{c}(l,r)\,, \end{aligned} \tag{3.35}$$

which naturally leads to

$$[[\mathbf{L},\mathbf{R}],\mathbf{R}] = 0\,. \tag{3.36}$$

Given that $e^{\mathbf{L}}|\Phi\rangle = 0$, the operator kernel from Eq. (3.32) reduces to

$$\frac{\langle\Phi(l)|O|\Phi(r)\rangle}{\langle\Phi(l)|\Phi\rangle\langle\Phi|\Phi(r)\rangle} \approx e^{\mathbf{c}(l,r)}\sum_{l,r=0}^{\infty}\frac{1}{l!r!}\langle\Phi|\tilde{C}_r(C_l(\mathbf{L},O),\mathbf{R})|\Phi\rangle\,, \tag{3.37}$$

whereas the norm kernel in Eq. (3.33) becomes

$$\frac{\langle\Phi(l)|\Phi(r)\rangle}{\langle\Phi(l)|\Phi\rangle\langle\Phi|\Phi(r)\rangle} \approx e^{\mathbf{c}(l,r)}\,, \tag{3.38}$$

the connected operator kernel becoming

$$\frac{\langle\Phi(l)|O|\Phi(r)\rangle}{\langle\Phi(l)|\Phi(r)\rangle} \approx \sum_{l,r=0}^{\infty}\frac{1}{l!r!}\langle\Phi|\tilde{C}_r(C_l(\mathbf{L},O),\mathbf{R})|\Phi\rangle\,. \tag{3.39}$$

The simplified bosonic algebra provided by the commutators in Eqs. (3.12) naturally truncates the expansion in Eq. (3.39) at order $n+1$ if an n-body operator O is considered. Thus, Eq. (3.39) can be written

$$\begin{aligned}\frac{\langle\Phi(l)|O|\Phi(r)\rangle}{\langle\Phi(l)|\Phi(r)\rangle} &\approx \sum_{l,r=0}^{l+r\leq n+1}\frac{1}{l!r!}\langle\Phi|\tilde{C}_r(C_l(\mathbf{L},O),\mathbf{R})|\Phi\rangle \\ &= \sum_{i=0}^{n+1}\sum_{l,r=0}^{l+r=i}\frac{1}{l!r!}\langle\Phi|\tilde{C}_r(C_l(\mathbf{L},O),\mathbf{R})|\Phi\rangle\,. \end{aligned} \tag{3.40}$$

In the notation of Eqs. (3.34), Eq. (3.40) reads as

$$\begin{aligned}\frac{\langle\Phi(l)|O|\Phi(r)\rangle}{\langle\Phi(l)|\Phi(r)\rangle} \approx \sum_{i=0}^{n+1}\sum_{l,r=0}^{l+r=i}\frac{1}{l!r!}\frac{1}{2^{l+r}}\sum_{\substack{\lambda_1\ldots\lambda_l\\ \rho_1\ldots\rho_r}}&[\mathbf{z}^{\dagger}_{\lambda_1}\ldots\mathbf{z}^{\dagger}_{\lambda_l}](l)[\mathbf{z}^{\rho_1}\ldots\mathbf{z}^{\rho_r}](r)\times \\ &\times\langle\Phi|[[[[B_{\lambda_1},[B_{\lambda_2},\ldots[B_{\lambda_l},O]\ldots]],B^{\dagger}_{\rho_1}],B^{\dagger}_{\rho_2}]\ldots,B^{\dagger}_{\rho_r}]|\Phi\rangle\,. \end{aligned} \tag{3.41}$$

Following Ref. [121] the transformed functions

$$\begin{aligned}\tilde{f}_{\nu}(l) &\equiv \sum_{r}\langle\Phi|\Phi(r)\rangle\exp\left[\frac{1}{4}\sum_{\gamma}\mathbf{z}^{\dagger}_{\gamma}(l)\mathbf{z}^{\gamma}(r)\right]f_{\nu}(r) \\ &= \sum_{r}\langle\Phi|\Phi(r)\rangle\, e^{\mathbf{c}(l,r)}f_{\nu}(r) \end{aligned} \tag{3.42}$$

are introduced. The functions $\tilde{f}_\nu(l)$ verify the equation

$$2\frac{\partial \tilde{f}_\nu(l)}{\partial \mathbf{z}^\dagger_\alpha(l)} = \sum_r \frac{1}{2}\mathbf{z}^\alpha(r)e^{\mathbf{c}(l,r)}f_\nu(r). \tag{3.43}$$

It is immediate to check that the quantities $\mathbf{z}^\dagger_\alpha(l)$ and $\frac{\partial}{\mathbf{z}^\dagger_\alpha(l)}$ behave like boson creation and annihilation operators respectively. Indeed, defining

$$b^\dagger_\alpha \equiv \frac{1}{2}\mathbf{z}^\dagger_\alpha(l), \tag{3.44a}$$

$$b_\alpha \equiv 2\frac{\partial}{\mathbf{z}^\dagger_\alpha(l)}, \tag{3.44b}$$

one can easily prove that the operators in Eqs. (3.44) satisfy the bosonic commutation rules from Eq. (3.12). Substituting Eq. (3.41) in the HWQ secular equation (1.9) of the GCM and using the notation introduced in Eqs. (3.44), Eq. (1.9) eventually reads

$$\Bigg[\sum_{i=0}^{n+1}\sum_{l,r=0}^{l+r=i}\frac{1}{l!r!}\sum_{\substack{\lambda_1\dots\lambda_l\\ \rho_1\dots\rho_r}} b^\dagger_{\lambda_1}\dots b^\dagger_{\lambda_l}b_{\rho_1}\dots b_{\rho_r}\langle\Phi|[[[[B_{\lambda_1},[B_{\lambda_2},\dots[B_{\lambda_l},H]\dots]],B^\dagger_{\rho_1}],B^\dagger_{\rho_2}]\dots,B^\dagger_{\rho_r}]|\Phi\rangle - E_\nu\Bigg]\tilde{f}_\nu(l) = 0\,, \tag{3.45}$$

where the normalisation $\langle\Phi(l)|\Phi\rangle$ is assumed to be non-vanishing in order to simplify it. The l coordinate appears in Eq. (3.45) only in $\tilde{f}_\nu(l)$, such that the solutions to Eq. (3.45) do not depend on the selected generator coordinates and the l dependence can actually be omitted.

3.5 Derivation of the QRPA equations

Equation (3.45) is now written in the more compact form

$$\Bigg[\sum_{i=0}^{n+1} M^{[i]} - E_\nu\Bigg]\tilde{f}_\nu(p) = 0\,, \tag{3.46}$$

where the contribution $M^{[i]}$ of order i in $\mathbf{z}$ is defined as

$$M^{[i]} \equiv \sum_{l,r=0}^{l+r=i}\frac{1}{l!r!}\sum_{\substack{\lambda_1\dots\lambda_l\\ \rho_1\dots\rho_r}} b^\dagger_{\lambda_1}\dots b^\dagger_{\lambda_l}b_{\rho_1}\dots b_{\rho_r}\langle\Phi|[[[[B_{\lambda_1},[B_{\lambda_2},\dots[B_{\lambda_l},H]\dots]],B^\dagger_{\rho_1}],B^\dagger_{\rho_2}]\dots,B^\dagger_{\rho_r}]|\Phi\rangle\,. \tag{3.47}$$

Contributions at different orders i are addressed separately in the following sections up to the second order. The usual QRPA equations are then showed to be recovered when a second-order truncation is indeed considered. Third-order contributions are provided in App. F, which may be of interest for the development of a set of QRPA equations explicitly considering the presence of three-body forces.

3.5.1 First order

Setting $i = 1$ in Eq. (3.47), the first order contribution is provided by

$$M^{[1]} = \sum_\lambda b^\dagger_\lambda\langle\Phi|[B_\lambda,H]|\Phi\rangle + \sum_\rho b_\rho\langle\Phi|[H,B^\dagger_\rho]|\Phi\rangle\,. \tag{3.48}$$

The Hamiltonian is then split according to its many-body content, so that the contributions coming from different terms can be computed separately upon the substitution of Eq. (3.13) into Eq. (A.2). The only non-vanishing contributions originate from the one-body normal-ordered part of H, i.e.

$$\begin{aligned}\langle\Phi|[B_{k_1l_1},\mathbf{H}^{[1]}]|\Phi\rangle &= \langle\Phi|[B_{k_1l_1},\mathbf{H}^{20}]|\Phi\rangle \\ &= \sum_{k_2l_2}\mathbf{h}^{k_2l_2}\langle\Phi|[B_{k_1l_1},B^\dagger_{k_2l_2}]|\Phi\rangle\,, \\ &= \mathbf{h}^{k_1l_1} \qquad (3.49a)\\ \langle\Phi|[\mathbf{H}^{[1]},B^\dagger_{k_1l_1}]|\Phi\rangle &= \langle\Phi|[\mathbf{H}^{02},B^\dagger_{k_1l_1}]|\Phi\rangle \\ &= \sum_{k_2l_2}\mathbf{h}_{k_2l_2}\langle\Phi|[B_{k_2l_2},B^\dagger_{k_1l_1}]|\Phi\rangle \\ &= \mathbf{h}_{k_1l_1}\,. \qquad (3.49b)\end{aligned}$$

Still, if the Hamiltonian is normal ordered with respect to the HFB solution $|\Phi\rangle$, as it is the case here, the terms $\mathbf{H}^{20}$ and $\mathbf{H}^{02}$ vanish identically, so that, overall

$$\langle\Phi|[B_{k_1l_1},\mathbf{H}^{[1]}]|\Phi\rangle = \langle\Phi|[\mathbf{H}^{[1]},B^\dagger_{k_1l_1}]|\Phi\rangle = 0\,, \qquad (3.50a)$$

$$\langle\Phi|[B_{k_1l_1},\mathbf{H}^{[2]}]|\Phi\rangle = \langle\Phi|[\mathbf{H}^{[2]},B^\dagger_{k_1l_1}]|\Phi\rangle = 0\,, \qquad (3.50b)$$

$$\langle\Phi|[B_{k_1l_1},\mathbf{H}^{[3]}]|\Phi\rangle = \langle\Phi|[\mathbf{H}^{[3]},B^\dagger_{k_1l_1}]|\Phi\rangle = 0\,, \qquad (3.50c)$$

and eventually

$$M^{[1]} = 0\,. \qquad (3.51)$$

3.5.2 Second order

Setting $i = 2$ Eq. (3.47) reduces to three possible combinations of l and r, i.e.

$$\begin{aligned}M^{[2]} =& \frac{1}{2}\sum_{\lambda_1\lambda_2} b^\dagger_{\lambda_1}b^\dagger_{\lambda_2}\langle\Phi|[B_{\lambda_1},[B_{\lambda_2},H]]|\Phi\rangle + \sum_{\lambda_1\rho_1} b^\dagger_{\lambda_1}b_{\rho_1}\langle\Phi|[[B_{\lambda_1},H],B^\dagger_{\rho_1}]]|\Phi\rangle \\ &+\frac{1}{2}\sum_{\rho_1\rho_2} b_{\rho_1}b_{\rho_2}\langle\Phi|[[H,B^\dagger_{\rho_1}],B^\dagger_{\rho_2}]|\Phi\rangle\,. \qquad (3.52)\end{aligned}$$

The non-vanishing contributions in Eq. (3.52) originate from the one-body normal-ordered part of H

$$\begin{aligned}\langle\Phi|[[B_{k_1l_1},\mathbf{H}^{[1]}],B^\dagger_{k_2l_2}]|\Phi\rangle &= \langle\Phi|[[B_{k_1l_1},\mathbf{H}^{11}],B^\dagger_{k_2l_2}]|\Phi\rangle \\ &= \sum_{\substack{k_3l_3\\ j}}\mathbf{h}^{k_3}{}_{l_3}\langle\Phi|[[B_{k_1l_1},B^\dagger_{k_3j}B_{l_3j}],B^\dagger_{k_2l_2}]|\Phi\rangle \\ &= \mathbf{h}^{k_1}{}_{k_2}\delta_{l_1l_2}\,, \qquad (3.53)\end{aligned}$$

as well as from the two-body normal-ordered part of H

$$\begin{aligned}\langle\Phi|[[B_{k_1l_1},\mathbf{H}^{[2]}],B^\dagger_{k_2l_2}]|\Phi\rangle &= \langle\Phi|[[B_{k_1l_1},\mathbf{H}^{22}],B^\dagger_{k_2l_2}]|\Phi\rangle \\ &= \frac{1}{4}\sum_{\substack{k_3l_3\\ k_4l_4}}\mathbf{h}^{k_3l_3}{}_{k_4l_4}\langle\Phi|[[B_{k_1l_1},B^\dagger_{k_3l_3}B_{k_4l_4}],B^\dagger_{k_2l_2}]|\Phi\rangle\end{aligned}$$

$$= \frac{1}{4}\mathbf{h}^{k_1 l_1}{}_{k_2 l_2}, \tag{3.54a}$$

$$\begin{aligned}\langle\Phi|[B_{k_1 l_1},[B_{k_2 l_2},\mathbf{H}^{[2]}]]|\Phi\rangle &= \langle\Phi|[B_{k_1 l_1},[B_{k_2 l_2},\mathbf{H}^{40}]]|\Phi\rangle \\ &= \frac{1}{4!}\sum_{\substack{k_3 l_3\\ k_4 l_4}} \mathbf{h}^{k_3 l_3 k_4 l_4}\langle\Phi|[B_{k_1 l_1},[B_{k_2 l_2},B^\dagger_{k_3 l_3}B^\dagger_{k_4 l_4}]]|\Phi\rangle \\ &= \frac{1}{12}\mathbf{h}^{k_1 l_1 k_2 l_2},\end{aligned} \tag{3.54b}$$

$$\begin{aligned}\langle\Phi|[[\mathbf{H}^{[2]},B^\dagger_{k_1 l_1}],B^\dagger_{k_2 l_2}]|\Phi\rangle &= \langle\Phi|[[\mathbf{H}^{04},B^\dagger_{k_1 l_1}],B^\dagger_{k_2 l_2}]|\Phi\rangle \\ &= \frac{1}{12}\mathbf{h}_{k_1 l_1 k_2 l_2}.\end{aligned} \tag{3.54c}$$

Upon the introduction of the matrices

$$\begin{aligned}A_{k_1 l_1 k_2 l_2} \equiv\ & [B_{k_1 l_1},[H,B^\dagger_{k_2 l_2}]] \\ =\ & [B_{k_1 l_1},[\mathbf{H}^{11}+\mathbf{H}^{22},B^\dagger_{k_2 l_2}]] \\ =\ & \mathbf{h}^{k_1}{}_{k_2}\delta_{l_1 l_2}+\frac{1}{4}\mathbf{h}^{k_1 l_1}{}_{k_2 l_2},\end{aligned} \tag{3.55a}$$

$$\begin{aligned}B_{k_1 l_1 k_2 l_2} \equiv & -[B_{k_1 l_1},[H,B_{k_2 l_2}]] \\ = & -[B_{k_1 l_1},[\mathbf{H}^{40},B_{k_2 l_2}]] \\ = & -\frac{1}{12}\mathbf{h}^{k_1 l_1 k_2 l_2},\end{aligned} \tag{3.55b}$$

Eq. (3.52) eventually reads

$$\begin{aligned}M^{[2]} &= \frac{1}{2}\sum_{\lambda_1\lambda_2} B_{\lambda_1\lambda_2}b^\dagger_{\lambda_1}b^\dagger_{\lambda_2}+\sum_{\lambda_1\rho_1}A_{\lambda_1\rho_1}b^\dagger_{\lambda_1}b_{\rho_1}+\frac{1}{2}\sum_{\rho_1\rho_2}B^*_{\rho_1\rho_2}b_{\rho_1}b_{\rho_2} \\ &= \sum_{\alpha\beta}\frac{1}{2}\Big[B_{\alpha\beta}b^\dagger_\alpha b^\dagger_\beta+B^*_{\alpha\beta}b_\alpha b_\beta+A_{\alpha\beta}b^\dagger_\alpha b_\beta+A^*_{\alpha\beta}b_\alpha b^\dagger_\beta-A_{\alpha\beta}\delta_{\alpha\beta}\Big].\end{aligned} \tag{3.56}$$

3.5.3 Solution of the differential equation for $n = 2$

Given the second-order contributions in Eq. (3.56), Eq. (3.45) reads

$$\sum_{\alpha\beta}\frac{1}{2}\Big[B_{\alpha\beta}b^\dagger_\alpha b^\dagger_\beta+B^*_{\alpha\beta}b_\alpha b_\beta+A_{\alpha\beta}b^\dagger_\alpha b_\beta+A^*_{\alpha\beta}b_\alpha b^\dagger_\beta-A_{\alpha\beta}\delta_{\alpha\beta}-2(E_\nu-E_0)\Big]\tilde{f}_\nu=0. \tag{3.57}$$

The solution of Eq. (3.57) amounts to diagonalising the reduced Hamiltonian (quadratic form)

$$\begin{aligned}\tilde{H} &= E_0-\frac{1}{2}\mathrm{Tr}A+\frac{1}{2}\begin{pmatrix}b^\dagger & b\end{pmatrix}\begin{pmatrix}A & B\\ B^* & A^*\end{pmatrix}\begin{pmatrix}b\\ b^\dagger\end{pmatrix} \\ &\equiv E_0-\frac{1}{2}\mathrm{Tr}A+\frac{1}{2}\begin{pmatrix}b^\dagger & b\end{pmatrix}\mathcal{S}\begin{pmatrix}b\\ b^\dagger\end{pmatrix},\end{aligned} \tag{3.58}$$

where the stability matrix S of the HFB solution $|\Phi\rangle$ has been introduced [124]. The diagonalisation problem for boson operators is addressed by introducing a Bogoliubov transformation in the form of Eq. (3.2) into Eq. (3.58)

$$\tilde{H}=E_0-\frac{1}{2}\mathrm{Tr}A+\frac{1}{2}\begin{pmatrix}\gamma^\dagger & \gamma\end{pmatrix}\mathcal{X}^\dagger\mathcal{S}\mathcal{X}\begin{pmatrix}\gamma\\ \gamma^\dagger\end{pmatrix}. \tag{3.59}$$

Equation (3.9) is then employed to recast the diagonalisation problem into the form

$$\eta\mathcal{S}\mathcal{X} = \mathcal{X}\eta\tilde{\Omega} \tag{3.60}$$

or, in extended form,

$$\begin{pmatrix} A & B \\ -B^* & -A^* \end{pmatrix}\begin{pmatrix} X & Y^* \\ Y & X^* \end{pmatrix} = \begin{pmatrix} \Omega^{(+)} & \mathbb{0} \\ \mathbb{0} & -\Omega^{(-)} \end{pmatrix}\begin{pmatrix} X & Y^* \\ Y & X^* \end{pmatrix}, \tag{3.61}$$

where $\Omega^{(+)}$ and $\Omega^{(-)}$ are diagonal matrices containing the eigenvalues of the problem. The explicit evaluation of the matrix product in Eq. (3.61) easily leads to the property

$$\Omega^{(-)} = \left(\Omega^{(+)}\right)^*, \tag{3.62}$$

so that defining

$$\Omega \equiv \Omega^{(+)} \tag{3.63}$$

the problem reduces, without redundancies, to

$$\begin{pmatrix} A & B \\ -B^* & -A^* \end{pmatrix}\begin{pmatrix} X \\ Y \end{pmatrix} = \begin{pmatrix} \Omega & \mathbb{0} \\ \mathbb{0} & -\Omega^* \end{pmatrix}\begin{pmatrix} X \\ Y \end{pmatrix}, \tag{3.64}$$

which is exactly the QRPA eigenvalue equation determining QRPA eigenfrequencies and eigenvectors. Having solved Eq. (3.64), the reduced Hamiltonian can be written as

$$\begin{aligned} \tilde{H} &= E_0 - \frac{1}{2}\mathrm{Tr}A + \frac{1}{2}\sum_\alpha (\Omega_\alpha \gamma^\dagger_\alpha \gamma_\alpha + \Omega^*_\alpha \gamma_\alpha \gamma^\dagger_\alpha) \\ &= E_0 - \frac{1}{2}\mathrm{Tr}A + \frac{1}{2}\sum_\alpha (\Omega_\alpha \gamma^\dagger_\alpha \gamma_\alpha + \Omega^*_\alpha \gamma^\dagger_\alpha \gamma_\alpha + \Omega^*_\alpha) \\ &= E_0 - \frac{1}{2}\mathrm{Tr}A + \frac{1}{2}\sum_\alpha \Omega^*_\alpha + \sum_\alpha \mathrm{Re}(\Omega_\alpha)\gamma^\dagger_\alpha \gamma_\alpha \,. \end{aligned} \tag{3.65}$$

The absolute energies of QRPA excited states are provided by

$$E_\alpha = E_0^{\mathrm{QRPA}} + \mathrm{Re}(\Omega_\alpha), \tag{3.66}$$

where

$$E_0^{\mathrm{QRPA}} \equiv E_0 - \frac{1}{2}\mathrm{Tr}A + \frac{1}{2}\sum_\alpha \Omega^*_\alpha \,. \tag{3.67}$$

An explicit form can be obtained for the collective wave-functions $\tilde{f}_\nu$. The ground-state wave-function represents the vacuum for the annihilation operators γ

$$\gamma_\alpha \tilde{f}_0 = 0\,, \tag{3.68}$$

and the excited states can be reached through the application of creation operators $\gamma^\dagger$ to the ground-state function f_0.

3.6 Boson expansion methods and self-consistent correction to QRPA

QRPA was derived is Sec. 3.5 as the formal solution of the Hill-Wheeler-Griffin equation under the QBA. Such an approximation represents the zeroth order of more refined techniques, routinely referred to as *boson expansion methods*. The existing link between the GCM and boson expansion techniques and their natural appearance in this context are briefly discussed in the present section.

3.6.1 Dyson expansion

It is here shown how the Dyson boson expansion naturally emerges within the GCM framework. The definitions of the norm overlap in Eq. (2.28) and of the elementary contractions in Eqs. (2.17) and (2.19) can be used to prove the relations

$$\mathcal{N}(\mathbf{z}^*,\mathbf{z}') = \exp\left\{\frac{1}{2}\mathrm{Tr}\ln\left(1-\mathbf{z}^*\cdot\mathbf{z}'\right)\right\}, \tag{3.69a}$$

$$\begin{aligned}\kappa_{kl}(\mathbf{z}^*,\mathbf{z}')\mathcal{N}(\mathbf{z}^*,\mathbf{z}') &= \left\{\mathbf{z}'\cdot\frac{1}{1-\mathbf{z}^*\cdot\mathbf{z}'}\right\}_{kl}\mathcal{N}(\mathbf{z}^*,\mathbf{z}') \\ &= \frac{\partial}{\partial\mathbf{z}^*_{kl}}\mathcal{N}(\mathbf{z}^*,\mathbf{z}'),\end{aligned} \tag{3.69b}$$

$$\begin{aligned}\bar{\kappa}^*_{kl}(\mathbf{z}^*,\mathbf{z}')\mathcal{N}(\mathbf{z}^*,\mathbf{z}') &= \left\{\frac{1}{1-\mathbf{z}^*\cdot\mathbf{z}'}\cdot\mathbf{z}^*\right\}\mathcal{N}(\mathbf{z}^*,\mathbf{z}') \\ &= \left(\mathbf{z}^*_{kl}+\sum_{ij}\mathbf{z}^*_{ki}\mathbf{z}^*_{jl}\frac{\partial}{\partial\mathbf{z}^*_{ji}}\right)\mathcal{N}(\mathbf{z}^*,\mathbf{z}') \\ &= \frac{\partial}{\partial\mathbf{z}'_{kl}}\mathcal{N}(\mathbf{z}^*,\mathbf{z}'),\end{aligned} \tag{3.69c}$$

$$\begin{aligned}\rho_{kl}(\mathbf{z}^*,\mathbf{z}')\mathcal{N}(\mathbf{z}^*,\mathbf{z}') &= -\left\{\mathbf{z}'\cdot\frac{1}{1-\mathbf{z}^*\cdot\mathbf{z}'}\cdot\mathbf{z}^*\right\}\mathcal{N}(\mathbf{z}^*,\mathbf{z}') \\ &= \sum_i \mathbf{z}^*_{li}\frac{\partial}{\partial\mathbf{z}^*_{ki}}\mathcal{N}(\mathbf{z}^*,\mathbf{z}').\end{aligned} \tag{3.69d}$$

Detailed derivations are provided in App. G. If $\mathbf{z}$ and $\mathbf{z}^*$ are used as independent variables the differential operator satisfies the canonical commutation rules

$$\left[\frac{\partial}{\partial\mathbf{z}^*_{kl}},\mathbf{z}^*_{mn}\right] = \delta_{km}\delta_{ln}-\delta_{kn}\delta_{lm}, \tag{3.70a}$$

$$\left[\frac{\partial}{\partial\mathbf{z}^*_{kl}},\mathbf{z}_{mn}\right] = 0 \tag{3.70b}$$

with respect to the norm overlap. Upon the introduction of boson creation and annihilation operators (equivalently to Sec. 3.4)

$$B^\dagger_{kl} \equiv \mathbf{z}^*_{kl}, \tag{3.71a}$$

$$B_{kl} \equiv \frac{\partial}{\partial\mathbf{z}^*_{kl}}, \tag{3.71b}$$

the contractions from Eqs. (3.69) are exactly expressed in terms of the Dyson boson expansion [125]

$$\beta_l\beta_k \to B_{kl}, \tag{3.72a}$$

$$\beta^\dagger_k\beta^\dagger_l \to B^\dagger_{kl}+\sum_{jm}B^\dagger_{kj}B^\dagger_{lm}B_{jm}, \tag{3.72b}$$

$$\beta^\dagger_k\beta_l \to \sum_j B^\dagger_{kj}B_{lj} \tag{3.72c}$$

acting on the norm kernel. This relates to the four fundamental contractions being fermionic pair operators, which can be re-expressed in terms of bosonic expansions. However, it should be stressed that in this case the expectation value of fermionic pairs is being considered, not the fermionic pairs themselves.

The Dyson boson expansion, differently from other examples, is finite. In this respect, it can only be used in its original form and it is not suitable for perturbative expansions. In the Dyson formalism operators are no longer Hermitian in the boson space, which has been shown to lead to the appearance of spurious states. The elimination of spurious solutions is to be ensured by the applications of projectors onto the physical boson subspace (see Ref. [126] for an extensive discussion) or deleting the states associated to vanishing values of the norm kernel (which is a customary practice in the numerical implementation of the GCM).

The origin of such an asymmetry is found in the choice of a specific variable to work with (in this case $\mathbf{z}^*$). However, as can be seen from Eq. (3.69c), the problem could be equally and symmetrically formulated in terms of the other variable, so that an equivalent formulation as a function of $\mathbf{z}'$ could be envisaged.

3.6.2 Holstein-Primakoff or Beliaev-Zelevinski expansion

A more symmetric infinite expansion allowing one to perform truncations with different levels of accuracy is the Holstein-Primakoff or Beliaev-Zelevinsky expansion [127, 128, 129, 130, 131]. In order to provide a link with the Dyson expansion, let us introduce the following change of variables

$$\begin{aligned}\mathbf{x} &\equiv \mathbf{z}' \cdot (1 - \mathbf{z}^* \cdot \mathbf{z}')^{-1/2} \\ &= (1 - \mathbf{z}' \cdot \mathbf{z}^*)^{-1/2} \cdot \mathbf{z}', \qquad (3.73a)\\ \mathbf{y} &\equiv -(1 - \mathbf{z}^* \cdot \mathbf{z}')^{-1/2} \cdot \mathbf{z}^* \\ &= -\mathbf{z}^* \cdot (1 - \mathbf{z}' \cdot \mathbf{z}^*)^{-1/2}, \qquad (3.73b)\end{aligned}$$

providing the relations

$$\begin{aligned}(1 - \mathbf{z}' \cdot \mathbf{z}^*)^{-1} &= 1 - \mathbf{x} \cdot \mathbf{y}, \qquad (3.74a)\\ -\mathbf{z}' \cdot \frac{1}{1 - \mathbf{z}^* \cdot \mathbf{z}'} \cdot \mathbf{z}^* &= \mathbf{x} \cdot \mathbf{y} \\ &= \rho(\mathbf{x}, \mathbf{y}), \qquad (3.74b)\\ \mathbf{z}' \cdot \frac{1}{1 - \mathbf{z}^* \cdot \mathbf{z}'} &= \sqrt{1 - \mathbf{x} \cdot \mathbf{y}} \cdot \mathbf{x} \\ &= \kappa(\mathbf{x}, \mathbf{y}), \qquad (3.74c)\\ \frac{1}{1 - \mathbf{z}^* \cdot \mathbf{z}'} \cdot \mathbf{z}^* &= -\mathbf{y} \cdot \sqrt{1 - \mathbf{x} \cdot \mathbf{y}} \\ &= \bar{\kappa}^*(\mathbf{x}, \mathbf{y}). \qquad (3.74d)\end{aligned}$$

The overlap kernel in terms of the new variable is re-expressed as

$$\mathcal{N}(\mathbf{x}, \mathbf{y}) = \exp\left\{ -\frac{1}{2} \mathrm{Tr} \ln \left(1 - \mathbf{y} \cdot \mathbf{x}\right)\right\}. \qquad (3.75)$$

Equations (3.74) are just the c-number form of the infinite boson expansion of Holstein and Primakoff. Since no approximation has been made up to this point (only a change of variables has been performed) the exact one-body densities are found. The same algebra of fermionic pairs provided in Eqs. (3.11) is found replacing the quantal commutators of operators A and B with Poisson brackets [130, 132] defined by

$$[A, B] \quad \longrightarrow \quad \frac{1}{2} \sum_{kl} \left[\frac{\partial A}{\partial \mathbf{x}_{kl}} \frac{\partial B}{\partial \mathbf{y}_{kl}} - \frac{\partial A}{\partial \mathbf{y}_{kl}} \frac{\partial B}{\partial \mathbf{x}_{kl}} \right] \equiv [\![A, B]\!]. \qquad (3.76)$$

Indeed, the following relations are obtained

$$[\![\kappa_{k_1 l_1}, \kappa_{k_2 l_2}]\!] = [\![\bar{\kappa}^*_{k_1 l_1}, \bar{\kappa}^*_{k_2 l_2}]\!] = 0, \qquad (3.77a)$$

$$[\![\kappa_{k_1 l_1}, \bar{\kappa}^*_{k_2 l_2}]\!] = \delta_{k_1 k_2}\delta_{l_1 l_2} - \delta_{l_1 k_2}\delta_{k_1 l_2} + \delta_{k_1 l_2}\rho_{l_1 k_2} + \delta_{l_1 k_2}\rho_{k_1 l_2} - \delta_{l_1 l_2}\rho_{k_1 k_2} - \delta_{k_1 k_2}\rho_{l_1 l_2}\,, \tag{3.77b}$$

$$[\![\kappa_{k_1 l_1}, \rho_{k_2 l_2}]\!] = \delta_{l_1 l_2}\kappa_{k_1 k_2} - \delta_{k_1 l_2}\kappa_{l_1 k_2}\,, \tag{3.77c}$$

$$[\![\rho_{k_1 l_1}, \rho_{k_2 l_2}]\!] = \delta_{k_1 l_2}\rho_{k_2 l_1} - \delta_{l_1 k_2}\rho_{k_1 l_2}\,, \tag{3.77d}$$

which are equivalent to Eqs. (3.11) when c-numbers are involved instead of fermionic pairs.

3.7 Summary

The link between the GCM based on Bogoliubov states and QRPA has been discussed in the present chapter. After having presented the Bogoliubov transformation for bosons in Sec. 3.1, the problem of mapping fermion pairs onto boson was introduced in Sec. 3.2, together with the QBA. The kernels evaluation problem was reformulated in Sec. 3.3 within a nested-commutator formalism, which proved to be particularly convenient upon the introduction of the QBA (Sec. 3.4). The QRPA equations are then derived in Sec. 3.5 solving the HWG equation within the QBA. The QBA based on a two-body Hamiltonian introduces a truncation of the problem at the harmonic level, making the QRPA the harmonic approximation of the GCM. The boson expansion theories of Dyson or Beliaev and Zelevinsky were then discussed in association to the GCM in Sec. 3.6.

The main drawback of the QBA relates to the Pauli principle violation associated to the equivalence assumption between the boson and the HFB ground state. Two different classes of strategies may alleviate this problem. A first solution, which met great success in the past, invokes more sophisticated boson mappings to reduce the Pauli principle violation, at the price of producing more elaborated theories [133, 134]. Alternatively, a self-consistent determination of the QRPA bosonic ground state [135, 136, 137, 138, 73] would solve the Pauli principle violation still dealing with a (consistently-treated) harmonic approximation.

Both ways are difficult to realise in practice, large-scale QRPA calculations already constituting a challenging numerical task. It is noticed here that the GCM does not suffer from any of these pathologies, i.e. the fermion pairs are exactly treated and no harmonic approximation is required. The price to pay is an explicit dependence on the generator coordinates, preventing in practice a systematic exploration of the parameters space. The comparison of *ab initio* (P)GCM calculations based on various sets of collective coordinates and of QRPA calculations is provided in Chap. 9 for a selection of nuclei of increasing complexity.

Chapter 4

Response functions and their moments

Contents

In this chapter the strength function induced by an external excitation is introduced in Sec. 4.1. The associated moments are shown to be representable in terms of the expectation value of n-body operators in the ground state (Secs. 4.2 and 4.3). Different approximations used for the evaluation of high moments are then discussed in Sec. 4.4. Eventually, the relation to physical observables is recalled in Sec. 4.5 for completeness.

4.1 Linear response theory: a primer

Let us consider a physical system in the presence of an external time-dependent scalar field $h(t)$ that couples to an observable of the system described by the Hermitian operator F. The total Hamiltonian can be written as

$$\begin{aligned} H(t) &= H + \tilde{F}(t) \\ &\equiv H + h(t)\,F\,, \end{aligned} \tag{4.1}$$

where H is the Hamiltonian in the absence of the external field. The external perturbation is turned on at time $t = 0$ such that $H(0) = H$. Let then $|\bar{\Psi}(t)\rangle$ be the solution of the time-dependent Schrödinger equation

$$i\frac{\partial}{\partial t}|\bar{\Psi}(t)\rangle = H(t)|\bar{\Psi}(t)\rangle\,, \tag{4.2}$$

while $|\Psi_0\rangle$ and $|\Psi_\nu\rangle$ denote, respectively, the normalised ground and excited states of the unperturbed system for $t \leq 0$, obeying the Schrödinger equation

$$H|\Psi_\nu\rangle = E_\nu|\Psi_\nu\rangle\,. \tag{4.3}$$

In the unperturbed case, the average value in the ground state of a generic operator O at time t is provided by[1]

$$\langle O\rangle(t) = \langle\Psi_0|e^{iHt}Oe^{-iHt}|\Psi_0\rangle\,. \tag{4.4}$$

whereas, when the system is subject to the external perturbation $\tilde{F}(t)$, it reads in Schrödinger's picture

$$\langle O\rangle_{\rm ex}(t) \equiv \langle\bar{\Psi}(t)|O|\bar{\Psi}(t)\rangle\,. \tag{4.5}$$

In the interaction representation one has

$$\langle\bar{\Psi}(t)|O|\bar{\Psi}(t)\rangle = \langle\bar{\Psi}_I(t)|e^{iHt}Oe^{-iHt}|\bar{\Psi}_I(t)\rangle\,. \tag{4.6}$$

The time-evolved state in the interaction picture $|\bar{\Psi}_I(t)\rangle$ is defined as

$$|\bar{\Psi}_I(t)\rangle = U_I(t,t_0)|\bar{\Psi}_I(t_0)\rangle\,. \tag{4.7}$$

The unitary *time-evolution operator* $U_I(t,t_0)$ reads as

$$U_I(t,t_0) = \mathrm{Texp}\Big\{-i\int_{t_0}^{t}dt'\,\tilde{F}_I(t')\Big\}, \tag{4.8}$$

or, equivalently, as

$$U(t,t_0) = \mathbb{1} + \sum_{n=1}^{\infty}\frac{(-i)^n}{n!}\int_{t_0}^{t}dt_1\ldots\int_{t_0}^{t}dt_n T[\tilde{F}_I(t_1)\ldots\tilde{F}_I(t_n)], \tag{4.9}$$

where $T[\ldots]$ stands for the *time-ordered product* of operators and the subscript I denotes the interaction picture. The latter is equivalent to the Heisenberg picture with respect to the time-independent Hamiltonian H, such that that

$$\begin{aligned}\tilde{F}_I(t) &\equiv h(t)F_I(t)\\ &\equiv h(t)e^{iHt}Fe^{-iHt}\,.\end{aligned} \tag{4.10}$$

Expanding Eq. (4.5) up to the linear order, $\langle O\rangle_{\rm ex}(t)$ reads for $t_0 = 0$

$$\begin{aligned}\langle O\rangle_{\rm ex}(t) &= \langle\Psi_0|\Big[\mathbb{1} + i\int_0^t dt'\tilde{F}_I(t') + \ldots\Big]e^{iHt}Oe^{-iHt}\Big[\mathbb{1} - i\int_0^t dt'\tilde{F}_I(t') + \ldots\Big]|\Psi_0\rangle\\ &= \langle O\rangle(t) + i\langle\Psi_0|\int_0^t dt'[\tilde{F}_I(t'), O_I(t)]|\Psi_0\rangle\\ &= \langle O\rangle(t) + i\langle\Psi_0|\int_0^t dt' h(t')[F_I(t'), O_I(t)]|\Psi_0\rangle\,.\end{aligned} \tag{4.11}$$

[1] Notice that $\langle O\rangle(t)$ is, in fact, independent of t, given that the system is in a stationary state of H.

Eventually, the linear response of the ground-state expectation value of the operator O is provided by the Green-Kubo formula [139, 140, 114]

$$\begin{aligned}\delta\langle O\rangle(t) &\equiv \langle O\rangle_{\rm ex}(t) - \langle O\rangle(t) \\ &= i\langle\Psi_0|\int_0^t dt' h(t')[F_I(t'), O_I(t)]|\Psi_0\rangle\,. \end{aligned} \tag{4.12}$$

As a specific case let us focus on the linear response of the external perturbation operator F itself

$$\begin{aligned}\delta\langle F\rangle(t) &= i\langle\Psi_0|\int_0^t dt' h(t')[F_I(t'), F_I(t)]|\Psi_0\rangle \\ &\equiv \int_{-\infty}^{+\infty} dt'\, C_F^R(t,t')\,h(t')\,. \end{aligned} \tag{4.13}$$

In Eq. (4.13) the retarded correlation function $C_F^R(t,t')$ has been introduced according to

$$iC_F^R(t,t') \equiv \vartheta(t-t')\langle\Psi_0|[F_I(t), F_I(t')]|\Psi_0\rangle\,. \tag{4.14}$$

Explicitly displaying the commutator and recurring to the identity resolution leads to

$$\begin{aligned} iC_F^R(t,t') &= \Big[\langle\Psi_0|F_I(t)F_I(t')|\Psi_0\rangle - \langle\Psi_0|F_I(t')F_I(t)|\Psi_0\rangle\Big]\vartheta(t-t') \\ &= \sum_\nu \Big[\langle\Psi_0|F_I(t)|\Psi_\nu\rangle\langle\Psi_\nu|F_I(t')|\Psi_0\rangle - \langle\Psi_0|F_I(t')|\Psi_\nu\rangle\langle\Psi_\nu|F_I(t)|\Psi_0\rangle\Big]\vartheta(t-t') \\ &= \sum_\nu \Big[e^{i(E_0-E_\nu)t}\langle\Psi_0|F|\Psi_\nu\rangle\langle\Psi_\nu|F|\Psi_0\rangle e^{i(E_\nu-E_0)t'} - e^{i(E_0-E_\nu)t'}\langle\Psi_0|F|\Psi_\nu\rangle\langle\Psi_\nu|F|\Psi_0\rangle e^{i(E_\nu-E_0)t}\Big]\vartheta(t-t') \\ &= \sum_\nu \Big[|\langle\Psi_\nu|F|\Psi_0\rangle|^2 e^{-i(E_\nu-E_0)(t-t')} - |\langle\Psi_\nu|F|\Psi_0\rangle|^2 e^{i(E_\nu-E_0)(t-t')}\Big]\vartheta(t-t')\,. \end{aligned} \tag{4.15}$$

The integral representation of the step function is then exploited

$$\vartheta(t-t') = \lim_{\eta\to 0^+} i\int_{-\infty}^{+\infty}\frac{dE}{2\pi}\frac{e^{-iE(t-t')}}{E+i\eta} \tag{4.16}$$

giving

$$\begin{aligned} iC_F^R(t,t') =& i\sum_\nu\int_{-\infty}^{+\infty}\frac{dE}{2\pi}\frac{e^{-iE(t-t')}}{E+i\eta}|\langle\Psi_\nu|F|\Psi_0\rangle|^2 e^{-i(E_\nu-E_0)(t-t')} \\ & -i\sum_\nu\int_{-\infty}^{+\infty}\frac{dE}{2\pi}\frac{e^{-iE(t-t')}}{E+i\eta}|\langle\Psi_\nu|F|\Psi_0\rangle|^2 e^{i(E_\nu-E_0)(t-t')}\,. \end{aligned} \tag{4.17}$$

The integration variable in the two terms of the sum is then changed according to

$$E \longrightarrow E' \equiv E \pm (E_\nu - E_0) \tag{4.18}$$

providing

$$iC_F^R(t,t') = i\sum_\nu\int_{-\infty}^{+\infty}\frac{dE}{2\pi}e^{-iE(t-t')}\Big[\frac{|\langle\Psi_\nu|F|\Psi_0\rangle|^2}{E-(E_\nu-E_0)+i\eta} - \frac{|\langle\Psi_\nu|F|\Psi_0\rangle|^2}{E+(E_\nu-E_0)+i\eta}\Big]$$

$$\equiv i \int_{-\infty}^{+\infty} \frac{dE}{2\pi} C_F^R(E) e^{-iE(t-t')}. \tag{4.19}$$

In the last line the retarded correlation function in the frequency domain has been introduced

$$C_F^R(E) \equiv \sum_\nu \left[\frac{|\langle \Psi_\nu | F | \Psi_0 \rangle|^2}{E - (E_\nu - E_0) + i\eta} - \frac{|\langle \Psi_\nu | F | \Psi_0 \rangle|^2}{E + (E_\nu - E_0) + i\eta} \right]. \tag{4.20}$$

This function only shows poles in the negative complex half plane, as it is always the case for retarded functions, and can be recast in terms of the *spectral* or *strength function* $S(E)$ through

$$C_F^R(E) = \int_{-\infty}^{+\infty} dE' \frac{S(E')}{E - E' + i\eta}, \tag{4.21}$$

where

$$S(E) = \vartheta(E) \sum_\nu |\langle \Psi_\nu | F | \Psi_0 \rangle|^2 \delta(E_\nu - E_0 - E) - \vartheta(-E) \sum_\nu |\langle \Psi_\nu | F | \Psi_0 \rangle|^2 \delta(E_\nu - E_0 + E). \tag{4.22}$$

The strength function clearly reduces to the more familiar definition

$$S(E) = \sum_\nu |\langle \Psi_\nu | F | \Psi_0 \rangle|^2 \delta(E_\nu - E_0 - E) \tag{4.23}$$

if only positive excitation energies are taken into account, as it will be the case from now on. The response of the ground-state of the nucleus to the action of a perturbation induced by a hermitian operator F is, thus, fully characterised by such a quantity.

4.2 Moments of the strength function

Strength function's moments provide an important and handful tool to characterise collective excitations. They allow, in many cases, to compute global properties in a simple way and are therefore useful to test and compare different approximation schemes, e.g. HFB, (P)GCM and (Q)RPA calculations, and different interactions. For many aspects, the present discussion follows the extensive review on sum rules provided in Ref. [141].

4.2.1 Setting

By convention, all the operators at play are redefined in such a way that their expectation value in the ground state is subtracted, i.e. for any operator[2] Q

$$\mathbf{Q} \equiv Q - \langle \Psi_0 | Q | \Psi_0 \rangle . \tag{4.25}$$

In general, the k-th moment of the strength distribution is defined as

$$m_k \equiv \int_0^{+\infty} E^k S(E) dE, \tag{4.26}$$

[2]Notice that Eq. (4.25) is no longer relevant as soon as one deals with commutators, since it is immediate to show that

$$[A - \langle A \rangle, B - \langle B \rangle] = [A, B]. \tag{4.24}$$

which, using Eq. (4.23), becomes

$$m_k = \sum_\nu (E_\nu - E_0)^k |\langle \Psi_\nu | \mathbf{F} | \Psi_0 \rangle|^2 . \tag{4.27}$$

Equation (4.27) has a straightforward physical meaning, as it is akin to the exact mathematical definition of the k-th moment of a discretised probability distribution associated with the transition probability generated by F. Let us remark that, except for m_0, as it will become evident below, there is no difference in using $\mathbf{F}$ or F in Eq. (4.27).

4.2.2 General properties

Two sets of quantities having the dimension of an energy are introduced

$$\bar{E}_k \equiv \frac{m_k}{m_{k-1}} , \tag{4.28a}$$

$$\tilde{E}_k \equiv \left(\frac{m_k}{m_{k-2}} \right)^{1/2} , \tag{4.28b}$$

and coincide for all k's if the strength distribution is concentrated in a single peak. The degree to which they differ reflects the fragmentation of the distribution. Notice that, by definition, the average value of the energy distribution is

$$\bar{E}_1 = \frac{m_1}{m_0} . \tag{4.29}$$

Schwartz's inequality[3] provides the following relations between the moments

$$\cdots \geq \frac{m_{k+2}}{m_{k+1}} \geq \sqrt{\frac{m_{k+2}}{m_k}} \geq \frac{m_{k+1}}{m_k} \geq \sqrt{\frac{m_{k+1}}{m_{k-1}}} \geq \cdots , \tag{4.33}$$

which represents a practical tool to set boundaries on a specific moment in case it cannot be easily computed. The variance of the strength distribution is shown to satisfy

$$\sigma^2 = \frac{m_2}{m_0} - \left(\frac{m_1}{m_0} \right)^2 \geq 0 . \tag{4.34}$$

Notice that, from a numerical standpoint, the above inequalities hold if the involved moments are all computed within the same approximation scheme.

[3] For $\rho(E)$ being a positive definite function and, thus, $\rho(E)dE$ a positive measure, Schwartz's inequality reads

$$\int f^2(E)\rho(E)dE \int g^2(E)\rho(E)dE \geq \left(\int f(E)g(E)\rho(E)dE \right)^2 , \tag{4.30}$$

with f and g two arbitrary functions. The strength function $S(E)$ is defined for positive values of E (see Eq. (4.23)), so that

$$\rho(E) \equiv E^k S(E) \tag{4.31}$$

is positive definite. For $f(E) = E$ and $g(E) = 1$ Eq. (4.30) reads

$$m_{k+2} m_k \geq m_{k+1}^2 , \tag{4.32}$$

which provides the sequence of inequalities in Eq. (4.33).

4.2.3 Commutators-based formulation

By means of the identity resolution on the A-body Hilbert space $\mathcal{H}_A$

$$\mathbb{1} = \sum_{\nu} |\Psi_\nu\rangle\langle\Psi_\nu| \,, \tag{4.35}$$

Eq. (4.27) can be rewritten as the ground-state expectation value

$$\begin{aligned} m_k &= \sum_{\nu} (E_\nu - E_0)^k \langle\Psi_0|\mathbf{F}|\Psi_\nu\rangle\langle\Psi_\nu|\mathbf{F}|\Psi_0\rangle \\ &= \sum_{\nu} \langle\Psi_0|\mathbf{F}(H-E_0)^k|\Psi_\nu\rangle\langle\Psi_\nu|\mathbf{F}|\Psi_0\rangle \\ &= \langle\Psi_0|\mathbf{F}(H-E_0)^k\mathbf{F}|\Psi_0\rangle \,. \end{aligned} \tag{4.36}$$

For $k \geq 0$, one can write Eq. (4.36) as

$$m_k = (-1)^i \langle\Psi_0|C_i C_j|\Psi_0\rangle \tag{4.37}$$

with[4]

$$\begin{aligned} C_l &\equiv \{H^l, F\} \\ &\equiv \underbrace{[H,[H,...[H,[H}_{l \text{ times}},F]]...]] \end{aligned} \tag{4.40}$$

[4]Similarly one could define m_k by means of the operators

$$\begin{aligned} \tilde{C}_l &\equiv \{F, H^l\} \\ &\equiv [[...[[F,\underbrace{H],H]...,H],H}_{l \text{ times}}], \end{aligned} \tag{4.38}$$

since $\tilde{C}_l$ is equal to C_l up to a sign, i.e. it is easy to check that

$$\tilde{C}_l = (-1)^l C_l \,. \tag{4.39}$$

and where i and j are integers fulfilling[5] $i+j=k$. For odd moments, moreover, Eq. (4.37) can be further rewritten in terms of a commutator, i.e.

$$m_k = \frac{1}{2}(-1)^i \langle\Psi_0|[C_i, C_j]|\Psi_0\rangle\,. \tag{4.45}$$

This provides a useful simplification to the structure of the operator whose ground-state expectation value is to be computed. Indeed, for F a one-body operator, while the product C_iC_j contains up to $[(n-1)k+2]$-body operators, n being the highest-rank component of H, the commutator contains only up to $[(n-1)k+1]$-body operators. This simplification has no counterpart for the even moments, since these can be written in terms of anti-commutators, instead of commutators, that have the same many-body rank as the product C_iC_j. Let us eventually introduce a definition for the *moment operator* of order k

$$\check{M}_k(i,j) \equiv (-1)^i C_i C_j \qquad \forall\ k \geq 0\,, \tag{4.46a}$$

$$M_k(i,j) \equiv \frac{1}{2}(-1)^i [C_i, C_j] \qquad \text{if } k = 2n+1,\ n \in \mathbb{N}\,, \tag{4.46b}$$

whose expectation value over $|\Psi_0\rangle$ delivers m_k.

4.2.4 Similarity-transformed-based formulation

Odd moments m_k ($k>0$) can be further linked to a similarity-transformed Hamiltonian defined as

$$\begin{aligned} H_k(\eta) &\equiv e^{-\eta G_k} H e^{\eta G_k} \\ &= H + \eta[H, G_k] + \frac{1}{2!}\eta^2[[H, G_k], G_k] + \mathcal{O}(\eta^3)\,, \end{aligned} \tag{4.47}$$

where the last equality expands the similarity transformation in powers of the parameter η by making use of the Baker-Campbell-Hausdorff's identity. To match the expression given in Eq. (4.46b) it is sufficient to take $i = j+1$ and define

$$G_k \equiv C_j \quad \text{with } k \equiv 2j+1\,, \tag{4.48}$$

[5] The proof of Eq. (4.37) is straightforward recalling that H can be redefined as

$$\mathbf{H} \equiv H - \langle\Psi_0|H|\Psi_0\rangle\,. \tag{4.41}$$

In such a case Eq. (4.36) reads as

$$\begin{aligned} m_k &= \langle\Psi_0|\mathbf{F}\mathbf{H}^k\mathbf{F}|\Psi_0\rangle \\ &= \langle\Psi_0|\mathbf{F}\mathbf{H}^i\mathbf{H}^j\mathbf{F}|\Psi_0\rangle \\ &= \langle\Psi_0|[\mathbf{F}, \mathbf{H}^i][\mathbf{H}^j, \mathbf{F}]|\Psi_0\rangle\,, \end{aligned} \tag{4.42}$$

with $i+j=k$ and where the property $\mathbf{H}|\Psi_0\rangle = 0$ deriving from Eq. (4.41) has been used. Since $[\mathbf{H}^n, \mathbf{F}] = [H^n, F]$ for $n \in \mathbb{N}$, the bold notation will be no longer used in the following. The commutators $[H^l, F]$ and $[F, H^l]$ can be rewritten [142] as

$$[H^l, F] = \sum_{n=0}^{l-1} \binom{l}{n} C_{l-n} H^n\,, \tag{4.43a}$$

$$[F, H^l] = \sum_{n=0}^{l-1} \binom{l}{n} H^n \tilde{C}_{l-n}\,, \tag{4.43b}$$

with C_l and $\tilde{C}_l$ defined, respectively, in Eq. (4.40) and (4.38). The only non-vanishing contributions to Eq. (4.42) are obtained for $n=0$ in Eqs. (4.43) since $H|\Psi_0\rangle = 0$ because of Eq. (4.41), such that

$$m_k = \langle\Psi_0|\tilde{C}_i C_j|\Psi_0\rangle \tag{4.44}$$

which, together with Eq. (4.39), proves the general formula in Eq. (4.37).

such that

$$M_k(j+1,j) = \frac{1}{2}(-1)^{j+1}\frac{\partial^2}{\partial\eta^2}H_k(\eta)\bigg|_{\eta=0}. \tag{4.49}$$

4.3 Explicit calculation of selected moments

The case where H contains up to three-body operators and F is a one-body operator is presently studied in detail. In what follows, the general strategy consists in generating an explicit algebraic expression of the operator $\check{M}_k$ or M_k for $k \geq 0$. Then, the corresponding expectation value m_k is computed over the (P)GCM state, which can be done numerically including up to three-body operators. The associated numerical results are delivered in Chap. 10. In what follows all operators are defined according to the general convention described in App. A.

4.3.1 m_0

According to Eq. (4.46), the m_0 operator is a two-body operator reading as

$$\check{M}_0(0,0) = \mathbf{F}^2, \tag{4.50}$$

with matrix elements

$$\check{M}_0^{[0]} = 0, \tag{4.51a}$$

$$\check{m}_{0,ab}^{11} \equiv \sum_c f_{ac}^{11} f_{cb}^{11}, \tag{4.51b}$$

$$\check{m}_{0,abcd}^{22} \equiv 2(f_{ac}^{11} f_{bd}^{11} - f_{bc}^{11} f_{ad}^{11}). \tag{4.51c}$$

4.3.2 m_1

There are two equivalent ways to obtain the odd-moment operators, namely given by Eqs. (4.46b) and (4.49). They are explored separately in the following subsections for m_1.

Similarity-transformed H

Using Eq. (4.49) for $k = 1$, the m_1 operator is given by

$$M_1(1,0) = -\frac{1}{2}\frac{\partial^2}{\partial\eta^2}H_1(\eta)\bigg|_{\eta=0} \tag{4.52}$$

with

$$H_1(\eta) = e^{-\eta F} H e^{\eta F}, \tag{4.53}$$

such that

$$\begin{aligned} H_1(\eta) =& H_1^{[0]}(\eta) \\ &+ \sum_{ab} h_{ab}^{11}\, e^{-\eta F} c_a^\dagger c_b e^{\eta F} \\ &+ \frac{1}{(2!)^2}\sum_{abcd} h_{abcd}^{22}\, e^{-\eta F} c_a^\dagger c_b^\dagger c_d c_c e^{\eta F} \end{aligned}$$

$$+\frac{1}{(3!)^2}\sum_{abcdef} h^{33}_{abcdef}\, e^{-\eta F} c_a^\dagger c_b^\dagger c_c^\dagger c_f c_e c_d e^{\eta F}\,. \tag{4.54}$$

As shown below, the similarity transformation, with F a one-body operator, does not change the rank of the operator, such that $M_1(1,0)$ has the same rank as H. Introducing the identity operator in-between each pair of creation and/or annihilation operators under the form

$$1 = e^{\eta F} e^{-\eta F}\,, \tag{4.55}$$

the similarity transformation is separately performed on each creation (annihilation) operator. The commutator

$$\begin{aligned}
[F, c_a^\dagger] &= \sum_{kl} f^{11}_{kl} c_k^\dagger c_l c_a^\dagger - c_a^\dagger F \\
&= \sum_{kl} f^{11}_{kl} c_k^\dagger (\delta_{la} - c_a^\dagger c_l) - c_a^\dagger F \\
&= \sum_{k} f^{11}_{ka} c_k^\dagger,
\end{aligned} \tag{4.56}$$

together with Baker-Campbell-Hausdorff's formula allows one to obtain

$$\begin{aligned}
e^{-\eta F} c_a^\dagger e^{\eta F} &= c_a^\dagger - \eta[F, c_a^\dagger] + \eta^2 \frac{1}{2!}[F,[F, c_a^\dagger]] - \eta^3 \frac{1}{3!}[F,[F,[F, c_a^\dagger]]] + \dots \\
&= c_a^\dagger - \eta \sum_k f^{11}_{ka} c_k^\dagger + \eta^2 \frac{1}{2!} \sum_{kl} f^{11}_{lk} f^{11}_{ka} c_l^\dagger - \eta^3 \frac{1}{3!} \sum_{klm} f^{11}_{ml} f^{11}_{lk} f^{11}_{ka} c_m^\dagger + \dots \\
&= c_a^\dagger - \eta \sum_k f^{11}_{ka} c_k^\dagger + \eta^2 \frac{1}{2!} \sum_{k} (f^{11})^2_{ka} c_k^\dagger - \eta^3 \frac{1}{3!} \sum_{k} (f^{11})^3_{ka} c_k^\dagger + \dots \\
&= \sum_k (e^{-\eta f^{11}})_{ka} c_k^\dagger.
\end{aligned} \tag{4.57a}$$

Similarly, one has

$$e^{-\eta F} c_a e^{\eta F} = \sum_k (e^{\eta f^{11}})_{ka} c_k\,. \tag{4.57b}$$

Eventually, Eq. (4.54) is written as

$$\begin{aligned}
H_1(\eta) =& H_1^{[0]}(\eta) \\
&+ \sum_{kl} h^{11}_{kl}(\eta)\, c_k^\dagger c_l \\
&+ \frac{1}{(2!)^2} \sum_{klmn} h^{22}_{klmn}(\eta)\, c_k^\dagger c_l^\dagger c_n c_m \\
&+ \frac{1}{(3!)^2} \sum_{\substack{klm \\ nop}} h^{33}_{klmnop}(\eta)\, c_k^\dagger c_l^\dagger c_m^\dagger c_p c_o c_n\,,
\end{aligned} \tag{4.58}$$

with

$$H_1^{[0]}(\eta) \equiv H^{[0]}\,, \tag{4.59a}$$

$$h^{11}_{kl}(\eta) \equiv \sum_{ab} h^{11}_{ab} (e^{-\eta f^{11}})_{ka} (e^{\eta f^{11}})_{lb} \,, \tag{4.59b}$$

$$h^{22}_{klmn}(\eta) \equiv \sum_{abcd} h^{22}_{abcd} (e^{-\eta f^{11}})_{ka} (e^{-\eta f^{11}})_{lb} (e^{\eta f^{11}})_{mc} (e^{\eta f^{11}})_{nd} \,, \tag{4.59c}$$

$$h^{33}_{klmnop}(\eta) \equiv \sum_{\substack{abc \\ def}} h^{33}_{abcdef} (e^{-\eta f^{11}})_{ka} (e^{-\eta f^{11}})_{lb} (e^{-\eta f^{11}})_{mc} (e^{\eta f^{11}})_{nd} (e^{\eta f^{11}})_{oe} (e^{\eta f^{11}})_{pf} \,. \tag{4.59d}$$

The similarity-transformed matrix elements on the left-hand side of Eqs. (4.59) naturally inherit the anti-symmetry of the original matrix elements, as it can be checked directly.

The second derivative with respect to η can now be explicitly performed to derive the matrix elements of $M_1(1,0)$, i.e.

$$M^{[0]}_1 = 0 \,, \tag{4.60a}$$

$$\begin{aligned} m^{11}_{1,kl}(1,0) &\equiv -\frac{1}{2} \frac{\partial^2}{\partial \eta^2} h^{11}_{kl}(\eta) \Big|_{\eta=0} \\ &= -\frac{1}{2} \sum_{ab} h^{11}_{ab} [(f^{11})^2_{ka} \delta_{lb} - 2 f^{11}_{ka} f^{11}_{lb} + \delta_{ka} (f^{11})^2_{lb}] \,, \end{aligned} \tag{4.60b}$$

$$\begin{aligned} m^{22}_{1,klmn}(1,0) &\equiv -\frac{1}{2} \frac{\partial^2}{\partial \eta^2} h^{22}_{klmn}(\eta) \Big|_{\eta=0} \\ &= -\frac{1}{2} \sum_{abcd} h^{22}_{abcd} [(f^{11})^2_{ka} \delta_{lb} \delta_{mc} \delta_{nd} + \delta_{ka} (f^{11})^2_{lb} \delta_{mc} \delta_{nd} + \delta_{ka} \delta_{lb} (f^{11})^2_{mc} \delta_{nd} \\ &\quad + \delta_{ka} \delta_{lb} \delta_{mc} (f^{11})^2_{nd} + 2 f^{11}_{ka} f^{11}_{lb} \delta_{mc} \delta_{nd} - 2 f^{11}_{ka} \delta_{lb} f^{11}_{mc} \delta_{nd} - 2 f^{11}_{ka} \delta_{lb} \delta_{mc} f^{11}_{nd} \\ &\quad - 2 \delta_{ka} f^{11}_{lb} f^{11}_{mc} \delta_{nd} - 2 \delta_{ka} f^{11}_{lb} \delta_{mc} f^{11}_{nd} + 2 \delta_{ka} \delta_{lb} f^{11}_{mc} f^{11}_{nd}] \,, \end{aligned} \tag{4.60c}$$

$$\begin{aligned} m^{33}_{1,klmnop}(1,0) &\equiv -\frac{1}{2} \frac{\partial^2}{\partial \eta^2} h^{33}_{klmnop}(\eta) \Big|_{\eta=0} \\ &= -\frac{1}{2} \sum_{\substack{abc \\ def}} h^{33}_{abcdef} [(f^{11})^2_{ka} \delta_{lb} \delta_{mc} \delta_{nd} \delta_{oe} \delta_{pf} + \delta_{ka} (f^{11})^2_{lb} \delta_{mc} \delta_{nd} \delta_{oe} \delta_{pf} + \delta_{ka} \delta_{lb} (f^{11})^2_{mc} \delta_{nd} \delta_{oe} \delta_{pf} \\ &\quad + \delta_{ka} \delta_{lb} \delta_{mc} (f^{11})^2_{nd} \delta_{oe} \delta_{pf} + \delta_{ka} \delta_{lb} \delta_{mc} \delta_{nd} (f^{11})^2_{oe} \delta_{pf} + \delta_{ka} \delta_{lb} \delta_{mc} \delta_{nd} \delta_{oe} (f^{11})^2_{pf} \\ &\quad + 2 f^{11}_{ka} f^{11}_{lb} \delta_{mc} \delta_{nd} \delta_{oe} \delta_{pf} + 2 f^{11}_{ka} \delta_{lb} f^{11}_{mc} \delta_{nd} \delta_{oe} \delta_{pf} - 2 f^{11}_{ka} \delta_{lb} \delta_{mc} f^{11}_{nd} \delta_{oe} \delta_{pf} \\ &\quad - 2 f^{11}_{ka} \delta_{lb} \delta_{mc} \delta_{nd} f^{11}_{oe} \delta_{pf} - 2 f^{11}_{ka} \delta_{lb} \delta_{mc} \delta_{nd} \delta_{oe} f^{11}_{pf} + 2 \delta_{ka} f^{11}_{lb} f^{11}_{mc} \delta_{nd} \delta_{oe} \delta_{pf} \\ &\quad - 2 \delta_{ka} f^{11}_{lb} \delta_{mc} f^{11}_{nd} \delta_{oe} \delta_{pf} - 2 \delta_{ka} f^{11}_{lb} \delta_{mc} \delta_{nd} f^{11}_{oe} \delta_{pf} - 2 \delta_{ka} f^{11}_{lb} \delta_{mc} \delta_{nd} \delta_{oe} f^{11}_{pf} \\ &\quad - 2 \delta_{ka} \delta_{lb} f^{11}_{mc} f^{11}_{nd} \delta_{oe} \delta_{pf} - 2 \delta_{ka} \delta_{lb} f^{11}_{mc} \delta_{nd} f^{11}_{oe} \delta_{pf} - 2 \delta_{ka} \delta_{lb} f^{11}_{mc} \delta_{nd} \delta_{oe} f^{11}_{pf} \\ &\quad + 2 \delta_{ka} \delta_{lb} \delta_{mc} f^{11}_{nd} f^{11}_{oe} \delta_{pf} + 2 \delta_{ka} \delta_{lb} \delta_{mc} f^{11}_{nd} \delta_{oe} f^{11}_{pf} + 2 \delta_{ka} \delta_{lb} \delta_{mc} \delta_{nd} f^{11}_{oe} f^{11}_{pf}] \,. \end{aligned} \tag{4.60d}$$

As for the matrix elements of the similarity-transformed Hamiltonian in Eq. (4.59), the matrix elements of $M_1(1,0)$ are manifestly antisymmetric.

Commutator form

The same expressions can be obtained from Eq. (4.46) for $k = 1$ (e.g. $i = 0$ and $j = 1$). This is achieved by applying Wick's theorem with respect to the particle vacuum $|0\rangle$. In this case the only non-vanishing contraction at play is

$$\overbrace{c_a \, c^\dagger_b} \equiv \langle 0 | c_a c^\dagger_b | 0 \rangle = \delta_{ab} \,. \tag{4.61}$$

The commutator $C_1 = [H, F]$ is computed separately for the various components of H

$$[H^{[0]}, F] = 0\,, \tag{4.62a}$$

$$\begin{aligned}
[H^{[1]}, F] &= \sum_{abcd} h^{11}_{ab} f^{11}_{cd} \{c^\dagger_a c_b c^\dagger_c c_d - c^\dagger_c c_d c^\dagger_a c_b\} \\
&= \sum_{abcd} h^{11}_{ab} f^{11}_{cd} \{c^\dagger_a c_d \delta_{bc} - c^\dagger_c c_b \delta_{ad}\} \\
&= \sum_{abc} \{h^{11}_{ac} f^{11}_{cb} - h^{11}_{cb} f^{11}_{ac}\} c^\dagger_a c_b \\
&\equiv \sum_{ab} c^{11}_{1,ab}\, c^\dagger_a c_b\,,
\end{aligned} \tag{4.62b}$$

$$\begin{aligned}
[H^{[2]}, F] &= \frac{1}{(2!)^2} \sum_{\substack{abc \\ def}} h^{22}_{abcd} f^{11}_{ef} \{c^\dagger_a c^\dagger_b c_d c_c c^\dagger_e c_f - c^\dagger_e c_f c^\dagger_a c^\dagger_b c_d c_c\} \\
&= \frac{1}{(2!)^2} \sum_{\substack{abc \\ def}} h^{22}_{abcd} f^{11}_{ef} \{c^\dagger_a c^\dagger_b c_d c_f \delta_{ce} - c^\dagger_a c^\dagger_b c_c c_f \delta_{de} + c^\dagger_e c^\dagger_a c_d c_c \delta_{fb} - c^\dagger_e c^\dagger_b c_d c_c \delta_{fa}\} \\
&= \frac{1}{(2!)^2} \sum_{\substack{abc \\ de}} \{h^{22}_{abed} f^{11}_{ec} + h^{22}_{abce} f^{11}_{ed} - h^{22}_{aecd} f^{11}_{be} - h^{22}_{ebcd} f^{11}_{ae}\} c^\dagger_a c^\dagger_b c_d c_c \\
&\equiv \frac{1}{(2!)^2} \sum_{abcd} c^{22}_{1,abcd}\, c^\dagger_a c^\dagger_b c_d c_c\,,
\end{aligned} \tag{4.62c}$$

$$\begin{aligned}
[H^{[3]}, F] &= \frac{1}{(3!)^2} \sum_{\substack{abcd \\ efgh}} h^{33}_{abcdef} f^{11}_{gh} \{c^\dagger_a c^\dagger_b c^\dagger_c c_f c_e c_d c^\dagger_g c_h - c^\dagger_g c_h c^\dagger_a c^\dagger_b c^\dagger_c c_f c_e c_d\} \\
&= \frac{1}{(3!)^2} \sum_{\substack{abcd \\ efgh}} h^{33}_{abcdef} f^{11}_{gh} \{c^\dagger_a c^\dagger_b c^\dagger_c c_f c_e c_h \delta_{dg} - c^\dagger_a c^\dagger_b c^\dagger_c c_f c_d c_h \delta_{eg} + c^\dagger_a c^\dagger_b c^\dagger_c c_e c_d c_h \delta_{fg} \\
&\qquad\qquad - c^\dagger_g c^\dagger_b c^\dagger_c c_f c_e c_d \delta_{ha} + c^\dagger_g c^\dagger_a c^\dagger_c c_f c_e d_h \delta_{hb} - c^\dagger_g c^\dagger_a c^\dagger_b c_f c_e c_d \delta_{hc}\} \\
&= \frac{1}{(3!)^2} \sum_{\substack{abcd \\ efg}} \{h^{33}_{abcgef} f^{11}_{gd} + h^{33}_{abcdgf} f^{11}_{ge} + h^{33}_{abcdeg} f^{11}_{gf} \\
&\qquad - h^{33}_{gbcdef} f^{11}_{ag} - h^{33}_{agcdef} f^{11}_{bg} - h^{33}_{abgdef} f^{11}_{cg}\} c^\dagger_a c^\dagger_b c^\dagger_c c_f c_e c_d \\
&\equiv \frac{1}{(3!)^2} \sum_{\substack{abc \\ def}} c^{33}_{1,abcdef} c^\dagger_a c^\dagger_b c^\dagger_c c_f c_e c_d\,.
\end{aligned} \tag{4.62d}$$

Reference [143] provides an equivalent, yet much more synthetic, writing of the anti-symmetrised two- and three-body matrix elements using permutation operators. This paper originally introduces a diagrammatic (and automated) way to evaluate commutators' anti-symmetrised matrix elements in Bogoliubov algebra but the same result can be exploited in this work by simply substituting quasiparticle operators $\beta^\dagger$ with single-particle operators $c^\dagger$ and taking the particle vacuum $|0\rangle$ instead of the Bogoliubov vacuum $|\Phi_{\text{HFB}}\rangle$. Naturally the single-particle formalism only needs to retain number-conserving components. Eventually, the matrix elements of the elementary commutator can be re-expressed as

$$c^{11}_{1,ab} = \sum_k h^{11}_{ak} f^{11}_{kb} - \sum_k f^{11}_{ak} h^{11}_{kb}\,, \tag{4.63a}$$

$$c^{22}_{1,abcd} = P(c/d)\sum_k h^{22}_{abck} f^{11}_{kd} - P(a/b)\sum_k f^{11}_{ak} h^{22}_{kbcd}\,, \tag{4.63b}$$

$$c^{33}_{1,abcdef} = P(de/f)\sum_k h^{33}_{abcdek} f^{11}_{kf} - P(a/bc)\sum_k f^{11}_{ak} h^{33}_{kbcdef}\,, \tag{4.63c}$$

with

$$P(a/b) \equiv 1 - P_{ab}\,, \tag{4.64a}$$

$$P(a/bc) \equiv 1 - P_{ab} - P_{ac}\,, \tag{4.64b}$$

$$P(ab/c) \equiv 1 - P_{ac} - P_{bc}\,, \tag{4.64c}$$

and where P_{ab} denotes the transposition operator exchanging indices a and b. The operator F being a one-body operator, the commutator preserves the n-body nature of the component $H^{[n]}$. The above result is exploited to readily compute the nested commutator needed to obtain the m_1 operator

$$M_1(1,0) \equiv -\frac{1}{2}[[H,F],F] = -\frac{1}{2}[C_1,F]\,, \tag{4.65}$$

by substituting H with C_1 in Eqs. (4.62). Eventually, the matrix elements of $M_1(1,0)$ are obtained as

$$M^{[0]}_1 = 0\,, \tag{4.66a}$$

$$\begin{aligned} m^{11}_{1,ab} &\equiv -\frac{1}{2}\sum_c \{c^{11}_{1,ac} f^{11}_{cb} - f^{11}_{ac} c^{11}_{1,cb}\} \\ &= -\frac{1}{2}\sum_{cd} \{\{h^{11}_{ad} f^{11}_{dc} - f^{11}_{ad} h^{11}_{dc}\} f^{11}_{cb} - f^{11}_{ac}\{h^{11}_{cd} f^{11}_{db} - f^{11}_{cd} h^{11}_{db}\}\} \\ &= -\frac{1}{2}\sum_{cd} h^{11}_{cd}\{(f^{11})^2_{db}\delta_{ac} - 2 f^{11}_{ac} f^{11}_{db} + (f^{11})^2_{ac}\delta_{db}\}\,, \end{aligned} \tag{4.66b}$$

$$\begin{aligned} m^{22}_{1,abcd} &\equiv -\frac{1}{2}\sum_e \{c^{22}_{1,abed} f^{11}_{ec} + c^{22}_{1,abce} f^{11}_{ed} - c^{22}_{1,aecd} f^{11}_{be} - c^{22}_{1,ebcd} f^{11}_{ae}\} \\ &= -\frac{1}{2}\sum_{ef} \{\{h^{22}_{abfd} f^{11}_{fe} + h^{22}_{abef} f^{11}_{fd} - h^{22}_{afed} f^{11}_{bf} - h^{22}_{fbed} f^{11}_{af}\} f^{11}_{ec} \\ &\qquad + \{h^{22}_{abfe} f^{11}_{fc} + h^{22}_{abcf} f^{11}_{fe} - h^{22}_{afce} f^{11}_{bf} - h^{22}_{fbce} f^{11}_{af}\} f^{11}_{ed} \\ &\qquad - \{h^{22}_{aefd} f^{11}_{fc} + h^{22}_{aecf} f^{11}_{fd} - h^{22}_{afcd} f^{11}_{ef} - h^{22}_{fecd} f^{11}_{af}\} f^{11}_{be} \\ &\qquad - \{h^{22}_{ebfd} f^{11}_{fc} + h^{22}_{ebcf} f^{11}_{fd} - h^{22}_{efcd} f^{11}_{bf} - h^{22}_{fbcd} f^{11}_{ef}\} f^{11}_{ae}\} \\ &= -\frac{1}{2}\sum_{efgh} h^{22}_{efgh}\{(f^{11})^2_{ae}\delta_{bf}\delta_{cg}\delta_{dh} + \delta_{ae}(f^{11})^2_{bf}\delta_{cg}\delta_{dh} + \delta_{ae}\delta_{bf}(f^{11})^2_{cg}\delta_{dh} + \delta_{ae}\delta_{bf}\delta_{cg}(f^{11})^2_{dh} \\ &\qquad + 2 f^{11}_{ae} f^{11}_{bf}\delta_{cg}\delta_{dh} - 2 f^{11}_{ae}\delta_{bf} f^{11}_{cg}\delta_{dh} + 2 f^{11}_{ae}\delta_{bf}\delta_{cg} f^{11}_{dh} \\ &\qquad - 2\delta_{ae} f^{11}_{bf} f^{11}_{cg}\delta_{dh} + 2\delta_{ae} f^{11}_{bf}\delta_{cg} f^{11}_{dh} - 2\delta_{ae}\delta_{bf} f^{11}_{cg} f^{11}_{gh}\}\,, \end{aligned} \tag{4.66c}$$

$$\begin{aligned} m^{33}_{1,abcdef} &\equiv -\frac{1}{2}\sum_g \{c^{33}_{1,abcgef} f^{11}_{gd} + c^{33}_{1,abcdgf} f^{11}_{ge} + c^{33}_{1,abcdeg} f^{11}_{gf} - c^{33}_{1,gbcdef} f^{11}_{ag} - c^{33}_{1,agcdef} f^{11}_{bg} - c^{33}_{1,abgdef} f^{11}_{cg}\} \\ &= -\frac{1}{2}\sum_{gh} \{\{h^{33}_{abchef} f^{11}_{hg} + h^{33}_{abcghf} f^{11}_{he} + h^{33}_{abcgeh} f^{11}_{hf} - h^{33}_{hbcgef} f^{11}_{ah} - h^{33}_{ahcgef} f^{11}_{bh} - h^{33}_{abhgef} f^{11}_{ch}\} f^{11}_{gd} \\ &\qquad + \{h^{33}_{abchgf} f^{11}_{hd} + h^{33}_{abcdhf} f^{11}_{hg} + h^{33}_{abcdgh} f^{11}_{hf} - h^{33}_{hbcdgf} f^{11}_{ah} - h^{33}_{ahcdgf} f^{11}_{bh} - h^{33}_{abhdgf} f^{11}_{ch}\} f^{11}_{ge} \end{aligned}$$

$$
\begin{aligned}
&+\{h^{33}_{abcheg}f^{11}_{hd}+h^{33}_{abcdhg}f^{11}_{he}+h^{33}_{abcdeh}f^{11}_{hg}-h^{33}_{hbcdeg}f^{11}_{ah}-h^{33}_{ahcdeg}f^{11}_{bh}-h^{33}_{abhdeg}f^{11}_{ch}\}f^{11}_{gf}\\
&-\{h^{33}_{gbchef}f^{11}_{hd}+h^{33}_{gbcdhf}f^{11}_{he}+h^{33}_{gbcdeh}f^{11}_{hf}-h^{33}_{hbcdef}f^{11}_{gh}-h^{33}_{ghcdef}f^{11}_{bh}-h^{33}_{gbhdef}f^{11}_{ch}\}f^{11}_{ag}\\
&-\{h^{33}_{agchef}f^{11}_{hd}+h^{33}_{agcdhf}f^{11}_{he}+h^{33}_{agcdeh}f^{11}_{hf}-h^{33}_{hgcdef}f^{11}_{ah}-h^{33}_{ahcdef}f^{11}_{gh}-h^{33}_{aghdef}f^{11}_{ch}\}f^{11}_{bg}\\
&-\{h^{33}_{abghef}f^{11}_{hd}+h^{33}_{abgdhf}f^{11}_{he}+h^{33}_{abgdeh}f^{11}_{hf}-h^{33}_{hbgdef}f^{11}_{ah}-h^{33}_{ahgdef}f^{11}_{bh}-h^{33}_{abhdef}f^{11}_{gh}\}f^{11}_{cg}\}\\
=&-\frac{1}{2}\sum_{ghilmn}h^{33}_{ghilmn}\{(f^{11})^2_{ag}\delta_{bh}\delta_{ci}\delta_{dl}\delta_{em}\delta_{fn}+\delta_{ag}(f^{11})^2_{bh}\delta_{ci}\delta_{dl}\delta_{em}\delta_{fn}+\delta_{ag}\delta_{bh}(f^{11})^2_{ci}\delta_{dl}\delta_{em}\delta_{fn}\\
&+\delta_{ag}\delta_{bh}\delta_{ci}(f^{11})^2_{dl}\delta_{em}\delta_{fn}+\delta_{ag}\delta_{bh}\delta_{ci}\delta_{dl}(f^{11})^2_{em}\delta_{fn}+\delta_{ag}\delta_{bh}\delta_{ci}\delta_{dl}\delta_{em}(f^{11})^2_{fn}\\
&+2f^{11}_{ag}f^{11}_{bh}\delta_{ci}\delta_{dl}\delta_{em}\delta_{fn}+2f^{11}_{ag}\delta_{bh}f^{11}_{ci}\delta_{dl}\delta_{em}\delta_{fn}-2f^{11}_{ag}\delta_{bh}\delta_{ci}f^{11}_{dl}\delta_{em}\delta_{fn}\\
&-2f^{11}_{ag}\delta_{bh}\delta_{ci}\delta_{dl}f^{11}_{em}\delta_{fn}-2f^{11}_{ag}\delta_{bh}\delta_{ci}\delta_{dl}\delta_{em}f^{11}_{fn}+2\delta_{ag}f^{11}_{bh}f^{11}_{ci}\delta_{dl}\delta_{em}\delta_{fn}\\
&-2\delta_{ag}f^{11}_{bh}\delta_{ci}f^{11}_{dl}\delta_{em}\delta_{fn}-2\delta_{ag}f^{11}_{bh}\delta_{ci}\delta_{dl}f^{11}_{em}\delta_{fn}-2\delta_{ag}f^{11}_{bh}\delta_{ci}\delta_{dl}\delta_{em}f^{11}_{fn}\\
&-2\delta_{ag}\delta_{bh}f^{11}_{ci}f^{11}_{dl}\delta_{em}\delta_{fn}-2\delta_{ag}\delta_{bh}f^{11}_{ci}\delta_{dl}f^{11}_{em}\delta_{fn}-2\delta_{ag}\delta_{bh}f^{11}_{ci}\delta_{dl}\delta_{em}f^{11}_{fn}\\
&+2\delta_{ag}\delta_{bh}\delta_{ci}f^{11}_{dl}f^{11}_{em}\delta_{fn}+2\delta_{ag}\delta_{bh}\delta_{ci}f^{11}_{dl}\delta_{em}f^{11}_{fn}+2\delta_{ag}\delta_{bh}\delta_{ci}\delta_{dl}f^{11}_{em}f^{11}_{fn}\},
\end{aligned}
\tag{4.66d}
$$

where it can be checked that the expressions in terms of the matrix elements of F and H are the same as those obtained in Sec. 4.3.2. Eventually, the use of permutation operators allows one to obtain the compact expressions

$$
\begin{aligned}
m^{22}_{1,abcd}&=\frac{1}{2}P(a/b)\sum_k f^{11}_{ak}c^{22}_{kbcd}-\frac{1}{2}P(c/d)\sum_k c^{22}_{abck}f^{11}_{kd}\\
&=\frac{1}{2}P(a/b)\sum_{kl}f^{11}_{ak}\{P(c/d)h^{22}_{kbcl}f^{11}_{ld}-P(k/b)f^{11}_{kl}h^{22}_{lbcd}\}\\
&\quad-\frac{1}{2}P(c/d)\sum_{kl}\{P(c/k)h^{22}_{abcl}f^{11}_{lk}-P(a/b)f^{11}_{al}h^{22}_{lbcd}\}f^{11}_{kd},
\end{aligned}
\tag{4.67a}
$$

$$
\begin{aligned}
m^{33}_{1,abcdef}&=\frac{1}{2}P(a/bc)\sum_k f^{11}_{ak}c^{33}_{kbcdef}-\frac{1}{2}P(de/f)\sum_k c^{33}_{abcdek}f^{11}_{kf}\\
&=\frac{1}{2}P(a/bc)\sum_{kl}f^{11}_{ak}\{P(de/f)h^{33}_{kbcdel}f^{11}_{lf}-P(k/bc)f^{11}_{kl}h^{33}_{lbcdef}\}\\
&\quad-\frac{1}{2}P(de/f)\sum_{kl}\{P(de/k)h^{33}_{abcdel}f^{11}_{kl}-P(a/bc)f^{11}_{al}h^{33}_{lbcdek}\}f^{11}_{kf},
\end{aligned}
\tag{4.67b}
$$

for the two- and three-body matrix elements.

4.3.3 m_2

Higher moments are defined Eq. (4.27) by substituting the appropriate k. In order to keep the highest rank component of moments operators under control, so to make the calculation manageable, m_2 and m_3 sum rules expressions are computed under the approximation

$$
C_1=[H,F]\approx[H^{[1]},F],
\tag{4.68}
$$

such that C_1 remains a one-body operator. This condition is not verified in general but is useful in giving an approximated value of higher-order moments. Under this approximation

$$
\breve{M}_2(1,1)=[H,F]^2
$$

$$\approx [H^{[1]}, F]^2, \tag{4.69}$$

is a two-body operator such that

$$\begin{aligned} \breve{M}_2(1,1) &= (C_1^{[0]} + C_1^{[1]})^2 \\ &= C_1^{[1]2}, \end{aligned} \tag{4.70}$$

since $C_1^{[0]} = 0$ as shown in Eq. (4.62a). Eventually, matrix elements of the approximate $\breve{M}_2(1,1)$ operator read

$$\breve{M}_2^{[0]} = 0, \tag{4.71a}$$

$$\begin{aligned} \breve{m}_{2,ab}^{11} &= \sum_c c_{1,ac}^{11} c_{1,cb}^{11} \\ &= \sum_{cde} (h_{ad}^{11} f_{dc}^{11} - h_{dc}^{11} f_{ad}^{11})(h_{ce}^{11} f_{eb}^{11} - h_{eb}^{11} f_{ce}^{11}), \end{aligned} \tag{4.71b}$$

$$\begin{aligned} \breve{m}_{2,abcd}^{22} &= 2P(c/d) c_{1,ad}^{11} c_{1,bc}^{11} \\ &= 2P(c/d) \sum_{ef} (h_{ae}^{11} f_{ed}^{11} - h_{ed}^{11} f_{ae}^{11})(h_{bf}^{11} f_{fc}^{11} - h_{fc}^{11} f_{bf}^{11}), \end{aligned} \tag{4.71c}$$

where Wick's theorem with respect to the particle vacuum $|0\rangle$ has been applied.

4.3.4 m_3

Under the approximation of Eq. (4.68), m_3 can be computed by replacing F with C_1 in Eq. (4.65)

$$M_3(2,1) \equiv \frac{1}{2}[[H,[H,F]],[H,F]] = \frac{1}{2}[[H,C_1],C_1]. \tag{4.72}$$

The matrix elements are immediately provided through

$$M_3^{[0]} = 0, \tag{4.73a}$$

$$m_{3,ab}^{11} = \frac{1}{2} \sum_{cd} h_{cd}^{11} \{(c_1^{11})_{db}^2 \delta_{ac} - 2c_{1,ac}^{11} c_{1,db}^{11} + (c_1^{11})_{ac}^2 \delta_{db}\}, \tag{4.73b}$$

$$\begin{aligned} m_{3,abcd}^{22} =& \frac{1}{2} P(c/d) \sum_{kl} \{P(c/k) h_{abcl}^{22} c_{1,lk}^{11} - P(a/b) c_{1,al}^{11} h_{lbcd}^{22}\} c_{1,kd}^{11} \\ & - \frac{1}{2} P(a/b) \sum_{kl} c_{1,ak}^{11} \{P(c/d) h_{kbcl}^{22} c_{1,ld}^{11} - P(k/b) c_{1,kl}^{11} h_{lbcd}^{22}\}, \end{aligned} \tag{4.73c}$$

$$\begin{aligned} m_{3,abcdef}^{33} =& \frac{1}{2} P(de/f) \sum_{kl} \{P(de/k) h_{abcdel}^{33} c_{1,kl}^{11} - P(a/bc) c_{1,al}^{11} h_{lbcdek}^{33}\} c_{1,kf}^{11} \\ & - \frac{1}{2} P(a/bc) \sum_{kl} c_{1,ak}^{11} \{P(de/f) h_{kbcdel}^{33} c_{1,lf}^{11} - P(k/bc) c_{1,kl}^{11} h_{lbcdef}^{33}\}. \end{aligned} \tag{4.73d}$$

4.3.5 m_{-1}

Moments m_k with $k \leq 0$ cannot be computed via the method exposed earlier for $k \geq 0$ since Eqs. (4.46) do not apply. In order to evaluate the m_{-1} sum rule, which is obtained from Eq. (4.27) for $k = -1$ as

$$m_{-1} = \sum_\nu \frac{|\langle \Psi_\nu | F | \Psi_0 \rangle|^2}{E_\nu - E_0}, \tag{4.74}$$

one employs time-independent perturbation theory. Perturbing the system (i.e. in the small λ limit) by an external field F, the Hamiltonian becomes

$$H(\lambda) \equiv H + \lambda F\,, \tag{4.75}$$

and the associated Schrödinger equation for the ground state is

$$H(\lambda)|\Psi_0(\lambda)\rangle = E_0(\lambda)|\Psi_0(\lambda)\rangle\,. \tag{4.76}$$

Perturbation theory allows one to expand $|\Psi_0(\lambda)\rangle$ in powers of λ [144] according to

$$|\Psi_0(\lambda)\rangle = |\Psi_0\rangle + \lambda \sum_\nu \frac{\langle\Psi_\nu|F|\Psi_0\rangle}{E_0 - E_\nu}|\Psi_\nu\rangle + \mathcal{O}(\lambda^2). \tag{4.77}$$

The variation of the ground-state expectation value of a generic operator Q and of H reads as

$$\begin{aligned}
\delta\langle Q\rangle &\equiv \langle\Psi_0(\lambda)|Q|\Psi_0(\lambda)\rangle - \langle\Psi_0|Q|\Psi_0\rangle \\
&= -\lambda \sum_\nu \left\{ \langle\Psi_0|Q|\Psi_\nu\rangle \frac{1}{E_\nu - E_0}\langle\Psi_\nu|F|\Psi_0\rangle + \langle\Psi_0|F|\Psi_\nu\rangle \frac{1}{E_\nu - E_0}\langle\Psi_\nu|Q|\Psi_0\rangle \right\} + \mathcal{O}(\lambda^2), \qquad \text{(4.78a)} \\
\delta\langle H\rangle &\equiv \langle\Psi_0(\lambda)|H|\Psi_0(\lambda)\rangle - \langle\Psi_0|H|\Psi_0\rangle \\
&= \lambda^2 \sum_\nu \frac{|\langle\Psi_\nu|F|\Psi_0\rangle|^2}{E_\nu - E_0} + \mathcal{O}(\lambda^3), \qquad \text{(4.78b)}
\end{aligned}$$

where the terms linear in λ disappear in Eq. (4.78b) due to the fact that $\{|\Psi_\nu\rangle\}$ constitutes the orthonormal eigenbasis of H. It is easy to see that both of these expressions provide a direct link to m_{-1} if $Q = F$, i.e.

$$m_{-1} = -\frac{1}{2}\frac{\partial\langle\Psi_0(\lambda)|F|\Psi_0(\lambda)\rangle}{\partial\lambda}\bigg|_{\lambda=0}, \tag{4.79a}$$

$$m_{-1} = \frac{1}{2}\frac{\partial^2\langle\Psi_0(\lambda)|H|\Psi_0(\lambda)\rangle}{\partial\lambda^2}\bigg|_{\lambda=0}. \tag{4.79b}$$

Notice that the first contribution to the variation of the ground-state energy is of order λ^2, which makes in general Eq. (4.79a) a more reliable numerical option to compute m_{-1}.

4.4 Approximation of higher moments

Throughout the evaluation of moments of different orders, a commutator hierarchy naturally emerges

$$\begin{aligned}
C_1 &= [H, F], \\
C_2 &= [H, C_1], \\
&\vdots \\
C_{k+1} &= [H, C_k].
\end{aligned}$$

The many-body complexity of such operators increases at each step, unless some approximation is made. Hence, in the present section, solutions aiming at keeping moments' operators at a low rank are presented. Focusing on moments of actual physical interest, i.e. m_2 and m_3, whose first set of approximated matrix elements were obtained in Secs. 4.3.3 and 4.3.4, other approximations restricting C_1 to be a one-body operator are now considered.

4.4.1 Momentum-independent local interactions

In phenomenological calculations one usually chooses to work within the approximation

$$C_1 \equiv [H,F] \approx [T,F], \tag{4.80}$$

with T the kinetic energy part of the Hamiltonian. Indeed in most cases phenomenological interactions are local and momentum independent. Given the class of excitation operators in use, one easily obtains in this case that

$$[v(\mathbf{r}),F(\mathbf{r})] = 0\,, \tag{4.81}$$

so that Eq. (4.80) is verified.

From a physical point of view, commutation operations involving the Hamiltonian are intimately linked to the time evolution in Heisenberg picture, according to

$$\frac{\partial}{\partial t}F(t) = i[H,F(t)] \tag{4.82}$$

(with $\hbar = 1$). Thus, higher moments involve time derivatives of higher and higher orders of the excitation operator F at use. Under the approximation given into Eq. (4.80), F evolves as it would if the system were composed of free fermions. The approximation at use in this work, provided in Eq. (4.68), can be more general than Eq. (4.80), as it will be shown in the next section. As an example, if the one-body part of the Hamiltonian also includes the mean field part of the interaction, then F evolves as it would in a mean-field potential.

4.4.2 Proposed approximations

The approximation exposed in Sec. 4.4.1 is essentially method-driven, since it is related to a peculiar property assumed to be fulfilled by phenomenological EDF interactions. In general, however, such an assumption may reveal too simplistic for the chiral Hamiltonians at use in *ab initio* calculations, that are neither local nor momentum independent. The eventual intent of the EDF approximation in Eq. (4.80) being to limit the many-body complexity of the moment operators at play, other solutions can be envisaged. This can be achieved limiting C_1 to a one-body operator, some solutions are now explored. Let us consider the two-body Hamiltonian

$$H^{[1]} = T = \sum_{ab} t_{ab} c_a^\dagger c_b\,, \tag{4.83a}$$

$$H^{[2]} = V = \frac{1}{4}\sum_{abcd} \bar{v}_{abcd} c_a^\dagger c_b^\dagger c_d c_c\,. \tag{4.83b}$$

If the two-body component of the Hamiltonian undertakes a normal-ordering procedure with respect to a Slater determinant[6], the matrix elements of the one-body (normal-ordered) part of the Hamiltonian modify according to

$$t_{ab} \to t_{ab} + \sum_{cd} \bar{v}_{acbd}\rho_{dc}\,. \tag{4.84}$$

To investigate the differences arising from the order of execution of normal ordering and commutation operations, Eqs. (4.62) are recalled, which provide the commutator matrix elements. If normal ordering

[6] Contractions are computed here with respect to a Slater determinant for simplicity. Actual calculations were performed with respect to a HFB vacuum and, thus, involving both normal and anomalous contractions.

is performed ***before*** the computation of C_1, i.e. the procedure is performed on the Hamiltonian, then the one-body matrix elements of C_1 are easily obtained combining Eqs. (4.62b) and (4.84) and read as

$$C^{11}_{1,ab} \approx \sum_c \left\{ t_{ac} f_{cb} + \sum_{de} \bar{v}_{adce} \rho_{ed} f_{cb} - f_{ac} t_{cb} - \sum_{de} f_{ac} \bar{v}_{cdbe} \rho_{ed} \right\}. \tag{4.85}$$

Discarding the higher-rank components of C_1, i.e. only the one-body matrix elements from Eq. (4.85) are retained, the approximation corresponds to using the mean-field Hamiltonian instead of T in Eq. (4.80).

On the other hand, if normal ordering is performed ***after*** the commutation, i.e. directly on the commutator, the normal ordering procedure is to be applied to Eq. (4.62c), providing

$$C^{11}_{1,ab} \approx \sum_c \left\{ t_{ac} f_{cb} - f_{ac} t_{cb} + \sum_{de} \left\{ \bar{v}_{aced} f_{eb} \rho_{dc} + \bar{v}_{acbe} f_{ed} \rho_{dc} - f_{ce} \bar{v}_{aebd} \rho_{dc} - f_{ae} \bar{v}_{ecbd} \rho_{dc} \right\} \right\}. \tag{4.86}$$

Comparing Eqs. (4.85) and (4.86) it appears clearly that commutation and normal-ordering operations do not ***commute*** if the operators are truncated at the one-body level, since only half of the two-body contributions appear in Eq. (4.85) when compared to Eq. (4.86). In particular, while the terms where the contraction with the one-body density is performed with V only appear in the two equations, mixed contractions involving both V and F only appear if the normal ordering is performed after the commutation. Of course, the two operations have to commute in an exact setting, such that and the difference originates from the truncation of the resulting C_1 operator at the one-body level.

Summary

Summing up the results from the previous subsections, three possibilities are considered to approximate the commutator C_1 at the one-body level, which are given by

$$C^{11(\mathrm{A})}_{1,ab} = \sum_c \left\{ t_{ac} f_{cb} - f_{ac} t_{cb} \right\}, \tag{4.87a}$$

$$C^{11(\mathrm{B})}_{1,ab} = \sum_c \left\{ t_{ac} f_{cb} + \sum_{de} \bar{v}_{adce} \rho_{ed} f_{cb} - f_{ac} t_{cb} - \sum_{de} f_{ac} \bar{v}_{cdbe} \rho_{ed} \right\}, \tag{4.87b}$$

$$C^{11(\mathrm{C})}_{1,ab} = \sum_c \left\{ t_{ac} f_{cb} - f_{ac} t_{cb} + \sum_{de} \left\{ \bar{v}_{aced} f_{eb} \rho_{dc} + \bar{v}_{acbe} f_{ed} \rho_{dc} - f_{ce} \bar{v}_{aebd} \rho_{dc} - f_{ae} \bar{v}_{ecbd} \rho_{dc} \right\} \right\}. \tag{4.87c}$$

The numerical performance of the three approximations is discussed in Sec. 10.4.

4.5 Relation to observables

The actual relation of the strength function to observable is hereby briefly discussed. At first order in perturbation theory, the transition rate $w_{0\to\nu}$ from the ground state $|\Psi_0\rangle$ to an excited state $|\Psi_\nu\rangle$ mediated by the time-independent operator F is provided by Fermi's golden rule

$$w_{0\to\nu} = 2\pi |\langle \Psi_\nu | F | \Psi_0 \rangle|^2 \delta(E_\nu - E_0 - E), \tag{4.88}$$

so that the corresponding cross section $\sigma_{0\to\nu}$ is easily obtained normalising the transition rate by the flux of incident particles and the number of scattering centers

$$\frac{d\sigma_{0\to\nu}}{dE} = w_{0\to\nu} \cdot \frac{1}{\text{flux}} \cdot \frac{1}{\#\text{ of sc. centers}}. \tag{4.89}$$

The total cross section is then obtained summing over all possible final states ν, so that, normalising with respect to the flux and the number of scattering centers it can be expressed as

$$\sigma = 2\pi \int_{-\infty}^{+\infty} S(E)dE = 2\pi m_0 . \tag{4.90}$$

In practice, double-differential cross sections are experimentally measured to perform a ***multipole-decomposition analysis*** (MDA), allowing to extract the multipole strength distributions [64]. In the MDA process, the experimental cross-sections at each angle are binned into small (typically, ≤ 1 MeV) excitation energy intervals. The laboratory angular distributions for each excitation-energy bin are then converted into the centre-of-mass frame using standard Jacobian and relativistic kinematics. For each excitation energy bin, the experimental angular distributions are fitted by means of the least-square method with the linear combination of the calculated double-differential cross sections associated to different multipoles:

$$\left.\frac{d^2\sigma^{\exp}}{d\Omega dE}\right|_{E_x} = \sum_{L=0}^{\infty} a_L(E_x) \left.\frac{d^2\sigma_L^{\mathrm{DWBA}}}{d\Omega dE}\right|_{E_x} , \tag{4.91}$$

where $a_L(E_x)$ is the m_1 sum rule fraction for the L-th component and the cross sections used for the fit procedure correspond to the 100% of m_1 for the L-th multipole at excitation energy E_x calculated using the distorted-wave Born approximation (DWBA). In such calculations an optical potential is used as scattering potential. The fractions of m_1, $a_L(E_x)$, for various multipole components are determined by minimising χ^2. Eventually, the strength distributions for different multipolarities are obtained by multiplying the extracted $a_L(E_x)$'s by the strength corresponding to 100% m_1 at the given energy E_x

$$S_L(E_x) = \frac{m_{L,1}}{E_x} a_L(E_x) . \tag{4.92}$$

One should point out that in such context, the energy-weighted sum rules $m_{L,1}$ for different L's are always computed within the assumption of local momentum-independent interactions, which allows to easily provide algebraic expressions for lower moments but cannot be considered exact in general, as discussed in Sec. 4.4.1.

Chapter 5

Angular Momentum Projection of Multipole Strengths

Contents

The (P)GCM and QRPA formalisms were introduced in Chaps. 1 and 3 respectively. In case the symmetry-projection is not explicitly taken into account before the diagonalisation and symmetry-breaking states are employed, the approximate solution of the Schrödinger equation typically breaks symmetries of the Hamiltonian. The symmetries of the problem can, however, be restored by projecting the symmetry-breaking solutions onto the good symmetry state. The effect of such a *projection after variation* (PAV) on multipole response functions is studied in this chapter focusing on *angular momentum projection* (AMP). After an introductory overview about rotations in quantum mechanics in Sec. 5.1, different levels of symmetry-restoration are introduced in Sec. 5.2. The AMP formula for transition amplitudes is derived in Sec. 5.3 and a specific development based on axially-deformed RPA states is introduced in Sec. 5.4, mostly following Ref. [145]. Several identity resolutions eventually used to benchmark the new development are derived in Sec. 5.6. Eventually, the presence of a coupling to spurious rotational states in symmetry-breaking theories is discussed in Sec. 5.7, together with subtraction techniques allowing for its removal. Results from calculations involving different levels of AMP in GCM are later discussed in Chap. 8. Numerical results of *a posteriori* angular-momentum-projected RPA (PAV RPA) calculations based on a Skyrme-EDF are presented in Chap. 12.

5.1 Introductory concepts

A survey of the necessary concepts needed to discuss angular momentum projection is provided in this section.

5.1.1 Eigenstates of angular momentum operators

Let us start introducing a quantum state carrying good quantum numbers J, M and α

$$|JM\alpha\rangle\,, \tag{5.1}$$

where J is the quantum number relative to the square of total angular momentum operator $\mathbf{J}^2 = J_x^2 + J_y^2 + J_z^2$, M is the quantum number relative to the total angular momentum projection on the z-axis J_z and α collects the remaining quantum numbers necessary to uniquely define the quantum state, such that

$$\mathbf{J}^2\,|JM\alpha\rangle = J(J+1)\,|JM\alpha\rangle\,, \tag{5.2a}$$
$$J_z\,|JM\alpha\rangle = M\,|JM\alpha\rangle\,. \tag{5.2b}$$

The choice of the z-axis only represents a conventional yet arbitrary choice: the operator $\mathbf{J}^2$ commutes with any of its components

$$[\mathbf{J}^2, J_k] = 0 \quad \forall k\,. \tag{5.3}$$

On the contrary, the total angular momentum components J_k being the generator of rotations around the axis k, they do not commute between themselves, satisfying instead the commutation relation

$$[J_i, J_j] = i\varepsilon_{ijk}J_k\,, \tag{5.4}$$

where ε_{ijk} is the Levi-Civita tensor. This reflects the fact that rotations belong to the $SU(2)$ *non-abelian* group, i.e. the generators of the infinitesimal transformations do not commute between them. Hence the necessity to choose only one out of the three components of $\mathbf{J}$ as an observable to be simultaneously diagonalised with $\mathbf{J}^2$.

5.1.2 Rotations

It is customary to express rotations by means of Euler angles

$$\Omega \equiv (\alpha, \beta, \gamma), \tag{5.5}$$

in relation to the unitary rotation transformation as

$$\mathcal{R}(\Omega) \equiv e^{-i\alpha J_z} e^{-i\beta J_y} e^{-i\gamma J_z}. \tag{5.6}$$

The matrix elements of the rotation operator are provided by the so-called Wigner D-matrix, which is defined as[1]

$$\begin{aligned}
\langle JM|\mathcal{R}(\Omega)|J'K\rangle &\equiv \mathcal{D}^J_{MK}(\Omega)\delta_{JJ'} \\
&\equiv \langle JM|\mathcal{R}(\Omega)|JK\rangle\,\delta_{JJ'} \\
&= e^{-iM\alpha}\langle JM|e^{-i\beta J_y}|JK\rangle e^{-iK\gamma}\delta_{JJ'} \\
&\equiv e^{-iM\alpha} d^J_{MK}(\beta) e^{-iK\gamma}\delta_{JJ'}.
\end{aligned} \tag{5.7}$$

Using the definition of Wigner D-matrices from Eq. (5.7), a rotated state $|JM'\Omega\rangle$ can be seen as a rotation acting on the original $|JM'\rangle$

$$\begin{aligned}
|JM'\Omega\rangle &= \mathcal{R}(\Omega)|JM'\rangle \\
&= \sum_M |JM\rangle\langle JM|\mathcal{R}(\Omega)|JM'\rangle \\
&\equiv \sum_M |JM\rangle \mathcal{D}^J_{MM'}(\Omega).
\end{aligned} \tag{5.8}$$

The $(2J+1)\times(2J+1)$ matrix provided by $\mathcal{D}^J_{MK}(\Omega)$ is referred to as the *irreducible representation* of dimension $(2J+1)$ of the rotation operator $\mathcal{R}(\Omega)$. This means that the matrix corresponding to an arbitrary rotation operator in the space of the kets, which are not necessarily characterised by a single value of J, can be transformed, by an appropriate basis choice, in a block-diagonal matrix. Every block is a square $(2J+1)\times(2J+1)$ matrix given by $\mathcal{D}^J_{MK}(\Omega)$ for a given J. Moreover, any square block cannot be further decomposed in smaller sub-blocks, independently of the basis of choice. It can be easily shown that rotation matrices for a given J form a group in the mathematical sense.

Useful formulæ

As a first application, let us compute the coupling constant between angular momenta expressed in a rotated state $\langle J_1 M_1 J_2 M_2 \Omega|J_3 M_3\rangle$. The straightforward application of Eq. (5.8) provides

$$\begin{aligned}
\langle J_1 M_1 J_2 M_2 \Omega|J_3 M_3\rangle &= \sum_{M'_1 M'_2} \langle J_1 M'_1 J_2 M'_2|J_3 M_3\rangle \mathcal{D}^{J_1}_{M_1 M'_1}(\Omega)\mathcal{D}^{J_2}_{M_2 M'_2}(\Omega) \\
&= \sum_{M'_3} \langle J_1 M_1 J_2 M_2 \Omega|J_3 M'_3 \Omega\rangle \mathcal{D}^{J_3 *}_{M_3 M'_3}(\Omega).
\end{aligned} \tag{5.9}$$

[1] Here the z-y-z convention for the Euler's angles is chosen. This convention has the advantage of delivering real $d^J_{KM}(\beta)$ functions. Other conventions (z-x-z for instance) could be envisaged, but they have less attractive properties and thus will not be discussed here.

In the second line the sum over M_3' implied by the rotation is suppressed by the requirement

$$M_1 + M_2 = M_3' . \tag{5.10}$$

The following properties are given without proof:

$$\mathcal{D}^{J*}_{MK}(\Omega) = (-1)^{M-K}\mathcal{D}^{J}_{-M-K}(\Omega) , \tag{5.11}$$

$$\frac{1}{8\pi^2}\int \mathrm{d}\Omega \mathcal{D}^{J_1*}_{M_1K_1}(\Omega)\mathcal{D}^{J_2*}_{M_2K_2}(\Omega)\mathcal{D}^{J_3*}_{M_3K3}(\Omega) = \begin{pmatrix} J_1 & J_2 & J_3 \\ M_1 & M_2 & M_3 \end{pmatrix}\begin{pmatrix} J_1 & J_2 & J_3 \\ K_1 & K_2 & K_3 \end{pmatrix}, \tag{5.12}$$

where the object

$$\begin{pmatrix} J_1 & J_2 & J_3 \\ M_1 & M_2 & M_3 \end{pmatrix} \tag{5.13}$$

is known under the name of $3j$ symbol. For further details, see Chapter 4 from Ref. [146].

5.1.3 Spherical tensors

A spherical tensor of rank λ is a set of operators $T_{\lambda\mu}$, with $\mu \in [-\lambda, +\lambda]$, transferring an angular momentum λ with projection μ. Spherical tensors are defined according to their behaviour with respect to rotations, i.e. they transform according to

$$\mathcal{R}^{\dagger}(\Omega)T_{\lambda\mu}\mathcal{R}(\Omega) = \sum_{\mu'=-\lambda}^{+\lambda} \mathcal{D}^{\lambda*}_{\mu'\mu}(\Omega)T_{\lambda\mu'} . \tag{5.14}$$

A nuclear transition $J_1 \rightarrow J_2$ involving the transfer of angular momentum λ can be described in terms of a transition operator $T_{\lambda\mu}$ summing over all the accepted combinations of M and μ. The total transition probability, summed over μ, M_1 and M_2 is given by

$$B(T_\lambda; J_1 \rightarrow J_2) \equiv \sum_{\substack{M_1M_2 \\ \mu}} |\langle J_1M_1|T_{\lambda\mu}|J_2M_2\rangle|^2 . \tag{5.15}$$

5.1.4 Reduced matrix elements

Let us recall a fundamental result in quantum mechanics, i.e. Wigner-Eckart's theorem: it is formulated, in the Racah-Wigner convention as

$$\langle J_1M_1|T_{\lambda\mu}|J_2M_2\rangle = (-1)^{J_1-M_1}\begin{pmatrix} J_1 & \lambda & J_2 \\ -M_1 & \mu & M_2 \end{pmatrix}\langle J_1\|T_\lambda\|J_2\rangle , \tag{5.16}$$

where $\langle J_1\|T_\lambda\|J_2\rangle$ is the so-called reduced matrix element. The theorem states that it is sufficient to know one combination (M_1, μ, M_2) of the transition amplitude between spherical states, while the others can be deduced geometrically. For further use, let use recall that the 3-j symbol is non-vanishing only under the assumption $M_2 = M_1 - \mu$, so that we may rewrite Eq. (5.16) as

$$\begin{aligned}\langle J_1M_1|T_{\lambda\mu}|J_2M_2\rangle &= (-1)^{J_1-M_1}\begin{pmatrix} J_1 & \lambda & J_2 \\ -M_1 & \mu & M_1-\mu \end{pmatrix}\langle J_1\|T_\lambda\|J_2\rangle \\ &= (-1)^{J_1-M_1}(-1)^{J_1+J_2+\lambda}\begin{pmatrix} J_1 & J_2 & \lambda \\ -M_1 & M_1-\mu & \mu \end{pmatrix}\langle J_1\|T_\lambda\|J_2\rangle\end{aligned}$$

$$= (-1)^{2J_1+J_2+\lambda-M_1} \begin{pmatrix} J_1 & J_2 & \lambda \\ -M_1 & M_1-\mu & \mu \end{pmatrix} \langle J_1 \| T_\lambda \| J_2 \rangle \,. \tag{5.17}$$

The reduced matrix elements can be extracted independently of the particular transition used in the calculation. However, this is true only if spherical states are used on both sides of the transition matrix element. Using Wigner-Eckart's theorem, the total transition probability can be re-expressed in terms of the reduced matrix element as

$$B(T_\lambda; J_1 \to J_2) = \frac{1}{2J_1+1} |\langle J_1 \| T_\lambda \| J_2 \rangle|^2 \,, \tag{5.18}$$

which reduces the number of quantities to be explicitly evaluated.

5.1.5 Angular momentum projection

The operator necessary to perform an AMP is given by[2]

$$P^J_{MK} = \frac{2J+1}{8\pi^2} \int \mathrm{d}\Omega \mathcal{D}^{J*}_{MK}(\Omega) \mathcal{R}(\Omega) \tag{5.19a}$$

$$\equiv \sum_\alpha |JM\alpha\rangle\langle JK\alpha| \tag{5.19b}$$

and fulfil the properties

$$P^{J\dagger}_{MK} = P^J_{KM} \,, \tag{5.20a}$$

$$P^J_{MK} P^{J'}_{M'K'} = \delta_{JJ'} \delta_{KM'} P^J_{MK'} \,. \tag{5.20b}$$

5.1.6 Projected states

A state with good angular momentum J and projection M was previously introduced as $|JM\alpha\rangle$, where α collects all remaining quantum numbers necessary to uniquely define the quantum state. As the latter index is not directly affected in this discussion, it will be hereafter omitted for notation's simplicity. A state $|JM\rangle$ can be obtained by projecting all K components of an arbitrary state $|\Phi\rangle$ (e.g. Slater determinant) onto the angular momentum values J and M via the projector P^J_{MK} and by finding the optimal superposition of these components

$$|JM\rangle = \sum_K g^J_K P^J_{MK} |\Phi\rangle \,. \tag{5.21}$$

The coefficients g^J_K must be determined variationally minimising the energy expectation value in the subspace of projected intrinsic states. In the case of present interest of axially deformed intrinsic states, $|\Phi\rangle$ carries a good quantum number associated to J_z, so that the coefficients g^J_K trivially vanish for all K's differing from the one carried by $|\Phi\rangle$, i.e. if

$$J_z |\Phi\rangle = K' |\Phi\rangle \,, \tag{5.22}$$

then

$$|JM\rangle = \sum_K g^J_K P^J_{MK} |\Phi\rangle$$

[2] In the present work J is always assumed to be an integer, such that the integration domain $\alpha \in [0, 2\pi]$, $\beta \in [0, \pi]$, $\gamma \in [0, 2\pi]$ and the normalising factor $1/8\pi^2$ are adopted. Half-integer values of J would demand to modify the γ integration domain to $\gamma \in [0, 4\pi]$ and, consequently, the normalising constant to $1/16\pi^2$.

Symmetry breaking	
GCM	**(Q)RPA**
Large-amplitude superposition of deformed HF(B) states	Harmonic fluctuations around a deformed HF(B) state
Status: developed	**Status**: developed
PAV GCM	**PAV (Q)RPA**
Angular-momentum projection of symmetry-breaking GCM spectra	Angular-momentum projection of symmetry-breaking (Q)RPA spectra
Status: developed in this work	**Status**: developed in this work[3]
PGCM	**P(Q)RPA**
Proper treatment of rotation-vibration coupling within the GCM	Proper treatment of rotation-vibration coupling within the (Q)RPA
Status: developed	**Status**: formal development [148] only
Symmetry conserving	

Table 5.1: Schematic representation of different projection levels based on symmetry-breaking GCM and (Q)RPA.

$$= \sum_K \delta_{KK'} g^J_K P^J_{MK} |\Phi\rangle$$
$$= g^J_{K'} P^J_{MK'} |\Phi\rangle \,, \tag{5.23}$$

such that $g^J_{K'}$ reduces to a normalisation factor.

5.2 Symmetry restoration and projection techniques

Symmetry restoration is generally achieved via the applications of projection operators. Projectors have the role of selecting the good-quantum-number components of symmetry-breaking states. The specific case of angular momentum was introduced in Eq. 5.19b and angular-momentum-projected states were discussed in Sec. 5.1.6.

Let us schematise, without loss of generality, that a symmetry-breaking solution is obtained via the diagonalisation of the nuclear Hamiltonian in a reduced Hilbert space on the basis of a many-body of choice. This is, for instance, the philosophy followed by variational methods, for which the energy is minimised in a restricted wave-function subspace.

In the GCM, for example, the minimisation is performed in the subspace spanned by HFB states obtained by constraining a selected set of generator coordinates, whereas in the (Q)RPA the solutions span the one-particle-one-hole (two-quasiparticle) subspace[4].

In this context, the symmetry projection may be performed before or after the diagonalisation process. In the *projection after variation* (PAV) scheme, the many-body solutions are first determined in a symmetry-breaking frame, whereas the projection is performed *a posteriori* to extract good-quantum-number components. In the *variation after projection* (VAP) scheme, instead, the projection is fully considered in the diagonalisation process, such that the minimisation is performed within an irreducible representation of the symmetry group. A schematic picture of different levels of projection in the GCM and (Q)RPA frameworks is shown in Tab. 5.1.

[3] Following the development first introduced in Ref. [147].

[4] Notice that, in all actual applications, (Q)RPA is not variational, since the QBA is always advocated for practical purposes. The variational principle would be satisfied if the (Q)RPA ground state were determined via a self-consistent process [149, 73]. The computational complexity associated to self-consistent (Q)RPA calculations has prevented any realistic implementation up to date.

The comparison between different levels of symmetry projections is addressed in this work for the first time in the field of nuclear vibrations. The necessary theoretical tools for the study of vibrational spectra are addressed in Sec. 5.2.2 for the GCM and in Sec. 5.4 for the RPA. For the latter, only the PAV scheme has been developed in the present work, whereas the VAP RPA is left to a future work.

5.2.1 Physical interpretation

A physical interpretation of the PAV and VAP schemes is given in the present section. In a simplified picture one may imagine that symmetry restoration is achieved by an intrinsically-deformed state via rotations. This reflects the PAV philosophy.

Assuming, as it is of interest in this work, that intrinsically deformed solutions are obtained diagonalising the nuclear Hamiltonian in the vibration subspace, then the PAV scheme assumes an exact decoupling between rotations and vibrations.

From a physical perspective this assumption states that vibrations and rotations are associated to completely different time scales, such that they can be addressed separately in a Born-Oppenheimer-like approximation. Specifically, rotations are assumed to be infinitely slower than nuclear vibrations, which is a direct consequence of the rotation being ideally associated with a zero-energy (Goldstone) mode.

Nuclear rotations, however, happen at finite frequencies, such that they cannot be fully decoupled *a posteriori* from vibrational modes [150]. Thus, the variational/diagonalisation process must be performed in a Hilbert subspace simultaneously spanning vibrations *and* rotations. This is achieved in the VAP scheme, which is, consequently, the method of choice to consistently treat the coupling effects between nuclear vibrations and rotations.

5.2.2 Symmetry restoration in the GCM

The application of the VAP and PAV schemes in the GCM are now distinguished. The GCM wave-function was introduced in Eq. (1.1). The unprojected **GCM** transition strength between the ground state and an arbitrary excited state mediated by any operator O is given by

$$\begin{aligned}\langle\Psi_0|O|\Psi_\nu\rangle &= \sum_{pq} f_0^*(p) f_\nu(q) \langle\Phi(p)|O|\Phi(q)\rangle \\ &\equiv \sum_{pq} f_0^*(p) O(p,q) f_\nu(q). \end{aligned} \tag{5.24}$$

Using more compact notations, one can write the transition matrix element between any two GCM states as

$$\begin{aligned}\langle\Psi_\mu|O|\Psi_\nu\rangle &\equiv \sum_{pq} f_{\mu p}^* O_{pq} f_{q\nu} \\ &\equiv (\mathbf{f}^\dagger \cdot \mathbf{O} \cdot \mathbf{f})_{\mu\nu}, \end{aligned} \tag{5.25}$$

where the indices of the matrix containing the operator kernel $O(p,q)$ run on the generator coordinates whereas the linear coefficient matrix $\mathbf{f}$ indices run on the generator coordinates for the lines and on the states for the columns.

The symmetry-projected version of the symmetry-breaking GCM strength can be computed, where the projection is thus performed after obtaining the solution of the HWG equation, and is referred in the following as **PAV GCM**. Projecting the GCM states one works with

$$|\tilde{\Psi}_\nu^J\rangle \equiv N_\nu^J P^J |\Psi_\nu\rangle$$

$$= N_\nu^J \sum_q f_\nu(q) P^J |\Phi(q)\rangle \,, \tag{5.26}$$

where N_ν^J is a normalising factor provided by

$$\begin{aligned} 1 &= \langle \tilde{\Psi}_\nu^J | \tilde{\Psi}_\nu^J \rangle \\ &= (N_\nu^J)^2 \sum_{pq} f_\nu^*(p) f_\nu(q) \langle \Phi(p) | P^J | \Phi(q) \rangle \,, \end{aligned} \tag{5.27}$$

such that

$$(N_\nu^J)^{-2} = \sum_{pq} f_\nu^*(p) f_\nu(q) \mathcal{N}^J(p,q). \tag{5.28}$$

The transition strength is then given by

$$\langle \tilde{\Psi}_0^J | O | \tilde{\Psi}_\nu^{\tilde{J}} \rangle = N_0^J N_\nu^{\tilde{J}} \sum_{pq} f_0(p) f_\nu(q) \langle \Phi(p) | P^{J\dagger} O P^{\tilde{J}} | \Phi(q) \rangle \,. \tag{5.29}$$

The PGCM wave-function was introduced in Eq. (1.2). Since the AMP is enforced in the solution of the HWG equation (the variation is performed *after* the projection), in the present context PGCM calculations will also be referred to as **VAP GCM**. The VAP GCM transition strength reads

$$\langle \Psi_0^J | O | \Psi_\nu^{\tilde{J}} \rangle = \sum_{pq} f_0^{J*}(p) f_\nu^{\tilde{J}}(q) \langle \Phi(p) | P^{J\dagger} O P^{\tilde{J}} | \Phi(q) \rangle \,. \tag{5.30}$$

Similarly to the GCM case one can introduce a more compact representation in matrix form as

$$\begin{aligned} \langle \Psi_\mu^J | O | \Psi_\nu^{\tilde{J}} \rangle &\equiv \sum_{pq} f_{\mu p}^{J*} O_{pq}^{J\tilde{J}} f_{q\nu}^{\tilde{J}} \\ &\equiv (\mathbf{f}^{J\dagger} \cdot \mathbf{O}^{J\tilde{J}} \cdot \mathbf{f}^{\tilde{J}})_{\mu\nu} \,. \end{aligned} \tag{5.31}$$

If the same collective space is considered for a pair of GCM and PGCM calculations, then, without changing the previously introduced notations, in matrix notation the PAV GCM transition amplitudes read

$$\langle \tilde{\Psi}_\mu^J | O | \tilde{\Psi}_\nu^{\tilde{J}} \rangle = N_\mu^J N_\nu^{\tilde{J}} (\mathbf{f}^\dagger \cdot \mathbf{O}^{J\tilde{J}} \cdot \mathbf{f})_{\mu\nu} \,. \tag{5.32}$$

Equation (5.32) shows that, up to a normalising factor, the transition amplitudes in the PAV frame are provided by the projected kernels from Eq. (5.32) combined with the unprojected linear coefficients of the GCM collective wave-function from Eq. (5.25).

5.3 Transition amplitudes for projected states

The general formula for angular-momentum-projected transition amplitudes between intrinsically deformed states is addressed in this section. This general derivation is reported in order to further introduce in Sec. 5.4 the PAV RPA formalism.

5.3.1 General case

Using the definition from Eq. (5.21) it is now possible to explicitly evaluate the transition amplitude between projected intrinsic states

$$\langle J_1 M_1 | T_{\lambda\mu} | J_2 M_2 \rangle = N_1 N_2 \sum_{K_1 K_2} g^{J_1}_{K_1} g^{J_2}_{K_2} \langle \Phi_1 | P^{J_1 \dagger}_{M_1 K_1} T_{\lambda\mu} P^{J_2}_{M_2 K_2} | \Phi_2 \rangle \,, \tag{5.33}$$

where the normalisation factors N_i are introduced as

$$\begin{aligned} N_i^{-1} &\equiv \sqrt{\sum_{K_1 K_2} g^{J_i}_{K_1} g^{J_i}_{K_2} \langle \Phi_i | P^{J_i \dagger}_{M_i K_1} P^{J_i}_{M_i K_2} | \Phi_i \rangle} \\ &= \sqrt{\sum_{K_1 K_2} g^{J_i}_{K_1} g^{J_i}_{K_2} \langle \Phi_i | P^{J_i}_{K_1 K_2} | \Phi_i \rangle} . \end{aligned} \tag{5.34}$$

Employing Eq. (5.19a), the transition amplitude reads as

$$\begin{aligned} \frac{(5.33)}{N_1 N_2} &= \frac{(2J_1+1)(2J_2+1)}{64\pi^4} \sum_{K_1 K_2} g^{J_1}_{K_1} g^{J_2}_{K_2} \int \mathrm{d}\Omega_1 \mathrm{d}\Omega_2 \mathcal{D}^{J_1}_{M_1 K_1}(\Omega_1) \mathcal{D}^{J_2 *}_{M_2 K_2}(\Omega_2) \langle \Phi_1 | \mathcal{R}^\dagger(\Omega_1) T_{\lambda\mu} \mathcal{R}(\Omega_2) | \Phi_2 \rangle \\ &= \frac{(2J_1+1)(2J_2+1)}{64\pi^4} \sum_{K_1 K_2} g^{J_1}_{K_1} g^{J_2}_{K_2} \int \mathrm{d}\Omega_1 \mathrm{d}\Omega_2 \mathcal{D}^{J_1}_{M_1 K_1}(\Omega_1) \mathcal{D}^{J_2 *}_{M_2 K_2}(\Omega_2) \langle \Phi_1 | \mathcal{R}^\dagger(\Omega_1) T_{\lambda\mu} \mathcal{R}(\Omega_1) \mathcal{R}^\dagger(\Omega_1) \mathcal{R}(\Omega_2) | \Phi_2 \rangle \\ &= \frac{(2J_1+1)(2J_2+1)}{64\pi^4} \sum_{\substack{K_1 K_2 \\ \mu'}} g^{J_1}_{K_1} g^{J_2}_{K_2} \int \mathrm{d}\Omega_1 \mathrm{d}\Omega_2 \mathcal{D}^{J_1}_{M_1 K_1}(\Omega_1) \mathcal{D}^{J_2 *}_{M_2 K_2}(\Omega_2) \mathcal{D}^{\lambda *}_{\mu\mu'}(\Omega_1) \langle \Phi_1 | T_{\lambda\mu'} \mathcal{R}^\dagger(\Omega_1) \mathcal{R}(\Omega_2) | \Phi_2 \rangle \,, \end{aligned} \tag{5.35}$$

where in the last line Eq. (5.14) has been used. The auxiliary definition

$$\mathcal{R}(\Omega) \equiv \mathcal{R}^\dagger(\Omega_1) \mathcal{R}(\Omega_2) \,, \tag{5.36}$$

is then introduced, which implies

$$\begin{aligned} \mathcal{D}^{J_2}_{M_2 K_2}(\Omega_2) &= \langle J_2 M_2 | \mathcal{R}(\Omega_2) | J_2 K_2 \rangle \\ &= \sum_{M'} \langle J_2 M_2 | \mathcal{R}(\Omega_1) | J_2 M' \rangle \langle J_2 M' | R(\Omega) | J_2 K_2 \rangle \\ &= \sum_{M'} \mathcal{D}^{J_2}_{M_2 M'}(\Omega_1) \mathcal{D}^{J_2}_{M' K_2}(\Omega) . \end{aligned} \tag{5.37}$$

Upon the introduction of Eqs. (5.36) and (5.37), Eq. (5.35) reads

$$\begin{aligned} (5.35) &= \frac{(2J_1+1)(2J_2+1)}{64\pi^4} \sum_{\substack{K_1 K_2 \\ M' \mu'}} g^{J_1}_{K_1} g^{J_2}_{K_2} \int \mathrm{d}\Omega_1 \mathrm{d}\Omega \mathcal{D}^{J_1}_{M_1 K_1}(\Omega_1) \mathcal{D}^{J_2 *}_{M_2 M'}(\Omega_1) \mathcal{D}^{J_2 *}_{M' K_2}(\Omega) \mathcal{D}^{\lambda *}_{\mu\mu'}(\Omega_1) \langle \Phi_1 | T_{\lambda\mu'} \mathcal{R}(\Omega) | \Phi_2 \rangle \\ &= \frac{(2J_1+1)(2J_2+1)}{64\pi^4} \sum_{\substack{K_1 K_2 \\ M' \mu'}} g^{J_1}_{K_1} g^{J_2}_{K_2} \int \mathrm{d}\Omega_1 \mathrm{d}\Omega (-1)^{M_1 - K_1} \mathcal{D}^{J_1 *}_{-M_1 -K_1}(\Omega_1) \mathcal{D}^{J_2 *}_{M_2 M'}(\Omega_1) \mathcal{D}^{\lambda *}_{\mu\mu'}(\Omega_1) \mathcal{D}^{J_2 *}_{M' K_2}(\Omega) \times \\ &\quad \times \langle \Phi_1 | T_{\lambda\mu'} \mathcal{R}(\Omega) | \Phi_2 \rangle \end{aligned}$$

$$= \frac{(2J_1+1)(2J_2+1)}{8\pi^2} \sum_{\substack{K_1 K_2 \\ M'\mu'}} g^{J_1}_{K_1} g^{J_2}_{K_2} (-1)^{M_1-K_1} \begin{pmatrix} J_1 & J_2 & \lambda \\ -M_1 & M_2 & \mu \end{pmatrix} \begin{pmatrix} J_1 & J_2 & \lambda \\ -K_1 & M' & \mu' \end{pmatrix} \int \mathrm{d}\Omega \mathcal{D}^{J_2 *}_{M'K_2}(\Omega) \langle \Phi_1 | T_{\lambda\mu'} \mathcal{R}(\Omega) | \Phi_2 \rangle \,, \tag{5.38}$$

where in the second and third lines Wigner D-matrix properties from Eqs. (5.11) and (5.12) have been respectively used. The first 3-j symbol imposes the condition $M_2 = M_1 - \mu$, and can be factorised out of the loop to make Eq. (5.38) consistent with Wigner-Eckart's theorem from Eq. (5.17). The second 3-j symbol imposes $M' = K_1 - \mu'$, so that

$$\begin{aligned} (5.38) = \frac{(2J_1+1)(2J_2+1)}{8\pi^2} & \begin{pmatrix} J_1 & J_2 & \lambda \\ -M_1 & M_1-\mu & \mu \end{pmatrix} \sum_{\substack{K_1 K_2 \\ \mu'}} g^{J_1}_{K_1} g^{J_2}_{K_2} (-1)^{M_1-K_1} \begin{pmatrix} J_1 & J_2 & \lambda \\ -K_1 & K_1-\mu' & \mu' \end{pmatrix} \times \\ & \times \int \mathrm{d}\Omega \mathcal{D}^{J_2 *}_{K_1-\mu' K_2}(\Omega) \langle \Phi_1 | T_{\lambda\mu'} \mathcal{R}(\Omega) | \Phi_2 \rangle \\ = (2J_1+1) & \begin{pmatrix} J_1 & J_2 & \lambda \\ -M_1 & M_1-\mu & \mu \end{pmatrix} \sum_{\substack{K_1 K_2 \\ \mu'}} g^{J_1}_{K_1} g^{J_2}_{K_2} (-1)^{M_1-K_1} \begin{pmatrix} J_1 & J_2 & \lambda \\ -K_1 & K_1-\mu' & \mu' \end{pmatrix} \langle \Phi_1 | T_{\lambda\mu'} P^{J_2}_{K_1-\mu' K_2} | \Phi_2 \rangle \,. \end{aligned} \tag{5.39}$$

Equating to Eq. (5.17) one finds

$$\begin{aligned} (-1)^{2J_1+J_2+\lambda-M_1} \frac{\langle J_1 \| T_\lambda \| J_2 \rangle}{N_1 N_2} &= (2J_1+1) \sum_{\substack{K_1 K_2 \\ \mu'}} g^{J_1}_{K_1} g^{J_2}_{K_2} (-1)^{M_1-K_1} \begin{pmatrix} J_1 & J_2 & \lambda \\ -K_1 & K_1-\mu' & \mu' \end{pmatrix} \langle \Phi_1 | T_{\lambda\mu'} P^{J_2}_{K_1-\mu' K_2} | \Phi_2 \rangle \\ &= (2J_1+1) \sum_{\substack{K_1 K_2 \\ \mu'}} g^{J_1}_{K_1} g^{J_2}_{K_2} (-1)^{M_1-K_1+J_1+J_2+\lambda} \begin{pmatrix} J_1 & \lambda & J_2 \\ -K_1 & \mu' & K_1-\mu' \end{pmatrix} \langle \Phi_1 | T_{\lambda\mu'} P^{J_2}_{K_1-\mu' K_2} | \Phi_2 \rangle \,, \end{aligned} \tag{5.40}$$

which eventually provides

$$\langle J_1 \| T_\lambda \| J_2 \rangle = N_1 N_2 (2J_1+1) \sum_{\substack{K_1 K_2 \\ \mu}} g^{J_1}_{K_1} g^{J_2}_{K_2} (-1)^{J_1-K_1} \begin{pmatrix} J_1 & \lambda & J_2 \\ -K_1 & \mu & K_1-\mu \end{pmatrix} \langle \Phi_1 | T_{\lambda\mu} P^{J_2}_{K_1-\mu, K_2} | \Phi_2 \rangle \,. \tag{5.41}$$

This is the textbook formula given, for instance, in Eq. (11.137) of Ref. [89].

The possibility based on Wigner-Eckart's theorem to extract the reduced matrix element from a single $T_{\lambda\mu}$ component of the spherical tensor is lost when employing good-angular-momentum states resulting from projected intrinsically-deformed states. Indeed, as Eq. (5.41) shows, the sum over μ needs to be explicitly performed to extract the reduced matrix elements.

5.3.2 Axial symmetry

As previously pointed out, limiting the discussion to axially-deformed intrinsic states makes the coefficients g^J_K appearing in Eq. (5.21) trivial. Thus, in the axial case Eq. (5.41) simplifies as

$$\langle J_1 \| T_\lambda \| J_2 \rangle = N_1 N_2 (2J_1+1) \sum_{\mu=-\lambda}^{+\lambda} (-1)^{J_1-K_1} \begin{pmatrix} J_1 & \lambda & J_2 \\ -K_1 & \mu & K_1-\mu \end{pmatrix} \langle \Phi_1 | T_{\lambda\mu} P^{J_2}_{K_1-\mu, K_2} | \Phi_2 \rangle \,, \tag{5.42}$$

where K_1 and K_2 are the quantum numbers carried by the states $|\Phi_1\rangle$ and $|\Phi_2\rangle$ respectively and where

$$N_i^{-1} = \sqrt{\langle\Phi_i|P^{J_i}_{K_iK_i}|\Phi_i\rangle}. \tag{5.43}$$

The projector can be further simplified, since due to axial symmetry the integration over α and γ can be resolved explicitly as shown in App. I.2, so that the only non-trivial integral to be performed is the one over β, providing an "effective" projection operator

$$P^J_{MK} = \frac{2J+1}{2}\int_{-1}^{+1} \mathrm{d}(\cos\beta) d^J_{MK}(\beta) e^{-i\beta J_y}. \tag{5.44}$$

5.4 Application to RPA

5.4.1 Original RPA formulation

Since the RPA formalism does not explicitly provide the wave-function neither of the ground-state nor of the excited states, some remarks are in order. The RPA excited states $|\omega\rangle$ relate to the RPA ground state via the action of an excitation operator resulting from the linear combination of one-particle-one-hole creation and annihilation operators, according to

$$Q^\dagger_\omega|\mathrm{RPA}\rangle = |\omega\rangle\,, \tag{5.45a}$$
$$Q_\omega|\mathrm{RPA}\rangle = 0\,, \tag{5.45b}$$

with

$$Q^\dagger_\omega \equiv \sum_{ph}\left\{X^\omega_{ph}c^\dagger_p c_h - Y^\omega_{ph}c^\dagger_h c_p\right\}. \tag{5.46}$$

In order to provide an explicit formulation of the projected transition amplitudes in the RPA framework, let us profit from the QBA. In this context the QBA boils down to replacing operators products with commutators and to substituting the actual RPA ground-state with the uncorrelated HF ground-state

$$|\mathrm{RPA}\rangle \approx |\mathrm{HF}\rangle\,. \tag{5.47}$$

The transition amplitude operated by the tensor operator $T_{\lambda\mu}$ between the ground state and any excited state is thus delivered by

$$\begin{aligned}\langle\mathrm{RPA}|T_{\lambda\mu}|\omega\rangle &= \langle\mathrm{RPA}|T_{\lambda\mu}Q^\dagger_\omega|\mathrm{RPA}\rangle \\ &= \langle\mathrm{RPA}|[T_{\lambda\mu},Q^\dagger_\omega]|\mathrm{RPA}\rangle \\ &\approx \langle\mathrm{HF}|[T_{\lambda\mu},Q^\dagger_\omega]|\mathrm{HF}\rangle\,.\end{aligned} \tag{5.48}$$

Expressing the RPA phonons in terms of their particle-hole components according to Eq. (5.46) leads to

$$\langle\mathrm{HF}|[T_{\lambda\mu},Q^\dagger_\omega]|\mathrm{HF}\rangle = \sum_{ph}\left\{X^\omega_{ph}\langle\mathrm{HF}|T_{\lambda\mu}c^\dagger_p c_h|\mathrm{HF}\rangle + Y^\omega_{ph}\langle\mathrm{HF}|c^\dagger_h c_p T_{\lambda\mu}|\mathrm{HF}\rangle\right\}. \tag{5.49}$$

If $T_{\lambda\mu}$ is a one-body operator, Eq. (5.49) reduces to

$$\langle\mathrm{RPA}|T_{\lambda\mu}|\omega\rangle \approx \sum_{ph}\left\{X^\omega_{ph}\langle h|T_{\lambda\mu}|p\rangle + Y^\omega_{ph}\langle p|T_{\lambda\mu}|h\rangle\right\}, \tag{5.50}$$

which is the standard formula implied in the evaluation of RPA strength functions.

5.4.2 General philosophy

Few words are in order before focusing on the possible ways to introduce symmetry restoration in the original symmetry-breaking RPA strength. Specifically, one should proceed keeping in mind the following question: what should the limit of the derivation be if the effect of projection is eventually removed? The answer which is proposed here is that Eq. (5.48) should be recovered once the projector is removed. Any reasonable formulation satisfying this condition is equally good *a priori*.

5.4.3 Naive projection

In principle, the easiest strategy could be straightforwardly derived from Eq. (5.42). However, the following lines will explain why this could actually pose a problem. If the canonical QBA steps leading to Eq. (5.48) are introduced into Eq. (5.42), with $\langle\Phi_1| \equiv \langle\text{RPA}|$ and $|\Phi_2\rangle \equiv |\omega\rangle$, the following controversial behaviour is found

$$\begin{aligned}\langle\text{RPA}|T_{\lambda\mu}P^{J_\omega}_{K_0-\mu,K_\omega}|\omega\rangle &= \langle\text{RPA}|T_{\lambda\mu}P^{J_\omega}_{K_0-\mu,K_\omega}Q^\dagger_\omega|\text{RPA}\rangle \\ &= \langle\text{RPA}|[T_{\lambda\mu}P^{J_\omega}_{K_0-\mu,K_\omega}, Q^\dagger_\omega]|\text{RPA}\rangle \\ &\approx \langle\text{HF}|[T_{\lambda\mu}P^{J_\omega}_{K_0-\mu,K_\omega}, Q^\dagger_\omega]|\text{HF}\rangle\,. \end{aligned} \tag{5.51}$$

Here J_ω is the total angular momentum of the excited state, K_0 refers to the J_z quantum number of the HF ground-state and the same for K_ω with respect to the excited state. The phonon $|\omega\rangle$ resulting from the linear combination of ph excitations carries the selection rule $K_\omega = K_{ph}$ for all involved ph excitations. If the definition of the RPA phonons from Eq. (5.46) is introduced, Eq. (5.51) reads

$$(5.51) = \sum_{ph}\left\{X^\omega_{ph}\langle\text{HF}|T_{\lambda\mu}P^{J_\omega}_{K_0-\mu,K_{ph}}c^\dagger_p c_h|\text{HF}\rangle + Y^\omega_{ph}\langle\text{HF}|c^\dagger_h c_p T_{\lambda\mu}P^{J_\omega}_{K_0-\mu,K_{ph}}|\text{HF}\rangle\right\}. \tag{5.52}$$

The second term in Eq. (5.52), i.e. the backward amplitude, raises a problem. Indeed, it vanishes for $K_{ph} \neq K_0$ (see Appendices I.1 and I.2). This same consideration had already been pointed out in Ref. [145]. This would typically mean that in even-even systems, where $K_0 = 0$, the backward amplitude would not vanish only if $\mu = 0$ excitations are considered. If Eq. (5.52) could set these specific projected spectra on a sound basis, nonetheless a more general derivation is in order for other kind of excitations.

Overall, the main problem is the ambiguity of the way one deals with the absence of an explicit wave-function for the RPA ground- and excited states, i.e. using commutators when product of operators are involved and substituting the RPA ground-state with the uncorrelated HF determinant is incompatible with an unambiguous inclusion of projectors.

TDA limit

As a counterexample, the inclusion of the projector in the Tamm-Dancoff Approximation (TDA) could be easily achieved in an unambiguous manner. If the TDA phonons are introduced as

$$Q^\dagger_{\omega_{\text{TDA}}} \equiv \sum_{ph} X^{\omega_{\text{TDA}}}_{ph} c^\dagger_p c_h\,, \tag{5.53}$$

then the TDA ground state corresponds to the uncorrelated HF ground state. The projected transition amplitudes are properly delivered by

$$\langle\text{TDA}|T_{\lambda\mu}P^{J_\omega}_{K_0-\mu K_\omega}|\omega_{\text{TDA}}\rangle = \langle\text{TDA}|T_{\lambda\mu}P^{J_\omega}_{K_0-\mu K_\omega}Q^\dagger_{\omega_{\text{TDA}}}|\text{TDA}\rangle$$

$$= \langle \mathrm{HF}|T_{\lambda\mu} P^{J_\omega}_{K_0-\mu K_\omega} Q^\dagger_{\omega_{\mathrm{TDA}}}|\mathrm{HF}\rangle \,. \tag{5.54}$$

Using Eq. (5.53) leads to

$$\langle \mathrm{TDA}|T_{\lambda\mu} P^{J_\omega}_{K_0-\mu K_\omega}|\omega_{\mathrm{TDA}}\rangle = \sum_{ph} X^{\omega_{\mathrm{TDA}}}_{ph} \langle \mathrm{HF}|T_{\lambda\mu} P^{J_\omega}_{K_0-\mu K_{ph}} c^\dagger_p c_h|\mathrm{HF}\rangle \,, \tag{5.55}$$

without any problem raised by the introduction of the projector.

5.4.4 Adopted strategy

Along the lines of what has previously mentioned in Sec. 5.4.2, let us formulate an alternative way to introduce symmetry restoration in a symmetry-breaking RPA strength function. The only criterion to be respected is that if the projector is taken away, Eq. (5.48) has to be recovered. With this in mind, let us more explicitly rewrite Eq. (5.48) as

$$\begin{aligned}
\langle \mathrm{RPA}|T_{\lambda\mu}|\omega\rangle &= \langle \mathrm{RPA}|T_{\lambda\mu} Q^\dagger_\omega|\mathrm{RPA}\rangle \\
&= \langle \mathrm{RPA}|T_{\lambda\mu} Q^\dagger_\omega|\mathrm{RPA}\rangle - \langle \mathrm{RPA}|Q^\dagger_\omega T_{\lambda\mu}|\mathrm{RPA}\rangle \\
&\approx \langle \mathrm{HF}|T_{\lambda\mu} Q^\dagger_\omega|\mathrm{HF}\rangle - \langle \mathrm{HF}|Q^\dagger_\omega T_{\lambda\mu}|\mathrm{HF}\rangle \,.
\end{aligned} \tag{5.56}$$

This is exactly what was achieved by the introduction of the commutator. Writing the phonons in terms of their ph components one obtains

$$\langle \mathrm{RPA}|T_{\lambda\mu}|\omega\rangle = \sum_{ph} \Big\{ X^\omega_{ph} \langle \mathrm{HF}|T_{\lambda\mu} c^\dagger_p c_h|\mathrm{HF}\rangle + Y^\omega_{ph} \langle \mathrm{HF}|c^\dagger_h c_p T_{\lambda\mu}|\mathrm{HF}\rangle \Big\} \tag{5.57}$$

which is the usual RPA expression. The projector can be introduced in Eq. (5.56) while making sure that the null term added in the second line involves a projector carrying the appropriate set of quantum numbers. More in detail

$$\begin{aligned}
\langle \mathrm{RPA}|T_{\lambda\mu} P^{J_\omega}_{K_0-\mu,K_{ph}}|\omega\rangle &= \langle \mathrm{RPA}|T_{\lambda\mu} P^{J_\omega}_{K_0-\mu,K_{ph}} Q^\dagger_\omega|\mathrm{RPA}\rangle \\
&= \langle \mathrm{RPA}|T_{\lambda\mu} P^{J_\omega}_{K_0-\mu,K_{ph}} Q^\dagger_\omega|\mathrm{RPA}\rangle - \langle \mathrm{RPA}|Q^\dagger_\omega P^{J_\omega}_{K_{ph},K_0+\mu} T_{\lambda\mu}|\mathrm{RPA}\rangle \\
&\approx \langle \mathrm{HF}|T_{\lambda\mu} P^{J_\omega}_{K_0-\mu,K_{ph}} Q^\dagger_\omega|\mathrm{HF}\rangle - \langle \mathrm{HF}|Q^\dagger_\omega P^{J_\omega}_{K_{ph},K_0+\mu} T_{\lambda\mu}|\mathrm{HF}\rangle \,.
\end{aligned} \tag{5.58}$$

If the phonons are expanded in terms of their ph components, then

$$(5.58) = \sum_{ph} \Big\{ X^\omega_{ph} \langle \mathrm{HF}|T_{\lambda\mu} P^{J_\omega}_{K_0-\mu,K_{ph}} c^\dagger_p c_h|\mathrm{HF}\rangle + Y^\omega_{ph} \langle \mathrm{HF}|c^\dagger_h c_p P^{J_\omega}_{K_{ph},K_0+\mu} T_{\lambda\mu}|\mathrm{HF}\rangle \Big\} . \tag{5.59}$$

The second term can be further elaborated

$$\begin{aligned}
Y^\omega_{ph} \langle \mathrm{HF}|c^\dagger_h c_p P^{J_\omega}_{K_{ph},K_0+\mu} T_{\lambda\mu}|\mathrm{HF}\rangle &= Y^\omega_{ph} \langle \mathrm{HF}|T^\dagger_{\lambda\mu} P^{J_\omega\dagger}_{K_{ph},K_0+\mu} c^\dagger_p c_h|\mathrm{HF}\rangle^* \\
&= (-1)^\mu Y^\omega_{ph} \langle \mathrm{HF}|T_{\lambda-\mu} P^{J_\omega}_{K_0+\mu,K_{ph}} c^\dagger_p c_h|\mathrm{HF}\rangle^* \\
&= (-1)^{-\mu'} Y^\omega_{ph} \langle \mathrm{HF}|T_{\lambda\mu'} P^{J_\omega}_{K_0-\mu',K_{ph}} c^\dagger_p c_h|\mathrm{HF}\rangle^* \,,
\end{aligned} \tag{5.60}$$

with $\mu' = -\mu$.The sum of the forward and backward contributions eventually gives

$$\langle \mathrm{RPA}|T_{\lambda\mu}P^{J_\omega}_{K_0-\mu,K_{ph}}|\omega\rangle \approx \sum_{ph}\left\{X^\omega_{ph}\langle \mathrm{HF}|T_{\lambda\mu}P^{J_\omega}_{K_0-\mu,K_{ph}}c^\dagger_p c_h|\mathrm{HF}\rangle + (-1)^{-\mu'}Y^\omega_{ph}\langle \mathrm{HF}|T_{\lambda\mu'}P^{J_\omega}_{K_0-\mu',K_{ph}}c^\dagger_p c_h|\mathrm{HF}\rangle^*\right\}. \tag{5.61}$$

If the sum over μ (μ') is inserted in order to rename dummy indices and the realness hypothesis is satisfied, then the expression

$$\langle \mathrm{RPA}||T_\lambda||\omega\rangle = N_0 N_\omega (2J_0+1)(-1)^{J_0-K_0}\sum_{ph}\sum_{\mu=-\lambda}^{+\lambda}\left\{X^\omega_{ph}+(-1)^\mu Y^\omega_{ph}\right\}\begin{pmatrix} J_0 & \lambda & J_\omega \\ -K_0 & \mu & K_0-\mu\end{pmatrix}\langle \mathrm{HF}|T_{\lambda\mu}P^{J_\omega}_{K_0-\mu,K_{ph}}c^\dagger_p c_h|\mathrm{HF}\rangle \tag{5.62}$$

is eventually obtained, with the normalising factors N_0 and N_ω defined below. Equation (5.62) is equivalent to Eq. (6.40) of Ref. [147] up to a phase factor in front of the backwards amplitude. Details about the actual implementation of Eq. (5.62) are given in App. J.

5.5 Normalising RPA factors

5.5.1 Original RPA condition

The RPA normalisation factors are provided recurring, again, to the sole QBA from Eq. (5.47), such that the original condition reads as

$$\begin{aligned}\langle \mathrm{RPA}|Q_\omega Q^\dagger_\omega|\mathrm{RPA}\rangle &= \langle \mathrm{RPA}|[Q_\omega, Q^\dagger_\omega]|\mathrm{RPA}\rangle \\ &\approx \langle \mathrm{HF}|[Q_\omega, Q^\dagger_\omega]|\mathrm{HF}\rangle\,.\end{aligned} \tag{5.63}$$

The explicit writing of the phonons according to Eq. (5.46) eventually leads to

$$\begin{aligned}(5.63) &= \sum_{ph}\left\{X^\omega_{ph}\langle \mathrm{HF}|[Q_\omega, c^\dagger_p c_h]|\mathrm{HF}\rangle - Y^\omega_{ph}\langle \mathrm{HF}|[Q_\omega, c^\dagger_h c_p]|\mathrm{HF}\rangle\right\} \\ &= \sum_{ph}\left\{X^\omega_{ph}\langle \mathrm{HF}|Q_\omega c^\dagger_p c_h|\mathrm{HF}\rangle + Y^\omega_{ph}\langle \mathrm{HF}|c^\dagger_h c_p Q_\omega|\mathrm{HF}\rangle\right\} \\ &= \sum_{\substack{ph\\qi}}\left\{X^\omega_{ph}X^\omega_{qi}\langle \mathrm{HF}|c^\dagger_i c_q c^\dagger_p c_h|\mathrm{HF}\rangle - Y^\omega_{ph}Y^\omega_{qi}\langle \mathrm{HF}|c^\dagger_h c_p c^\dagger_q c_i|\mathrm{HF}\rangle\right\} \\ &= \sum_{\substack{ph\\qi}}\left\{X^\omega_{ph}X^\omega_{qi} - Y^\omega_{ph}Y^\omega_{qi}\right\}\langle \mathrm{HF}|c^\dagger_i c_q c^\dagger_p c_h|\mathrm{HF}\rangle \\ &= \sum_{ph}\left\{X^\omega_{ph}X^\omega_{ph} - Y^\omega_{ph}Y^\omega_{ph}\right\} \\ &= 1\,,\end{aligned} \tag{5.64}$$

which is the standard normalisation condition of RPA states.

5.5.2 Naive projection

If, in line with what has been previously done in Sec. 5.4.3 for the transitions amplitudes, a projector is inserted before invoking a commutator, the following result is obtained

$$\langle \mathrm{RPA}|Q_\omega P^{J_\omega}_{K_{ph},K_{ph}}Q^\dagger_\omega|\mathrm{RPA}\rangle = \langle \mathrm{RPA}|[Q_\omega P^{J_\omega}_{K_{ph},K_{ph}}, Q^\dagger_\omega]|\mathrm{RPA}\rangle$$

$$\approx \langle \mathrm{HF}|[Q_\omega P^{J_\omega}_{K_{ph},K_{ph}}, Q^\dagger_\omega]|\mathrm{HF}\rangle\,. \tag{5.65}$$

Further elaborating via Eq. (5.46) leads to

$$\begin{aligned}
(5.65) &= \sum_{ph}\left\{X^\omega_{ph}\langle \mathrm{HF}|[Q_\omega P^{J_\omega}_{K_{ph},K_{ph}}, c^\dagger_p c_h]|\mathrm{HF}\rangle - Y^\omega_{ph}\langle \mathrm{HF}|[Q_\omega P^{J_\omega}_{K_{ph},K_{ph}}, c^\dagger_h c_p]|\mathrm{HF}\rangle\right\}\\
&= \sum_{ph}\left\{X^\omega_{ph}\langle \mathrm{HF}|Q_\omega P^{J_\omega}_{K_{ph},K_{ph}} c^\dagger_p c_h|\mathrm{HF}\rangle + Y^\omega_{ph}\langle \mathrm{HF}|c^\dagger_h c_p Q_\omega P^{J_\omega}_{K_{ph},K_{ph}}|\mathrm{HF}\rangle\right\}\\
&= \sum_{\substack{ph\\qi}}\left\{X^\omega_{ph}X^\omega_{qi}\langle \mathrm{HF}|c^\dagger_i c_q P^{J_\omega}_{K_{ph},K_{ph}} c^\dagger_p c_h|\mathrm{HF}\rangle - Y^\omega_{ph}Y^\omega_{qi}\langle \mathrm{HF}|c^\dagger_h c_p c^\dagger_q c_i P^{J_\omega}_{K_{ph},K_{ph}}|\mathrm{HF}\rangle + Y^\omega_{ph}X^\omega_{qi}\langle \mathrm{HF}|c^\dagger_h c_p c^\dagger_i c_q P^{J_\omega}_{K_{ph},K_{ph}}|\mathrm{HF}\rangle\right\}\\
&= \sum_{\substack{ph\\qi}} X^\omega_{ph}X^\omega_{qi}\langle \mathrm{HF}|c^\dagger_i c_q P^{J_\omega}_{K_{ph},K_{ph}} c^\dagger_p c_h|\mathrm{HF}\rangle - \sum_{ph} Y^{\omega\,2}_{ph}\langle \mathrm{HF}|P^{J_\omega}_{K_{ph},K_{ph}}|\mathrm{HF}\rangle + \sum_{\substack{ph\\qi}} Y^\omega_{ph}X^\omega_{qi}\langle \mathrm{HF}|c^\dagger_h c_p c^\dagger_i c_q P^{J_\omega}_{K_{ph},K_{ph}}|\mathrm{HF}\rangle\,.
\end{aligned} \tag{5.66}$$

The normalising factor displays the aforementioned ambiguity regarding the indices of the projector. Eventually three different terms remain, the first one representing the projected overlap between two ph states in the forward channel, the second one being the projected overlap between HF states multiplied by the backward amplitudes and the third one representing a projected overlap between 2p2h states and the HF state multiplied by an admixture of forward and backward amplitudes. However, as shown in App. I.1, only projectors matching the good quantum numbers of the intrinsic states provide non-vanishing contributions, which would eventually result in the sole forward component.

5.5.3 Adopted strategy

The ground state norm in presence of the projection is straightforwardly obtained as

$$N_0^{-1} = \sqrt{\langle \mathrm{HF}|P^{J_0}_{K_0K_0}|\mathrm{HF}\rangle}, \tag{5.67}$$

As for the excited states, along the lines of what was done in Sec. (5.4.4), the following derivation is proposed. The original object to compute is

$$\langle \mathrm{RPA}|Q_\omega P^{J_\omega}_{K_\omega,K_\omega} Q^\dagger_\omega|\mathrm{RPA}\rangle\,. \tag{5.68}$$

As usual, nothing forbids the introduction of a vanishing quantity with appropriate anticipated properties once the QBA is applied. Doing so leads to

$$\begin{aligned}
\langle \mathrm{RPA}|Q_\omega P^{J_\omega}_{K_\omega,K_\omega} Q^\dagger_\omega|\mathrm{RPA}\rangle &= \langle \mathrm{RPA}|Q_\omega P^{J_\omega}_{K_\omega,K_\omega} Q^\dagger_\omega|\mathrm{RPA}\rangle - \langle \mathrm{RPA}|Q^\dagger_\omega P^{J_\omega}_{K_\omega,K_\omega} Q_\omega|\mathrm{RPA}\rangle\\
&\approx \langle \mathrm{HF}|Q_\omega P^{J_\omega}_{K_\omega,K_\omega} Q^\dagger_\omega|\mathrm{HF}\rangle - \langle \mathrm{HF}|Q^\dagger_\omega P^{J_\omega}_{K_\omega,K_\omega} Q_\omega|\mathrm{HF}\rangle\,,
\end{aligned} \tag{5.69}$$

where in the second line the QBA from Eq. (5.47) has been introduced. If the projector is taken away, the RPA normalisation is recovered. Further elaborating via Eq. (5.46) gives

$$\begin{aligned}
(5.69) &= \sum_{\substack{ph\\qi}}\left\{X^\omega_{ph}X^\omega_{qi}\langle \mathrm{HF}|c^\dagger_i c_q P^{J_\omega}_{K_{qi},K_{ph}} c^\dagger_p c_h|\mathrm{HF}\rangle - Y^\omega_{ph}Y^\omega_{qi}\langle \mathrm{HF}|c^\dagger_h c_p P^{J_\omega}_{K_{qi},K_{ph}} c^\dagger_q c_i|\mathrm{HF}\rangle\right\}\\
&= \sum_{\substack{ph\\qi}}\left\{X^\omega_{ph}X^\omega_{qi} - Y^\omega_{ph}Y^\omega_{qi}\right\}\langle \mathrm{HF}|c^\dagger_i c_q P^{J_\omega}_{K_{qi},K_{ph}} c^\dagger_p c_h|\mathrm{HF}\rangle\,,
\end{aligned} \tag{5.70}$$

where in the second line summed indices have been renamed for compactness' sake. Equation (5.70) is equivalent to Eq. (6.43) from Ref. [147]. Details about the actual implementation of Eq. (5.70) are given in App. J.

5.6 Identity resolutions involving the AMP

Projected quantities, such as transition matrix elements and states overlap, which are involved in the calculation of the projected strength function, offer a tool to test the correctness of the implementation itself. Indeed, in the case of RPA this projection technique has been implemented only in one case [147] in the literature, such that strong internal benchmarks are essential. Moreover, many other insights are provided at the same time to further investigate the nature of the particle-hole excitations and the collective phonons themselves, which also has no priors in literature to the best of our knowledge.

The identity resolution on a set of states carrying good angular momentum quantum numbers is introduced as

$$\mathbb{1} = \sum_{JM\alpha} |JM\alpha\rangle\langle JM\alpha| \tag{5.71a}$$

$$= \sum_{JM} P^J_{MM}\,, \tag{5.71b}$$

where the definition of the projector provided by Eqs. (5.19a) and (5.19b) has been used.

Starting from the simplest case of a Slater determinant $|\Phi\rangle$, the identity resolution from Eq. (5.71b) can be employed to decompose the normalised state into its good angular momentum components

$$\begin{aligned}\langle\Phi|\Phi\rangle &= \sum_{JM\alpha} \langle\Phi|JM\alpha\rangle\langle JM\alpha|\Phi\rangle \\ &= \sum_{J\alpha} \langle\Phi|JK\alpha\rangle\langle JK\alpha|\Phi\rangle \\ &= \sum_{J} \langle\Phi|P^J_{KK}|\Phi\rangle\,,\end{aligned} \tag{5.72}$$

where in the second line the property $J_z|\Phi\rangle = K|\Phi\rangle$, which is verified in axial symmetry, has been used. This provides the sum rule

$$\sum_J \langle\Phi|P^J_{KK}|\Phi\rangle = 1\,, \tag{5.73}$$

which is verified both for the HF ground state and for each ph excitation contributing to the RPA phonons (and has been checked for all the presented results, see Chap. 12).

The RPA states $|\omega\rangle$ being normalised according to Eq. (5.64) ($\langle\omega|\omega\rangle = 1$), the same decomposition can be verified for all the phonons according to

$$\sum_J \langle\omega|P^j_{K_\omega K_\omega}|\omega\rangle = 1\,, \tag{5.74}$$

and similarly for ph states

$$\sum_J \langle ph|P^j_{K_\omega K_\omega}|ph\rangle = 1\,. \tag{5.75}$$

One can proceed similarly for the overlap between the HF ground state and an arbitrary phonon excitation,

$$\langle \mathrm{HF}|\omega\rangle = \sum_{JM\alpha} \langle \mathrm{HF}|JM\alpha\rangle\langle JM\alpha|\omega\rangle$$

$$
\begin{aligned}
&= \sum_{J\alpha} \langle \mathrm{HF}|JK_0\alpha\rangle\langle JK_{ph}\alpha|\omega\rangle\,\delta_{K_0K_\omega} \\
&= \sum_{J} \langle \mathrm{HF}|P^J_{K_0K_\omega}|\omega\rangle\,\delta_{K_0K_\omega}\,,
\end{aligned} \tag{5.76}
$$

eventually leading to the sum rule

$$
\sum_{J} \langle \mathrm{HF}|P^J_{K_0K_\omega}|\omega\rangle\,\delta_{K_0K_\omega} = 0, \tag{5.77}
$$

which provides a benchmark tool for phonon excitations with $K_\omega = K_0 = 0$. A sum rule involving transition matrix elements is also provided

$$
\begin{aligned}
\langle \mathrm{HF}|T_{\lambda\mu}|\omega\rangle &= \sum_{JM\alpha} \langle \mathrm{HF}|T_{\lambda\mu}|JM\alpha\rangle\langle JM\alpha|\omega\rangle \\
&= \sum_{JM} \langle \mathrm{HF}|T_{\lambda\mu}P^J_{MM}|\omega\rangle \\
&= \sum_{J} \langle \mathrm{HF}|T_{\lambda\mu}P^J_{K_0-\mu,K_\omega}|\omega\rangle\,\delta_{K_0-\mu,K_\omega}
\end{aligned} \tag{5.78}
$$

whenever $T_{\lambda\mu}$ is a one-body operator. All these rules have been numerically tested for the RPA implementation and some of them are detailed in Chap. 12. It is found that all the presented results satisfy these identities to high numerical accuracy, testifying the trustfulness of the numerical implementation of the projection technique in RPA.

5.7 Spurious coupling to rotational states

In this section the concept of coupling to spurious rotational states in symmetry-breaking theories is introduced. While originally inspired by the usual derivation of RPA spurious states [151, 152, 89], the discussion is conducted on a more general level.

5.7.1 Origin of spurious rotations

Among the different possibilities to derive RPA and beyond-RPA theories one can start from the ***Equation Of Motion*** (EOM) technique by Rowe [135], which is particularly suited for the present discussion. The *exact* EOM reads as

$$
\langle 0|\Big[\delta Q,[H,Q^\dagger_\nu]\Big]|0\rangle = (E_\nu - E_0)\,\langle 0|[\delta Q,Q^\dagger_\nu]|0\rangle\,, \tag{5.79}
$$

where the excitation operator $Q^\dagger_\nu$ links the exact ground state $|0\rangle$ to the exact excited state $|\nu\rangle$ according to

$$
Q^\dagger_\nu|0\rangle = |\nu\rangle\,. \tag{5.80}
$$

Symmetry-breaking theories provide approximate symmetry-breaking solutions $|\Psi_0\rangle$ and $|\Psi_\nu\rangle$. In this case, Eq. (5.79) demonstrates that the corresponding symmetry operator commuting with the Hamiltonian delivers a zero-energy solution of the problem[5]. This phenomenon is usually referred to as the appearance of a Goldstone mode.

In the case of present interest one considers rotations by an (Euler) angle Ω. In this case the phonon operator reads as

$$
Q^\dagger_\nu \equiv \mathcal{R}(\Omega)\,, \tag{5.81}
$$

[5] This is only true for the symmetry generator corresponding to the broken symmetry. Indeed, the right-hand-side matrix element in Eq. (5.79) is zero for other symmetries, such that one does not find a solution with $E_\nu - E_0 = 0$.

such that the condition

$$[H, Q_\nu^\dagger] = [H, \mathcal{R}(\Omega)] = 0 \tag{5.82}$$

is satisfied. Consequently, one finds $E_\nu = E_0$ on the right hand side of Eq. (5.79), given that the associated matrix element is non-zero. Let us define the state corresponding to the associated Goldstone mode as

$$|R_\Psi(\Omega)\rangle \equiv \mathcal{R}(\Omega)|\Psi_0\rangle\,. \tag{5.83}$$

These are simply rotated versions of the symmetry-breaking ground state $|\Psi_0\rangle$.

5.7.2 Spurious rotations in RPA

The appearance of spurious coupling to rotational states is now addressed in the RPA context. In RPA the phonons $Q_\omega^\dagger$ are assumed to be the most general combination of 1p-1h excitations. In this sense, arbitrary rotational states cannot be a solution of the usual RPA equations, because a rotation by a finite angle cannot be represented by 1p-1h excitations.

However, in the small-angle limit one can expand the rotation operator $\mathcal{R}(\Omega)$ at first order and retain only its 1p-1h components. This amounts to considering the generator of the rotations as the RPA excitation operator, i.e. the angular momentum operators, which thus delivers a zero-energy solution of the RPA equation. This situation is traditionally denoted as spurious, given that it does not correspond to a genuine vibration.

For axially deformed systems, if rotations about the y-axis are considered, then J_y delivers a zero-energy spurious solution of the RPA equations. Its matrix elements are non-vanishing only in the $K = 1$ channel, given that $J_y = \frac{1}{2i}(J_+ - J_-)$ links single-particle states differing by one unit of J_z. The spurious state being a proper solution of the RPA equations it is by definition orthogonal to all the other RPA solutions. However, in all channels K, it may happen that the phonons are not orthogonal to the non-infinitesimal rotational states, such that

$$\langle R_{\mathrm{RPA}}(\Omega)|\omega\rangle \neq 0\,. \tag{5.84}$$

Such an overlap can be explicitly evaluated via the QBA as

$$\begin{aligned}\langle R_{\mathrm{RPA}}(\Omega)|\omega\rangle &= \langle \mathrm{RPA}|\mathcal{R}^\dagger(\Omega)Q_\omega^\dagger|\mathrm{RPA}\rangle \\ &\approx \langle \mathrm{HF}|[\mathcal{R}^\dagger(\Omega), Q_\omega^\dagger]|\mathrm{HF}\rangle\,.\end{aligned} \tag{5.85}$$

Restricting to axially-deformed systems one eventually obtains

$$\begin{aligned}\langle R_{\mathrm{RPA}}(\beta)|\omega\rangle &\approx \langle \mathrm{HF}|[e^{i\beta J_y}, Q_\omega^\dagger]|\mathrm{HF}\rangle \\ &= \sum_{ph}\Big[(e^{i\beta J_y})_{ph}X_{ph} - (e^{i\beta J_y})_{ph}Y_{ph}\Big].\end{aligned} \tag{5.86}$$

The integration over β of such quantity exactly provides, up to a multiplicative factor, the RPA strength of the projection operator P_{00}^0

$$\langle \mathrm{RPA}|P_{00}^0|\omega\rangle = \frac{1}{2}\int_{-1}^{+1} \mathrm{d}(\cos\beta)\,\langle \mathrm{RPA}|e^{-i\beta J_y}|\omega\rangle\,, \tag{5.87}$$

so that the latter quantity directly provides a quantitative measure of the spurious coupling to the rotational state. The rotational state is, thus, defined in RPA as

$$|\mathrm{ROT}\rangle \equiv N_{\mathrm{ROT}}P_{00}^0|\mathrm{RPA}\rangle\,, \tag{5.88}$$

with N_{ROT} a normalising constant enforcing the condition

$$\langle \mathrm{ROT}|\mathrm{ROT}\rangle = 1\,. \tag{5.89}$$

The overlap between the rotational state and the RPA phonons is then introduced as

$$\begin{aligned} a_\omega &\equiv \langle \mathrm{ROT}|\omega\rangle \\ &= N_{\mathrm{ROT}}\,\langle \mathrm{RPA}|P^0_{00}|\omega\rangle\,. \end{aligned} \tag{5.90}$$

The normalisation condition from Eq. (5.89) is actually ill-defined within RPA. Indeed in RPA no expression is provided for the $|\mathrm{RPA}\rangle$ ground state, so that the uncorrelated Hartree-Fock ground state is adopted instead. Such a discrepancy does not represent necessarily an issue by itself. Relative quantities involving transitions between the ground and the excited states encode such correlation in the RPA coefficients amplitudes. However, when the uncorrelated normalising constant is used with other quantities implicitly encoding RPA correlations, inconsistencies may show up. An example of such a problem is addressed in Chap. 12.

5.7.3 Spurious rotations in GCM

For the reasons mentioned in Sec. 5.7.1, when AMP is not considered in GCM calculations, the solutions of the HWG equation may be non-orthogonal to the rotational state. Similarly to the RPA case from Sec. 5.7.2, let us define the rotational state as

$$|\mathrm{ROT}\rangle \equiv N_{\mathrm{ROT}} P^0_{00}\,|\Psi_0\rangle\,, \tag{5.91}$$

with $|\Psi_0\rangle$ the GCM ground state. The overlap between the rotational state and a GCM excited state $|\Psi_\nu\rangle$ is then introduced as

$$\begin{aligned} a_\nu &\equiv \langle \mathrm{ROT}|\Psi_\nu\rangle \\ &= N_{\mathrm{ROT}}\,\langle \Psi_0|P^0_{00}|\Psi_\nu\rangle\,. \end{aligned} \tag{5.92}$$

Naturally, no spurious coupling to any rotational state appears in full PGCM calculations, since the AMP is enforced in the solution of the HWG equation (the variation is performed *after* the projection).

5.7.4 Subtraction of spurious rotational components

The spurious coupling to the rotational state can be explicitly subtracted by defining a new set of states. The procedure is independent of the method of choice, and can thus be applied to both GCM and RPA calculations (the only disclaimer for RPA calculations being the ill-defined normalising constant of the rotational state discussed in Sec. 5.7.2). Thus, in this section $|\Psi_0\rangle$ and $|\Psi_\nu\rangle$ represent the generic ground and excited states, respectively, of a symmetry-breaking theory.

A set of subtracted states is introduced as [153]

$$|\tilde{\Psi}_\nu\rangle \equiv N_{\tilde{\nu}}\Big[\,|\Psi_\nu\rangle - a_\nu\,|\mathrm{ROT}\rangle\,\Big], \tag{5.93}$$

where the coefficients a_ν are determined such that the condition

$$\langle \mathrm{ROT}|\tilde{\Psi}_\nu\rangle = 0 \tag{5.94}$$

is fulfilled. It is immediate to check that Eq. (5.94) is satisfied for a_ν defined as in Eq. (5.92) (hence the notation). The normalisation constant $N_{\tilde{\nu}}$ thus reads

$$(N_{\tilde{\nu}})^{-2} = 1 - |a_\nu|^2\,. \tag{5.95}$$

The transition amplitude with respect to such subtracted states then reads

$$\langle\Psi_0|O|\tilde{\Psi}_\nu\rangle = N_{\tilde{\nu}}\Big[\langle\Psi_0|O|\Psi_\nu\rangle - N_{\mathrm{ROT}}a_\nu\langle\Psi_0|OP^0_{00}|\Psi_0\rangle\Big]. \tag{5.96}$$

For the GCM, Eq. (5.96) is referred to as the **subtracted GCM** transition amplitude.

One may also introduce a subtracted variant of the projected states from Eq. (5.26) as

$$|\check{\Psi}^J_\nu\rangle \equiv N^J_{\check{\nu}}\Big[P^J|\Psi_\nu\rangle - a_\nu|\mathrm{ROT}\rangle\Big], \tag{5.97}$$

where the coefficients a_ν are defined such that the condition

$$\langle\mathrm{ROT}|\check{\Psi}^J_\nu\rangle = 0 \tag{5.98}$$

is satisfied. Notice that because of the definition of $|\mathrm{ROT}\rangle$ in Eq. (5.91), the states $|\check{\Psi}^J_\nu\rangle$ differ from the PAV states in Eq. (5.26) only for $J = 0$, in which case the coefficients a_ν are again defined as in Eq. (5.92) and the normalising factor $N^0_{\check{\nu}}$ reads

$$(N^0_{\check{\nu}})^{-2} = \langle\Psi_\nu|P^0_{00}|\Psi_\nu\rangle - |a_\nu|^2. \tag{5.99}$$

The transition amplitudes relative to the states $|\check{\Psi}^J_\nu\rangle$ are, thus, only given in the monopole case, reading

$$\langle\tilde{\Psi}^0_0|T_{00}|\check{\Psi}^0_\nu\rangle = N^0_0 N^0_{\check{\nu}}\Big[\langle\Psi_0|T_{00}P^0_{00}|\Psi_\nu\rangle - N_{\mathrm{ROT}}a_\nu\langle\Psi_0|T_{00}P^0_{00}|\Psi_0\rangle\Big]. \tag{5.100}$$

For the GCM, Eq. (5.100) is referred to as the **subtracted PAV GCM** transition amplitudes, whereas in RPA it will be referred to as **subtracted PAV RPA**.

Part II

Results

Chapter 6

GMR in PGCM: a systematic convergence study

Contents

In this and in the following chapters PGCM calculations in axial symmetry are performed in order to access the monopole response of several nuclei of interest in the light- and medium-mass region of the nuclear chart. The monopole response being mostly associated to radial vibrations of the nuclear surface, the mean square radius r represents a natural choice for the main generator coordinate. Since it is known that deformation may also importantly affect the monopole response (see, for instance, Refs. [69, 154]), the parameter

$$\beta_2 \equiv \frac{4\pi}{3R^2A}\langle Q_{20}\rangle\,, \tag{6.1}$$

with $R \equiv 1.2A^{1/3}$, is also considered as a relevant degree of freedom. While other collective coordinates could eventually prove to be relevant, the present work focuses on the description provided by the combination of these two generator coordinates (r, β_2). In order to investigate coupling effects between the

monopole and the quadrupole resonances, the $K = 0$ component of the quadrupole response is also analysed. The evaluation of $K \neq 0$ components would require triaxial effects to be included, i.e. the breaking of axial symmetry in the generation of HFB vacua employed in the PGCM ansatz. This is not addressed in the present work and is left for future developments.

^{46}Ti has been chosen as a study case for a systematic investigation of PGCM calculations in an *ab initio* framework. It is expected that ensuring the convergence of calculations for a medium-mass system also guarantees the reliability of the calculations in lighter systems. This chapter is devoted to a systematic convergence study of the calculations in ^{46}Ti and develops as follows. In Sec. 6.1 details about the nuclear Hamiltonians and many-body basis used in this work are given. In Sec. 6.2 the convergence of the monopole and quadrupole responses with respect to harmonic oscillator basis parameters is addressed. The chiral order and SRG dependence are investigated in Secs. 6.3 and 6.4 respectively. Other families of interactions are explored in Sec. 6.5. Eventually, the convergence with respect to the selected HFB vacua in the PGCM ansatz is also addressed in Sec. 6.6.

6.1 Details of the calculations

6.1.1 Nuclear Hamiltonian

Several two- plus three-nucleon (2N+3N) chiral Hamiltonians were used in the present work. A first family of interactions up to N3LO in the chiral expansion [6] was used. These include the 2N interaction by Entem and Machleidt [3, 155] with a consistent treatment of 3N forces with respect to chiral order, non-local regulator and cut-off value. The 2N low-energy constants (LECs) were fitted to two-nucleon scattering data, while 3N LECs were fixed using the ground-state energies of ^{3}H and ^{16}O.

The second used Hamiltonian, named NNLO$_{\text{sat}}$, was introduced in Ref. [156] with the objective of providing an improved description of saturation properties, such that the LECs were simultaneously fitted to few-body systems as well as chosen ground-state energies and radii of Carbon and Oxygen isotopes.

Eventually, the EM 1.8/2.0 interaction from Ref. [157, 158] was also employed. This Hamiltonian is based on the similarity-renormalisation-group (SRG) transformation of 2N interactions [3, 155] augmented with leading 3N contributions adjusted to data from A =3,4 systems. This interaction yields saturation point for nuclear matter around the empirical value [158] and accurate predictions for binding energies in medium-mass nuclei [159].

6.1.2 SRG evolution

Chiral Hamiltonians are normally softer than semi-phenomenological potentials used in seminal *ab initio* calculations of light systems. This relates to the implicit treatment of high-energy degrees of freedom in chiral Hamiltonians, which is associated to lower resolution scale and the absence of coupling to high nuclear momenta.

This effect is often further amplified via SRG techniques, which improve the convergence properties of the Hamiltonian by the use of unitary transformations decoupling low- and high-momentum modes. In practice, bare (i.e., unevolved) interactions are relatively hard and the corresponding HFB solutions are shallowly bound (if not at all). The SRG flow smooths out the convergence of the many-body perturbative series, approaching more and more the HFB solution to the exact many-body solution. The drawback is represented by the appearance of additional three-body (and higher) contributions; this effect is what determines the need for an optimal value of the flow parameter, maximising the gain provided by the smoothening with respect to the introduction of many-body forces.

The SRG evolution of the Hamiltonians adopted in this work is briefly reviewed. The chiral Hamiltonians from Ref. [6] are evolved to two values of the low-momentum scale, namely $\lambda = 1.88$ fm^{-1} (flow parameter α=0.08 fm^4) and $\lambda = 2.24$ fm^{-1} (α=0.04 fm^4).

$\mathrm{NNLO_{sat}}$ is SRG unevolved (bare), since non-negligible contributions from induced three- and four-body components were observed, making it unmanageable in actual implementations.

The EM 1.8/2.0 Hamiltonian is evolved to $\lambda = 1.8$ fm^{-1} ($\alpha = 0.0953$ fm^4) in the 2N sector, whereas the 3N regulator is directly set to $\lambda = 2.0$ fm^{-1} without further explicit SRG evolution.

6.1.3 Three-body treatment

Three-body forces (native or induced) are treated following the protocol developed in Ref. [160]. In practice the original or SRG-evolved Hamiltonian is used to perform a spherical HFB calculation with full treatment of two- and three-body components. A symmetry-conserving density operator is produced retaining the sole normal part of the one-body HFB density. The three-body operators are then convoluted with such a density matrix to produce a two-body symmetry-conserving effective Hamiltonian even in open-shell nuclei. This procedure reduces to standard normal-ordered two-body approximation for closed-shell systems. Used with low-resolution chiral Hamiltonians this approximation has shown to induce errors below 2-3% across a large selection of nuclei, observables and many-body methods [160].

6.1.4 Model-space

In actual implementations one needs to specify the basis in which the many-body tensors are expanded on. For a k-body operator the k-fold tensor product of one-body harmonic oscillator (HO) basis is adopted in this work. The HO basis includes states up to $e_{\mathrm{max}} \equiv \max(2n + l)$, with n the principal quantum number and l the orbital angular momentum quantum number. Several values of e_{max} are explored in the following, ranging from 4 to 12. While the two-body operators are consistently truncated in a two-body basis with $e_{\mathrm{2max}} = 2e_{\mathrm{max}}$, three-body operators are further restricted, due to computational limitations, to $e_{\mathrm{3max}} < 3e_{\mathrm{max}}$. In this work the value $e_{\mathrm{3max}} = 14$ was systematically adopted (except for $e_{\mathrm{max}} = 4$ calculations, in which case $e_{\mathrm{3max}} = 12$ represents a consistent and tractable choice).

A variation of the HO frequency $\hbar\omega$ was systematically performed for all investigated nuclei, in order to identify the optimal frequency. Converged observables should not carry any explicit dependence on the chosen $\hbar\omega$, but due to the finite basis size (especially for three-body operators) some frequencies actually produce faster convergence patterns. Values ranging from 12 to 24 MeV were tested. In general it is observed that in the mass region $A \leq 46$, $\hbar\omega = 12$ MeV represents an optimal choice at the HFB level.

6.1.5 Lorentzian smearing

In the following, monopole and quadrupole responses are systematically addressed. PGCM calculations provide a set of discrete (excited) states, given by the diagonalisation of the reduced Hamiltonian appearing in the HWG equation. In order to increase the readability of multipole responses, discrete spectra are here convoluted via a Lorentzian function of width Γ=0.5 MeV, unless specified differently. Such value does not excessively deteriorate the information of the PGCM spectra still allowing for a better visual comparison. It is also observed that experimental responses come, in most cases, with a finite energy resolution determined by the energy-bin width of 500 keV. It is reasonable to assume that the finite bin dimension can be reproduced by the smearing provided by the Lorentzian function when comparing theoretical results to experimental data.

6.2 Model space convergence

6.2.1 HFB convergence

The main body of this study has been realised using the family of chiral Hamiltonians from Ref. [6] as an input. Such chiral Hamiltonians are available for various values of the Harmonic Oscillator (HO) basis

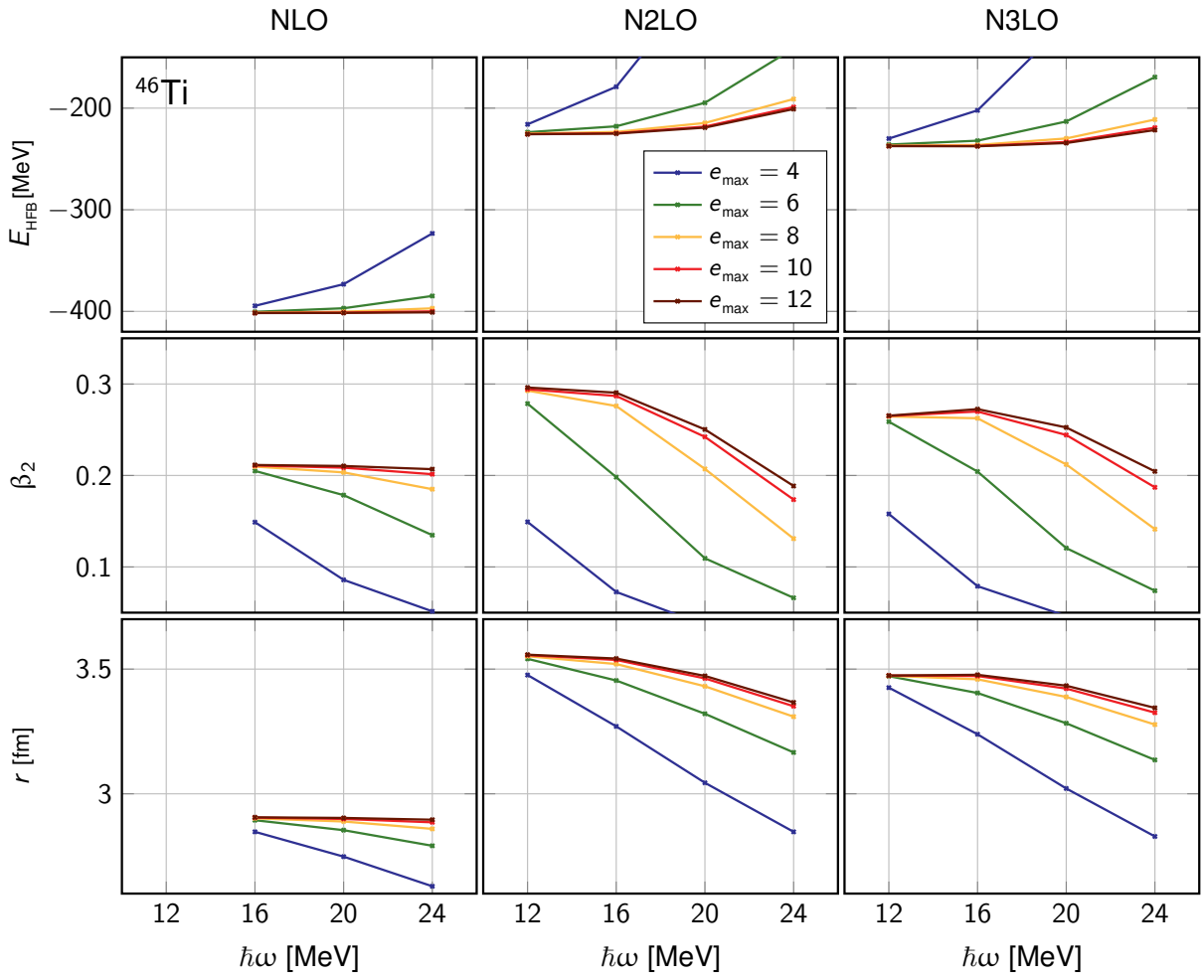

Figure 6.1: Total energy E_{HFB}, axial deformation β_2 and root mean square radius r of the HFB minimum in ^{46}Ti as a function of $\hbar\omega$ for different values of $e_{\max}$ at several chiral orders. The χEFT Hamiltonians are evolved to $\lambda_{\text{srg}} = 1.88$ fm^{-1}.

parameters ($\hbar\omega$, $e_{\max}$), for different SRG flow parameters and at several chiral orders. Properties of the HFB minimum, specifically the total energy of the HFB solution E_{HFB}, its mean square radius r and the axial deformation parameter β_2, for the three available chiral orders are reported in Fig. 6.1 as a function of $\hbar\omega$ for several values of $e_{\max}$.

As far as the energy is concerned, the typical pattern for successive chiral orders is found, i.e. a net decrease of the HFB binging energy from NLO to N2LO followed by a milder difference between NNLO and N3LO. As far as the $e_{\max}$ convergence is concerned, an interesting feature is observed: at NLO the $e_{\max}$ convergence is observed (more or less exactly for all quantities under exam) for all $\hbar\omega$ investigated, whereas at N2LO and N3LO the energy is converged with respect to $e_{\max}$ at $e_{\max} = 12$ only for low $\hbar\omega$ values, i.e. 12 and 16 MeV. This is conjectured to be linked to three-body forces: indeed, at NLO no original three-body force is present. Three-body operators are induced by the SRG flow, but to a sub-leading extent, so that if the convergence is achieved at the two-body level, then for some big-enough value of $e_{\max}$ it should be achieved independently on $\hbar\omega$.

At N2LO and N3LO, instead, where three-body forces are natively present, and not simply due to the SRG process, such consistency is not achieved. In such cases, the normal-ordering procedure through which

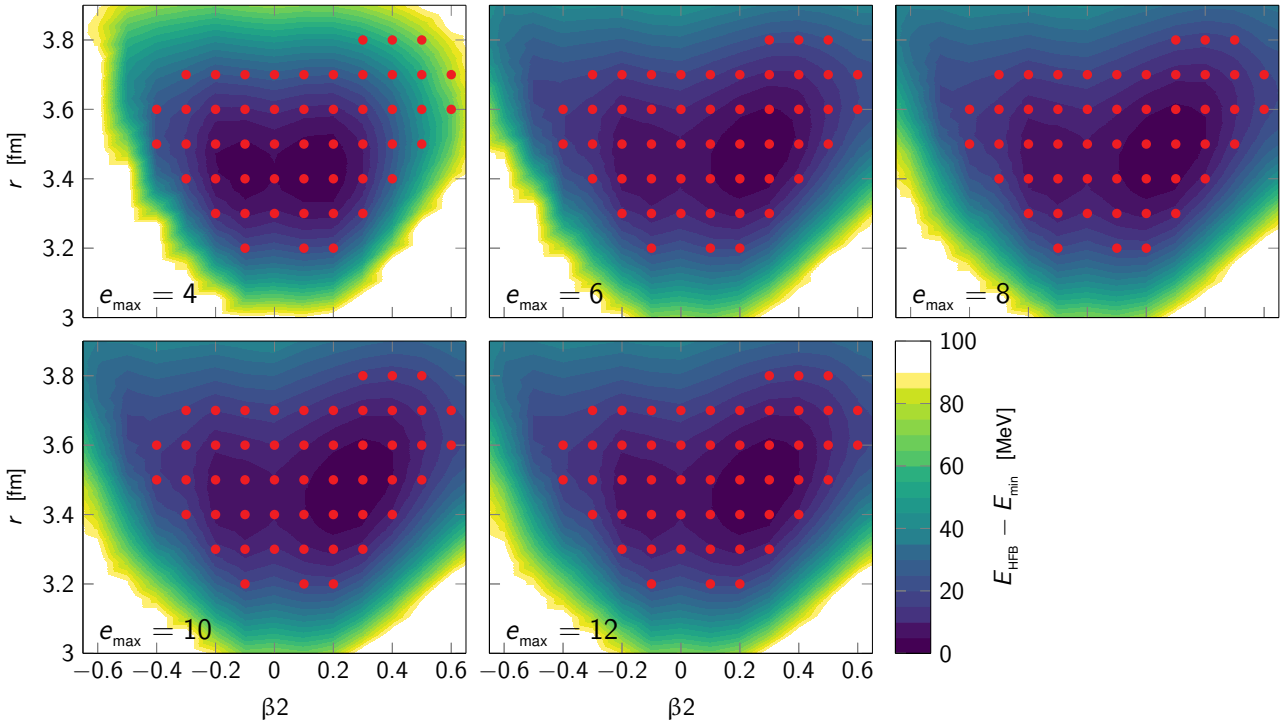

Figure 6.2: HFB total energy surface of ^{46}Ti for different values of e_{max} at N3LO ($\lambda_{srg} = 1.88$ fm^{-1}) with $\hbar\omega = 12$ MeV. The energy is plotted with respect to the minimal HFB energy for the respective e_{max} value.

three-body forces are treated in this work [160], is including most but not all the three-body content of the original Hamiltonian, so that an optimal choice of the $\hbar\omega$ parameter is key.

Figure 6.1 shows how the mean-field properties of the HFB solution can be severely affected by a non-optimal choice of $\hbar\omega$, especially as far as r and β_2 are concerned. In the following it will be shown how these features may strongly affect the determination of the giant resonance. In general the e_{max} convergence is best achieved for $\hbar\omega = 12$ MeV, which is an optimal choice for nuclei from $A \sim 20$ to $A \sim 50$. This parameter will, thus, be chosen for all the upcoming comparisons, unless stated differently.

6.2.2 PGCM convergence wrt model space size

Convergence with respect to e_{max} is here investigated at N3LO (which will be used for cases of actual physical interest). The optimal $\hbar\omega = 12$ parameter is considered. Figure 6.2 shows the total energy surface (TES) rescaled to the HFB minimum as a function of the r and β_2 for different values of e_{max}. Red dots, here as in all the following pictures, represent the HFB states that are actually included in the PGCM ansatz.

A good convergence is achieved already for $e_{max} = 8$. A more quantitative statement about the convergence of the total energy surface can be inferred from Fig. 6.3, where the difference of the total energy surface with respect to the $e_{max} = 12$ one is shown. Whereas for small basis size ($e_{max} = 4$) the difference is clearly visible, which translates into a much stiffer surface when going further from the HFB minimum, at $e_{max} = 8$ a good quantitative agreement is reached, which is confirmed at $e_{max} = 10$, where differences are smaller than 1 MeV for all the considered points on the surface.

Focusing on the low-energy response, the ground-state rotational band is displayed in Fig. 6.4, showing a good convergence pattern with respect to the harmonic oscillator basis size.

Eventually, the corresponding PGCM monopole response for different values of e_{max} is displayed in Fig. 6.5. PGCM calculations for different e_{max} were performed with the exact same set of HFB states

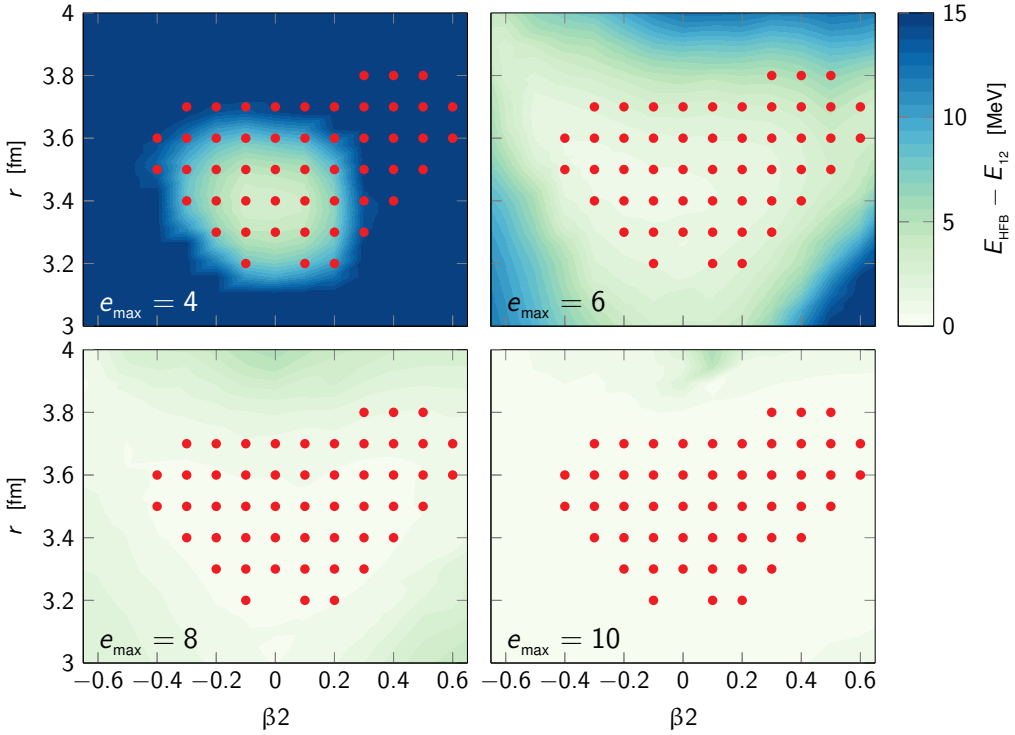

Figure 6.3: Same as Fig. 6.2 but plotted as the difference with respect to the $e_{max} = 12$ results.

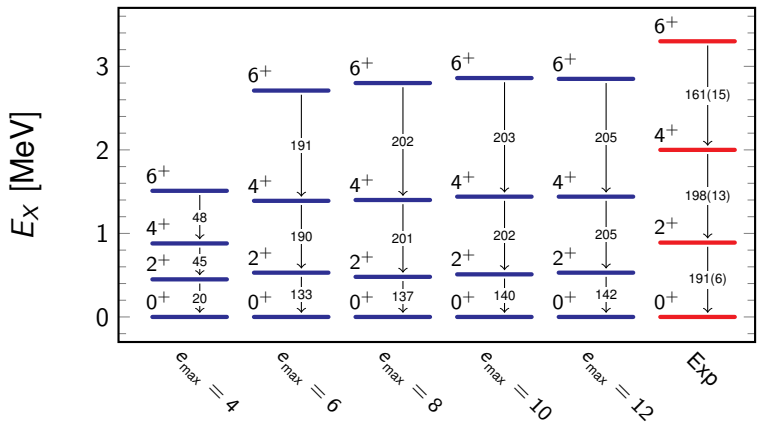

Figure 6.4: ^{46}Ti ground-state rotational band computed at N3LO ($\lambda_{srg} = 1.88$ fm^{-1}) for different values of e_{max} ($\hbar\omega = 12$ MeV) and compared to experimental data [161].

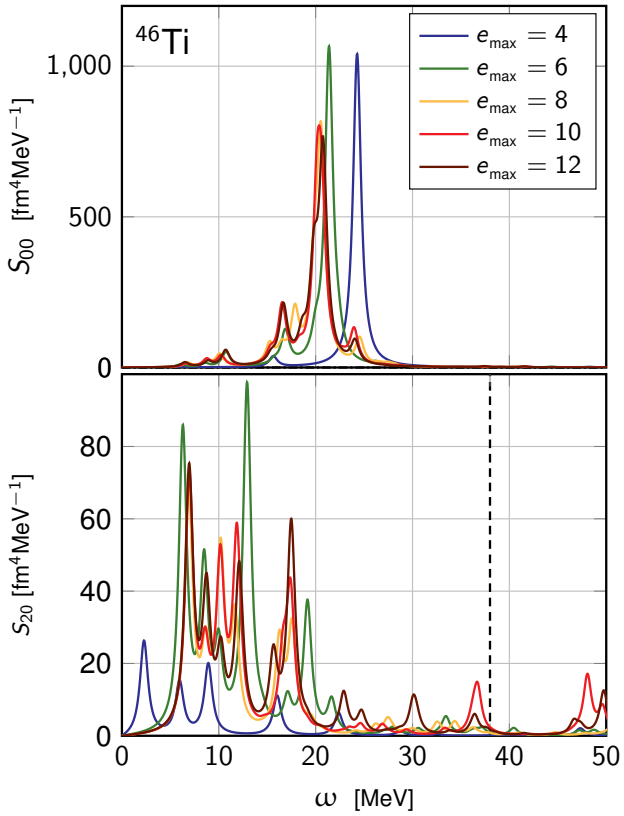

Figure 6.5: Monopole (top) and quadrupole (bottom) response in ^{46}Ti at N3LO ($\lambda_{\text{srg}} = 1.88$ fm^{-1}) for different values of e_{max} ($\hbar\omega = 12$ MeV). The dashed line in the quadrupole response represents the experimental cut-off at 38 MeV.

included in the ansatz. The aforementioned stiffness for small model spaces directly reflects into a higher-energy positioning of the giant resonance at $e_{\text{max}} = 4$, then converging with e_{max} towards ~ 21 MeV. In addition to the position of the main peak, an accurate convergence is also achieved with respect to the finer structures over the complete energy range, such that the $e_{\text{max}} = 10$ and $e_{\text{max}} = 12$ spectra are quantitatively very similar also for secondary peaks.

The quadrupole response (bottom panel of Fig. 6.5), displays, instead, a slower convergence pattern. While the overall structure is similar for $e_{\text{max}} = 10$ and $e_{\text{max}} = 12$ calculations, high-energy states are not converged. Similar trends in the quadrupole response are also observed in the next sections.

Moment's evaluation for spectra is also a good indicator of the overall convergence of the monopole and quadrupole responses. In this chapter, moments are evaluated according to Eq. (4.27), which relies on the knowledge of all the excited states of the system, the objective being to assess the convergence of the spectrum as a whole. Results are presented in the form of weighted averages (see the general formulæ in Eqs. (4.28a)). Specifically, the following quantities are computed

$$\tilde{E}_1 \equiv \frac{m_1}{m_0}, \tag{6.2a}$$

$$\tilde{E}_3 \equiv \sqrt{\frac{m_3}{m_1}}, \tag{6.2b}$$

$$\tilde{E}_1 \equiv \sqrt{\frac{m_1}{m_{-1}}}, \tag{6.2c}$$

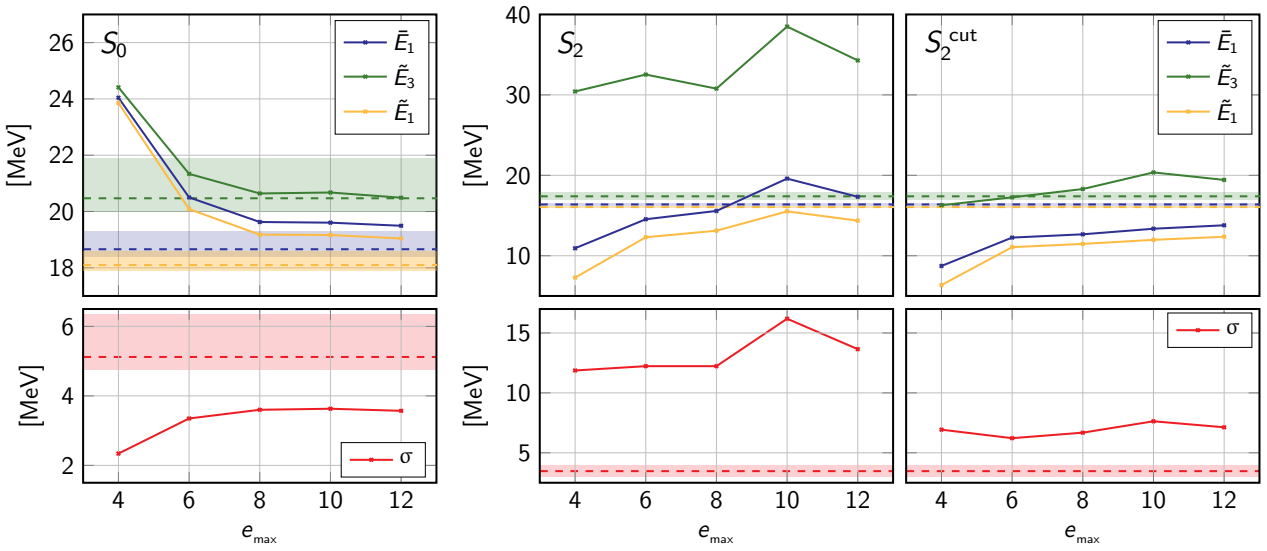

Figure 6.6: Weighted averages (see Eqs. (6.2) and (6.3) for details) as obtained from the moments of the monopole (left) and quadrupole (right) responses of ^{46}Ti for different values of e_{max} ($\hbar\omega$ = 12 MeV) at N3LO (λ_{srg} = 1.88 fm^{-1}). Dashed lines represent the corresponding experimental values, with the shaded areas standing for the corresponding error, from [162]. For the quadrupole response results with (S_2^{cut}) and without (S_2) cut-off at 38 MeV are shown.

and

$$\sigma \equiv \sqrt{\frac{m_2}{m_0} - \left(\frac{m_1}{m_0}\right)^2}. \tag{6.3}$$

The quantities from Eqs. (6.2) provide an information about the average value of the spectrum. If all the strength were concentrated in only one state all these quantities would coincide; their dispersion is an indicator of the fragmentation of the response. $\bar{E}_1$ clearly represents the centroid of the spectrum, $\tilde{E}_3$ is more sensitive to the presence of high-energy strength by definition. This is also true for σ, which stands for the standard deviation of the distribution.

The convergence of such quantities in PGCM calculations with respect to the model space size is displayed in Fig. 6.6 (right) for the monopole response. Experimental data from Ref. [162] are displayed as dashed lines, the shadowing representing the associated uncertainty. A clear convergence pattern is observed for all theoretical quantities. The fragmentation of the theoretical monopole spectrum underestimates the experimental one, the centroid of the latter being ∼1 MeV lower than the predicted value. This underestimation reflects that the many-body calculation does not account for all many-body effects, such as the coupling to the continuum, not presently taken into account explicitly.

The clean convergence picture observed in the monopole case is not as witnessed for the quadrupole. This different trend is visible in Fig. 6.6 (right). Plotted quantities strongly oscillate when increasing the model-space size. This effect reflects the appearance of higher-energy peaks beyond 30 MeV for $e_{\text{max}} = 10, 12$, as observed in Fig. 6.5. Theses states are not spurious (at least from the numerical point of view), as will also be attested in Sec. 6.4 when testing different SRG flow parameters.

Independently on the physical nature of those high-lying states, experimental spectra include a cut-off, which in Ref. [162] was set at 38 MeV. Taking into account such a cut-off, theoretical results are displayed in Fig. 6.6 (right). The oscillations associated with the enlargement of the model space are strongly reduced, attesting a good convergence in the $\omega < 38$ MeV region.

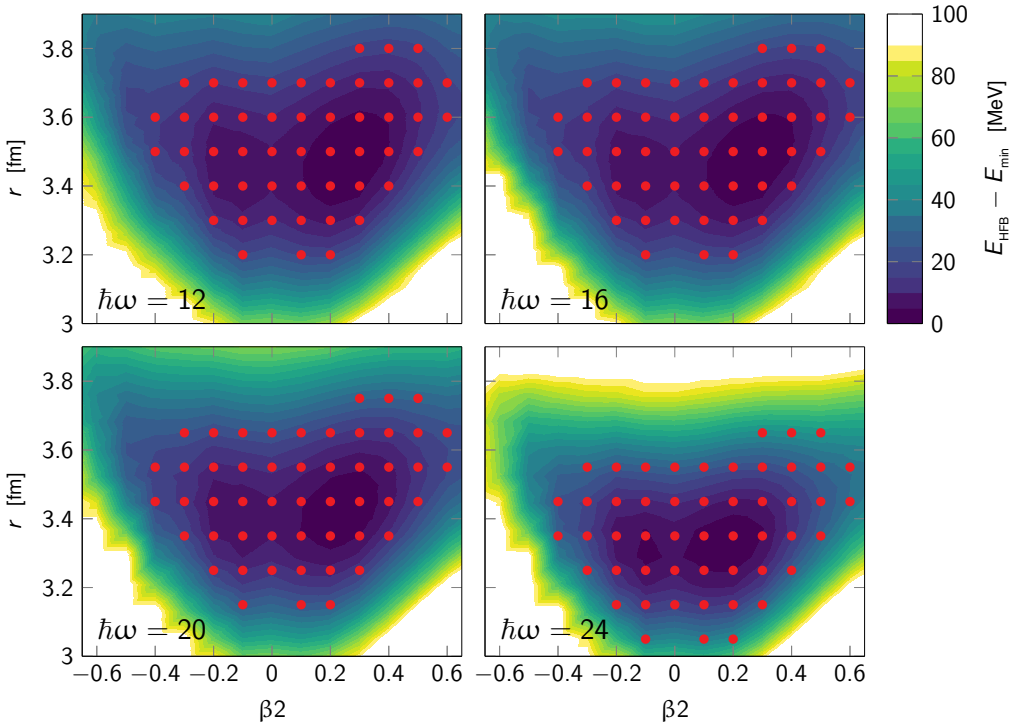

Figure 6.7: HFB total energy surface of ^{46}Ti for different values of $\hbar\omega$ at N3LO ($\lambda_{srg} = 1.88$ fm^{-1}) with $e_{max} = 10$. The energy is plotted with respect to the minimal HFB energy for the respective $\hbar\omega$ value.

6.2.3 PGCM convergence wrt harmonic oscillator width

Convergence with respect to $\hbar\omega$ for a fixed value of $e_{max} = 10$ is now illustrated. Contrarily to the previous model-space convergence, a different set of HFB states is included in the PGCM ansatz in each case. Indeed, the change of $\hbar\omega$ produces surfaces differing significantly from the optimal value $\hbar\omega = 12$, producing surfaces which can significantly differ from the optimal $\hbar\omega = 12$ MeV value, as clearly shown in Fig. 6.8. This requires to select optimal HFB states in each case separately. Since, as Fig. 6.8 shows, the energy difference mostly depends on the radius rather than on the axial deformation (the difference is quite uniform for fixed values of r) the set was simply shifted with respect to the radial coordinate.

The low-lying ground-state rotational band is exhibited in Fig. 6.9. Globally a good convergence towards $\hbar\omega = 12$ MeV is achieved both in terms of energy positioning and transition probabilities.

Results for the monopole response are presented in Fig. 6.10. Due to the stiffer energy surfaces for $\hbar\omega = 20, 24$ MeV and to the lower value for the radial minimum the giant resonance is at higher energy in these cases. Contrarily, the resonance energy and the overall structure of the spectrum for $\hbar\omega = 16$ MeV is similar to the $\hbar\omega = 12$ MeV case. This reflects the mild differences between the two energy surfaces, as visible in Fig. 6.8.

The convergence pattern is less straightforward for the quadrupole response, even if lower-energy structures are stable for $\hbar\omega = 12 - 20$ MeV. Higher-energy structures appear for the optimal $\hbar\omega = 12$ MeV case but not for the other $\hbar\omega$ values.

The overall convergence of the spectrum with respect to $\hbar\omega$ is evaluated via the computation of moments. Monopole weighted averages are displayed in Fig. 6.11 (top-left panel). A good convergence pattern is observed for the monopole response from higher $\hbar\omega$ towards the optimal value $\hbar\omega = 12$ MeV, the latter being close to the corresponding experimental values. The response fragmentation, characterised by σ (bottom-left panel), is quite stable with respect to variations in $\hbar\omega$, and systematically under-reproduces the

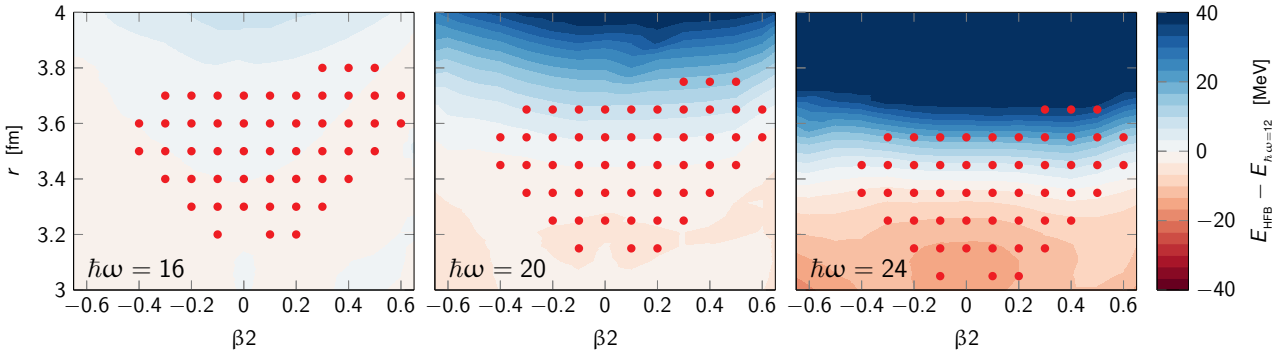

Figure 6.8: Same as Fig. 6.7 but plotted as the difference with respect to the $\hbar\omega = 12$ MeV results.

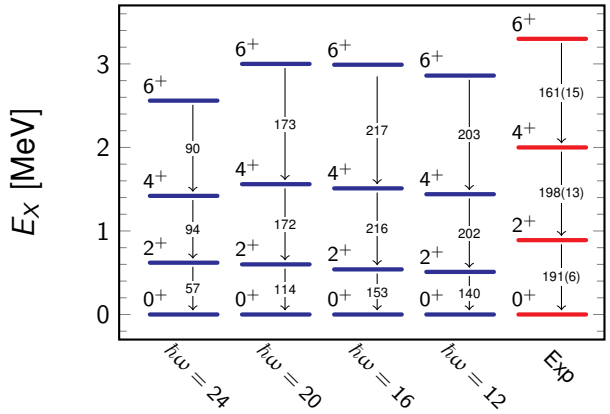

Figure 6.9: ^{46}Ti ground-state rotational band computed at N3LO ($\lambda_{srg} = 1.88$ fm^{-1}) for different values of $\hbar\omega$ ($e_{max} = 10$) and compared to experimental data [161].

experimental value.

The behaviour of the moments is erratic for the quadrupole response (Fig. 6.11 (right)), for reasons mentioned in Sec. 6.2.2. Without the use of an energy cut-off (middle panel), no clear pattern is observed, especially for higher moments. When the experimental cut-off of 38 MeV is applied (right panel), all plotted moments display a more stable behaviour.

6.3 Convergence wrt chiral order

In the following chapters the N3LO Hamiltonian [6] is used for actual calculations. In order to make a statement about the convergence with respect to the chiral order, results obtained at NLO and N2LO are presently compared. The total HFB energies, radii and β_2 parameters were displayed in Fig. 6.1. A good convergence pattern was observed at the HFB level: all quantities are strongly modified going from NLO to N2LO, whereas the change is significantly milder going from N2LO to N3LO.

The total HFB energy in the (β_2, r) plane is shown in Fig. 6.12 for the three chiral orders. Given the smaller HFB radius at NLO, the energy surface is shifted by approximately -0.6 fm with respect to the surfaces at N2LO and N3LO and is significantly stiffer.

Properties of the total HFB energy surfaces directly translate into the monopole response displayed in Fig. 6.13 (top panel). NLO results are very distinct from N2LO and N3LO ones with the stiffer surface leading to a GMR located ~8 MeV higher in energy. Moreover, the magnitude of the strength is significantly

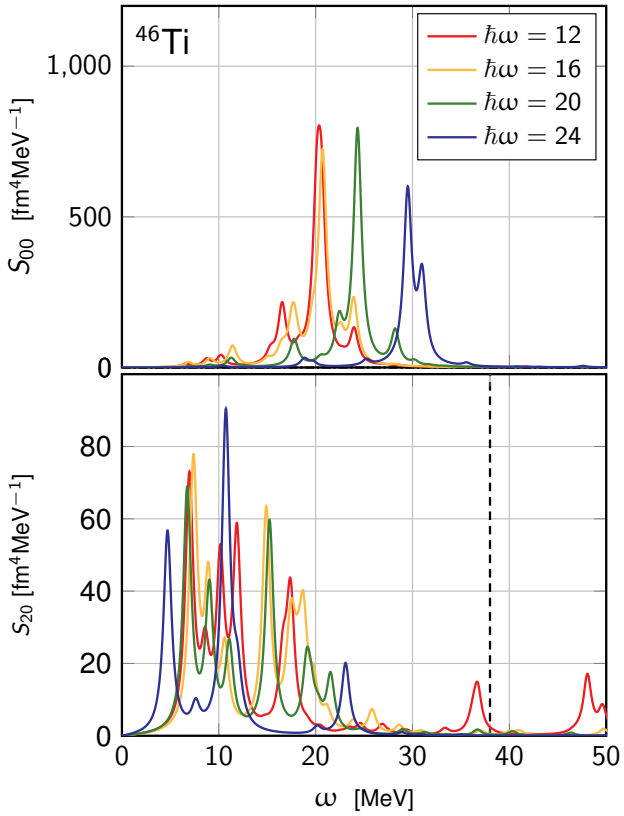

Figure 6.10: Monopole (top) and quadrupole (bottom) response of ^{46}Ti at N3LO ($\lambda_{\text{srg}} = 1.88$ fm^{-1}) for different values of $\hbar\omega$ ($e_{\text{max}} = 10$). The dashed line in the quadrupole response represents the experimental cut-off at 38 MeV.

smaller than at N3LO. Contrarily, N2LO and N3LO perform similarly even if N2LO GMR is ~1 MeV higher in energy than at N3LO.

Similar observations concern the quadrupole response in Fig. 6.13 (bottom panel). The NLO response exhibits little resemblance to N2LO and N3LO responses. The latter two are similar even though the highly fragmented response below 20 MeV is still significantly modified going from N2LO to N3LO.

The ground-state rotational band is displayed in Fig. 6.14 for the three chiral orders. N2LO and N3LO are in good agreement both for excitation energies and transition probabilities. NLO strongly underestimates the transition probabilities within the band, whereas excitation energies are not dramatically different and are (accidentally) in better agreement with experimental results.

The overall convergence properties of the spectra are once more rated through the evaluation of the associated moments. The corresponding weighted averages for the monopole response are displayed in Fig. 6.15 (top left). A converging trend is observed with N3LO results approaching experimental values. Accidentally the NLO dispersion (bottom-left panel) displays a good agreement with experiment, masking the fact that the NLO spectrum does not display any *giant* resonance accounting for a large part of the monopole strength.

A similar convergence pattern is observed when the moments of the quadrupole response are addressed in Fig. 6.15 (right). Indeed, applying the cut-off at 38 MeV generates a good convergence pattern going from NLO to N3LO.

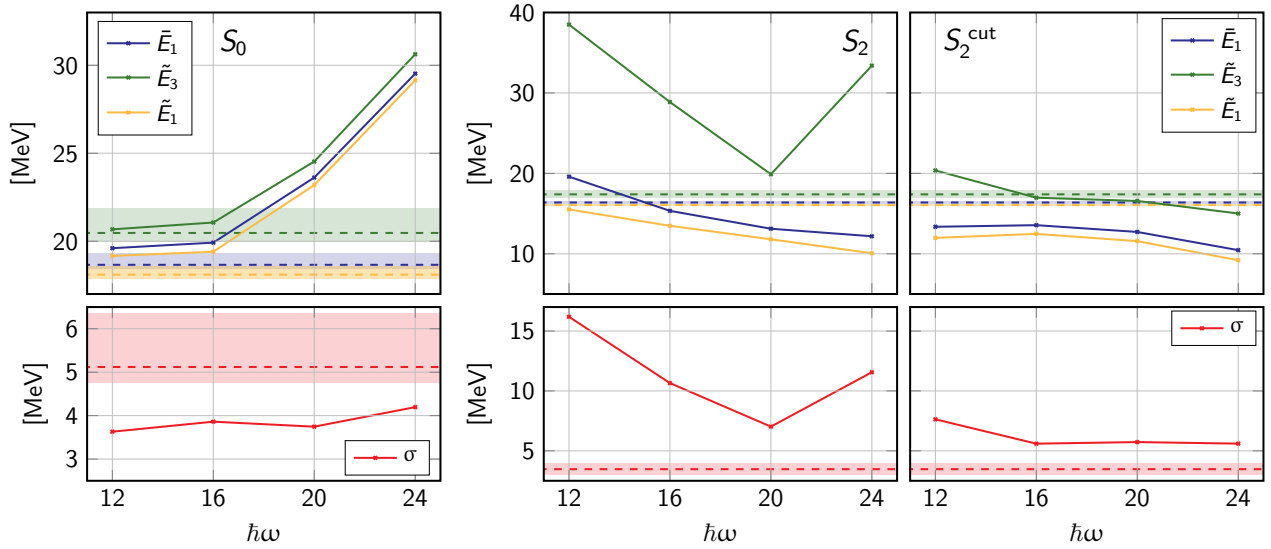

Figure 6.11: Weighted averages (see Eqs. (6.2) and (6.3) for details) as obtained from the moments of the monopole (left) and quadrupole (right) responses of ^{46}Ti for different values of $\hbar\omega$ ($e_{\max} = 10$) at N3LO ($\lambda_{\text{srg}} = 1.88$ fm^{-1}). Dashed lines represent the corresponding experimental values, with the shaded areas standing for the corresponding error, from [162]. For the quadrupole response results with (S_2^{cut}) and without (S_2) cut-off at 38 MeV are shown.

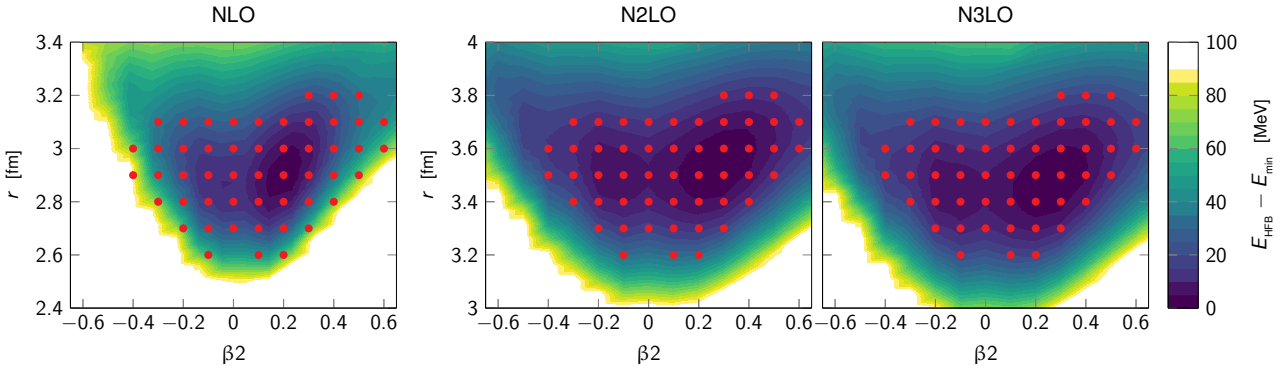

Figure 6.12: HFB total energy surface of ^{46}Ti at different chiral orders ($\lambda_{\text{srg}} = 1.88$ fm^{-1}) with $\hbar\omega = 16$ MeV and $e_{max} = 10$. The energy is plotted with respect to the minimal HFB energy for the respective chiral order.

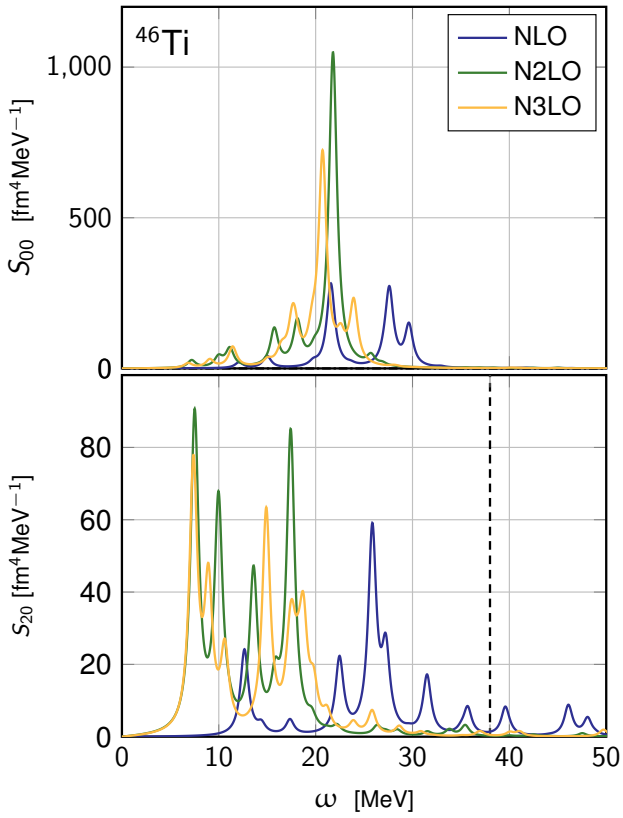

Figure 6.13: Monopole (top) and quadrupole (bottom) response of ^{46}Ti at different chiral orders (λ_{srg} = 1.88 fm^{-1}) for $\hbar\omega$ = 16 MeV and e_{max} = 10. The dashed line in the quadrupole response represents the experimental cut-off at 38 MeV.

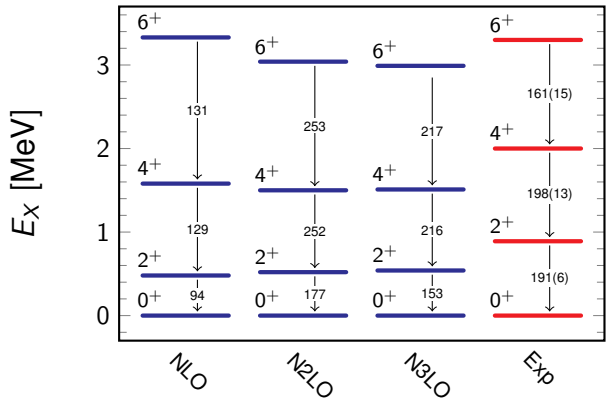

Figure 6.14: ^{46}Ti ground-states rotational band computed at different chiral orders (λ_{srg} = 1.88 fm^{-1}) for $\hbar\omega$ = 16 MeV and e_{max} = 10 and compared to experimental data [161].

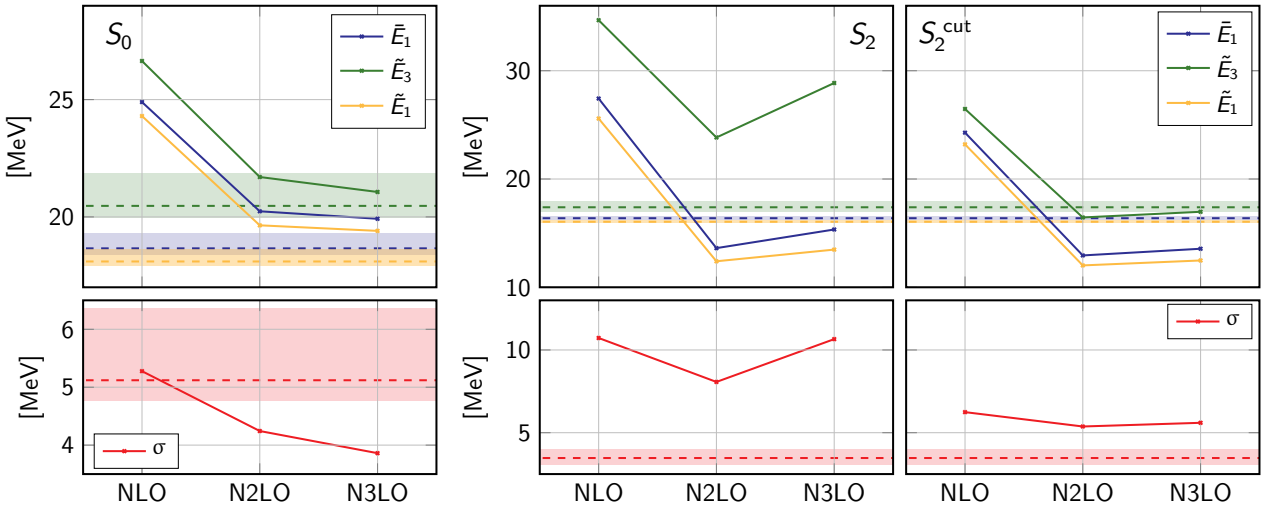

Figure 6.15: Weighted averages (see Eqs. (6.2) and (6.3) for details) as obtained from the moments of the monopole (left) and quadrupole (right) responses of ^{46}Ti at different chiral orders ($\lambda_{srg} = 1.88$ fm^{-1}), with $\hbar\omega = 16$ MeV and $e_{max} = 10$. Dashed lines represent the corresponding experimental values, with the shaded areas standing for the corresponding error, from [162]. For the quadrupole response results with (S_2^{cut}) and without (S_2) cut-off at 38 MeV are shown.

6.4 SRG dependence

The evolution of the monopole response in PGCM calculations with respect to the SRG flow parameter is now addressed. Fully converged *ab initio* observables should not carry any explicit dependence on the SRG evolution, which is in principle a unitary transformation of the original Hamiltonian. In this sense, the residual dependence on the SRG scale is an indicator of the breaking of such a unitarity in practical applications. In this context, results obtained for two different values ($\alpha = 0.04$ fm^4 and $\alpha = 0.08$ fm^4) of the flow parameters are compared.

The HFB energy, radius and deformation are presented in Fig. 6.16 for different basis parameters and for the two values of α. The total HFB energy for $\alpha = 0.04$ fm^4 is about 100 MeV higher than for $\alpha = 0.08$ fm^4. The radii behave accordingly.

The basis parameters $e_{max} = 10$ and $\hbar\omega$ =12 MeV are then chosen to perform the PGCM calculations. The total HFB energy surface in the (β_2, r) plane are displayed in Fig. 6.17. Due to the difference in the HFB radii the selected HFB points were shifted by 0.2 fm between the two different cases.

Globally, the surface stiffness increases with the flow parameter. This effect is more clearly visible in Fig. 6.18, where one-dimensional cuts of the energy surfaces through the HFB minimum are shown. Both the radial and the β_2 dependence are stiffer for α =0.08 fm^4. Softer interactions (i.e. with bigger α values) encompass more dynamical correlations at the mean-field level, whereas residual dynamical correlations (whose cancellation in spectroscopic quantities is only approximate [43]) are suppressed. This makes the mean-field solution closer to the exact many-body solution of the problem. Thus, moving away from the optimal mean-field parameters (i.e. from the HFB minimum) is energetically less favourable, and the energy surface is, consequently, stiffer.

This observation straightforwardly translates into the behaviour of the monopole and quadrupole responses, shown in Fig. 6.19. The monopole responses (top panel) display a qualitatively similar behaviour but with the α =0.04 fm^4 strength being lowered by ∼1 MeV compared to the α =0.08 fm^4 result.

The quadrupole responses (Fig. 6.19, bottom panel) are also similar in both cases. They eventually differ by an energy shift close to the one observed in the monopole channel. Interestingly the high-energy

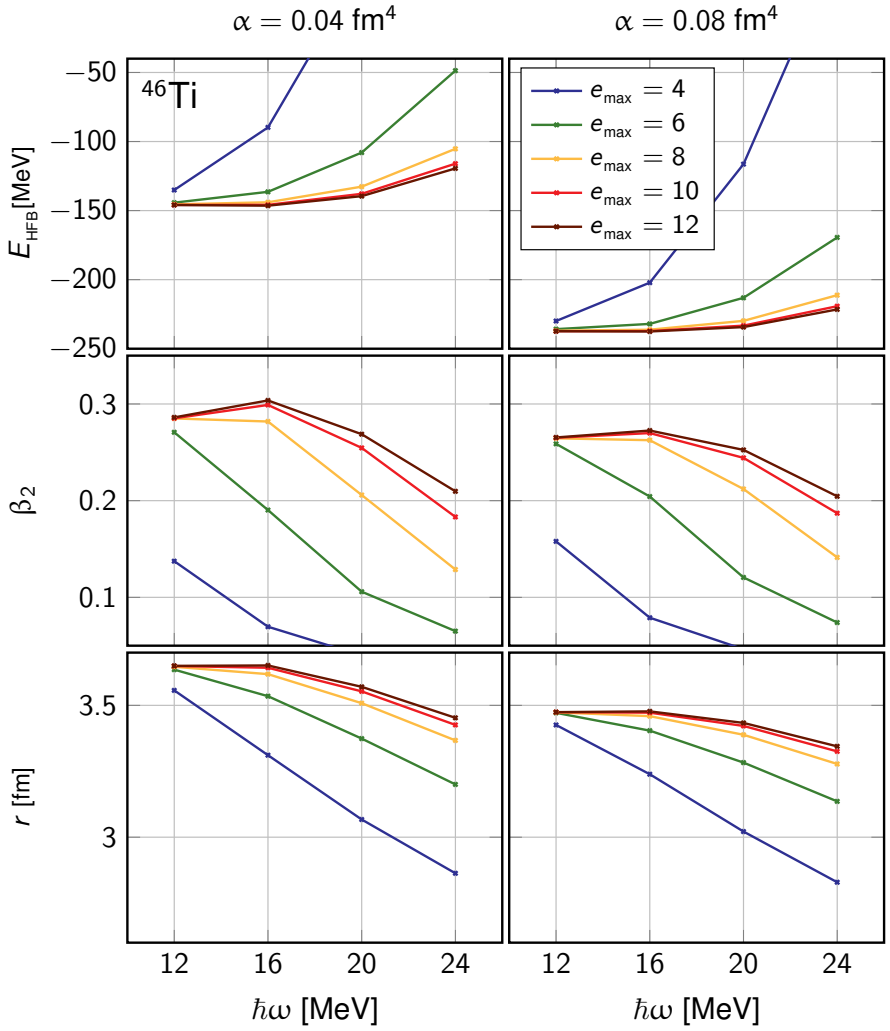

Figure 6.16: Total energy E_{HFB}, axial deformation β_2 and root mean square radius r of the HFB minimum in ^{46}Ti as a function of $\hbar\omega$ for different values of $e_{\max}$ at different values of the SRG flow parameter.

structures appearing between 30 and 50 MeV appear both for α =0.04 fm^4 and α =0.08 fm^4. They represent high-lying physical states which are actually provided by present PGCM calculations.

The ground-state rotational band is shown in Fig. 6.20. Results are close except that the α =0.04 fm^4 spectrum is slightly more compressed than its α =0.08 fm^4 counterpart, whereas transitions are also slightly overestimated in the former case.

The previous observations about the monopole response are quantitatively resumed through the SRG dependence of the strength moments, shown in Fig. 6.21 (left). The shift towards lower energies for α =0.04 fm^4 is observable for the three weighted averages. The same trend is visible in Fig. 6.21 (right) for the quadrupole response.

Overall an anti-correlation between the softness of the interaction and the centroid of the monopole and quadrupole responses is found. The same behaviour was observed from RPA calculations of spherical systems [55]. A more detailed study relying on larger set of flow parameter values would be beneficial in view of providing a clearer picture, and to show a convergence scheme for larger α's.

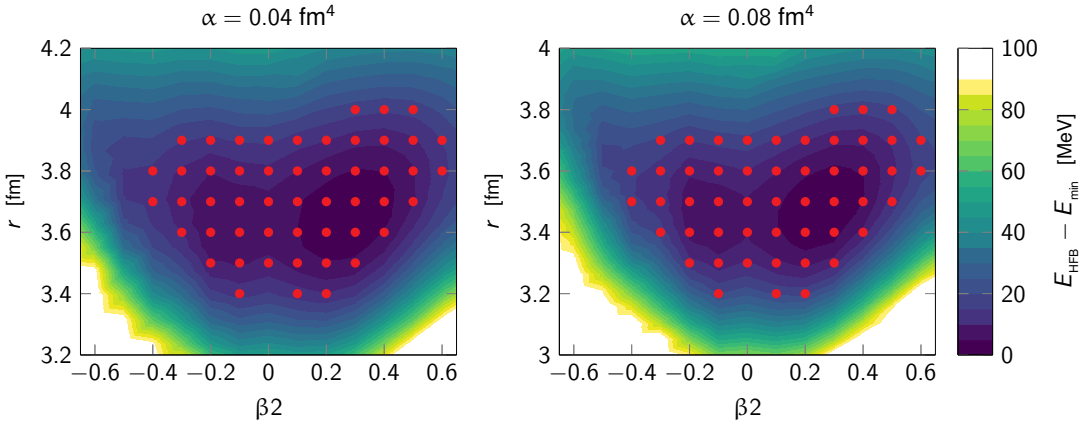

Figure 6.17: HFB total energy surface of ^{46}Ti at N3LO for different values of the flow parameter, with $\hbar\omega = 12$ MeV and $e_{max} = 10$. The energy is plotted with respect to the minimal HFB energy for the respective flow parameter.

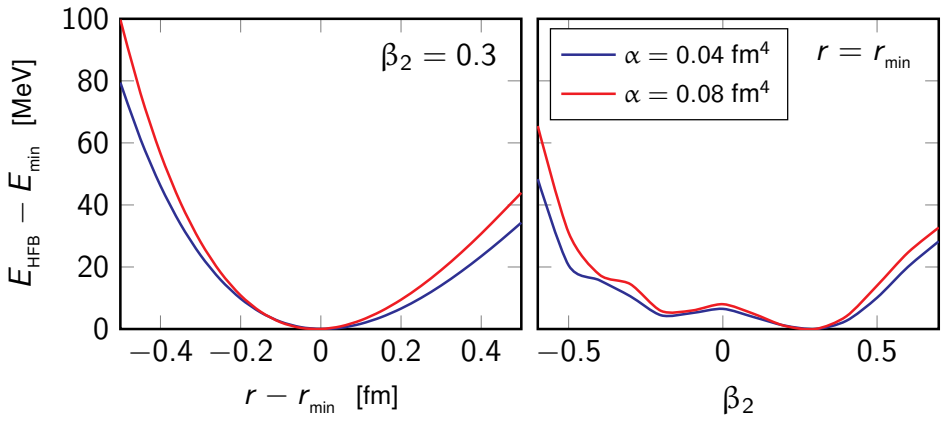

Figure 6.18: One-dimensional cut of the total energy surfaces of ^{46}Ti from Fig. 6.17 for r and β_2 minimising the HFB total energy.

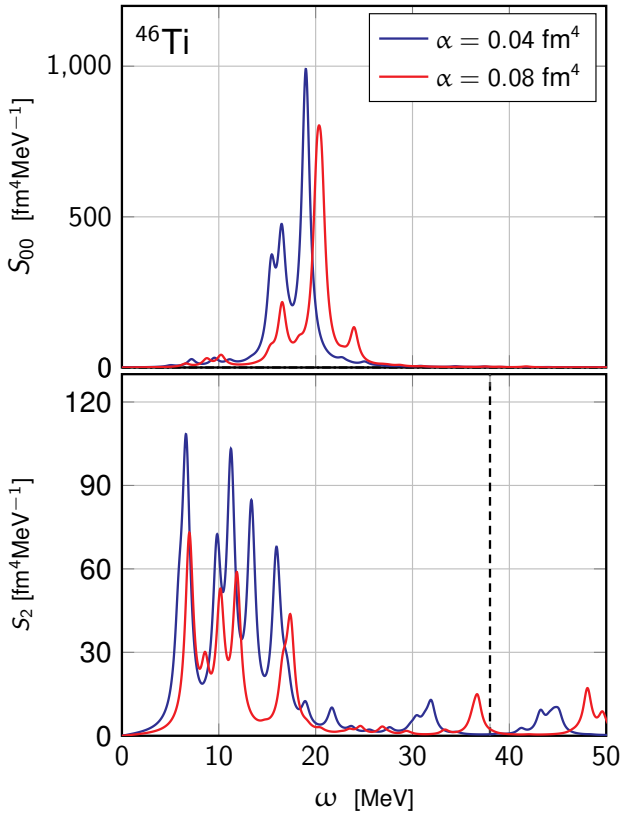

Figure 6.19: Monopole (top) and quadrupole (bottom) response of ^{46}Ti for different values of the flow parameter at N3LO, with $\hbar\omega = 12$ and $e_{\max} = 10$. The dashed line in the quadrupole response represents the experimental cut-off at 38 MeV.

6.5 Comparison of different interactions

Giant monopole resonances provide an indirect access to nuclear incompressibility [61, 62, 88]. They also represent an interesting phenomenon to characterise global properties of nuclear interactions. In this section, three different chiral-based nuclear Hamiltonians are tested in order to characterise their predictions of nuclear vibrations, i.e. the N3LO [6], NNLO$_{\text{sat}}$ [156] and EM 1.8/2.0 [157, 158] Hamiltonians.

HFB results are displayed in Fig. 6.22. NNLO$_{\text{sat}}$ is used without any SRG evolution: it is indeed known that its SRG evolution induces large three- and four-body contributions. Consequently, the system is very shallowly bound at the HFB level. EM 1.8/2.0 is evolved (in the NN sector) with at a flow parameter α =0.0953 fm^4, which coherently lowers the total HFB energy by about 50 MeV with respect to N3LO ($\alpha = 0.08$ fm^4). Radii predictions are poorer for EM 1.8/2.0, as already known from the literature [163].

The optimal basis parameters ($e_{\max} = 10$, $\hbar\omega = 12$ MeV) are the same for all three Hamiltonians. The corresponding total HFB energy surfaces in the (β_2, r) plane are displayed in Fig. 6.23. A first observation reveals their qualitatively different nature and the variation in the predicted deformations and radii. Compared to N3LO, NNLO$_{\text{sat}}$ is extremely soft against changes in β_2 and r, such that very large deformations are favoured. EM 1.8/2.0 instead behaves similarly to N3LO, even if radii, which are key in the description of the monopole response, are shifted by ~ -0.2 fm.

A more quantitative statement about the surfaces' stiffness can be inferred from Fig. 6.24, where the one-dimensional cuts through the HFB minimum are shown. As far as radial variations are concerned, N3LO and EM 1.8/2.0 behave very similarly; in contrast, NNLO$_{\text{sat}}$ is much softer both with respect to compression

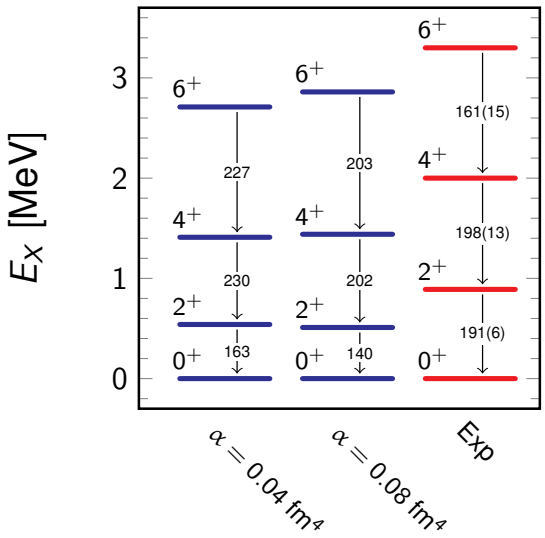

Figure 6.20: ^{46}Ti ground-states rotational band computed at N3LO for different values of the flow parameter, for $\hbar\omega = 12$ and $e_{\max} = 10$ and compared to experimental data [161].

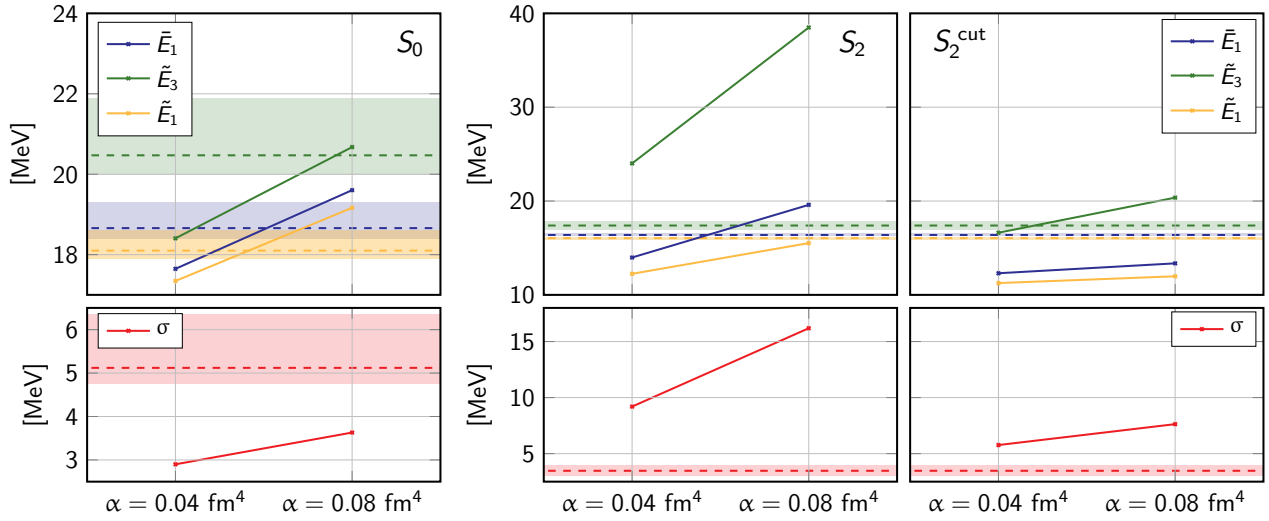

Figure 6.21: Weighted averages (see Eqs. (6.2) and (6.3) for details) as obtained from the moments of the monopole (left) and quadrupole (right) responses of ^{46}Ti for different values of the flow parameter ($\hbar\omega = 12$ and $e_{\max} = 10$) at N3LO. Dashed lines represent the corresponding experimental values, with the shaded areas standing for the corresponding error, from [162]. For the quadrupole response results with (S_2^{cut}) and without (S_2) cut-off at 38 MeV are shown.

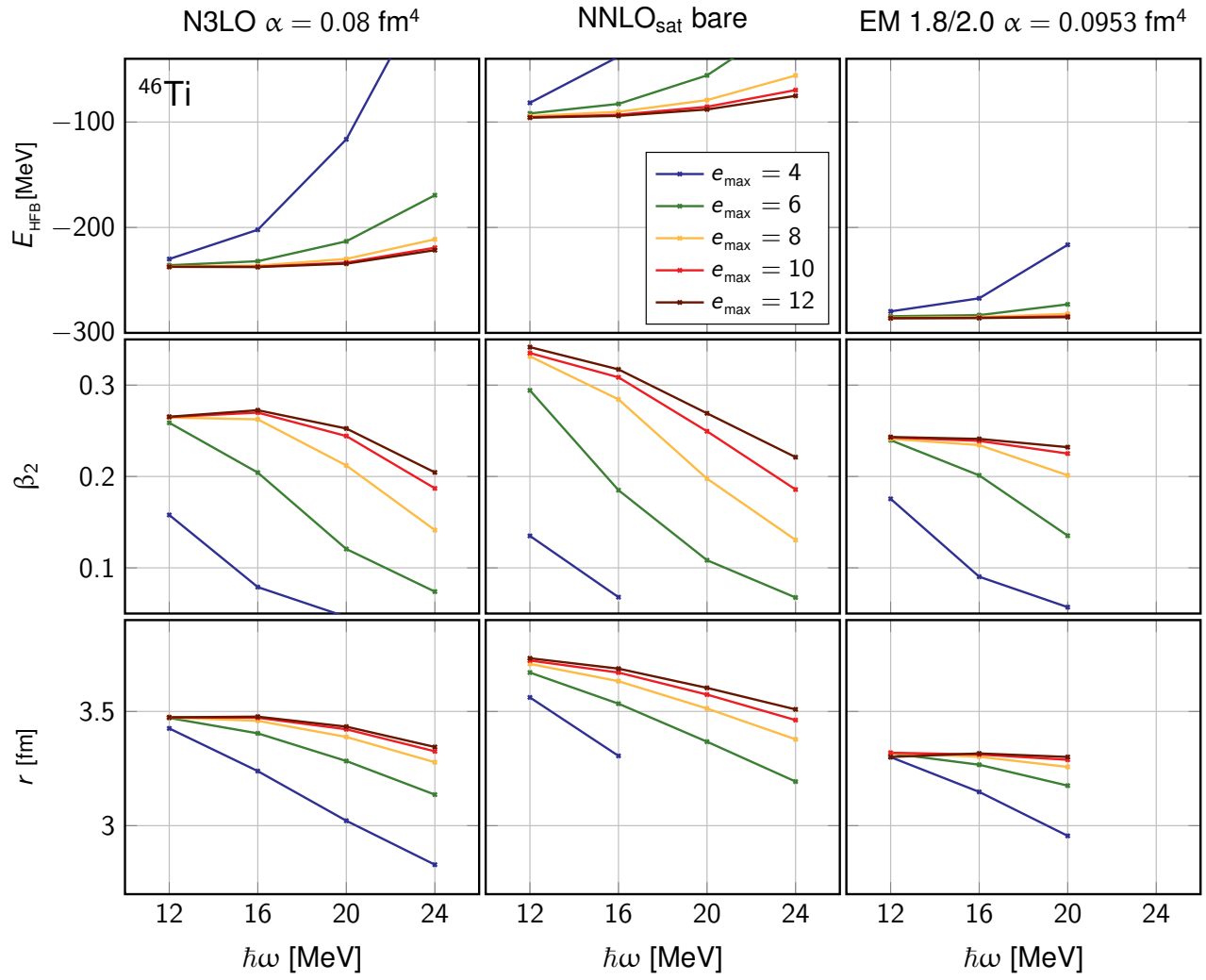

Figure 6.22: Total energy E_{HFB}, axial deformation β_2 and root mean square radius r of the HFB minimum in ^{46}Ti as a function of $\hbar\omega$ for different values of $e_{\max}$ for different interactions.

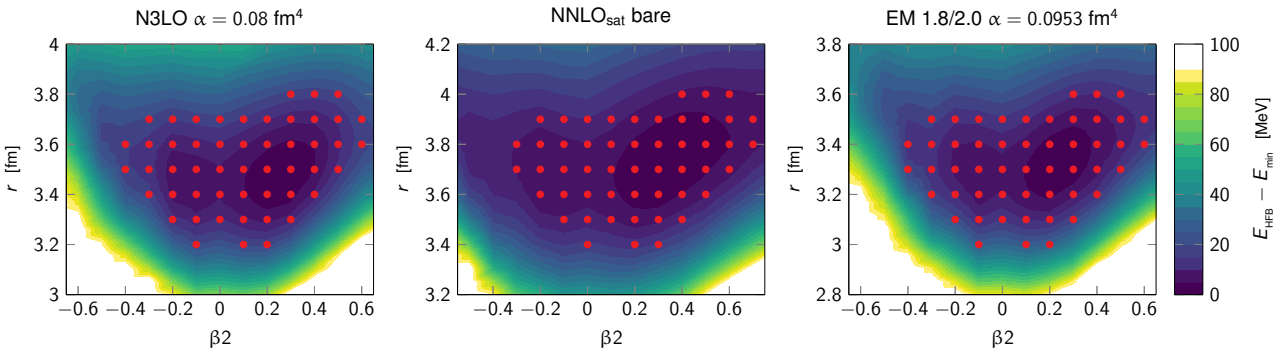

Figure 6.23: HFB total energy surface of ^{46}Ti at comparison for different interactions, with $\hbar\omega = 12$ MeV and $e_{\max} = 10$. The energy is plotted with respect to the minimal HFB energy for the respective interaction.

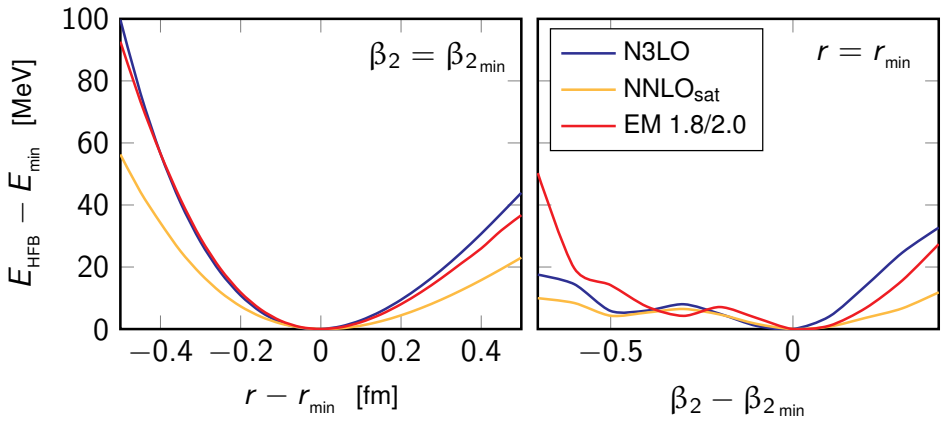

Figure 6.24: One-dimensional cut of the total energy surfaces of ^{46}Ti from Fig. 6.23 for r and β_2 minimising the HFB total energy.

and dilatation. Combining the information from Sec. 6.4, one may infer that the SRG evolution impacts significantly the energy surface characteristics.

These remarks directly transpose into the monopole responses shown in Fig. 6.25 (top panel). Taking N3LO as a reference, NNLO$_{sat}$ produces a highly fragmented monopole response, strongly shifted towards lower energies. EM 1.8/2.0, on the other hand, provides as well a fragmented response but in the correct energy region, probably linked to the similar radial response (but different with respect to β_2).

The behaviour of the quadrupole response is different (Fig. 6.25, bottom). Similarly to N3LO, NNLO$_{sat}$ displays a fragmented response below 20 MeV, although shifted towards lower energies due to the softer TES against β_2 variations. EM 1.8/2.0 oddly shows a very strong response (notice the 0.1 factor) that can hardly be related to other results.

The ground-state rotational band do not change dramatically (Fig. 6.26): NNLO$_{sat}$ produces very strong transition probabilities, whereas EM 1.8/2.0 provides a more dilated spectrum. Overall results are reasonable as far as the rotational spectra are concerned, which is in contrast, especially for EM 1.8/2.0, to its very different quadrupole response.

Moments of the monopole response are provided in Fig. 6.27 (left). Weighted averages reflect the comments made in connection with Fig. 6.25 (top): NNLO$_{sat}$ predicts the centroid of the monopole response at much lower energy than N3LO (∼6 MeV difference), whereas EM 1.8/2.0 is comparable to N3LO.

As for the quadrupole response, weighted averages are shown in Fig. 6.27 (right). NNLO$_{sat}$ again displays a shift towards lower energies compared to N3LO. However, when addressing average properties the quadrupole response from EM 1.8/2.0 does not reveal such a peculiar nature as it was observed in its spectrum. Its centroid is, instead, very close to experimental results.

Let us point out that NNLO$_{sat}$ and EM 1.8/2.0 calculations were not performed at the same level of convergence (with respect to the used parameters and the selection of PGCM points) as for N3LO calculations. However, global trends and general features can be already inferred from present calculations, so that qualitative statements about the behaviour of NNLO$_{sat}$ and EM 1.8/2.0 are valid.

6.6 Convergence wrt to selected HFB states

One of the drawbacks of PGCM calculations is a lack of systematicity in the choice of the HFB vacua to be included in the PGCM ansatz, as well as in the choice of the generator coordinates. If the generator coordinates, however, can be selected according to the physics one is aiming at describing, there is no unique criterion to select HFB vacua for a fixed set of generating coordinates (see [164] for a recent study).

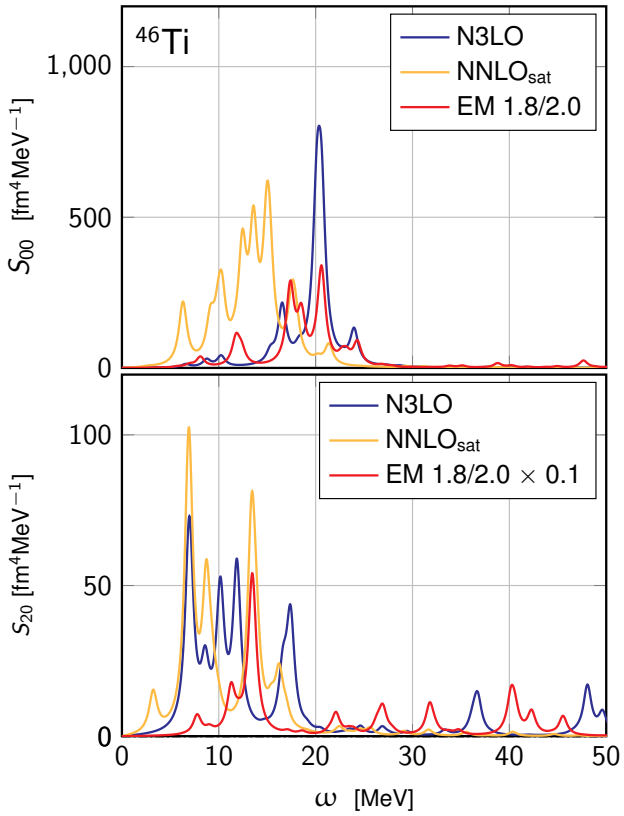

Figure 6.25: Monopole (top) and quadrupole (bottom) response of ^{46}Ti for the different interactions at use, with $\hbar\omega = 12$ and $e_{\max} = 10$.

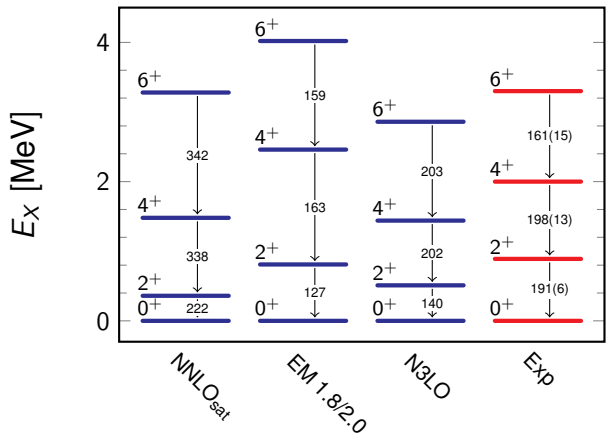

Figure 6.26: ^{46}Ti ground-states rotational computed with different interactions ($\hbar\omega = 12$ and $e_{\max} = 10$) and compared to experimental data [161].

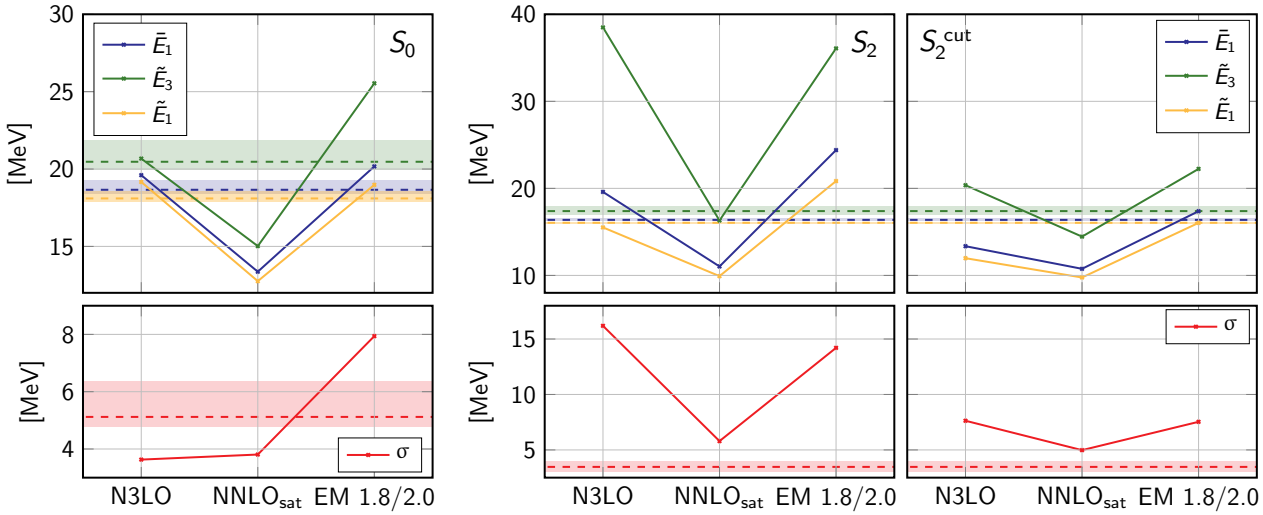

Figure 6.27: Weighted averages (see Eqs. (6.2) and (6.3) for details) as obtained from the moments of the monopole (left) and quadrupole (right) responses of ^{46}Ti for different interactions ($\hbar\omega = 12$ and $e_{\text{max}} = 10$). Dashed lines represent the corresponding experimental values, with the shaded areas standing for the corresponding error, from [162]. For the quadrupole response results with (S_2^{cut}) and without (S_2) cut-off at 38 MeV are shown.

In this section, two criteria are employed to select the HFB states. The first relies on the distance between HFB vacua on the generator coordinate mesh, whereas the second relates to the energy difference with respect to the HFB minimum. Examples are provided for one- and two-dimensional PGCM calculations in the following.

6.6.1 One-dimensional case

One-dimensional PGCM is first addressed in order to decouple the complexity of the problem. Calculations were performed using $\hbar\omega = 12$ MeV and $e_{\text{max}} = 10$. HFB calculations are performed constraining the generating coordinate r. The parameter β_2 (as well as any other parameter) is left free to adjust through the energy minimisation.

Mesh resolution

The total HFB energy as a function of the constrained radius is shown in Fig. 6.28 (top panel), together with the associated variation of β_2. The deformation varies almost linearly with r, such that the position of the quadrupole resonance is likely to be strongly correlated with the monopole resonance. For comparison, the *same* HFB energy is also plotted as a function of β_2 (bottom panel). The profile of the energy curve remains the same, due to the almost linear relation between r and β_2. A slight difference is only detectable for small β_2 (compression), since the dependence between r and β_2 deviates from the purely linear trend in this regime.

The sets of HFB points included in the different PGCM calculations are also shown, going from a spaced (a) to a very dense mesh (d) going from left to right. The grid refinement is doubled at each step.

Monopole and quadrupole responses from the one-dimensional PGCM calculations are displayed in Fig. 6.29 (top and bottom respectively). Given the almost linear correlation between r and β_2 in this one-dimensional calculation, the resonant states in the 0^+ and 2^+ channels are observed at the same energy. Strikingly, results are independent of the chosen mesh. Plotting the strength in logarithmic scale (right

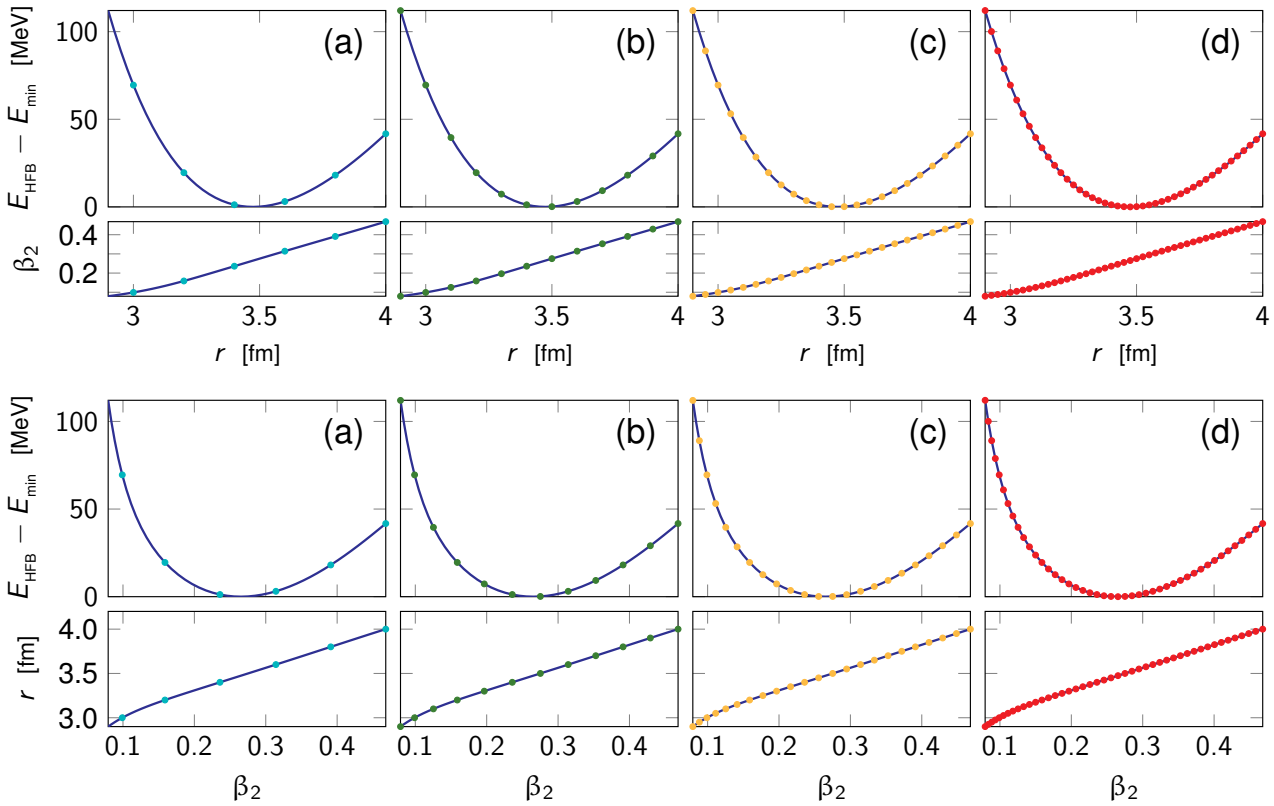

Figure 6.28: HFB one-dimensional total energy surface of ^{46}Ti as a function of r (**top panel**) and β_2 (**bottom panel**). In both panels a constrain on r is imposed, whereas the parameter β_2 is free. The distance on the radial coordinate between the selected states for the PGCM ansatz is 0.2 fm (a) (6 points), 0.1 fm (b) (12 points), 0.05 fm (c) (23 points) and 0.025 fm (d) (45 points).

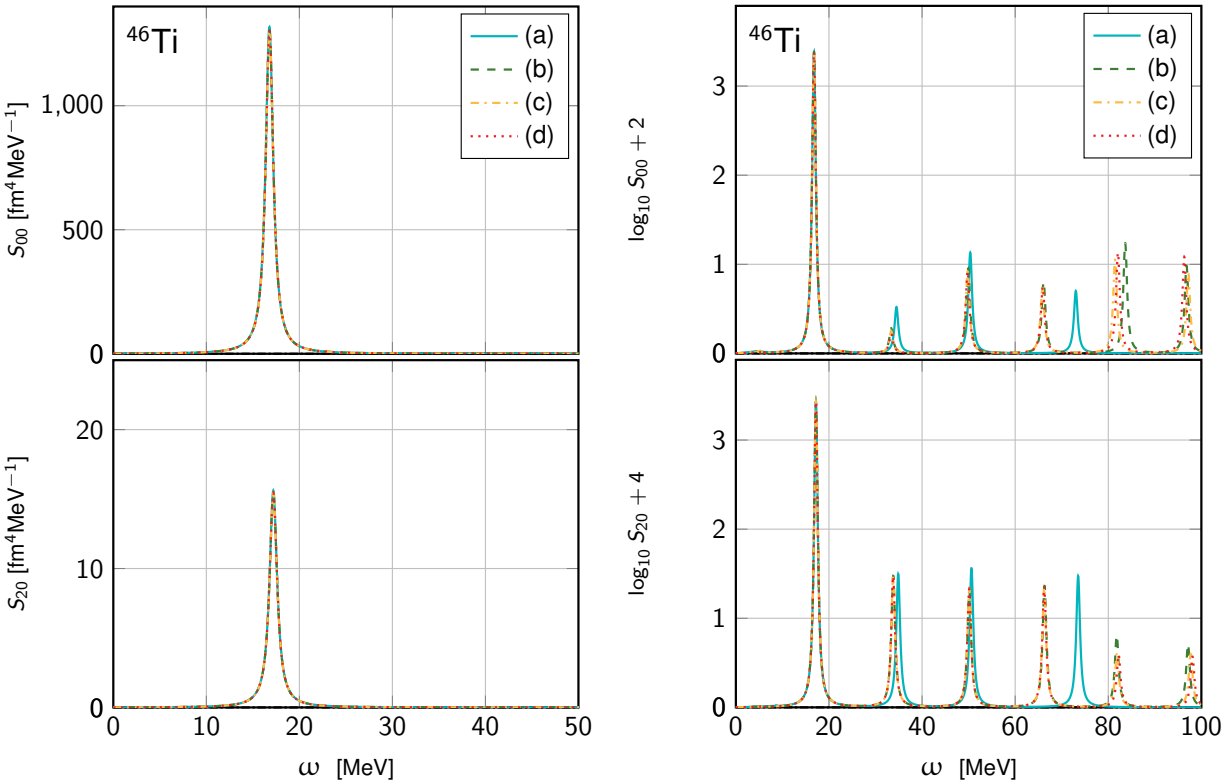

Figure 6.29: Monopole (top) and quadrupole (bottom) response of ^{46}Ti at N3LO, with $\hbar\omega = 12$ MeV and $e_{\max} = 10$ computed from the four energy surfaces shown in Fig. 6.28. Linear (left) and logarithmic (right) scales are employed. See Fig. 6.28 for details on labels and calculation parameters.

panel), slight differences are visible in high-energy peaks with tiny transition amplitudes. Such higher-energy states are shown to be multi-phonon states in Chap. 11, where their convergence is addressed.

The presence of high-energy states has a direct impact on the convergence properties of moments, even though those states carry little strength (Fig. 6.30). The quantities involving higher moments, such as $\tilde{E}_3$ and σ, are very sensitive to high-energy states and thus display large oscillations when increasing the mesh refinement. Lower moments, instead, are little or not affected, which is coherent with the stability of the GMR. If a cut-off is applied, the aforementioned oscillations disappear and results smoothly stabilise for both monopole and quadrupole responses (Fig. 6.31). The differences between $\tilde{E}_3$ and $\bar{E}_1$ reflect the presence of the small contributions from high-energy states. Contrarily $\tilde{E}_1$ and $\bar{E}_1$ are almost perfectly superposed, due to the absence of states below the GMR.

Energy window

The second criterion explored in this convergence study is related to the energy window of the selected PGCM points with respect to the minimal HFB energy. The same one-dimensional setting is exploited and four sets of points corresponding to maximum HFB excitation energies from 10 to 40 MeV are selected, as illustrated in Fig. 6.32.

The resulting monopole and quadrupole responses are shown in Fig. 6.33. Using a linear scale (left panel), no difference is visible. Using a logarithmic scale (right panel), tiny variations are visible for high-energy states, even though the convergence is rather quickly achieved there as well. It is thus quite striking to observe that PGCM solutions located between 50 and 100 MeV excitations are well converged using HFB states located only 40 MeV (or less) above the HFB minimum.

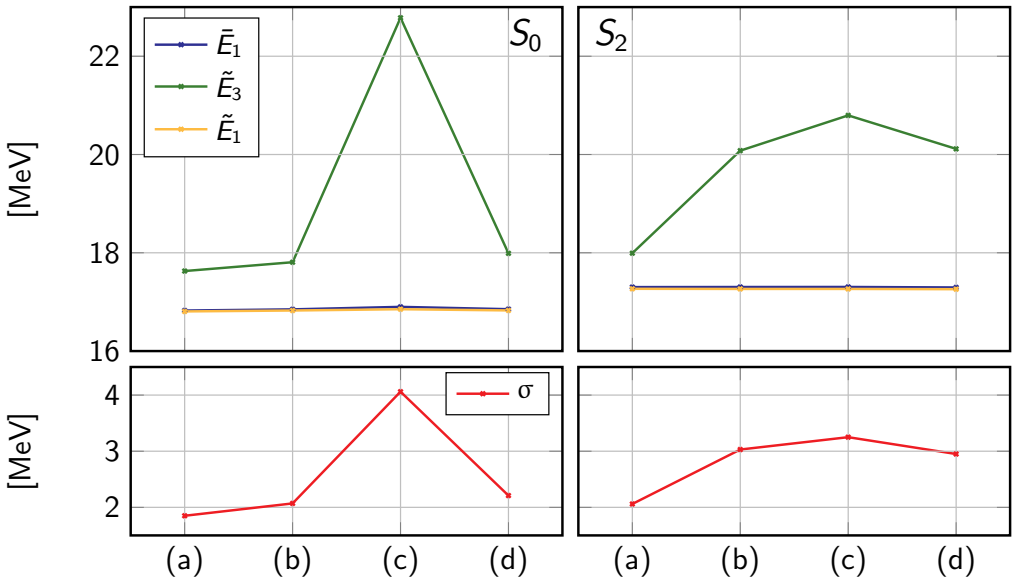

Figure 6.30: Weighted averages (see Eqs. (6.2) and (6.3) for details) as obtained from the moments of the monopole (**left**) and quadrupole (**right**) responses of ^{46}Ti from Fig. 6.29. Moments are evaluated summing over all the states issued from the PGCM calculation.

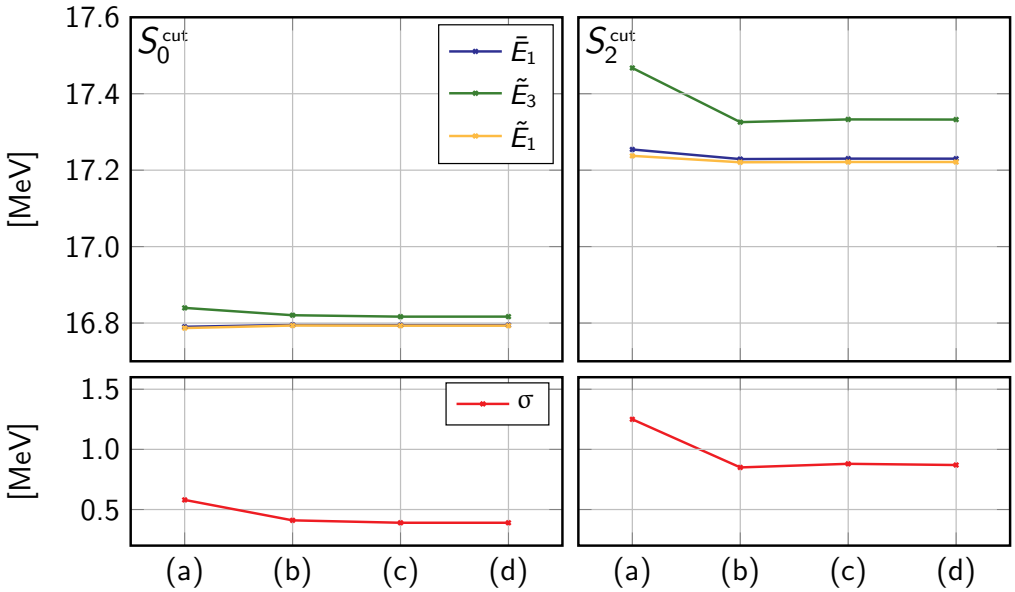

Figure 6.31: Weighted averages (see Eqs. (6.2) and (6.3) for details) as obtained from the moments of the monopole (**left**) and quadrupole (**right**) responses of ^{46}Ti from Fig. 6.29. Moments are evaluated applying a cut-off at 50 MeV.

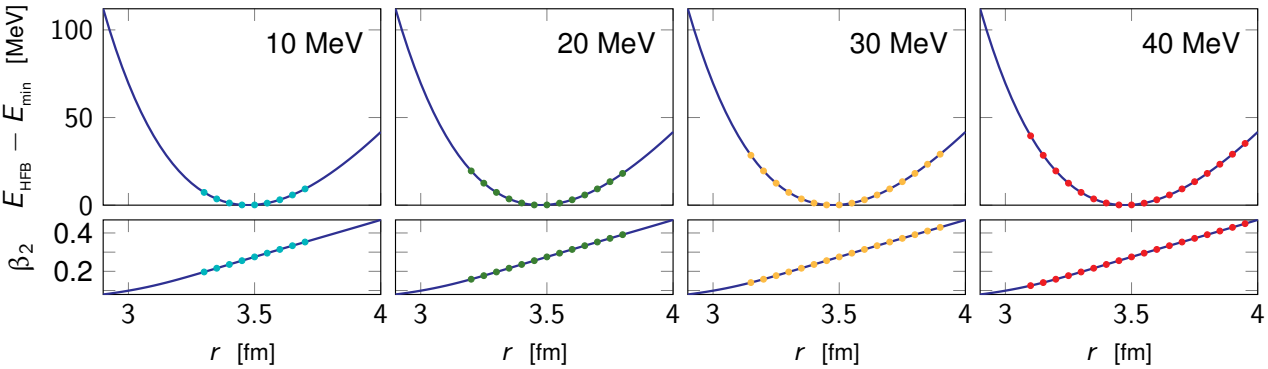

Figure 6.32: HFB one-dimensional total energy surface of ^{46}Ti as a function of r. A constrain on r is imposed, whereas the parameter β_2 is free. Different energy windows are explored for the selection of the points to include in the PGCM ansatz: 10 MeV (9 points), 20 MeV (13 points), 30 MeV (16 points) and 40 MeV (18 points). The distance on the radial coordinate between the selected states is 0.05 fm.

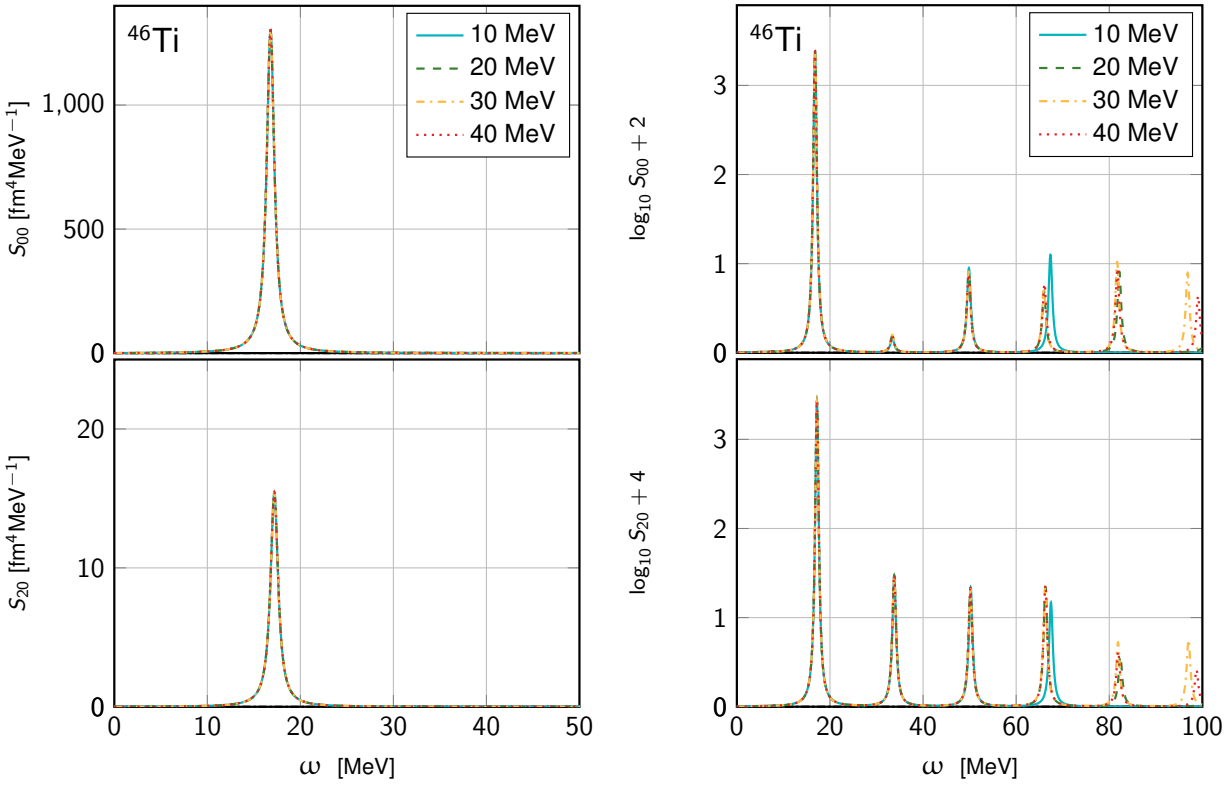

Figure 6.33: Monopole (top) and quadrupole (bottom) response of ^{46}Ti at N3LO, with $\hbar\omega = 12$ and MeV $e_{max} = 10$ in linear (left) and logarithmic (right) scale. See Fig. 6.32 for details on labels and calculations parameters.

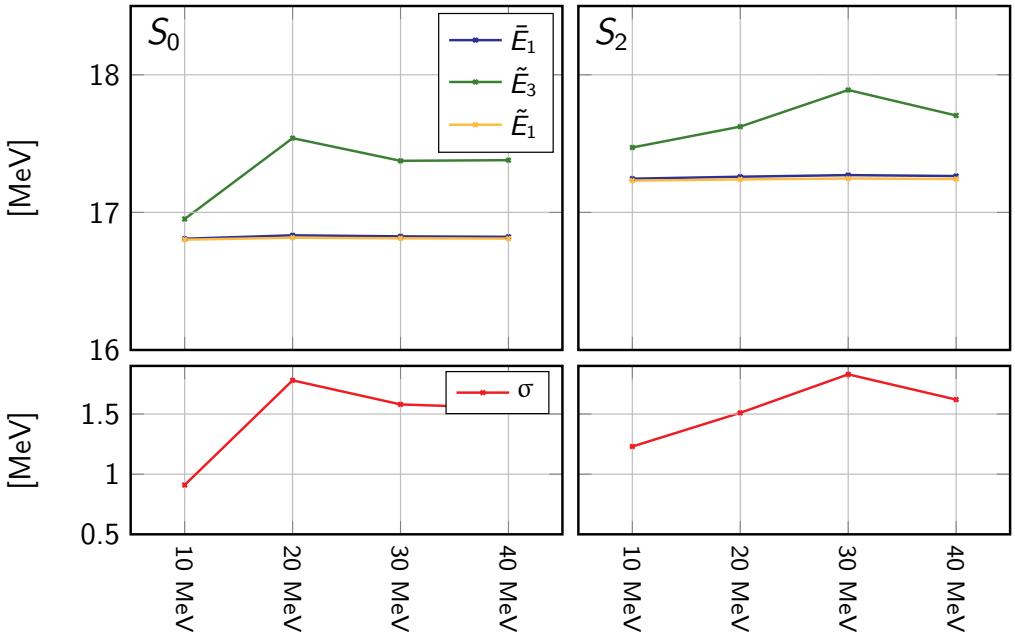

Figure 6.34: Weighted averages (see Eqs. (6.2) and (6.3) for details) as obtained from the moments of the monopole (**left**) and quadrupole (**right**) responses of ^{46}Ti from Fig. 6.33. Moments are evaluated summing over all the states issued from the PGCM calculation.

Mild variations in strength moments are mostly linked to variations of high-energy states. This is shown in Fig. 6.34. However, such variations are less pronounced than in the previous case from Fig. 6.30, so that the convergence of high-lying states is better managed via this second criterion. Eventually, once the cut-off is applied, results solidly stabilise independently on the considered energy window, as visible in Fig. 6.35.

6.6.2 Two-dimensional case

Realistic calculations aiming at investigating the coupling between monopole and quadrupole modes require the use of more than one generating coordinate. When two or more coordinates are considered simultaneously, the convergence pattern is more complicated to assess than in the one-dimensional case. The two criteria explored in the one-dimensional case are now also explored in two-dimensional calculations.

Mesh resolution

Calculations from Sec. 6.2.2 at N3LO with $\hbar\omega = 12$ MeV and $e_{\max} = 10$ are considered. Different spacing between the selected points are considered, as depicted in Fig. 6.36. The previously performed calculation corresponds to configuration (c). Starting from there, selected points are rarefied by withdrawing one every two HFB points, in two successive iterations. This results in the number of HFB points being reduced by a factor of two in (b) and four in (a).

The corresponding monopole and quadrupole responses are displayed in Fig. 6.37. The energy of the main GMR peak is very stable, whereas secondary structures change rapidly as the mesh grid is decreased. The quadrupole response is even more seriously affected by the reduction of HFB points: while the strength below 15 MeV is qualitatively reproduced by coarser meshes, this is not the case for the GQR.

Weighted averages are shown in Fig. 6.38. Since the GMR is rather stable these moments are very solid against variations in the mesh grid. Quadrupole moments are more affected. Overall, weighted averages migrate towards higher energies when going from a less to a more refined mesh (from (a) to (c)). This is an

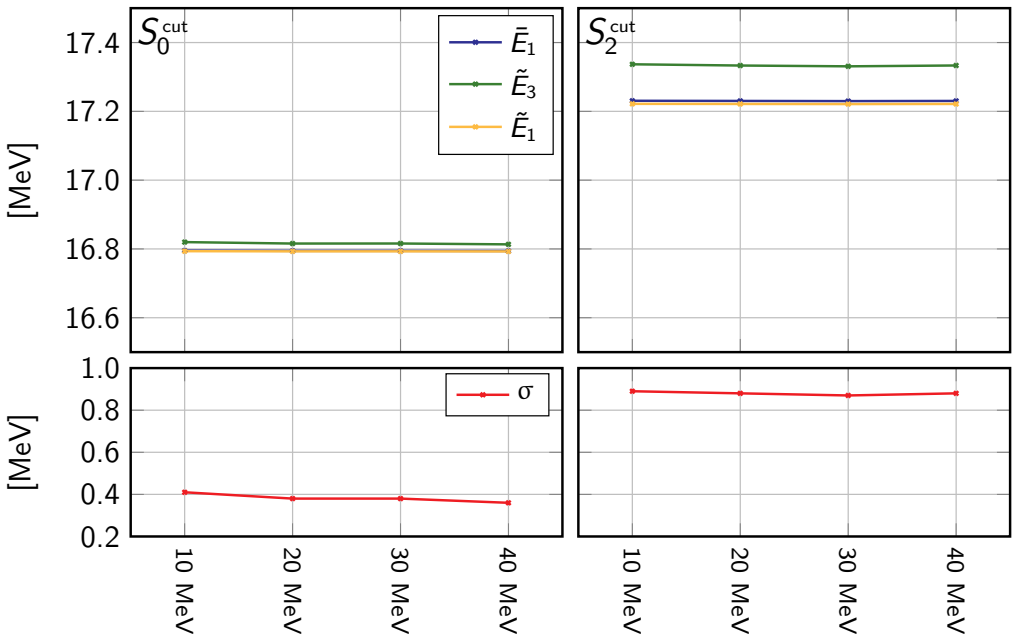

Figure 6.35: Weighted averages (see Eqs. (6.2) and (6.3) for details) as obtained from the moments of the monopole (**left**) and quadrupole (**right**) responses of ^{46}Ti from Fig. 6.33. Moments are evaluated applying a cut-off at 50 MeV.

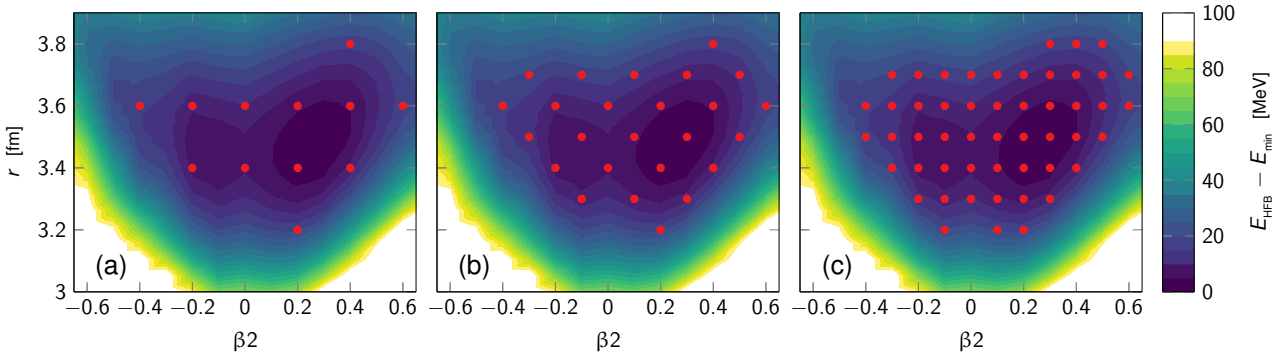

Figure 6.36: HFB total energy surface of ^{46}Ti at N3LO ($\hbar\omega$ = 12 MeV and e_{max} = 10) showing different mesh distancing of the points included in the PGCM ansatz. The meshes (a), (b) and (c) include, respectively, 12, 25 and 51 points.

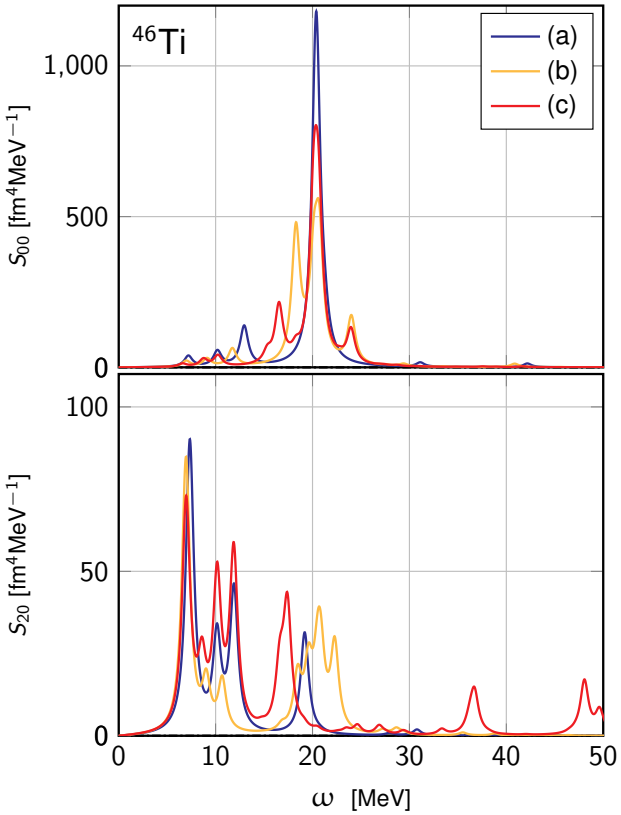

Figure 6.37: Monopole (top) and quadrupole (bottom) response of ^{46}Ti at N3LO, with $\hbar\omega = 12$ and $e_{\max} = 10$, computed from the three meshes displayed in Fig. 6.36.

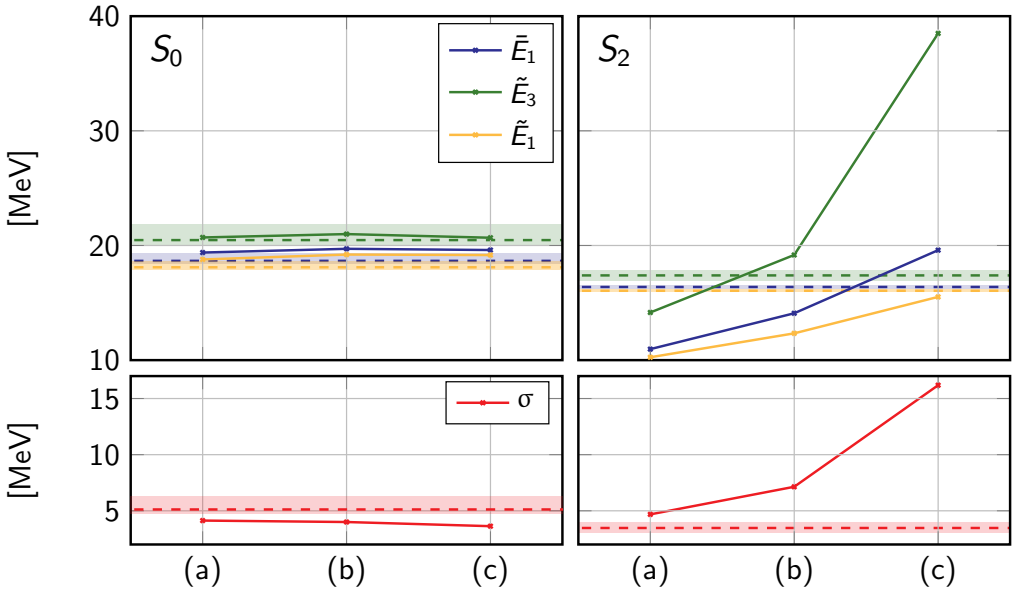

Figure 6.38: Weighted averages (see Eqs. (6.2) and (6.3) for details) as obtained from the moments of the monopole (**left**) and quadrupole (**right**) responses of ^{46}Ti from Fig. 6.37. Moments are evaluated summing over all the states issued from the PGCM calculation.

immediate consequence of the high-lying strength above 35 MeV appearing in (c).

If the 38 MeV cut-off is applied (Fig. 6.39), monopole averages remain almost unchanged and a good agreement with experimental data is observed. The quadrupole averages are more radically affected by the cut-off. The centroid, in particular, is lowered by ∼6 MeV and displays a convergent trend, whereas $\tilde{E}_3$, more sensitive to high-energy states, is still significantly higher in (c).

Energy window

To investigate the convergence of the PGCM results with respect to the maximum energy of the selected HFB states, three values, from 10 to 20 MeV, are utilised, as illustrated in Fig. 6.40.

The corresponding monopole and quadrupole responses are displayed in Fig. 6.41. In the monopole channel, at 10 MeV the spectrum is already nicely converged. Comparing the 15 MeV and the 20 MeV cases, an accurate reproduction is observed, both concerning the main GMR peak and the peak associated with the coupling to the GQR at ∼17 MeV.

For the quadrupole the situation is unusually satisfying. The GQR is correctly determined already at 10 MeV, and lower-energy structures are also qualitatively reproduced. At 15 MeV an excellent agreement with the target 20 MeV result is observed, both for the GQR and the lower-energy strength. The only difference lies in the determination of states at higher energy, which are not observed with points up to 15 MeV.

The associated weighted averages are plotted in Fig. 6.42. Monopole moments are very stable with respect to the considered energy windows. Quadrupole weighted averages being affected by high-energy strength are significantly changed in the 20 MeV case. While the use of the 38 MeV cut-off does not influence monopole moments, it mitigates to a large extent the quadrupole moments dependence on the considered energy window.

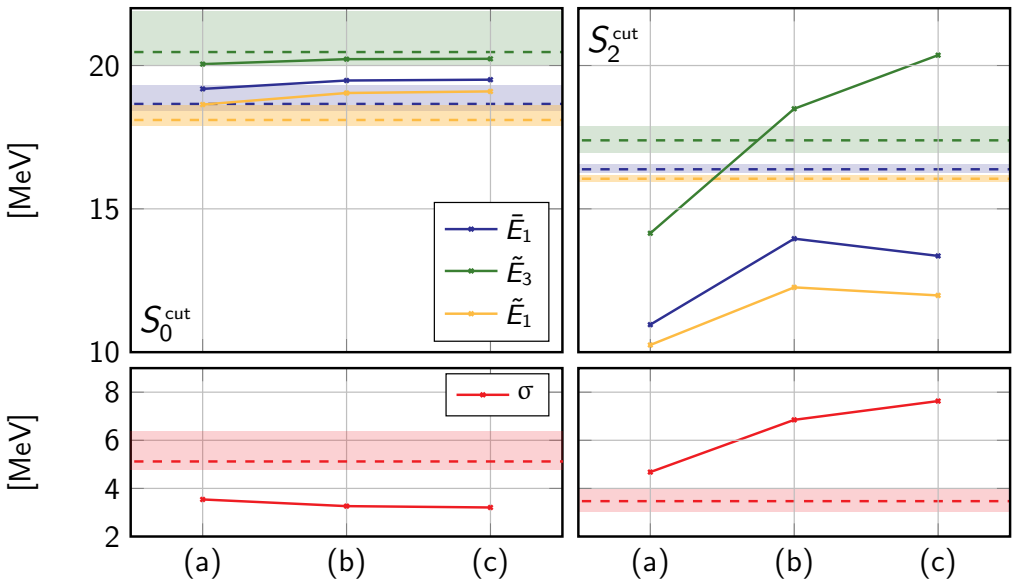

Figure 6.39: Weighted averages (see Eqs. (6.2) and (6.3) for details) as obtained from the moments of the monopole (**left**) and quadrupole (**right**) responses of ^{46}Ti from Fig. 6.37. Moments are evaluated applying a cut-off at 38 MeV.

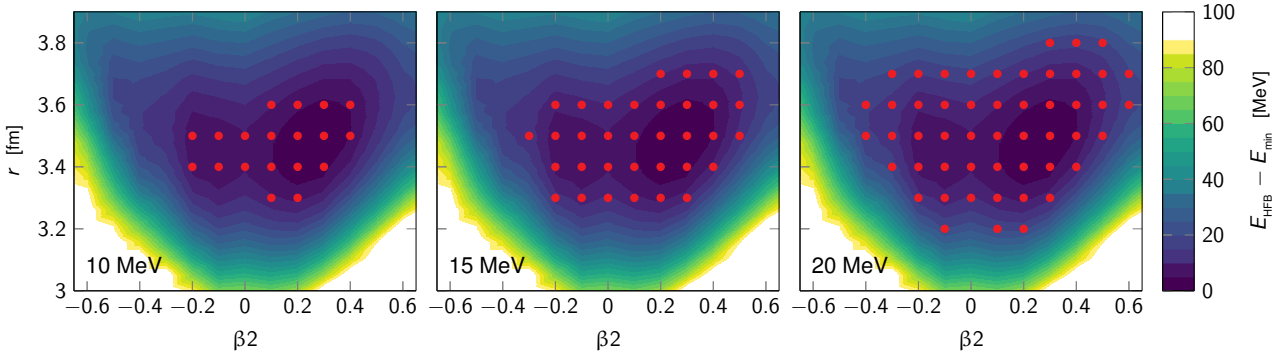

Figure 6.40: HFB total energy surface of ^{46}Ti at N3LO ($\hbar\omega = 12$ MeV and $e_{\text{max}} = 10$) showing different energy windows to select the points included in the PGCM ansatz: from left to right, 10 MeV (19 points), 15 MeV (34 points) and 20 MeV (51 points).

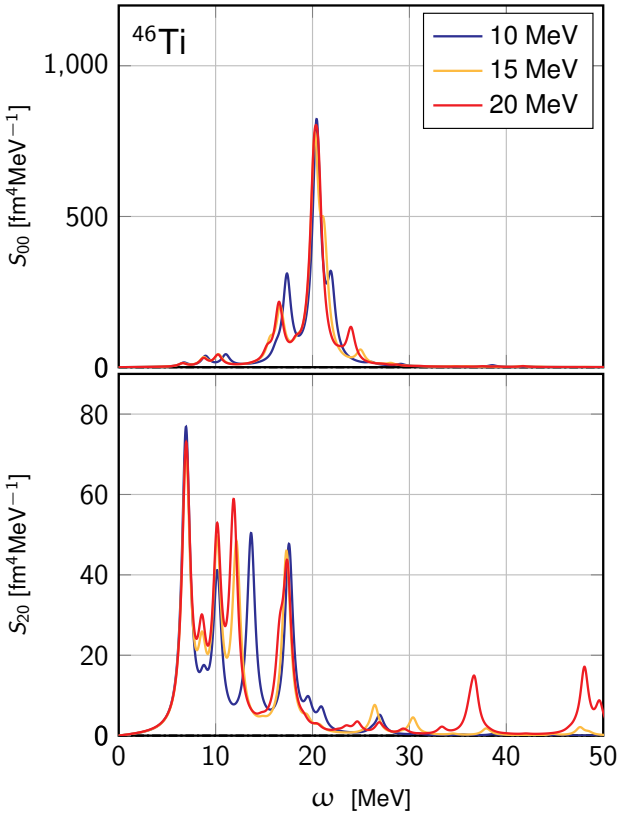

Figure 6.41: Monopole (top) and quadrupole (bottom) responses of ^{46}Ti at N3LO, with $\hbar\omega = 12$ MeV and $e_{\max} = 10$, computed from the three meshes displayed in Fig. 6.40.

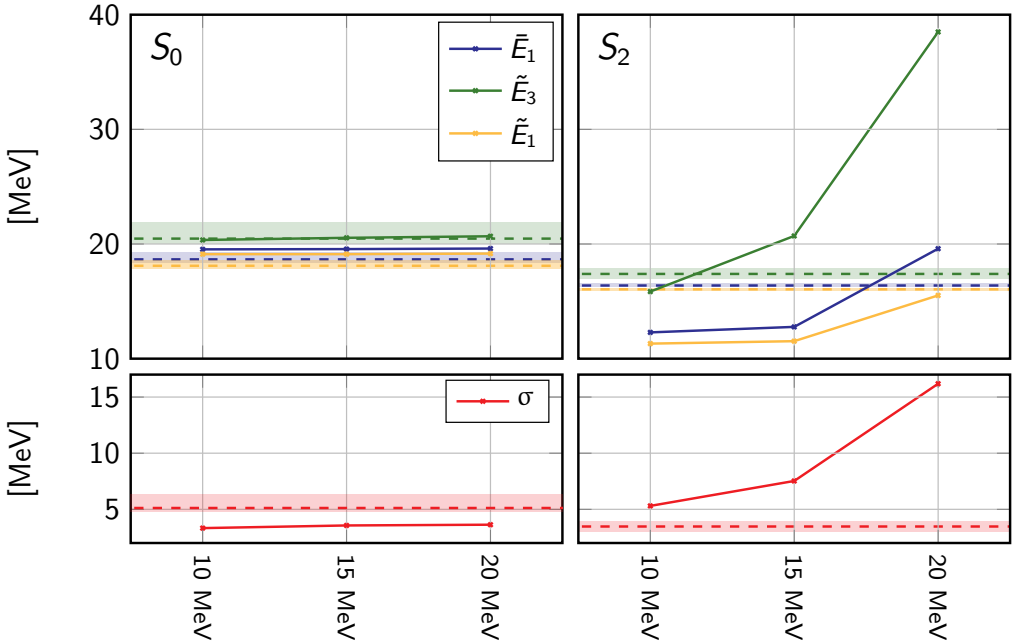

Figure 6.42: Weighted averages (see Eqs. (6.2) and (6.3) for details) as obtained from the moments of the monopole (**left**) and quadrupole (**right**) responses of ^{46}Ti from Fig. 6.41. Moments are evaluated summing over all the states issued from the PGCM calculation.

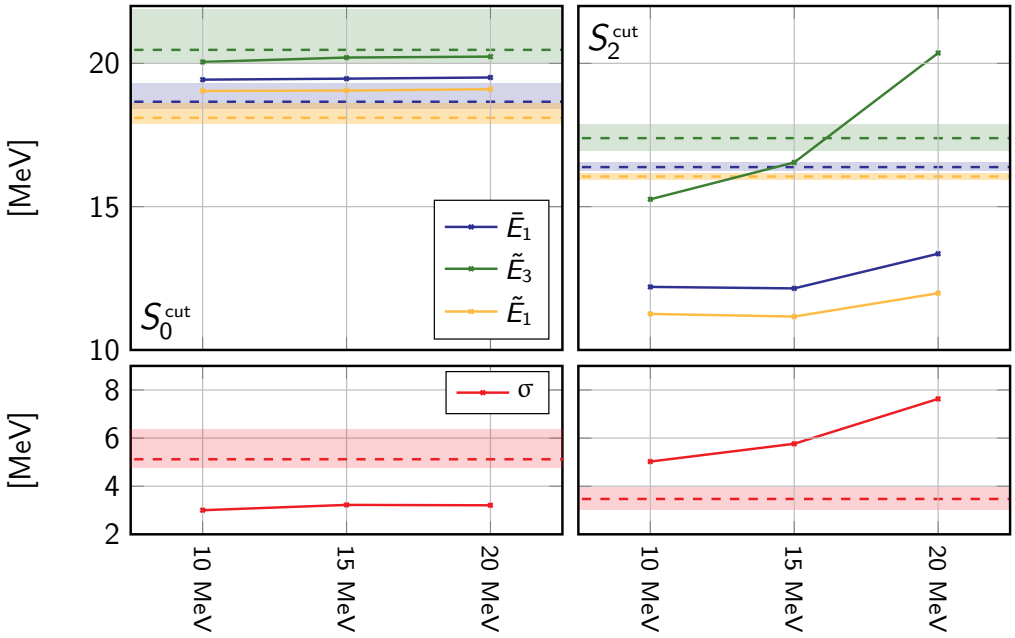

Figure 6.43: Weighted averages (see Eqs. (6.2) and (6.3) for details) as obtained from the moments of the monopole (**left**) and quadrupole (**right**) responses of ^{46}Ti from Fig. 6.41. Moments are evaluated applying a cut-off at 38 MeV.

6.6.3 Summary

Two criteria to optimise the selection of the HFB vacua to be included in the PGCM ansatz were briefly explored. A first criterion relying on the notion of distance in the generator coordinates space and a second one associated with the maximal energy difference to the HFB minimum were examined. Both one- and two-dimensional PGCM calculations were performed. The most relevant outcomes of this investigation are that

- In one-dimensional calculations both the energy-based and the mesh-density criteria allow on to achieve converged results on the basis of a small number of points.
- Two-dimensional calculations are affected to a greater extent by the choice of HFB states, such that the two criteria perform differently for a given number of points.
- Two-dimensional calculations are overly sensitive to changes in the mesh grid in the generator coordinates space. The strategy of reducing the number of HFB states by increasing the distance between them in a fixed energy window revealed unsatisfying.
- Thus, an energy-based selection, with a fixed mesh density is the most appropriate. The use of a relatively narrow energy window (up to ∼15 MeV) provides a sufficiently precise description of high-lying states up to about ∼80 MeV excitations.

Chapter 7

Results of physical interest

Contents

As illustrated in Chap. 6, where the deformed nucleus ^{46}Ti was studied to characterise numerical convergence aspects, deformed systems display a significant fragmentation of the monopole strength. Such a fragmentation is even more pronounced in some of the lighter systems addressed in this chapter. In Sec. 7.1 results about the spherical, doubly-closed-shell system ^{16}O are presented, just in order to provide a clear comparison between PGCM and QRPA. The physics of GMR-GQR coupling in PGCM calculations is discussed in Sec. 7.2 for ^{46}Ti. The possible effects of shape-coexistence on the GMR in ^{28}Si are addressed in Sec. 7.3. Eventually, the case of a highly-fragmented monopole response is investigated in Sec. 7.4 for ^{24}Mg.

All calculations presented in this and in the following chapters are realised in a harmonic oscillator basis space with $\hbar\omega = 12$ MeV and $e_{\max} = 10$, at N3LO [6]. PGCM and QFAM calculations are performed in axial symmetry. The generator coordinates (r, β_2) are explored in PGCM calculations.

7.1 ^{16}O: an archetypical spherical system

PGCM calculations in ^{16}O are now addressed in order to explore the GMR physics in an easier spherical system. The HFB energy surface adopted for PGCM calculations is displayed in Fig. 7.1, showing without ambiguities a well defined spherical minimum and a smooth behaviour with respect to both the radial and

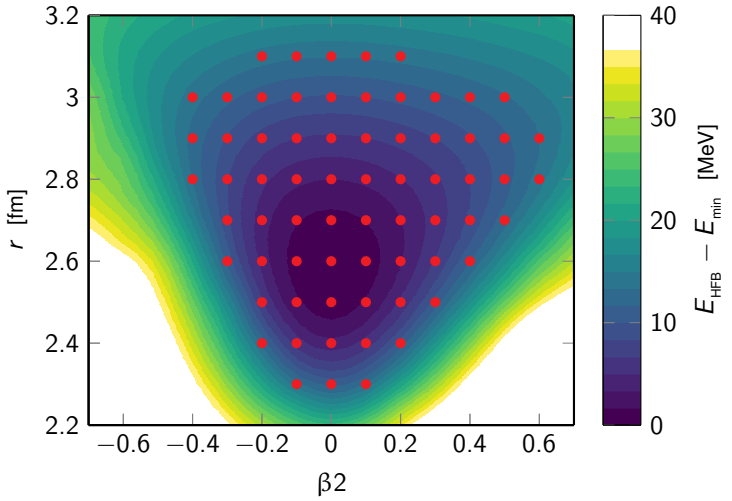

Figure 7.1: HFB total energy surface for ^{16}O. The red dots correspond to the constrained quasiparticle vacua included in the PGCM ansatz.

the β_2 coordinates. The corresponding PGCM monopole response is shown in Fig. 7.2 and compared to Finite Amplitude Method-QRPA (QFAM) results[1] obtained using the same numerical setting and the same spherical HFB minimum. The PGCM monopole response results in a very compact spectrum, with a single GMR peak at ∼19 MeV followed by smaller peaks at higher energies. QRPA, instead, provides a more fragmented monopole strength; the peak at ∼22 MeV is associated to the breathing mode for reasons that are exposed in the following. Thus, the GMR positioning in QRPA is ∼ 3 MeV higher than in PGCM.

An interpretation of such differences is given on the basis of Fig. 7.3. One-dimensional cuts of the HFB energy surface from Fig. 7.1 as a function of r (β_2) while fixing β_2 (r) at the HFB-minimum value. A harmonic fit is also provided in each case. Details on the fitting procedure are given in Sec. 9.2. The eigenfrequencies extracted from the fitting parameters are $\hbar\omega$ =22.6 MeV for the monopole response and $\hbar\omega$ =22.3 MeV for the quadrupole response. This crude estimate provides a good degree of agreement with the QRPA results: the values a_r = 98.91 MeV fm^{-2} and a_β = 96.18 MeV provide, respectively, the eigenfrequencies $\hbar\omega$ = 22.6 MeV (the first monopole peak of QFAM being at 22.7 MeV) and $\hbar\omega$ = 22.3 MeV (the quadrupole response in QFAM has its main peak at 21.9 MeV). Overall, the following comments are in order

a. The harmonic total energy surface approximates the reference HFB one in such a way that the energy is underestimated for negative variations of the rms radius, whereas it overestimates the energy for positive variations of the coordinate (i.e. the nucleus is actually stiffer when addressing compression and softer when dilations are concerned).

b. Similarly, even if in a less pronounced fashion, the energy change associated to negative (positive) variations of the axial deformation parameter β_2 are underestimated (overestimated) by the harmonic approximations.

c. Overall, the softer nature of the total HFB energy surface compared to its harmonic approximation explains the ∼3 MeV shift of the PGCM response to lower energies if compared to the QRPA response.

d. The fragmentation of the QRPA spectrum is *not* a consequence of anharmonic effects, that are not taken into account in QRPA by definition. It must be due to the fact that QRPA is not limited to

[1]The QFAM technique is briefly introduced in Chap. 9. In this context it can be considered a synonym of QRPA.

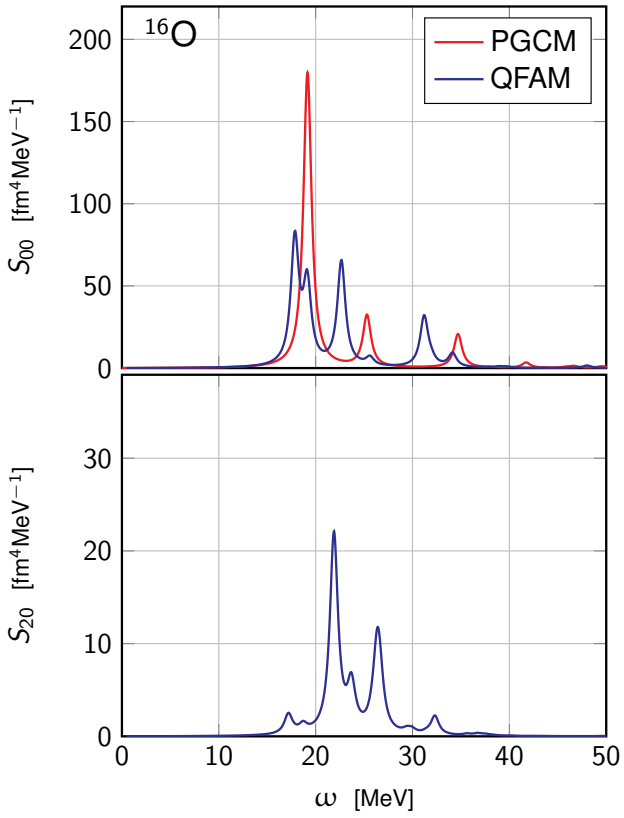

Figure 7.2: Monopole (top) and quadrupole (bottom) response in ^{16}O for PGCM and QFAM calculations. The PGCM ansatz results from the combination of the points displayed in Fig. 7.1, whereas the QFAM calculations were performed starting from the corresponding spherical minimum. PGCM quadrupole response is missing due to numerical issues intervened for this specific calculation when projecting on $J = 2$.

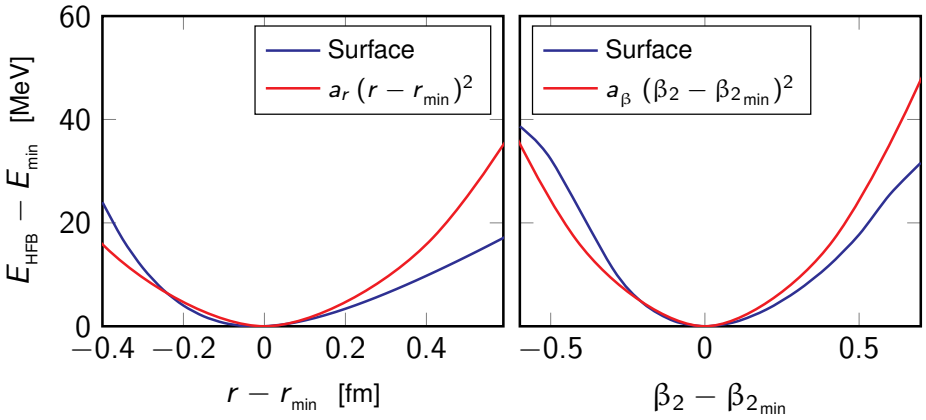

Figure 7.3: One-dimensional cuts from the HFB energy surface from Fig. 7.1 for $\beta_2 = 0$ (left) and $r = r_{\min}$ (right) compared to the respective harmonic fit.

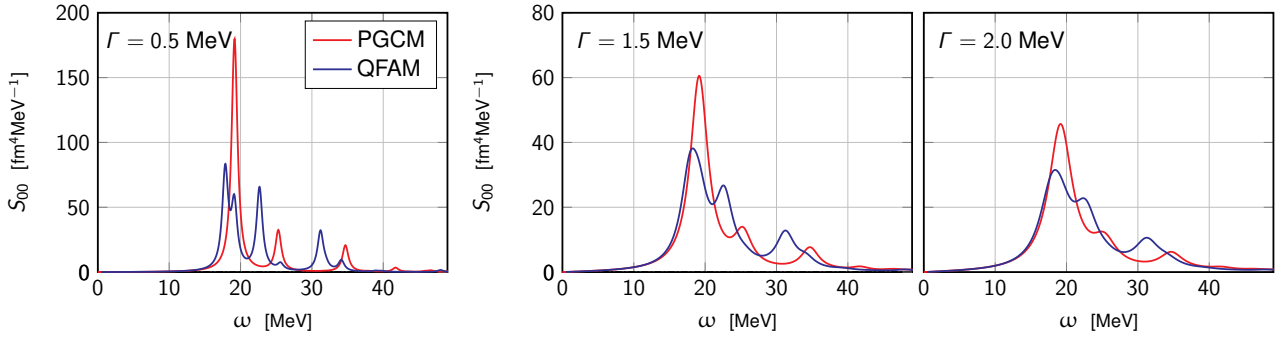

Figure 7.4: Monopole response in ^{16}O for PGCM and QFAM calculations for different values of the smearing parameter Γ. The $\Gamma = 0.5$ MeV results have been plotted with a different vertical scale in order not to excessively compress the other cases.

exploring two collective coordinates. This fragmentation is absent from present PGCM results, that explore only two collective coordinates (albeit without any harmonic approximation).

Eventually, different smearing parameters are explored. Increasing Γ to 1.5 MeV or 2.0 MeV, the difference between PGCM and QFAM results becomes less and less pronounced, as visible in Fig. 7.4. In such cases, a global agreement between QFAM and PGCM spectra is observed.

7.2 Deformation effects in ^{46}Ti

Results concerning numerical convergence aspects in ^{46}Ti were extensively discussed in Chap. 6. A more physical perspective is now adopted to investigate the nature of the observed resonances, with a specific interest to deformation effects, as well as in the coupling between the monopole and the quadrupole resonances.

The HFB total energy surface is displayed in Fig. 7.5. Coloured lines in this picture point to specific (uncoupled) one-dimensional PGCM calculations performed at fixed deformation, either spherical (purple line) or at the optimal β_2 value (light blue line), or fixed radius (orange line). The one-dimensional PGCM calculation resulting from a pure constrain on the radius while leaving β_2 free to adjust through the energy minimisation (black line) is also showed for comparison. The total energy curves corresponding to these one-dimensional cuts are shown in Fig. 7.6 to better analyse the outcome of the different calculations.

The monopole and quadrupole response for the different sets of PGCM calculations are displayed in Fig. 7.7. The monopole response from the full two-dimensional PGCM calculation displays a slightly fragmented structure, whose peaks of greater importance can now be analysed. The one-dimensional and full two-dimensional calculations are commented on in the following subsections while referring to the PGCM collective wave-functions associated to the main states of interest displayed in Fig. 7.8.

7.2.1 Monopole vibrations (breathing mode)

The main peak (b) visible in Fig. 7.7 is the manifestation of the standard giant monopole resonance, whose collective PGCM wave-function is presented in Fig. 7.8 (middle left). This state presents a well-defined radial node with respect to the ground-state configuration (top left) such that the GMR clearly manifests as a radial vibration on top of the ground-state. This statement is confirmed by the light-blue monopole response in Fig. 7.7, originating from the pure radial (one-dimensional) vibration at the fixed deformation corresponding to the HFB minimum: the corresponding single-peak GMR is found to be almost superposed to the GMR peak (b) from the two-dimensional PGCM calculation.

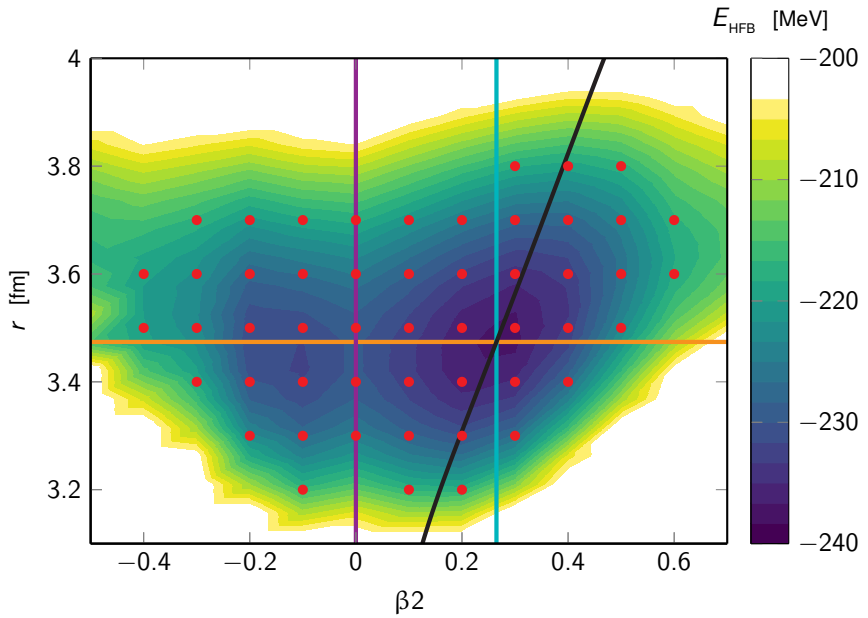

Figure 7.5: HFB total energy surface for ^{46}Ti. The red dots correspond to the constrained quasiparticle vacua included in the PGCM ansatz. Coloured lines represents the different one-dimensional cuts used in the PGCM analysis, see text for details. The same colour code is used in Figs. 7.6 and 7.7.

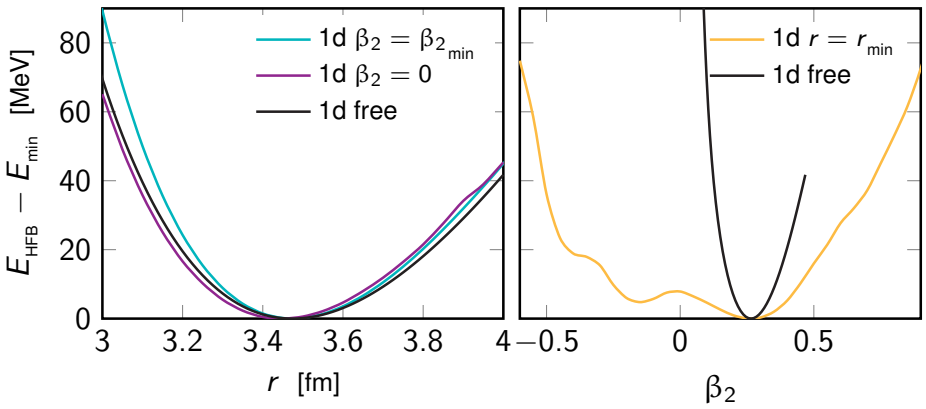

Figure 7.6: One-dimensional cuts from the HFB energy surface in Fig. 7.5 for fixed values of r and β_2. The free one-dimensional cut is also shown, whose points minimise the HFB total energy for assigned values of r while leaving β_2 free to move towards the energetically more convenient configuration.

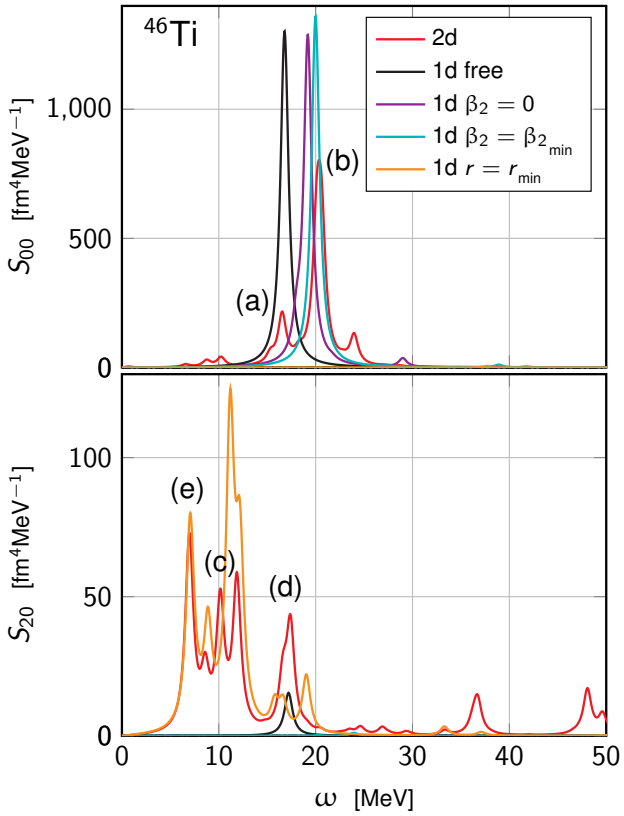

Figure 7.7: Monopole (top) and quadrupole (bottom) response in ^{46}Ti for the different sets of PGCM calculations discussed in Fig. 7.5. Labels (a) - (e) identify different parts of the spectra discussed in the text.

The pure radial vibration computed at sphericity (purple line) delivers a single-peak GMR that is slightly shifted towards lower energy compared to the GMR peak (b). Such a shift can be explained from the one-dimensional cuts at fixed β_2 values displayed in Fig. 7.6: the deformed energy profile is stiffer than its spherical counterpart, especially against compression, which explains the slightly higher energy of the resonance in this case. Such a tendency is in qualitative agreement with Ref. [165], where a shift towards higher energies is associated to an increase in the deformation parameter in a fluiddynamical model.

7.2.2 Quadrupole vibrations

Pure quadrupole vibrations are obtained through an uncoupled one-dimensional PGCM calculation along the β_2 coordinate with fixed radius values. This is represented by the yellow line in Fig. 7.5 and in Fig. 7.6 for the corresponding one-dimensional HFB-energy curve. The associated quadrupole response is provided in Fig. 7.7 (bottom). Compared to the full two-dimensional PGCM calculation in red, one observes that the two responses below 15 MeV are qualitatively (and in some cases quantitatively). The nature of this excitations is now briefly discussed.

Such states can be in some cases associated to individual modes: this is the case, for instance, of peak (c), whose collective PGCM wave-function is depicted in Fig. 7.8 (bottom left) and is characterised by a sharp displacement with respect to β_2. Neighbouring states displays similar features.

Alternatively, a low-lying 2^+ rotational state built on the oblate-shape isomer is observed at ~6.5 MeV (e). The corresponding collective PGCM wave-function is displayed in Fig. 7.9 (bottom right) and compared to the one associated with the 2^+ rotational state built on the ground state (bottom left). The energy of the oblate-shape isomer (~6.6 MeV) is found to be coherent with the energy difference between the oblate and

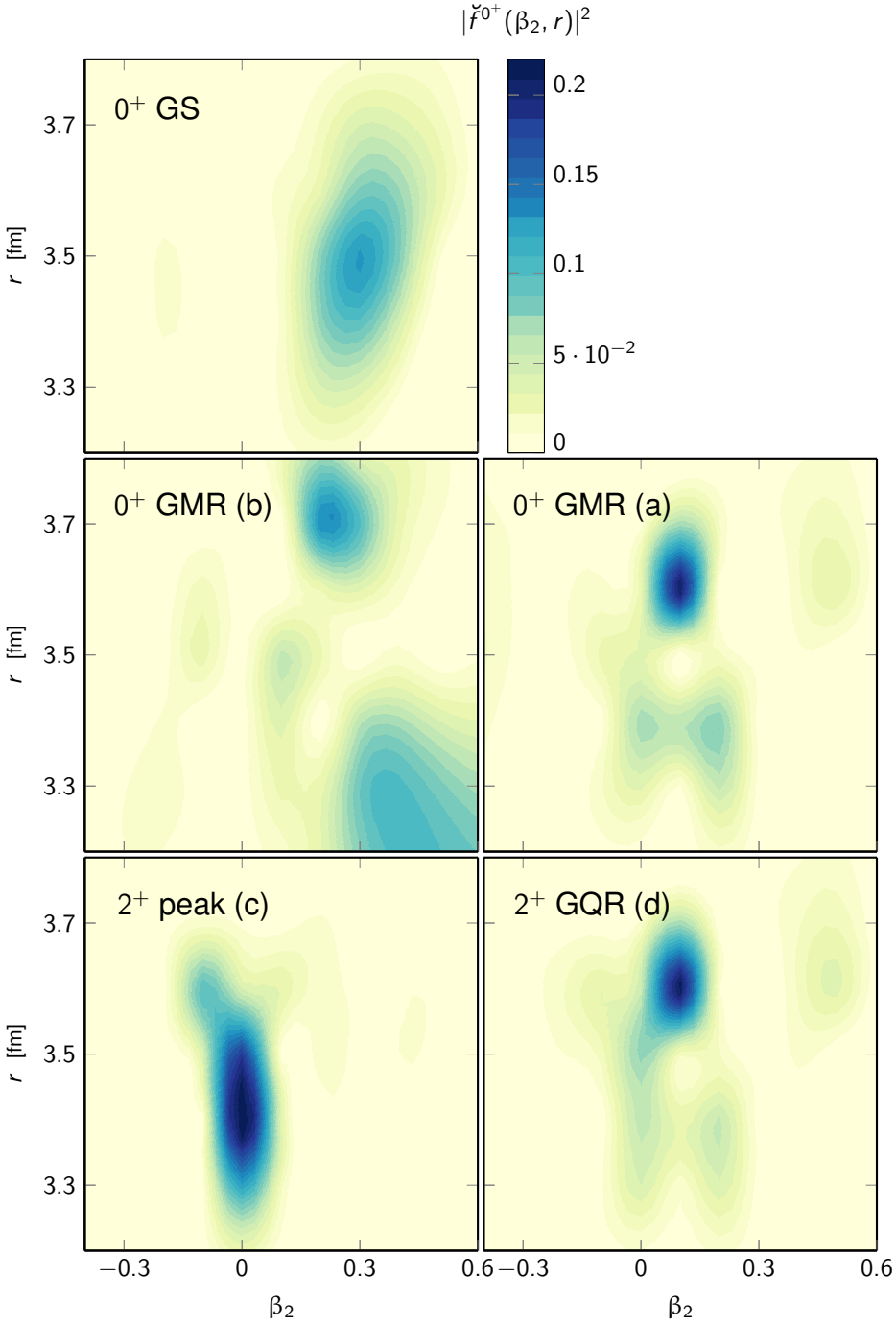

Figure 7.8: Intrinsic collective PGCM wave-functions in the (r, β_2) plane of some specific states of interest (labels are referred to Fig. 7.7), specifically: 0^+ ground state (top left); main (b) 0^+ component of the giant monopole resonance (middle left); lower energy (a) 0^+ component of the giant monopole resonance (middle right), coupling to (bottom right) the 2^+ giant quadrupole resonance (d); lower energy 2^+ state (bottom left).

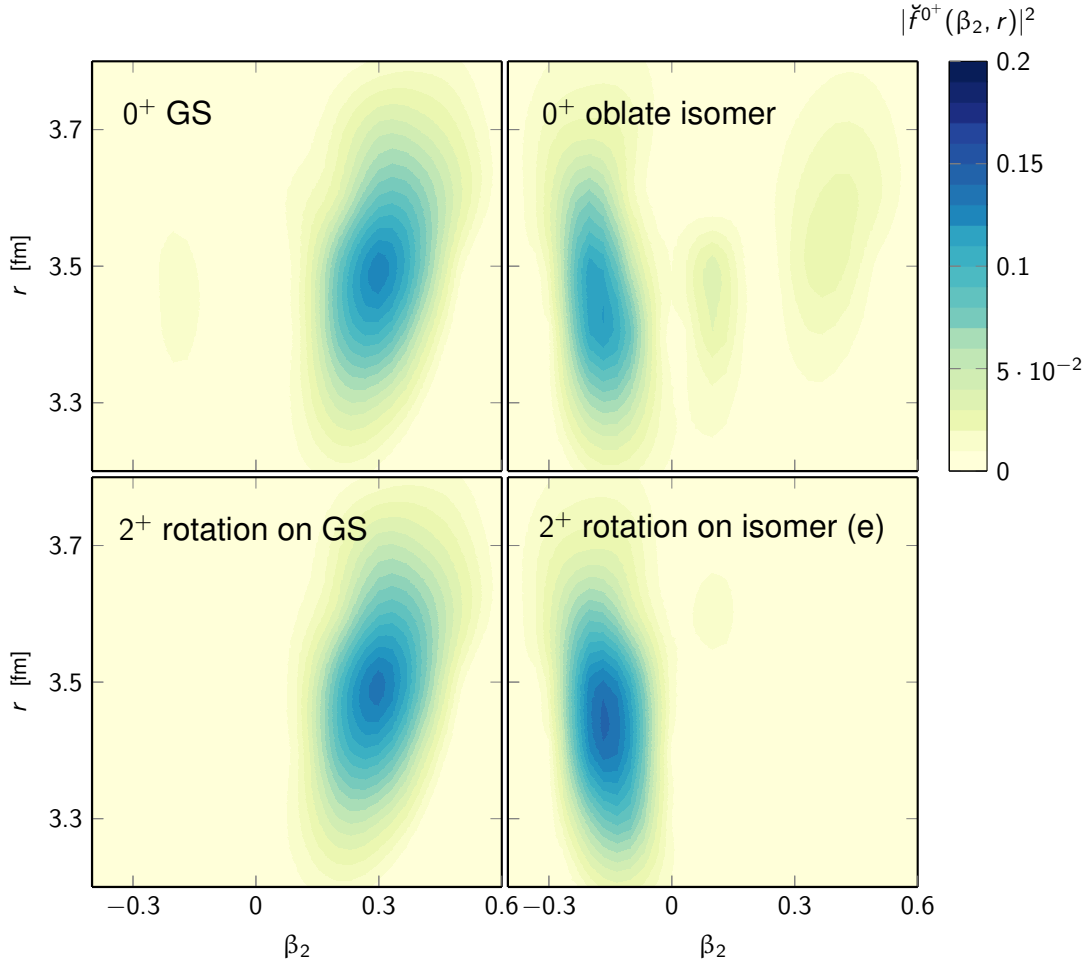

Figure 7.9: Intrinsic collective PGCM wave-functions in the (r, β_2) plane of some specific states of interest (labels are referred to Fig. 7.7), specifically: 0^+ ground state (top left); 2^+ rotation on the ground state (bottom left); 0^+ oblate-shape isomer (top right); 2^+ rotation on the oblate-shape isomer (bottom right).

the prolate minima in Fig. 7.5 (energy difference between prolate and oblate minima ∼6.1 MeV).

7.2.3 Coupling to quadrupole resonance

The lower-energy component (a) of the monopole resonance at ∼16.5 MeV (associated collective wave-function in Fig. 7.8, middle right) is also shown to correspond to a radial vibration, like the breathing mode (b), but with a central node located at smaller deformation ($\beta_2 \sim 0.1$), thus implying a change of static deformation. Peak (a) appears at nearly the same energy as the GQR peak (d) at ∼17.1 MeV. This feature is usually referred to as the GMR-GQR coupling [69, 154]. The collective PGCM wave-function of the GQR 2^+ state is displayed in Fig. 7.8 (bottom right). The striking similarity between the 0^+ and 2^+ collective wave-functions of the GMR-GQR coupled state shows how PGCM identifies such states as one intrinsic coupled vibrational state, subsequently disentangled by the projection on different angular momenta.

Eventually, $B(E2)$ transition probabilities between all 0^+ and 2^+ states are systematically displayed in Fig. 7.10. In this plot the probability always relates to the upwards transition, i.e. only excitation processes are represented in the figure; see Fig. 7.10 for further details on the employed representation. Even if *all* possible transitions are displayed, only few of them are actually visible due to the choice of making

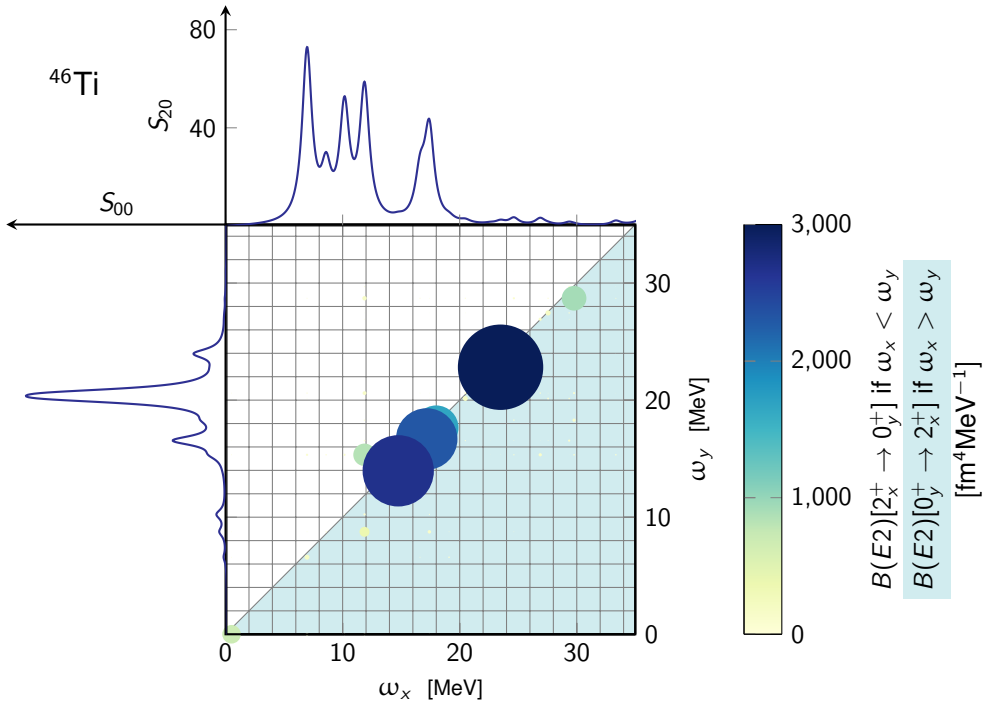

Figure 7.10: Inter-state $B(E2)$ transitions between all 0^+ and 2^+ states issued from the two-dimensional PGCM calculation. The dots are located at the intersection of the energies between 0^+ (vertical axis) and 2^+ (horizontal axis) states. The monopole (quadrupole) response of the ground state is also shown for comparison on the vertical (horizontal) axis, in order to provide a clearer picture of possible coupling between different resonant channels. Transition amplitudes are also rescaled so to refer to upwards transitions (excitations); the size of the dots is proportional to the magnitude of the transition (same information provided by the colour code).

the points' size proportional to the magnitude of the corresponding transition. This shows that only very few transitions actually display large probabilities, many of which concentrate in the energy region corresponding to the GQR. This is interpreted as an additional signal of the so-called coupling between the $K = 0$ component of the GQR and the lowest peak of the GMR in prolate deformed systems. The sizes of these few transitions are comparable to the expectation value of the transition operator in the corresponding 2^+ state. Focusing on the transition between the 0^+ state at 16.5 MeV (first GMR peak) and the 2^+ state at 17.1 MeV ($K = 0$ component of the GQR), the transition amplitude is $|\langle 2^+_{\text{GQR}}|Q_{20}|0^+_{\text{GQR}}\rangle|^2 = 294$ fm^{4}MeV^{-1}, which shall be compared to $|\langle 2^+_{\text{GQR}}|Q_{20}|2^+_{\text{GQR}}\rangle|^2 = 464$ fm^{4}MeV^{-1}.

Comment on the notion of coupling

The presence of neighbouring states with $J = 0$ and $J = 2$ displaying strong transitions in the GQR region indicates that the PGCM captures what is usually referred to as the GMR-GQR coupling in intrinsically-deformed nuclei.

Such states relate to a single intrinsic state in symmetry-breaking frameworks, such as deformed (Q)RPA or GCM (without AMP). There, an intrinsically-deformed state contributes to both the $K = 0$ component of the GQR and to the first peak of the GMR. PGCM relying on symmetry restoration *prior* to the diagonalisation in the reduced Hilbert space, every $J = J_i$ subspace is independent from the others. Still, the notion of coupling in the intrinsic state seems not to be lost even once the symmetries have been fully restored.

A simple explanation of the coupling mechanism is now presented. For the time being, let us disregard the projection effects. One can interpret the underlying mechanism by means of a coupled harmonic oscillator problem with two proper frequencies.

In this naive picture, if the coupling is ignored, two sets of independent solutions are found as vibrational modes. This is what happens in the present case (without harmonic assumption) when one-dimensional calculations are performed separately for radial and quadrupole vibrations around the HFB minimum (in Figs. 7.5 and 7.7 light-blue and orange curves respectively). In this case, none of the modes originating from the first (second) calculation contributes to the quadrupole (monopole) strength.

When the coupling is switched on the eigen-solutions of the problem are modified such that the new eigen-states are linear combinations of the original uncoupled solutions. One can understand that such a process is indeed at play in two-dimensional GCM results displayed in Fig. 7.7. The coupled calculation is not the straightforward combination of the independent radial and quadrupolar vibrations, rather a linear combination of those.

Not all states are equally affected by the coupling. The low-lying quadrupole response in Fig. 7.7, for instance, is basically unchanged, since these radial vibration states lie at energies far from the radial eigen-frequency. The monopole and quadrupole resonances, instead, are modified by their mutual coupling. The main consequences are (i) a slight modification of their frequencies and (ii) the appearance of a secondary peak in the monopole spectrum. This latter aspect is the manifestation of the monopole component of the coupled state (which is a linear combination of the purely radial and quadrupole phonons). The quadrupole counterpart at the energy of the GMR is hindered with respect to the monopole case, such that no prominent quadrupole resonance is observed at the GMR energy [165].

The explicit AMP before the variational solution of the HWG equation introduces an additional coupling to rotational states of the intrinsically-deformed ground state. This aspect was discussed in Sec. 5.2.1. AMP projects each (coupled) intrinsic state onto one $J = 0$ component and one $J = \lambda$ component retaining the memory of their common intrinsic vibrational structure. Rotational-coupling effects are expected to be more prominent at low energy, i.e. close to the energy of rotational states. Slight differences, however, are still observed in the GRs region, since the GQR and its monopole counterpart lie at close but not identical energies, which can be understood in terms of different coupling effects to rotations.

The observation of GMR-GQR coupling in a symmetry-conserving theory is an unprecedented result of

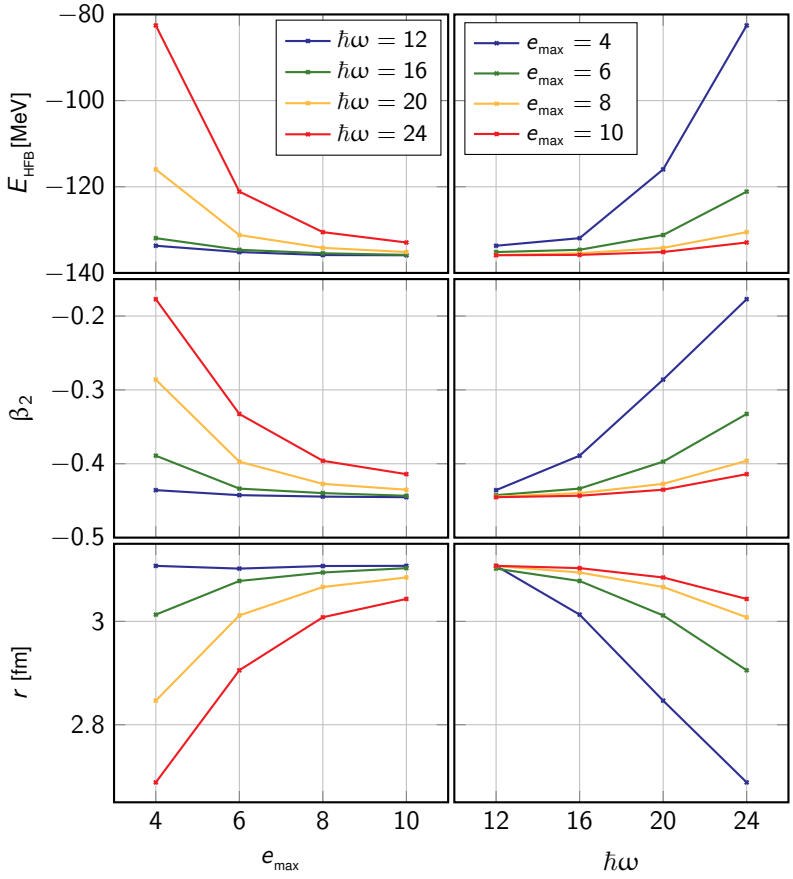

Figure 7.11: Total energy E_{HFB}, axial deformation β_2 and root mean square radius r of the oblate HFB minimum in ^{28}Si (left) as a function of e_{max} for different values of $\hbar\omega$ and (right) as a function of $\hbar\omega$ for different values of e_{max}.

this work: no other symmetry-conserving method is able to fully take into account the effects of projection on giant resonances (for intrinsically deformed systems). The very notion of coupling, and the way it emerges here, should not be taken for obvious. One may imagine that such effect is a feature linked to the concept of deformation in the intrinsic reference frame, and that the projection of the first GMR peak on $J = 0$ may erase it due to its quadrupolar nature. This will be shown not to be the case in Chap. 8, where an extensive discussion is given about the effects of projection on different levels in GCM calculations.

7.3 Shape coexistence in ^{28}Si

Results for the oblate-shape nucleus ^{28}Si are now presented. In this nucleus, a prolate-shape isomer has been both predicted theoretically [166] and observed experimentally [167, 168]. Contrary to QRPA, the PGCM can fully take into account shape-coexistence and shape-mixing effects, and predictions of the monopole resonance for such a case are displayed here for the first time.

Having studied the convergence of the HFB ground-state energy, axial deformation and radius with respect to the model space parameters (see Fig. 7.11), the optimal numerical parameters $\hbar\omega = 12$ MeV and $e_{max} = 10$ are employed.

Figure 7.12 displays the total HFB energy surface in the (r, β_2) plane. Two distinct minima are observed, the first being associated to the oblate ground state of the system ($\beta_2 \approx -0.45$) and the second producing a

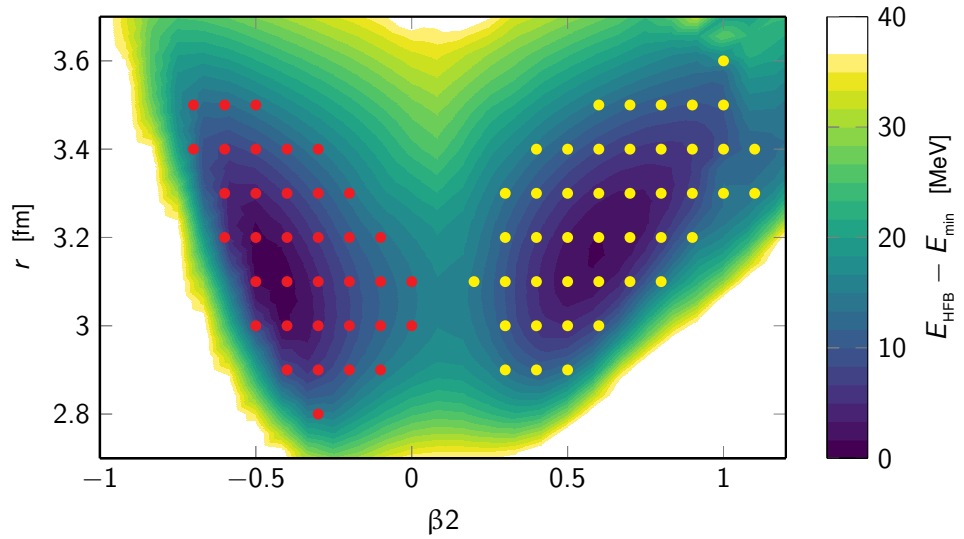

Figure 7.12: HFB total energy surface for ^{28}Si in the (β_2, r) plane. The red (yellow) dots correspond to the oblate (prolate) configurations included in the PGCM ansatz.

prolate-shape isomer ($\beta_2 \approx 0.55$) differing from the ground state by less than 1 MeV. Given the clear separation of the two minima, three distinct PGCM calculations are performed: one only including oblate points, one only including prolate points and a third one including both oblate and prolate HFB configurations. A colour code is adopted in this section: blue is associated to the results of the full two-dimensional PGCM, whereas red (yellow) refers to the PGCM calculation restricted to oblate (prolate) configurations.

7.3.1 Ground-state response

The monopole and quadrupole responses relative to the ground state are displayed in Fig. 7.13 (left). A giant monopole resonance is identified at ∼18 MeV, accompanied by isolated minor peaks both at lower and higher energies. The main GMR peak is slightly more fragmented in the full calculation, due to the larger employed Hilbert space than when restricting it to oblate configurations. In general, though, results of the two calculations are very similar, showing that the two wells are fully decoupled as far as the description of the GMR is concerned.

As for the quadrupole response, two well separated peaks are associated to the first two peaks in the monopole response. Some strength at 25 - 35 MeV is present in both calculations, with a greater fragmentation in the full calculation.

For completeness the ground-state rotational band is displayed in Fig. 7.14 (left), which is very similar in the two calculations.

7.3.2 Shape-isomer response

Calculations including the sole prolate configurations or the full set of HFB states were performed to calculate the transition built on the first excited 0^+ state (corresponding to the prolate-shape isomer) rather than on the oblate ground state.

The rotational band on top of the prolate-shape isomer is provided in Fig. 7.14 (right). A global picture of rotational bands built both on the ground and prolate-isomer states is given in Fig. 7.15, where a comparison to experimental data is also offered. Data relative to the direct decay from the 2^+ to the supposed isomeric 0^+ are absent, and two very close 2^+ states were observed (which explains the splitting of the strength). The rotational spectrum relative to the ground state is, in this calculation, less compressed than the experimental

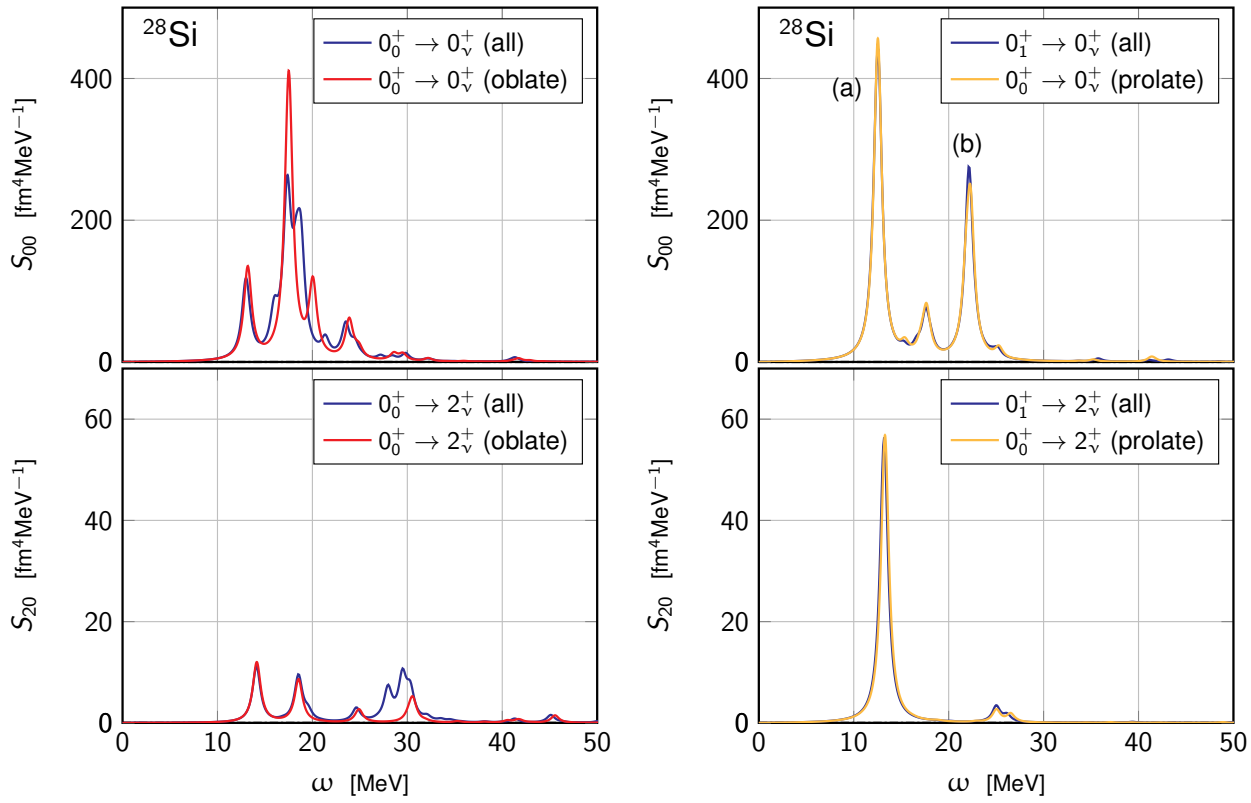

Figure 7.13: **Left**: Monopole (top panel) and quadrupole (bottom panel) response relative to the oblate ground state of ^{28}Si. The red plot is referred to the PGCM calculation including only the oblate configurations, whereas the blue plot is the result of the full calculation including both oblate and prolate configurations. **Right**: Monopole (top panel) and quadrupole (bottom panel) response relative to the prolate-shape isomer. The yellow plot is referred to the PGCM calculation including only the prolate configurations (whose ground state corresponds to the prolate isomer by construction), whereas the blue plot is the result of the full calculation, where the transitions are evaluated with respect to the first excited 0^+ state, corresponding to the prolate-shape isomer.

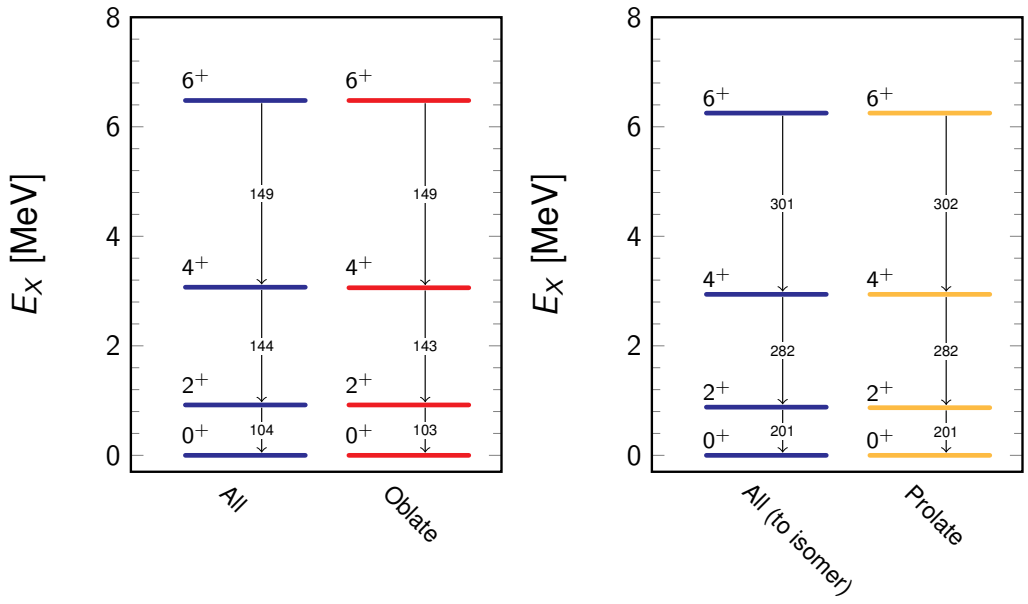

Figure 7.14: **Left**: ^{28}Si ground-state rotational band from PGCM calculations. **Right**: ^{28}Si prolate isomer rotational band from PGCM calculations. The same colour code of Fig. 7.13 is adopted.

results, whereas the opposite situation emerges for the prolate-shape isomer. The main difference, however, is linked to the determination of the energy associated to the isomeric state itself, which differs by ~ 6 MeV between theory and experiment.

Monopole and quadrupole responses are shown in Fig. 7.13 (right). The overlap of the spectra obtained from the two calculations is striking. The monopole response displays a typical structure with two well-separated main peaks. The quadrupole response is concentrated approximately at the same energy of the first peak of the monopole response. If compared to the oblate-GS response, the quadrupole spectrum built on the prolate-shape isomer displays a much larger strength, and consequently the coupling to the monopole response is highly enhanced, as clearly visible from the prominence of the 0^+ peak at ~12.2 MeV.

7.3.3 Discussion

The nature of the different resonances and the coupling between quadrupole and monopole resonance in deformed systems are now addressed via the use of the collective PGCM wave-functions and transition probabilities between 2^+ and 0^+ states. Labels are referred to Fig. 7.13.

The GMR based on the oblate ground state is the manifestation, as previously showed for ^{46}Ti, of a breathing mode, i.e. a radial vibration around the ground-state configuration. This is visible comparing the radial node in the PGCM collective wave-function of the GMR in Fig. 7.16 (middle left) with the wave-function of the ground state (top left). The GMR peak (b), whose wave-function in displayed in Fig. 7.16 (middle right) is a breathing mode built on the prolate-shape isomer (top centre).

The lower-energy monopole peak (a) at ~12.2 MeV reflects a vibration along both the β_2 and radial coordinates, which is visible in Fig. 7.16 (middle centre). The wave-function of the corresponding 2^+ peak, namely the GQR, is also shown for comparison (bottom centre). The two wave-functions are basically one, supporting the interpretation discussed in Sec. 7.2.3 that the lower-energy GMR peak and the GQR originate from the same intrinsic vibrational state. The exact degeneracy is lifted by the projection on different values of J, i.e. the excitation energy is ~12.6 MeV for the 0^+ and ~13.2 MeV for the 2^+).

The prolate-shape isomer in ^{28}Si is an excellent case to corroborate the interpretation of this coupling

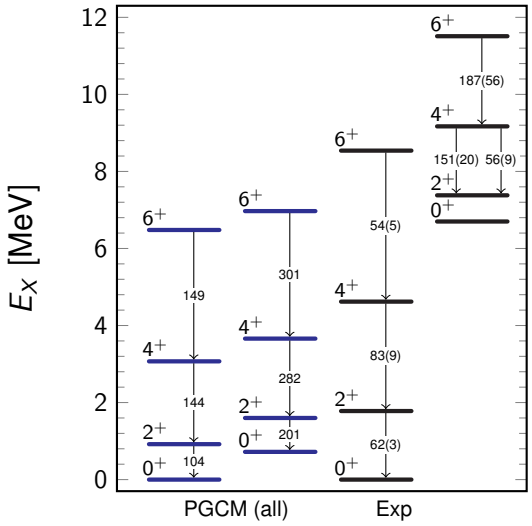

Figure 7.15: ^{28}Si rotational bands both for the ground state and for the prolate-shape isomer. Experimental data from [168].

due to the magnitude of the quadrupolar strength and to the clean separation of the monopole peaks. Eventually $B(E2)$ transition probabilities between all 2^+ and 0^+ states are also provided in Fig. 7.17. A large coupling links the GQR and the lower-energy peak of the GMR built on the prolate-shape isomer. The corresponding transition amplitude $|\langle 0^+_{\text{GQR}}|Q_{20}|2^+_{\text{GQR}}\rangle|^2 = 1408$ fm^{4}MeV^{-1} shall be compared to the quadrupole moment $|\langle 2^+_{\text{GQR}}|Q_{20}|2^+_{\text{GQR}}\rangle|^2 = 2229$ fm^{4}MeV^{-1}.

7.3.4 Comparison to experiment

The monopole response of the oblate ground state from the previously discussed PGCM calculations is eventually compared to recent experimental data. Both calculations including only oblate or both oblate and prolate configurations are displayed in Fig. 7.18 at comparison with data from Refs. [169, 170, 171]. Notice that numerical results are multiplied by a factor 0.5. The PGCM strength is smeared via a Lorentzian function of width $\Gamma = 0.5$ MeV. This width has been chosen to allow a better readability of discrete states and to simulate the finite bin width of experimental data. Continuum coupling effects may be relevant in the lowering of the discrete strength, but they are not taken into account in this model. Let us mention, however, that experimental data also carry elements of incertitude in the evaluation of the normalising constant, such that the difference with respect to theoretical values should be further investigated.

Overall the results of this work are in good agreement with the experimental data. The positioning of the main GMR peak is accurately reproduced with respect to all data sets. The structure at ∼13 MeV, associated to the GQR coupling, is also reproduced, especially for the positioning of the resonance, which is in agreement with the experimental data.

The lower-energy fragmentation, which is testified by the three sets of data, even if not in a univocal way, fails to be described by the PGCM calculation. It was suggested [168] that such states could be considered as potential band-heads for super-deformed bands.

Eventually, the high-energy part of the spectrum is also qualitatively reproduced, with the exception of the data from Ref. [170] (left plot), which displays a systematically greater strength for all the points at energy higher than the GMR, such that these data are not in agreement with the other two sets.

A quantitative comparison of moments and associated weighted averages is left to Chap. 10.

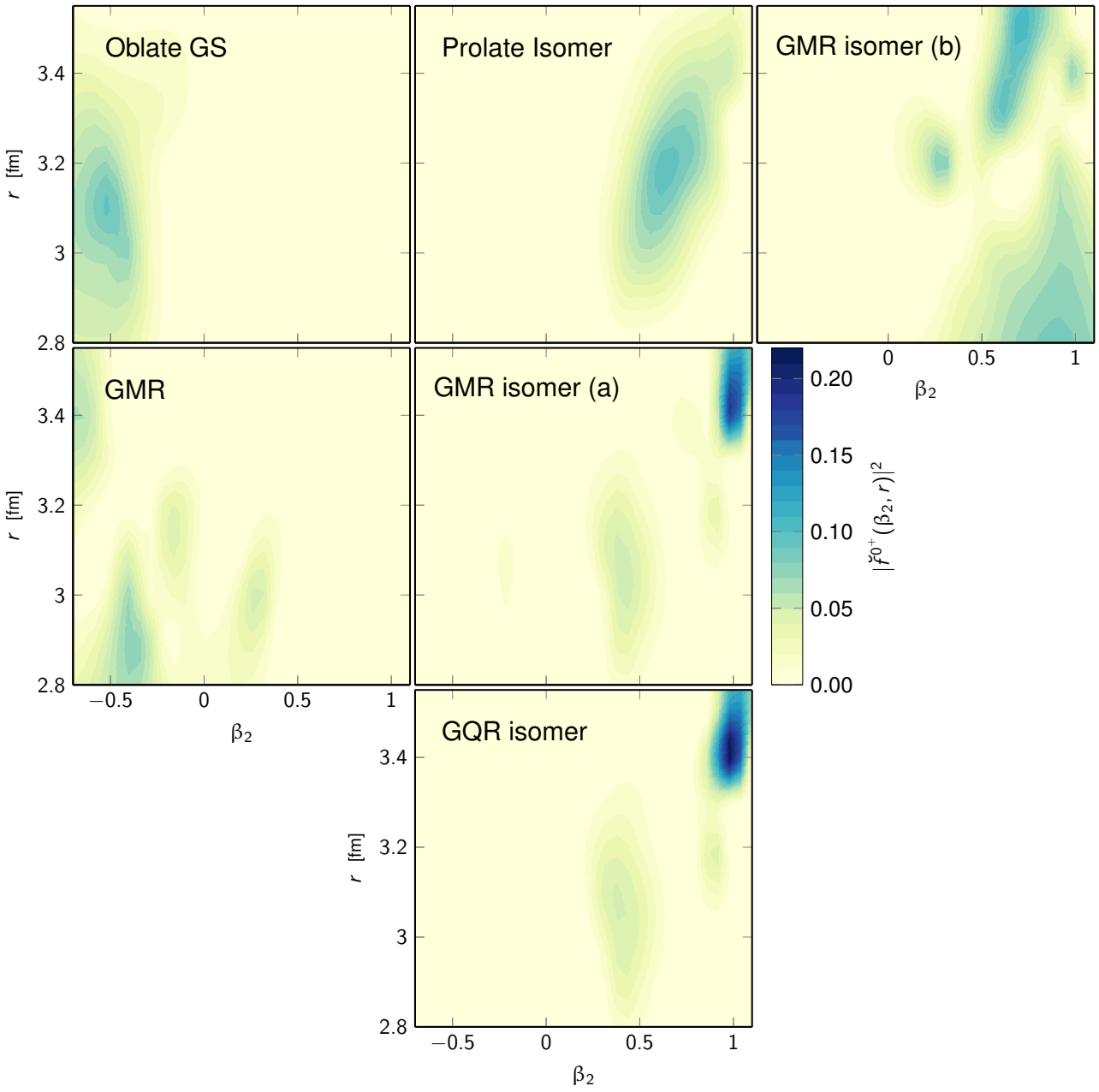

Figure 7.16: Intrinsic collective PGCM wave-functions in the (r, β_2) plane of some specific states of interest (labels are referred to Fig. 7.13), specifically: 0^+ oblate ground state (top left); 0^+ GMR on the oblate ground state (middle left); 0^+ prolate-shape isomer (top center); 0^+ peak (a) on the prolate-shape isomer (middle center) coupled to: 2^+ GQR prolate-shape isomer (bottom center); 0^+ GMR (b) on the prolate-shape isomer (middle right).

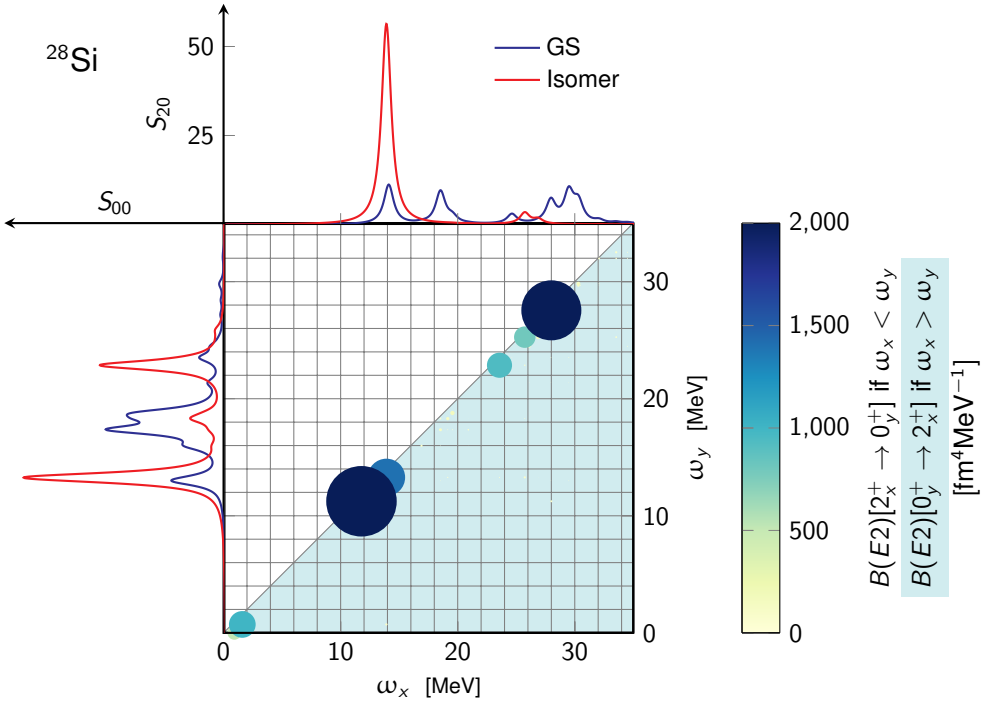

Figure 7.17: Inter-state transitions between all the 0^+ and 2^+ states issued from the two-dimensional PGCM calculation. The dots are located at the intersection of the energies between 0^+ (vertical axis) and 2^+ (horizontal axis) states. The monopole (quadrupole) response of the ground state is also shown for comparison on the vertical (horizontal) axis, in order to provide a clearer picture of possible coupling between different resonant channels. The transition amplitude is also rescaled so to refer to upwards transitions (excitations); the size of the dots is proportional to the magnitude of the transition (same information provided by the colourbar).

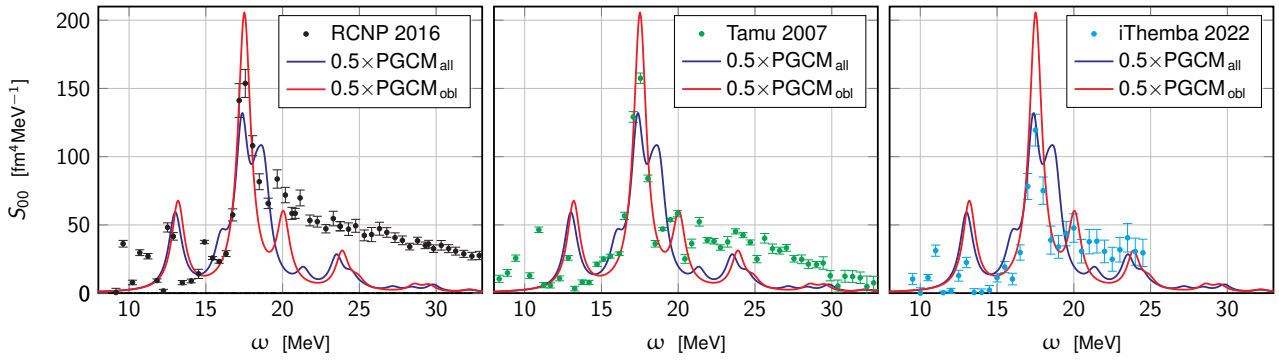

Figure 7.18: Comparison of experimental monopole response from Refs. [170, 169, 171] (left, centre and right respectively). Both the PGCM calculations including the oblate and all the configurations are shown. Theoretical results are multiplied by a 0.5 factor.

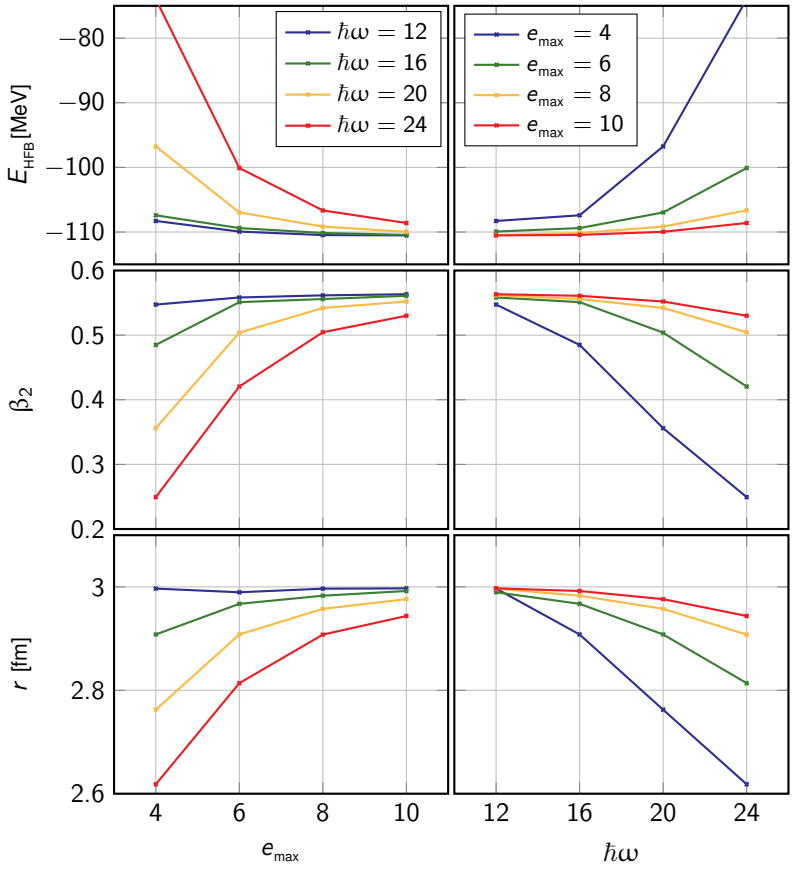

Figure 7.19: Total energy E_{HFB}, axial deformation β_2 and root mean square radius r in ^{24}Mg (left) as a function of e_{max} for different values of $\hbar\omega$ and (right) as a function of $\hbar\omega$ for different values of e_{max}.

7.4 Highly fragmented response in ^{24}Mg

In the previous sections several physical aspects rising from PGCM calculations for GMR in deformed systems were discussed. A particular attention was dedicated to GMR-GQR coupling effects in ^{46}Ti and ^{28}Si. However, some systems may display a more complex response, whose structure cannot be easily explained in terms of well-defined coupling effects between different multipolarities in the intrinsic state. This is the case, for instance, of ^{24}Mg, which is addressed in the present section.

7.4.1 PGCM results

The HFB energy, deformation and rms radius are displayed in Fig. 7.19 for different model space parameters. The optimal parameter $\hbar\omega$=12 MeV allows a fast convergence with respect to the dimensions of the model space. Calculations are thus performed for e_{max} =10.

The total HFB energy surface in the (β_2, r) plane is showed in Fig. 7.20. A well-defined minimum in the prolate region is found, accompanied by a secondary minimum in the oblate sector ∼7 MeV above the HFB ground state. The HFB vacua included in the PGCM ansatz are represented by red dots, both prolate and oblate configurations within an excitation energy window of 15 MeV were employed.

The rotational band on top of the prolate-shape ground state is provided in Fig. 7.21, showing a good agreement with experimental data.

The monopole and quadrupole responses issued from the PGCM calculation are displayed in Fig. 7.22.

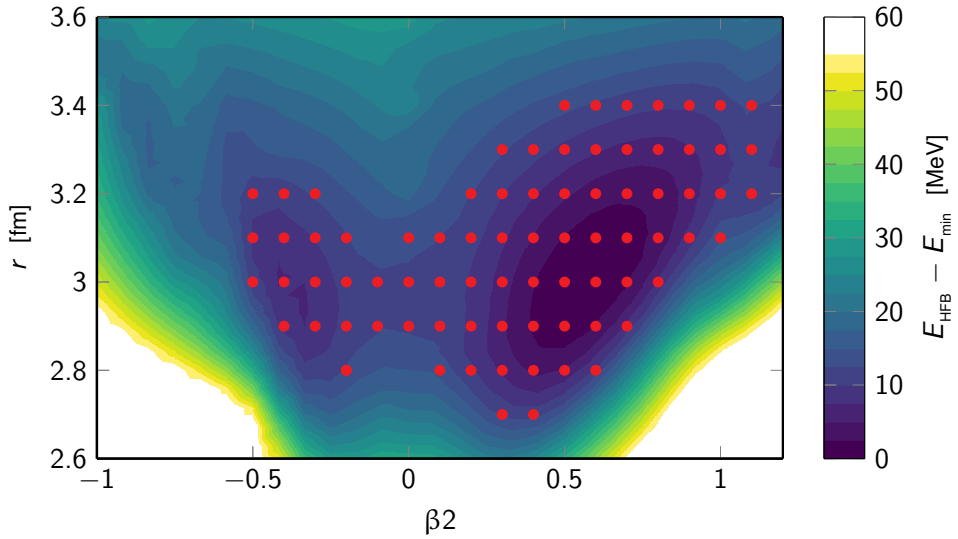

Figure 7.20: HFB total energy surface for ^{24}Mg in the (β_2, r) plane at N3LO with $e_{max} = 10$ and $\hbar\omega$ =12 MeV. The red dots correspond to the configurations included in the PGCM ansatz.

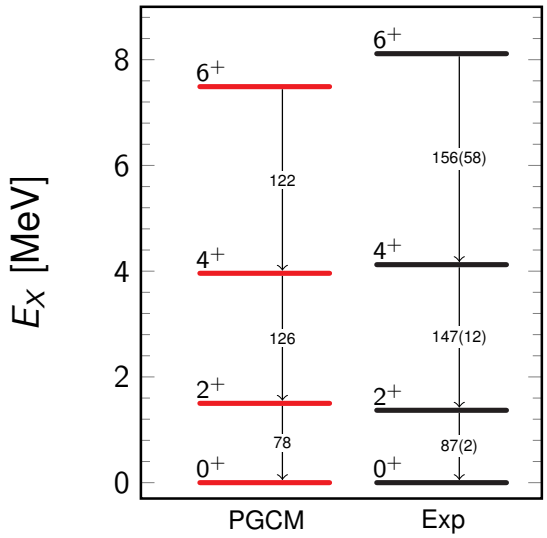

Figure 7.21: ^{24}Mg ground-state rotational bands from PGCM calculations compared to experimental data [172].

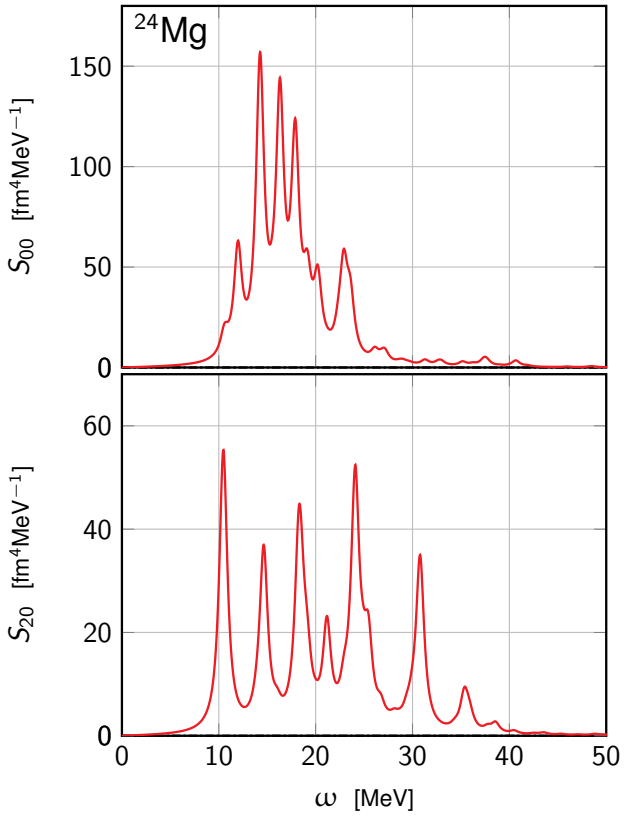

Figure 7.22: Monopole (top) and quadrupole (bottom) response of ^{24}Mg.

Differently from previously discussed cases, both responses are extremely fragmented, so that no easy correspondence between the two spectra can be found. In previous examples the coupled monopole response could be decomposed in a pure dominant breathing mode and a lower-energy state originating from the coupling with the GQR, accompanied by minor structures. Here, many states appear carrying a relatively similar strength, so that the identification of a dominant mode is more difficult.

$B(E2)$ transition probabilities between all 2^+ and 0^+ states are presented in Fig. 7.23 in order to help identifying specific couplings between resonant states. The picture is not decisive in this respect. Except for the large coupling between the two resonant structures at ∼14.5 MeV in the monopole and quadrupole responses, no other significant strength between major structures is present (the strong signal at ∼9 MeV being associated to a rotation on the oblate-shape isomer).

One must notice that the numerical stability of the response has been tested with respect to the linear independence of the norm eigenvalues, so that the great fragmentation is not associated to any numerical problem. The convergence with respect to the set of selected HFB points has not been tested, such that one may expect the fine positioning or the height of the peaks in the monopole response to be susceptible to slight changes. However, the highly fragmented nature of the monopole response in ^{24}Mg can be considered to be an actual feature of this system. This statement is supported in the following section by the comparison to experimental data.

7.4.2 Comparison to experiment

The PGCM monopole response is compared to different sets of experimental data [173, 174, 175, 176, 177] in Fig. 7.24. A smearing of Γ =0.5 MeV is employed to produce the theoretical results. Given the very fragmented nature of the PGCM results for ^{24}Mg, a larger value of Γ results into a single very broad

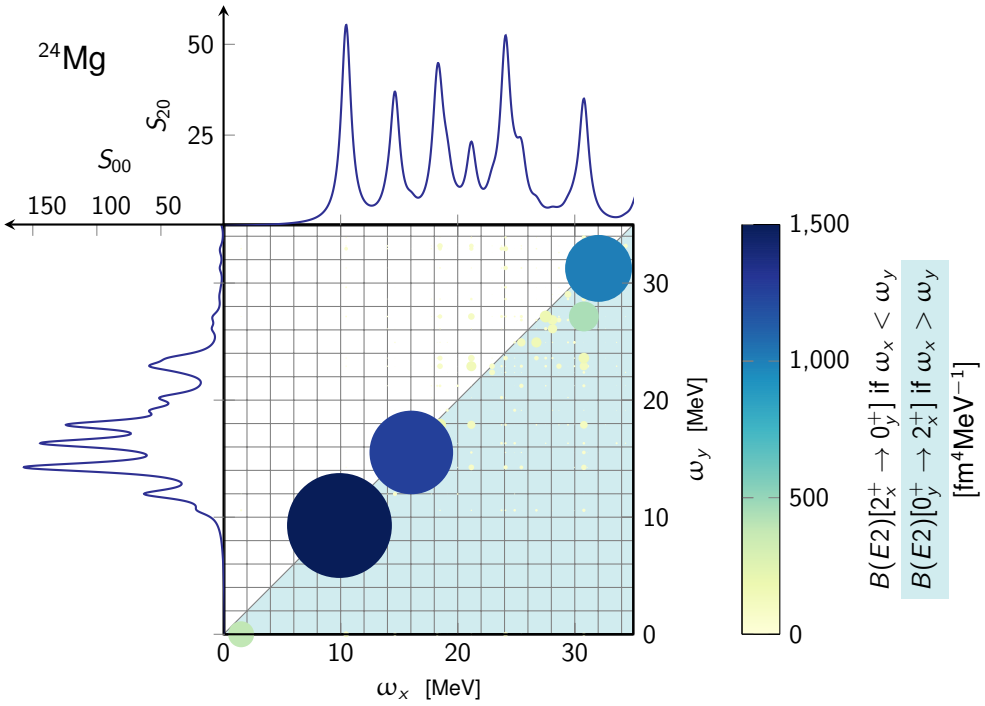

Figure 7.23: Inter-state transitions between all the 0^+ and 2^+ states issued from the two-dimensional PGCM calculation. The dots are located at the intersection of the energies between 0^+ (vertical axis) and 2^+ (horizontal axis) states. The monopole (quadrupole) response of the ground state is also shown for comparison on the vertical (horizontal) axis, in order to provide a clearer picture of possible coupling between different resonant channels. The transition amplitude is also rescaled so to refer to upwards transitions (excitations); the size of the dots is proportional to the magnitude of the transition (same information provided by the colourbar).

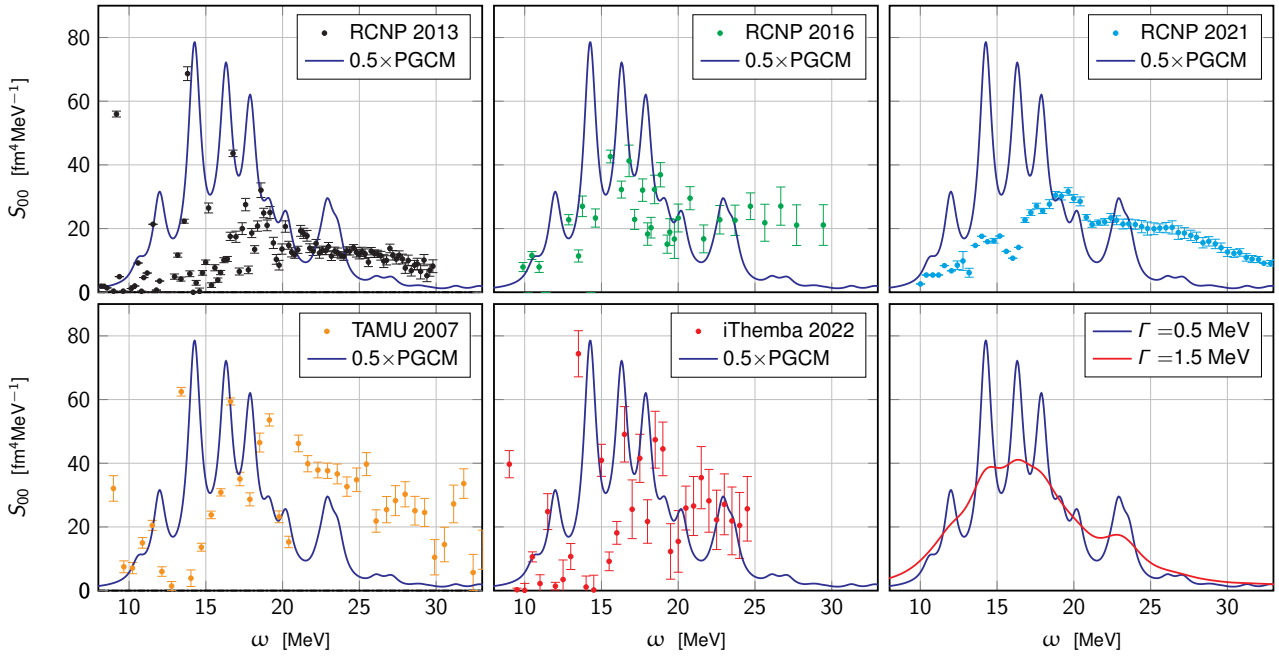

Figure 7.24: Comparison of the PGCM monopole response with experimental data from Refs. [175] (top left), [173, 174] (top centre), [176] (top right), [177] (bottom left) and [171] (bottom centre). When compared to experimental data, PGCM results are convoluted with a Lorentzian function of width Γ =0.5 MeV. Two different values of the smearing parameter Γ are also shown (bottom right). Theoretical results are multiplied by a 0.5 factor.

response as also shown in Fig. 7.24 (bottom right). The same considerations about the 0.5 multiplicative factor from Sec. 7.3.4 also apply here.

One must first observe that the experimental monopole responses from different references are, at best, in weak agreement between each other. In some cases they could also be referred to as incompatible. This is true not only when comparing results from different facilities, but also when successive campaigns from the same infrastructure (RCNP) are juxtaposed.

However, in all cases (except for Ref. [176], Fig. 7.24 top right), all data agree in finding a highly fragmented monopole response in ^{24}Mg, which results in sudden jumps of the strength in a small energy interval. This feature then naturally reflects in a high uncertainty linked to the extraction of monopole response from double-differential cross section (which is the only available observable not subject to strong model dependence), whose data analysis invokes many theoretical assumptions and approximations. An essential overview about the observables relation to the response function is given in Sec. 4.5.

Chapter 8

Angular Momentum Projection in GCM

Contents

The effects of angular momentum projection are here addressed in detail. GCM calculations without angular momentum projection are performed using numerical parameters identical to those used for the PGCM calculations reported in Chap. 7.

Starting from GCM calculations, intermediate steps of angular momentum projection are considered, following the possibilities envisaged in Sec. 5.7. A parallel procedure was developed for the PAV method in the EDF-RPA calculations whose results are discussed in Chap. 12. A fully symmetry-conserving (Q)RPA [148] realisation has not been implemented yet.

Referring to Sec. 5.7, the different flavours of projection compared in this chapter are now summarised for clarity. Particle-number projection is included by default, such that only the impact of angular-momentum projection is addressed. The acronyms are hereafter listed and explained

- **GCM**: no angular momentum projection at all, spectrum follows Eq. (5.25).
- $\mathbf{a}_\omega$: (Eq. (5.92)) overlap between the excited GCM state at energy ω and the rotational state.
- **sub GCM**: GCM with explicit subtraction of the rotational contribution, see Eq. (5.96).
- **PAV GCM**: symmetry-breaking GCM solutions projected *a posteriori* on good J's (Eq. (5.32)).
- **sub PAV GCM**: PAV GCM but with subtraction of rotational contribution (Eq. (5.100)).
- **VAP GCM**: full PGCM with projection included before solving the HWG equation (Eq. (5.31)).

All these quantities are compared in the next sections for several nuclei. The significant coupling to the rotational state in PAV GCM calculations is discussed first. Once this contribution has been explicitly removed, subtracted PAV GCM spectra are displayed.

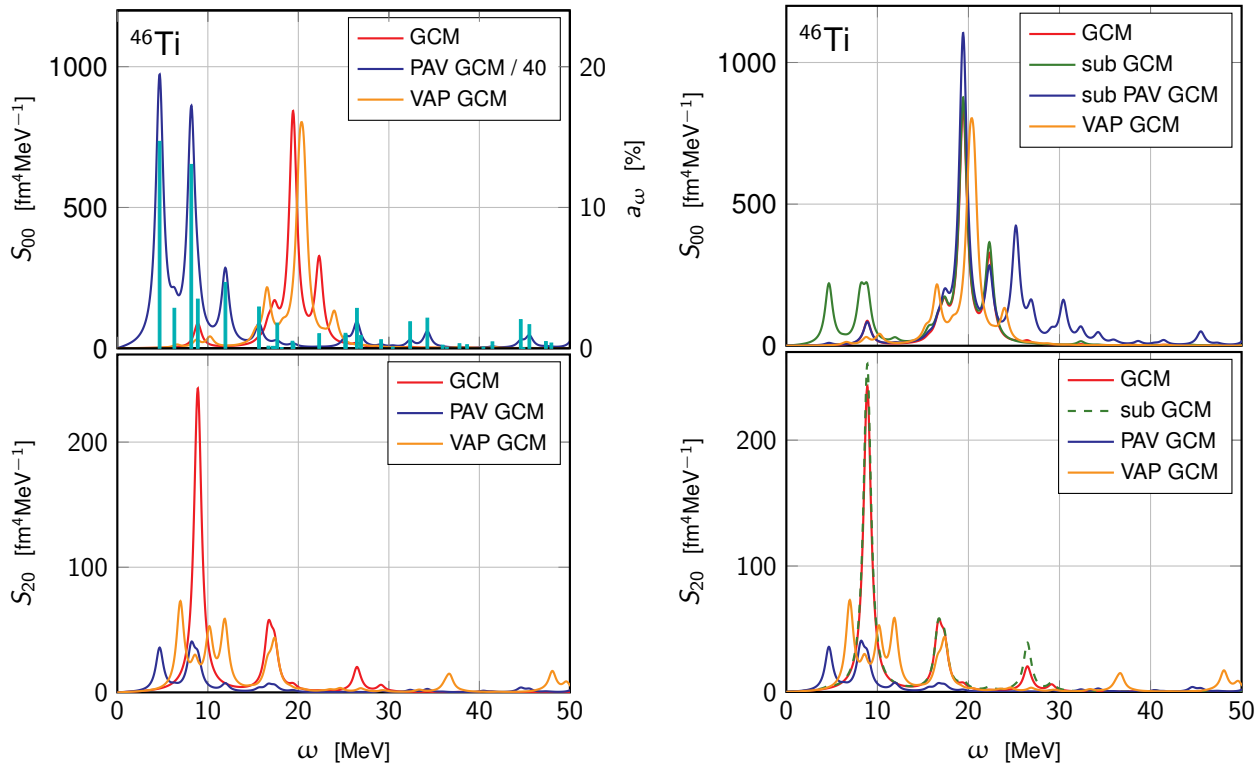

Figure 8.1: **Left**: monopole (top) and quadrupole (bottom) responses for GCM, PAV GCM and VAP GCM calculations in ^{46}Ti. For the monopole response, the overlap between GCM states and the rotational state is also plotted, the corresponding scale being shown on the right y-axis. **Right**: monopole (top) and quadrupole (bottom) responses for (sub) GCM, (sub) PAV GCM and VAP GCM calculations.

8.1 ^{46}Ti

Results for ^{46}Ti are first addressed; see Sec. 7.2 for details about the calculation parameters and for the selected HFB vacua included in the (P)GCM ansatz. The differently projected GCM spectra are compared in Fig. 8.1.

A significant overlap between excited GCM states and the rotational state is observed, reaching ∼15% for some low-energy states. Many higher-energy states are also affected on a few percent level.

The PAV GCM monopole response is significantly affected by the rotational content, i.e. a large monopole strength appears in regions (notice the factor 1/40 for the PAV GCM response) in direct correspondence to the states that couple the most to the rotational state although no associated GCM strength was originally present. The GCM monopole response is thus highly sensitive to this spurious behaviour when eventually rotated.

When the rotational content is explicitly removed from GCM states following the prescription given in Eq. (5.93) the picture radically changes. This can be appreciated in the right panel of Fig. 8.1. While the subtracted GCM spectrum is close to the original GCM one, the same becomes true for the subtracted PAV GCM spectrum. Eventually, differences are only observed in the low-energy sector (for the subtracted GCM) and above 25 MeV (for the subtracted PAV GCM spectrum).

This pathological behaviour is not observed in the quadrupole response, where the PAV GCM response is more similar to the VAP GCM counterpart in the low-energy sector. The GQR at ∼17 MeV is also greatly diminished.

Also based on examples provided in the next sections, GCM, subtracted GCM and subtracted PAV

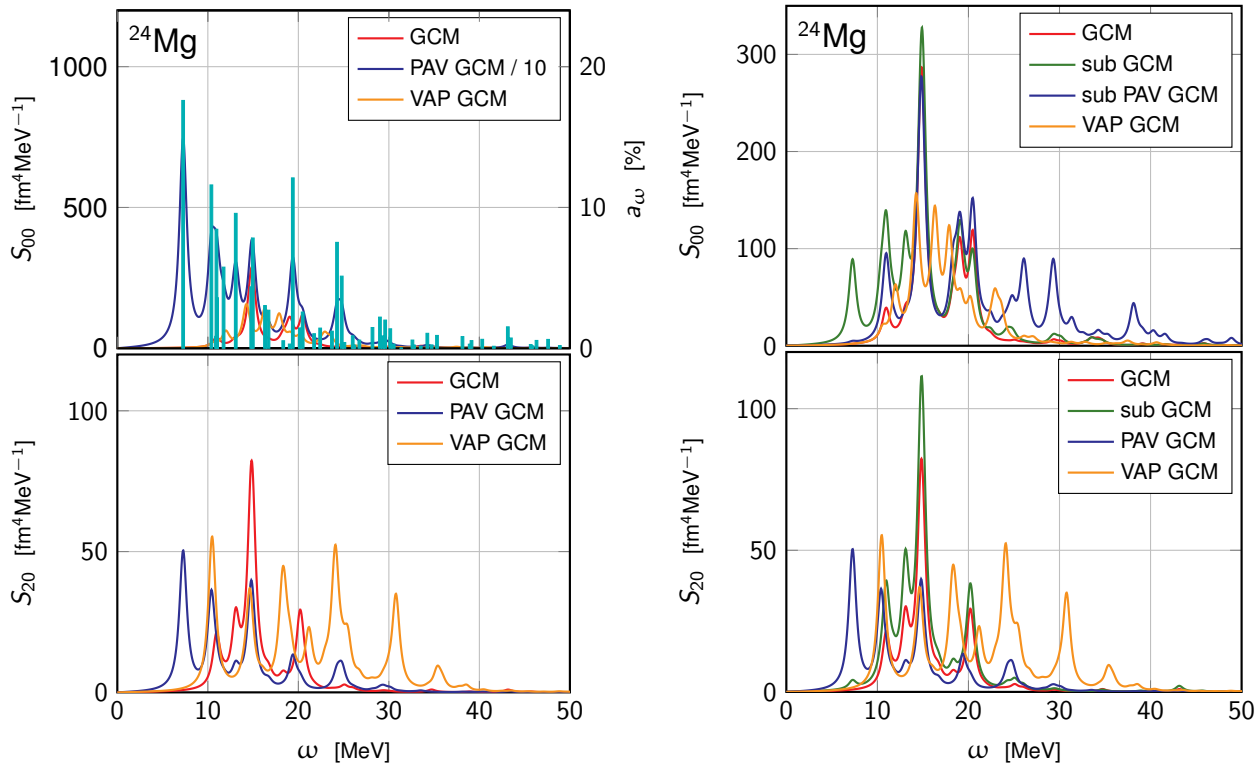

Figure 8.2: **Left**: monopole (top) and quadrupole (bottom) responses for GCM, PAV GCM and VAP GCM calculations in ^{24}Mg. For the monopole response, the overlap between GCM states and the rotational state is also plotted, the corresponding scale being shown on the right y-axis. **Right**: monopole (top) and quadrupole (bottom) responses for (sub) GCM, (sub) PAV GCM and VAP GCM calculations.

GCM can be said to provide very similar monopole responses, i.e. once the rotational coupling is removed the monopole spectrum is weakly affected by projection.

8.2 ^{24}Mg

The same analysis is now proposed for ^{24}Mg. Details of the (P)GCM results are found in Sec. 7.4. Again, GCM states are strongly coupled to the rotational state, as shown in Fig. 8.2 (left). Such a coupling engenders a strong enhancement in the PAV GCM monopole response (notice the 1/10 factor).

Once the rotational coupling has been explicitly removed, the subtracted monopole spectra, both with and without projection, are close to the original GCM spectrum. This can be observed in Fig. 8.2. Differences above 25 MeV are observed like in ^{46}Ti. Compared to GCM and subtracted PAV GCM spectra, the VAP GCM monopole response is significantly more fragmented. This is an unexpected and non-trivial effect of AMP, which is interpreted in terms of the larger (monopole) Hilbert subspace accessible to VAP GCM calculations.

The quadrupole response is interestingly modified. The subtracted GCM spectrum is very similar to the original GCM response. However, once projection is considered (PAV GCM), the response is closer to the PGCM case (VAP GCM). Indeed, the GCM quadrupole spectrum is strongly modified. Three main peaks appear, which are akin to the VAP GCM (PGCM) peaks below 20 MeV but shifted towards lower energies by ∼4 MeV. The remarkable energy shift is postulated to be linked to the non-variational nature of the projection in PAV GCM, which fails, consequently, at correctly reproducing the 2^+ states energies. The

same effect is also observed in ^{28}Si (see Sec. 8.3).

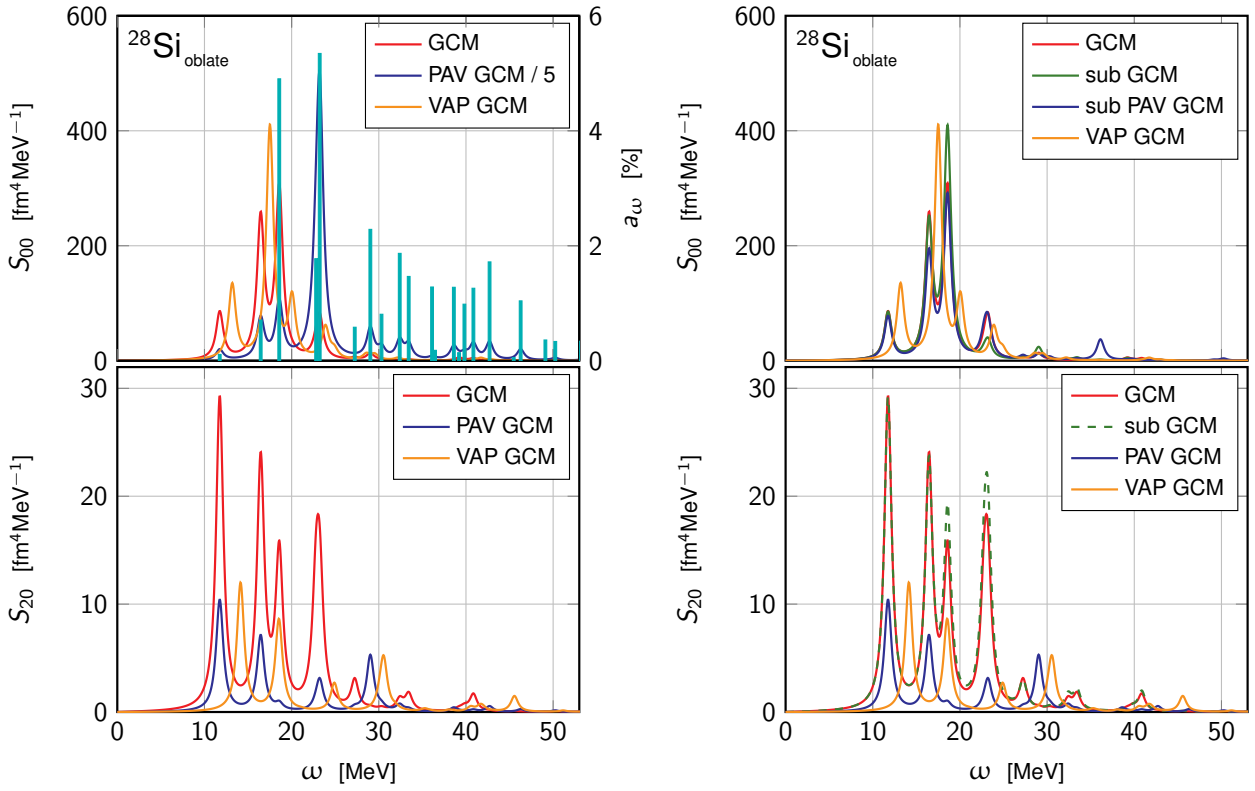

Figure 8.3: **Left**: monopole (top) and quadrupole (bottom) responses for GCM, PAV GCM and VAP GCM calculations for the oblate ground state of ^{28}Si. For the monopole response, the overlap between GCM states and the rotational state is also plotted, the corresponding scale being shown on the right y-axis. **Right**: monopole (top) and quadrupole (bottom) responses for (sub) GCM, (sub) PAV GCM and VAP GCM calculations.

Indeed, when angular momentum projection is performed before diagonalising the reduced Hamiltonian, ground- and excited-states energies explicitly take into account the configuration mixing associated with the rotational motion. As shown in Tab. 9.1, the ground state typically gain ∼5 MeV correlation energy from AMP in strongly deformed systems. Projection affects excited states in a similar but not identical way, such that the combined effect for ground- and excited-states is at the origin of the shift between PAV and VAP GCM spectra.

Eventually, the absence of relevant structures above 20 MeV in the PAV GCM quadrupole response also questions the trustfulness of high-energy resonances in VAP GCM (PGCM) calculations in the same region. Such statement is also supported by the deviating behaviour of VAP GCM (PGCM) quadrupole moments observed in Sec. 10.5.

8.3 ^{28}Si

The main observations reported in previous sections are here corroborated by the particularly clear situation encountered in ^{28}Si. Results relative to both the oblate ground state and to the prolate-shape isomer are respectively displayed in Fig. 8.3 and 8.4. Calculations were detailed in Sec. 7.3.

In the two cases GCM states are less coupled to the rotational states than in previous examples (notice the a_ω scale on the right axis of the left panels in Figs. 8.3 and 8.4). Thus, the repercussions of the

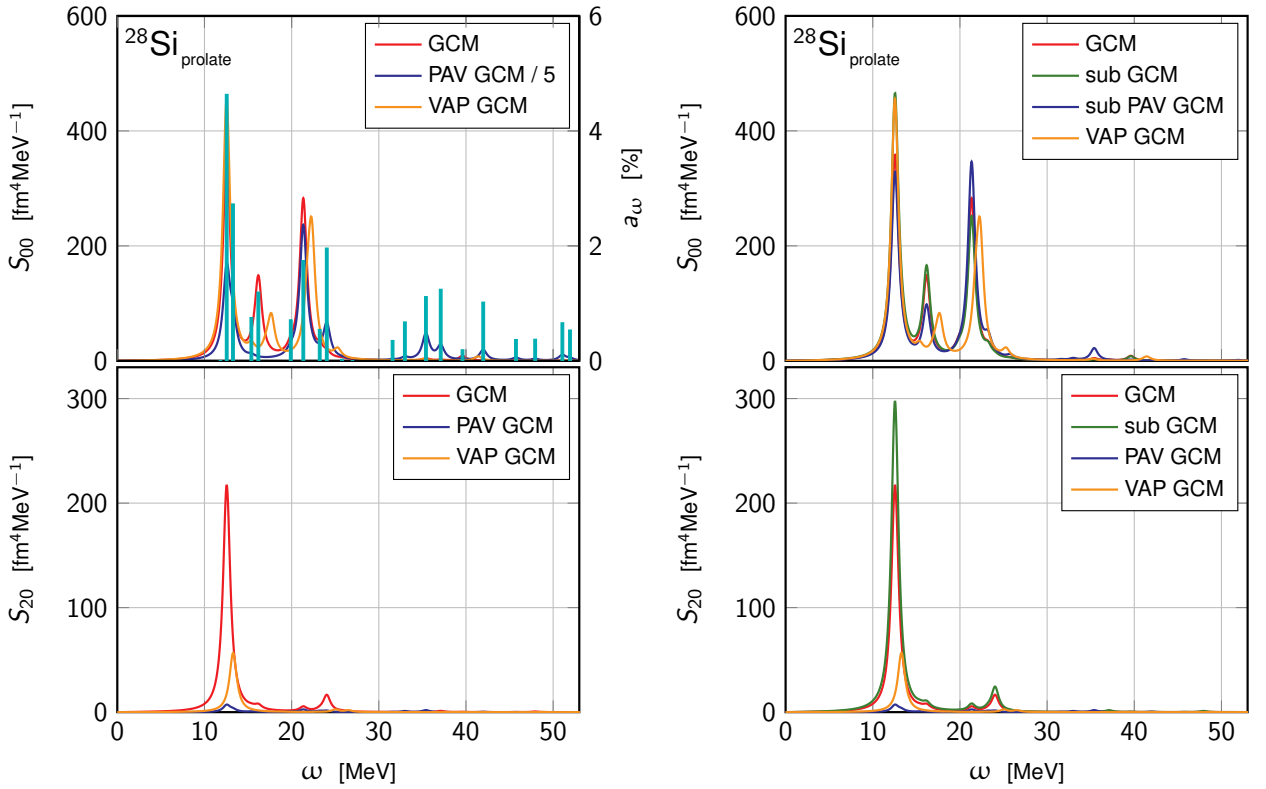

Figure 8.4: **Left**: monopole (top) and quadrupole (bottom) responses for GCM, PAV GCM and VAP GCM calculations for the prolate-shape isomer of ^{28}Si. For the monopole response, the overlap between GCM states and the rotational state is also plotted, the corresponding scale being shown on the right y-axis. **Right**: monopole (top) and quadrupole (bottom) responses for (sub) GCM, (sub) PAV GCM and VAP GCM calculations.

rotational coupling are less pronounced in the PAV GCM monopole response of ^{28}Si than in ^{46}Ti and ^{24}Mg (still, a factor 1/5 is introduced to allow for a comparison with GCM and PGCM spectra). Eventually, once the subtraction of the rotational contribution has been performed, the monopole projected spectra are extremely close to the original GCM response.

Projection effects on the quadrupole response can also be clearly interpreted. The oblate ground state quadrupole response of ^{28}Si is represented in Fig. 8.3 (bottom panels). Results support the interpretation already offered for ^{24}Mg: the quadrupole GCM response is entirely modified by the action of projection, PAV GCM basically corresponding to the VAP GCM (PGCM) spectrum up to an energy shift. The PAV and VAP GCM quadrupole spectra are essentially one same spectrum shifted by ∼2-3 MeV. The origin of the shift was already explained for ^{24}Mg in the previous section.

Projection effects on the quadrupole response of the prolate-shape isomer are exhibited in Fig. 8.4. The GCM response appears over-estimated with respect to symmetry-conserving VAP GCM calculations. After projection, the GQR is strongly attenuated in the PAV GCM response.

8.4 Summary

It has been shown that different levels of symmetry breaking and restoration provide novel insights in the understanding of general physical properties of many-body methods, which represents an original finding of this work. In this respect, the *intermediate* PAV GCM projection should not be judged as an actual method

of interest for realistic calculations, but as a tool to connect GCM and PGCM results. In principle the same philosophy can be extrapolated to other many-body methods. A concrete example concerning EDF-RPA is discussed in Chap. 12.

The main findings of the present chapter are summarised hereafter

- Without an appropriate treatment of rotations, which can only be achieved with proper VAP GCM (PGCM) calculations, GCM states incorporate a coupling to rotational states.
- GCM states are, thus, an admixture of vibrational and (unphysical) rotational states.
- Projection on $J = 0$ is strictly equivalent to a pure rotation. Thus, PAV GCM monopole spectra bring the rotational content of GCM states out. The excitation operator now probes both the vibrational and (spurious) rotational content of intrinsically deformed GCM states.
- Projection on $J = 2$ naturally embodies a selection rule which prevents the spurious rotational state to infect PAV GCM quadrupole spectra (the rotational state being by definition projected on $J = 0$).
- Quadrupole strengths are over-reproduced by GCM and projection on $J = 2$ is necessary for realistic evaluations.

None of the previous statements is constrained to specific properties of GCM, such that similar outcomes are to be expected in any symmetry-breaking formalism whenever symmetry restoration is considered.

Finally, it is deduced that a solid simultaneous treatment of vibrations and rotations can only be achieved by VAP methods, i.e. projection onto good angular momenta (but the same is true for any rotation) must be performed before diagonalising the reduced Hamiltonian in the Hilbert subspace of interest.

Chapter 9

Comparison to QFAM

Contents

In this chapter, previously discussed (P)GCM calculations for monopole and quadrupole responses are compared to QRPA calculations. Ab initio QRPA calculations are here performed via the *Finite Amplitude Method* (FAM) [60]. The FAM has been developed in recent years within an EDF setting, first addressing closed-shell systems [178]. It was later generalised to open-shell systems via the generalisation to the quasi-particles realm [179], producing the so-called *Quasiparticle Finite Amplitude Method* (QFAM). The (Q)FAM approach is strictly equivalent to the traditional (Q)RPA.

An *ab initio* realisation of QFAM was recently achieved [60] for axially- and triaxially-deformed systems. While the code can access any multipolarity of choice, it is here exploited for monopole and quadrupole response calculations only.

The comparison between QRPA and (P)GCM calculation provides useful benchmarks, keeping in mind that QRPA and (P)GCM are not expected to provide the same results. It was previously proven (see Chap. 3) that QRPA represents the harmonic approximation of GCM. At the same time, however, QRPA explores the complete manifold of Bogoliubov states allowed by the symmetry restrictions of the specific implementation, such that the accessible phase space is systematically probed. The compromise between the harmonic approximation and the systematic exploration of the generator coordinates space is here investigated via the explicit comparison between QRPA and (P)GCM. Effects of angular-momentum projection are also addressed in comparing GCM and PGCM calculations.

9.1 Ground-state properties

Results presented in Chaps. 7 and 8 from PGCM and GCM calculations respectively, are compared to QFAM calculations in a consistent setting. QFAM calculations were performed using the N3LO interaction [6] in a model space with $e_{\max} = 10$ and $\hbar\omega = 12$ MeV. Properties of the HFB minima chosen as ground states for QFAM calculations are listed in Tab. 9.1 and compared to (P)GCM results.

	E_{GS} [MeV]			r [fm]			β_2	
	HFB	GCM	PGCM	HFB	GCM	PGCM	HFB	GCM
^{16}O	-79.55	-79.68	-79.92	2.580	2.581	2.583	0.00	0.00
^{46}Ti	-237.30	-237.64	-240.69	3.474	3.474	3.483	0.27	0.26
^{24}Mg	-110.52	-111.16	-116.03	2.997	3.006	3.011	0.56	0.57
^{28}Si	-135.89	-136.11	-140.95	3.107	3.109	3.116	-0.45	-0.45
^{28}Si$_{\mathrm{iso}}$	-134.41	-135.05	-140.23	3.168	3.179	3.199	0.60	0.61

Table 9.1: Total energy, rms radius and quadrupole deformation β_2 of the HFB minima employed in QFAM calculations. The same quantities for the relative (P)GCM solutions are also reported for comparison. Results for the prolate-shape isomer of ^{28}Si are also reported.

	a_2 [MeV fm^{-2}]	a_3 [MeV fm^{-3}]	a_4 [MeV fm^{-4}]	a_2/A [MeV fm^{-2}]	a_3/A [MeV fm^{-3}]	a_4/A [MeV fm^{-4}]
^{16}O	98.91	-141.37	90.10	6.18	-8.84	5.63
^{46}Ti	265.44	-248.26	100.20	5.77	-5.40	2.18
^{24}Mg	154.18	-212.12	102.23	6.42	-8.84	4.26
^{28}Si	178.09	-231.77	116.75	6.36	-8.28	4.17
^{28}Si$_{\mathrm{iso}}$	197.10	-278.76	155.20	7.04	-9.96	5.54

Table 9.2: Fitting parameters relative to the functions plotted in Fig. 9.1. The function from Eq. (9.1) with $k = 4$ was used. Values of the fitting parameters divided by the mass number are also reported.

Ground-state energies are not significantly lowered by the configuration mixing included in the GCM, i.e. by typically less than 1 MeV. Projection allows instead to gain up to an additional ∼6 MeV in doubly open-shell nuclei. Radii are essentially not affected by beyond-mean-field corrections, which makes an accurate reproduction at the HFB level a crucial aspect even for more involved calculations. The quadrupole deformation β_2 is also stable going from HFB to GCM. PGCM results are not displayed since PGCM ground states have a good angular momentum $J = 0$ by definition.

9.2 Evaluation of anharmonic effects

In order to comment on anharmonic effects in the following sections, a quantitative analysis of beyond-quadratic corrections is now proposed. One-dimensional energy surfaces for fixed $\beta_2 = \beta_{2\,\mathrm{min}}$ and $r = r_{\mathrm{min}}$ are considered for the investigated nuclei. The class of polynomials

$$f_k(x) \equiv \sum_{l=2}^{k} a_l x^l \tag{9.1}$$

is employed to fit the dependence of the energy surface with respect to the variable of interest. Polynomials of fourth order are found to accurately describe the observed radial behaviour, which is shown in Fig. 9.1, while the convergence is more involved for the β_2 dependence, given its less regular behaviour, as shown in Fig. 9.2. The quadratic, cubic and quartic fitting functions are also displayed for comparison. The fitting parameters relative to Figs. 9.1 and 9.2 are reported in Tabs. 9.2 and 9.3 respectively.

Once the harmonic fitting parameter has been determined, the eigen-frequency $\hbar\omega$ of the associated quantum harmonic oscillator problem can be evaluated. The extracted numerical values are tabulated in Tab. 9.4 for radial vibrations, where the GMR energy from QFAM calculations are also anticipated. The

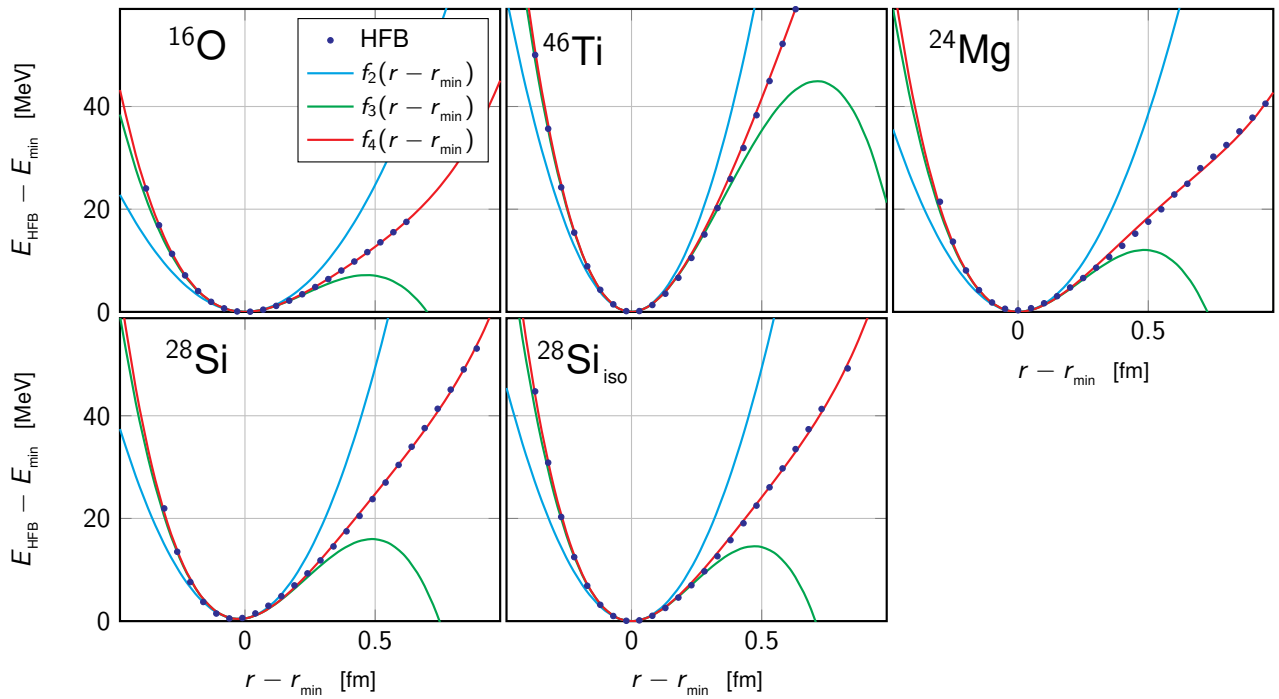

Figure 9.1: One-dimensional total HFB energy surface for fixed $\beta_2 = \beta_{2\,min}$. Polynomial fits (see Eq. (9.1)) are also reported for different values of k. The fitting parameters are reported in Tab. 9.2.

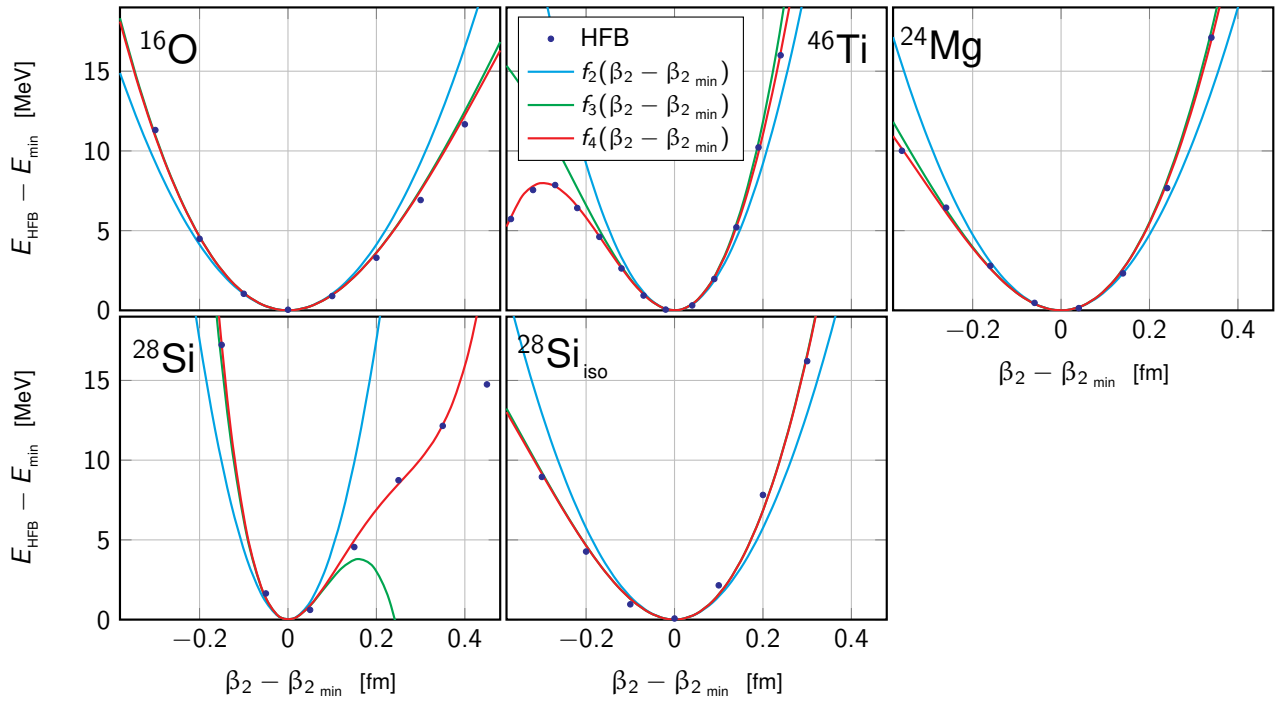

Figure 9.2: One-dimensional total HFB energy surface for fixed $r = r_{min}$. Polynomial fits (see Eq. (9.1)) are also reported for different values of k. The fitting parameters are reported in Tab. 9.3.

	a_2 [MeV fm^{-2}]	a_3 [MeV fm^{-3}]	a_4 [MeV fm^{-4}]	a_2/A [MeV fm^{-2}]	a_3/A [MeV fm^{-3}]	a_4/A [MeV fm^{-4}]
^{16}O	103.11	-62.61	-9.98	6.44	-3.91	-0.62
^{46}Ti	230.03	325.70	-483.85	5.00	7.08	-10.52
^{24}Mg	118.72	96.94	-42.88	4.95	4.04	-1.79
^{28}Si	401.94	-1338.51	1365.91	14.36	-47.80	48.78
^{28}Si$_{\text{iso}}$	143.71	136.87	-10.64	5.13	4.89	-0.38

Table 9.3: Fitting parameters relative to the functions plotted in Fig. 9.2. The function from Eq. (9.1) with $k = 4$ was used. Values of the fitting parameters divided by the mass number are also reported.

	a_2 [MeV fm^{-2}]	$\hbar\omega$ [MeV]	$E^{\text{GMR}}_{\text{QFAM}}$ [MeV]	ΔE_{sph} [MeV]	$\lvert\beta_2\rvert$
^{16}O	98.91	22.62	22.70	-0.08	0.00
^{46}Ti	265.44	21.85	19.80	2.05	0.27
^{24}Mg	154.18	23.06	17.10	5.96	0.56
^{28}Si	178.09	22.94	17.90	5.04	0.45
^{28}Si$_{\text{iso}}$	197.10	24.14	17.30	6.84	0.60

Table 9.4: Eigen-frequencies extrapolated from the harmonic approximation to one-dimensional energy surfaces at fixed $\beta_2 = \beta_{2\,\text{min}}$ from Fig. 9.1. The GMR energy from QFAM calculations are also reported for comparison.

energy difference

$$\Delta E_{\text{sph}} \equiv \hbar\omega - E^{\text{GMR}}_{\text{QFAM}} \tag{9.2}$$

is evaluated to quantify departures from the harmonic limit.

A quantitative agreement between this crude approximation and QFAM calculations is only observed for ^{16}O. Indeed, when extracting the eigen-frequencies of the problem from one-dimensional energy surfaces, the monopole resonance is implicitly assumed to be decoupled from other oscillating modes. This hypothesis is well verified for spherical systems, like ^{16}O. However, when deformed systems are addressed, the quadrupole resonance couples to the GMR, so that a coupled anisotropic harmonic oscillator should be considered instead. The difference from the uncoupled (spherical) case is proportional to the deformation of the system [165]. Such a trend is indeed exhibited in Fig. 9.3 (left panel).

Overall, a fully quantitative statement about anharmonicities can only be made in spherical systems. In deformed systems the coupling to quadrupole resonances does not allow to properly qualify anharmonic effects via this simple model. However, the magnitude of the fitting coefficients beyond the quadratic order represents also an indicator. The ratio of the cubic and quartic coefficients with respect to the harmonic coefficient is plotted in Fig. 9.3 (right panel) as a function of the mass number of the system for the radial dependence.

Both cubic and quartic coefficients are relatively more important for lighter systems, and they decrease with increasing mass numbers. In this respect, ^{16}O is the *least harmonic* nucleus, whereas ^{46}Ti is the *most harmonic* one. This is coherent with the Pauli principle violation (which is implicit in the Quasi Boson Approximation determining the harmonic approximation, see Sec. 3.4 for details) being less severe for more collective states and, thus, in heavier systems [89]. Globally, deviations between QFAM and GCM are expected, thus, to be more prominent in lighter nuclei.

Given the magnitude of the anharmonic coefficients in Tab. 9.2 (which are relatively as important as the harmonic coefficient), a perturbative analysis of beyond-quadratic corrections may not be satisfactory due

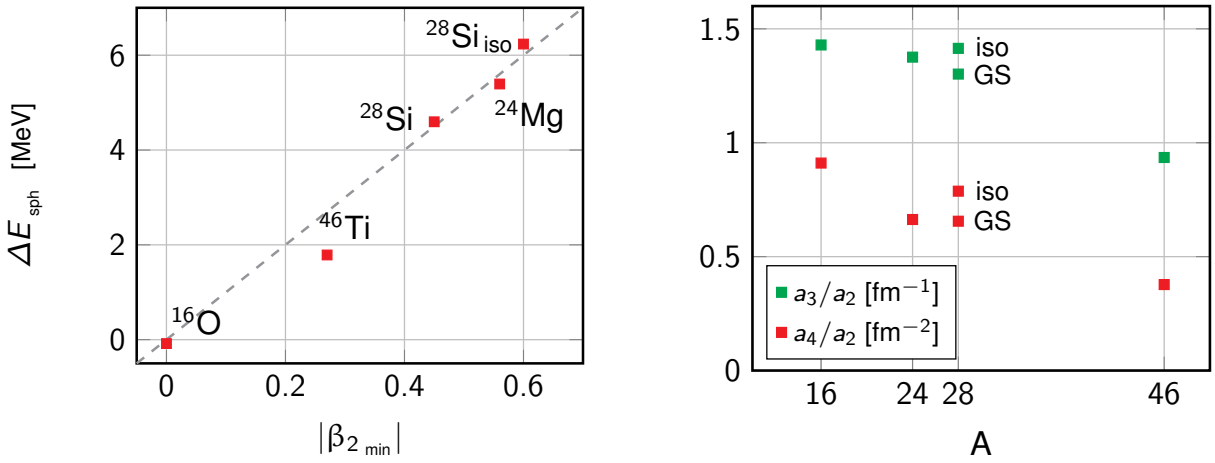

Figure 9.3: **Left**: Effects of deformation on the GMR positioning in QFAM. **Right**: beyond-quadratic fitting parameters as a function of the mass number.

	$\hbar\omega$	$E_0^{(2,3)}$	$E_0^{(1,4)}$	$E_0^{(2,4)}$	$E_1^{(2,3)}$	$E_1^{(1,4)}$	$E_1^{(2,4)}$	$\hbar\omega^{(1+2)}$
^{16}O	22.618	-1.816	0.883	-0.161	-11.720	4.416	-1.265	15.143
^{46}Ti	21.851	-0.270	0.127	-0.003	-1.746	0.637	-0.027	20.862
^{24}Mg	23.056	-1.122	0.429	-0.037	-7.240	2.143	-0.292	18.397
^{28}Si	22.941	-0.860	0.363	-0.027	-5.553	1.816	-0.211	19.518
^{28}Si$_{iso}$	24.135	-1.016	0.436	-0.037	-6.558	2.182	-0.289	20.086

Table 9.5: First- and second-order perturbative corrections to the harmonic-oscillator (r) eigen-energies for the ground state and the first excited state (resonance) associated to the fitting parameters from Tab. 9.2. All values are expressed in MeV units. See Appendix K for details on labels.

to the nature of the problem. Analytical corrections to the eigen-energies are given in App. K up to second order in perturbation theory. Still, numerical values for the first- and second-order perturbative corrections to the ground-state and the first-excited-state (resonance) energies are given in Tabs. 9.5 and 9.6 for the one-dimensional $\beta_2 = \beta_{2\,\text{min}}$ (radial vibrations) and $r = r_{\,\text{min}}$ (deformation vibrations) surfaces respectively.

As proven in App. K first-order cubic corrections $E_n^{(1,3)}$ vanish identically, hence they are not displayed. Second-order cubic corrections $E_n^{(2,3)}$ are more relevant in light systems, which is symptomatic of important anharmonic effects. Possibly third-order corrections may be necessary in order to converge the perturbative series. Quartic corrections are less important for all observed cases, and a clear convergent trend is visible when going from first ($E_n^{(1,4)}$) to second order ($E_n^{(2,4)}$), except for β_2 vibrations in ^{28}Si (which is imputed to bad numerical properties of the fitting parameters). In general, comparing Tabs. 9.5 and 9.6 (see, for instance, ^{16}O and ^{46}Ti) one observes that for a given system the perturbative correction (and thus the anharmonicity degree) can be more or less pronounced depending on the considered generator coordinate.

A full understanding of the energy shift provided by anharmonic effects would require a coupled analysis of r and β_2. However, the uncoupled evaluation of perturbative corrections to the harmonic picture already provides a qualitative indicator to explain possible differences between QFAM and GCM calculations.

	$\hbar\omega$	$E_0^{(2,3)}$	$E_0^{(1,4)}$	$E_0^{(2,4)}$	$E_1^{(2,3)}$	$E_1^{(1,4)}$	$E_1^{(2,4)}$	$\hbar\omega^{(1+2)}$
^{16}O	23.092	-0.328	-0.094	-0.002	-2.115	-0.469	-0.014	20.917
^{46}Ti	20.342	-0.620	-0.709	-0.115	-4.001	-3.547	-0.907	13.332
^{24}Mg	20.232	-0.395	-0.233	-0.013	-2.550	-1.167	-0.099	17.057
^{28}Si	34.465	-5.633	1.883	-0.480	-36.357	9.415	-3.772	7.981
^{28}Si $_{\text{iso}}$	20.608	-0.461	-0.041	0.000	-2.974	-0.205	-0.003	17.928

Table 9.6: First- and second-order perturbative corrections to the harmonic-oscillator (β_2) eigenenergies for the ground state and the first excited state (resonance) associated to the fitting parameters from Tab. 9.3. All values are expressed in MeV units. See Appendix K for details on labels.

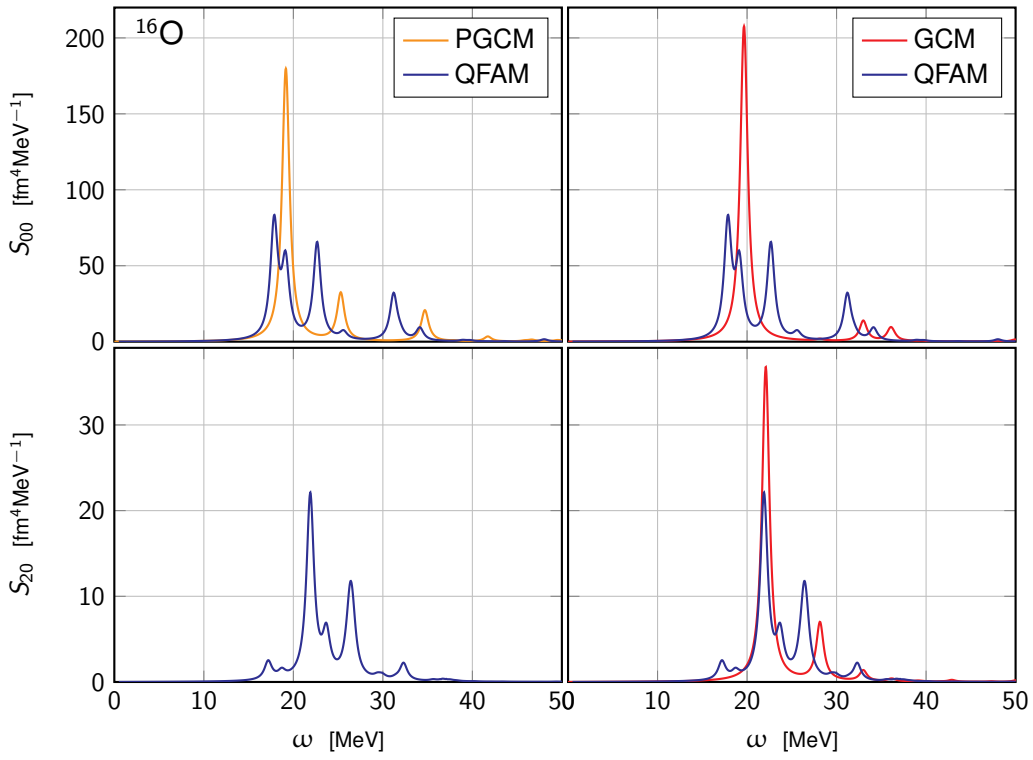

Figure 9.4: Monopole (top) and quadrupole (bottom) response in ^{16}O for QFAM calculations compared to PGCM (left) and GCM (right) calculations.

9.3 ^{16}O

Results relative to the spherical system ^{16}O were addressed in Sec. 7.1. QFAM results were shown to be easily interpreted in terms of an harmonic approximation of the exact (r, β_2) energy surface. Several smearing parameters were also tested to verify the compatibility between PGCM and QFAM results.

Here, GCM results without explicit projection on angular momentum are also compared to QFAM calculations. Monopole and quadrupole responses of QFAM and (P)GCM calculations are displayed in Fig. 9.4.

The monopole response is first addressed. QFAM displays a rather fragmented monopole spectrum, which is not observed for (P)GCM calculations. Such a fragmentation cannot be the outcome of anharmonic effects in (r, β_2), which are not allowed for in QRPA calculations and which would be explicitly captured by (P)GCM calculations. The different modes must be, thus, associated to vibrations along collective coordinates that are not explicitly considered in the presently used (P)GCM ansatz, i.e. different from r and β_2. Given ^{16}O spherical nature the peak most naturally associated with the GMR is the one at 22.7 MeV, since it corresponds to a pure one-dimensional harmonic oscillator model along the r coordinate.

The GMR predicted by PGCM and GCM are highly similar. Their positions differ by less than ∼500 keV and the associated transition amplitudes (before convoluting them with a Lorentzian function) vary by approximately 40 fm^{4}MeV^{-1}. The projected spectrum is slightly more fragmented than the original GCM one. This effect is traced back to projected calculations having access to a larger Hilbert space than pure GCM calculations.

The main effect of anharmonicities (ser Tab. 9.5) is found in the shift of the (P)GCM main peak with respect to QFAM, the latter being ∼3.0 MeV (∼3.5 MeV) higher than in (P)GCM calculations. The position of the QFAM main peak was shown to be in quantitative agreement with a simple quantum harmonic oscillator picture in Tab. 9.4 and associated text. The perturbative estimates of anharmonic corrections to the GMR energy in Tab. 9.5 predict a shift down by ∼7.5 MeV, which is overestimated but in qualitative agreement with the (P)GCM result.

As for the quadrupole response, the GQR is very similar in QFAM and GCM calculations, the main peak being positioned at ∼21.9 MeV and ∼22.0 respectively, as discussed in connection with Fig. 7.3. This is an evidence that the behavior with respect to the quadrupole deformation is better reproduced in the harmonic approximation than the radial dependence. This result demonstrates that in a given system different generator coordinates may agree to different extents with the harmonic assumption implicit in QRPA calculations, which can be inferred comparing Tabs. 9.5 and 9.6.

9.4 ^{46}Ti

QFAM results for ^{46}Ti are compared to (P)GCM calculations in Fig. 9.5. The monopole response is studied first. The three methods agree on the position of the GMR peak, which is at ∼19.8 MeV for QFAM, ∼20.4 MeV for PGCM and ∼19.4 MeV for GCM calculations. The consistent description of the GMR testifies the validity of the harmonic approximation in ^{46}Ti (with respect to the radial dependence).

The coupling to the GQR is, however, poorly reproduced by QFAM. The first peak of the QFAM monopole response at ∼18.4 MeV is clearly associated to the quadrupole peak at the same energy. Its positioning is in poor agreement with PGCM 0^+ first peak at ∼16.5 MeV, which is coupled with the 2^+ GQR state at ∼17.1 MeV. These values are to be compared to the experimental value of ∼16.8 MeV for the centroid of the fitted Gaussian from Ref. [162].

The low-energy quadrupole response is different for the three methods. The low-energy quadrupole strength arising from PGCM calculations in ^{46}Ti was already addressed in Sec. 7.2.2. The GCM quadrupole response in the 5-15 MeV region is different from its projected counterpart. One strong transition is observed at ∼9 MeV instead of many fragmented peaks. However, the associated physical content is

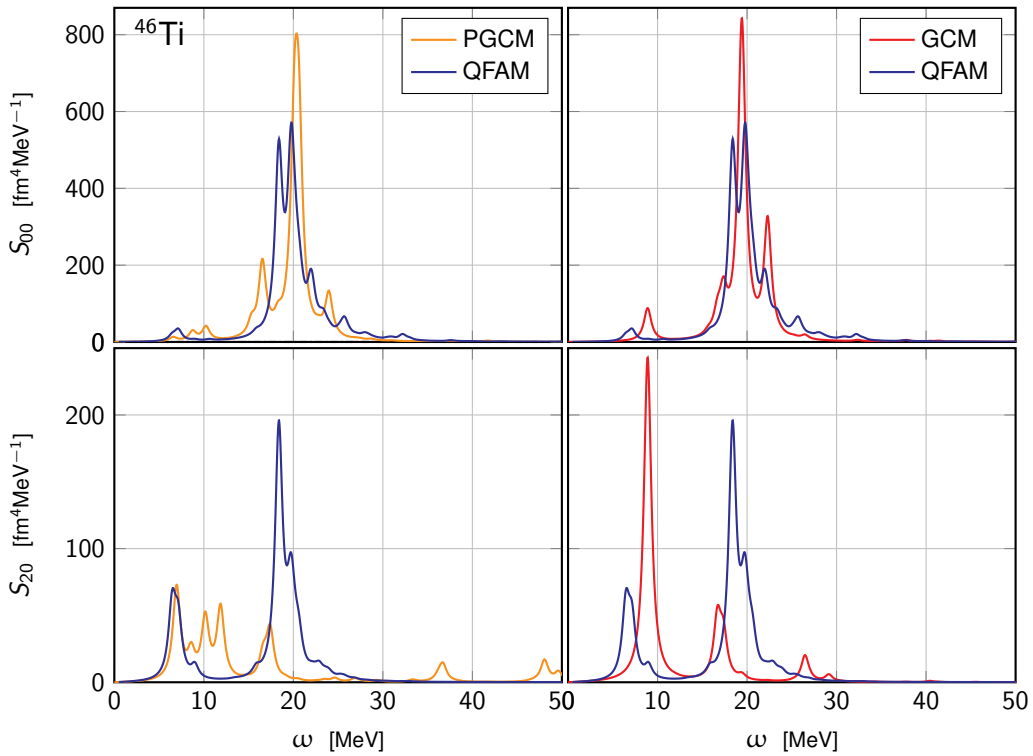

Figure 9.5: Monopole (top) and quadrupole (bottom) response in ^{46}Ti for QFAM calculations compared to PGCM (left) and GCM (right) calculations.

similar. A similar response is also observed, even if at lower energies, for the QFAM quadrupole response. The collective GCM wave-function of the 9 MeV quadrupole peak is compared to one of the 2^+ PGCM states at ~ 10 MeV in Fig. 9.6. The strong quadrupole vibration is visible in both cases.

Overall, a better agreement between (P)GCM and QFAM calculations is observed in ^{46}Ti for the monopole rather than for the quadrupole response. The GQR amplitude and the corresponding manifestation in the GMR is larger in QFAM than in (P)GCM, and the associated GMR splitting is underestimated with respect to (P)GCM calculations.

9.5 ^{24}Mg

The highly-fragmented monopole response of ^{24}Mg in PGCM calculations was discussed in Sec. 7.4. A comparison to QFAM and GCM is presently provided. The (P)GCM monopole and quadrupole responses are confronted to QFAM calculations in Fig. 9.7.

A qualitative agreement is observed comparing the GCM monopole response to QFAM. The GCM GMR peak at ~14.8 MeV is slightly lower than the QFAM peak at ~15.6 MeV. The small energy difference is postulated to be linked to anharmonic effects, which is qualitatively motivated by the analysis in Tab. 9.5, in which a strong lowering (~5 MeV) due to anharmonic perturbations is observed. Overall a two-peak structure is similarly produced by QFAM and GCM. When projection is taken into account, however, the response is drastically modified. PGCM monopole response results into a significantly more fragmented strength than in both GCM and QFAM calculations.

In this respect the effects of projection are not trivial in the well-deformed ^{24}Mg nucleus. The larger Hilbert space accessible to projected calculations is speculated to be at the origin of the higher fragmentation. Similar effects shall be expected in QRPA calculations as well, such that projected-QRPA may represent

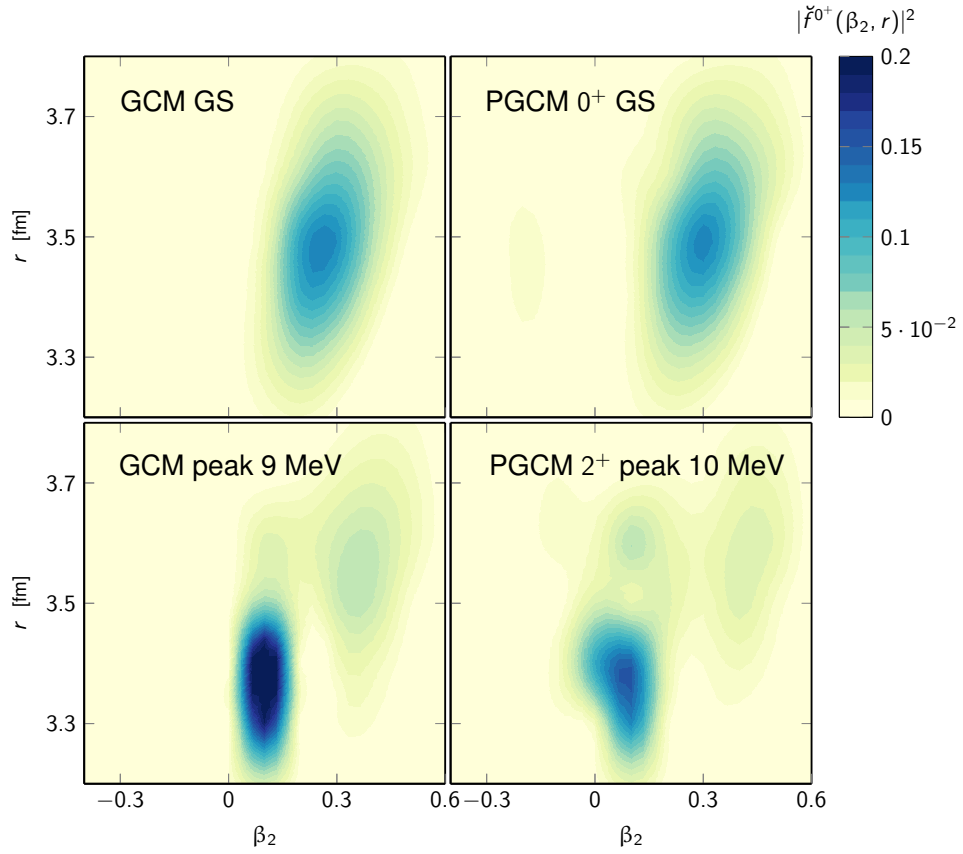

Figure 9.6: Intrinsic collective (P)GCM wave-functions for the ground state and for low-energy quadrupole transitions in ^{46}Ti.

a necessary step forward in the investigation of non-trivial systems.

The quadrupole response displays even more diverse behaviours depending on the method of choice. QFAM and GCM calculations are first compared. The reliability of GCM quadrupole response is testified by the consistency of the associated moments when computed using different evaluation methods and their coherence with respect to QFAM calculations (please refer to Chap. 10 for quantitative information). In this respect, even if QFAM should *not* be considered an exact result to aim at, the qualitative agreement between GCM and QFAM results is encouraging. QFAM and GCM quadrupole responses are not qualitatively dissimilar, but the GQR energy differs by roughly 2 MeV (14.8 MeV for GCM and 17.2 MeV for QFAM calculations). Such a difference is again imputed to anharmonic effects in ^{24}Mg, especially as far as quadrupole vibrations are concerned (see Tab. 9.6).

Based on moments evaluation (see Sec. 10.2.2) the PGCM quadrupole response cannot be considered trustworthy, such that no proper comparison to QFAM is practicable. Indeed, PGCM quadrupole moments strongly diverge from both GCM and QFAM calculations. However, following the discussion of Sec. 8.2, the PGCM quadrupole response below 20 MeV appears to be more reliable. If a qualitative comparison limited to this energy region is to be made, a very different behaviour is observed, both relative to GCM and QFAM calculations. As in the monopole case, angular momentum projection greatly affects the quadrupole response, as testified by the difference between GCM and PGCM results. There is no reason why QRPA should behave differently with respect to projection, such that the relevance to developing the projected-QRPA is confirmed for quadrupole calculations as well.

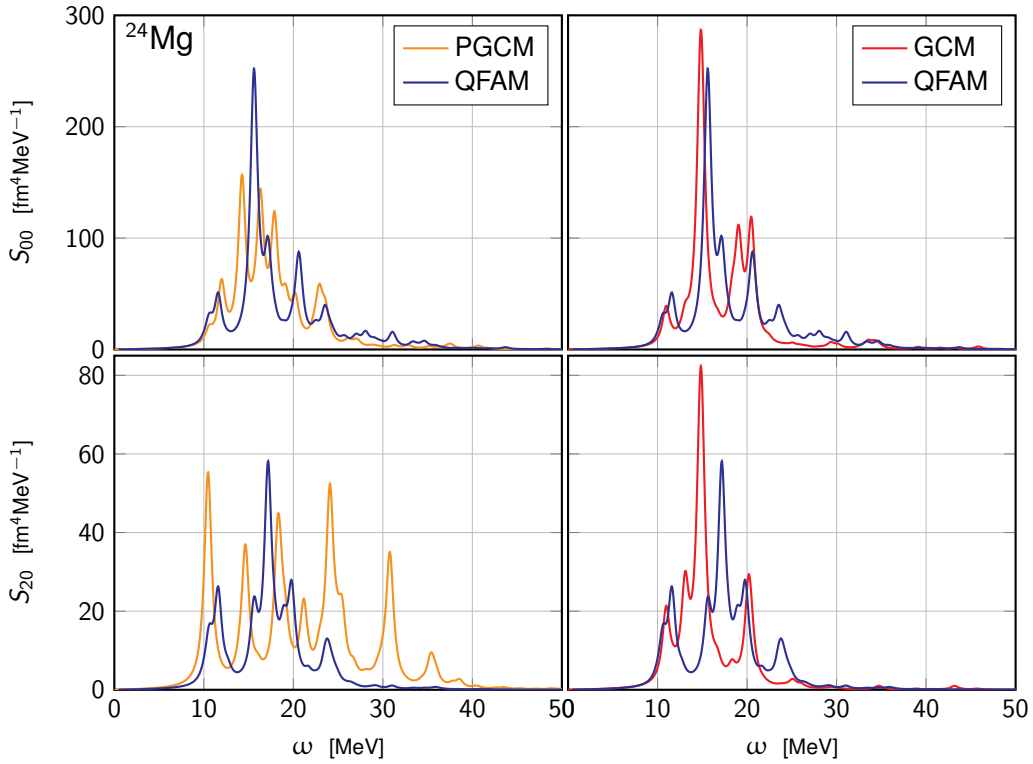

Figure 9.7: Monopole (top) and quadrupole (bottom) response in ^{24}Mg for QFAM calculations compared to PGCM (left) and GCM (right) calculations.

9.6 ^{28}Si

QFAM results for both the oblate-shape ground state and the prolate-shape isomer of ^{28}Si are presented and compared to (P)GCM calculations in Figs. 9.8 and 9.9 respectively.

In the monopole response of the oblate ground state the GMR is coherently predicted by both QFAM and (P)GCM calculations: the breathing mode is observed at ∼17.5 MeV, accompanied by some fragmentation at higher energies. The main difference is the presence of a peak at ∼13 MeV in (P)GCM calculations which is not observed in QFAM.

As for the ground-state quadrupole channel, the three methods agree in determining a faint response. This is in line with the very partial exhaustion of the associated EWSR in QFAM and (P)GCM calculations, which is reported in Sec. 10.6.1. This effect is associated to the exploration of the sole $K = 0$ component of the quadrupole resonance: the ground state of ^{28}Si being strongly oblate, quadrupolar vibrations are expected to be more prominent perpendicularly to the symmetry axis. Such kind of quadrupolar vibrations would demand the inclusion of $K \neq 0$ components, requiring triaxiality to be considered.

The prolate-shape isomer is hereby addressed, starting from the monopole response (upper panels of Fig. 9.9). QFAM and (P)GCM calculations agree in the identifications of three main regions of interest. The first one at ∼13 MeV is unambiguously identified by both QFAM and (P)GCM as the manifestation of the GMR-GQR coupling, as already discussed in Sec. 7.3. The second peak at ∼17 MeV has greater prominence in non-projected calculations, since both QFAM and GCM associate a relevant strength to such a state, which is instead diminished in PGCM results. The third peak at ∼22 MeV is associated to the breathing mode of the prolate isomer, whose collective PGCM wave-function was shown in Fig. 7.3. This state's strength is lower in QFAM calculations.

GCM and QFAM quadrupole spectra display a very similar shape, with GCM being shifted down by

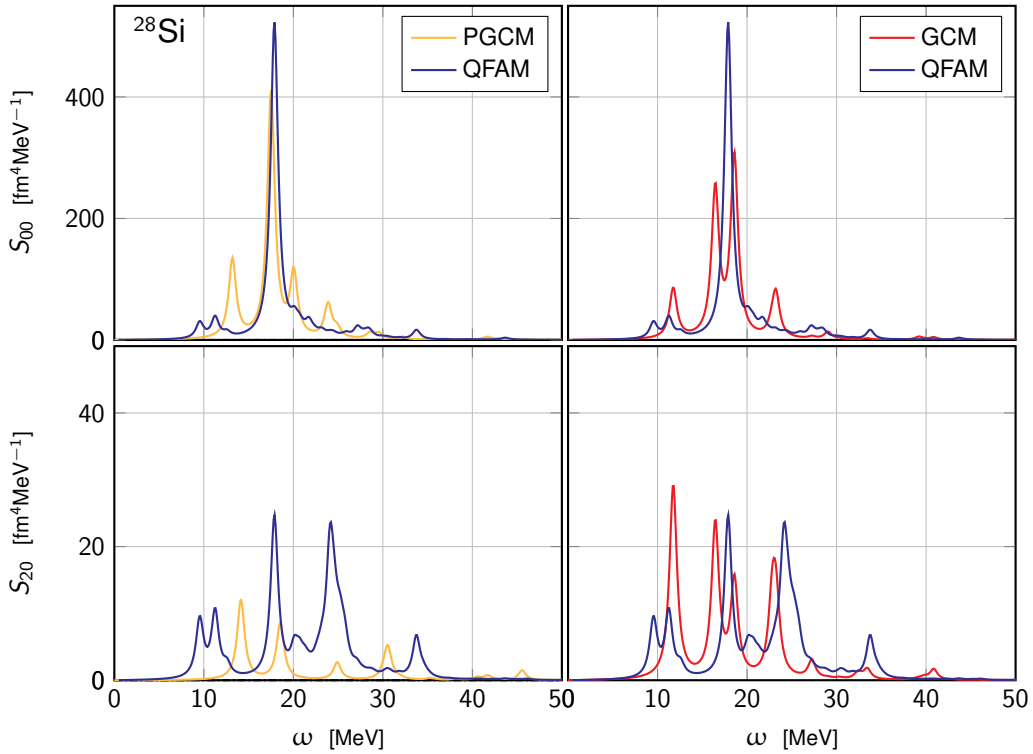

Figure 9.8: Monopole (top) and quadrupole (bottom) response in ^{28}Si for QFAM calculations compared to PGCM (left) and GCM (right) calculations.

roughly 1-2 MeV. This effect is assumed to be produced by anharmonicities based on data from Tab. 9.6. However, projection largely reduces the strength associated to the GQR in GCM calculations, such that a similar effect shall be expected in projected-QRPA calculations.

9.7 Conclusions

QFAM calculations were compared to (P)GCM results. In all the observed cases the various strengths were in qualitative agreement. However, in some cases, anharmonic effects have a significant impact in the energy positioning of the resonances. Such an effect is detectable by comparing QFAM and GCM calculations.

Anharmonic effects are shown in Sec. 9.2 to be magnified when different generator coordinates are considered separately. Coupling between different modes, which is properly described both in (P)GCM and QRPA, strongly reduces the impact of anharmonic corrections. Indeed, (P)GCM and QFAM results differ the most in ^{16}O, where the GMR-GQR coupling does not appear due to the spherical shape of the nuclear ground state, such that anharmonic effects in the uncoupled breathing mode can manifest to the greatest extent. Further formal investigations are in order for a more quantitative description of the competing effects of anharmonicities and coupling between different modes.

Projection also has, in some cases, non-trivial consequences on both the monopole and quadrupole responses (this is the case, for instance, of ^{24}Mg). Such consequences are appreciated by comparing GCM calculations with their angular-momentum-projected counterpart. Similar effects are likely to manifest in PQRPA as well, which represents a stimulus in implementing a full-fledged projected version of this formalism.

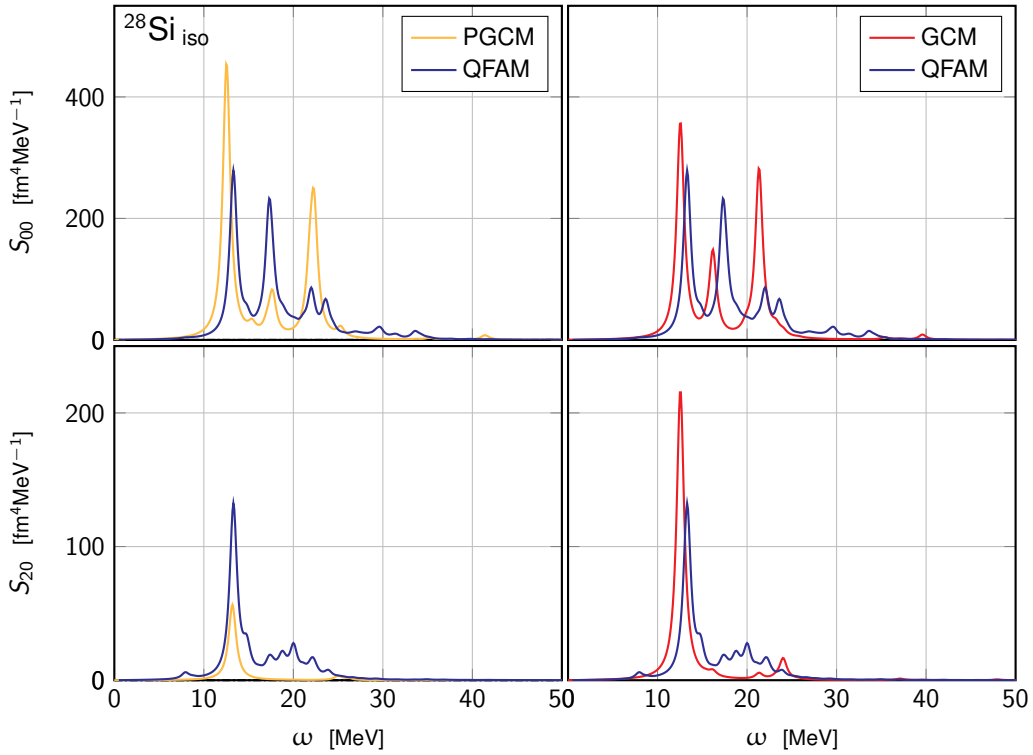

Figure 9.9: Monopole (top) and quadrupole (bottom) response in the prolate-shape isomer of ^{28}Si for QFAM calculations compared to PGCM (left) and GCM (right) calculations.

Chapter 10

Moments evaluation: numerical results

Contents

Multipole responses moments are numerically evaluated in this chapter, following their theoretical introduction in Chap. 4. While moments are used in Chap. 6 to provide a global characterisation of strength functions, the present chapter focuses on theoretical and technical concerns.

In Chap. 4 two possibilities to compute the moments m_k of the strength distributions were discussed and formally defined, namely Eqs. (4.27) and (4.46). Equation (4.27) relies on the explicit knowledge of all excited states of the system, whereas Eq. (4.46) defines a *moment operator* whose average computed in the ground state delivers, in principle, the same information. Numerical results are provided in Sec. 10.1 for both techniques for different GCM and PGCM calculations, so to test the assumption underlying the identity resolution in Eq. (4.35).

The effects of different types of correlations are also addressed. Specifically, the effects of projection are discussed in Sec. 10.2 comparing GCM and PGCM results, while anharmonic effects are discussed in Sec. 10.3 by comparing QFAM to GCM.

Moments operators engender a numerical complexity linked to their intrinsic many-body nature, such that only the zeroth moment m_0 and the first moment m_1 were actually implemented in an exact fashion. Approximations for higher moments proposed in Sec. 4.4 are tested numerically in Sec. 10.4.

	^{16}O		^{24}Mg		^{46}Ti		^{28}Si		^{28}Si$_{\text{iso}}$	
	Sum	GS	Sum	GS	Sum	GS	Sum	GS	Sum	GS
m_0 [fm^{4}MeV^{-1}]	369	284	955	1314	2226	2366	1154	1670	1299	1328
m_1 [fm^4]	7940	8611	16676	17850	43185	46776	21046	22384	22104	23625

Table 10.1: Monopole moments computed using the excited-state- and the ground-state-based approaches for GCM calculations.

	^{16}O		^{24}Mg		^{46}Ti		^{28}Si		^{28}Si$_{\text{iso}}$	
	Sum	GS	Sum	GS	Sum	GS	Sum	GS	Sum	GS
m_0 [fm^{4}MeV^{-1}]	377	378	969	1025	2264	2383	1165	1022	1355	1406
m_1 [fm^4]	8386	8617	17178	17978	44392	47046	21490	22526	22846	24016

Table 10.2: Monopole moments computed using the excited-state- and the ground-state-based approaches for PGCM calculations.

The Energy Weighted Sum Rule and the relative exhaustion by QFAM and (P)GCM calculations is addressed in Secs. 10.5 and 10.6 in order to quantify the non-locality of the chiral Hamiltonian at use in the present work.

PGCM calculations employed in the present chapter were discussed in details in Sec. 7.1 for ^{16}O, Sec. 7.4 for ^{24}Mg, Sec. 7.3 for ^{28}Si (ground state and prolate-shape isomer) and Sec. 7.2 for ^{46}Ti. GCM calculations are taken from Chap. 8, whereas QFAM calculations were presented in Chap. 9.

10.1 Comparison of the two calculation methods

The two approaches for the evaluation of spectral moments are here compared for GCM and PGCM calculations. The equivalence of the two techniques relies on the completeness assumption from Eq. (4.35), which allows for the use of the identity resolution. Such completeness may not be justified *a priori* for (P)GCM calculations that do not provide exact and complete solutions of the A-body Schrödinger equation. A formal proof for GCM calculations employing Slater determinants built from harmonic oscillator wavefunctions was provided in Appendix C of Ref. [85]. A direct extension of this proof to GCM states based on HFB vacua with non-local momentum-dependent interactions is not immediate and is left to future developments.

Since an exact implementation of moment operators has been realised for m_0 and m_1, only these two quantities are compared. The effect of approximations on higher moments excessively deteriorates the quality of the obtained information, as will be shown in Sec. 10.4, so that their comparison in this context is not relevant.

Here and in the remaining of this chapter the label *Sum* refers to the excited-state-based evaluation of moments from Eq. (4.27), whereas the label *GS* refers to the ground-state formulation from Eq. (4.46). Results for monopole and quadrupole responses are separately addressed in the following.

10.1.1 Monopole

GCM results are first addressed in Tab. 10.1. As will become clearer in the following, m_0 is strongly affected by the method of choice, with numerical differences of 45% in ^{28}Si representing the most extreme variation. Differently, m_1 is relatively stable, displaying variations always smaller than ∼8%.

The same quantities are presented in Tab. 10.2 for PGCM calculations. Compared to GCM results, m_0 values obtained via the two different evaluation methods are closer in PGCM, with variations smaller

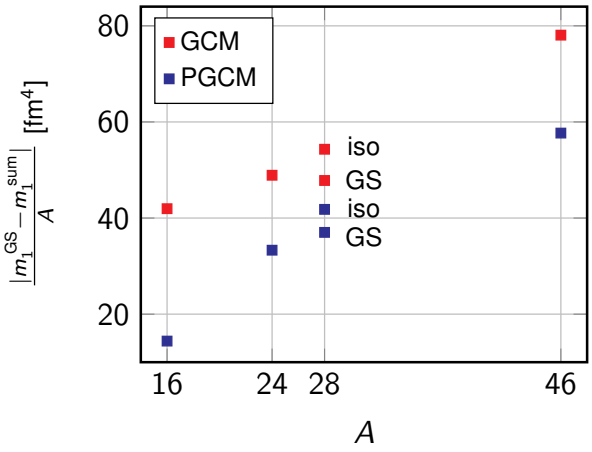

Figure 10.1: Difference between the GS- and the excited-state-based monopole m_1 values as a function of A in (P)GCM calculations. The factor $1/A$ is included to remove trivial A dependencies (see Eq. (10.1a)).

than 12% (^{28}Si) and typically assessing around 5% (or less). Given the aforementioned high sensitivity of m_0 to the ground-state convergence, the compatibility between the two evaluation methods is a signal of numerical convergence (as far as the many-body method itself is concerned). This improvement is attributed to the benefits of the symmetry restoration: symmetry contaminants originally present in the GCM ground state are removed by the angular momentum projection, such that the use of the completeness relation in Eq. (4.35) is better realised for PGCM calculations, i.e. the projection on $J = 0$ explicitly restrains to a Hilbert subspace which is essentially closed with respect to the r^2 operator. This further corroborates the correctness of PGCM results in the monopole channel discussed in Chap. 7. Moreover, the same improvement is observed for m_1: the difference between the two evaluation methods is reduced for all presented results, with an average variation of 5%. Overall, a good agreement between the two methods is observed in the monopole channel for GCM and PGCM calculations.

Eventually, the numerical difference between the two evaluation methods for m_1 is plotted in Fig. 10.1 as a function of the mass number A for both GCM and PGCM calculations. In both cases a correlation with A is observed, pointing at the fact that the completeness assumption in Eq. (4.35) is less verified in heavier systems or, in other words, the hypotheses in Appendix C of Ref. [85] are not satisfied to a larger extent.

10.1.2 Quadrupole

Results obtained from the two evaluation methods are now discussed for the quadrupole response. Results from GCM calculations are listed in Tab. 10.3. The difference with the monopole moments is clear: the sensitivity of m_0 to the method of choice manifests here to a greater extent. With the exception of the prolate-shape isomer of ^{28}Si, all calculations are far from being consistent for the quadrupole strength, with variations spanning from 20% to 550%. Significant differences between the two evaluation methods are also visible for m_1, where variations from 10% to 58% are observed, except for ^{16}O, where a 1% difference is found.

PGCM moments are reported in Tab. 10.4 for ^{46}Ti. The two evaluation methods are now more consistent as far as m_1 is concerned. However, m_0 results differ by roughly 36% if the GS-based value is taken as a reference.

	^{16}O		^{24}Mg		^{46}Ti		^{28}Si		^{28}Si$_{\text{iso}}$	
	Sum	GS	Sum	GS	Sum	GS	Sum	GS	Sum	GS
m_0 [fm^{4}MeV^{-1}]	72	467	264	455	552	664	150	257	387	391
m_1 [fm^4]	1709	1721	4194	4622	6801	10750	2748	3425	5377	6185

Table 10.3: Quadrupole moments computed using the excited-state- and the ground-state-based approaches for GCM calculations.

	^{46}Ti	
	Sum	GS
m_0 [fm^{4}MeV^{-1}]	511	799
m_1 [fm^4]	10002	10110

Table 10.4: Quadrupole moments computed using the excited-state- and the ground-state-based approaches for PGCM calculations.

10.2 Effects of the angular momentum projection

The explicit effect of AMP on the moments evaluation is hereby analysed by comparing results from GCM and PGCM calculations. The sum and GS approaches are analysed independently. Monopole and quadrupole responses are presented separately in the following sections.

10.2.1 Monopole

Monopole moments for GCM and PGCM calculations are compared in Tabs. 10.5 and 10.6 for the excited-state-based approach. A global trend is observed for all computed quantities, for which PGCM values are systematically larger than GCM ones. Higher moments ($k > 1$) are naturally more prone to the variations already observed for m_1, since they are more sensitive to higher-energy states differences.

The effects on the GS-based formulation turn out to be quite different, see Tab. 10.7. As previously noticed, m_0 can be very sensitive to the GS wave-function of choice. Differently, m_1 is quite insensitive to the inclusion of the symmetry projection, with variations between the methods always smaller than 1%.

Overall, the projection on good angular momentum does not affect strongly the results in the monopole channel. As already observed in Chap. 8, where such a comparison was made, the coarse structure of the monopole response is not affected dramatically by the symmetry restoration.

	^{16}O		^{24}Mg		^{46}Ti	
	GCM	PGCM	GCM	PGCM	GCM	PGCM
m_0 [fm^{4}MeV^{-1}]	369	377	955	969	2226	2264
m_1 [fm^4]	7940	8386	16676	17178	43185	44392
m_2 [fm^{4}MeV]	182667	205277	315053	329629	871376	900105
m_3 [fm^{4}MeV^2]	4718706	5887075	6661187	7031885	18469397	18976050
m_{-1} [fm^{4}MeV^{-2}]	17.83	17.90	57.95	58.16	120.75	120.86

Table 10.5: Monopole moments computed using the excited-state-based approach for GCM and PGCM calculations.

	^{28}Si		^{28}Si $_{\text{iso}}$	
	GCM	PGCM	GCM	PGCM
m_0 [fm^{4}MeV^{-1}]	1154	1165	1299	1355
m_1 [fm^4]	21046	21490	22104	22846
m_2 [fm^{4}MeV]	407130	421980	409871	425302
m_3 [fm^{4}MeV^2]	8598128	9120720	8449724	8895435
m_{-1} [fm^{4}MeV^{-2}]	66.37	66.07	82.11	87.33

Table 10.6: Monopole moments computed using the excited-state-based approach for GCM and PGCM calculations.

	^{16}O		^{24}Mg		^{46}Ti		^{28}Si		^{28}Si $_{\text{iso}}$	
	GCM	PGCM	GCM	PGCM	GCM	PGCM	GCM	PGCM	GCM	PGCM
m_0 [fm^{4}MeV^{-1}]	284	378	2366	2383	1670	1022	1328	1406	1314	1025
m_1 [fm^4]	8611	8617	46776	47046	22384	22526	23625	24016	17850	17978

Table 10.7: Monopole moments computed using the GS-based approach for GCM and PGCM calculations.

10.2.2 Quadrupole

The effect of AMP on the moments of the quadrupole strength is displayed in Tab. 10.8 for the excited-state-based approach. The difference between GCM and PGCM is significant (up to 400%) for all computed cases, with ^{46}Ti being a unique exception. More precise statements are prevented by the poor convergence properties of quadrupole spectra in PGCM, previously ascribed to the insufficient set of collective coordinates employed. Ground-state-based results are also shown in Tab. 10.9 for ^{46}Ti. In this specific case the effects of projection are not drastic, which parallels the observation of excited-states results for this same system.

Quadrupole GCM responses are shown in the following section to be consistent with QFAM calculations modulo the potential presence of anharmonic effects. Thus, the associated quadrupole response can be considered reliable and the large numerical differences encountered in the quadrupole channel are assumed to be mostly driven by angular momentum projection.

	^{24}Mg		^{46}Ti		^{28}Si		^{28}Si $_{\text{iso}}$	
	GCM	PGCM	GCM	PGCM	GCM	PGCM	GCM	PGCM
m_0 [fm^{4}MeV^{-1}]	264	465	552	511	150	51	387	97
m_1 [fm^4]	4194	9782	6801	10002	2748	1141	5377	1412
m_2 [fm^{4}MeV]	72025	236886	103680	329731	57089	31044	81991	22651
m_3 [fm^{4}MeV^2]	1397322	6540569	2030609	14821641	1375429	1036111	1494175	452028
m_{-1} [fm^{4}MeV^{-2}]	17.53	25.69	51.95	41.54	9.10	2.63	29.25	7.03

Table 10.8: Quadrupole moments computed using the excited-state-based approach for GCM and PGCM calculations.

	^{46}Ti	
	GCM	PGCM
m_0 [fm^{4}MeV^{-1}]	664	799
m_1 [fm^4]	10750	10110

Table 10.9: Quadrupole moments computed using the GS-based approach for GCM and PGCM calculations.

	^{16}O		^{24}Mg		^{46}Ti	
	QFAM	GCM	QFAM	GCM	QFAM	GCM
m_0 [fm^{4}MeV^{-1}]	374	369	946	955	2302	2226
m_1 [fm^4]	8356	7940	17478	16676	46387	43185
m_2 [fm^{4}MeV]	198143	182667	352512	315053	970709	871376
m_3 [fm^{4}MeV^2]	5038020	4718706	7848770	6661187	21106400	18469397

Table 10.10: Monopole moments computed using the excited-state-based approach for GCM calculations compared to QFAM moments.

10.3 Comparison to QFAM results

Moments originating from QFAM calculations presented in Chap. 9 are now compared to GCM ones. This comparison not only allows one to gauge the performance of two different methods, but also can provide a useful insight on the role of correlations. In Sec. 10.2 the impact of AMP was addressed. Here the comparison of GCM to QFAM allows one to make a statement about beyond-mean-field and beyond-QRPA correlations, without any interference with the effects of AMP.

QFAM moments have been computed following the prescription from Ref. [180]. In the following, excited- and ground-state-based evaluation of moments for GCM are independently compared to QFAM results.

It is recalled in App. H.1 that odd QRPA moments can be evaluated using Eq. (H.8). This is strictly equivalent to the evaluation of Eq. 4.46 based on the HFB ground state [151, 181]. Any beyond-mean-field correction is effectively absent from the evaluation of odd-k moments in QRPA. In this respect, GS-based results from (P)GCM calculations are, by definition, superior to QRPA ones, given that the (P)GCM ground state includes more correlations that an individual HFB state, even for a limited number of generator coordinates.

10.3.1 Monopole

A comparison between QFAM and GCM excited-state-based moments for the monopole response is performed in Tabs. 10.10 and 10.11. An excellent agreement is observed for all presented cases. Given the approximations at the heart of QRPA, larger differences are expected for systems further away from the harmonic hypothesis. One would thus expect the agreement between QFAM and GCM to be driven by the *harmonicity* degree of the considered system. Larger systems are supposed to better fulfil the harmonic hypothesis due to less pronounced violations of the Pauli principle in QRPA [89], which was indeed observed in Sec. 9.2.

The difference between the QFAM and the excited-state-based GCM m_1 values is plotted as a function of A in Fig. 10.2 (left). The difference is found to be proportional to A. This observation contradicts the assumption that the harmonic hypothesis is better fulfilled by larger nuclei. Ground-state-based moments are, hence, compared to QFAM calculations in Tabs. 10.12. Concerning m_1, a good agreement is observed between QFAM and GCM monopole moments. The anomalous behaviour reported in Fig. 10.2 (left) for the

	^{28}Si		^{28}Si$_{\text{iso}}$	
	QFAM	GCM	QFAM	GCM
m_0 [fm^{4}MeV^{-1}]	1170	1154	1267	1299
m_1 [fm^4]	22080	21046	23075	22104
m_2 [fm^{4}MeV]	444208	407130	456313	409871
m_3 [fm^{4}MeV^2]	9651280	8598128	9889420	8449724

Table 10.11: Monopole moments computed using the excited-state-based approach for GCM calculations compared to QFAM moments.

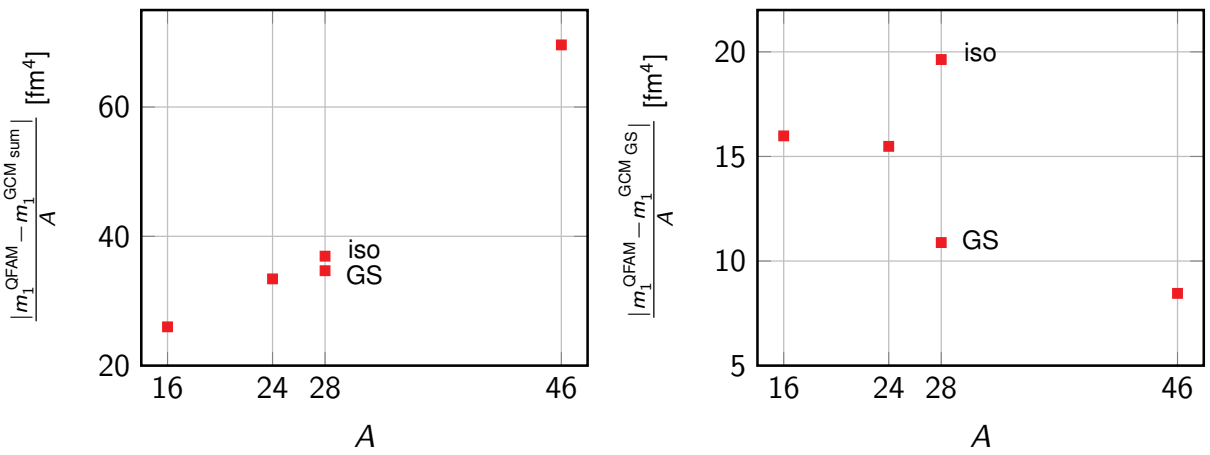

Figure 10.2: Difference between the QFAM and (left) the excited-state-based (right) the GS-based GCM monopole m_1 values as a function of A. The factor $1/A$ is included to remove trivial A dependencies (see Eq. (10.1a)).

	^{16}O		^{24}Mg		^{46}Ti		^{28}Si		^{28}Si$_{\text{iso}}$	
	QFAM	GCM	QFAM	GCM	QFAM	GCM	QFAM	GCM	QFAM	GCM
m_0 [fm^{4}MeV^{-1}]	374	284	946	1314	2302	2366	1170	1670	1267	1328
m_1 [fm^4]	8356	8611	17478	17850	46387	46776	22080	22384	23075	23625

Table 10.12: Monopole moments computed using the GS-based approach for GCM calculations compared to QFAM moments.

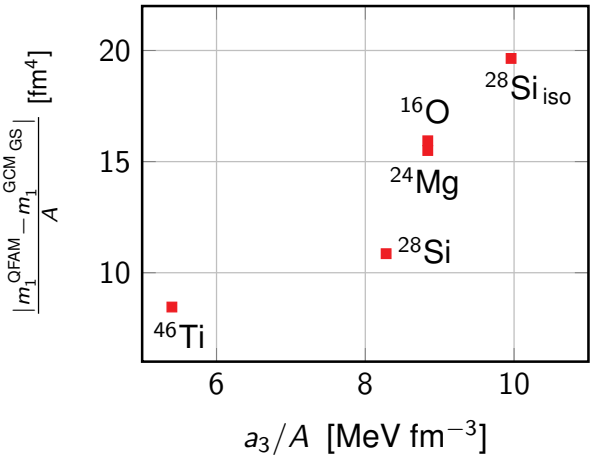

Figure 10.3: Difference between the QFAM and the gound-state-based GCM monopole m_1 values as a function of the cubic coefficients a_3/A (see Sec. 9.2). The factor $1/A$ is included to remove trivial A dependencies (see Eq. (10.1a)).

	^{16}O		^{24}Mg		^{46}Ti	
	QFAM	GCM	QFAM	GCM	QFAM	GCM
m_0 [fm^{4}MeV^{-1}]	72	72	264	264	660	552
m_1 [fm^4]	1712	1709	4571	4194	10736	6801
m_2 [fm^{4}MeV]	41877	41832	84212	72025	195735	103680
m_3 [fm^{4}MeV^2]	1050870	1074434	1655270	1397322	3788380	2030609

Table 10.13: Quadrupole moments computed using the excited-state-based approach for GCM calculations compared to QFAM moments.

excited-state-based m_1 is not found in this case. The difference between the QFAM and the GS-based GCM m_1 values is indeed plotted as a function of A in Fig. 10.2 (right). Coherently with the better fulfilment of the harmonic hypothesis in heavier systems, a negative correlation with A is found, contrarily to the excited-state-based method. Supported by the observed trend in Fig. 10.1 concerning the violation of the completeness relation in Eq. (4.35), thus, the GS-based method is found to provide more reliable information on the m_1 moments in (P)GCM calculations.

As expected, the difference between QFAM and GCM is now proved to be driven by anharmonic effects, as shown in Fig. 10.3, where the difference between QFAM and ground-state-based GCM m_1 moments is plotted as a function of the cubic coefficients a_3 extracted in Sec. 9.2. Larger values of a_3 are associated to larger differences between GCM and QFAM, which hints at the presence of anharmonic effects not accounted for in QFAM.

10.3.2 Quadrupole

The same comparison is now performed in the quadrupole channel. The excited-state-based evaluation of moment is first addressed. Numerical values in GCM and QFAM are compared in Tabs. 10.13 and 10.14. In general GCM predictions are conform to QFAM, with quantitative differences that do not compromise the qualitative similarities. In analogy to the monopole case the difference between QFAM and excited-state-based GCM moments correlates to the mass number, implying worse fulfilment of the completeness relation in Eq. (4.35) for heavier systems.

	^{28}Si		^{28}Si$_{\text{iso}}$	
	QFAM	GCM	QFAM	GCM
m_0 [fm^{4}MeV^{-1}]	162	150	380	387
m_1 [fm^4]	3393	2748	6074	5377
m_2 [fm^{4}MeV]	78754	57089	103751	81991
m_3 [fm^{4}MeV^2]	1984110	1375429	1919930	1494175

Table 10.14: Quadrupole moments computed using the excited-state-based approach for GCM calculations compared to QFAM moments.

	^{16}O		^{24}Mg		^{46}Ti		^{28}Si		^{28}Si$_{\text{iso}}$	
	QFAM	GCM	QFAM	GCM	QFAM	GCM	QFAM	GCM	QFAM	GCM
m_0 [fm^{4}MeV^{-1}]	72	467	264	455	660	664	162	257	380	391
m_1 [fm^4]	1712	1721	4571	4622	10736	10750	3393	3425	6074	6185

Table 10.15: Quadrupole moments computed using the GS-based approach for GCM calculations compared to QFAM moments.

The comparison of the GCM GS-based moments with QFAM results is displayed in Tab. 10.15. A quantitative agreement is observed for m_1 in all studied cases, with differences always smaller than ∼1%. Results are more scattered for m_0, given the high sensibility of this physical quantity.

10.4 Approximations on commutators

Moments operators, introduced in Chap. 4, are many-body operators whose rank increases with the moment's degree. Considering a two-body Hamiltonian, only m_0 and m_1 deliver two-body operators, knowing that this is the maximum rank that can be easily handled in the current PGCM code. In Sec. 4.4 different approximations were proposed to overcome such a limitation for higher moments. In particular, Eqs. (4.87) provide three approximate expressions for the commutator C_1 (see Eq.(4.40)).

The performance of such approximations is tested for monopole operators in PGCM calculations using m_1, for which exact calculations are available as a benchmark. Results are reported in Tab. 10.16. Going from (a) to (c) in Eqs. (4.87), approximations are expected to proceed from a lower to a higher degree of accuracy. The observed trend is actually opposite in numerical applications. Approximation (a) deviates by ∼10% from the exact value in all observed cases. The deviation is about 33% for approximation (b), whereas approximation (c) out-predicts the exact value by a factor 4-5. This results disqualify approximations (b) and (c) for concrete applications.

Approximation (a) is then tested for m_2 and m_3 moments. Results are listed in Tab. 10.17. The relative

	Exact	(a)	(b)	(c)	Err % (a)	Err % (b)	Err % (c)
^{24}Mg	17978	16263	23851	92484	9.5	32.7	414.4
^{28}Si	22526	20379	30074	124854	9.5	33.5	454.3
^{28}Si$_{\text{iso}}$	24016	21496	32191	142629	10.5	34.0	493.9

Table 10.16: Monopole m_1 computed using the GS-based approach in PGCM calculations. Approximations from Eqs. (4.87) are compared to the exact value, relative errors with respect to exact value are also reported. Absolute quantities are in units of fm^4.

	^{24}Mg			^{28}Si			^{28}Si$_{\text{iso}}$		
	Sum	(a)	Err %	Sum	(a)	Err %	Sum	(a)	Err %
m_1 [fm^4]	17178	16263	5.3	21490	20379	5.2	22846	21496	5.9
m_2 [fm^{4}MeV]	329629	293642	10.9	421980	371820	11.9	425302	382864	10.0
m_3 [fm^{4}MeV^2]	7031885	23573901	235.2	9120720	30439415	233.7	8895435	31148633	250.2

Table 10.17: Monopole moments computed using the GS-based approach in PGCM calculations using approximation (a) from Eqs. (4.87). Excited-state-based values are used as a reference.

EWSR	QFAM	GCM	PGCM	Exp
^{16}O	8832	8841	8852	9623
^{24}Mg	17880	17990	18047	18600
^{28}Si	22422	22448	22546	22648
^{28}Si$_{\text{iso}}$	23306	23474	23771	
^{46}Ti	46046	46053	46293	49607

Table 10.18: Isoscalar monopole EWSR from Eq. (10.1a) for different nuclei under different approximations compared to experimental results. Experimental values for radii have been taken from [183]. All results are expressed in fm^4 units.

error rapidly increases with the order of the computed moment. A clear trend in the error propagation is difficult to establish due to the fact that excited-state-based moments are used as benchmarks. Eventually, this behaviour is not dissimilar from recent observations of spurious isospin-symmetry-breaking effects in the IMSRG [182], where an exponential error on the similarity-transformed Hamiltonian is introduced by the normal-ordered two-body approximation when evaluating nested commutators.

Eventually, none of the proposed approximations can be considered reliable to evaluate GS-based moments beyond m_0 and m_1.

10.5 Energy Weighted Sum Rule

The Energy Weighted Sum Rule (EWSR) is a standard quantity in GRs studies and provides a good indicator of the degree of collectivity of nuclear excitations. It relies on the evaluation of m_1 from Eq. (4.46), i.e. based on the GS approach, with the assumption of a momentum-independent local Hamiltonian [141, 64], leading to the analytical results

$$\text{EWSR}(E0) = \frac{2\hbar^2 A \langle r^2 \rangle_{gs}}{m} \tag{10.1a}$$

$$\text{EWSR}(E2) = \frac{25\hbar^2 A \langle r^2 \rangle_{gs}}{4\pi m} \tag{10.1b}$$

for the isoscalar monopole and quadrupole response, respectively, with m the nucleon mass. EWSRs solely rely on the knowledge of the ground-state mean-square nuclear charge radius. Different values for the EWSR are presented in Tabs. 10.18 and 10.19 for monopole and quadrupole calculations respectively. HFB values for radii are consistently used in QFAM calculations, while (P)GCM radii must be used to evaluate (P)GCM sum rules. Experimental nuclear radii are taken from [183] to evaluate the experimental EWSR.

As far as monopole EWSRs from Tab. 10.18 are concerned, the numerical dispersion between QFAM, GCM and PGCM is very small. This is consistent with Eq. 10.1a showing that $\langle r^2 \rangle_{gs}$ is the sole ingredient to

	QFAM	GCM	PGCM	Exp
^{16}O	8785	8795	8805	9573
^{24}Mg	17785	17895	17951	18502
^{28}Si	22304	22329	22427	22528
^{28}Si $_{\text{iso}}$	23183	23350	23646	
^{46}Ti	45803	45809	46048	49345

Table 10.19: Isoscalar quadrupole EWSR from Eq. (10.1b) for different nuclei under different approximations compared to experimental results. Experimental values for radii have been taken from [183]. All results are expressed in fm^4 units.

the calculation of the EWSR. Generally speaking, nuclear radii are not strongly affected by beyond-mean-field corrections, such that the HFB value already provides a good approximation of the exact many-body counterpart [184, 185]. Experimental values are slightly under-predicted, but a slow trend is observed in all the investigated systems towards experimental results when going from QFAM to GCM and PGCM calculations. Besides the imperfection of the presently employed nuclear Hamiltonian, further improvements may be provided by increasing the number of considered generator coordinates or via the addition of perturbative corrections on top of PGCM [41, 43].

Since the quadrupole EWSR from Eq. (10.1b) is identical to its monopole counterpart up to a multiplicative factor, the same remarks also apply for the quadrupolar response. The relative numerical values are provided in Tab. 10.19.

10.6 EWSR exhaustion and Hamiltonian momentum independence

Since the EWSRs from Eqs. (10.1a) and (10.1b) are derived under the assumption of a local momentum-independent interaction, it is of interest to analyse to which extent such rules are exhausted by different *ab initio* methods, making use of a chiral Hamiltonian neither local nor momentum independent. In the following sections the isoscalar monopole and quadrupole EWSRs are addressed separately. Data are expressed as percentage of exhaustion of the EWSR relative to the corresponding *theoretical* quantities evaluated in Sec. 10.5.

Since the EWSRs derivation also assumes the resolution of identity in Eq. (4.35), only GS-based results are employed. In this way the completeness relation is assumed to be verified and only the Hamiltonian momentum independence hypothesis is probed. If the latter were satisfied, a 100 % exhaustion would be observed, independently on the method at use. Departures from the total exhaustion represent, thus, a quantitative measure of the momentum dependence of the employed chiral Hamiltonian.

10.6.1 Monopole

The EWSR exhaustion in the monopole channel is summarised in Tab. 10.20 for previously discussed (P)GCM and QFAM calculations. No significant difference is observed between GCM and PGCM calculations, with variations smaller than 0.4% for all studied cases. In general, a good agreement with the monopole EWSR is observed both for GCM and PGCM calculations; small deviations from the EWSR are a signal that the hypothesis of momentum independence on nuclear interaction made to obtain Eq. (10.1a) is (more or less strongly) violated.

GCM moments can also be compared to QFAM calculations. The accordance with the EWSR is systematically improved by GCM for all the observed cases except ^{46}Ti (which represents the *most harmonic* among the analysed nuclei, see Sec. 9.2). The interaction at use being the same for both QFAM and GCM

% of EWSR	^{16}O	^{24}Mg	^{46}Ti	^{28}Si	^{28}Si $_{\text{iso}}$
QFAM	94.6	97.8	100.7	98.5	99.0
GCM	97.4	99.2	101.6	99.7	100.6
PGCM	97.3	99.6	101.6	99.9	101.0

Table 10.20: Percentage of exhaustion of the EWSR for monopole m_1 from (P)GCM and QFAM calculations. Both the excited-state- and the ground-state-based approaches are displayed for (P)GCM. QFAM moments are evaluated following the prescription from Ref. [180].

% of EWSR	^{16}O	^{24}Mg	^{46}Ti	^{28}Si	^{28}Si $_{\text{iso}}$
QFAM	19.5	25.7	23.4	15.2	26.2
GCM	19.6	25.8	23.5	15.3	26.5
PGCM			22.0		

Table 10.21: Percentage of exhaustion of the EWSR for quadrupole m_1 from (P)GCM and QFAM calculations. Both the excited-state- and the ground-state-based approaches are displayed for (P)GCM. QFAM moments are evaluated following the prescription from Ref. [180].

calculations, the locality and momentum-independent hypotheses violation could be expected to be similar.

The effect can be better isolated by assuming that the Hamiltonian is decomposed into a momentum-independent and a momentum-dependent component according to

$$H \equiv H_{\not k} + \delta H_k \,. \tag{10.2}$$

The m_1 moment, consequently, splits into two different terms, reading, in the monopole case

$$\begin{aligned} m_1 &= \frac{1}{2}\langle\Psi_0|[r^2,[H,r^2]]|\Psi_0\rangle \\ &= \frac{1}{2}\langle\Psi_0|[r^2,[H_{\not k},r^2]]|\Psi_0\rangle + \frac{1}{2}\langle\Psi_0|[r^2,[\delta H_k,r^2]]|\Psi_0\rangle \\ &= \mathrm{EWSR}(E0) + \frac{1}{2}\langle\Psi_0|[r^2,[\delta H_k,r^2]]|\Psi_0\rangle \\ &\equiv \mathrm{EWSR}(E0) + \delta m_k \,. \end{aligned} \tag{10.3}$$

Equation (10.3) isolates the component responsible for the deviations from the EWSR. The dimensionless quantity

$$\varepsilon_k \equiv \frac{m_1}{\mathrm{EWSR}(E0)} - 1 \tag{10.4}$$

is then introduced in order to quantify the momentum-dependence effect. Numerical values are plotted in Figs. 10.4. Globally one observes that ε_k increases with the mass number and going from QFAM to (P)GCM, suggesting that the exact wave-function should present a non-vanishing expectation value. It is observed that the difference between QFAM and (P)GCM values is larger in lighter systems, in agreement with the harmonic hypothesis being better satisfied in heavy systems. However, the degree of momentum dependence also depends on the considered nucleus.

Overall, none of the employed methods manifests strong violations of the monopole EWSR with the specific interaction at use [6]. Eventually, a pictorial view summarising data from Tab. 10.20 is given in Fig. 10.5.

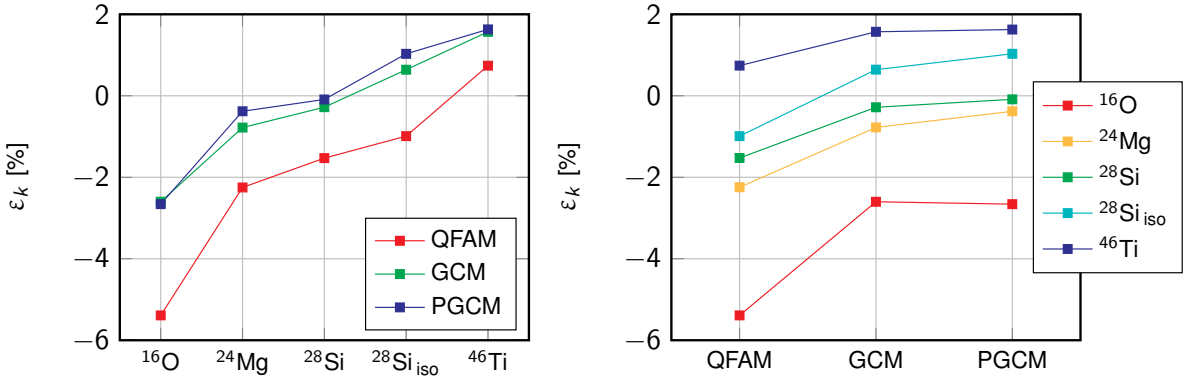

Figure 10.4: Percent variation from the momentum-independence hypothesis within different methods.

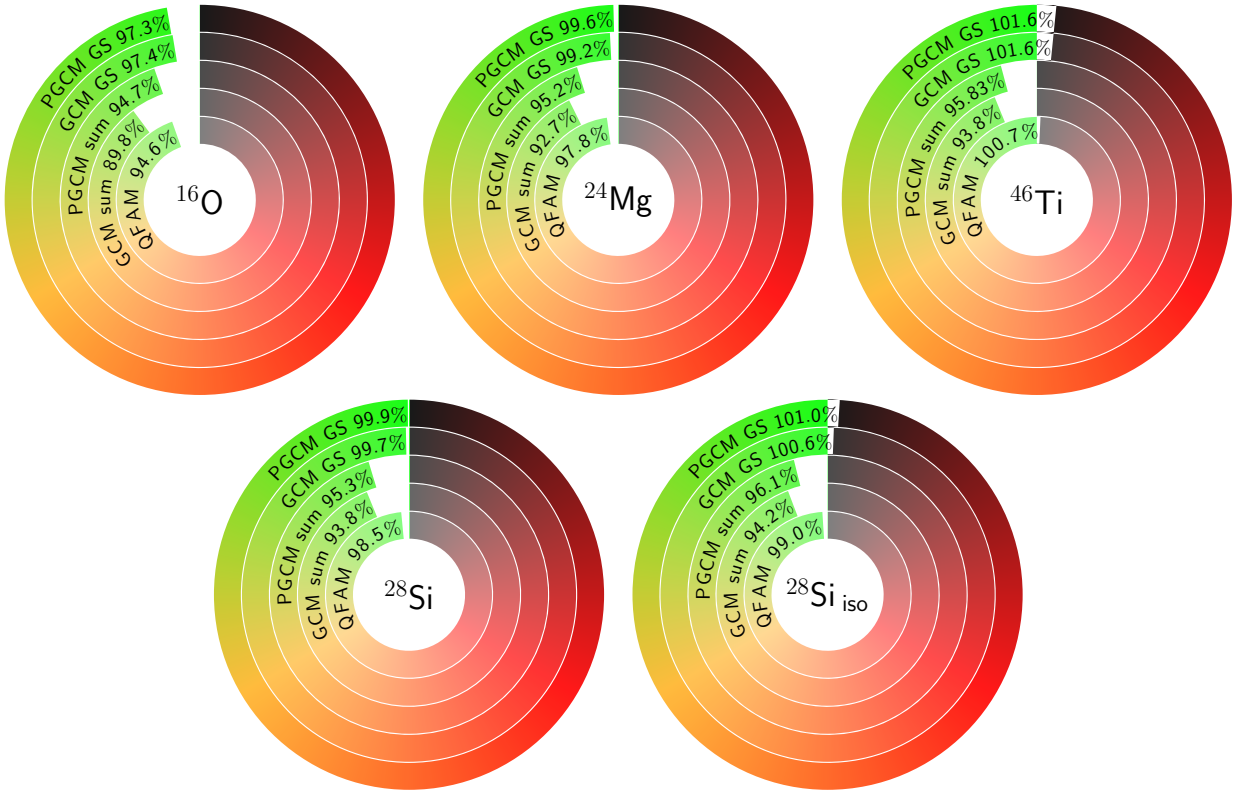

Figure 10.5: Percentage of exhausted EWSR in the monopole channel for different nuclei and methods.

10.6.2 Quadrupole

Data relative to the quadrupole EWSR are reported in Tab. 10.21. Percentages are far from being close to 100%, generally oscillating around 20% instead. This is due to the axial symmetry of the HFB states at use. Because of such a limitation only the $K = 0$ component of the quadrupole response can be computed. The $K = \pm 1, \pm 2$ channels not considered here also contribute to exhaust the total EWSR. For spherical systems the strength is equally distributed among the five different K channels, such that for a momentum-independent interaction the limit of 20% is expected for each K channel.

It is difficult, thus, to make any quantitative statement without the computation of $K \neq 0$ channels, which would demand triaxial calculations to be performed. However, some comments are in order. One however observes a good agreement with the 20% limit in ^{16}O, a spherical system, both for QFAM and GCM calculations. This testifies a weak violation of the quadrupole EWSR as in the monopole case. Prolate systems exceed the 20% limit by an amount proportional to the quadrupole deformation parameter β_2 (^{46}Ti being less deformed than ^{24}Mg, being in turn less deformed than the prolate isomer of ^{28}Si, see Tab. 9.1 for numerical values), whereas oblate systems (^{28}Si) underpredict the limit value. This is in line with the systematic trend observed in Ref. [78] for time-dependent HF+BCS EDF calculations.

In summary, QFAM and GCM calculations present similar levels of exhaustion of the quadrupole EWSR, whereas no precise statement can be made about PGCM results. An illustrated synthesis is also available in Fig. 10.6.

10.7 Summary

The main findings of this chapter are here itemised for clarity:

- In its operatorial implementation m_0 is sensitive to ground-state wave-function numerical convergence, whereas m_1 is more stable and has better convergence properties.
- In all considered inquiries (P)GCM calculations in the plane (β_2, r) confirmed their solid ground and self-coherence, proving a suitable tool to address monopole resonances.
- A qualitative agreement between (P)GCM results and QFAM is observed, with quantitative differences linked to anharmonic and symmetry-restoring effects.
- The momentum-dependent content of the chiral Hamiltonian manifests to different extents in the EWSR according to the employed many-body method. It is also observed that the departure from the momentum-independence hypothesis depends on the nucleus under exam, with m_1 increasing with the mass of the system.
- The EWSR is not a sensitive quantity when aiming at the characterisation of different many-body techniques, given their trivial dependence on nuclear radii, which are not greatly affected by the many-body method at use themselves.

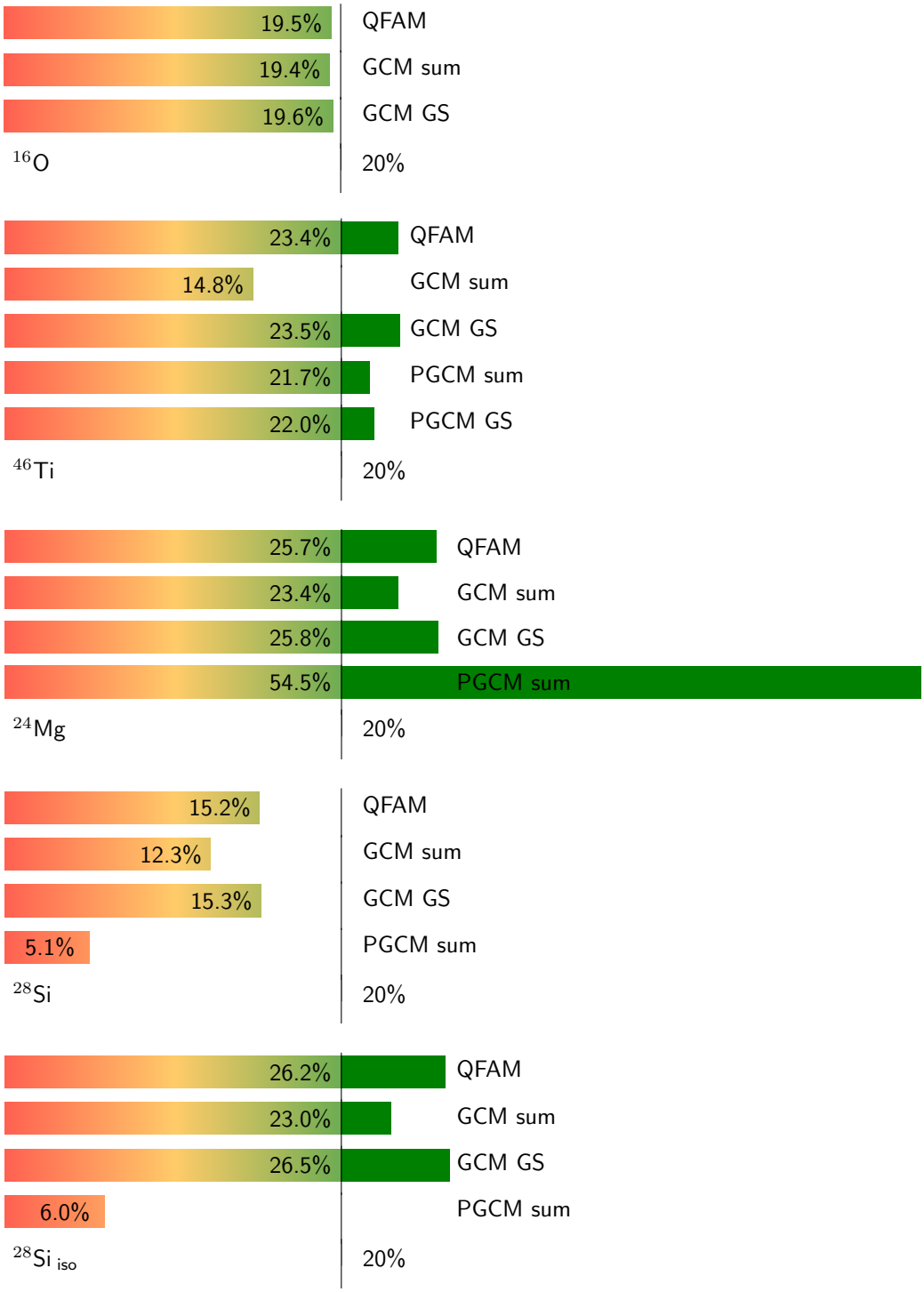

Figure 10.6: Percentage of exhausted EWSR in the quadrupole channel for different nuclei and methods. The 20% limit is also shown for reference.

Chapter 11

Multi-phonon states

Contents

In the previous chapters giant monopole resonances were addressed via the PGCM. The $K = 0$ component of quadrupolar resonances was also discussed. Giant resonances, in general, are understood as the first oscillator quantum of collective vibrations. Higher quanta are also expected in this vibrational picture, which are known in literature as multi-phonon states. Two-phonon states, for instance, can be portrayed as a giant resonance built on top of the *normal* giant resonance instead of on top of the nuclear ground state.

The experimental and theoretical investigation of multi-phonon states knew a discrete success in past years, especially regarding dipole and quadrupole resonances, see Refs. [186, 187] for a summary on this topic. Recent theoretical results [79] based on realistic multi-configuration time-dependent calculations suggest a good agreement with experimental data for two- and three-phonon quadrupole resonances in ^{40}Ca [188, 189].

Theoretical calculations of multi-phonon states are challenging when employing standard techniques for giant resonances investigations. Indeed, (Q)RPA describes, by definition, resonant states in terms of one-boson excitations. More sophisticated theories are, thus, necessary in order to attack the multi-phonon problem, such as boson expansions [89], beyond-(Q)RPA [73] or multi-reference theories. In this context, PGCM naturally offers a tool to investigate multi-phonon states.

11.1 One-dimensional study case in ^{46}Ti

A first study of multi-phonon states is now proposed on one-dimensional calculations described in Sec. 6.6.1. The one-dimensional case offers simplifications allowing for a gradual and controlled investigation, namely

i) It represents a textbook study case of multi-phonon states allowing one to grasp the main physical features associated with it and to compare it to simpler models. It offers the possibility to check global trends and certify the trustfulness and meaningfulness of the calculations.

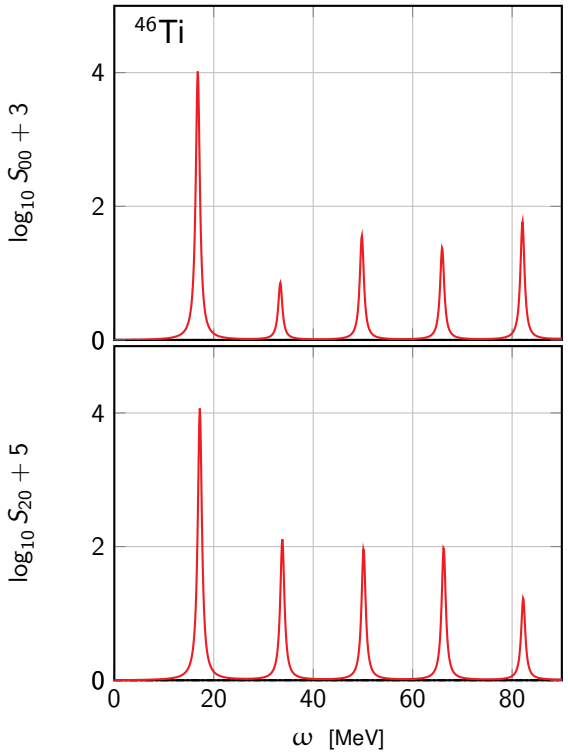

Figure 11.1: Monopole (top) and quadrupole (bottom) response in ^{46}Ti for one-dimensional PGCM calculations from Sec. 6.6.1 plotted in logarithmic scale.

ii) A proper convergence study of high-lying multi-phonon states can be readily provided.

In this section both monopole and quadrupole multi-phonon states for the one-dimensional case are investigated in two separate subsections. A simple explanation of observed trends is also provided, re-enforcing the robustness of the observations.

11.1.1 Monopole resonances

Monopole and quadrupole responses obtained from the one-dimensional calculations were described in Sec. 6.6.1 using a set of HFB solutions constrained on different values of the rms radius. The parameter β_2 was left free to vary throughout the minimisation of the HFB energy and came out linearly correlated with the rms radius. Overall, as observed, for instance, in Fig. 6.33, both the monopole and the quadrupole spectra consist of one peak, whose convergence in terms of HFB points had been thoroughly checked.

Higher-energy states were also produced, even if the corresponding transitions to the ground state were not strong enough to be visible in linear scale. The monopole and quadrupole responses from Figs. 6.33 are presented in Fig. 11.1 in logarithmic scale to appreciate the presence of states other than the giant resonance. These regularly spaced high-lying states are identified as multi-phonon states built on top of the main giant resonance.

These results can be usefully compared to a naive one-dimensional quantum harmonic oscillator model, which is discussed, together with perturbative corrections to it, in App. K. Effects associated with AMP, however, are not considered in the harmonic model. In the pure harmonic model, excited states are equally spaced and transitions are non-vanishing only between neighbouring states.

The PGCM energy spectrum of 0^+ states is compared to the harmonic limit obtained in App. K.1 in Fig. 11.2. Cubic and quartic corrections up to second order in perturbation theory (see App. K.2) are

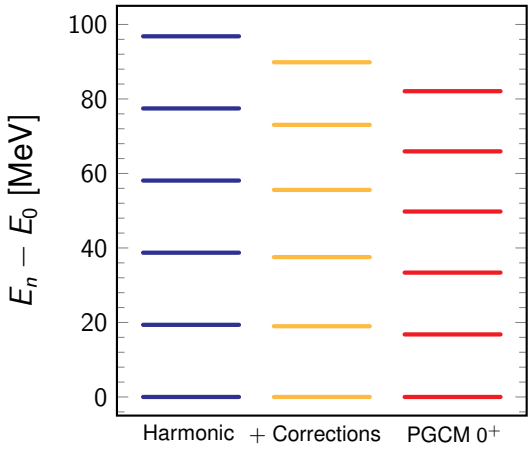

Figure 11.2: Energy spectrum of 0^+ states from a one-dimensional PGCM calculation along the radial coordinate in ^{46}Ti. Results are compared to the harmonic oscillator limit and to its perturbatively-corrected version.

shown for comparison. The inclusion of perturbative corrections improves the overall agreement between the PGCM spectrum and the pure harmonic oscillator model, illustrating how anharmonicities slightly compress the harmonic spectrum.

Monopole transition probabilities between 0^+ states are shown in Fig. 11.3. All possible transitions are displayed, with the exception of transitions between the same state, which amounts to evaluating radii of excited states. Interestingly, only the transitions between neighbouring phonons are strong enough to be visible in Fig. 11.3. The transition between the giant resonance and the next state appears almost exactly at twice the GR's energy, which is highlighted by the presence of the straight lines $\omega_{y(x)} = 2\omega_{x(y)}$. Also, the transitions between neighbouring phonons are extremely close to the anti-diagonal straight lines. They would lie exactly on such lines in the pure harmonic limit.

In Fig. 11.3 the magnitude of the transitions between neighbouring states happens to increase linearly with the degree of the considered phonons. This pattern is highlighted in Fig. 11.4 (left), where the transition probability between neighbouring phonons is displayed as a function of the phonon's number. The linear trend is confirmed, in agreement with the pure quantum harmonic oscillator model, see Eq. (K.7). Anharmonic effects on transition probabilities are thus not significant, even though the very presence of non-vanishing transition probabilities between multi-phonon states and the ground state is a finger print of such anharmonic effects.

The comparison to the quantum harmonic oscillator is extremely useful, and can be pushed further for the benefit of the interpretation of these results. One-dimensional PGCM collective wave-functions are displayed in Fig. 11.4 (right) for the ground state, the giant resonance and the two-phonon state. The resemblance to the eigen-functions of the quantum harmonic oscillator is clear, establishing the second excited state as a phonon built on top of the giant resonance.

11.1.2 Quadrupole resonances

The same analysis is now proposed for quadrupole excitations. Compared to the monopole case, where only $0^+ \to 0^+$ transitions were involved, the landscape is complicated by the possibility for quadrupole transitions to connect states of different angular momentum. While the GQR links the 0^+ ground state to an excited 2^+ state, a subsequent phonon may link such a 2^+ state to a 0^+, 2^+ or 4^+ state, and so on for higher phonons. This is schematised in Fig. 11.5 for the one-dimensional PGCM results. More generally, for J_i being the angular momentum of the initial state and λ the multipolarity of the transition, all the angular

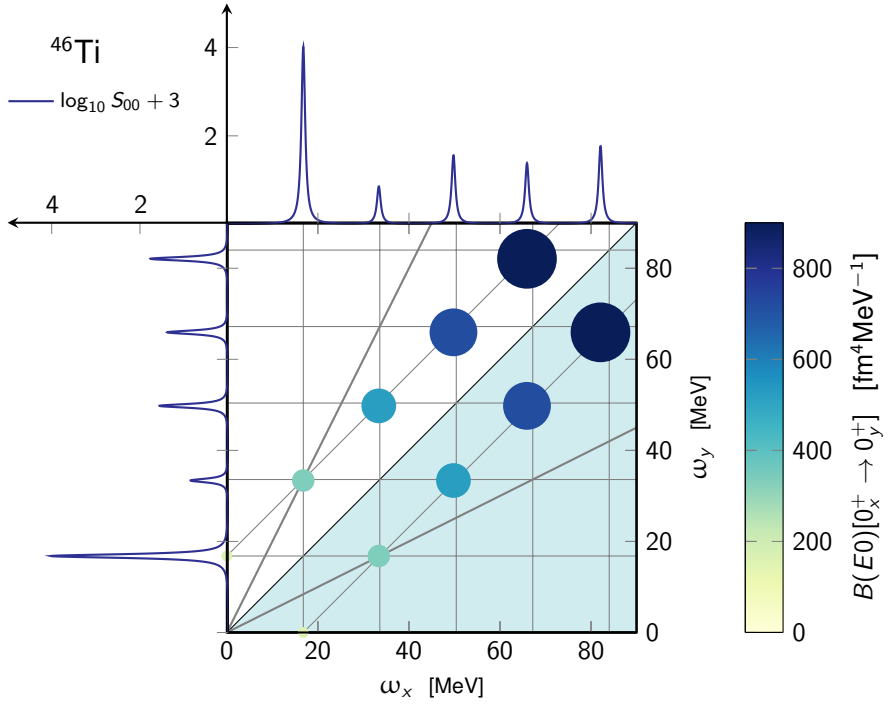

Figure 11.3: Inter-state monopole transitions from the one-dimensional PGCM calculation in ^{46}Ti from Sec. 6.6.1. The ground-state monopole response in logarithmic scale is displayed on the vertical and horizontal axis for comparison. The size of the dots is proportional to the magnitude of the transition probability and re-enforces the color-code content. Grid lines are set at exact multiples of the first-excited-state energy (giant resonance) to accentuate the analogy to the quantum harmonic oscillator (see text for details). In the same spirit the anti-diagonal lines at the crossing between neighbouring phonons are also shown, as well as the straight lines $\omega_{y(x)} = 2\omega_{x(y)}$. All inter-states transitions are included in the plotted data, except those relative to the diagonal (average value of the excited states).

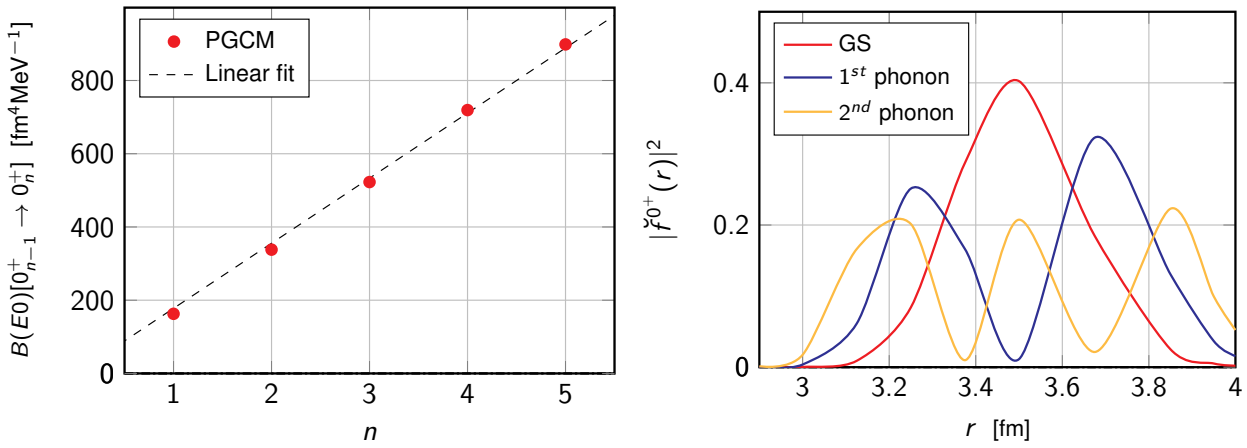

Figure 11.4: **Left**: transition probabilities between neighbouring phonons as a function of the phonons' degree. One-dimensional PGCM results are shown in red together with a dashed lines resulting from a linear fit of the computed points. **Right**: one-dimensional PGCM collective wave-functions in ^{46}Ti relative to ground state and to the two first excited states (giant resonance and two-phonon state).

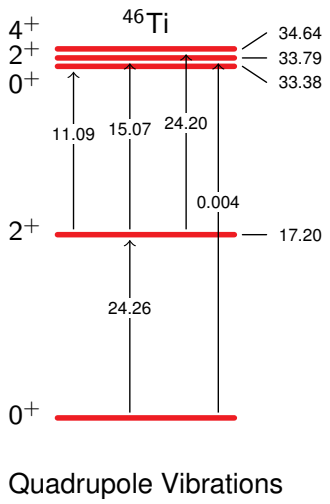

Figure 11.5: Spectrum associated with quadrupole vibrations in ^{46}Ti one-dimensional PGCM calculations. Two successive quadrupole phonons are shown, the second one being made of a triplet of (quasi-degenerate) $J^\pi = 0^+, 2^+, 4^+$ states, see Eq. (11.1). Energies are in MeV and transition probabilities in fm^{4}MeV^{-1}.

momenta

$$J_f \in \{|J_i - \lambda|, |J_i - \lambda| + 1, \ldots, J_i + \lambda - 1, J_i + \lambda\} \tag{11.1}$$

are accessible via such a transition.

Transitions from 2^+ states to 0^+, 2^+ and 4^+ states are represented in Figs. 11.6, 11.7 and 11.8 respectively, leading to the following comments

a) The two halves of the energy-energy planes are asymmetric as far as transition probabilities are concerned. Indeed, since amplitudes are associated with upwards transitions (excitations) from lower to higher energies, the angular momenta of the initial and final states are inverted once the diagonal $\omega_y = \omega_x$ is overcome. Thus, the implicit multiplicities in the definitions of the transition probabilities must change accordingly, following the relation

$$B(E\lambda, f \to i) = \frac{2J_i + 1}{2J_f + 1} B(E\lambda, i \to f). \tag{11.2}$$

b) The dots corresponding to transition probabilities to 0^+ and 4^+ are slightly misaligned with respect to the quadrupole response of the ground state. This effect is due to the fact that the energies of the 2^+ states in the ground-state response and the energies of the 0^+ and 4^+ states involved in the graph are not perfectly degenerate, as visible in Fig. 11.5.

c) The transitions testify the presence of multi-phonon states for all relevant J^π states and the linear trend of the transition probabilities with respect to the phonon number is also reproduced.

Eventually, the prediction of quasi-harmonic multi-phonon states from the one dimensional PGCM calculation is clear for both monopole and quadrupole channels.

11.1.3 Convergence of multi-phonon states

Since multi-phonon states lie at high energies, their convergence is a primary concern in the present investigation. To this purpose, let us recall the tests from Sec. 6.6.1. These calculations explore the numerical

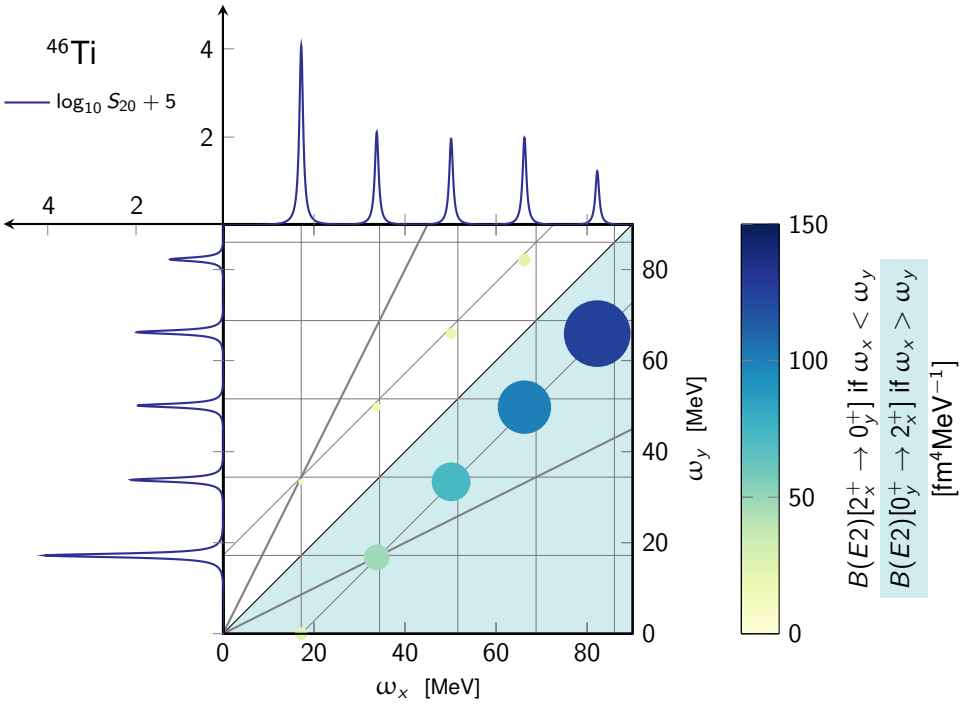

Figure 11.6: Same as Fig. 11.3 for quadrupole transitions from 2^+ to 0^+ states. The quadrupole response to the ground state in logarithmic scale is shown for comparison on the vertical and horizontal axes. Only upwards transitions are displayed (excitations). With respect to the monopole case from Fig. 11.3, the two halves of the plane are asymmetric (as far as the transition probabilities magnitude is concerned) due to the different multiplicities of the initial and final states, see Eq. (11.2).

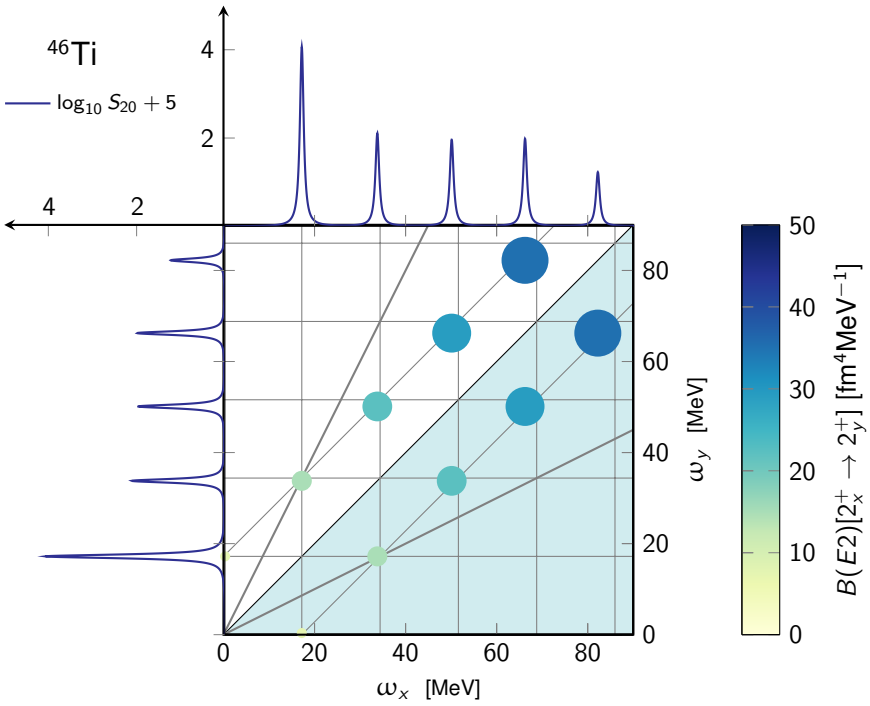

Figure 11.7: Same as Fig. 11.6 for quadrupole transitions from 2^+ to 2^+ states.

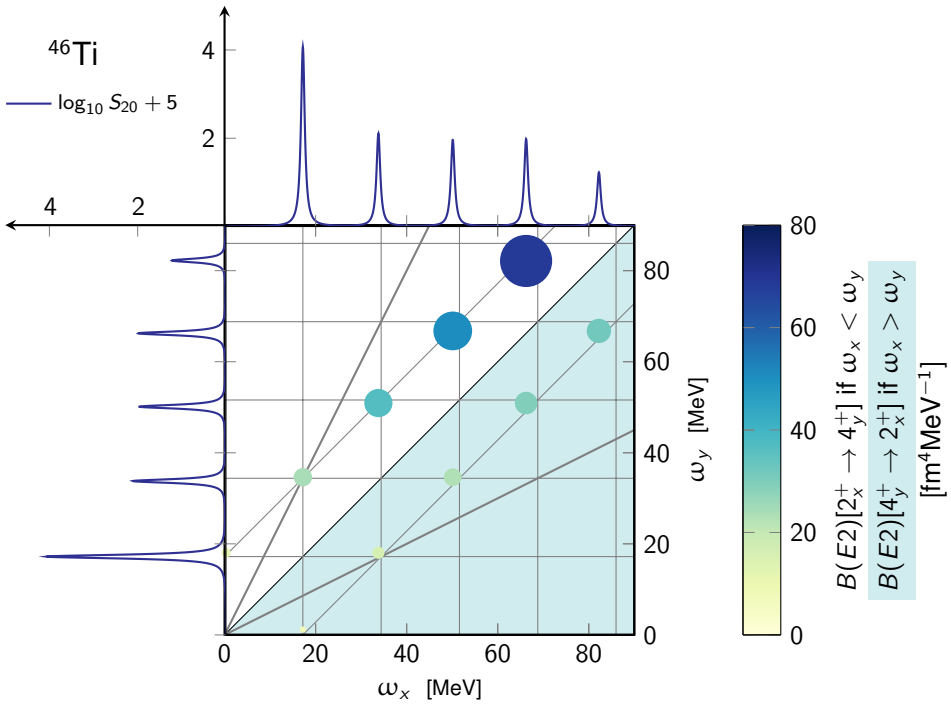

Figure 11.8: Same as Fig. 11.6 for quadrupole transitions from 2^+ to 4^+ states.

stability of PGCM solutions with respect to the energy window of the HFB states included in the PGCM ansatz. It was shown in Sec. 6.6.1 that the giant resonance, in the one-dimensional case, is fully stable in this respect. To investigate higher excited states the quantity

$$\Delta_n\omega \equiv \frac{\omega_n - n\omega_1}{n}, \tag{11.3}$$

ω_1 being the energy of the giant resonance (first excited state) and ω_n the energy of the n-th phonon, is shown in Fig. 11.9. This quantity allows to check simultaneously the numerical convergence and the anhamornicity (the latter manifesting as a departure from zero) of the excited energies.

Values of $\Delta_n\omega$ are negative both in the 0^+ and 2^+ channels, indicating spectra that are more compressed than in the pure harmonic limit, as already illustrated in Fig. 11.2. However, such a compression is mild, i.e. of the order of 0.5 MeV per phonon, to be compared to a phonon energy of ~20 MeV, so that in the one-dimensional case the harmonic limit provides a good description of multi-phonon states.

A similar analysis is carried out for transition probabilities between neighbouring phonons. Figure 11.10 displays the quantity

$$\Delta_n B(E\lambda) \equiv \frac{B(E\lambda, n-1 \to n) - nB(E\lambda, 0 \to 1)}{n} \tag{11.4}$$

for multi-phonon states built on both the GMR and the GQR. The factor $1/n$ is included to remove the trivial dependence on n previously pointed out and formalised in Eq. (K.7). This quantity provides access both to numerical instabilities and departures from the harmonic limit. As for the energy eigen-values, results from Fig. 11.10 both confirm a close relation to the harmonic limit (order of 1% difference per phonon) and a sound numerical convergence of high-lying multi-phonon states.

These results are particularly interesting as they indicate that PGCM states located 60-80 MeV above the ground state are well converged when including points in the total HFB energy surface lying only within a 20 MeV window above the minimum.

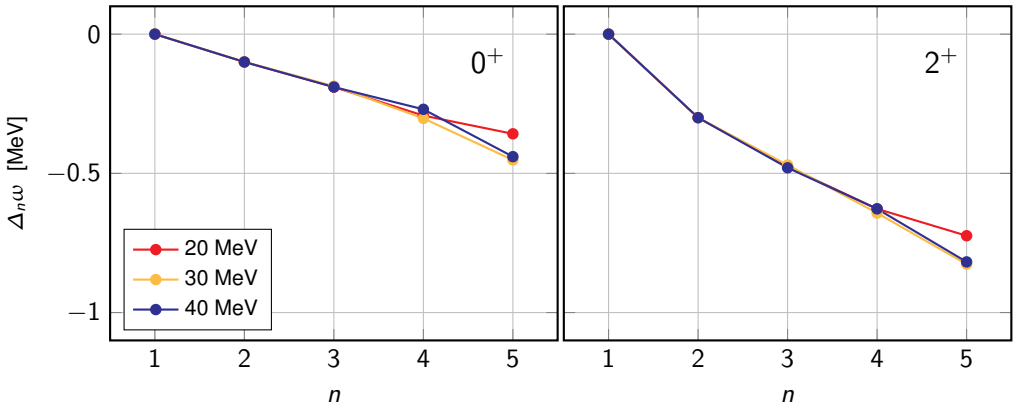

Figure 11.9: Numerical convergence of the excited-states energies as a function of the phonon number for (**left**) 0^+ and (**right**) 2^+ excited states for different PGCM calculations (labels are referred to Fig. 6.32). Different energy labels relate to the maximal energy difference with respect to the HFB minimum of the HFB states entering the PGCM ansatz.

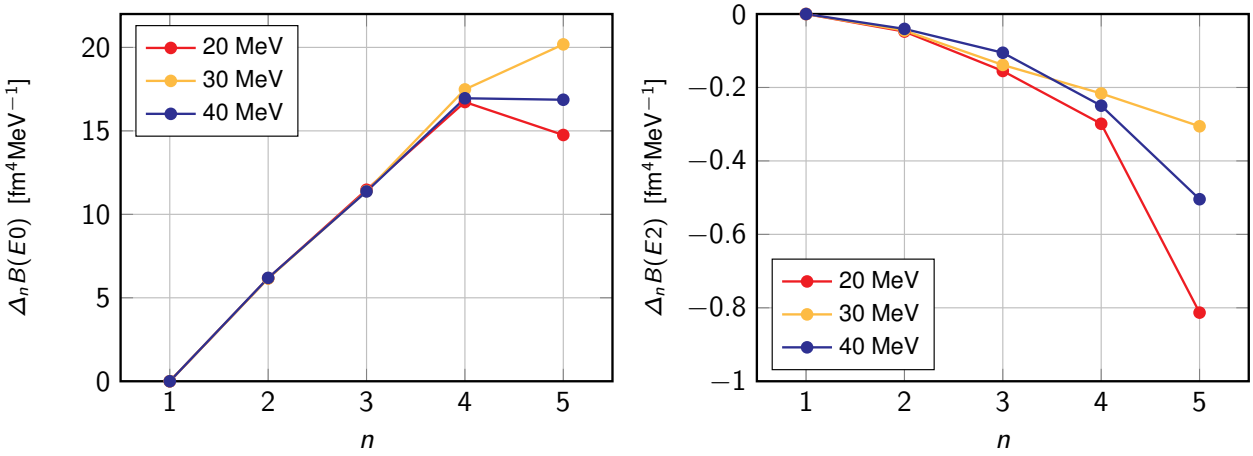

Figure 11.10: Numerical convergence of the transition probabilities between neighbouring phonon states as a function of the phonon number for (**left**) 0^+ and (**right**) 2^+ excited states for different PGCM calculations (labels are referred to Fig. 6.32). Different energy labels relate to the maximal energy difference with respect to the HFB minimum of the HFB states entering the PGCM ansatz.

11.1.4 Remarks

As a summary, four criteria are listed to characterise multi-phonon states in PGCM calculations

1. States shall exist at energies close to integer multiples of the giant-resonance energy,
2. Transition probabilities must be maximised between neighbouring phonons,
3. A linear trend in the transition probability between neighbouring phonons must be observed,
4. Intrinsic PGCM collective wave-functions must validate the multi-phonon character of the excited states.

If quadrupole states are addressed

5. States associated with all accessible angular momenta must be quasi-degenerate and fulfil the above conditions.

While these observations concern multi-phonon states built on giant resonances nothing prevents multi-phonon states to be built on excited states other than the giant resonances [186]. Consequently, fully realistic calculations may display more involved situations than the one described above for one-dimensional PGCM calculations. This will be exemplified in the following sections.

11.2 Realistic calculations

In the previous section an extensive study about the appearance of multi-phonon states in a simple one-dimensional PGCM calculation was presented. Such states naturally emerge from PGCM, such that they are expected to manifest also in more complex multi-dimensional calculations. In that case, however, one expects the situation to be possibly less transparent. In this section, results in ^{46}Ti and ^{28}Si, previously shown in Sects. 7.2 and 7.3 respectively, are further analysed to investigate the possible occurrence of multi-phonon states. This possibility is scrutinised in the monopole channel for ^{46}Ti and in the quadrupole one for ^{28}Si.

11.2.1 Multi-phonon monopole states in ^{46}Ti

Results from the two-dimensional PGCM calculation in the (r, β_2) plane for ^{46}Ti were extensively discussed in Chaps. 6 and 7. The energy spectrum gathering the three first 0^+ states is displayed in Fig. 11.11, whereas monopole transition probabilities are shown in Fig. 11.12. The ground-state monopole response is also plotted in logarithmic scale along the vertical and horizontal axes.

The landscape is necessarily more complex than in the one-dimensional calculation. Indeed, many strong transitions appear between states that are seemingly not directly connected to the GMR. Candidates for multi-phonon GMR states are, however, found. In Fig. 11.12 coloured dashed lines highlight the energies of the GMR and the two- and three-phonon states candidates built on it, appearing close to integer multiples of the GMR energy. $B(E0)$ strength mildly emerges with respect to the surrounding states. The crossing of such coloured lines is marked by significant monopole strength, increasing linearly with respect to the phonon numbers. Numerical values relative to these states are compared in Tab. 11.1 to predictions of the pure harmonic oscillator model. For both energy and transition probabilities a good agreement is observed.

The intrinsic PGCM collective wave-function of the candidate two-phonon state is compared in Fig. 11.13 to those of the ground-state and of the GMR. The wave-function distribution along the radial coordinate is qualitatively coherent with a quantum harmonic oscillator picture. Especially, the disposition of nodes and maxima going from ground- to first- and to second-excited state is respected.

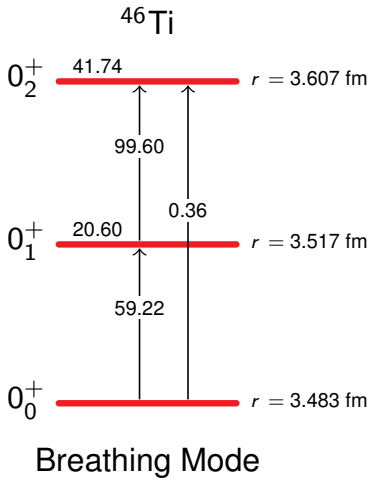

Figure 11.11: 0^+ spectrum in ^{46}Ti from two-dimensional PGCM. Energies are in MeV and transition probabilities in fm^{4}MeV^{-1}.

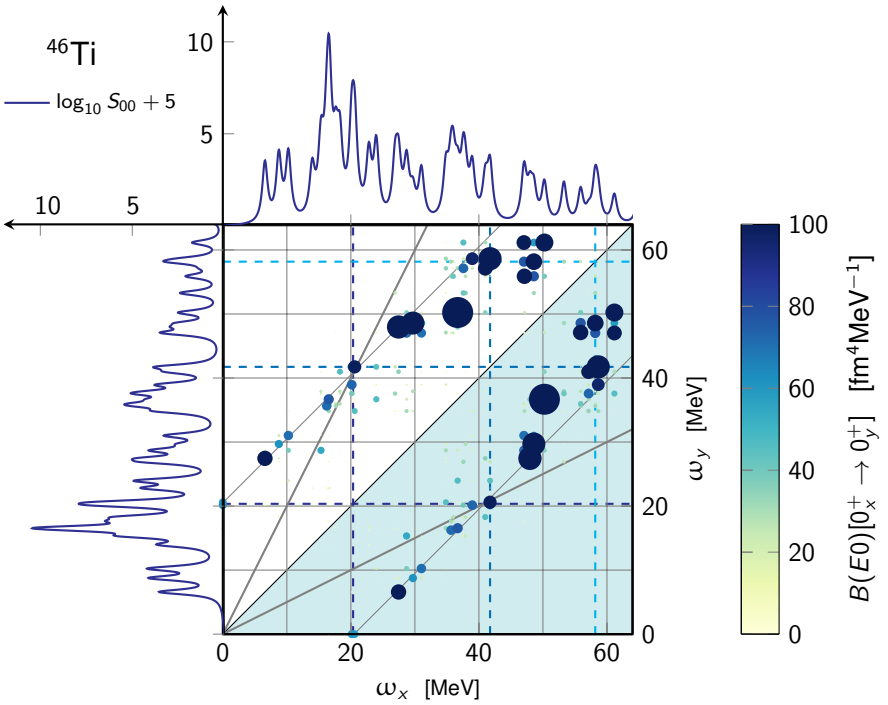

Figure 11.12: Inter-state monopole transitions from the two-dimensional PGCM calculation in the (r, β_2) for ^{46}Ti from Sec. 7.2. The ground-state monopolar response in logarithmic scale is displayed on the vertical and horizontal axis for comparison. The size of the dots is proportional to the magnitude of the transition probability and reinforces the colour-code content. Dashed lines are drawn in correspondence of high-lying states that are expected to represent the multi-phonon states of the GMR. The anti-diagonal lines highlights the locus of suitable points for multi-phonon states to appear, the straight lines $\omega_{y(x)} = 2\omega_{x(y)}$ are also shown. All inter-states transitions are included in the plotted data, excepting those relative to the diagonal (average value of excited states).

n	ω_n [MeV]	$n\omega_1$ [MeV]	$B(E0)_n$ [fm^{4}MeV^{-1}]	$nB(E0)_1$ [fm^{4}MeV^{-1}]
1	20.6	20.6	59.2	59.2
2	41.7	41.2	99.6	118.4
3	58.6	61.8	174.4	177.7

Table 11.1: Energy eigenvalues and transition probabilities for the giant monopole resonance and candidate two- and three-phonon states in ^{46}Ti obtained via PGCM calculations from Sec. 7.2, compared with integer multiples of the GMR values expected in the harmonic trend.

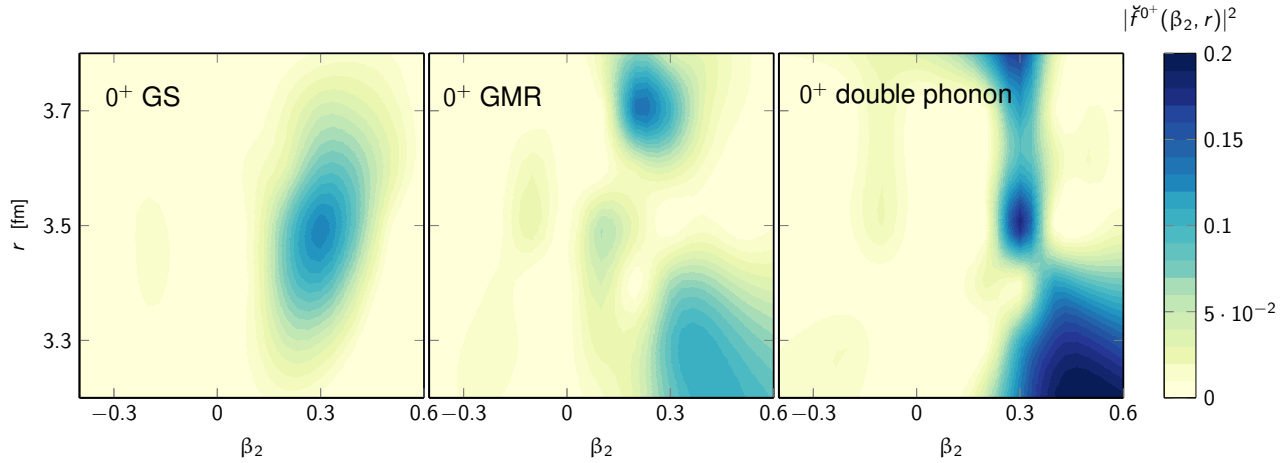

Figure 11.13: Intrinsic collective PGCM wave-functions in the plane (β_2, r) for the 0_0^+ ground state (left), the 0_1^+ GMR (centre) and the candidate two-phonon 0_2^+ state (right) in ^{46}Ti.

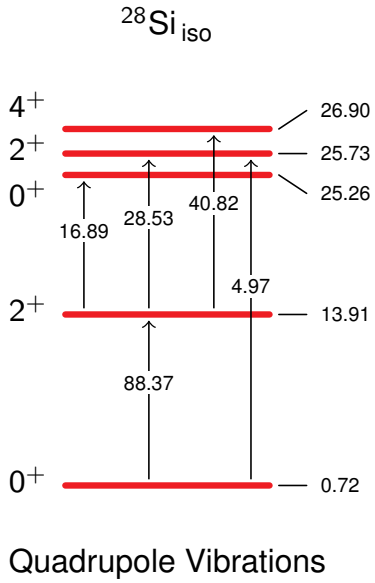

Figure 11.14: Spectrum associated with quadrupole vibrations in ^{28}Si. The lowest state is the prolate-shape isomer. Two successive quadrupole phonons are shown, the second one being made of a triplet of (quasi-degenerate) $J^\pi = 0^+, 2^+, 4^+$ states, see Eq. (11.1). Energies are in MeV and transition probabilities in fm^{4}MeV^{-1}.

Eventually, all the criteria proposed in Sec. 11.1.4 on the basis of a simple one-dimensional description are satisfied by the multi-phonon candidates in the two-dimensional PGCM calculation. ^{46}Ti is, thus, proposed as a potential system suitable for the investigation of multi-phonon states built on the GMR.

11.2.2 Multi-phonon quadrupole states in ^{28}Si

In Sec. 7.3, a giant quadrupolar resonance based on the prolate-shape isomer state of ^{28}Si was predicted. In this section multi-phonon states built on this GQR are investigated. The excitation spectrum associated with the two first quadrupolar phonons is displayed in Fig. 11.14: the multi-phonon picture is very well satisfied, which can be also noticed comparing to the ideal one-dimensional case in Fig. 11.5 for ^{46}Ti.

The inter-state $B(E2)$ are shown in Figs. 11.15, 11.16 and 11.17 for transitions from 2^+ states to 0^+, 2^+ and 4^+ states respectively. The prolate-shape isomer quadrupole response in logarithmic scale is also plotted along the vertical and horizontal axes. As for realistic monopole transitions in ^{46}Ti, a large set of transitions emerges for all three final-state angular momenta due to the large number of accessible states in the two-dimensional PGCM calculation.

Overall, three well-defined peaks are distinguished in the isomer response. The corresponding energies are highlighted with coloured dashed lines. Large transition probabilities are located at the crossing of such lines or in their immediate vicinity (mild shift are produced by the non-exact degeneracy of the corresponding 0^+, 2^+ and 4^+ states). However, $B(E2)$ transition probabilities between neighbouring candidates do not increase linearly with the phonon number as expected for ideal multi-phonon states.

The intrinsic collective PGCM wave-functions of the prolate isomer, the GQR and the candidate two-phonon state are compared in Fig. 11.18. Imagining the $K = 0$ component of the quadrupole resonance to be associated to vibration along the β_2 coordinate, the positioning of maxima and nodes with respect to such coordinate is close to a quantum-harmonic-oscillator-like trend, which supports the argument for the

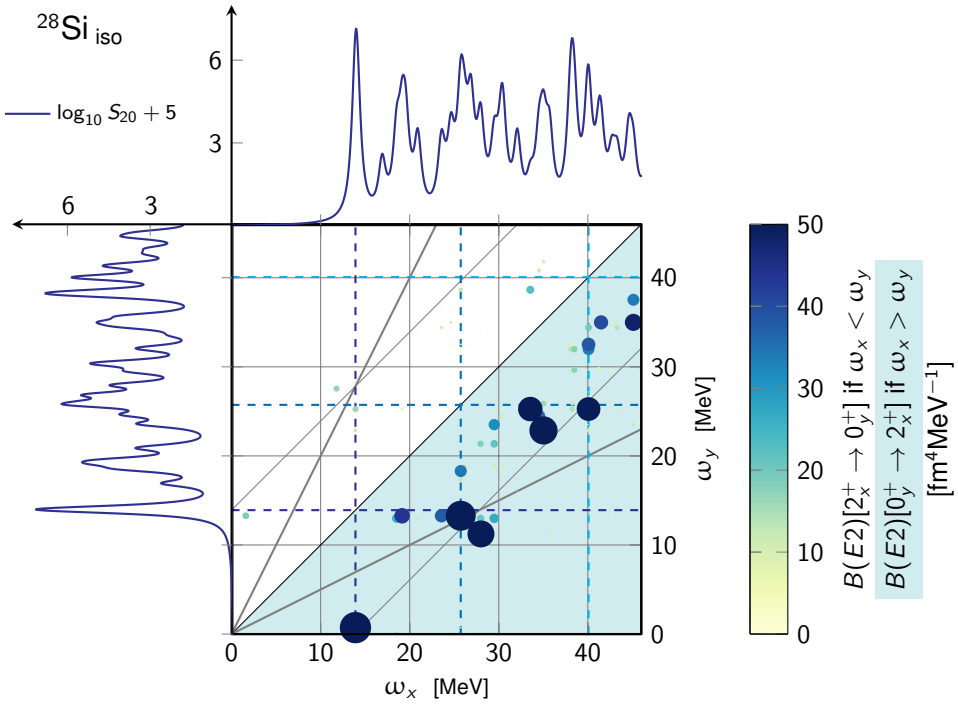

Figure 11.15: Inter-state quadrupole transitions from 2^+ to 0^+ states for two-dimensional PGCM calculations in the (r, β_2) for ^{28}Si from Sec. 7.3. The prolate-isomer quadrupolar response in logarithmic scale is displayed on the vertical and horizontal axis for comparison. The size of the dots is proportional to the magnitude of the transition probability and reinforces the colour-code content. Dashed lines are drawn in correspondence of high-lying states that are expected to represent the multi-phonon states of the GQR. The anti-diagonal lines highlights the locus of suitable points for multi-phonon states to appear, the straight lines $\omega_{y(x)} = 2\omega_{x(y)}$ are also shown. All inter-states transitions are included in the plotted data, excepting those for which the condition $|\omega_x - \omega_y|$ <2 MeV is verified. Only upwards transitions are displayed (excitations). The two halves of the plane are asymmetric (as far as the transition probabilities magnitude is concerned) due to the different multiplicities of the initial and final states, see Eq. (11.2).

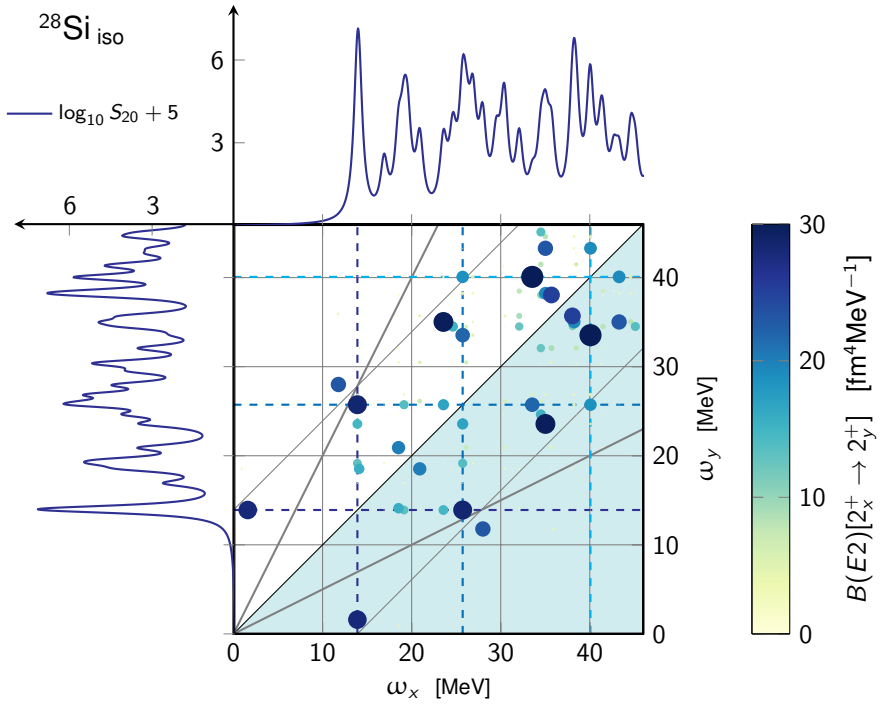

Figure 11.16: Same as Fig. 11.15 for 2^+ to 2^+ quadrupolar transitions.

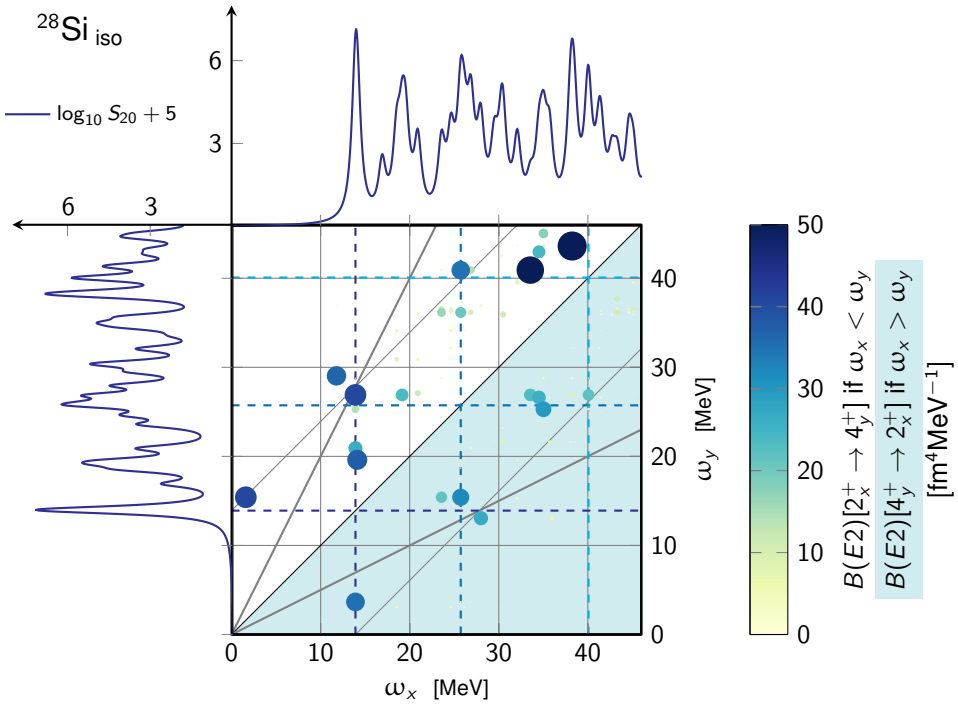

Figure 11.17: Same as Fig. 11.15 for 2^+ to 4^+ quadrupolar transitions.

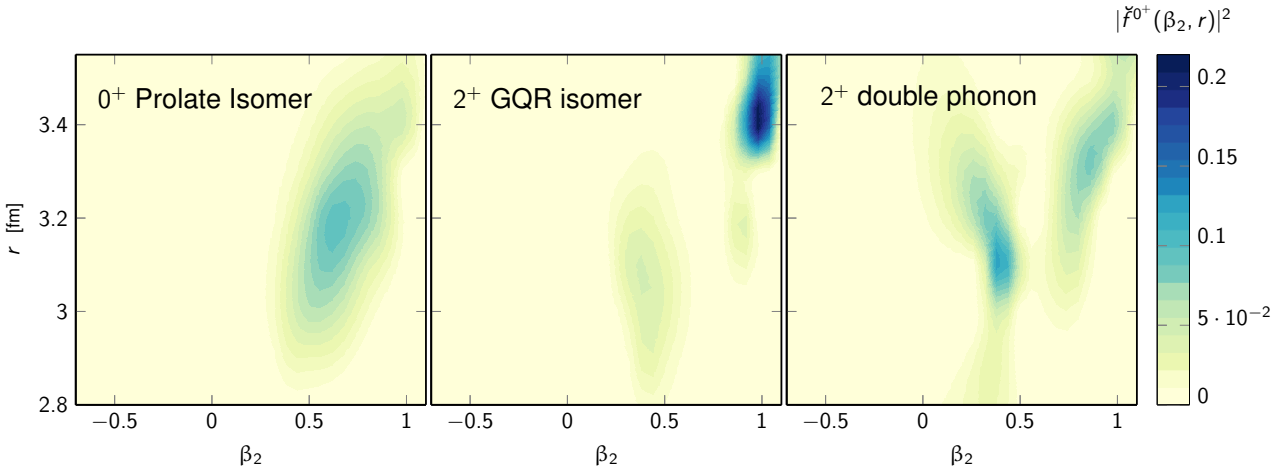

Figure 11.18: Intrinsic collective PGCM wave-function in the plane (β_2, r) for the 0^+ ground state (left), the 2^+ GQR (center) and the candidate two-phonon state (right) in ^{28}Si.

presence of multi-phonon GQR states on top of the prolate shape isomer in ^{28}Si.

Eventually, multi-phonon states are predicted, even though their identification with harmonic phonons is less clear than for multi-phonon states built on top of the GMR in ^{46}Ti due to the absence of a linear increase of $B(E2)$ transition probabilities in ^{28}Si. It was pointed out in Sec. 9.2 that ^{28}Si deviates more from a pure harmonic limit than ^{46}Ti based on the evaluation of cubic and quartic perturbative corrections. Hence, larger deviations from the harmonic trend could indeed be expected regarding multi-phonon states.

Chapter 12

Numerical Results in PAV RPA

Contents

> If you try and take a cat apart to see how it works, the first thing you have on your hands is a non-working cat.
>
> Douglas Adams

Three levels of rotational symmetry breaking and restoration were systematically introduced in Sec. 5.2, in order to account for rotation-vibration coupling effects on different levels. A program to develop such formalisms within GCM and (Q)RPA was proposed in Tab. 5.1. All three levels, i.e. unprojected, PAV AMP and VAP AMP, are already accessible within GCM, and their differences were discussed in Chap. 8. In this chapter numerical results relative to the *a posteriori* angular-momentum projected RPA (PAV RPA) strengths [147, 145], introduced in Chap. 5 are presented. This parallels PAV GCM results from Chap. 8 within the *ab initio* framework. An implementation of PAV QRPA in our *ab initio* QFAM numerical code being more involved due to the lack of an explicit wave-function representation of the QRPA phonons, PAV RPA has been implemented in an existing EDF-QRPA framework.

A QRPA code allowing for axially-deformed calculations [70, 154] was used as a base and the SkM* functional [190] was employed. The implementation was realised without taking into account pairing correlations, such that axially-deformed[1] HF solutions were used as reference states. Basic properties of the HF

[1]The axial quadrupole deformation parameter, defined in this chapter as [191]

$$\beta \equiv \sqrt{\frac{\pi}{5}} \frac{\langle Q_{20} \rangle_\pi + \langle Q_{20} \rangle_\nu}{\langle r^2 \rangle_\pi + \langle r^2 \rangle_\nu} \tag{12.1}$$

, is employed to generate the reference state of the QRPA solution.

	E_{HF} [MeV]	r [fm]	β
^{4}He	-26.63	1.984	0.00
^{20}Ne	-155.94	2.876	0.35
^{24}Mg	-195.65	2.991	0.38
^{28}Si	-235.72	3.027	-0.21

Table 12.1: Hartree-Fock ground-state energy E_{HF}, root mean square radius r and axial quadrupole deformation β of the HF vacuum adopted for RPA calculations in this chapter.

vacua obtained for the nuclei of present interest are reported in Tab. 12.1. Unless stated otherwise, calculations were performed in an $e_{\max} = 6$ model space, with $\hbar\omega = 17$ MeV. RPA calculations were performed in the $K = 0$ channel and a ph excitation energy cut-off $E_{cut} = 100$ MeV was applied for all presented results, unless differently specified. The spectra are convoluted with a Lorentzian function making use of a smearing parameter $\Gamma = 0.5$ MeV for a better readability.

In the forthcoming sections the ***reduced matrix elements*** associated with the unperturbed response (Eq. (5.62))

$$\langle \mathrm{HF}||Q_\lambda||ph\rangle = \sum_{\mu=-\lambda}^{+\lambda} \begin{pmatrix} J_0 & \lambda & J \\ -K_0 & \mu & K_0-\mu \end{pmatrix} \langle \mathrm{HF}|Q_{\lambda\mu} P^J_{K_0-\mu,K_{ph}} c_p^\dagger c_h|\mathrm{HF}\rangle \,, \tag{12.2}$$

are computed to analyse the effects of AMP on RPA strength functions. This corresponds to setting ($X^\omega_{ph} = 1$, $Y^\omega_{ph} = 0$) for the ph excitation of interest while neglecting the others, i.e. it allows to study the unperturbed one-particle-one-hole response of the nucleus under examination.

In Sec. 12.1 the PAV RPA code is benchmarked on a spherical system to ensure the correctness of the implementation. In Sec. 12.2 results obtained for the prolate nucleus ^{24}Mg are presented. Systematic calculations follow in Sec. 12.3 in order to address the numerical stability of the observed results. Eventually Sec. 12.4 discusses the nature of the vibration-rotation coupling in deformed systems.

12.1 Benchmark in ^{4}He

Because of its closed-shell nature and its simple structure, ^{4}He represents an excellent candidate to test the projection tool. In particular, the HF ground state is spherical, such that no effect from the AMP is expected, i.e.

$$N_0 = \langle \mathrm{HF}|P^0_{00}|\mathrm{HF}\rangle\big|_{^4\mathrm{He}} = 1 \,, \tag{12.3}$$

as is visible from the J-decomposition of the HF ground state in Fig. 12.1 (left). The J-decomposition of the $K_{ph} = 0$ ph elementary excitations is displayed in Fig. 12.1 (right). For all ph excitations under study the sum rule obtained in Eq. (5.73) is satisfied, which constitutes a strong benchmark of the projection. While the HF ground state can only contain even-J components due to reflection symmetry, ph excitations may carry odd-J components.

The unperturbed lp-lh monopole response is analysed with and without AMP in Fig. 12.2 (left). No appreciable difference between the two sets of matrix elements is observed. Eventually, the full RPA monopole response is plotted in Fig. 12.2 (right) together with its projected version, both in the isoscalar and isovector channels. The HF ground state carrying a good $J = 0$ angular momentum and given the monopole nature of the excitation, the original and projected spectra exactly coincide. The same analysis is carried in Figs. 12.3 for the $K = 0$ component of the quadrupole response, leading to analogous results.

In Fig. 12.4 the dominant ph components making up the monopole and quadrupole RPA peaks are characterised. The RPA normalising condition from Eq. (5.64) provides access to the weight of each ph

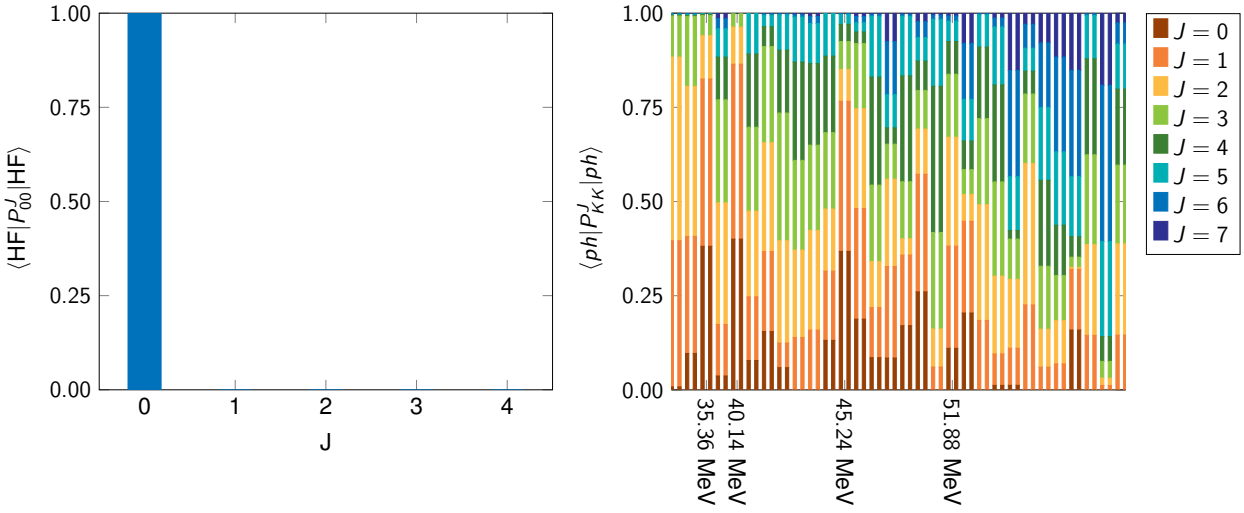

Figure 12.1: **Left**: J decomposition of the HF ground state in ^{4}He. **Right**: J decomposition of the ph states with $K_{ph} = 0$ in ^{4}He. While ph excitations are sorted according to their unperturbed excitation energy $e_p - e_h$, their position along the x-axis is not linear with respect to it. Certain energies are explicitly quoted in connection with the main transitions visible in Figs. 12.2 and 12.3.

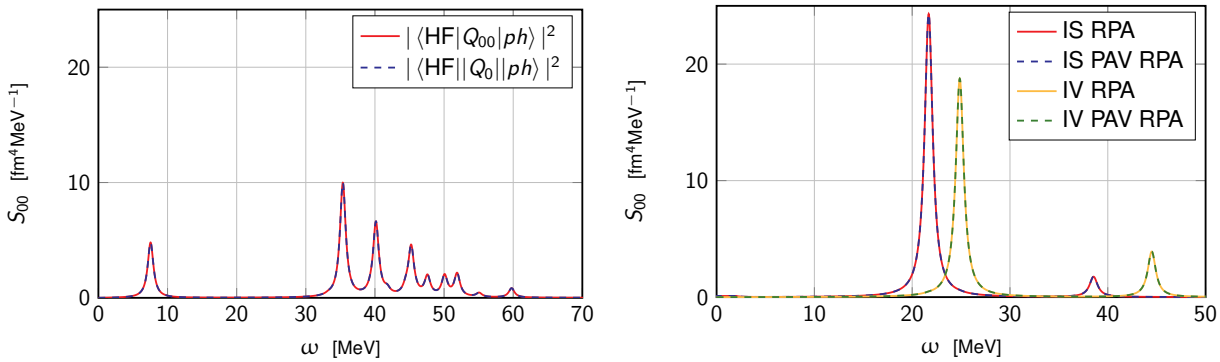

Figure 12.2: ^{4}He monopole response: **Left**: unperturbed 1p-1h response, **Right**: full RPA response.

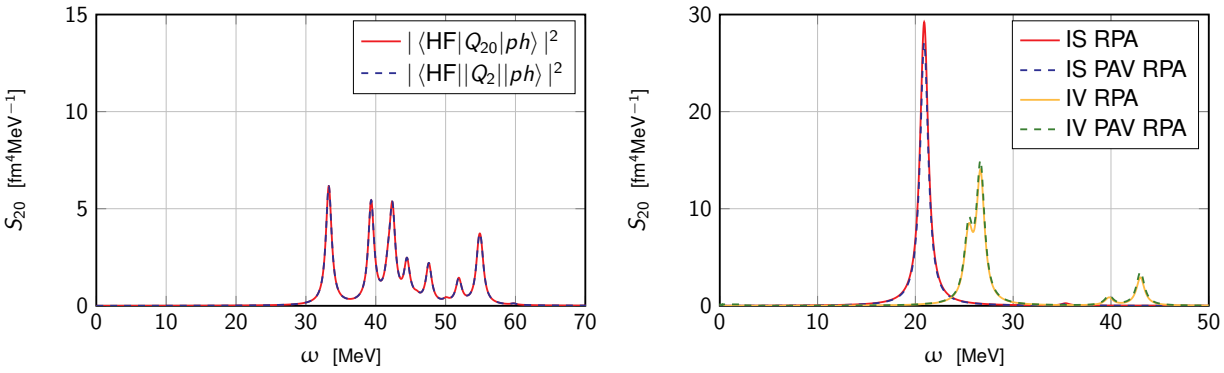

Figure 12.3: ^{4}He quadrupole response in the $K = 0$ channel: **Left**: unperturbed 1p-1h response **Right**: full RPA response.

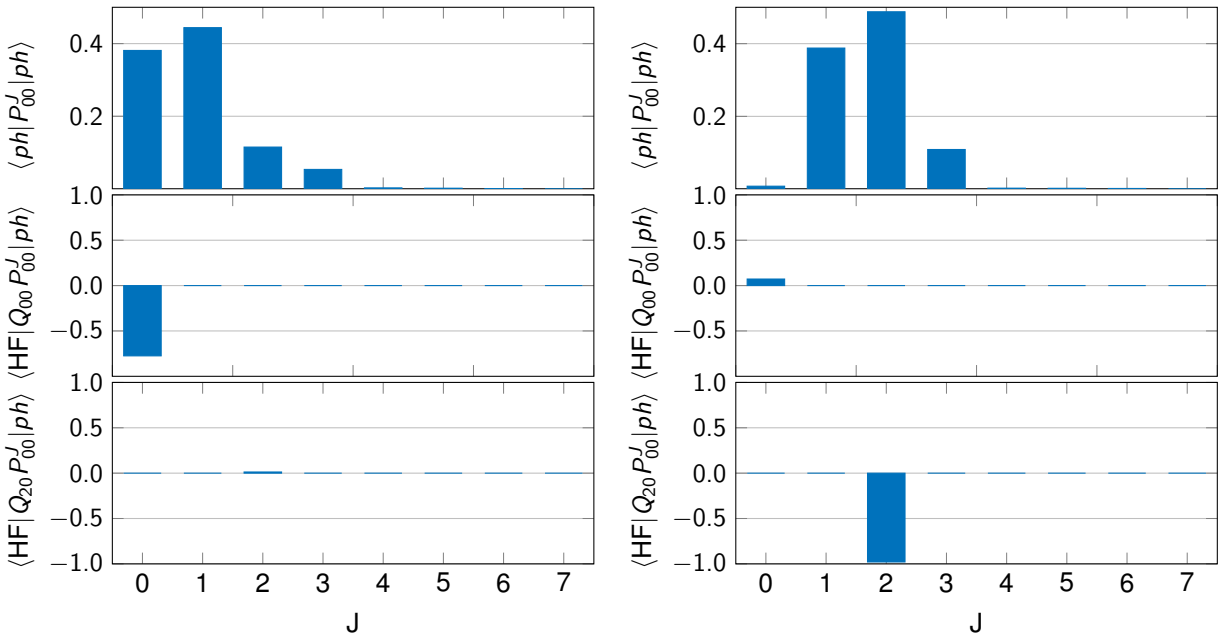

Figure 12.4: **Left**: Dominant ($\zeta^{\omega}_{ph} \sim 0.32$ for protons and $\zeta^{\omega}_{ph} \sim 0.18$ for neutrons) ph components in the isoscalar monopole resonance at ~ 21.7 MeV in ^{4}He. **Right**: Dominant ($\zeta^{\omega}_{ph} \sim 0.20$ for protons and $\zeta^{\omega}_{ph} \sim 0.20$ for neutrons) ph components in the isoscalar quadrupole resonance at ~ 20.9 MeV in the $K = 0$ channel in ^{4}He. See text for details.

component in a phonon according to

$$\zeta^{\omega}_{ph} \equiv |X^{\omega}_{ph}|^2 - |Y^{\omega}_{ph}|^2 , \tag{12.4}$$

such that

$$\sum_{ph} \zeta^{\omega}_{ph} = 1 . \tag{12.5}$$

Essentially, ζ^{ω}_{ph} allows one to identify the dominant ph component for any RPA phonon $|\omega\rangle$. Figure 12.4 (left) characterises the dominant ph component of the ISGMR displayed in Fig. 12.2 (right). The J distribution of this ph component is mostly located in $J = 0, 1$ channels, with less relevant contributions from higher J's. The response of the monopole operator is fully provided by the $J = 0$ component, given the spherical nature of the HF ground state. The same analysis is shown in Fig. 12.4 (right) for the dominant component of the ISGQR from Fig. 12.3 (right). In this case the dominant ph component is mostly of $J = 2$ character and the response of the operator Q_{20} is entirely due to this component.

Overall, the sum rules from Eqs. (5.73), (5.74), (5.75), (5.77) and (5.78) have all been numerically checked. It is found that projected and unprojected RPA responses are strictly identical, as expected for a spherical system, which is a necessary condition to validate the numerical implementation.

12.2 ^{24}Mg

The aim of AMP being to restore the rotational symmetry in the strength functions of intrinsically-deformed nuclei, let us now focus on ^{24}Mg as case of greater interest. The HF ground state is found to minimise the HF energy for a deformation parameter $\beta = 0.38$. Correspondingly, the J decomposition of the HF wave-function is spread over several (even) J's. As shown in Fig. 12.5, the dominant components are found to be $J = 2, 4$. Notice that Eq. (5.73) is satisfied such that the J-components sum up to the unity.

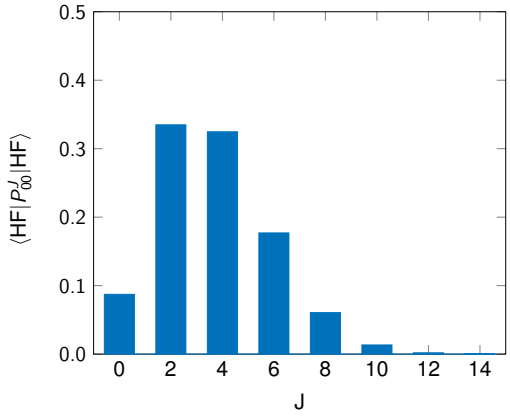

Figure 12.5: J decomposition of the HF ground state in ^{24}Mg

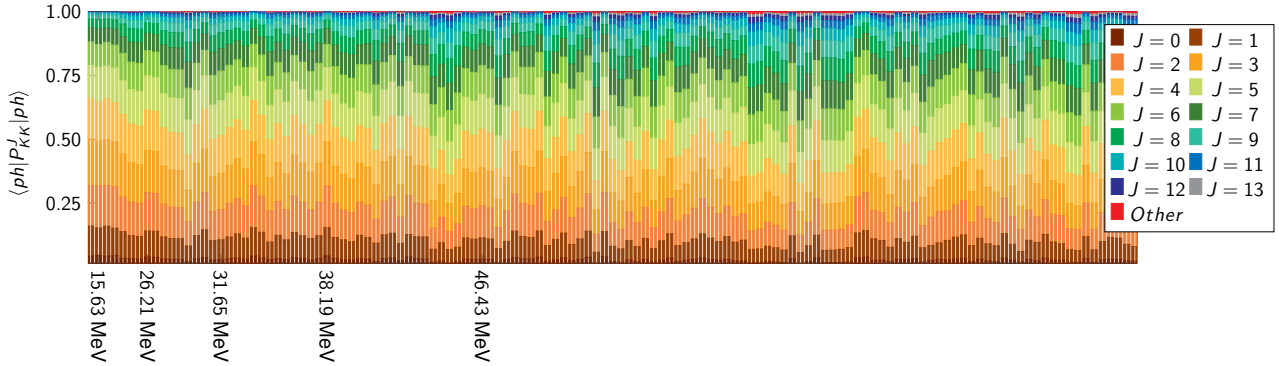

Figure 12.6: J decomposition of the ph states carrying $K_{ph} = 0$ in ^{24}Mg. While ph excitations are sorted according to their unperturbed excitation energy $e_p - e_h$, their position along the x-axis is not linear with it. Certain energies are quoted in connection with the main transitions visible in Figs. 12.9 (right) and 12.10 (right).

The J distribution of ph excitations is more homogeneous than for a spherical HF ground state, as visible in Fig. 12.6. Simultaneously, each ph state spreads over many more J's values up to high angular momenta: whereas in ^{4}He (Fig. 12.1 (right)) the sum rule in Eq. (5.75) was basically exhausted at $J = 7$, ph states in ^{24}Mg shows non-negligible components up to $J = 14$.

The sum rule in Eq. (5.74) is verified for all $K_\omega = 0$ phonons as visible from Fig. (12.7). It is interesting to observe that only natural-parity states are obtained, i.e. states of positive (negative) parity only display even (odd) J components.

The identities from Eq. (5.77) and (5.78) were also numerically validated. An example of the exhaustion of both sum rules is provided in Fig. 12.8 for two selected phonons. Despite the orthogonality between the HF ground state and the phonons, the different J components of the HF and phonon states are not separately orthogonal, but the different J projections eventually sum up to zero. A similar effect is observed for the matrix element of Q_{00}, where the various J components eventually sum up to the original RPA value but low and high J values contributing with opposite signs.

The projected monopole unperturbed strength is compared to the unprojected one in Fig. 12.9 (left). Differently from ^{4}He the large deformation of the ^{24}Mg HF ground state leads to a strong suppression of most matrix elements. Indeed, except for two ph excitations at ∼15 MeV, all amplitudes are strongly reduced due to the AMP on $J = 0$.

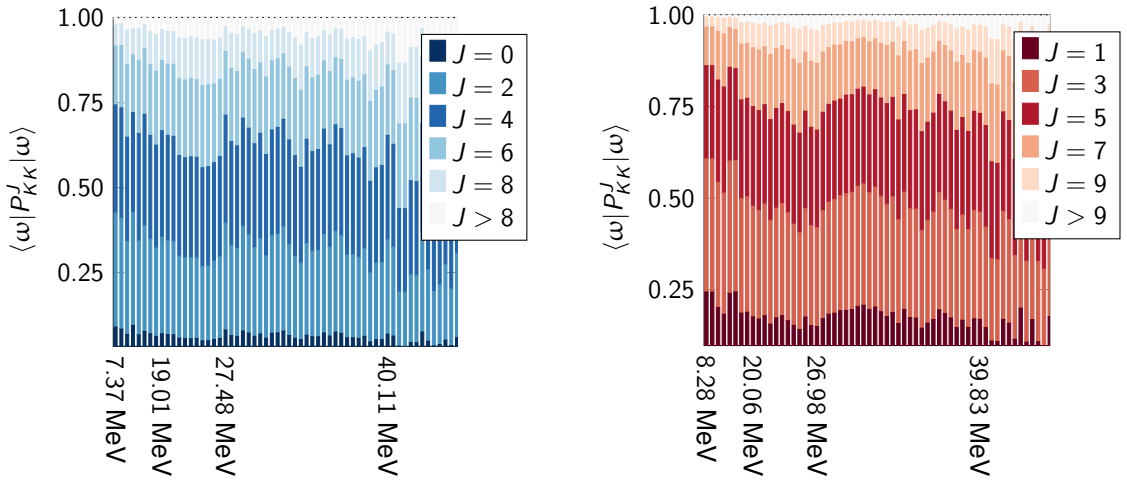

Figure 12.7: J decomposition over even **(left)** and odd **(right)** J values for RPA phonons carrying $K_\omega = 0$ in ^{24}Mg. While phonon excitations are sorted according to their excitation energy, their position along the x-axis is not linear with respect to it. Certain energies are explicitly quoted in connection with the main transition visible in Figs. 12.9 (right) and 12.10 (right).

Moving to the RPA response the situation is very different from the one encountered in ^{4}He, as seen in Fig. 12.9 (right). While only minor changes are identified in the IV channel, the IS response is dramatically affected (notice the factor 1/10 in front of the projected IS monopole response) by the AMP, which was also observed in Refs. [147, 145]. The most remarkable effect is the appearance of a prominent strength in the $5-15$ MeV region. This effect is not associated to an anomalous behaviour of the phonons' normalisation factor, as visible from the bottom panel of Fig. 12.9.

The differences between unprojected and projected spectra are similar in the unperturbed and RPA cases. The unperturbed 1p-1h response displays a sharp increase for two excitations around 15 MeV whereas a global suppression occurs for excitations between 20 and 40 MeV. As a direct consequence, a significant amount of strength appears in the RPA response for a few phonons in the 8-15 MeV interval.

The $K = 0$ component of the quadrupolar response is analysed in Fig. 12.10. The matrix elements are more uniformly affected than in the monopole case, as can be appreciate in the left panel. Indeed, all ph transition amplitudes are strongly suppressed. The magnification of the ph transitions at ~15 MeV is no longer observed. Consequently, the projected RPA response (right panel) shows little difference with respect to the original RPA response, both in the IS and IV channels.

The appearance of a large monopole strength in the 5-15 MeV region when projection is introduced is shown to be associated with a strong overlap with the rotational state defined in Eq. (5.88). The quantity a_ω defined in Eq. (5.90) requires the knowledge of the normalising constant of the rotational state. However, it cannot be properly determined for the RPA ground state; i.e. only for the uncorrelated HF ground state. Thus, the quantity

$$|\langle \mathrm{RPA}|P^0|\omega\rangle|^2 = |a_\omega|^2 N^{-2}_{\mathrm{ROT}} \tag{12.6}$$

is plotted instead in Fig. 12.11, together with the monopole RPA and PAV RPA responses. It is observed that the projected response is magnified for the phonons whose overlap with the rotational state is large. The same effect was observed in PAV GCM calculations in Chap. 8.

Figure 12.12 shows, in linear and logarithmic scale, the rotational strength of the RPA phonons as a function of the rotation angle. The strength is strongly concentrated in the low-energy states where the anomalous appearance of monopole strength is identified. The maximal overlap is mostly concentrated around a finite rotation angle $\beta \approx \pi/6$ and is symmetric with respect to $\pi/2$.

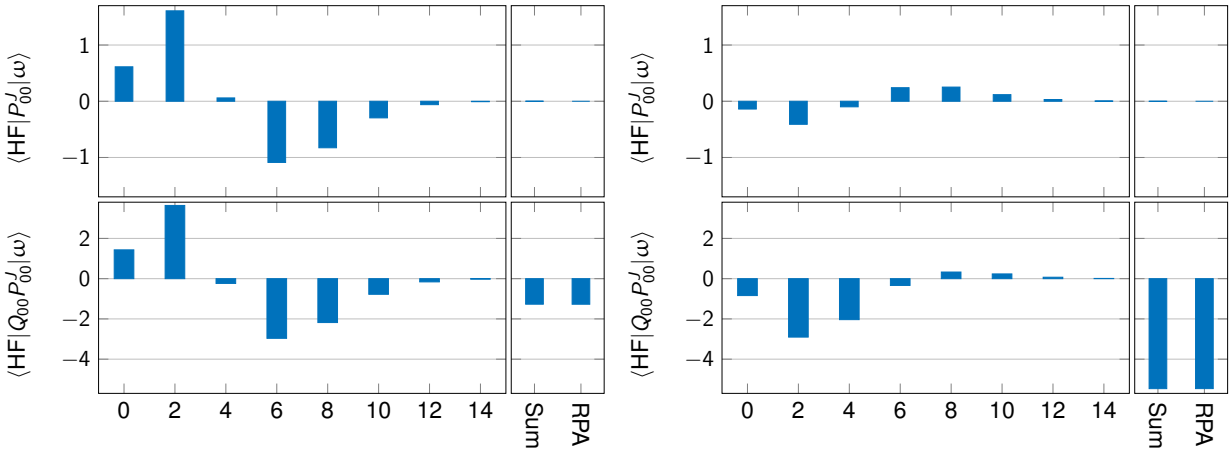

Figure 12.8: ^{24}Mg J-decomposition of the (bottom) monopole transition strength and (top) ground state-phonon overlap for (**left**) the phonon at 11.60 MeV and (**right**) the GMR phonon at 27.48 MeV.

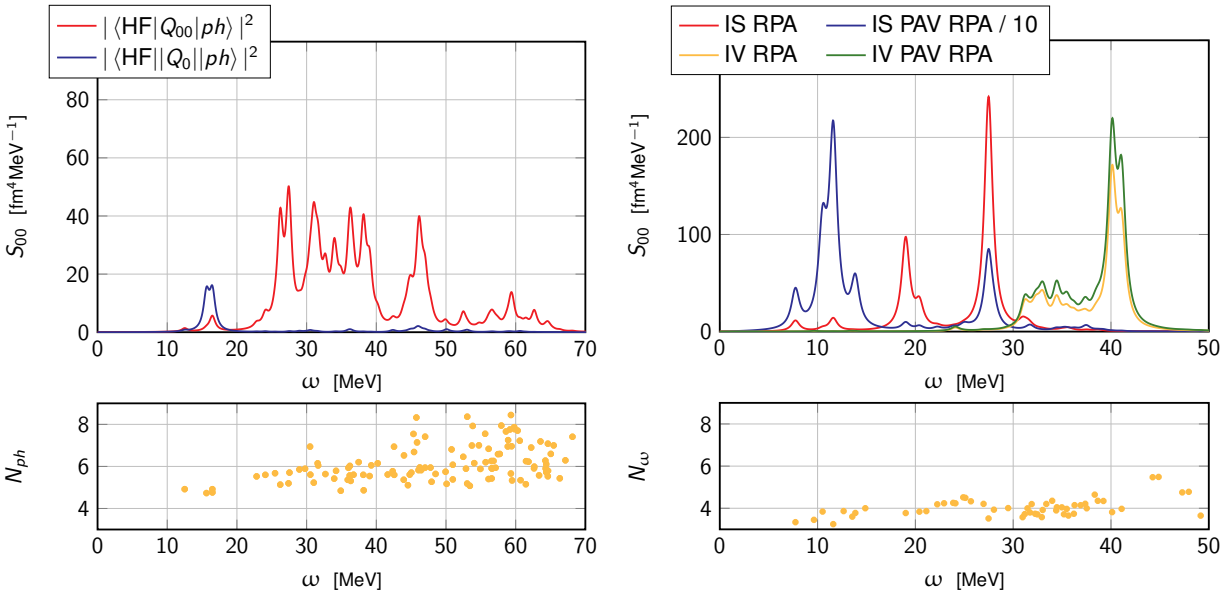

Figure 12.9: ^{24}Mg monopole response: **(left)** unperturbed 1p-1h response **(right)** RPA response. In the bottom panels the corresponding normalising factors are shown for comparison.

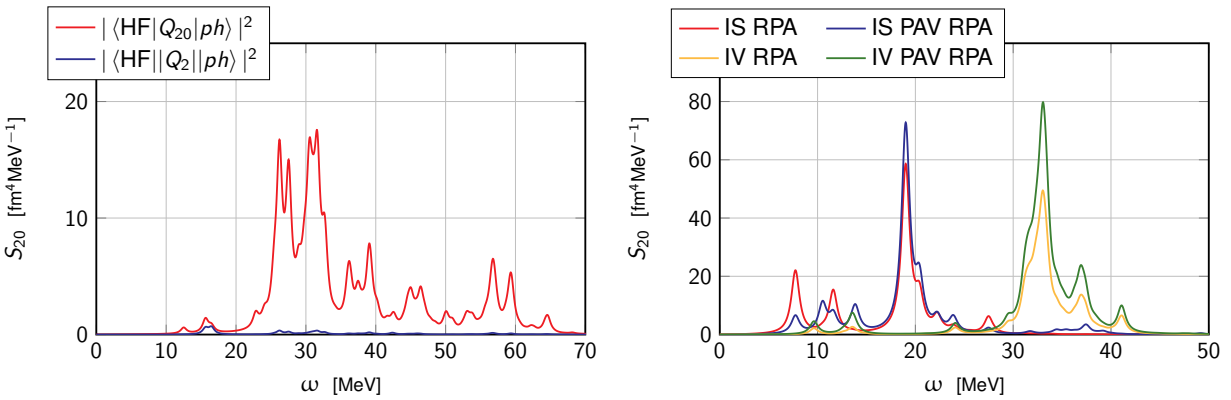

Figure 12.10: ^{24}Mg quadrupole response: **(left)** unperturbed 1p-1h response **(right)** RPA response.

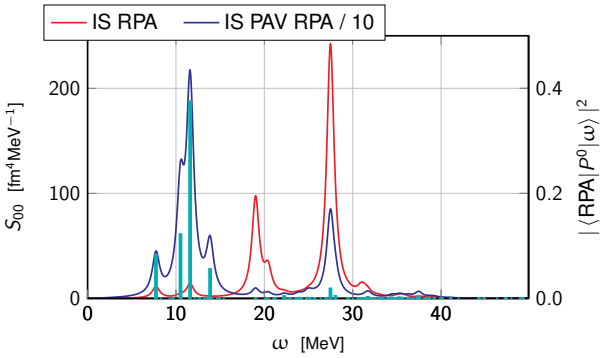

Figure 12.11: ^{24}Mg monopole response for RPA and PAV RPA calculations (left axis) and overlap with the rotational state (see Eq.(12.6)) of the RPA phonons (right axis).

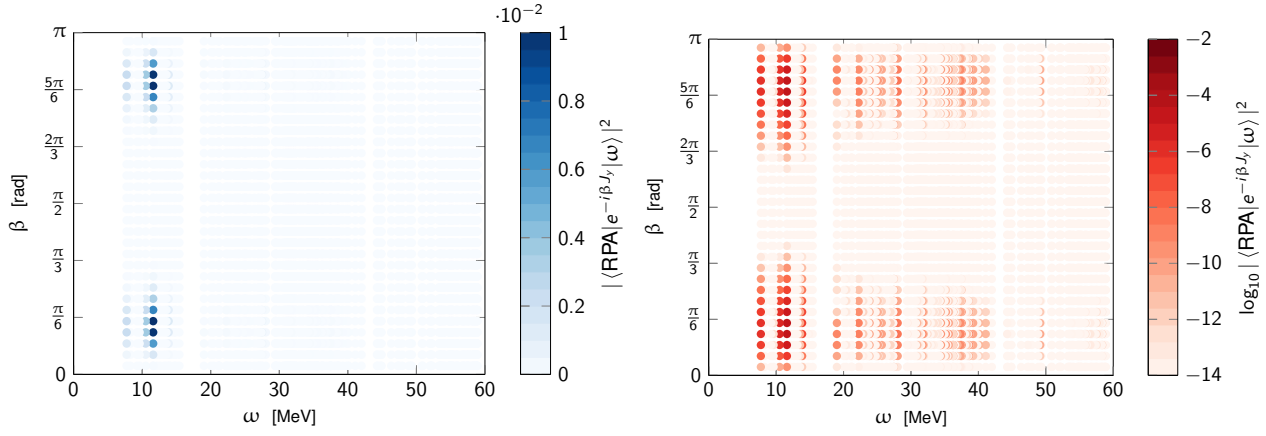

Figure 12.12: ^{24}Mg rotational RPA strength as a function of the rotation angle in **(left)** linear **(right)** logarithmic scale.

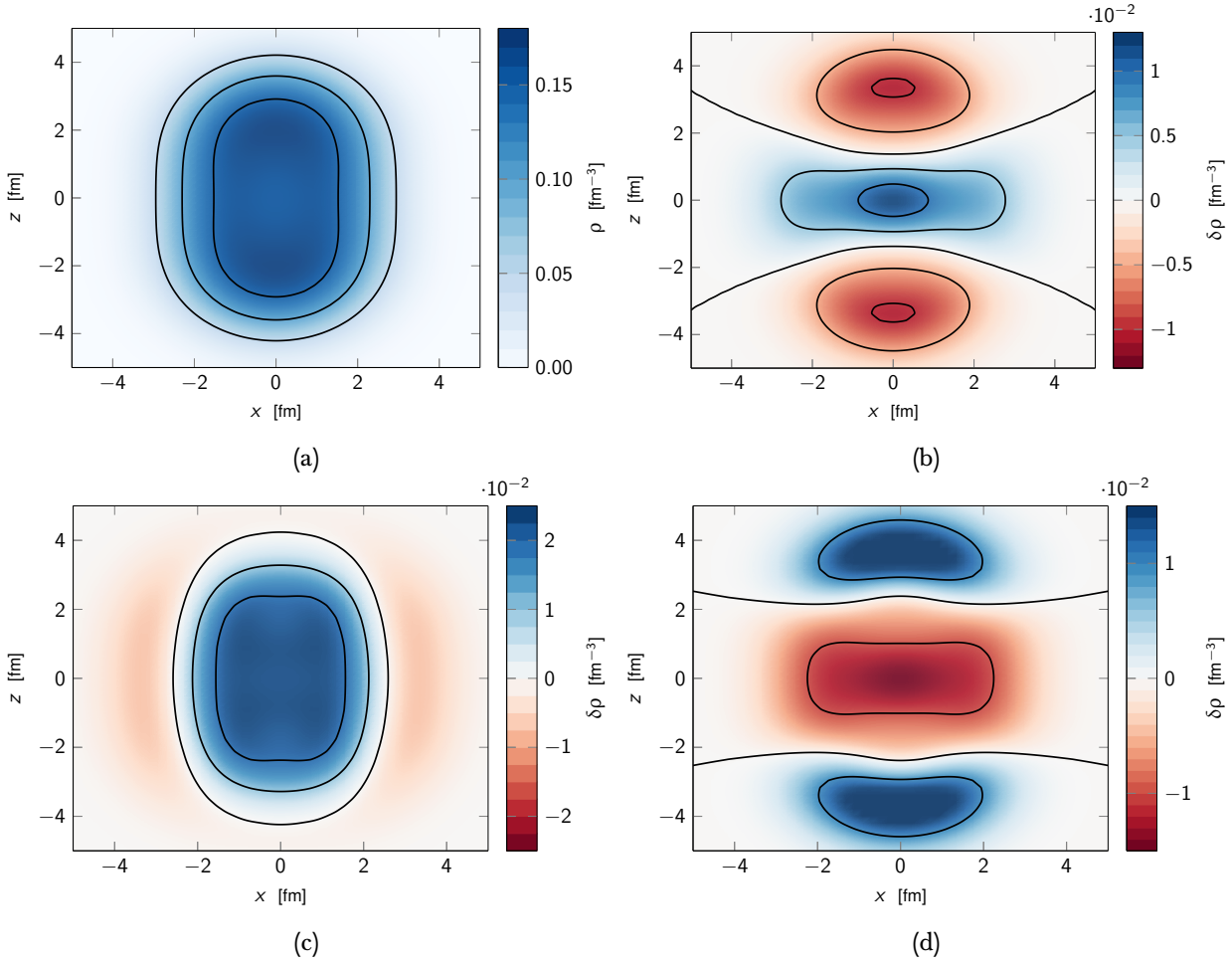

Figure 12.13: ^{24}Mg **(a)** one-body intrinsic matter density of the HF ground state **(b)** intrinsic RPA transition density for the rotational phonon at $\omega = 11.60$ MeV **(c)** intrinsic RPA transition density for the ISGMR phonon at $\omega = 27.48$ MeV and **(d)** intrinsic RPA transition density for the ISGQR phonon at $\omega = 19.01$ MeV.

In order to access the physical content of the different phonons the intrinsic ground-state and transition densities associated to three phonons of interest are shown in Fig. 12.13. The transition density associated to the breathing mode at ∼27 MeV (c) globally preserves the original shape of the HF ground state (a). The quadrupole resonance at ∼19 MeV (d), instead, displays a strong depletion in the equatorial region and a significant enhancement around the poles. This is associated to a shape modification with respect to the HF ground state and is understood in terms of quadrupole vibration. The anomalous phonon at ∼11 MeV (b) also looks similar, such that its rotational content is not detectable from the associated transition density. Thus, the coupling to the rotational state is further investigated in the following sections.

12.3 Systematic study

In order to ensure that the anomalous effects from AMP in the monopole channel are not due to poor convergence properties of the RPA calculation, a systematic study of the model space parameters is now presented. Results relative to the HF ground state are reported in Tab. 12.2.

$e_{\max}$	E_{HF} [MeV]	r [fm]	β
4	-192.29	2.911	0.292
6	-195.65	2.991	0.378
8	-196.21	3.009	0.392
10	-196.93	3.011	0.383
12	-197.15	3.016	0.390

Table 12.2: Hartree-Fock ground-state energy E_{HF}, root mean square radius r and deformation β of the HF vacuum adopted for the convergence study in ^{24}Mg.

12.3.1 $e_{\max}$ convergence

The convergence with respect to the harmonic oscillator basis size $e_{\max}$ is first addressed for a fixed value of the maximal ph-excitation energy value $E_{\mathrm{cut}} = 100$ MeV. The original RPA response displays a converging pattern in the quadrupole channel, as seen in the bottom panel of Fig. 12.14 (left). The low-energy component of the monopole response also converges for relatively small $e_{\max}$. However, the high-energy component shows a strong dependence on the dimension of the harmonic oscillator basis and the fragmentation is still increasing for the largest model space employed. This phenomenon was also observed in Ref. [192] and attributed to high-lying excitations involving states in the continuum.

When projection is considered (Fig. 12.14 (right)) the effects observed in Sec. 12.2 are recovered, both in the isoscalar monopole and quadrupole responses, such that strong effects are only observed in the monopole case. Overall, the same convergence trend with respect to $e_{\max}$ is observed in the unprojected and projected responses. As for the monopole response, the strong enhancement of the response in the $5-15$ MeV region is quickly stable for increasing $e_{\max}$ and thus cannot be attributed to poor convergence properties with respect to $e_{\max}$.

The IV channel is also analysed here for completeness. Numerical results are displayed in Fig. 12.15. The original RPA response (left) shows a significant dependence on the harmonic oscillator basis size. Both the IV monopole and quadrupole responses are concentrated above ~25 MeV, where the coupling to continuum states is expected to be important, such that details of single-particle configurations strongly affect the global response. Eventually both unprojected and projected responses are not fully converged yet for $e_{\max} = 12$.

12.3.2 E_{cut} convergence

The dependence on the ph excitation energy cut-off E_{cut} is now addressed for a fixed number of harmonic oscillator shells $e_{\max} = 10$. Unprojected and projected isoscalar RPA responses are displayed in Fig. 12.16. A converging pattern is observed, results for $E_{\mathrm{cut}} = 100$ MeV and $E_{\mathrm{cut}} = 120$ MeV being practically identical. A similar analysis made in the IV channel is shown in Fig. 12.17. The convergent pattern is also observed.

12.3.3 Coupling to the rotational state

Convergence properties of the rotational coupling with respect to the model space size are addressed in Fig. 12.18. The quantity $|\langle \mathrm{RPA}|P^0|\omega\rangle|^2$ converges both with respect to $e_{\max}$ and E_{cut}, see Fig. 12.18. Thus, the coupling to the rotational state from Eq. (5.88) is not an artefact related to unachieved convergence of the RPA spectrum.

The rotational component of RPA phonons is then subtracted from the projected RPA response following the prescription from Eq. (5.100). As previously mentioned, the normalising constant of the rotational state N_{ROT} is ill-defined for RPA. If the uncorrelated HF ground state is used to compute N_{ROT}, the phonon normalising constant $N_{\tilde{\nu}}$ from Eq. (5.99) was found to be negative in some cases. Methods [193, 194, 195, 196]

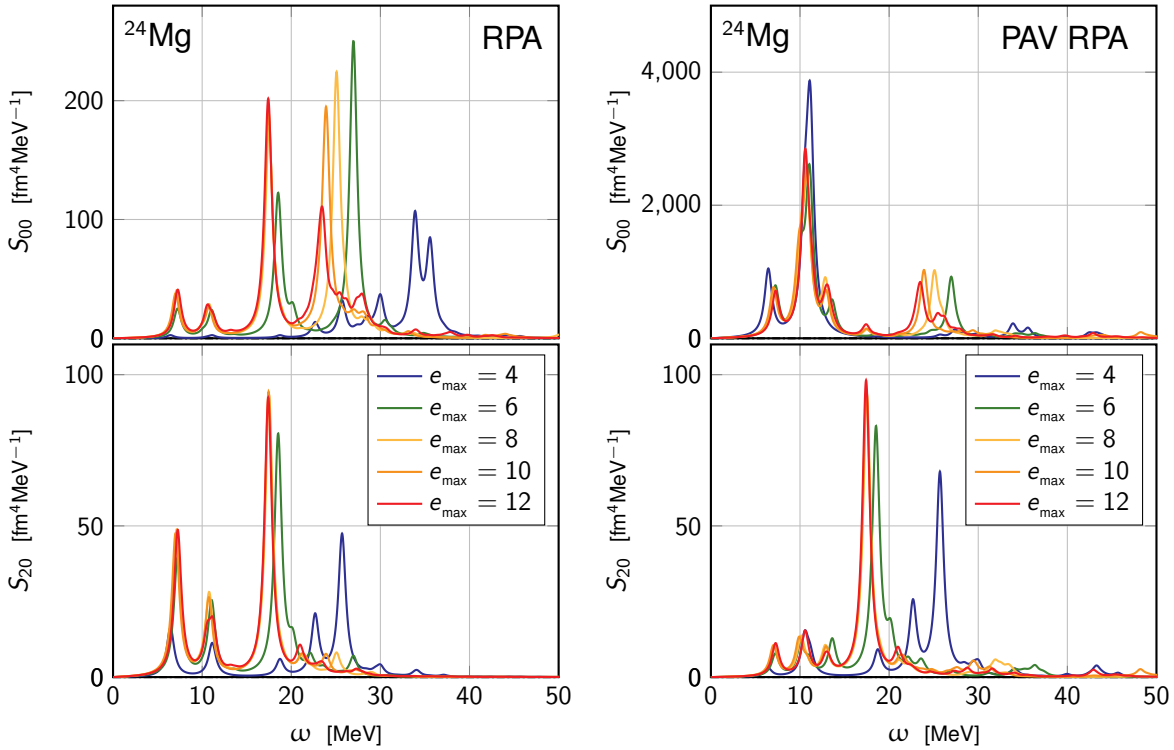

Figure 12.14: Original **(left)** and projected **(right)** RPA **isoscalar** response for different model space dimensions ($E_{\text{cut}} = 100$ MeV).

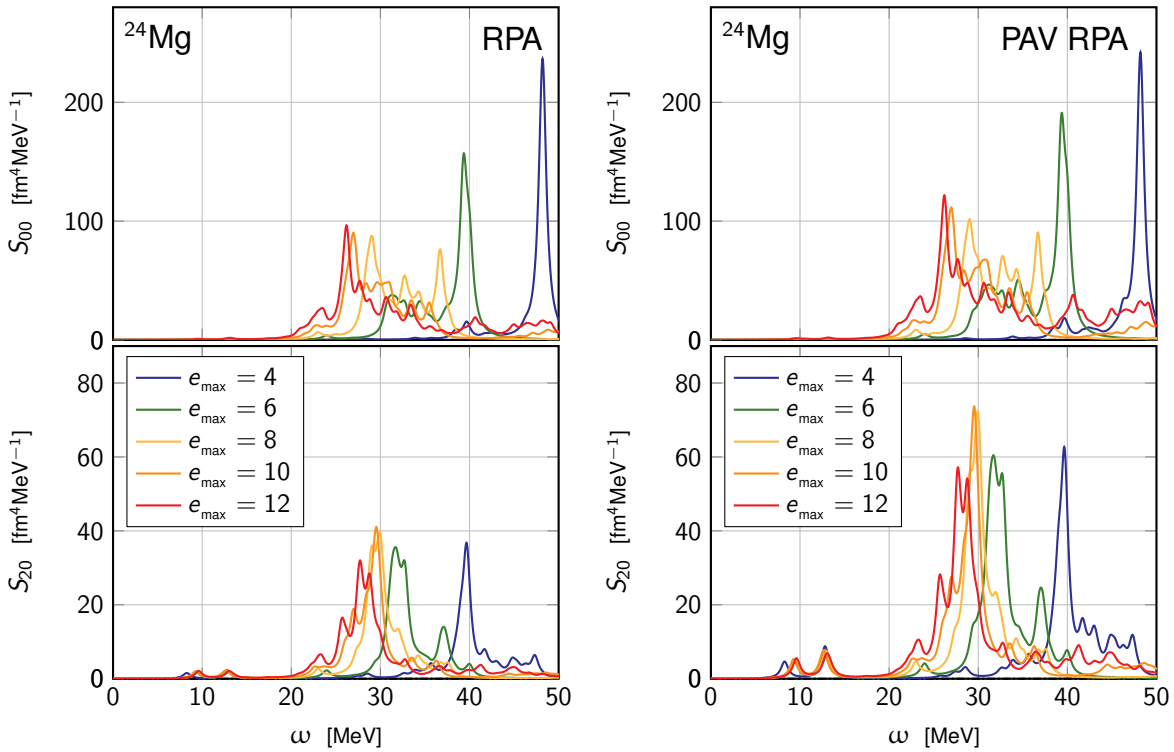

Figure 12.15: Original **(left)** and projected **(right)** RPA **isovector** response for different model space dimensions ($E_{\text{cut}} = 100$ MeV).

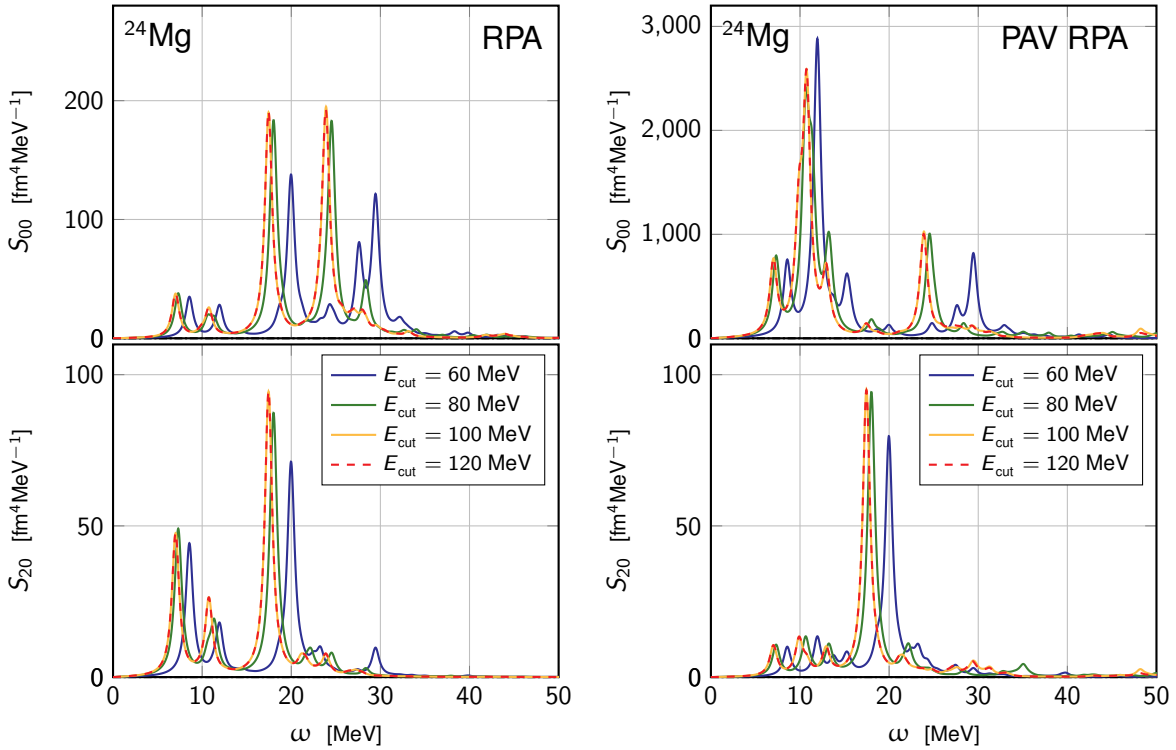

Figure 12.16: Original **(left)** and projected **(right)** RPA **isoscalar** response for different values of E_{cut} ($e_{\text{max}} = 10$).

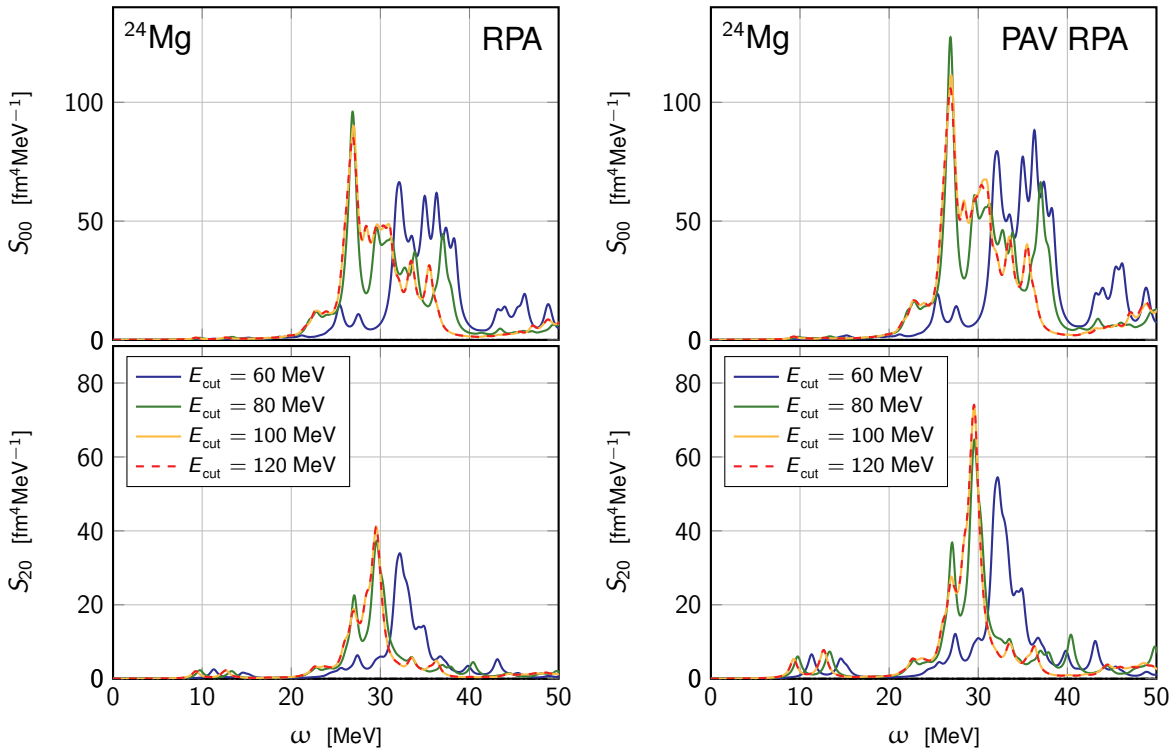

Figure 12.17: Original **(left)** and projected **(right)** RPA **isovector** response for different values of E_{cut} ($e_{\text{max}} = 10$).

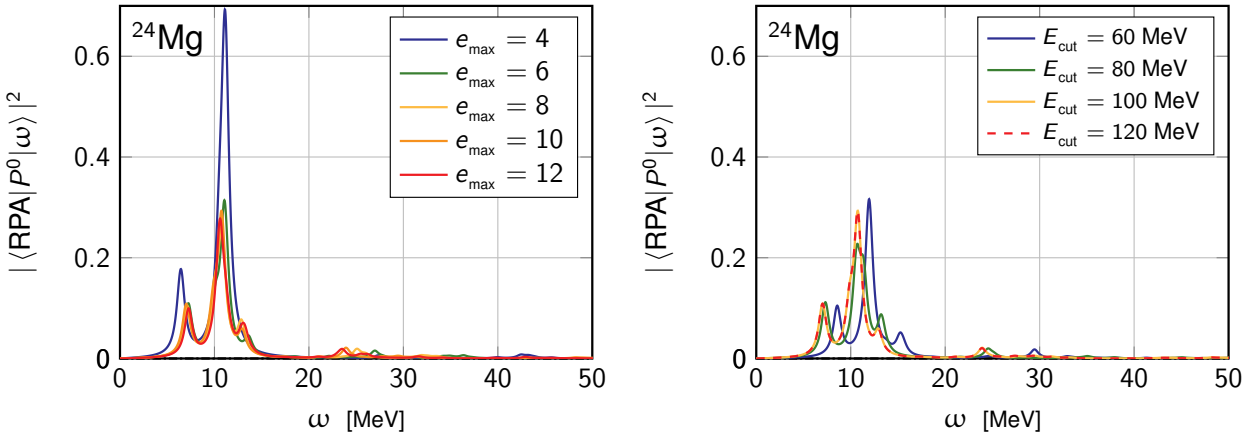

Figure 12.18: **Left**: RPA **isoscalar** rotational response for different model space dimensions ($E_{\text{cut}} = 100$ MeV); **Right**: RPA **isoscalar** rotational response for different values of E_{cut} ($e_{\text{max}} = 10$). The **isovector** rotational response vanishes identically for all studied cases.

exist to compute the $|\text{RPA}\rangle$ ground state but they are highly non-trivial, such that the determination of the RPA ground state goes beyond the objectives of the present discussion. Hence, in the present study N_{ROT} is fixed to fulfil the condition $N^0_{\tilde{\nu}} = 0$ (Eq. 5.99) for the RPA phonon that most strongly couples to the rotational state. Subtracted PAV RPA spectra are displayed in Fig. 12.19. A convergence pattern similar to the one observed for the unprojected RPA spectra is recovered, both with respect to e_{max} and E_{cut}.

Eventually, unprojected and projected responses are compared in Fig. 12.20. Once the rotational component has been removed according to Eq. (5.100), the monopole response becomes also weakly affected by the AMP, except for the strength of the GMR that is enhanced relative to the peak associated with the coupling with the GQR.

12.4 Discussion

The effects of AMP on the strength distributions originating from symmetry-breaking RPA calculations have been studied for the well-deformed prolate system ^{24}Mg in Secs. 12.2 and 12.3. The appearance of a large monopole strength at low energy was observed and shown to be due to a coupling to the (non-infinitesimal) rotational motion. Analogous effects were observed in other systems such as ^{20}Ne and ^{28}Si whose monopole and quadrupole RPA responses are displayed in Fig. 12.21, together with the information concerning the overlap between the RPA phonons and the rotational state.

A similar behaviour was in fact previously identified in Chap. 8 for PAV GCM calculations. Hence, the coupling to the rotational state is related to the symmetry-breaking nature of the reference state and is not peculiar to the specific many-body method used to compute vibrational excitations. The finite frequency of the rotational motion induces a coupling with the vibrational motion. Compared to GCM results, RPA limits the effect of such a coupling to the low-energy ($\lesssim 15$ MeV) region.

Traditionally, the rotation is discussed in connection with the presence of a solution in the $K = 1$ channel associated with an infinitesimal rotation (see Ref. [197] for instance) in deformed RPA calculations. Since RPA is not suited to provide genuine rotation-like excitations (for collective rotations no restoring force prevents the expansion parameters $\mathbf{z}$ in Eq. (3.41) from becoming large), only an infinitesimal rotation can be explicitly developed as a zero-energy solution.

While rotation-vibration coupling effects in $K \neq 1$ solutions cannot be addressed within RPA, they could be addressed in more phenomenological theories [150] via beyond-first-order effects in the $K = 0$ channel.

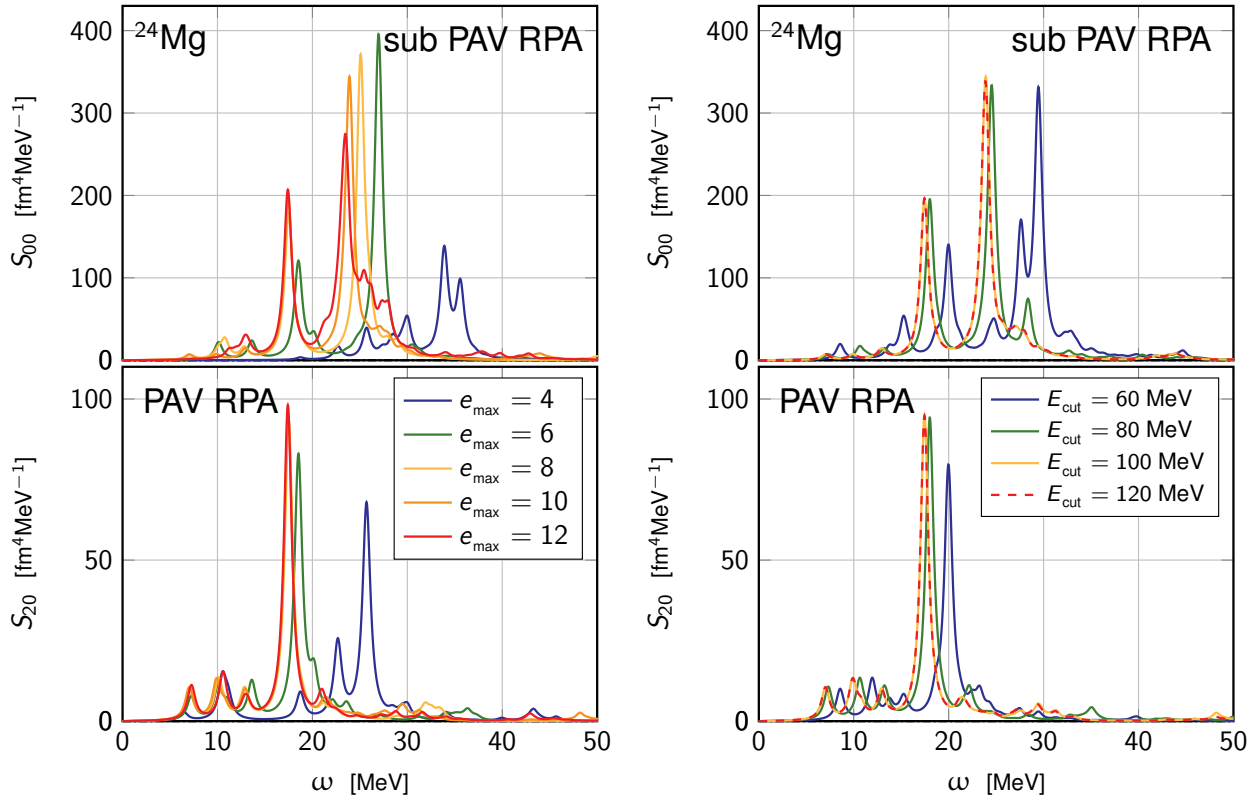

Figure 12.19: **Left**: subtracted PAV RPA **isoscalar** monopole response for different model space dimensions ($E_{\text{cut}} = 100$ MeV) compared to the projected quadrupolar response; **Right**: subtracted PAV RPA **isoscalar** monopole response for different values of E_{cut} ($e_{\text{max}} = 10$) compared to the projected quadrupolar response.

A strategy to explicitly isolate and subtract the rotational content of the RPA phonons was introduced in Sec. 5.7.4. Except for ambiguities concerning the normalising constant of the rotational state (a method to circumvent such issue was proposed in Sec. 12.3.3), the rotational coupling can be explicitly removed *a posteriori*. Eventually, the physical picture provided in this chapter is similar to the one at play in PAV GCM calculations.

eventually, a proper treatment of rotational effects can only be achieved if they are explicitly considered when solving the (Q)RPA equations. This demands the implementation of the full-fledged projected (Q)RPA, where the symmetry restoration is performed before diagonalising the reduced Hamiltonian of the problem. Such *variation after projection* (Q)RPA (VAP-QRPA) has been formally introduced in Ref. [148], but no realistic implementation has been realised so far. Developments in this direction are thus welcome to parallel PGCM calculations.

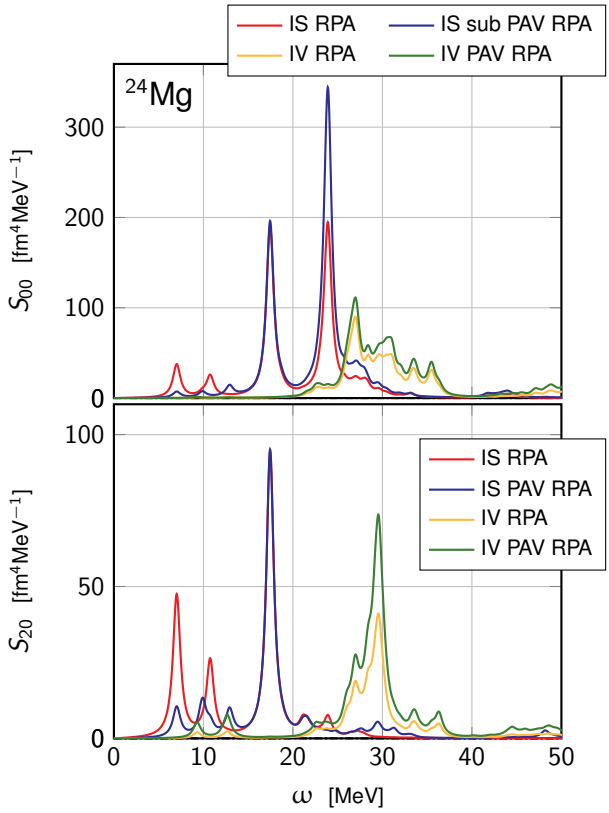

Figure 12.20: Original and projected RPA responses ($e_{\max} = 10$, $E_{\text{cut}} = 100$ MeV). For the projected isoscalar monopole case the subtracted PAV RPA response is shown.

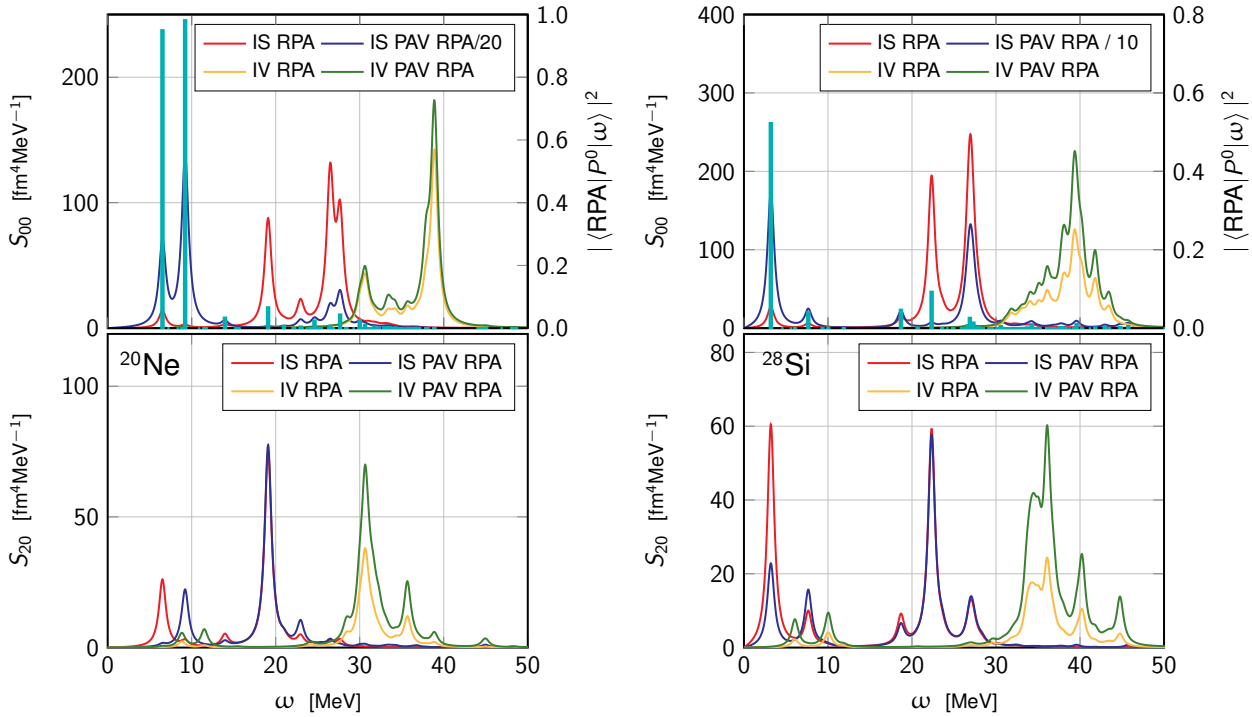

Figure 12.21: ^{20}Ne (**left**) and ^{28}Si (**right**) response for the monopole and the $K = 0$ component of the quadrupole channel. The overlap between the RPA phonons and the rotational state is also reported (right axis).

Conclusions

There is a destination but no way there.

Franz Kafka

In recent years *ab initio* methods have paved their own way through the nuclear chart. The *ab initio* description of ground-state nuclear properties is nowadays a mature field, yet living a continual renewal and evolution. In contrast to earlier times, when only few-nucleon systems could be accessed employing essentially exact techniques at the price of huge computational costs scaling exponentially with the system's size, nuclei up to $A \sim 130$ are consistently described today from first principles, with isolated highlights as heavy as ^{208}Pb [15]. Expansion methods represent the game-changer on the playground: all such methods present a more gentle polynomial scaling when truncated at a given order. Together with the use of symmetry-breaking reference states and similarity-evolved Hamiltonians, recent developments made possible to explore (doubly-)open shell nuclei from light to medium-heavy systems.

The gold rush towards heavier nuclei, however, is not the only frontier in contemporary *ab initio* nuclear theory. Today several paths are being explored in order to answer the many challenges issued by modern physics, ranging from the quest for ever-increasing accuracy to a sound uncertainty quantifications [198], and from the study of nuclear reactions [199] to the access to nuclear spectroscopy. This last aspect has been the centre of interest of the present work.

The description of collective vibrational excitations in the *ab initio* field has been mostly limited to spherical, i.e. doubly- and singly-closed shell, systems. Relatively few techniques are available compared to the wide portfolio of methods addressing nuclear ground states. Except for the CC-LIT method [48], most of the available alternative rely on (Q)RPA-inspired techniques, where several strategies to correlate the ground and excited states have been inspected [55, 54, 56]. Recently, a deformed FAM-QRPA solver was also developed [60] to access axially- and triaxially-deformed nuclei. Supported by the observation that dynamical correlations mostly cancel out when addressing collective excitations [55, 43], *ab initio* (Q)RPA has proven to be a reliable device for nuclear spectroscopy.

Stimulated by these findings and inspired by pioneering phenomenological calculations [81, 83, 85, 84], PGCM has been employed in the present work to address the GMR in closed- and open-shell nuclei from an *ab initio* standpoint for the first time. The mean-square radius and the quadrupolar deformation were chosen as relevant collective coordinates to access the nuclear breathing mode and quadrupolar vibrations, as well as the coupling between them. Resonating states in the energy region of interest were observed for all investigated nuclei and compared to experimental data whenever possible.

The numerical convergence properties of the calculations were addressed in Chap. 6, observing a satisfactory behaviour with respect to the variable parameters of the calculation. An exploratory study about the optimal choice of HFB vacua to be included in the PGCM ansatz was also carried out, suggesting that an accurate description of the immediate neighbourhood of the HFB minimum can provide converged results even for high-lying vibrational excitations. Several cases of physical and experimental interest have been discussed in Chap. 7. A detailed discussion of the GMR-GQR coupling in ^{46}Ti was presented, with a special attention to the mechanisms responsible for it in a symmetry-conserving formalism like PGCM. The

use of a fully symmetry-conserving formalism in the investigation of giant resonances stands as an element of novelty *per se*, and the description of the coupling between different multipolarities in this context also represents an innovation. The effects of shape coexistence and shape mixing were investigated in ^{28}Si, where no relevant coupling between different minima was observed. Along the way, predictions based on the prolate-shape isomer with an extreme GMR-GQR coupling were provided. Eventually, the study of ^{24}Mg revealed a largely fragmented monopole response, in agreement with several experimental data sets [171, 173, 174, 176, 177].

Anharmonic effects on the monopole response were discussed in Chap. 9, where PGCM and QRPA results obtained in a consistent setting were compared. A simple model was proposed to evaluate the degree of anharmonicity in a given nucleus and correlate it with the observed differences between the two sets of calculations. It was observed that light systems diverge the most from the harmonic hypothesis underlying QRPA calculations, which is in line with the common understanding of Pauli principle violation. The impact of the projection on good angular momentum was further analysed in Chap. 8. The presence of a spurious coupling between rotational and vibrational states was observed when AMP is not included in the solution of the secular equation but performed *a posteriori*. Analogous results were obtained in Chap. 12 for RPA in an EDF implementation. The observation of a spurious coupling between the monopole and the rotational responses in RPA is an original finding of this work and constitutes an element of formal interest.

The possibility to describe high-lying multi-phonon states by means of the PGCM was discussed in Chap. 11, where detailed calculations supported the presence of such states, also providing precise criteria to infer on them. Eventually, an extensive discussion on the moments of the collective responses was provided in Chap. 10, where a novel solution introduced in Chap. 4 to access such quantity was compared to more traditional approaches.

Original formal achievements were also presented. A diagrammatic approach [110] to consistently evaluate the norm and the operator kernels at play in the PGCM is exposed in Chap. 2. This novel method may reveal useful in other contexts, e.g. to design approximations in variational coupled cluster theory. The formal connection between GCM and QRPA was presented in Chap. 3 from a new perspective, allowing to generalise QRPA equations to a higher many-body content.

Perspectives

The PGCM results on giant resonances presented in this manuscript are the first of their kind in the *ab initio* community and represent, hence, an exploratory work. Many ways open to further improve the findings of this work, in particular as far as the building of the PGCM ansatz is concerned. It was mentioned in several occasions that PGCM lacks a systematic criterion to select the relevant collective coordinates of the problem, such that a physical guidance is often invoked in the choice of the relevant degrees of freedom. A collective coordinate may in principle be extracted unambiguously starting from the Self-consistent Collective Coordinate method (SCC) [200, 201, 202], by projecting the collective motion onto a specific function space. In this formalism the collective coordinates and the associated conjugate momenta are treated on the same footage. However, a configuration mixing does not appear explicitly in the SCC formulation, such that its application to PGCM is not trivial. Other collective coordinates should, thus, be systematically explored to further correlate the PGCM wave-function, with special attention on the dynamical degrees of freedom represented by conjugate momenta. Such an extension of the GCM formalism goes under the name of Dynamical GCM (DGCM) [203, 204] and has revealed to successfully improve on some limitations observed in GCM-EDF calculations [205, 206].

Another open point is how to effectively choose, for a given set of collective coordinates, the most relevant HFB vacua. The arbitrariness in the selection of such states constitutes a weakness point of PGCM calculations, such that a definite criterion would be key in this respect. One interesting direction in this sense is represented by Eigenvector Continuation (EC) [207]. This technique, recently introduced in nuclear

structure theory, allows to emulate a large number of solutions of the many-body problem. In particular, the similar formal ground with respect to PGCM makes natural to apply it to the present context, aiming at understanding the theoretical foundations underlying the optimal selection of the HFB vacua. The similarity (see, for instance Ref. [208]) is also supported by the present observation that high-lying states in one-dimensional PGCM calculations are easily converged even including few points in the surrounding of the HFB minimum. Eigenvector Continuation may help in obtaining similar results in two-dimensional (ore more) calculations as well; uncertainty quantification also may benefit from the same formalism [209].

The non-trivial effects of projection observed in comparing (P)GCM calculations in Chap. 8, as well as the presence of rotational-vibrational coupling in GCM and RPA calculations (see Chap. 12), strongly suggest that AMP (and projection in general) must be properly treated in deformed QRPA calculations. A fully symmetry-conserving version of the (Q)RPA (projected (Q)RPA) was formally defined and developed [148, 210] but, due to its prohibitive computational cost, no realistic implementation was ever realised in nuclear physics. Given the increased computational capabilities of current large scale infrastructures, as well as the re-formulation of QRPA in the form of QFAM, an ***ab initio*** implementation of projected QRPA may be at reach in the near future.

Part III

Appendices

Appendix A

Normal-ordered operators

An arbitrary rank-N particle-number-conserving fermionic operator O can be written as

$$O \equiv \sum_{n=0}^{N} O^{nn}, \tag{A.1}$$

where

$$O^{mn} \equiv \frac{1}{m!}\frac{1}{n!} \sum_{\substack{a_1 \cdots a_m \\ b_1 \cdots b_n}} o^{a_1 \cdots a_m}_{b_1 \cdots b_n} c^\dagger_{a_1} \cdots c^\dagger_{a_m} c_{b_n} \cdots c_{b_1}, \tag{A.2}$$

contains $m(n)$ particle creation (annihilation) operators. The zero-body part O^{00} is the scalar obtained as the expectation value of O in the particle vacuum

$$O^{00} = \langle 0|O|0\rangle. \tag{A.3}$$

In Eq. (A.2), matrix elements are fully anti-symmetric under the exchange of any pair of upper or lower indices, i.e.

$$o^{a_1 \cdots a_m}_{b_1 \cdots b_n} = \epsilon(\sigma_u)\epsilon(\sigma_l)\, o^{\sigma_u(a_1 \cdots a_m)}_{\sigma_l(b_1 \cdots b_n)}, \tag{A.4}$$

where $\epsilon(\sigma_u)$ ($\epsilon(\sigma_l)$) refers to the signature of the permutation $\sigma_u(\ldots)$ ($\sigma_l(\ldots)$) of the m (n) upper (lower) indices. In case the particle-number conserving operator is hermitian, each term O^{nn} is hermitian with its matrix elements fulfilling

$$o^{a_1 \cdots a_n}_{b_1 \cdots b_n} = \left(o^{b_1 \cdots b_n}_{a_1 \cdots a_m}\right)^*. \tag{A.5}$$

By virtue of standard Wick's theorem [211], the operator O can be normal ordered with respect to the Bogoliubov vacuum $|\Phi\rangle$

$$O \equiv \sum_{n=0}^{N} \mathbf{O}^{[2n]} \equiv \sum_{n=0}^{N} \sum_{\substack{i,j=0 \\ i+j=2n}}^{2n} \mathbf{O}^{ij} \tag{A.6}$$

where the component

$$\mathbf{O}^{ij} \equiv \frac{1}{i!j!} \sum_{\substack{k_1 \ldots k_i \\ l_1 \ldots l_j}} \mathbf{o}^{k_1 \ldots k_i}_{l_1 \ldots l_j} \beta^\dagger_{k_1} \ldots \beta^\dagger_{k_i} \beta_{l_j} \ldots \beta_{l_1} \tag{A.7}$$

contains $i(j)$ quasi-particle creation (annihilation) operators. The zero-body part $\mathbf{O}^{[0]}$ is the scalar obtained as the expectation value of O in the Bogoliubov vacuum

$$\mathbf{O}^{00} = \langle \Phi|O|\Phi\rangle. \tag{A.8}$$

In Eq. (A.7), matrix elements are fully anti-symmetric under the exchange of any pair of upper or lower indices, i.e.

$$\mathbf{o}^{k_1\cdots k_i}_{l_1\cdots l_j} = \epsilon(\sigma_u)\epsilon(\sigma_l)\,\mathbf{o}^{\sigma_u(k_1\cdots k_i)}_{\sigma_l(l_1\cdots l_j)} \,. \tag{A.9}$$

These matrix elements are functionals of the Bogoliubov matrices $(\mathcal{U},\mathcal{V})$ associated with $|\Phi\rangle$ and of the matrix elements $\{o^{a_1\cdots a_n}_{b_1\cdots b_n}\}$ initially defining the operator O. As such, the content of each operator $\mathbf{O}^{ij}$ depends on the rank N of O. For more details about the normal ordering procedure and for explicit expressions of the matrix elements up to $N = 3$, see Refs. [102, 30, 31, 212].

In case the operator is hermitian, each component $\mathbf{O}^{[2n]}$ is itself hermitian with $\mathbf{O}^{ij} = \mathbf{O}^{ji\dagger}$ such that matrix elements satisfy

$$\mathbf{o}^{k_1\cdots k_i}_{l_1\cdots l_j} = \left(\mathbf{o}^{l_1\cdots l_j}_{k_1\cdots k_i}\right)^* \,. \tag{A.10}$$

Appendix B

Diagrammatic rules for kernels evaluation

The present appendix is dedicated to setting up the diagrammatic rules used in Sec. 2.1.1, allowing one to compute matrix elements of the form

$$\langle_s|^i{}_j|^t\rangle \equiv \frac{1}{s!}\frac{1}{t!}\langle\Phi|\mathbf{L}^s\mathbf{O}^{ij}\mathbf{R}^t|\Phi\rangle, \tag{B.1a}$$

$$\langle_s||^t\rangle \equiv \frac{1}{s!}\frac{1}{t!}\langle\Phi|\mathbf{L}^s\mathbf{R}^t|\Phi\rangle, \tag{B.1b}$$

where $\mathbf{O}^{ij}$ takes the form given in Eq. (A.7) and where $\mathbf{R}$ ($\mathbf{L}$) is a one-body[1] excitation (de-excitation) operator as defined in Eq. (2.4a) (Eq. (2.4b)).

The diagrammatic rules are also worked out to compute a second category of matrix elements of present interest

$$\langle_s|^{k_2}||_{k_1}|^t\rangle \equiv \frac{1}{s!}\frac{1}{t!}\langle\Phi|\mathbf{L}^s\beta^\dagger_{k_2}\beta_{k_1}\mathbf{R}^t|\Phi\rangle, \tag{B.2a}$$

$$\langle_s|_{k_2}||_{k_1}|^t\rangle \equiv \frac{1}{s!}\frac{1}{t!}\langle\Phi|\mathbf{L}^s\beta_{k_2}\beta_{k_1}\mathbf{R}^t|\Phi\rangle, \tag{B.2b}$$

$$\langle_s|^{k_2}||^{k_1}|^t\rangle \equiv \frac{1}{s!}\frac{1}{t!}\langle\Phi|\mathbf{L}^s\beta^\dagger_{k_2}\beta^\dagger_{k_1}\mathbf{R}^t|\Phi\rangle, \tag{B.2c}$$

$$\langle_s|_{k_2}||^{k_1}|^t\rangle \equiv \frac{1}{s!}\frac{1}{t!}\langle\Phi|\mathbf{L}^s\beta_{k_2}\beta^\dagger_{k_1}\mathbf{R}^t|\Phi\rangle. \tag{B.2d}$$

These matrix elements differ from the two introduced in Eq. (B.1) by the presence of two "external/fixed" quasi-particle operators, i.e. quasi-particle operators whose indices are not summed over.

The diagrammatic rules follow from the straight application of standard Wick's theorem with respect to the Bogoliubov vacuum $|\Phi\rangle$. The application of Wick's theorem delivers the complete set of fully contracted terms associated with the operator product entering the matrix element of interest. Given that the operators at play are all conveniently expressed in the quasi-particle basis associated with the Bogoliubov vacuum $|\Phi\rangle$, the four possible elementary contractions take the simplest possible form

$$\begin{aligned}\mathbf{R}_{k_1k_2} &= \begin{pmatrix} \frac{\langle\Phi|\beta^\dagger_{k_2}\beta_{k_1}|\Phi\rangle}{\langle\Phi|\Phi\rangle} & \frac{\langle\Phi|\beta_{k_2}\beta_{k_1}|\Phi\rangle}{\langle\Phi|\Phi\rangle} \\ \frac{\langle\Phi|\beta^\dagger_{k_2}\beta^\dagger_{k_1}|\Phi\rangle}{\langle\Phi|\Phi\rangle} & \frac{\langle\Phi|\beta_{k_2}\beta^\dagger_{k_1}|\Phi\rangle}{\langle\Phi|\Phi\rangle} \end{pmatrix} \\ &\equiv \begin{pmatrix} R^{+-}_{k_1k_2} & R^{--}_{k_1k_2} \\ R^{++}_{k_1k_2} & R^{-+}_{k_1k_2} \end{pmatrix}\end{aligned}$$

[1]The diagrammatic rules can be straightforwardly generalised to operators $\mathbf{R}$ and $\mathbf{L}$ of higher, and possibly different, ranks.

$$= \begin{pmatrix} 0 & 0 \\ 0 & \delta_{k_1 k_2} \end{pmatrix}, \tag{B.3}$$

such that the sole non-zero contraction $R^{-+}_{k_1 k_2} = \delta_{k_1 k_2}$ needs to be considered.

B.1 Diagrammatic representation

The diagrammatic representation of the various contributions to the matrix elements of interest relies on the definition of the following building blocks

1. As illustrated in Fig. B.1, the normal-ordered operator $\mathbf{O}^{ij}$ entering the matrix element $\langle_s|^i{}_j|^t\rangle$ is represented by a Hugenholtz vertex with i (j) lines traveling out of (into) it and representing quasi-particle creation (annihilation) operators. The algebraic factor $\mathbf{o}^{k_1 \ldots k_i}_{l_1 \ldots l_j}$ is associated to the vertex while assigning indices $k_1 \ldots k_i$ consecutively from the leftmost to the rightmost line above the vertex and indices $l_1 \ldots l_j$ consecutively from the leftmost to the rightmost line below the vertex.

2. As illustrated in Fig. B.2, the operator $\mathbf{L}$ ($\mathbf{R}$) entering all matrix elements of present interest is represented by a vertex of the $\mathbf{O}^{02}$ ($\mathbf{O}^{20}$) type and carry the associated algebraic factor $\mathbf{z}^*_{l_1 l_2}(l)$ ($\mathbf{z}^{k_1 k_2}(r)$).

3. The only non-zero contraction $R^{-+}_{k_1 k_2} = \delta_{k_1 k_2}$ is represented in Fig. B.3 and connects two up-going lines associated with one annihilation and one creation operator, both carrying the same quasi-particle index. For simplicity, one can eventually represent the contraction as a line carrying a single up-going arrow along with one quasi-particle index.

B.2 Diagrams generation

With these building blocks at hand, one can construct the diagrams gathering all contributions to the matrix elements introduced in Eqs (B.1) and (B.2). The basic rules to do so are as follows

1. Diagrams contain s square vertices ($\mathbf{L}$) and t triangle vertices ($\mathbf{R}$), the former being located above the latter. This is consistent with the convention that the left-to-right reading of a matrix element corresponds to the up-down reading of the diagram.

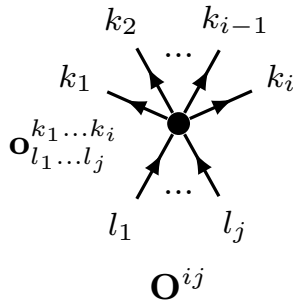

Figure B.1: Diagrammatic representation of the normal-ordered operator $\mathbf{O}^{ij}$ as a fully anti-symmetric Hugenholtz vertex.

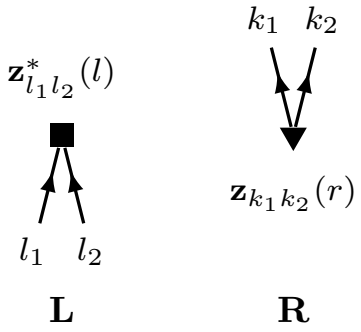

Figure B.2: Diagrammatic representation of the two Thouless operators **L** (left) and **R** (right).

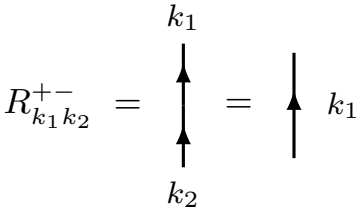

Figure B.3: Diagrammatic representation of the single non-zero elementary contraction. The convention is that the left-to-right reading of a matrix element corresponds to the up-down reading of the diagram.

2. Diagrams making up the two matrix elements introduced in Eqs. (B.1) are *vacuum-to-vacuum* diagrams with no line leaving the diagram. In $\langle_s|^i{}_j|^t\rangle$, a dot vertex ($\mathbf{O}^{ij}$) is located in between the square and triangle vertices. This is consistent with the convention that the left-to-right reading of a matrix element corresponds to the up-down reading of the diagram.

3. Diagrams making up the four matrix elements introduced in Eqs. (B.2) are *linked* with two external lines associated with the operators $\beta^{(\dagger)}_{k_2}$ and $\beta^{(\dagger)}_{k_1}$. The two lines leave the diagram on the same side to the, e.g., left such that (i) both lines are asymptotically in between the square ($\mathbf{L}$) and triangle ($\mathbf{R}$) vertices and such that (ii) the line carrying index k_2 is asymptotically located above the line carrying index k_1. This is consistent with the convention that the left-to-right reading of a matrix element corresponds to the up-down reading of the diagram. The arrow carried by each of the two lines points towards the interior (exterior) of the diagram if it is associated with a quasi-particle creation (annihilation) operator.

4. The fact that $R^{-+}_{k_1k_2}$ is the sole non-zero contraction implies that the number of quasi-particle creation operators involved in a given matrix element is equal to the number of quasi-particle annihilation operators. Given that each operator $\mathbf{L}$ ($\mathbf{R}$) contains two quasi-particle annihilation (creation) operators, this property require the following conditions to be fulfilled

   (a) $\langle_s|^i{}_j|^t\rangle$ demands $t = s + (i-j)/2$,
   (b) $\langle_s||^t\rangle$ demands $t = s$,
   (c) $\langle_s|^{k_2}||_{k_1}|^t\rangle$ demands $t = s$,
   (d) $\langle_s|_{k_2}||_{k_1}|^t\rangle$ demands $t = s+1$,
   (e) $\langle_s|^{k_2}||^{k_1}|^t\rangle$ demands $t = s-1$,
   (f) $\langle_s|_{k_2}||^{k_1}|^t\rangle$ demands $t = s$.

   such that $t \geq (i-j)/2$, $t \geq 1$ and $s \geq 1$ in case (a), (d) and (e), respectively.

5. Given the above considerations, one must construct all possible *topologically distinct unlabelled* diagrams from the building blocks; i.e., contract together the lines belonging to the s square ($\mathbf{L}$) vertices and to the t triangle ($\mathbf{R}$) vertices, along with those belonging to the dot ($\mathbf{O}^{ij}$) vertex or to the two external ($\beta^{(\dagger)}_{k_2}$ and $\beta^{(\dagger)}_{k_1}$) lines whenever applicable, in all possible ways. Unlabelled diagrams correspond to diagrams in which $\mathbf{L}$ ($\mathbf{R}$) vertices are not distinguished by a label. Topologically distinct unlabelled diagrams cannot be obtained from one another via a mere displacement, i.e. translation, of the vertices in the plane of the drawing.

6. The above process is constrained by the following properties

   (a) Because the operators $\mathbf{L}$, $\mathbf{R}$, and $\mathbf{O}^{ij}$ are in normal-ordered form with respect to $|\Phi\rangle$, self-contractions must be ignored.
   (b) Because $R^{-+}_{k_1k_2}$ is the sole non-zero contraction, $\mathbf{L}$ ($\mathbf{R}$) operators cannot display contractions among themselves, i.e. they necessarily contract with $\mathbf{R}$ ($\mathbf{L}$) operators, along with the i (j) quasi-particle creation (annihilation) operators inside $\mathbf{O}^{ij}$ or with $\beta^\dagger_{k_2}$ (β_{k_2}) and/or $\beta^\dagger_{k_1}$ (β_{k_1}) whenever applicable.

7. The diagrams making up the various matrix elements of interest display different typical topologies. Indeed, each contribution generated via the application of Wick's theorem can be expressed as a product of *strings of contractions*, each of which involves a subset of the $\mathbf{L}$ and $\mathbf{R}$ operators at play. As for $\langle_s|^i{}_j|^t\rangle$ with $(i+j) \geq 4$, several such strings actually involve quasi-particle operators belonging

to $\mathbf{O}^{ij}$, thus forming an overall closed string that is said to be *connected* to $\mathbf{O}^{ij}$. Translated into diagrammatic language, closed strings correspond to topologically *disjoint* closed sub-diagrams. In the case of $\langle_s|^i{}_j|^t\rangle$, any given diagram is thus made out of disjoint closed sub-diagrams, one of which is connected. As for the matrix elements introduced in Eqs. (B.2), one set of contractions must form a connected string involving the operators $\beta^{(\dagger)}_{k_2}$ and $\beta^{(\dagger)}_{k_1}$. These two operators cannot belong to two disjoint strings given that any string necessarily involves an even number of quasi-particle operators. Eventually, the diagrams making up the matrix elements introduced in Eqs. (B.2) are made out of disjoint closed sub-diagrams, one of which is connected to the external lines. Last but not least, each diagram contributing to $\langle_s||^t\rangle$ is made out of disjoint closed sub-diagrams, none of which is connected.

B.3 Diagrams evaluation

Once all the diagrams are drawn, one must compute their expressions. The rules to do so are the following

1. Label all quasi-particle lines and associate the appropriate factor to each vertex, i.e. a factor $\mathbf{z}^*_{l_1 l_2}(l)$ ($\mathbf{z}^{k_1 k_2}(r)$) to each vertex $\mathbf{L}$ ($\mathbf{R}$) and a factor $\mathbf{o}^{k_1 \ldots k_i}_{l_1 \ldots l_j}$ to the vertex $\mathbf{O}^{ij}$, respectively.

2. Sum over all internal line labels.

3. Include a factor $(n_e!)^{-1}$ for each set of n_e equivalent internal lines. Equivalent internal lines are those connecting identical vertices.

4. For any topologically distinct unlabelled diagram Γ, a symmetry factor S_Γ^{-1} must be considered. Given a *labelled* version of Γ, i.e. a version in which each operator $\mathbf{L}$ and $\mathbf{R}$ carries a specific label, S_Γ is equal to the number of permutations of the $\mathbf{L}$ and $\mathbf{R}$ operators delivering a topologically equivalent labelled diagram. The most obvious cases correspond to *equivalent subgroups* of $\mathbf{L}$ and $\mathbf{R}$ operators whose overall permutations lead to topologically equivalent labelled diagrams. The simplest example concerns two $\mathbf{L}$ ($\mathbf{R}$) operators that are doubly connected to $\mathbf{O}^{ij}$ or singly connected to $\mathbf{O}^{ij}$ and to the same operator $\mathbf{R}$ ($\mathbf{L}$). These $n_o \equiv 2$ operators $\mathbf{L}$ ($\mathbf{R}$) are equivalent and contribute a factor 2! to S_Γ. The next simplest example corresponds to $n_o > 2$ operators $\mathbf{L}$ ($\mathbf{R}$) fully connected to $\mathbf{O}^{ij}$. These $n_o > 2$ operators are indeed equivalent[2] such that their permutations contribute a factor $n_o!$ to S_Γ. Beyond those two examples, a set of $\mathbf{L}$ and $\mathbf{R}$ operators can form a string of contractions that is equivalent to other identical strings. Such n_s strings are said to be equivalent and contribute a factor $n_s!$ to S_Γ. Eventually, less obvious permutations can deliver topologically equivalent labelled diagrams and thus contribute to S_Γ[3].

5. Provide the diagram with a sign $(-1)^{\ell_c}$, where ℓ_c is the number of line crossings in the diagram. For diagrams containing external lines, their potential crossing must be counted.

[2] Note that $n_o > 2$ operators $\mathbf{L}$ ($\mathbf{R}$) cannot be equivalent if any of them is connected to an operator $\mathbf{R}$ ($\mathbf{L}$) given that the latter cannot entertain the same contraction pattern with $n_o > 2$ operators $\mathbf{L}$ ($\mathbf{R}$). More general patterns would however occur if $\mathbf{L}$ and $\mathbf{R}$ were of higher ranks.

[3] There is no general rule to identify them such that the symmetry factor associated with each topologically distinct unlabelled diagram must be identified on a case by case basis.

Appendix C

Asymmetric approach to kernels evaluation

The asymmetric approach constitutes the standard path to the off-diagonal Wick theorem at play in the computation of the connected operator kernel [105, 89]. Employing the simplified notation

$$\mathbf{R} \equiv \mathbf{Z}^{20}(l,r) = \frac{1}{2}\sum_{k_1 k_2} \mathbf{z}^{k_1 k_2}(l,r)\beta^\dagger_{k_1}(l)\beta^\dagger_{k_2}(l), \tag{C.1}$$

for the Thouless operator introduced in Eq. (1.25b) and satisfying $\langle\Phi(l)|\mathbf{R} = 0$, the connected operator kernel reads as

$$\begin{aligned}\frac{\langle\Phi(l)|O|\Phi(r)\rangle}{\langle\Phi(l)|\Phi(r)\rangle} &\equiv \sum_{n=0}^{N}\sum_{\substack{i,j=0\\ i+j=2n}}^{2n} \langle\Phi(l)|\mathbf{O}^{ij}e^{\mathbf{R}}|\Phi(l)\rangle, \\ &= \sum_{n=0}^{N}\sum_{\substack{i,j=0\\ i+j=2n}}^{2n} \langle\Phi(l)|{}^R\mathbf{O}^{ij}|\Phi(l)\rangle,\end{aligned} \tag{C.2}$$

where the operator

$$\begin{aligned}{}^R\mathbf{O}^{ij} &\equiv e^{-\mathbf{R}}\mathbf{O}^{ij}e^{\mathbf{R}} \\ &= \frac{1}{i!j!}\sum_{\substack{k_1\ldots k_i\\ l_1\ldots l_j}} \mathbf{o}^{k_1\ldots k_i}_{l_1\ldots l_j}\, {}^R\beta^\dagger_{k_1}\ldots{}^R\beta^\dagger_{k_i}\,{}^R\beta_{l_j}\ldots{}^R\beta_{l_1},\end{aligned} \tag{C.3}$$

formally reads as $\mathbf{O}^{ij}$ but with the quasi-particle operators replaced by their similarity-transformed partners

$$\begin{pmatrix}{}^R\beta_k \\ {}^R\beta^\dagger_k\end{pmatrix} \equiv e^{-\mathbf{R}}\begin{pmatrix}\beta_k \\ \beta^\dagger_k\end{pmatrix}e^{\mathbf{R}}. \tag{C.4}$$

Given that the similarity-transformed quasi-particle operators satisfy anticommutation relations

$$\{{}^R\beta^\dagger_{k_1}, {}^R\beta^\dagger_{k_2}\} = e^{-\mathbf{R}}\{\beta^\dagger_{k_1},\beta^\dagger_{k_2}\}e^{\mathbf{R}} = 0, \tag{C.5a}$$

$$\{{}^R\beta_{k_1}, {}^R\beta_{k_2}\} = e^{-\mathbf{R}}\{\beta_{k_1},\beta_{k_2}\}e^{\mathbf{R}} = 0, \tag{C.5b}$$

$$\{{}^R\beta_{k_1}, {}^R\beta^\dagger_{k_2}\} = e^{-\mathbf{R}}\{\beta_{k_1},\beta^\dagger_{k_2}\}e^{\mathbf{R}} = \delta_{k_1 k_2}, \tag{C.5c}$$

standard Wick's theorem with respect to $|\Phi(l)\rangle$ applies and can be used to compute the matrix elements entering the right-hand side of Eq. (C.2). This results into the standard set of fully contracted terms, except that the elementary contractions at play do not involve the original quasi-particle operators but rather the similarity-transformed ones. The latter are related to the former via a non-unitary Bogoliubov transformation that is now detailed to compute the relevant elementary contractions.

Using Baker-Campbell-Hausdorff (BCH) identity, one first evaluates Eq. (C.4) according to

$$ {}^{R}\beta_{k_1}^{(\dagger)} = \beta_{k_1}^{(\dagger)} - [\mathbf{R}, \beta_{k_1}^{(\dagger)}] + \frac{1}{2!}[\mathbf{R}, [\mathbf{R}, \beta_{k_1}^{(\dagger)}]] + \dots . \tag{C.6} $$

Given the two elementary commutators

$$ \left[\beta_k^\dagger(l)\beta_{k'}^\dagger(l), \beta_{k_1}(l)\right] = \beta_k^\dagger(l)\delta_{k'k_1} - \beta_{k'}^\dagger(l)\delta_{kk_1}\,, \tag{C.7a} $$

$$ \left[\beta_k^\dagger(l)\beta_{k'}^\dagger(l), \beta_{k_1}^\dagger(l)\right] = 0\,, \tag{C.7b} $$

it is straightforward to prove

$$ \begin{aligned}
\left[\mathbf{R}, \beta_{k_1}\right] &= -\sum_{k_2}\left[U(l)\mathbf{z}(l,r)\right]_{k_1k_2}\beta_{k_2}^\dagger(l)\,,\\
\left[\mathbf{R}, \left[\mathbf{R}, \beta_{k_1}\right]\right] &= 0\,,\\
\left[\mathbf{R}, \dots \left[\mathbf{R}, \beta_{k_1}\right] \dots\right] &= 0\,,\\
\left[\mathbf{R}, \beta_{k_1}^\dagger\right] &= -\sum_{k_2}\left[V(l)\mathbf{z}(l,r)\right]_{k_1k_2}\beta_{k_2}^\dagger(l)\,,\\
\left[\mathbf{R}, \left[\mathbf{R}, \beta_{k_1}^\dagger\right]\right] &= 0\,,\\
\left[\mathbf{R}, \dots \left[\mathbf{R}, \beta_{k_1}^\dagger\right] \dots\right] &= 0\,,
\end{aligned} $$

such that

$$ \begin{aligned}
{}^{R}\beta_{k_1} &= \sum_{k_2} U_{k_1k_2}(l)\beta_{k_2}(l)\\
&\quad + \left[V^*(l) + U(l)\mathbf{z}(l,r)\right]_{k_1k_2}\beta_{k_2}^\dagger(l)\,, \qquad \text{(C.8a)}\\
{}^{R}\beta_{k_1}^\dagger &= \sum_{k_2} V_{k_1k_2}(l)\beta_{k_2}(l)\\
&\quad + \left[U^*(l) + V(l)\mathbf{z}(l,r)\right]_{k_1k_2}\beta_{k_2}^\dagger(l)\,, \qquad \text{(C.8b)}
\end{aligned} $$

which can be compacted in matrix form according to the non-unitary Bogoliubov transformation

$$ \begin{pmatrix} {}^{R}\beta \\ {}^{R}\beta^\dagger \end{pmatrix} = \begin{pmatrix} U(l) & V^*(l) + U(l)\mathbf{z}(l,r) \\ V(l) & U^*(l) + V(l)\mathbf{z}(l,r) \end{pmatrix}\begin{pmatrix} \beta(l) \\ \beta^\dagger(l) \end{pmatrix}. \tag{C.9} $$

As Eqs. (C.8-C.9) testify, the infinite expansion in Eq. (C.6), originating from the presence of $e^{\mathbf{R}}$ in Eq. (2.1), *naturally terminates*, i.e. it stops after two terms. Eventually, the four elementary contractions read as

$$ \rho_{k_1k_2}(l,r) = \langle\Phi(l)|{}^{R}\beta_{k_2}^\dagger\,{}^{R}\beta_{k_1}|\Phi(l)\rangle \tag{C.10a} $$

$$
\begin{aligned}
&= \Big[V^*(l) V^T(l) + U(l) \mathbf{z}(l,r) V^T(l) \Big]_{k_1 k_2} \\
&= +\rho_{k_1 k_2}(l,l) + \Big[U(l) \mathbf{z}(l,r) V^T(l) \Big]_{k_1 k_2} \, , \\
\kappa_{k_1 k_2}(l,r) &= \langle \Phi(l)|^R \beta_{k_2} \, {}^R \beta_{k_1} |\Phi(l)\rangle \qquad \text{(C.10b)} \\
&= \Big[V^*(l) U^T(l) + U(l) \mathbf{z}(l,r) U^T(l) \Big]_{k_1 k_2} \\
&= +\kappa_{k_1 k_2}(l,l) + \Big[U(l) \mathbf{z}(l,r) U^T(l) \Big]_{k_1 k_2} \, , \\
-\bar{\kappa}^*_{k_1 k_2}(l,r) &= \langle \Phi(l)|^R \beta^\dagger_{k_2} \, {}^R \beta^\dagger_{k_1} |\Phi(l)\rangle \qquad \text{(C.10c)} \\
&= \Big[U^*(l) V^T(l) + V(l) \mathbf{z}(l,r) V^T(l) \Big]_{k_1 k_2} \\
&= -\bar{\kappa}^*_{k_1 k_2}(l,l) + \Big[V(l) \mathbf{z}(l,r) V^T(l) \Big]_{k_1 k_2} \, , \\
-\sigma^*_{k_1 k_2}(l,r) &= \langle \Phi(l)|^R \beta_{k_2} \, {}^R \beta^\dagger_{k_1} |\Phi(l)\rangle \qquad \text{(C.10d)} \\
&= \Big[U^*(l) U^T(l) + V(l) \mathbf{z}(l,r) U^T(l) \Big]_{k_1 k_2} \\
&= -\sigma^*_{k_1 k_2}(l,l) + \Big[V(l) \mathbf{z}(l,r) U^T(l) \Big]_{k_1 k_2} \, ,
\end{aligned}
$$

where Eqs. (C.8-C.9) have been used. This completes the derivation of the off-diagonal Wick theorem where the explicit form of the elementary off-diagonal contractions in Eq. (C.10) reflects the asymmetric character of the approach, i.e. the expressions are anchored on the bra state $\langle \Phi(l)|$ and are a functional of the Thouless matrix $\mathbf{z}(l,r)$ associated with the transition Bogoliubov transformation of Eqs. (1.22-1.24).

Starting from Eq. (C.10) and using repeatedly relations associated with the unitarity of $W(l)$ (Eq. (1.17)), one can symmetrise the elementary contractions by expressing them in terms of the Thouless matrices $\mathbf{z}(l)$ and $\mathbf{z}(r)$ associated with the left and right states, respectively. Doing so, one recovers exactly Eqs. (2.17) and (2.19) obtained directly via the symmetric approach.

Appendix D

Connected kernel of a rank-3 operator

According to Eq. (2.16), the connected kernel associated with a rank-3 operator $O \equiv \mathbf{O}^{[0]} + \mathbf{O}^{[2]} + \mathbf{O}^{[4]} + \mathbf{O}^{[6]}$ reads in terms of the off-diagonal elementary contractions as

$$
\begin{aligned}
\frac{\langle\Phi(l)|O|\Phi(r)\rangle}{\langle\Phi(l)|\Phi(r)\rangle} &= \mathbf{O}^{[0]} + \frac{1}{2}\sum_{k_1k_2}\mathbf{o}^{k_1k_2}\bar{\kappa}^*_{k_1k_2}(l,r) + \sum_{k_1l_1}\mathbf{o}^{k_1}_{l_1}\rho_{l_1k_1}(l,r) + \frac{1}{2}\sum_{l_1l_2}\mathbf{o}_{l_1l_2}\kappa_{l_1l_2}(l,r) \\
&+ \frac{1}{8}\sum_{k_1k_2k_3k_4}\mathbf{o}^{k_1k_2k_3k_4}\bar{\kappa}^*_{k_1k_2}(l,r)\bar{\kappa}^*_{k_3k_4}(l,r) + \frac{1}{2}\sum_{k_1k_2k_3l_1}\mathbf{o}^{k_1k_2k_3}_{l_1}\rho_{l_1k_1}(l,r)\bar{\kappa}^*_{k_2k_3}(l,r) \\
&+ \frac{1}{2}\sum_{k_1k_2l_1l_2}\mathbf{o}^{k_1k_2}_{l_1l_2}\rho_{l_1k_1}(l,r)\rho_{l_2k_2}(l,r) + \frac{1}{4}\sum_{k_1k_2l_1l_2}\mathbf{o}^{k_1k_2}_{l_1l_2}\bar{\kappa}^*_{k_1k_2}(l,r)\kappa_{l_1l_2}(l,r) \\
&+ \frac{1}{2}\sum_{k_1l_1l_2l_3}\mathbf{o}^{k_1}_{l_1l_2l_3}\rho_{l_1k_1}(l,r)\kappa_{l_2l_3}(l,r) + \frac{1}{8}\sum_{l_1l_2l_3l_4}\mathbf{o}_{l_1l_2l_3l_4}\kappa_{l_1l_2}(l,r)\kappa_{l_3l_4}(l,r) \\
&+ \frac{1}{48}\sum_{k_1k_2k_3k_4k_5k_6}\mathbf{o}^{k_1k_2k_3k_4k_5k_6}\bar{\kappa}^*_{k_1k_2}(l,r)\bar{\kappa}^*_{k_3k_4}(l,r)\bar{\kappa}^*_{k_5k_6}(l,r) \\
&+ \frac{1}{8}\sum_{k_1k_2k_3k_4k_5l_1}\mathbf{o}^{k_1k_2k_3k_4k_5}_{l_1}\rho_{l_1k_1}(l,r)\bar{\kappa}^*_{k_2k_3}(l,r)\bar{\kappa}^*_{k_4k_5}(l,r) \\
&+ \frac{1}{16}\sum_{k_1k_2k_3k_4l_1l_2}\mathbf{o}^{k_1k_2k_3k_4}_{l_1l_2}\bar{\kappa}^*_{k_1k_2}(l,r)\bar{\kappa}^*_{k_3k_4}(l,r)\kappa_{l_1l_2}(l,r) \\
&+ \frac{1}{4}\sum_{k_1k_2k_3k_4l_1l_2}\mathbf{o}^{k_1k_2k_3k_4}_{l_1l_2}\rho_{l_1k_1}(l,r)\rho_{l_2k_2}(l,r)\bar{\kappa}^*_{k_3k_4}(l,r) \\
&+ \frac{1}{6}\sum_{k_1k_2k_3l_1l_2l_3}\mathbf{o}^{k_1k_2k_3}_{l_1l_2l_3}\rho_{l_1k_1}(l,r)\rho_{l_2k_2}(l,r)\rho_{l_3k_3}(l,r) \\
&+ \frac{1}{4}\sum_{k_1k_2k_3l_1l_2l_3}\mathbf{o}^{k_1k_2k_3}_{l_1l_2l_3}\rho_{l_1k_1}(l,r)\bar{\kappa}^*_{k_2k_3}(l,r)\kappa_{l_2l_3}(l,r) \\
&+ \frac{1}{16}\sum_{k_1k_2l_1l_2l_3l_4}\mathbf{o}^{k_1k_2}_{l_1l_2l_3l_4}\bar{\kappa}^*_{k_1k_2}(l,r)\kappa_{l_1l_2}(l,r)\kappa_{l_3l_4}(l,r) \\
&+ \frac{1}{4}\sum_{k_1k_2l_1l_2l_3l_4}\mathbf{o}^{k_1k_2}_{l_1l_2l_3l_4}\rho_{l_1k_1}(l,r)\rho_{l_2k_2}(l,r)\kappa_{l_3l_4}(l,r)
\end{aligned}
$$

$$+\frac{1}{8}\sum_{k_1 l_1 l_2 l_3 l_4 l_5} \mathbf{o}^{k_1}_{l_1 l_2 l_3 l_4 l_5} \rho_{l_1 k_1}(l,r)\kappa_{l_2 l_3}(l,r)\kappa_{l_4 l_5}(l,r)$$
$$+\frac{1}{48}\sum_{l_1 l_2 l_3 l_4 l_5 l_6} \mathbf{o}_{l_1 l_2 l_3 l_4 l_5 l_6} \kappa_{l_1 l_2}(l,r)\kappa_{l_3 l_4}(l,r)\kappa_{l_5 l_6}(l,r). \tag{D.1}$$

Appendix E

Proofs involving nested commutators

E.1 Nested commutator property

This appendix extends a well known commutator identity to nested commutators. The result, which is proven below, is

$$C_n(L,AB) = \sum_{k=0}^{n} \binom{n}{k} C_{n-k}(L,A) C_k(L,B). \tag{E.1}$$

Proof. Equation (E.1) is proven by induction. For $n = 1$ the formula reduces to the well known commutator property

$$[L,AB] = A[L,B] + [L,A]B. \tag{E.2}$$

Assuming then Eq. (E.1) to be verified for n, let us show that it holds for $(n+1)$ as well

$$\begin{aligned}
C_{n+1}(L,AB) &= \underbrace{[L,[L,\ldots[L,[L}_{n+1 \text{ times}},AB]]\ldots]] \\
&= \underbrace{[L,[L,\ldots[L,[L}_{n \text{ times}},[L,A]B]]\ldots]] + \underbrace{[L,[L,\ldots[L,[L}_{n \text{ times}},A[L,B]]]\ldots]] \\
&= C_n(L,[L,A]B) + C_n(L,A[L,B]) \\
&= \sum_{k=0}^{n} \binom{n}{k} C_{n-k}(L,[L,A]) C_k(L,B) + \sum_{k=0}^{n} \binom{n}{k} C_{n-k}(L,A) C_k(L,[L,B]) \\
&= \sum_{k=0}^{n} \binom{n}{k} C_{n+1-k}(L,A) C_k(L,B) + \sum_{k=0}^{n} \binom{n}{k} C_{n-k}(L,A) C_{k+1}(L,B) \\
&= \sum_{k=0}^{n} \binom{n}{k} C_{n+1-k}(L,A) C_k(L,B) + \sum_{k=1}^{n+1} \binom{n}{k-1} C_{n+1-k}(L,A) C_k(L,B) \\
&= \sum_{n=1}^{n} \left[\binom{n}{k} + \binom{n}{k-1} \right] C_{n+1-k}(L,A) C_k(L,B) + C_{n+1}(L,A)B + AC_{n+1}(L,B) \\
&= \sum_{n=1}^{n} \binom{n+1}{k} C_{n+1-k}(L,A) C_k(L,B) + C_{n+1}(L,A)B + AC_{n+1}(L,B) \\
&= \sum_{n=0}^{n+1} \binom{n+1}{k} C_{n+1-k}(L,A) C_k(L,B).
\end{aligned} \tag{E.3}$$

This proves Eq. (E.1). □

E.2 Recursive formula

The identity from Eq. (E.1) is hereby used to proof the identity

$$\sum_{l=0}^{\infty}\frac{1}{l!}C_l(L,R^r)=\left\{\sum_{k=0}^{\infty}\frac{1}{k!}C_k(L,R)\right\}^r. \tag{E.4}$$

Proof. Equation (E.1) is first used to write

$$\begin{aligned}C_l(L,R^r)&=C_l(L,R\cdot R^{r-1})\\&=\sum_{k=0}^{l}\binom{l}{k}C_{l-k}(L,R)C_k(L,R^{r-1}).\end{aligned} \tag{E.5}$$

Let us now compute the series

$$\begin{aligned}\sum_{l=0}^{\infty}\frac{1}{l!}C_l(L,R^r)&=\sum_{l=0}^{\infty}\frac{1}{l!}\sum_{k=0}^{l}\frac{l!}{k!(l-k)!}C_{l-k}(L,R)C_k(L,R^{r-1})\\&=\sum_{k=0}^{\infty}\sum_{l=k}^{\infty}\frac{1}{k!(l-k)!}C_{l-k}(L,R)C_k(L,R^{r-1})\\&=\sum_{k=0}^{\infty}\sum_{i=0}^{\infty}\frac{1}{k!i!}C_i(L,R)C_k(L,R^{r-1})\\&=\left\{\sum_{i=0}^{\infty}\frac{1}{i!}C_i(L,R)\right\}\sum_{l=0}^{\infty}\frac{1}{l!}C_l(L,R^{r-1}).\end{aligned} \tag{E.6}$$

A recursive relation is, thus, provided, such that after r times one exactly finds Eq. (E.4), which proves our initial claim. □

E.3 Commutator series truncation

For **L** and **R** defined in Eqs. (2.4) one finds

$$\begin{aligned}[L,R]&=\frac{1}{4}\sum_{\substack{k_1l_1\\k_2l_2}}\mathbf{z}^*_{k_1l_1}(l)\mathbf{z}^{k_2l_2}(r)[b_{k_1l_1},b^\dagger_{k_2l_2}]\\&=\frac{1}{2}\mathrm{Tr}\left\{\mathbf{z}^\dagger(l)\mathbf{z}(r)\right\}+\sum_{kl}\left[\mathbf{z}^*(l)\mathbf{z}(r)\right]_{kl}a_{kl}\,,\end{aligned} \tag{E.7a}$$

$$\begin{aligned}[L,[L,R]]&=\frac{1}{2}\sum_{\substack{k_1l_1\\k_2l_2}}\mathbf{z}^*_{k_1l_1}(l)\left[\mathbf{z}^*(l)\mathbf{z}(r)\right]_{k_2l_2}[b_{k_1kl_1},a_{k_2l_2}]\\&=\sum_{kl}\left[\mathbf{z}^*(l)\mathbf{z}(r)\mathbf{z}^*(l)\right]_{kl}b_{kl}\,,\end{aligned} \tag{E.7b}$$

$$\underbrace{[L,[L,\ldots[L,[L}_{l\text{ times}},R]]]]=0\qquad\forall\ l>2\,, \tag{E.7c}$$

and similarly

$$[[L,R],R] = \sum_{kl} \Big[\mathbf{z}(r)\mathbf{z}^*(l)\mathbf{z}(r)\Big]_{kl} b^\dagger_{kl}\,, \tag{E.7d}$$

$$[[[[\underbrace{L,R],R]\ldots,R],R}_{r \text{ times}}] = 0 \qquad \forall\ r > 2\,. \tag{E.7e}$$

Appendix F

Evaluation of Eq. (3.47) for $i = 3$

Setting $i = 3$ Eq. (3.47) reduces to four possible combinations of l and r, i.e.

$$M^{[3]} = \frac{1}{6}\sum_{\lambda_1\lambda_2\lambda_3} b^\dagger_{\lambda_1} b^\dagger_{\lambda_2} b^\dagger_{\lambda_3} \langle\Phi|[B_{\lambda_1},[B_{\lambda_2},[B_{\lambda_3},H]]]|\Phi\rangle + \frac{1}{2}\sum_{\lambda_1\lambda_2\rho_1} b^\dagger_{\lambda_1} b^\dagger_{\lambda_2} b_{\rho_1} \langle\Phi|[[B_{\lambda_1},[B_{\lambda_2},H]],B^\dagger_{\rho_1}]]|\Phi\rangle$$
$$+\frac{1}{2}\sum_{\lambda_1\rho_1\rho_2} b^\dagger_{\lambda_1} b_{\rho_1} b_{\rho_2} \langle\Phi|[[[B_{\lambda_1},H],B^\dagger_{\rho_1}],B^\dagger_{\rho_2}]|\Phi\rangle + \frac{1}{6}\sum_{\rho_1\rho_2\rho_3} b_{\rho_1} b_{\rho_2} b_{\rho_3} \langle\Phi|[[[H,B^\dagger_{\rho_1}],B^\dagger_{\rho_2}],B^\dagger_{\rho_3}]|\Phi\rangle\,. \quad \text{(F.1)}$$

Equation (F.1) can be recast in a more symmetric way, similarly to the $i = 2$ case,

$$\begin{aligned} M^{[3]} &= \sum_{\alpha\beta\gamma} \left[\frac{1}{6} b^\dagger_\alpha b^\dagger_\beta b^\dagger_\gamma \mathcal{E}_{\alpha\beta\gamma} + \frac{1}{2} b^\dagger_\alpha b^\dagger_\beta b_\gamma \mathcal{F}_{\alpha\beta}{}^{\gamma} + \frac{1}{2} b^\dagger_\alpha b_\beta b_\gamma \mathcal{H}^{*}{}_{\alpha}{}^{\beta\gamma} + \frac{1}{6} b_\alpha b_\beta b_\gamma \mathcal{E}^{*\alpha\beta\gamma} \right] \\ &= \sum_{\alpha\beta\gamma} \frac{1}{6}\Big[b^\dagger_\alpha b^\dagger_\beta b^\dagger_\gamma \mathcal{E}_{\alpha\beta\gamma} + b^\dagger_\alpha b^\dagger_\beta b_\gamma \mathcal{F}_{\alpha\beta}{}^{\gamma} + b^\dagger_\alpha b_\beta b^\dagger_\gamma \mathcal{G}_{\alpha}{}^{\beta}{}_{\gamma} + b_\alpha b^\dagger_\beta b^\dagger_\gamma \mathcal{H}^{\alpha}{}_{\beta\gamma} \\ &\qquad + b^\dagger_\alpha b_\beta b_\gamma \mathcal{H}^{*}{}_{\alpha}{}^{\beta\gamma} + b_\alpha b^\dagger_\beta b_\gamma \mathcal{G}^{*\alpha}{}_{\beta}{}^{\gamma} + b_\alpha b_\beta b^\dagger_\gamma \mathcal{F}^{*\alpha\beta}{}_{\gamma} + b_\alpha b_\beta b_\gamma \mathcal{E}^{*\alpha\beta\gamma} \Big] \\ &\quad - \sum_{\alpha\beta} \frac{1}{2}\Big[b^\dagger_\alpha \mathcal{F}_{\alpha\beta}{}^{\beta} + b_\alpha \mathcal{F}^{*\alpha\beta}{}_{\beta} \Big], \end{aligned} \quad \text{(F.2)}$$

where the matrices

$$\mathcal{E}_{\alpha\beta\gamma} \equiv \langle\Phi|[B_\alpha,[B_\beta,[B_\gamma,H]]]|\Phi\rangle\,, \quad \text{(F.3a)}$$
$$\mathcal{F}_{\alpha\beta}{}^{\gamma} \equiv \langle\Phi|[[B_\alpha,[B_\beta,H]],B^\dagger_\gamma]|\Phi\rangle\,, \quad \text{(F.3b)}$$
$$\mathcal{G}_{\alpha}{}^{\beta}{}_{\gamma} \equiv -\langle\Phi|[[[B_\alpha,H],B^\dagger_\beta],B_\gamma]|\Phi\rangle = \mathcal{F}_{\alpha\gamma}{}^{\beta}\,, \quad \text{(F.3c)}$$
$$\mathcal{H}^{\alpha}{}_{\beta\gamma} \equiv \langle\Phi|[[[H,B^\dagger_\alpha],B_\beta],B_\gamma]|\Phi\rangle = \mathcal{F}_{\gamma\beta}{}^{\alpha}\,, \quad \text{(F.3d)}$$

have been introduced. All objects in Eqs. (F.3) are symmetric with respect to exchange of indices of the same kind (upper or lower) due to the Jacobi identity. Eventually, Eq. (F.2) is written in the form

$$M^{[3]} = \frac{1}{6} b^\dagger \begin{pmatrix} b^\dagger & b \end{pmatrix} \begin{pmatrix} \mathcal{F} & \mathcal{E} \\ \mathcal{H}^* & \mathcal{G} \end{pmatrix} \begin{pmatrix} b \\ b^\dagger \end{pmatrix} + \frac{1}{6} b \begin{pmatrix} b^\dagger & b \end{pmatrix} \begin{pmatrix} \mathcal{G}^* & \mathcal{H} \\ \mathcal{E}^* & \mathcal{F}^* \end{pmatrix} \begin{pmatrix} b \\ b^\dagger \end{pmatrix} - \sum_{\alpha\beta} \frac{1}{2}\Big[b^\dagger_\alpha \mathcal{F}_{\alpha\beta}{}^{\beta} + b_\alpha \mathcal{F}^{*\alpha\beta}{}_{\beta} \Big]. \quad \text{(F.4)}$$

Equation (F.4) may be used for the definition of a set of QRPA equations consistently treating three-body forces. The non-vanishing contributions to the matrix elements are provided, at the two-body level, by

$$\langle\Phi|[[B_{k_1 l_1},[B_{k_2 l_2},\mathbf{H}^{[2]}]],B^\dagger_{k_3 l_3}]|\Phi\rangle = \langle\Phi|[[B_{k_1 l_1},[B_{k_2 l_2},\mathbf{H}^{31}]],B^\dagger_{k_3 l_3}]|\Phi\rangle$$

$$= \frac{1}{6}\sum_{\substack{k_4 l_4 \\ k_5 l_5 \\ j}} \mathbf{h}^{k_4 l_4 k_5}{}_{l_5} \langle\Phi|[[B_{k_1 l_1}, [B_{k_2 l_2}, B^\dagger_{k_4 l_4} B^\dagger_{k_5 j} B_{l_5 j}]], B^\dagger_{k_3 l_3}]|\Phi\rangle$$

$$= \frac{1}{6}\Big\{\mathbf{h}^{k_1 k_2 l_2}{}_{k_3}\delta_{l_1 l_3} + \mathbf{h}^{k_1 l_1 k_2}{}_{k_3}\delta_{l_2 l_3}\Big\}, \tag{F.5a}$$

$$\langle\Phi|[[[B_{k_1 l_1}, \mathbf{H}^{[2]}], B^\dagger_{k_2 l_2}], B^\dagger_{k_3 l_3}]|\Phi\rangle = \langle\Phi|[[[B_{k_1 l_1}, \mathbf{H}^{13}], B^\dagger_{k_2 l_2}], B^\dagger_{k_3 l_3}]|\Phi\rangle$$

$$= \frac{1}{6}\sum_{\substack{k_4 l_4 \\ k_5 l_5 \\ j}} \mathbf{h}^{k_4}{}_{k_5 l_5 l_4} \langle\Phi|[[[B_{k_1 l_1}, B^\dagger_{k_4 j} B_{l_4 j} B_{k_5 l_5}], B^\dagger_{k_2 l_2}], B^\dagger_{k_3 l_3}]|\Phi\rangle$$

$$= \frac{1}{6}\Big\{\mathbf{h}^{k_1}{}_{k_2 l_2 k_3}\delta_{l_1 l_3} + \mathbf{h}^{k_1}{}_{k_3 l_3 k_2}\delta_{l_1 l_2}\Big\} \tag{F.5b}$$

and, at the three-body level, by

$$\langle\Phi|[B_{k_1 l_1}, [B_{k_2 l_2}, [B_{k_3 l_3}, \mathbf{H}^{[3]}]]]|\Phi\rangle = \langle\Phi|[B_{k_1 l_1}, [B_{k_2 l_2}, [B_{k_3 l_3}, \mathbf{H}^{60}]]]|\Phi\rangle$$

$$= \frac{1}{6!}\sum_{\substack{k_4 k_5 k_6 \\ l_4 l_5 l_6}} \mathbf{h}^{k_4 l_4 k_5 l_5 k_6 l_6} \langle\Phi|[B_{k_1 l_1}, [B_{k_2 l_2}, [B_{k_3 l_3}, B^\dagger_{k_4 l_4} B^\dagger_{k_5 l_5} B^\dagger_{k_6 l_6}]]]|\Phi\rangle$$

$$= \frac{1}{5!}\mathbf{h}^{k_1 l_1 k_2 l_2 k_3 l_3}, \tag{F.6a}$$

$$\langle\Phi|[[[\mathbf{H}^{[3]}, B^\dagger_{k_1 l_1}], B^\dagger_{k_2 l_2}], B^\dagger_{k_3 l_3}]|\Phi\rangle = \langle\Phi|[[[\mathbf{H}^{06}, B^\dagger_{k_1 l_1}], B^\dagger_{k_2 l_2}], B^\dagger_{k_3 l_3}]|\Phi\rangle$$

$$= \frac{1}{6!}\sum_{\substack{k_4 k_5 k_6 \\ l_4 l_5 l_6}} \mathbf{h}_{k_6 l_6 k_5 l_5 k_4 l_4} \langle\Phi|[[[B_{k_4 l_4} B_{k_5 l_5} B_{k_6 l_6}, B^\dagger_{k_1 l_1}], B^\dagger_{k_2 l_2}], B^\dagger_{k_3 l_3}]|\Phi\rangle$$

$$= \frac{1}{5!}\mathbf{h}_{k_1 l_1 k_2 l_2 k_3 l_3}, \tag{F.6b}$$

$$\langle\Phi|[[B_{k_1 l_1}, [B_{k_2 l_2}, \mathbf{H}^{[3]}]], B^\dagger_{k_3 l_3}]|\Phi\rangle = \langle\Phi|[[B_{k_1 l_1}, [B_{k_2 l_2}, \mathbf{H}^{42}]], B^\dagger_{k_3 l_3}]|\Phi\rangle$$

$$= \frac{1}{2\cdot 4!}\sum_{\substack{k_4 k_5 k_6 \\ l_4 l_5 l_6}} \mathbf{h}^{k_4 l_4 k_5 l_5}{}_{k_6 l_6} \langle\Phi|[[B_{k_1 l_1}, [B_{k_2 l_2}, B^\dagger_{k_4 l_4} B^\dagger_{k_5 l_5} B_{k_6 l_6}]], B^\dagger_{k_3 l_3}]|\Phi\rangle$$

$$= \frac{1}{4!}\mathbf{h}^{k_1 l_1 k_2 l_2}{}_{k_3 l_3}, \tag{F.6c}$$

$$\langle\Phi|[[[B_{k_1 l_1}, \mathbf{H}^{[3]}], B^\dagger_{k_2 l_2}], B^\dagger_{k_3 l_3}]|\Phi\rangle = \langle\Phi|[[[B_{k_1 l_1}, \mathbf{H}^{24}], B^\dagger_{k_2 l_2}], B^\dagger_{k_3 l_3}]|\Phi\rangle$$

$$= \frac{1}{2\cdot 4!}\sum_{\substack{k_4 k_5 k_6 \\ l_4 l_5 l_6}} \mathbf{h}^{k_4 l_4}{}_{k_6 l_6 k_5 l_5} \langle\Phi|[[[B_{k_1 l_1}, B^\dagger_{k_4 l_4} B_{k_5 l_5} B_{k_6 l_6}], B^\dagger_{k_2 l_2}], B^\dagger_{k_3 l_3}]|\Phi\rangle$$

$$= \frac{1}{4!}\mathbf{h}^{k_1 l_1}{}_{k_2 l_2 k_3 l_3}, \tag{F.6d}$$

which leads to

$$\mathcal{E}_{k_1 l_1 k_2 l_2 k_3 l_3} = \frac{1}{5!}\mathbf{h}^{k_1 l_1 k_2 l_2 k_3 l_3}, \tag{F.7a}$$

$$\mathcal{F}_{k_1 l_1 k_2 l_2}{}^{k_3 l_3} = \frac{1}{6}\Big\{\mathbf{h}^{k_1 k_2 l_2}{}_{k_3}\delta_{l_1 l_3} + \mathbf{h}^{k_1 l_1 k_2}{}_{k_3}\delta_{l_2 l_3}\Big\} + \frac{1}{4!}\mathbf{h}^{k_1 l_1 k_2 l_2}{}_{k_3 l_3}, \tag{F.7b}$$

$$\mathcal{H}^*_{k_1 l_1}{}^{k_2 l_2 k_3 l_3} = \frac{1}{6}\Big\{\mathbf{h}^{k_1}{}_{k_2 l_2 k_3}\delta_{l_1 l_3} + \mathbf{h}^{k_1}{}_{k_3 l_3 k_2}\delta_{l_1 l_2}\Big\} + \frac{1}{4!}\mathbf{h}^{k_1 l_1}{}_{k_2 l_2 k_3 l_3}. \tag{F.7c}$$

Appendix G

Identities for boson expansion methods

In the present appendix the explicit calculations necessary in Sec. 3.6 are performed in detail. Let us redefine the Thouless' matrices inherent to the two Bogoliubov vacua $\langle\Phi(l)|$ and $|\Phi(r)\rangle$ as

$$\mathbf{z}(l) \equiv \mathbf{z}, \tag{G.1a}$$
$$\mathbf{z}(r) \equiv \mathbf{z}'. \tag{G.1b}$$

The norm kernel reads, in the newly introduced variables,

$$\mathcal{N}(\mathbf{z}^*, \mathbf{z}') = \exp\left[\frac{1}{2}\mathrm{Tr}\left\{\ln\left(1 - \mathbf{z}^*\mathbf{z}'\right)\right\}\right]. \tag{G.2}$$

G.1 Matrix calculus properties

Let us start recalling some important properties of matrix calculus. For $\mathbf{U}$ a matrix generically depending on $\mathbf{z}$, i.e. $\mathbf{U} = f(\mathbf{z})$, the chain rule for the derivative of a matrix reads

$$\frac{\partial g(\mathbf{U})}{\partial \mathbf{z}_{kl}} = \mathrm{Tr}\left[\left(\frac{\partial g(\mathbf{U})}{\partial \mathbf{U}}\right)^{\mathrm{T}} \frac{\partial \mathbf{U}}{\partial \mathbf{z}_{kl}}\right]. \tag{G.3}$$

Another important property valid when differentiating the trace of a function with respect to its variable is the following

$$\frac{\partial \mathrm{Tr}\Big(F(\mathbf{U})\Big)e}{\partial \mathbf{U}} = f(\mathbf{U})^{\mathrm{T}}, \tag{G.4}$$

where f is the scalar derivative of F, i.e.

$$f(\cdot) \equiv F'(\cdot). \tag{G.5}$$

G.2 Norm kernel derivative

The first step in the derivation of Eqs. (3.69) is the differentiation of the norm kernel given in Eq. (G.2). Replacing

$$\mathbf{U} \equiv \mathbf{z}^* \cdot \mathbf{z}' \tag{G.6}$$

into Eq. (G.2) and using the properties Eqs. (G.3) and (G.4) the derivative of the norm kernel can be computed without ambiguities

$$\frac{\partial \mathcal{N}(\mathbf{z}^*, \mathbf{z}')}{\partial \mathbf{z}^*_{kl}} = \mathcal{N}(\mathbf{z}^*, \mathbf{z}')\frac{1}{2}\mathrm{Tr}\left[\left(\frac{\partial}{\partial \mathbf{U}}\mathrm{Tr}\,\ln(1-\mathbf{U})\right)^{\mathrm{T}} \frac{\partial \mathbf{U}}{\partial \mathbf{z}^*_{kl}}\right]$$

$$
\begin{aligned}
&= \mathcal{N}(\mathbf{z}^*,\mathbf{z}')\frac{1}{2}\mathrm{Tr}\Big[-\Big(\frac{1}{1-\mathbf{U}}\Big)\frac{\partial \mathbf{U}}{\partial \mathbf{z}^*_{kl}}\Big] \\
&= \mathcal{N}(\mathbf{z}^*,\mathbf{z}')\frac{1}{2}\sum_{abc}\Big[-\Big(\frac{1}{1-\mathbf{z}^*\cdot\mathbf{z}'}\Big)_{ab}\frac{\partial}{\partial \mathbf{z}^*_{kl}}\mathbf{z}^*_{bc}\mathbf{z}'_{ca}\Big] \\
&= \mathcal{N}(\mathbf{z}^*,\mathbf{z}')\frac{1}{2}\sum_{abc}\Big[-\Big(\frac{1}{1-\mathbf{z}'\cdot\mathbf{z}^*}\Big)_{ba}(\delta_{kb}\delta_{lc}-\delta_{kc}\delta_{lb})\mathbf{z}'_{ca}\Big] \\
&= \mathcal{N}(\mathbf{z}^*,\mathbf{z}')\frac{1}{2}\sum_{a}\Big[-\Big(\frac{1}{1-\mathbf{z}'\cdot\mathbf{z}^*}\Big)_{ka}\mathbf{z}'_{la}+\Big(\frac{1}{1-\mathbf{z}'\cdot\mathbf{z}^*}\Big)_{la}\mathbf{z}'_{ka}\Big] \\
&= \mathcal{N}(\mathbf{z}^*,\mathbf{z}')\frac{1}{2}\sum_{a}\Big[\Big(\frac{1}{1-\mathbf{z}'\cdot\mathbf{z}^*}\Big)_{ka}\mathbf{z}'_{al}+\mathbf{z}'_{ka}\Big(\frac{1}{1-\mathbf{z}^*\cdot\mathbf{z}'}\Big)_{al}\Big],
\end{aligned}
\tag{G.7}
$$

where the property

$$
\begin{aligned}
(1-\mathbf{z}^*\cdot\mathbf{z}')^{-1} &= \Big[\Big[(1-\mathbf{z}^*\cdot\mathbf{z}')^{-1}\Big]^{\mathrm{T}}\Big]^{\mathrm{T}} \\
&= \Big[\Big[(1-\mathbf{z}^*\cdot\mathbf{z}')^{\mathrm{T}}\Big]^{-1}\Big]^{\mathrm{T}} \\
&= \Big[(1-\mathbf{z}'\cdot\mathbf{z}^*)^{-1}\Big]^{\mathrm{T}}
\end{aligned}
\tag{G.8}
$$

has been used. Recalling the relation

$$
\begin{aligned}
\mathbf{z}'\cdot\Big(\frac{1}{1-\mathbf{z}^*\cdot\mathbf{z}'}\Big) &= \sum_{n=0}^{\infty}\mathbf{z}'\cdot(\mathbf{z}^*\cdot\mathbf{z}')^n \\
&= \sum_{n=0}^{\infty}(\mathbf{z}'\cdot\mathbf{z}^*)^n\cdot\mathbf{z}' \\
&= \Big(\frac{1}{1-\mathbf{z}'\cdot\mathbf{z}^*}\Big)\cdot\mathbf{z}',
\end{aligned}
\tag{G.9}
$$

Eq. (G.7) eventually reads

$$
\frac{\partial \mathcal{N}(\mathbf{z}^*,\mathbf{z}')}{\partial \mathbf{z}^*_{kl}} = \Big[\mathbf{z}'\cdot\Big(\frac{1}{1-\mathbf{z}^*\cdot\mathbf{z}'}\Big)\Big]_{kl}\mathcal{N}(\mathbf{z}^*,\mathbf{z}').
\tag{G.10}
$$

The derivative with respect to the matrix $\mathbf{z}'$ is also computed,

$$
\begin{aligned}
\frac{\partial \mathcal{N}(\mathbf{z}^*,\mathbf{z}')}{\partial \mathbf{z}'_{kl}} &= \mathcal{N}(\mathbf{z}^*,\mathbf{z}')\frac{1}{2}\mathrm{Tr}\Big[\Big(\frac{\partial}{\partial \mathbf{U}}\mathrm{Tr}\ln(1-\mathbf{U})\Big)^{\mathrm{T}}\frac{\partial \mathbf{U}}{\partial \mathbf{z}'_{kl}}\Big] \\
&= \mathcal{N}(\mathbf{z}^*,\mathbf{z}')\frac{1}{2}\mathrm{Tr}\Big[-\Big(\frac{1}{1-\mathbf{U}}\Big)\frac{\partial \mathbf{U}}{\partial \mathbf{z}'_{kl}}\Big] \\
&= \mathcal{N}(\mathbf{z}^*,\mathbf{z}')\frac{1}{2}\sum_{abc}\Big[-\Big(\frac{1}{1-\mathbf{z}^*\cdot\mathbf{z}'}\Big)_{ab}\frac{\partial}{\partial \mathbf{z}'_{kl}}\mathbf{z}^*_{bc}\mathbf{z}'_{ca}\Big] \\
&= \mathcal{N}(\mathbf{z}^*,\mathbf{z}')\frac{1}{2}\sum_{abc}\Big[-\Big(\frac{1}{1-\mathbf{z}'\cdot\mathbf{z}^*}\Big)_{ba}\mathbf{z}^*_{bc}(\delta_{kc}\delta_{la}-\delta_{ka}\delta_{lc})\Big] \\
&= \mathcal{N}(\mathbf{z}^*,\mathbf{z}')\frac{1}{2}\sum_{a}\Big[-\Big(\frac{1}{1-\mathbf{z}'\cdot\mathbf{z}^*}\Big)_{bl}\mathbf{z}^*_{bk}+\Big(\frac{1}{1-\mathbf{z}'\cdot\mathbf{z}^*}\Big)_{bk}\mathbf{z}^*_{bl}\Big] \\
&= \mathcal{N}(\mathbf{z}^*,\mathbf{z}')\frac{1}{2}\sum_{a}\Big[\mathbf{z}^*_{kb}\Big(\frac{1}{1-\mathbf{z}'\cdot\mathbf{z}^*}\Big)_{bl}+\Big(\frac{1}{1-\mathbf{z}^*\cdot\mathbf{z}'}\Big)_{kb}\mathbf{z}^*_{bl}\Big]
\end{aligned}
$$

$$= \left[\left(\frac{1}{1-\mathbf{z}^*\cdot\mathbf{z}'}\right)\cdot\mathbf{z}^*\right]_{kl}\mathcal{N}(\mathbf{z}^*,\mathbf{z}'). \tag{G.11}$$

G.3 Anomalous densities

The comparison of Eq. (3.69b) to Eq. (G.10) allows to recover the desired result for the anomalous density matrix, since

$$\begin{aligned}\kappa_{kl}(\mathbf{z}^*,\mathbf{z}')\mathcal{N}(\mathbf{z}^*,\mathbf{z}') &= \left[\mathbf{z}'\cdot\left(\frac{1}{1-\mathbf{z}^*\cdot\mathbf{z}'}\right)\right]_{kl}\mathcal{N}(\mathbf{z}^*,\mathbf{z}')\\ &= \frac{\partial}{\partial\mathbf{z}^*_{kl}}\mathcal{N}(\mathbf{z}^*,\mathbf{z}').\end{aligned} \tag{G.12}$$

The validity of Eq. (3.69c) is now proven

$$\begin{aligned}\left(\mathbf{z}^*_{kl}+\sum_{ij}\mathbf{z}^*_{ki}\mathbf{z}^*_{jl}\frac{\partial}{\partial\mathbf{z}^*_{ij}}\right)\mathcal{N}(\mathbf{z}^*,\mathbf{z}') &= \left\{\mathbf{z}^*_{kl}+\sum_{ij}\mathbf{z}^*_{ki}\mathbf{z}^*_{jl}\left[\mathbf{z}'\cdot\left(\frac{1}{1-\mathbf{z}^*\cdot\mathbf{z}'}\right)\right]_{ij}\right\}\mathcal{N}(\mathbf{z}^*,\mathbf{z}')\\ &= \left[\mathbf{z}^*+\mathbf{z}^*\cdot\mathbf{z}'\cdot\left(\frac{1}{1-\mathbf{z}^*\cdot\mathbf{z}'}\right)\cdot\mathbf{z}^*\right]_{kl}\mathcal{N}(\mathbf{z}^*,\mathbf{z}')\\ &= \left[(1-\mathbf{z}^*\cdot\mathbf{z}')\cdot\left(\frac{1}{1-\mathbf{z}^*\cdot\mathbf{z}'}\right)\cdot\mathbf{z}^*+\mathbf{z}^*\cdot\mathbf{z}'\cdot\left(\frac{1}{1-\mathbf{z}^*\cdot\mathbf{z}'}\right)\cdot\mathbf{z}^*\right]_{kl}\mathcal{N}(\mathbf{z}^*,\mathbf{z}')\\ &= \left[\left(\frac{1}{1-\mathbf{z}^*\cdot\mathbf{z}'}\right)\cdot\mathbf{z}^*\right]_{kl}\mathcal{N}(\mathbf{z}^*,\mathbf{z}').\end{aligned} \tag{G.13}$$

Comparing to Eq. (3.69c) one gets

$$\begin{aligned}\kappa_{kl}(\mathbf{z}',\mathbf{z}^*)\mathcal{N}(\mathbf{z}^*,\mathbf{z}') &= \left[\left(\frac{1}{1-\mathbf{z}^*\cdot\mathbf{z}'}\right)\cdot\mathbf{z}^*\right]_{kl}\mathcal{N}(\mathbf{z}^*,\mathbf{z}')\\ &= \left(\mathbf{z}^*_{kl}+\sum_{ij}\mathbf{z}^*_{ki}\mathbf{z}^*_{jl}\frac{\partial}{\partial\mathbf{z}^*_{ij}}\right)\mathcal{N}(\mathbf{z}^*,\mathbf{z}').\end{aligned} \tag{G.14}$$

G.4 Normal density

The same steps are now used to prove Eq. (3.69d). The quantity

$$\begin{aligned}\sum_i\mathbf{z}^*_{li}\frac{\partial}{\partial\mathbf{z}^*_{ki}}\mathcal{N}(\mathbf{z}^*,\mathbf{z}') &= \sum_i\mathbf{z}^*_{li}\left[\mathbf{z}'\cdot\left(\frac{1}{1-\mathbf{z}^*\cdot\mathbf{z}'}\right)\right]_{ki}\mathcal{N}(\mathbf{z}^*,\mathbf{z}')\\ &= -\left[\mathbf{z}'\cdot\left(\frac{1}{1-\mathbf{z}^*\cdot\mathbf{z}'}\right)\cdot\mathbf{z}^*\right]_{kl}\mathcal{N}(\mathbf{z}^*,\mathbf{z}')\end{aligned} \tag{G.15}$$

is evaluated. Comparing to Eq. (3.69d) the equivalence is proven

$$\begin{aligned}\rho_{kl}(\mathbf{z}^*,\mathbf{z}')\mathcal{N}(\mathbf{z}^*,\mathbf{z}') &= -\left[\mathbf{z}'\cdot\left(\frac{1}{1-\mathbf{z}^*\cdot\mathbf{z}'}\right)\cdot\mathbf{z}^*\right]_{kl}\mathcal{N}(\mathbf{z}^*,\mathbf{z}')\\ &= \sum_i\mathbf{z}^*_{li}\frac{\partial}{\partial\mathbf{z}^*_{ki}}\mathcal{N}(\mathbf{z}^*,\mathbf{z}').\end{aligned} \tag{G.16}$$

Appendix H

Moments evaluation based on the HFB ground state

H.1 Odd moments

In this appendix a short focus on the derivation of the (Q)RPA odd-moments is reported. Particular attention is put on the fact that (Q)RPA odd moments can be computed knowing the sole HF(B) ground state. The reason why the same does not apply to even moments is shortly addressed. In what follows the procedure from Refs. [151, 181] is followed.

Let us write the transition matrix elements of F in the (Q)RPA as

$$\langle \Psi_0 | F | \Psi_\nu \rangle = (F^\dagger, F^\intercal) \begin{pmatrix} X^\nu \\ Y^\nu \end{pmatrix}. \tag{H.1}$$

Notice that in QRPA the matrix elements of F in the above equation are replaced by their two-quasiparticle components F^{20} (see App. A). Rising (Q)RPA equations (see Eq. (3.64)) to the power k one obtains

$$\begin{pmatrix} A & B \\ -B^* & -A^* \end{pmatrix}^k \begin{pmatrix} X^\nu \\ Y^\nu \end{pmatrix} = E_\nu^k \begin{pmatrix} X^\nu \\ Y^\nu \end{pmatrix}, \tag{H.2}$$

with of A and B defined by

$$A_{ph,p'h'} \equiv \langle \Phi | [c_h^\dagger c_p, [H, c_{h'}^\dagger c_{p'}]] | \Phi \rangle , \tag{H.3a}$$
$$B_{ph,p'h'} \equiv -\langle \Phi | [c_h^\dagger c_p, [H, c_{p'}^\dagger c_{h'}]] | \Phi \rangle , \tag{H.3b}$$

in RPA and by

$$A_{ab,cd} \equiv \langle \Phi | [\beta_b \beta_a, [H, \beta_c^\dagger \beta_d^\dagger]] | \Phi \rangle , \tag{H.4a}$$
$$B_{ab,cd} \equiv -\langle \Phi | [\beta_b \beta_a, [H, \beta_c \beta_d]] | \Phi \rangle \tag{H.4b}$$

in QRPA. If $2N$ is the total number of (Q)RPA solutions, half of them relate to positive eigenvalues whereas the other half relate to negative energies equal to the previous ones in absolute value. If $\nu \in [1, N]$ denotes the positive solutions and $\nu \in [N+1, 2N]$ the negative ones, this symmetry can be exploited to write

$$2m_k = 2 \sum_{\nu=1}^{N} E_\nu^k |\langle \Psi_\nu | F | \Psi_0 \rangle|^2$$

$$= \sum_{\nu=1}^{2N} |E_\nu^k| |\langle \Psi_\nu | F | \Psi_0 \rangle|^2 \tag{H.5}$$

$$= \left(\sum_{\nu=1}^{N} - \sum_{\nu=N+1}^{2N} \right) (F^\dagger, F^\intercal) \begin{pmatrix} X^\nu \\ Y^\nu \end{pmatrix} E_\nu^k (X^{\nu\dagger}, Y^{\nu\dagger}) \begin{pmatrix} F \\ F^* \end{pmatrix} \tag{H.6}$$

$$= \left(\sum_{\nu=1}^{N} - \sum_{\nu=N+1}^{2N} \right) (F^\dagger, F^\intercal) \begin{pmatrix} A & B \\ -B^* & -A^* \end{pmatrix}^k \begin{pmatrix} X^\nu \\ Y^\nu \end{pmatrix} (X^{\nu\dagger}, -Y^{\nu\dagger}) \begin{pmatrix} F \\ -F^* \end{pmatrix}.$$

Then the (Q)RPA identity

$$\left(\sum_{\nu=1}^{N} - \sum_{\nu=N+1}^{2N} \right) \begin{pmatrix} X^\nu \\ Y^\nu \end{pmatrix} (X^{\nu\dagger}, -Y^{\nu\dagger}) = \mathbb{1} \tag{H.7}$$

is used to eventually write

$$m_k = \frac{1}{2} (F^\intercal, F^\dagger) \begin{pmatrix} A & B \\ -B^* & -A^* \end{pmatrix}^k \begin{pmatrix} F \\ -F^* \end{pmatrix}, \tag{H.8}$$

Inserting Eqs. (H.3) and (H.4) into Eq. (H.8) for $k = 1$ leads to

$$\frac{1}{2} (F^\intercal, F^\dagger) \begin{pmatrix} A & B \\ -B^* & -A^* \end{pmatrix} \begin{pmatrix} F \\ -F^* \end{pmatrix} = \frac{1}{2} \langle \Phi | [F, [H, F]] | \Phi \rangle \tag{H.9}$$

is thus proving the equivalence between (Q)RPA 1-st order moment and the HF(B) expectation value of Eq. (4.46b) for $k = 1$. However, one should stress, and this is missing in Ref. [181], that going from Eq. (H.5) to Eq. (H.6) the sum splitting can only be performed for odd k values. The peculiar structure of the (Q)RPA identity resolution from Eq. (H.7) can be thus exploited for the computation of *odd* moments only.

H.2 Even moments

In what follows, the even moments computed from an HFB state are shown to be equal in the isoscalar and isovector channels. Beside its formal interest, such a property delivers a useful benchmark for the numerical calculations. Explicit derivations are presently performed for $\breve{M}_0(0,0)$ only but the extension to any higher even moment is straightforward.

Let us at first redefine the operator at use subtracting its mean value, as specified in Section 4.2, computed at the HFB level $\langle F \rangle_{\text{HFB}} \equiv \langle \Phi | F | \Phi \rangle$

$$\mathbf{F} \equiv F - \langle F \rangle_{\text{HFB}}, \tag{H.10a}$$

$$\mathbf{F}^2 \equiv F^2 - 2 \langle F \rangle_{\text{HFB}} F + \langle F \rangle_{\text{HFB}}^2. \tag{H.10b}$$

Compared to Eqs. (4.51) the matrix elements associated to $\breve{M}_0(0,0)$ become

$$\breve{M}_0^{[0]} = \langle F \rangle_{\text{HFB}}^2, \tag{H.11a}$$

$$\breve{m}_{0,ab}^{11} = \sum_c f_{ac}^{11} f_{cb}^{11} - 2 \langle F \rangle_{\text{HFB}} f_{ab}^{11}, \tag{H.11b}$$

$$\breve{m}_{0,abcd}^{22} = 2 (f_{ac}^{11} f_{bd}^{11} - f_{bc}^{11} f_{ad}^{11}). \tag{H.11c}$$

The average of $\breve{M}_0(0,0)$ with respect to an HFB state $|\Phi\rangle$ is

$$m_0^{\text{HFB}} \equiv \langle \Phi | \breve{M}_0(0,0) | \Phi \rangle$$

$$= \breve{M}_0^{[0]} + \sum_{ab} \breve{m}^{11}_{0,ab}\rho_{ba} + \frac{1}{2}\sum_{abcd} \breve{m}^{22}_{0,abcd}\rho_{ca}\rho_{db} + \frac{1}{4}\sum_{abcd} \breve{m}^{22}_{0,abcd}\kappa_{ba}\kappa_{dc}\,. \tag{H.12}$$

The notation

$$\begin{aligned} O &= \sum_{ab\in\pi} o_{ab}c_a^\dagger c_b \pm \sum_{ab\in\nu} o_{ab}c_a^\dagger c_b \\ &\equiv O_\pi \pm O_\nu \end{aligned} \tag{H.13}$$

is adopted to specify the two isospin components of a generic one-body operator O, which is feasible if the operator is block-diagonal with respect to isospin. Respectively, the plus and minus sign refer to isoscalar and isovector operators. The same is presently supposed to be true for the one-body HFB density matrices ρ and κ. Separately computing the different terms in Eq. (H.12) one then obtains

$$\begin{aligned} \breve{M}_0^{[0]} &= \langle F\rangle^2_{\text{HFB}} \\ &= \Big[\text{tr}(F_\pi\cdot\rho_\pi \pm F_\nu\cdot\rho_\nu)\Big]^2 && \text{(H.14a)} \\ \sum_{ab}\breve{m}^{11}_{0,ab}\rho_{ba} &= \sum_{abc} f^{11}_{ac}f^{11}_{cb}\rho_{ba} - 2\langle F\rangle_{\text{HFB}}\sum_{ab} f^{11}_{ab}\rho_{ba} \\ &= \text{tr}(F_\pi\cdot F_\pi\cdot\rho_\pi + F_\nu\cdot F_\nu\cdot\rho_\nu) - 2\Big[\text{tr}(F_\pi\cdot\rho_\pi \pm F_\nu\cdot\rho_\nu)\Big]^2 && \text{(H.14b)} \\ \frac{1}{2}\sum_{abcd}\breve{m}^{22}_{0,abcd}\rho_{ca}\rho_{db} &= \sum_{abcd}(f^{11}_{ac}f^{11}_{bd} - f^{11}_{bc}f^{11}_{ad})\rho_{ca}\rho_{db} \\ &= \Big[\text{tr}(F_\pi\cdot\rho_\pi) \pm \text{tr}(F_\nu\cdot\rho_\nu)\Big]^2 - \text{tr}(F_\pi\cdot\rho_\pi\cdot F_\pi\cdot\rho_\pi + F_\nu\cdot\rho_\nu\cdot F_\nu\cdot\rho_\nu) && \text{(H.14c)} \\ \frac{1}{4}\sum_{abcd}\breve{m}^{22}_{0,abcd}\kappa_{ba}\kappa^*_{dc} &= \frac{1}{2}\sum_{abcd}(f^{11}_{ac}f^{11}_{bd} - f^{11}_{bc}f^{11}_{ad})\kappa_{ba}\kappa^*_{dc} \\ &= -\frac{1}{2}\text{tr}(F_\pi\cdot\kappa_\pi\cdot F_\pi\cdot\kappa^*_\pi + F_\nu\cdot\kappa_\nu\cdot F_\nu\cdot\kappa^*_\nu) + \frac{1}{2}\text{tr}(F_\pi\cdot\kappa_\pi\cdot F_\pi\cdot\kappa^*_\pi + F_\nu\cdot\kappa_\nu\cdot F_\nu\cdot\kappa^*_\nu) \\ && \text{(H.14d)} \end{aligned}$$

so that when summing up the only non-vanishing terms are

$$m_0^{\text{HFB}} = \text{tr}(F\cdot F\cdot\rho) + \text{tr}(F\cdot\rho\cdot F\cdot\rho)\,. \tag{H.15}$$

Both terms being quadratic in F the result is the same in isoscalar and isovector channels. This statement can be extended with no loss of generality to any square product of one-body hermitian operators, whenever the isospin block-diagonal structure of the operator is preserved. This case applies to $\breve{M}_2(1,1)$ if the hypothesis (4.68) is taken into account. The HFB isoscalar-isovector invariance of even moments in such an hypothesis has been numerically checked both for closed- and (doubly) open-shell nuclei. Calculations relative to $\breve{M}_2(1,1)$ are even simpler, since any expectation value linear in the commutator of two hermitian operators vanishes by definition[1], so that only quadratic contributions appear. Thus, the isospin character of the operator itself is lost.

[1] Let us consider the commutator

$$C = [H,F]. \tag{H.16}$$

The condition

$$C^\dagger = -C \tag{H.17}$$

is verified due to the hermiticity of operators H and F. Thus, it is immediate to check that

$$\text{tr}(C) = -\text{tr}(C^\dagger) = 0\,, \tag{H.18}$$

Naively, the present result seems to be in contradiction with numerical values of *even* moments in (Q)RPA, that differ depending on the selected isospin channel. This contradiction is only apparent. Only *odd* (Q)RPA moments can be computed as the expectation value of the moment operator with respect to the HF(B) solution. This is not the case for *even* moments, which must be computed through Eq. (4.27) and that do not display this equality between their isoscalar and isovector components .

since hermiticity in general implies the trace of an hermitian operator to be real. One can simply show that

$$\begin{aligned} \rho \cdot C &= -\rho^{\dagger} \cdot C^{\dagger} \\ &= -(C \cdot \rho)^{\dagger}. \end{aligned} \tag{H.19}$$

In this way one proofs that

$$\begin{aligned} \mathrm{tr}(\rho \cdot C) &= -\mathrm{tr}(C \cdot \rho)^{\dagger} \\ &= \mathrm{tr}(C \cdot \rho) \\ &= 0, \end{aligned} \tag{H.20}$$

where in the first equivalence Eq. (H.19) has been used, the second equivalence exploits the cyclic character of the trace and the last one follows from Eq. (H.18).

Appendix I

Proofs involving projectors

I.1 Projected overlap between states with different K

The selection rule employed in Sec. 5.5.2 is proven in the following.

$$\begin{aligned}
\langle\Phi_{M'}|P^J_{MK}|\Phi_{K'}\rangle &= \frac{2J+1}{8\pi^2}\int \mathrm{d}\Omega \mathcal{D}^{J*}_{MK}(\Omega)\langle\Phi_{M'}|\mathcal{R}(\Omega)|\Phi_{K'}\rangle \\
&= \frac{2J+1}{8\pi^2}\int_0^{2\pi}\mathrm{d}\alpha\int_{-1}^{+1}\mathrm{d}(\cos\beta)\int_0^{2\pi}\mathrm{d}\gamma\; e^{iM\alpha}d^J_{MK}(\beta)e^{iK\gamma}\langle\Phi_{M'}|e^{-i\alpha J_z}e^{-i\beta J_y}e^{-i\gamma J_z}|\Phi_{K'}\rangle \\
&= \frac{2J+1}{8\pi^2}\int_0^{2\pi}\mathrm{d}\alpha\; e^{i(M-M')\alpha}\int_0^{2\pi}\mathrm{d}\gamma\; e^{i(K-K')\gamma}\int_{-1}^{+1}\mathrm{d}(\cos\beta)\; d^J_{MK}(\beta)\langle\Phi_{M'}|e^{-i\beta J_y}|\Phi_{K'}\rangle \\
&= \frac{2J+1}{2}\delta_{MM'}\delta_{KK'}\int_{-1}^{+1}\mathrm{d}(\cos\beta)\; d^J_{MK}(\beta)\langle\Phi_{M'}|e^{-i\beta J_y}|\Phi_{K'}\rangle\,. \qquad \text{(I.1)}
\end{aligned}$$

I.2 Projected transition amplitude between states with different K

The selection rule employed in Sec. 5.4.3 is proven in the following. Spherical tensors fulfil the commutation relations (see, for instance, Ref. [146])

$$[J_z, T_{\lambda\mu}] = \mu T_{\lambda\mu}\,, \qquad \text{(I.2a)}$$

$$[J_\pm, T_{\lambda\mu}] = \sqrt{\lambda(\lambda+1)-\mu(\mu\pm1)}\,T_{\lambda,\mu\pm1}\,. \qquad \text{(I.2b)}$$

In particular, Eq. (I.2a) allows to provide the following derivation

$$\begin{aligned}
\langle\Phi_{M'}|T_{\lambda\mu}P^J_{MK}|\Phi_{K'}\rangle &= \frac{2J+1}{8\pi^2}\int_0^{2\pi}\mathrm{d}\alpha\int_{-1}^{+1}\mathrm{d}(\cos\beta)\int_0^{2\pi}\mathrm{d}\gamma\; \mathcal{D}^{J*}_{MK}(\alpha,\beta,\gamma)\langle\Phi_{M'}|T_{\lambda\mu}\mathcal{R}(\alpha,\beta,\gamma)|\Phi_{K'}\rangle \\
&= \frac{2J+1}{8\pi^2}\int_0^{2\pi}\mathrm{d}\alpha\int_{-1}^{+1}\mathrm{d}(\cos\beta)\int_0^{2\pi}\mathrm{d}\gamma\; e^{iM\alpha}d^J_{MK}(\beta)e^{iK\gamma}\langle\Phi_{M'}|T_{\lambda\mu}e^{-i\alpha J_z}e^{-i\beta J_y}e^{-i\gamma J_z}|\Phi_{K'}\rangle \\
&= \frac{2J+1}{4\pi}\delta_{KK'}\int_0^{2\pi}\mathrm{d}\alpha\int_{-1}^{+1}\mathrm{d}(\cos\beta)\; e^{iM\alpha}d^J_{MK}(\beta)\langle\Phi_{M'}|T_{\lambda\mu}e^{-i\alpha J_z}e^{-i\beta J_y}|\Phi_{K'}\rangle \\
&= \frac{2J+1}{4\pi}\delta_{KK'}\int_0^{2\pi}\mathrm{d}\alpha\int_{-1}^{+1}\mathrm{d}(\cos\beta)\; e^{iM\alpha}d^J_{MK}(\beta)\sum_{n=0}^{\infty}\frac{1}{n!}\langle\Phi_{M'}|T_{\lambda\mu}(-i\alpha J_z)^n e^{-i\beta J_y}|\Phi_{K'}\rangle \\
&= \frac{2J+1}{4\pi}\delta_{KK'}\int_0^{2\pi}\mathrm{d}\alpha\int_{-1}^{+1}\mathrm{d}(\cos\beta)\; e^{iM\alpha}d^J_{MK}(\beta)\sum_{n=0}^{\infty}\frac{1}{n!}\langle\Phi_{M'}|[(-i\alpha J_z+i\alpha\mu)^n T_{\lambda\mu}]e^{-i\beta J_y}|\Phi_{K'}\rangle
\end{aligned}$$

$$= \frac{2J+1}{4\pi}\delta_{KK'}\int_0^{2\pi}\mathrm{d}\alpha\int_{-1}^{+1}\mathrm{d}(\cos\beta)\; e^{iM\alpha}d^J_{MK}(\beta)e^{-i\alpha(M'-\mu)}\langle\Phi_{M'}|T_{\lambda\mu}e^{-i\beta J_y}|\Phi_{K'}\rangle$$

$$= \frac{2J+1}{2}\delta_{KK'}\delta_{M,M'-\mu}\int_{-1}^{+1}\mathrm{d}(\cos\beta)\; d^J_{MK}(\beta)\langle\Phi_{M'}|T_{\lambda\mu}e^{-i\beta J_y}|\Phi_{K'}\rangle\,. \tag{I.3}$$

For states $|\Phi_K\rangle$ carrying a good J_z quantum number, the projected transition amplitudes vanish if the lower projection indices do not match the quantum numbers of the symmetry-breaking states.

Appendix J

Matrix elements in the HF basis

This appendix develops the necessary details for numerical implementations of Secs. 5.4.4 and 5.5.3.

J.1 Hartree-Fock single-particle basis

The Hartree-Fock ground-state is referred to as $|\mathrm{HF}\rangle$. It is expressed, as well as one-particle-one-hole states resulting from an excitation acting on it, as a Slater determinant of the **occupied** single-particle states $|\varphi_i\rangle$ constituting it, i.e.

$$|\mathrm{HF}\rangle = |\varphi_1 \varphi_2 ... \varphi_A\rangle \,, \tag{J.1}$$

with A being the number of nucleons in the system and $\{\varphi_i\}_{i=1,...,N}$ the basis set of HF single-particle states. The basis is made up of N single-particle states, whereas the A-body state Slater determinant is the anti-symmetrised product of A **occupied** single-particle states, with $A \leq N$. Single-particle states can be expanded onto an arbitrary basis $\{a\}_N$ of choice through a unitary transformation C ($N \times N$ matrix)

$$\begin{aligned} |\varphi_i\rangle &= \sum_a |a\rangle\langle a|\varphi_i\rangle \\ &= \sum_a C_{ai}\,|a\rangle \,. \end{aligned} \tag{J.2}$$

This work relies on the use of axially deformed states with a good angular-momentum projection quantum number, such that they are eigenstates of J_z but not of $\mathbf{J}^2$, i.e.

$$J_z|\Phi_K\rangle = K\,|\Phi_K\rangle, \tag{J.3}$$

with $|\Phi_K\rangle$ being any possible Slater determinant made up of A such HF single-particle states. In this context a standard choice for the underlying basis is the **cylindrical** harmonic oscillator basis (CHO). The CHO basis states are denoted as

$$|n_z n_r m_l m_s\rangle \,, \tag{J.4}$$

where n_z (n_r) is the principal quantum number relative to the z (r) coordinate, indicating the number of nodes of the axially-symmetric wave-function in this direction, and m_l (m_s) is the z-projection component of the orbital (spin) angular momentum. The direct transformation is the one going from the CHO to the HF basis,

$$|a\rangle \xrightarrow{C} |\varphi_i\rangle \,, \tag{J.5}$$

thus having the row index for the CHO basis and the column index for the HF basis. Operators are introduced in the CHO basis. In order to express an operator O in the HF basis its matrix elements must

undergo the unitary transformation

$$\begin{aligned}\tilde{O}_{ij} &= \langle\varphi_i|O|\varphi_j\rangle \\ &= \sum_{ab}\langle\varphi_i|a\rangle\langle a|O|b\rangle\langle b|\varphi_j\rangle \\ &= \sum_{ab} C^*_{ia} O_{ab} C_{bj} \\ &= (C^\dagger O C)_{ij}\,. \end{aligned} \tag{J.6}$$

J.2 Angular momentum matrix elements

In the **spherical** harmonic oscillator basis (SHO), the basis states are denoted as

$$|nljm\rangle\,, \tag{J.7}$$

where n is the principal quantum number, indicating the number of nodes of the spherically-symmetric wavefunction, l is the orbital angular momentum quantum number, j refers to the total angular momentum of the state and m is its projection on the z-axis. Thus, basis states fulfil

$$\mathbf{L}^2|nljm\rangle = l(l+1)|nljm\rangle\,, \tag{J.8a}$$
$$\mathbf{J}^2|nljm\rangle = j(j+1)|nljm\rangle\,, \tag{J.8b}$$
$$J_z|nljm\rangle = m|nljm\rangle\,. \tag{J.8c}$$

Ladder operators for the total angular momentum act on the basis states according to

$$J_+|nljm\rangle = \sqrt{j(j+1)-m(m+1)}|nlj,m+1\rangle\,, \tag{J.9a}$$
$$J_-|nljm\rangle = \sqrt{j(j+1)-m(m-1)}|nlj,m-1\rangle\,, \tag{J.9b}$$

so that the matrix element of J_y are obtained as

$$\begin{aligned}\langle n_1 l_1 j_1 m_1|\,J_y|n_2 l_2 j_2 m_2\rangle &= \frac{1}{2i}\langle n_1 l_1 j_1 m_1|\,J_+|n_2 l_2 j_2 m_2\rangle - \frac{1}{2i}\langle n_1 l_1 j_1 m_1|\,J_-|n_2 l_2 j_2 m_2\rangle \\ &= \frac{1}{2i}\delta_{n_1 n_2}\delta_{l_1 l_2}\delta_{j_1 j_2}\Big\{\sqrt{j_2(j_2+1)-m_2(m_2+1)}\langle m_1|m_2+1\rangle \\ &\qquad - \sqrt{j_2(j_2+1)-m_2(m_2-1)}\langle m_1|m_2-1\rangle\Big\} \\ &= \frac{1}{2i}\delta_{n_1 n_2}\delta_{l_1 l_2}\delta_{j_1 j_2}\Big\{\delta_{m_1,m_2+1}\sqrt{j_2(j_2+1)-m_2(m_2+1)} \\ &\qquad - \delta_{m_1,m_2-1}\sqrt{j_2(j_2+1)-m_2(m_2-1)}\Big\}. \end{aligned} \tag{J.10}$$

The matrix elements of J_y originally given in the SHO basis according to Eq. (J.10) can then be transformed into the CHO basis through

$$J_y^{(\mathrm{CHO})} = U J_y^{(\mathrm{SHO})} U^\dagger \tag{J.11}$$

where matrix elements of the unitary transformation U are provided by the overlaps between the two bases

$$U_{nljm,n_z n_r m_l m_s} = \langle nljm|n_z n_r m_l m_s\rangle\,. \tag{J.12}$$

J.3 Overlap evaluation

The overlap between two non-orthogonal Slater determinants $|\Phi\rangle$ and $|\Xi\rangle$ is computed (see, for instance, Ref. [115]) as a determinant

$$\langle\Phi|\Xi\rangle = \det M(\Phi,\Xi), \tag{J.13}$$

where $M(\Phi,\Xi)$ is the matrix of the overlaps between the single-particle states $|\varphi_i\rangle$ **occupied** in $|\Phi\rangle$ and the single-particle states $|\xi_i\rangle$ **occupied** in $|\Xi\rangle$, i.e.

$$\begin{aligned} M_{ij}(\Phi,\Xi) &\equiv \langle\varphi_i|\xi_j\rangle \\ &= \sum_a \langle\varphi_i|a\rangle\langle a|\xi_j\rangle \\ &= \sum_a C^*_{(\Phi)ia} C_{(\Xi)aj} \\ &= (C^\dagger_{(\Phi)} C_{(\Xi)})_{ij}, \end{aligned} \tag{J.14}$$

where the matrix $C_{(\Phi)}$ is a $N \times A$ rectangular matrix, whose row index run on basis states, whose total number is N, and column index runs on occupied single-particle states, whose number equates the number of nucleons A. The $C_{(\Phi)}$ matrix is built retaining the columns in the basis-change matrix C corresponding to the occupied single-particle states $|\varphi_i\rangle$ in $|\Phi\rangle$. Alternatively, when $|\Phi\rangle$ and $|\Xi\rangle$ are different Slater determinants expressed with respect the same HF single-particle states (e.g. the $|\mathrm{HF}\rangle$ state and a ph excitation $|ph\rangle \equiv c_p^\dagger c_h|\mathrm{HF}\rangle$), one can compute the product $C^\dagger C$ using the whole transformation matrix C linking the Hartree-Fock and CHO bases, and then retaining only the rows (columns) corresponding to the occupied single-particle states in $\langle\Phi|$ ($|\Xi\rangle$). In this case the overlap can be written as

$$\begin{aligned} M_{ij}(\Phi,\Xi) &\equiv \langle\varphi_i|\xi_j\rangle \\ &= \sum_a \langle\varphi_i|a\rangle\langle a|\xi_j\rangle \\ &= \sum_a C^*_{ia} C_{aj} \\ &= (C^\dagger C)^{\mathrm{occ}}_{ij}, \end{aligned} \tag{J.15}$$

where indices i and j run over occupied single-particle states in $\langle\Phi|$ and $|\Xi\rangle$, respectively. This is the solution used in the present implementation. When AMP is involved, one has to evaluate rotated overlaps of the form

$$\langle\Phi|\mathcal{R}(\Omega)|\Xi\rangle = \det M(\Phi,\Xi;\Omega). \tag{J.16}$$

In axial symmetry, this amounts to evaluating

$$\begin{aligned} M_{ij}(\Phi,\Xi;\beta) &\equiv \langle\varphi_i|e^{-i\beta J_y}|\xi_j\rangle \\ &= \sum_{ab} \langle\varphi_i|a\rangle\langle a|e^{-i\beta J_y}|b\rangle\langle b|\xi_j\rangle \\ &= \sum_{ab} C^*_{(\Phi)ia} (e^{-i\beta J_y})_{ab} C_{(\Xi)bj} \\ &= (C^\dagger_{(\Phi)} e^{-i\beta J_y} C_{(\Xi)})_{ij}. \end{aligned} \tag{J.17}$$

Two equivalent ways can again be envisioned to provide this expression. First, one considers matrices $C_{(\Phi)}$ and $C_{(\Xi)}$ obtained by retaining the columns relative to the occupied HF states in the determinant of choice.

If the Slater determinants refer to the same HF single-particle basis as in Eq. (J.15), one can rather perform the matrix product using the complete transformation matrix C and solely retaining the rows/columns relative to the occupied HF states in the left/right Slater determinant

$$\begin{aligned} M_{ij}(\Phi,\Xi;\beta) &\equiv \langle\varphi_i|e^{-i\beta J_y}|\xi_j\rangle \\ &= \sum_{ab}\langle\varphi_i|a\rangle\langle a|e^{-i\beta J_y}|b\rangle\langle b|\xi_j\rangle \\ &\equiv \sum_{ab}\langle\varphi_i|a\rangle\langle a|r(\beta)|b\rangle\langle b|\xi_j\rangle \\ &= \sum_{ab} C^*_{ia} r_{ab}(\beta) C_{bj} \\ &= (C^\dagger e^{-i\beta J_y} C)^{\text{occ}}_{ij}\,. \end{aligned} \tag{J.18}$$

This second choice is preferable, for two reasons. First, there is no ambiguity regarding the way the elements in the matrix are sorted. Second, it is computationally more optimal, given that only the information relative to the occupied states in each Slater determinant needs to be stored out of the full matrix

$$(C^\dagger e^{-i\beta J_y} C)_{pq}\,,$$

simply corresponding to the rotation matrix expressed in the HF basis.

Matrix exponential

For a $N\times N$ matrix A, let V be the unitary transformation diagonalising A. Naturally, V is made out of the N eigenvectors of A. Let Λ be the diagonal matrix whose elements are the eigenvalues $\{\lambda_a\}_{a=1,\dots,N}$ of A. Given the eigenvalue equation

$$AV = \Lambda V\,, \tag{J.19}$$

it is easy to show that the matrix exponential is nothing but

$$e^A = V^\dagger e^\Lambda V\,, \tag{J.20}$$

where the exponential of Λ is the diagonal matrix with elements $\{e^{\lambda_a}\}_{a=1,\dots,N}$. This scheme is particularly convenient as far as the computational cost is concerned. Indeed, once A has been diagonalised, V and Λ can be stored for successive iterative uses. This is of interest when integrating during the projection process, since one deals with the iterated evaluation of

$$e^{\beta A} = V^\dagger e^{\beta\Lambda} V \tag{J.21}$$

for many β's, which is easily achieved multiplying the eigenvalues $\{\lambda_a\}_{a=1,\dots,N}$ by β.

J.4 Off-diagonal density matrix

The computation of transition strengths implies the evaluation of many off-diagonal matrix elements of the form

$$\begin{aligned} \langle\Phi|T|\Xi\rangle &= \frac{\langle\Phi|T|\Xi\rangle}{\langle\Phi|\Xi\rangle}\langle\Phi|\Xi\rangle \\ &= \sum_{ab} T_{ab}\frac{\langle\Phi|c^\dagger_a c_b|\Xi\rangle}{\langle\Phi|\Xi\rangle}\langle\Phi|\Xi\rangle \end{aligned}$$

$$\equiv \mathrm{Tr}\{T \cdot \rho(\Phi,\Xi)\}\langle\Phi|\Xi\rangle\,, \tag{J.22}$$

involving the knowledge of the off-diagonal density matrix $\rho(\Phi,\Xi)$. Dealing with Slater determinants, the latter can be expressed as [115]

$$\begin{aligned}\rho_{ab}(\Phi,\Xi) &= \frac{\langle\Phi|c_b^\dagger c_a|\Xi\rangle}{\langle\Phi|\Xi\rangle} \\ &= \sum_{i,j=1}^{A} \langle a|\xi_i\rangle M^{-1}(\Phi,\Xi)_{ij}\langle\varphi_j|b\rangle \\ &= \sum_{i,j=1}^{A} C_{(\Xi)ai} M^{-1}(\Phi,\Xi)_{ij} C^*_{(\Phi)jb}\,.\end{aligned} \tag{J.23}$$

If, as for the overlap in Eq. (J.15), the states $|\Phi\rangle$ and $|\Xi\rangle$ are Slater determinants built out of the same set of HF single-particle states, the transition matrix element can be expressed as

$$\begin{aligned}\langle\Phi|T|\Xi\rangle &= \sum_{ab} T_{ab}\frac{\langle\Phi|c_a^\dagger c_b|\Xi\rangle}{\langle\Phi|\Xi\rangle}\langle\Phi|\Xi\rangle \\ &= \sum_{i,j=1}^{A}\sum_{ab} T_{ab}C_{bi}M^{-1}(\Phi,\Xi)_{ij}C^*_{ja}\langle\Phi|\Xi\rangle \\ &= \sum_{i,j=1}^{A}(C^\dagger TC)_{ji}M^{-1}(\Phi,\Xi)_{ij}\langle\Phi|\Xi\rangle \\ &\equiv \mathrm{Tr}\{\tilde{T}(\Phi,\Xi)M^{-1}(\Phi,\Xi)\}\langle\Phi|\Xi\rangle\,,\end{aligned} \tag{J.24}$$

where

$$\tilde{T}(\Phi,\Xi) \equiv (C^\dagger TC)^{\mathrm{occ}} \tag{J.25}$$

is the sub-matrix made out of the occupied row and column indices of $|\Phi\rangle$ and $|\Xi\rangle$, respectively, of the operator T expressed in the HF single-particle basis. As for the overlap matrix M, the matrix $\tilde{T}(\Phi,\Xi)$ is constructed by first evaluating the complete product $C^\dagger TC$ (which amounts to computing T in the HF single-particle basis) and by retaining the rows (columns) corresponding to the occupied single-particle states in $\langle\Phi|$ ($|\Xi\rangle$). The overlap matrix $M(\Phi,\Xi)$ is block-diagonal with respect to isospin (proton and neutron states are orthogonal since they span different sub-spaces of the one-body Hilbert space), such that the inverse matrix is block diagonal as well. Thus, one is allowed to write

$$\langle\Phi|T|\Xi\rangle = \mathrm{Tr}\{\tilde{T}_\pi \cdot M_\pi^{-1}(\Phi,\Xi) + \tilde{T}_\nu \cdot M_\nu^{-1}(\Phi,\Xi)\}\langle\Phi|\Xi\rangle\,, \tag{J.26}$$

where the subscripts π and ν stands for proton and neutron sub-blocks, respectively. The overlap $\langle\Phi|\Xi\rangle$ factorises, for the same reason, into a proton and a neutron component

$$\langle\Phi|\Xi\rangle = \langle\Phi|\Xi\rangle_\pi\langle\Phi|\Xi\rangle_\nu\,. \tag{J.27}$$

The inverse of a matrix is related to its cofactor matrix $\mathfrak{C}$ by the relation (see, e.g., Ref. [213])

$$M^{-1} = \frac{1}{\det M}\mathfrak{C}^{\mathrm{T}}\,. \tag{J.28}$$

Since the determinant of the overlap matrix corresponds to the overlap itself, one can write

$$\langle\Phi|T|\Xi\rangle = \mathrm{Tr}\{\frac{\tilde{T}_\pi(\Phi,\Xi)\cdot\mathfrak{C}^{\mathrm{T}}_\pi(\Phi,\Xi)}{\langle\Phi|\Xi\rangle_\pi} + \frac{\tilde{T}_\nu(\Phi,\Xi)\cdot\mathfrak{C}^{\mathrm{T}}_\nu(\Phi,\Xi)}{\langle\Phi|\Xi\rangle_\nu}\}\langle\Phi|\Xi\rangle_\pi\langle\Phi|\Xi\rangle_\nu \tag{J.29}$$

$$= \mathrm{Tr}\{\tilde{T}_\pi(\Phi,\Xi)\cdot\mathfrak{C}^{\mathrm{T}}_\pi(\Phi,\Xi)\}\langle\Phi|\Xi\rangle_\nu + \mathrm{Tr}\{\tilde{T}_\nu(\Phi,\Xi)\cdot\mathfrak{C}^{\mathrm{T}}_\nu(\Phi,\Xi)\}\langle\Phi|\Xi\rangle_\pi\,. \tag{J.30}$$

This writing has the advantage to be well-defined for orthogonal states as well, which is of interest in this specific application, where by definition ph excitation are orthogonal to the HF state, whereas the original formulation demands a matrix inversion, which is ill defined if the determinant of the matrix (overlap) is zero. Let us consider the particular case

$$|\Xi\rangle = c_p^\dagger c_h|\Phi\rangle\,. \tag{J.31}$$

According to the isospin character of the ph excitation, either the proton or the neutron overlap are vanishing, i.e for a proton (neutron) ph excitation the overlap $\langle\Phi|\Xi\rangle_\pi$ ($\langle\Phi|\Xi\rangle_\nu$) vanishes and the overlap $\langle\Phi|\Xi\rangle_\nu = 1$ ($\langle\Phi|\Xi\rangle_\pi = 1$). As an example, for a proton ph state one obtains

$$\langle\Phi|T|\Xi\rangle = \mathrm{Tr}\{\tilde{T}_\pi(\Phi,\Xi)\cdot\mathfrak{C}^{\mathrm{T}}_\pi(\Phi,\Xi)\}\,. \tag{J.32}$$

This is no longer true in the case of non-orthogonal states, which is the situation emerging when dealing with projectors. In this case both the proton and the neutron component may be present at the same time, as clearly appears in Eq. (J.30). When rotation is involved, the definition from Eq. (J.25) is straightforwardly modified (see Ref. [214]) according to

$$\tilde{T}(\Phi,\Xi;\beta) \equiv (C^\dagger T e^{-i\beta J_y} C)^{\mathrm{occ}}\,, \tag{J.33}$$

and $\mathfrak{C}(\Phi,\Xi;\beta)$, i.e. the cofactor matrix of $M(\Phi,\Xi;\beta)$, is employed instead of $\mathfrak{C}(\Phi,\Xi)$. Overall, one obtains

$$\langle\Phi|T|\Xi(\beta)\rangle = \mathrm{Tr}\{T_\pi(\Phi,\Xi;\beta)\cdot\mathfrak{C}^{\mathrm{T}}_\pi(\Phi,\Xi;\beta)\}\langle\Phi|\Xi(\beta)\rangle_\nu + \mathrm{Tr}\{T_\nu(\Phi,\Xi;\beta)\cdot\mathfrak{C}^{\mathrm{T}}_\nu(\Phi,\Xi;\beta)\}\langle\Phi|\Xi(\beta)\rangle_\pi\,. \tag{J.34}$$

Appendix K

Quantum Harmonic Oscillator and Perturbative Corrections

K.1 Problem setting

Perturbative corrections to the eigen-energies of the one-dimensional quantum harmonic oscillator (QHO) are here computed for a perturbation having both a cubic and a quartic terms up to second order[1]. The Hamiltonian

$$H = H_0 + \lambda H_1 \tag{K.1}$$

is given, with

$$H_0 \equiv \frac{p^2}{2m} + \frac{1}{2} m\omega^2 q^2 , \tag{K.2a}$$

$$H_1 \equiv -\mu q^3 + \xi q^4 , \tag{K.2b}$$

representing the unperturbed QHO and the perturbation respectively. The canonical coordinate and momentum are expressed in terms of ladder operators

$$q = \sqrt{\frac{\hbar}{2m\omega}} (a^\dagger + a) , \tag{K.3a}$$

$$p = i\sqrt{\frac{m\omega}{2\hbar}} (a^\dagger - a) , \tag{K.3b}$$

with the action of $a^\dagger$ and a being defined by

$$a^\dagger |n\rangle = \sqrt{n+1}\, |n+1\rangle , \tag{K.4a}$$

$$a |n\rangle = \sqrt{n}\, |n-1\rangle , \tag{K.4b}$$

where $|n\rangle$ are the eigen-states of the QHO defined by the Schrödinger equation

$$H_0 |n\rangle = \left(n + \frac{1}{2}\right) \hbar\omega\, |n\rangle . \tag{K.5}$$

The matrix elements of the operator q are determined using the representation from Eq. (K.3a), providing

$$\langle m|q|n\rangle = \sqrt{\frac{\hbar}{2m\omega}} [\sqrt{n}\delta_{m,n-1} + \sqrt{n+1}\delta_{m,n+1}] . \tag{K.6}$$

[1] The perturbation theory for the q^4 correction to the QHO is known to diverge (zero radius of convergence) [215, 216, 217].

The transition probability between neighbouring states is given by

$$|\langle n-1|q|n\rangle|^2 = \frac{\hbar}{2m\omega} n. \tag{K.7}$$

K.2 Eigen-energies correction

Eigen-energies corrections at first and second order in perturbation theory are provided, respectively, by

$$E_n^{(1)} = \lambda \langle n|H_1|n\rangle\,, \tag{K.8a}$$

$$E_n^{(2)} = \lambda^2 \sum_{m\neq n} \frac{|\langle n|H_1|m\rangle|^2}{E_n^{(0)} - E_m^{(0)}}, \tag{K.8b}$$

with $E_n^{(0)}$ standing for the eigen-energies of H_0, i.e.

$$E_n^{(0)} \equiv \langle n|H_0|n\rangle = \hbar\omega\left(n + \frac{1}{2}\right). \tag{K.9}$$

The cubic and the quartic contributions to the first-order term read as

$$\begin{aligned} E_n^{(1,3)} &\equiv -\langle n|\mu q^3|n\rangle \\ &= -\mu\left(\frac{\hbar}{2m\omega}\right)^{\frac{3}{2}} \langle n|(a^\dagger + a)^3|n\rangle \\ &= 0\,, \end{aligned} \tag{K.10a}$$

$$\begin{aligned} E_n^{(1,4)} &\equiv \langle n|\xi q^4|n\rangle \\ &= \xi\left(\frac{\hbar}{2m\omega}\right)^2 \langle n|(a^\dagger + a)^4|n\rangle \\ &= \xi\left(\frac{\hbar}{2m\omega}\right)^2 3(2n^2 + 2n + 1). \end{aligned} \tag{K.10b}$$

The cubic term does not contribute at first order, since its expansion only provides unequal powers of $a^\dagger$ and a. The second-order contributions are computed via tedious but straightforward algebraic calculations eventually reading as

$$\begin{aligned} E_n^{(2,3)} &\equiv \sum_{m\neq n} \frac{|\langle n|\mu q^3|m\rangle|^2}{E_n^{(0)} - E_m^{(0)}} \\ &= \frac{\mu^2}{\hbar\omega}\left(\frac{\hbar}{2m\omega}\right)^3 \sum_{m\neq n} \frac{|\langle n|(a^\dagger + a)^3|m\rangle|^2}{n-m} \\ &= -\frac{\mu^2}{\hbar\omega}\left(\frac{\hbar}{2m\omega}\right)^3 (30n^2 + 30n + 11), \end{aligned} \tag{K.11a}$$

$$\begin{aligned} E_n^{(2,4)} &\equiv \sum_{m\neq n} \frac{|\langle n|\xi q^4|m\rangle|^2}{E_n^{(0)} - E_m^{(0)}} \\ &= \frac{\xi^2}{\hbar\omega}\left(\frac{\hbar}{2m\omega}\right)^4 \sum_{m\neq n} \frac{|\langle n|(a^\dagger + a)^4|m\rangle|^2}{n-m} \\ &= -\frac{\xi^2}{\hbar\omega}\left(\frac{\hbar}{2m\omega}\right)^4 (68n^3 + 102n^2 + 118n + 42). \end{aligned} \tag{K.11b}$$

Eventually, the perturbatively-corrected eigen-energies are defined as

$$E_n^{(1+2)} \equiv E_n^{(0)} + E_n^{(2,3)} + E_n^{(1,4)} + E_n^{(2,4)}, \tag{K.12}$$

and, consequently, the perturbed eigen-frequencies as

$$\hbar\omega^{(1+2)} \equiv E_n^{(1+2)} - E_0^{(1+2)}. \tag{K.13}$$

Résumé en français

À partir des années 2000, les méthodes *ab initio* en structure nucléaire théorique ont été extrêmement prolifiques dans la description des observables expérimentales sur la base des théories chirales des champs effectives (EFT), où les degrés de liberté des quarks sont intégrés et la force forte entre nucléons est moyennée par les pions comme bosons de Goldstone de la brisure de symétrie spontanée associée à la symétrie chirale. Spécifiquement, les EFT chirales représentent une conjonction solide à la chromodynamique quantique (QCD), la théorie de champ sous-jacente de la force forte. La construction de l'hamiltonien à partir des principes premiers combinée à des techniques à N corps d'avant-garde offre une direction vers un cadre de travail universel pour décrire les propriétés du noyau atomique, de l'énergie de liaison jusqu'aux rayons de charge et aux excitations collectives.

Techniques à N corps

Les méthodes *ab initio* jouent un rôle essentiel pour attaquer des systèmes quantiques fortement corrélés tels que le noyau atomique, de telle sorte que le développement et l'extension des nouvelles techniques pour résoudre l'équation de Schrödinger à A corps sont centrales pour la description des observables nucléaires à partir des principes premiers. Une solution essentiellement exacte du problème à N corps quantique est fournie par les méthodes de diagonalisation, telles que le modèle en couches sans cœur (NCSM), ou les méthodes Monte-Carlo. Cependant, lié à l'augmentation exponentielle du coût computationnel par rapport au nombre de nucléons A du système, ces méthodes ne sont limitées qu'aux noyaux légers, avec $A \lesssim 12$, bien que les techniques de troncation par importance (IT) puissent élargir leur étendu jusqu'à certains isotopes de l'Oxygène e du Calcium.

Une avancée majeure dans le développement des méthodes *ab initio* pour la description de noyaux de masse moyenne a été marquée par la (ré)introduction des méthodes dites d'expansion, où l'action d'un *opérateur d'onde* agissant sur un état de référence gagne la corrélation manquante dans l'état initial choisi de manière appropriée à travers une expansion contrôlée, qui peut être de nature perturbative ou non-perturbative. Si on tronque l'expansion à un ordre fini, toutes ces méthodes partagent une augmentation polynomiale du coût computationnel par rapport à la dimension de l'espace d'Hilbert à un corps. Par conséquent, aujourd'hui une grande variété d'observables est couramment accessible dans des systèmes avec $A \lesssim 100$ et, dans certains cas spécifiques, même dans des noyaux beaucoup plus lourds. Le développement de l'application de ces techniques se décline par rapport aux spécificités de l'état de départ. Les toute premières applications basées sur un unique déterminant de Slater optimisé via un calcul de champ moyen Hartree-Fock (HF) respectant les symétries de l'Hamiltonien ont permis, a partir du 2005, d'aborder les propriétés nucléaires des noyaux doublement magiques. Des exemples sont la théorie des perturbations à A corps (MBPT), la méthode des clusters couplés (CC), du groupe de transformation similaire dans le milieu (IMSRG) ou des fonctions de Green auto-cohérentes (SCGF) dans le formalisme de Dyson.

Un état de référence respectant les symétries de l'Hamiltonien demeure quand-même inadéquat pour la description des systèmes à couches ouverte, faute à l'occupation partielle des couches de valence dégenrées et à l'apparition conséquente des corrélations statiques fortes. À fin d'inclure d'une façon efficiente ces

corrélations statiques il est nécessaire un état de référence plus général. Une possibilité est d'utiliser un état de référence qui brise spontanément une ou plusieurs symétries de l'hamiltonien sous-jacent. À partir du 2011 des états de référence de Hartree-Fock-Bogoliubov (HFB) brisant la symétrie lié au bon nombre de particules ont été utilisés dans l'extension de Gor'kov de la méthode SCGF pour le calcul des propriétés de l'état fondamental le long des chaînes isotopiques des noyaux de masse moyenne semi-magiques. Une option similaire est disponible dans le contexte d'une méthode conceptuellement plus simple et numériquement plus abordable telle que la Bogoliubov MBPT (BMBPT). Par ailleurs, des extensions de la théorie CC qui permettent de briser et restaurer les symétries $U(1)$ et $SU(2)$ ont été formulées et appliquées. Bien que la restauration consistante de $U(1)$ et $SU(2)$ aient été élaborées sur le plan formel dans le schéma CC, le développement du même cadre dans le cas des Gor'kov SCGF pose des soucis de nature théorique encore irrésolus.

Des états brisant le symétries de l'Hamiltonien peuvent aussi être utilisés comme une étape intermédiaire dans la définition des états multi-référence qui avec des bons nombres quantiques, utilisés, à leur tour, comme états de référence pour des théories plus élaborées. Cette stratégie s'est révélée gagnante dans le contexte des extensions multi-référence de IMSRG (MR-IMSRG) permettant de calculer des énergie de liaison des noyaux à couches ouvertes, tout ensemble avec la méthode de la coordonnée génératrice projetée (PGCM), qui s'est démontrée en temps récents un excellent choix si l'on est intéressés aux propriétés spectroscopiques avec un haut niveau de précision. Récemment, de plus, la PGCM a été utilisée comme état de départ multi-référence elle même pour une d'entre les théories de perturbations à N corps les plus sophistiquées des nos jours en physique nucléaire, à savoir la théorie de perturbation basée sur un état PGCM (PGCM-PT), livrant des prédictions précises à la fois pour l'état fondamental et pour les excitations collectives rotationnelles et vibrationnelles.

Accès aux états excités

La plupart des méthodes discutées dans la section précédente, malgré l'énorme effort associé à leur développement formel et numérique, est plutôt limité par rapport aux propriétés des états excités. Ainsi, quant à l'accès aux états excités, le paysage est en quelque sorte dans son plus jeune âge, même si le panorama reste quand même large par rapport à la variété de techniques qui ont été développées au cours de ces dernières années.

Une méthode s'adressant aux états excités dans le contexte de l'IMSRG est son extension dans l'espace de valence (VS-IMSRG). Cette méthode, toutefois, présente un coût computationnel à l'augmentation hybride polynomiale-exponentielle, à cause d'une partie du calcul nécessitant des calculs à configurations interagissantes (CI), de telle sorte que son application est aujourd'hui limitée aux noyaux dans les couches *sd* ou *pf*. Dans le même esprit, les techniques relatant de l'équation du mouvement (EOM), où l'on commence de la solutions corrélée d'un noyau à couches fermées et on décrit les états excités comme le résultat de l'action d'un opérateur linéaire sur l'état fondamental, ont été largement utilisées dans la théorie CC. Une extension EOM de l'IMSRG pour la description des spectres des noyaux à couches fermées a été aussi élaborée. Des telles méthodes permettent d'accéder à la spectroscopie de basse énergie pour des excitation faiblement collectives, c'est à dire, des excitations essentiellement concentrées dans des excitations à peu de paires particule-trou.

Quant aux excitations collectives, des techniques de la transformée intégrale de Lorentz (LIT) permettent d'acceder aux réponses multipolaires dans les noyaux doublement magiques. Cependant, ces méthodes souffrent des instabilités numériques liées à des problèmes d'inversion et elles ne sont fiables que dans des cas où la réponse multipolaire elle même est concentrée dans un ou deux pics. Plus récemment il a été démontré que ces problématiques peuvent être contournées au moyen des techniques plus sophistiquées telles que l'expansion de Chebyshev.

Plus récemment, PGCM-PT a brillamment été utilisé pour une description *ab initio* précise et des

états rotationnels et des états vibrationnels. En particulier, il a été démontré que, lorsque les corrélations dynamiques sont essentielles pour accéder aux énergies absolues, elles s'annulent en grande partie dans la description des excitations collectives, ce qui justifie l'usage que de la PGCM comme méthode autonome pour la spectroscopie *ab initio*. Telle neutralisation a été observée, dans le contexte *ab initio*, pour la description des résonances géantes, ce qui rend la QRPA, elle même l'approximation harmonique de la GCM, une excellente description initiale.

Dans le même esprit, beaucoup de méthodes ont été développées à l'ombre des possibles déclinaisons de la QRPA, connaissant un grand succès entre les usagers. Des calculs RPA utilisant des propagateurs habillés ressortissant des calculs SCGF ont été utilisés pour étudier des excitations géantes de dipôle dans des systèmes magiques. Toutes ces méthodes, cependant, sont limitées dans leur application aux systèmes sphériques, ce qui limite énormément leur réussite. Le développement récent dans le groupe de Saclay d'une version à méthode des ampleurs finie (FAM) pour la QRPA a permis d'adresser les systèmes à double couche ouverte, qu'il s'agisse de noyaux intrinsèquement déformés de façon axiale ou triaxiale. Encore plus récemment la même méthode e été améliorée pour adresser également les noyaux pair-impair.

Résonances Géantes

Les résonances géantes (GRs) sont entre les manifestations les plus évidentes des mouvements de nature collective au sein du noyau. Elles correspondent à des excitations collectives dans lesquelles la plupart, si ce n'est la totalité des nucléons sont impliqués dans le procès. Les résonances géantes sont catégorisées selon leur multipolarité et leur spin isotopique et l'on peut les imaginer comme des vibrations de la surface nucléaire dans une peinture de type goutte liquide. La résonance géante monopolaire isoscalaire (ISGMR), qui est adressée dans ce travail, est aussi appelée *mode de respiration* et, étant donnée sa nature compressionnelle, on s'attend à qu'elle puisse fournir des informations relatives à l'incompressibilité de la matière nucléaire infinie, ce qui représente une quantité fondamentale faisant partie de l'équation d'état (EoS) nucléaire.

Puisqu'elles sont situées à des énergies de l'ordre de la séparation entre couches majeures, les résonances géantes sont incorporées dans un fond d'excitations particule-trou, dans lesquelles elles peuvent, en principe, décroître. La décroissance des vibrations collectives dans des excitations particule-trou est un phénomène très connu en physique des solides, dénommé amortissement de Landau. De plus, les résonances géantes se situent au-delà de la seuil d'émission de particules: par conséquent, elles peuvent se coupler à la décroissance par émission de particules dans le continuum. Enfin, elles peuvent aussi s'amortir à travers le couplage au champ électromagnétique en menant à l'émission d'un photon.

La description théorique des résonances géantes est un champ de recherche dans sa maturité. En particulier, leur nature d'excitations particule-trou cohérentes demeure au cœur de la RPA et des méthodes dérivées. La (Q)RPA implémentée dans le contexte des théories phénoménologiques de la fonctionnelle de la densité (EDF) s'est démontrée extrêmement prospère pour la description systématique des résonances géantes: des calculs déformés utilisant la QRPA tout au long de la charte des noyaux ont été réalisés, en obtenant globalement une bonne représentativité des donnés expérimentaux et qui ont significativité amélioré la compréhension théorique des effets de la déformation sur la GMR et le couplage avec la résonance géante de quadrupôle (GQR). Des calculs allant au delà de la RPA se sont aussi démontrés une progression remarquable pour la compréhension des effets non-triviaux. Parmi les nombreux exemples on citera la RPA auto-cohérent (SCRPA) et théories par elle inspirées, la seconde RPA (SRPA) et le couplage particule-vibration (PVC).

Une autre classe de théories relate de la description dépendante du temps des systèmes nucléaires dans le cas une perturbation multipolaire externe soit appliquée. Si l'on performe l'évolution temporelle sur un déterminant de Slater (vide de Bogoliubov) on peut démontrer que des telles théories sont strictement équivalentes à une formulation traditionnelle de la (Q)RPA, même si conceptuellement différentes. Des extension

à des états multi-référence des théories dépendants du temps, pourtant, représentent une alternative valide à fin d'aller au delà de la RPA traditionnelle.

Origines de ce travail

Entre les nombreuses méthodes à A corps s'adressant à une description formelle des résonances géantes, un certain intérêt fut montré pour la GCM dans plusieurs travaux exploratoires, qui jetèrent des bases formelles solides prouvant que la GCM demeure un outil fiable pour l'étude des états collectifs de nature vibrationnelle. Il fut également observé que les effets d'anharmonicité peuvent impacter d'une façon non-négligeable la détermination de l'incompressibilité nucléaire, ce qui fait de la GCM un outil essentiel à cet égard. Cependant, différemment de la (Q)RPA aucun usage extensif de la GCM suivi ces travaux pionniers dans la description théorique des résonances géantes.

Alimentés par ces travaux précurseurs et soutenus par l'observation que les corrélations dynamique se neutralisent dans une mesure majeure dans la description des excitations collectives, des calculs PGCM *ab initio* sont ici réalisés pour la première fois pour l'investigation de la résonance géante monopolaire et, dans une certaine mesure, quadrupolaire, dans des noyaux légers et de masse moyenne. On démontre que, au prix d'une choix moins systématique des degrés de liberté fondamentaux du problème, la PGCM peut traiter exactement les effets de non-harmonicité, ainsi que produire une solution qui respecte les symétries de l'hamiltonien et pour l'état fondamental et pour les états excités. Ces deux aspects sont abordés séparément et comparés à des calcules déformés en QRPA *ab initio*.

Définition du formalisme PGCM et algèbre de Bogoliubov

La première partie du manuscrit est vouée à l'introduction des concepts théoriques nécessaires aux développements suivants, aussi bien qu'à des avancées formelles constituant une partie originelle de ce travail.

Dans le Chapitre 1 on introduit le formalisme PGCM, qui constitue l'outil théorique centrale de ce travail. La fonction d'onde PGCM est définie à partir de la superposition linéaire des états de Bogoliubov contraints à différentes valeurs des coordonnées collectives. Les coefficients linéaires sont déterminés à partir d'une équation variationnelle menant à une équation aux valeurs propres similaires à l'équation de Schrödinger, nommée équation de Hill-Wheeler-Griffin (HWG). Les symétries sont restaurés à l'aide d'un projecteur sur les bons nombre quantiques, de telle sorte que les solutions de l'équation HWG respectent les symétries de l'hamiltonien. Les fondamentaux de l'algèbre de Bogoliubov sont donc rappelés en fin de chapitre.

Calculs des *kernels*

La résolution de l'équation HWG requiert l'évaluation numérique d'une classe d'objets nommés *kernels*. Deux catégories existent, notamment le *kernel* de la norme, à savoir la superposition entre deux états de Bogoliubov non-orthogonaux, et les *kernel* des opérateurs, correspondant à l'élément de matrice des opérateurs à un ou deux corps entre les deux états. Dans la pratique ces deux catégories invoquent deux pratiques conceptuellement différentes: le *kernel* de la norme est évalué en utilisant le *pfaffien*, qui généralise le concept de déterminant dans des matrices antisymétriques, lorsque les opérateurs demandent une généralisation du théorème de Wick dans la formulation de Balian and Brezin. On propose ici dans le Chapitre 2 une nouvelle approche reposant sur une technique diagrammatique permettant de formuler les deux catégories dans un cadre formel homogène et qui permet de retrouver les formules standard.

Dérivation de la QRPA à partir de la GCM

On parle couramment de la RPA comme de la limite harmonique de la GCM, ce qui correspond à un constat observé par Jancovici et Schiff peu après l'apparition de la GCM. Dans le Chapitre 3 on généralise la démonstration à des calculs GCM utilisant des états de Bogoliubov et à des Hamiltonien à N corps. À l'aide de l'approximation de *quasi-boson* (QBA) l'équation QRPA est retrouvée au cas où l'on considère un hamiltonien à deux corps. Cette dérivation originale est opéré en introduisant une autre formulation des *kernel* reposant sur l'usage des commutateurs imbriqués. Le lien entre la GCM et des théories d'expansion bosonique est aussi rappelé.

Fonctions de réponse et moments associés

À l'aide de la théorie de la réponse linéaire, la définition de fonction réponse est introduite dans le Chapitre 4. Cette quantité représente le point de contact entre la théorie et les observable expérimentales. L'attention se déplace donc sur le calcul de moments de la fonction réponse, dont on fournit une méthode d'évaluation basée seulement sur la connaissance de l'état fondamental su système. L'implémentation numérique de cette méthode représente un autre élément de nouveauté de ce travail.

La performance numérique des deux méthodes est présentée dans le Chapitre 10. L'on observe que globalement l'évaluation basée sur la nouvelle méthode résulte mieux convergé, ce qui est lié au fait que l'état fondamental est généralement mieux convergé que les états excités. Concernant l'évaluation des règles de somme, on ne retrouve pas des forts signaux de violation de l'hypothèse de localité liés à l'utilisation des hamiltoniens *ab initio*.

Projection sur J des fonctions de réponse

La projection sur le moment angulaire des fonctions de réponse obtenue à partir d'un calcul déformé est abordée dans le Chapitre 5. Les concepts fondamentaux de la rotation en mécanique quantique sont introduit pour permettre un accès graduel à la notion de projecteur, ce qui représente l'objet centrale dans une démarche de restauration de symétrie. L'application des techniques de projection à la fonction réponse des systèmes déformés est donc introduite dans le formalisme RPA. La présence du couplage entre un état rotationnel et les états excités de nature vibrationnelle ressortissant des calculs déformés est adressée d'un point de vue formel, aussi bien que une méthode pour le supprimer d'une façon explicite.

Étude systématique des résonances géantes en utilisant la PGCM

La deuxième partie du manuscrit est consacrée à l'exposition des résultats numériques de ce travail et se développe sur plusieurs chapitres. Dans le Chapitre 6 on s'intéresse, d'abord, à la convergence des calculs PGCM *ab initio* vis à vis des paramètres de l'hamiltonien utilisée et de la dimension de l'espace modèle employé dans le cas du ^{46}Ti. La fonction de réponse monopolaire est choisie comme quantité clef pour cet étude. On en retrouve une bonne notion de convergence par rapport aux paramètres de la base d'oscillateur harmonique utilisée, au même titre qu'à propos de l'ordre chiral de l'hamiltonien. Ensuite, la convergence de la fonction de réponse en termes des états de Bogoliubov insérés dans la fonction d'onde PGCM est adressée. On observe que si on considère des calculs PGCM effectués avec une seule coordonnée génératrice, la convergence ne représente point un problème, de telle sorte que peu de points aux alentours du minimum HFB suffisent pour déterminer des états excités jusqu'à très haute énergie. Quand deux coordonnées génératrices sont explorées au même temps, ce qui est nécessaire dans des calculs réalistes, la convergence est obtenue avec une plus grande difficulté. On constate, toutefois, qu'un critère de sélection reposant sur la différence en énergie par rapport au minimum HFB garantit des meilleurs résultats si

comparés à ce que l'on obtient quand un jugement de valeur s'appuyant sur la distance (dans l'espace des coordonnées collectives) entre les différents états HFB est choisi.

Résultats d'intérêt physique

Après une investigation systématique de la convergence des calculs PGCM *ab initio*, les enseignements tirés du Chapitre 6 sont mis en pratique dans le Chapitre 7 à fin d'étudier des systèmes physiques de plus grand intérêt. On commence en présentant un cas sphérique simple, tel que l'^{16}O, à fin d'analyser d'une façon claire la différence entre deux méthodes différentes, telle que la PGCM et la QRPA. On poursuit en analysant le contenu physique des résultats relatifs au ^{46}Ti, avec un focus particulier sur les effets de la déformation et sur le couplage entre GMR et GQR et comment cela se manifeste au sein des calculs PGCM. Les possible effets de la coexistence de formes sont abordés dans le ^{28}Si, sans observer des mélanges significatifs entre les minima oblate et prolate. Toutefois, la réponse de l'isomère de forme prolate est aussi obtenue, montrant des effets de couplage très prononcés avec la résonance quadrupolaire. Finalement, des calculs relatifs au ^{24}Mg sont présentés. La réponse monopolaire associée résulte extrêmement fragmentée et, bien qu'une interprétation physique de chaque excitation ne soit pas envisageable, un bon accord avec l'expérience est observé, ce qui contribue à expliquer la difficulté expérimentale rencontrée dans l'analyse de ce système.

Effets de la projection sur J des fonctions de réponse

Des calculs sans restauration de symétrie explicite ont été réalisés pour les mêmes noyaux adressés dans le Chapitre 7 pour analyser les effets de la projection. Puisque sans projection sur le moment angulaire la fonction d'onde GCM brise la symétrie par invariance rotationnelle, la technique détaillée dans le Chapitre 5 a été appliquée à des calculs GCM, dont les résultats sont présentés dans le Chapitre 8, et à des calculs EDF RPA dans le Chapitre 12. Dans les deux cas on apprend de l'existence d'un couplage entre un état rotationnel étant le Boson de Goldstone du groupe $SU(2)$ et les états excités vibrationnels. Cette observation n'ayant aucun précédent en littérature, spécialement par rapport à des vibrations monopolaires, elle représente un ultérieur élément de nouveauté de ce travail. On constate également qu'une fois les états vibrationnels explicitement orthogonalisés par rapport à l'état rotationnel, la réponse monopolaire demeure inchangée relativement à la contrepartie non-projetée.

Comparaison avec la QRPA

Les calculs PGCM relatifs au Chapitre 7 sont systématiquement comparés aux analogues QRPA dans le Chapitre 9. À l'aide des quantificateurs de non-harmonicité définis à travers la théorie des perturbations en première quantification, on analyse les différences plus ou moins prononcés entre les réponses monopolaires obtenues à partir des deux méthodes en les associant à des effets non-harmoniques. Globalement on rencontre un degré de non-harmonicité tant plus marqué pour les systèmes légers, lorsque un bon accord entre les deux méthodes est observé pour les noyaux plus lourds.

Observation des états de multi-phonon

Par sa nature la PGCM permet, contrairement à la QRPA, d'accéder à des états autres que des pures excitations de phonon, c'est à dire des excitations collectives qui peuvent être décrites comme l'action d'un opérateur bosonique d'excitation agissant sur l'état fondamental du système. Des états à plus hautes énergies, connus sous le nom de multi-phonons, peuvent également se manifester. Les multi-phonons sont le produit de l'action d'un opérateur d'excitation sur des états excités, notamment de phonons simples.

Dans le cas des résonances géantes, des états de multi-phonon correspondent à des états de résonance bâtis non pas sur l'état fondamental mais sur la résonance elle-même. Des résultats numériques relatifs à des tels états sont présentés dans le Chapitre 11. Après l'exposition d'un cas d'étude obtenu à partir des calculs simple dans une seule dimension, l'on présente des résultats réalistes pour des états de multi-phonon monopolaires dans le ^{46}Ti et quadrupolaires dans l'isomère de forme du ^{28}Si. Des critère généraux pour discriminer la présence des tels états dans des calculs théorique sont également donnés.

Conclusions et développements futurs

Dans ce travail la méthode PGCM a été utilisée pour la première fois pour un étude systématique des résonances géantes monopolaires en utilisant des hamiltoniens *ab initio*. Grâce à l'analyse détaillée des propriétés de convergence on peut affirmer que cette technique constitue un outil fiable pour l'investigation des résonances géantes. Contrairement à la QRPA, qui représente la méthode de référence dans le domaine, la PGCM peut décrire des effets de non-harmonicité et prend en compte explicitement les effets de couplage avec les états rotationnelles de basse énergie, produisant donc des solutions qui ne brisent pas les symétries fondamentales du problème.

Grâce à cette méthode différents aspects concernant les résonances géantes ont été analysés; parmi d'autres les conséquences des déformations intrinsèques, le couplage avec des états rotationnels, les effets de non-harmonicité e la présence des états de multi-phonon. Chaque aspect représente un élément de nouveauté quant à la description des résonances géantes dans la communauté *ab initio*.

Différemment de la QRPA la méthode PGCM présente, dans des applications réalistes, une ambiguïté de fond relativement au choix des coordonnées génératrices, ce qui représente la faiblesse la plus grande de cette technique. L'exploration des coordonnées supplémentaires est, pourtant, un point clef dans un étude plus systématique des résonances géantes, à même titre que l'ajout des moments conjugués; ce dernier point est explicitement pris en compte dans la GCM dynamique.

Une autre possibilité relative à une analyse plus systématique de l'espace des coordonnées génératrices est représentée par la méthode de la *continuation des vecteurs propres* (EC). Ce formalisme présente des fortes ressemblances formelles avec la GCM et semble indiquer que une description détaillée des coordonnées génératrices aux alentours de l'état fondamental peut fournir des informations précis relatifs aux états excités aussi, ce qui faciliterait énormément la sélection dans l'espace des coordonnées. EC pourrait également être utilisée pour une détermination quantitative des incertitudes liées au choix des coordonnées génératrices, ce qui constitue un point cardinal entre les défis majeurs de la structure nucléaire *ab initio* aujourd'hui.

Finalement, vus les effets non triviaux liés au couplage entre rotations et vibrations observés dans la GCM en ce travail et l'observation des certaines similarités à cet égard entre GCM et RPA, on encourage fortement le développement d'une version projetée de la QRPA, à même titre que la PGCM. Une telle technique a été en effet formalisé d'un point de vue théorique, mais des implémentations réalistes ont été développées seulement en chimie quantique. Vue les avancées actuelles concernant les ressources computationnelles disponibles et la reformulation de la QRPA dans le contexte de la méthode de l'ampleur finie (FAM), un tel objectif pourrait ne plus être si irréaliste comme à l'époque de son introduction théorique.

Bibliography

[1] V. Bontems, T. Duguet, G. Hagen, and V. Somà, "Topical issue on the tower of effective (field) theories and the emergence of nuclear phenomena," *The European Physical Journal A*, vol. 57, pp. 42–44, 2021.

[2] S. Rivat and A. Grinbaum, "Philosophical foundations of effective field theories," *The European Physical Journal A*, vol. 56, pp. 90–199, 2020.

[3] D. Entem and R. Machleidt, "Accurate charge-dependent nucleon-nucleon potential at fourth order of chiral perturbation theory," *Physical Review C*, vol. 68, no. 4, p. 041001, 2003.

[4] E. Epelbaum, H.-W. Hammer, and U.-G. Meißner, "Modern theory of nuclear forces," *Reviews of Modern Physics*, vol. 81, no. 4, p. 1773, 2009.

[5] V. Somà, "From the liquid drop model to lattice QCD," *The European Physical Journal Plus*, vol. 133, no. 10, pp. 1–22, 2018.

[6] T. Hüther, K. Vobig, K. Hebeler, R. Machleidt, and R. Roth, "Family of chiral two-plus three-nucleon interactions for accurate nuclear structure studies," *Physics Letters B*, vol. 808, p. 135651, 2020.

[7] R. Machleidt and F. Sammarruca, "Can chiral EFT give us satisfaction?," *The European Physical Journal A*, vol. 56, pp. 95–118, 2020.

[8] P. Navrátil, S. Quaglioni, I. Stetcu, and B. Barrett, "Recent developments in no-core shell-model calculations," *Journal of Physics G: Nuclear and Particle Physics*, vol. 36, no. 8, p. 083101, 2009.

[9] R. Roth, J. Langhammer, A. Calci, S. Binder, and P. Navrátil, "Similarity-Transformed Chiral NN+ 3N Interactions for the Ab Initio Description of ^{12}C and ^{16}O," *Physical Review Letters*, vol. 107, no. 7, p. 072501, 2011.

[10] B. Barrett, P. Navrátil, and J. Vary, "Ab initio no core shell model," *Progress in Particle and Nuclear Physics*, vol. 69, pp. 131–181, 2013.

[11] J. Carlson, S. Gandolfi, F. Pederiva, S. Pieper, R. Schiavilla, K. Schmidt, and R. Wiringa, "Quantum Monte Carlo methods for nuclear physics," *Reviews of Modern Physics*, vol. 87, no. 3, p. 1067, 2015.

[12] S. Gandolfi, D. Lonardoni, A. Lovato, and M. Piarulli, "Atomic nuclei from quantum Monte Carlo calculations with chiral EFT interactions," *Frontiers in Physics*, vol. 8, p. 117, 2020.

[13] R. Roth, "Importance truncation for large-scale configuration interaction approaches," *Physical Review C*, vol. 79, no. 6, p. 064324, 2009.

[14] R. Roth and P. Navrátil, "Ab Initio Study of ^{40}Ca with an Importance-Truncated No-Core Shell Model," *Physical review letters*, vol. 99, no. 9, p. 092501, 2007.

[15] B. Hu, W. Jiang, T. Miyagi, Z. Sun, A. Ekström, C. Forssén, G. Hagen, J. Holt, T. Papenbrock, S. Stroberg, *et al.*, "Ab initio predictions link the neutron skin of ^{208}Pb to nuclear forces," *Nature Physics*, pp. 1–5, 2022.

[16] A. Tichai, J. Langhammer, S. Binder, and R. Roth, "Hartree-Fock many-body perturbation theory for nuclear ground-states," *Physics Letters B*, vol. 756, pp. 283–288, 2016.

[17] A. Tichai, R. Roth, and T. Duguet, "Many-body perturbation theories for finite nuclei," *Frontiers in Physics*, vol. 8, p. 164, 2020.

[18] K. Kowalski, D. Dean, M. Hjorth-Jensen, T. Papenbrock, and P. Piecuch, "Coupled cluster calculations of ground and excited states of nuclei," *Physical Review Letters*, vol. 92, no. 13, p. 132501, 2004.

[19] R. Roth, S. Binder, K. Vobig, A. Calci, J. Langhammer, and P. Navrátil, "Medium-mass nuclei with normal-ordered chiral NN+ 3N interactions," *Physical Review Letters*, vol. 109, no. 5, p. 052501, 2012.

[20] G. Hagen, T. Papenbrock, M. Hjorth-Jensen, and D. Dean, "Coupled-cluster computations of atomic nuclei," *Reports on Progress in Physics*, vol. 77, no. 9, p. 096302, 2014.

[21] G. Hagen, A. Ekström, C. Forssén, G. Jansen, W. Nazarewicz, T. Papenbrock, K. Wendt, S. Bacca, N. Barnea, B. Carlsson, *et al.*, "Neutron and weak-charge distributions of the ^{48}Ca nucleus," *Nature Physics*, vol. 12, no. 2, pp. 186–190, 2016.

[22] K. Tsukiyama, S. Bogner, and A. Schwenk, "In-medium similarity renormalization group for nuclei," *Physical review letters*, vol. 106, no. 22, p. 222502, 2011.

[23] H. Hergert, S. Bogner, T. Morris, A. Schwenk, and K. Tsukiyama, "The in-medium similarity renormalization group: A novel ab initio method for nuclei," *Physics reports*, vol. 621, pp. 165–222, 2016.

[24] W. Dickhoff and C. Barbieri, "Self-consistent Green's function method for nuclei and nuclear matter," *Progress in Particle and Nuclear Physics*, vol. 52, no. 2, pp. 377–496, 2004.

[25] A. Cipollone, C. Barbieri, and P. Navrátil, "Isotopic chains around oxygen from evolved chiral two-and three-nucleon interactions," *Physical Review Letters*, vol. 111, no. 6, p. 062501, 2013.

[26] A. Cipollone, C. Barbieri, and P. Navrátil, "Chiral three-nucleon forces and the evolution of correlations along the oxygen isotopic chain," *Physical Review C*, vol. 92, no. 1, p. 014306, 2015.

[27] V. Somà, T. Duguet, and C. Barbieri, "Ab initio self-consistent Gorkov-Green's function calculations of semimagic nuclei: Formalism at second order with a two-nucleon interaction," *Physical Review C*, vol. 84, no. 6, p. 064317, 2011.

[28] V. Somà, C. Barbieri, and T. Duguet, "Ab initio Gorkov-Green's function calculations of open-shell nuclei," *Physical Review C*, vol. 87, no. 1, p. 011303, 2013.

[29] V. Somà, C. Barbieri, T. Duguet, and P. Navrátil, "Moving away from singly-magic nuclei with Gorkov-Green's function theory," *The European Physical Journal A*, vol. 57, no. 4, pp. 1–17, 2021.

[30] A. Tichai, P. Arthuis, T. Duguet, H. Hergert, V. Somá, and R. Roth, "Bogoliubov many-body perturbation theory for open-shell nuclei," *Physics Letters B*, vol. 786, pp. 195–200, 2018.

[31] P. Arthuis, T. Duguet, A. Tichai, R.-D. Lasseri, and J.-P. Ebran, "ADG: Automated generation and evaluation of many-body diagrams I. Bogoliubov many-body perturbation theory," *Computer Physics Communications*, vol. 240, pp. 202–227, 2019.

[32] P. Demol, M. Frosini, A. Tichai, V. Somà, and T. Duguet, "Bogoliubov many-body perturbation theory under constraint," *Annals of Physics*, vol. 424, p. 168358, 2021.

[33] T. Duguet, "Symmetry broken and restored coupled-cluster theory: I. Rotational symmetry and angular momentum," *Journal of Physics G: Nuclear and Particle Physics*, vol. 42, no. 2, p. 025107, 2014.

[34] T. Duguet and A. Signoracci, "Symmetry broken and restored coupled-cluster theory: II. Global gauge symmetry and particle number," *Journal of Physics G: Nuclear and Particle Physics*, vol. 44, no. 1, p. 015103, 2016.

[35] A. Signoracci, T. Duguet, G. Hagen, and G. Jansen, "Ab initio Bogoliubov coupled cluster theory for open-shell nuclei," *Physical Review C*, vol. 91, no. 6, p. 064320, 2015.

[36] G. Hagen, S. Novario, Z. Sun, T. Papenbrock, G. Jansen, J. Lietz, T. Duguet, and A. Tichai, "Angular-momentum projection in coupled-cluster theory: Structure of ^{34}Mg," *Physical Review C*, vol. 105, no. 6, p. 064311, 2022.

[37] Q. Yuan, S. Fan, B. Hu, J. Li, S. Zhang, S. Wang, Z. Sun, Y. Ma, and F. Xu, "Deformed in-medium similarity renormalization group," *Physical Review C*, vol. 105, no. 6, p. L061303, 2022.

[38] H. Hergert, S. Bogner, T. Morris, S. Binder, A. Calci, J. Langhammer, and R. Roth, "Ab initio multireference in-medium similarity renormalization group calculations of even calcium and nickel isotopes," *Physical Review C*, vol. 90, no. 4, p. 041302, 2014.

[39] H. Hergert, "In-medium similarity renormalization group for closed and open-shell nuclei," *Physica Scripta*, vol. 92, no. 2, p. 023002, 2016.

[40] J. Yao, J. Engel, L. Wang, C. Jiao, and H. Hergert, "Generator-coordinate reference states for spectra and $0\nu\beta\beta$ decay in the in-medium similarity renormalization group," *Physical Review C*, vol. 98, no. 5, p. 054311, 2018.

[41] M. Frosini, T. Duguet, J.-P. Ebran, and V. Somà, "Multi-reference many-body perturbation theory for nuclei: I. Novel PGCM-PT formalism," *The European Physical Journal A*, vol. 58, no. 4, p. 62, 2022.

[42] M. Frosini, T. Duguet, J.-P. Ebran, B. Bally, T. Mongelli, T. Rodríguez, R. Roth, and V. Somà, "Multi-reference many-body perturbation theory for nuclei: II. Ab initio study of Ne isotopes via PGCM and IM-NCSM calculation," *The European Physical Journal A*, vol. 58, p. 63, Apr 2022.

[43] M. Frosini, T. Duguet, J.-P. Ebran, B. Bally, H. Hergert, T. Rodríguez, R. Roth, J. Yao, and V. Somà, "Multi-reference many-body perturbation theory for nuclei: III. Ab initio calculations at second order in PGCM-PT," *The European Physical Journal A*, vol. 58, no. 4, p. 64, 2022.

[44] S. Stroberg, A. Calci, H. Hergert, J. Holt, S. Bogner, R. Roth, and A. Schwenk, "Nucleus-dependent valence-space approach to nuclear structure," *Physical Review Letters*, vol. 118, no. 3, p. 032502, 2017.

[45] S. Stroberg, H. Hergert, S. K. Bogner, and J. Holt, "Nonempirical interactions for the nuclear shell model: an update," *Annual Review of Nuclear and Particle Science*, vol. 69, pp. 307–362, 2019.

[46] G. Hagen, G. Jansen, and T. Papenbrock, "Structure of ^{78}Ni from First-Principles Computations," *Physical Review Letters*, vol. 117, no. 17, p. 172501, 2016.

[47] N. Parzuchowski, T. Morris, and S. Bogner, "Ab initio excited states from the in-medium similarity renormalization group," *Physical Review C*, vol. 95, no. 4, p. 044304, 2017.

[48] S. Bacca, N. Barnea, G. Hagen, G. Orlandini, and T. Papenbrock, "First Principles Description of the Giant Dipole Resonance in ^{16}O," *Physical Review Letters*, vol. 111, no. 12, p. 122502, 2013.

[49] J. Sobczyk and A. Roggero, "Spectral density reconstruction with Chebyshev polynomials," *Physical Review E*, vol. 105, no. 5, p. 055310, 2022.

[50] J. Sobczyk, S. Bacca, G. Hagen, and T. Papenbrock, "Spectral function for ^{4} He using the Chebyshev expansion in coupled-cluster theory," *arXiv preprint arXiv:2205.03592*, 2022.

[51] N. Paar, P. Papakonstantinou, H. Hergert, and R. Roth, "Collective multipole excitations based on correlated realistic nucleon-nucleon interactions," *Physical Review C*, vol. 74, no. 1, p. 014318, 2006.

[52] H. Hergert, P. Papakonstantinou, and R. Roth, "Quasiparticle random-phase approximation with interactions from the similarity renormalization group," *Physical Review C*, vol. 83, no. 6, p. 064317, 2011.

[53] R. Trippel and R. Roth, "Random-phase approximation with chiral two-plus three-body interactions," *Verhandlungen der Deutschen Physikalischen Gesellschaft*, 2013.

[54] R. Trippel and R. Roth, "Second random-phase approximation with chiral two-plus three-body interactions," *Verhandlungen der Deutschen Physikalischen Gesellschaft*, 2015.

[55] R. Trippel, "Collective excitations with chiral NN+ 3N interactions from coupled-cluster and in-medium SRG," 2016.

[56] R. Trippel and R. Roth, "Correlated random-phase approximation from densities and in-medium matrix elements," *Verhandlungen der Deutschen Physikalischen Gesellschaft*, 2016.

[57] P. Papakonstantinou, R. Trippel, and R. Roth, "From chiral NN (N) interactions to giant and pygmy resonances via extended RPA," *arXiv preprint arXiv:1704.08429*, 2017.

[58] F. Raimondi and C. Barbieri, "Nuclear electromagnetic dipole response with the self-consistent Green's function formalism," *Physical Review C*, vol. 99, no. 5, p. 054327, 2019.

[59] F. Raimondi and C. Barbieri, "Core-polarization effects and effective charges in O and Ni isotopes from chiral interactions," *Physical Review C*, vol. 100, no. 2, p. 024317, 2019.

[60] Y. Beaujeault-Taudière, M. Frosini, J.-P. Ebran, T. Duguet, R. Roth, and V. Somà", "Zero-and finite-temperature electromagnetic strength distributions in closed-and open-shell nuclei from first principles," *Physical Review C*, vol. 107, no. 2, p. L021302, 2023.

[61] J. Blaizot, D. Gogny, and B. Grammaticos, "Nuclear compressibility and monopole resonances," *Nuclear Physics A*, vol. 265, no. 2, pp. 315–336, 1976.

[62] J.-P. Blaizot, "Nuclear compressibilities," *Physics Reports*, vol. 64, no. 4, pp. 171–248, 1980.

[63] E. Khan, N. Paar, D. Vretenar, L.-G. Cao, H. Sagawa, and G. Colò, "Incompressibility of finite fermionic systems: Stable and exotic atomic nuclei," *Physical Review C*, vol. 87, no. 6, p. 064311, 2013.

[64] U. Garg and G. Coló, "The compression-mode giant resonances and nuclear incompressibility," *Progress in Particle and Nuclear Physics*, vol. 101, pp. 55–95, 2018.

[65] G. Bertsch, P. Bortignon, and R. Broglia, "Damping of nuclear excitations," *Reviews of Modern Physics*, vol. 55, no. 1, p. 287, 1983.

[66] P. Bortignon, A. Bracco, and R. Broglia, *Giant Resonances: Nuclear structure at finite temperature.* CRC Press, 2019.

[67] S. Péru, H. Goutte, and J. Berger, "Giant and pygmy resonances within axial-deformed QRPA with the Gogny force," *Nuclear Physics A*, vol. 788, no. 1-4, pp. 44–49, 2007.

[68] K. Yoshida and N. Van Giai, "Deformed quasiparticle-random-phase approximation for neutron-rich nuclei using the Skyrme energy density functional," *Physical Review C*, vol. 78, no. 6, p. 064316, 2008.

[69] S. Péru and H. Goutte, "Role of deformation on giant resonances within the quasiparticle random-phase approximation and the Gogny force," *Physical Review C*, vol. 77, no. 4, p. 044313, 2008.

[70] C. Losa, A. Pastore, T. Døssing, E. Vigezzi, and R. Broglia, "Linear response of light deformed nuclei investigated by self-consistent quasiparticle random-phase approximation," *Physical Review C*, vol. 81, no. 6, p. 064307, 2010.

[71] M. Martini, S. Goriely, S. Hilaire, and S. Péru, "Large scale QRPA calculations for dipole excitations based on a Gogny force," in *AIP Conference Proceedings*, vol. 1491, pp. 160–161, American Institute of Physics, 2012.

[72] S. Péru, I. Deloncle, S. Hilaire, S. Goriely, and M. Martini, "Study of dipole excitations in even-even $^{156-166}$Dy with QRPA using the Gogny force," *The European Physical Journal A*, vol. 55, pp. 1–11, 2019.

[73] P. Schuck, D. Delion, J. Dukelsky, M. Jemai, E. Litvinova, G. Röpke, and M. Tohyama, "Equation of Motion Method for strongly correlated Fermi systems and Extended RPA approaches," *Physics Reports*, vol. 929, pp. 1–84, 2021.

[74] D. Gambacurta, M. Grasso, and F. Catara, "Collective nuclear excitations with Skyrme-second random-phase approximation," *Physical Review C*, vol. 81, no. 5, p. 054312, 2010.

[75] D. Gambacurta and M. Grasso, "Second RPA calculations with the Skyrme and Gogny interactions," *The European Physical Journal A*, vol. 52, pp. 1–8, 2016.

[76] E. Litvinova, P. Ring, and V. Tselyaev, "Particle-vibration coupling within covariant density functional theory," *Physical Review C*, vol. 75, no. 6, p. 064308, 2007.

[77] G. Scamps and D. Lacroix, "Systematics of isovector and isoscalar giant quadrupole resonances in normal and superfluid spherical nuclei," *Physical Review C*, vol. 88, no. 4, p. 044310, 2013.

[78] G. Scamps and D. Lacroix, "Systematic study of isovector and isoscalar giant quadrupole resonances in normal and superfluid deformed nuclei," *Physical Review C*, vol. 89, no. 3, p. 034314, 2014.

[79] P. Marević, D. Regnier, and D. Lacroix, "Quantum fluctuations induce collective multi-phonons in finite Fermi liquids," *arXiv preprint arXiv:2304.07380*, 2023.

[80] E. Caurier, B. Bourotte-Bilwes, and Y. Abgrall, "Microscopic treatment of the coupled monopole and quadrupole vibrations in light nuclei," *Physics Letters B*, vol. 44, no. 5, pp. 411–415, 1973.

[81] Y. Abgrall and E. Caurier, "On the monopole and quadrupole isoscalar giant resonances in ^{4}He, ^{16}O, ^{20}Ne and ^{40}Ca," *Physics Letters B*, vol. 56, no. 3, pp. 229–231, 1975.

[82] B. Giraud and B. Grammaticos, "Collective potentials and inertia parameters (II)," *Nuclear Physics A*, vol. 255, no. 1, pp. 141–156, 1975.

[83] H. Flocard and D. Vautherin, "Generator coordinate calculations of monopole and quadrupole vibrations with Skyrme's interaction," *Physics Letters B*, vol. 55, no. 3, pp. 259–262, 1975.

[84] S. Krewald, R. Rosenfelder, J. Galonska, and A. Faessler, "Selfconsistent generator coordinate method for giant monopole resonances," *Nuclear Physics A*, vol. 269, no. 1, pp. 112–124, 1976.

[85] H. Flocard and D. Vautherin, "Generator coordinate calculations of giant resonances with the Skyrme interaction," *Nuclear Physics A*, vol. 264, no. 2, pp. 197–220, 1976.

[86] F. Arickx and J. Broeckhove, "The generator coordinate method and collective Hamiltonians for the isoscalar monopole vibrations," *Journal of Physics G: Nuclear Physics*, vol. 9, no. 3, p. 285, 1983.

[87] M. Stoitsov, P. Ring, and M. Sharma, "Generator coordinate calculations for breathing-mode giant monopole resonance in the relativistic mean-field theory," *Physical Review C*, vol. 50, no. 3, p. 1445, 1994.

[88] J.-P. Blaizot, J. Berger, J. Dechargé, and M. Girod, "Microscopic and macroscopic determinations of nuclear compressibility," *Nuclear Physics A*, vol. 591, no. 3, pp. 435–457, 1995.

[89] P. Ring and P. Schuck, *The nuclear many-body problem.* Springer-Verlag, 1980.

[90] M. Bender, P.-H. Heenen, and P.-G. Reinhard, "Self-consistent mean-field models for nuclear structure," *Rev. Mod. Phys.*, vol. 75, p. 121, 2003.

[91] T. Niksic, D. Vretenar, and P. Ring, "Relativistic Nuclear Energy Density Functionals: Mean-Field and Beyond," *Prog. Part. Nucl. Phys.*, vol. 66, pp. 519–548, 2011.

[92] L. Robledo, T. Rodríguez, and R. Rodríguez-Guzmán, "Mean field and beyond description of nuclear structure with the Gogny force: A review," *J. Phys. G*, vol. 46, no. 1, p. 013001, 2019.

[93] Z.-C. Gao, M. Horoi, and Y. Chen, "Variation after projection with a triaxially deformed nuclear mean field," *Phys. Rev. C*, vol. 92, no. 6, p. 064310, 2015.

[94] C. Jiao, J. Engel, and J. Holt, "Neutrinoless double-beta decay matrix elements in large shell-model spaces with the generator-coordinate method," *Phys. Rev. C*, vol. 96, no. 5, p. 054310, 2017.

[95] B. Bally, A. Sánchez-Fernández, and T. Rodríguez, "Variational approximations to exact solutions in shell-model valence spaces: calcium isotopes in the pf-shell," *Phys. Rev. C*, vol. 100, no. 4, p. 044308, 2019.

[96] N. Shimizu, T. Mizusaki, K. Kaneko, and Y. Tsunoda, "Generator-coordinate methods with symmetry-restored Hartree-Fock-Bogoliubov wave functions for large-scale shell-model calculations," *Phys. Rev. C*, vol. 103, no. 6, p. 064302, 2021.

[97] A. Sánchez-Fernández, B. Bally, and T. Rodríguez, "Variational approximations to exact solutions in shell-model valence spaces: Systematic calculations in the sd-shell," *Physical Review C*, vol. 104, no. 5, p. 054306, 2021.

[98] J. Yao, B. Bally, J. Engel, R. Wirth, T. Rodríguez, and H. Hergert, "*Ab Initio* Treatment of Collective Correlations and the Neutrinoless Double Beta Decay of ^{48}Ca," *Phys. Rev. Lett.*, vol. 124, no. 23, p. 232501, 2020.

[99] J. Yao, J. Engel, L. Wang, C. Jiao, and H. Hergert, "Generator-coordinate reference states for spectra and $0\nu\beta\beta$ decay in the in-medium similarity renormalization group," *Phys. Rev. C*, vol. 98, no. 5, p. 054311, 2018.

[100] D. Hill and J. Wheeler, "Nuclear constitution and the interpretation of fission phenomena," *Physical Review*, vol. 89, no. 5, p. 1102, 1953.

[101] J. Griffin and J. Wheeler, "Collective motions in nuclei by the method of generator coordinates," *Physical Review*, vol. 108, no. 2, p. 311, 1957.

[102] T. Duguet and A. Signoracci, "Symmetry broken and restored coupled-cluster theory: II. Global gauge symmetry and particle number," *Journal of Physics G: Nuclear and Particle Physics*, vol. 44, no. 1, p. 015103, 2016.

[103] B. Bally and T. Duguet, "Norm overlap between many-body states: Uncorrelated overlap between arbitrary Bogoliubov product states," *Physical Review C*, vol. 97, no. 2, p. 024304, 2018.

[104] D. Thouless, "Perturbation theory in statistical mechanics and the theory of superconductivity," *Annals of Physics*, vol. 10, no. 4, pp. 553–588, 1960.

[105] R. Balian and E. Brezin, "Nonunitary Bogoliubov transformations and extension of Wick's theorem," *Il Nuovo Cimento B (1965-1970)*, vol. 64, no. 1, pp. 37–55, 1969.

[106] N. Onishi and S. Yoshida, "Generator coordinate method applied to nuclei in the transition region," *Nuclear Physics*, vol. 80, no. 2, pp. 367–376, 1966.

[107] L. Robledo, "Sign of the overlap of Hartree-Fock-Bogoliubov wave functions," *Physical Review C*, vol. 79, no. 2, p. 021302, 2009.

[108] T. Mizusaki and M. Oi, "A new formulation to calculate general HFB matrix elements through Pfaffian," *Phys. Lett. B*, vol. 715, pp. 219–224, 2012.

[109] T. Mizusaki, M. Oi, F.-Q. Chen, and Y. Sun, "Grassmann integral and Balian-Brézin decomposition in Hartree-Fock-Bogoliubov matrix elements," *Phys. Lett. B*, vol. 725, pp. 175–179, 2013.

[110] A. Porro and T. Duguet, "On the off-diagonal Wick's theorem and Onishi formula: Alternative and consistent approach to off-diagonal operator and norm kernels," *The European Physical Journal A*, vol. 58, no. 10, p. 197, 2022.

[111] R. Bartlett and J. Noga, "The expectation value coupled-cluster method and analytical energy derivatives," *Chemical physics letters*, vol. 150, no. 1-2, pp. 29–36, 1988.

[112] J. Robinson and P. Knowles, "Quasi-variational coupled cluster theory," *The Journal of chemical physics*, vol. 136, no. 5, p. 054114, 2012.

[113] A. Marie, F. Kossoski, and P.-F. Loos, "Variational coupled cluster for ground and excited states," *The Journal of Chemical Physics*, vol. 155, no. 10, p. 104105, 2021.

[114] Q. Fetter and J. Walecka, *Quantum Theory of Many-Particle Systems (Dover Books on Physics)*. Dover Publications, 2003.

[115] J. Blaizot and G. Ripka, *Quantum theory of finite systems*. Cambridge, Mass: MIT Press, 1986.

[116] T. Mizusaki, M. Oi, and N. Shimizu, "Why does the sign problem occur in evaluating the overlap of HFB wave functions?," *Physics Letters B*, vol. 779, pp. 237–243, 2018.

[117] K. Neergård and E. Wüst, "On the calculation of matrix elements of operators between symmetry-projected Bogoliubov states," *Nuclear Physics A*, vol. 402, pp. 311–321, 1983.

[118] M. Oi, T. Mizusaki, N. Shimizu, and Y. Sun, "Hidden symmetries in the HFB norm overlap functions," *EPJ Web Conf.*, vol. 223, p. 01047, 2019.

[119] M. Krivoruchenko, "Trace Identities for Skew-Symmetric Matrices," *Mathematics and Computer Science*, vol. 1, no. 2, p. 21, 2016.

[120] E. Caianiello, *Combinatorics and renormalization in quantum field theory.* WA Benjamin, Inc., Reading, MA, 1973.

[121] B. Jancovici and D. Schiff, "The collective vibrations of a many-fermion system," *Nuclear Physics*, vol. 58, pp. 678–686, 1964.

[122] D. Brink and A. Weiguny, "The generator coordinate theory of collective motion," *Nuclear Physics A*, vol. 120, no. 1, pp. 59–93, 1968.

[123] G. Gallatin, "A useful formula for evaluating commutators," *Journal of Mathematical Physics*, vol. 24, no. 11, pp. 2564–2565, 1983.

[124] D. Thouless, "Stability conditions and nuclear rotations in the Hartree-Fock theory," *Nuclear Physics*, vol. 21, pp. 225–232, 1960.

[125] F. Dyson, "General theory of spin-wave interactions," *Physical review*, vol. 102, no. 5, p. 1217, 1956.

[126] D. Janssen, F. Dönau, S. Frauendorf, and R. Jolos, "Boson description of collective states:(I). Derivation of the boson transformation for even fermion systems," *Nuclear Physics A*, vol. 172, no. 1, pp. 145–165, 1971.

[127] T. Holstein and H. Primakoff, "Field dependence of the intrinsic domain magnetization of a ferromagnet," *Physical Review*, vol. 58, no. 12, p. 1098, 1940.

[128] S. T. Beliaev and V. Zelevinsky, "Anharmonic effects of quadrupole oscillations of spherical nuclei," *Nuclear Physics*, vol. 39, pp. 582–604, 1962.

[129] E. Marshalek, "On the relation between Beliaev-Zelevinsky and Marumori boson expansions," *Nuclear Physics A*, vol. 161, no. 2, pp. 401–409, 1971.

[130] E. Marshalek and G. Holzwarth, "Boson expansions and Hartree-Bogoliubov theory," *Nuclear Physics A*, vol. 191, no. 2, pp. 438–448, 1972.

[131] E. Marshalek, "Perturbative boson expansions to all orders for even and odd nuclei:(I). Formal properties," *Nuclear Physics A*, vol. 224, no. 2, pp. 221–244, 1974.

[132] J. Blaizot and E. Marshalek, "Boson expansions and quantization of time-dependent self-consistent fields (I). Particle-hole excitations," *Nuclear Physics A*, vol. 309, no. 3, pp. 422–452, 1978.

[133] J. Da Providência, "An extension of the random phase approximation," *Nuclear Physics A*, vol. 108, no. 3, pp. 589–608, 1968.

[134] M. Sambataro and F. Catara, "Extended random-phase approximation in a boson formalism with Pauli principle," *Physical Review C*, vol. 51, no. 6, p. 3066, 1995.

[135] D. Rowe, "Equations-of-motion method and the extended shell model," *Reviews of Modern Physics*, vol. 40, no. 1, p. 153, 1968.

[136] P. Schuck and S. Ethofer, "Self-consistent (nuclear) phonons," *Nuclear Physics A*, vol. 212, no. 2, pp. 269–286, 1973.

[137] D. Janssen and P. Schuck, "On some aspects of selfconsistent RPA theory," *Zeitschrift für Physik A Hadrons and Nuclei*, vol. 339, pp. 43–50, 1991.

[138] M. Jemai, D. Delion, and P. Schuck, "Self-consistent random-phase approximation from a coupled-cluster wave function perspective," *Physical Review C*, vol. 88, no. 4, p. 044004, 2013.

[139] M. Green, "Markoff random processes and the statistical mechanics of time-dependent phenomena. II. Irreversible processes in fluids," *The Journal of chemical physics*, vol. 22, no. 3, pp. 398–413, 1954.

[140] R. Kubo, "Statistical-mechanical theory of irreversible processes. I. General theory and simple applications to magnetic and conduction problems," *Journal of the Physical Society of Japan*, vol. 12, no. 6, pp. 570–586, 1957.

[141] O. Bohigas, A. Lane, and J. Martorell, "Sum rules for nuclear collective excitations," *Physics Reports*, vol. 51, no. 5, pp. 267–316, 1979.

[142] G. Gallatin, "A useful formula for evaluating commutators," *Journal of Mathematical Physics*, vol. 24, pp. 2564–2565, Nov. 1983.

[143] A. Tichai, P. Arthuis, H. Hergert, and T. Duguet, "ADG: automated generation and evaluation of many-body diagrams: III. Bogoliubov in-medium similarity renormalization group formalism," *The European Physical Journal A*, vol. 58, no. 1, p. 2, 2022.

[144] J. Sakurai and J. Napolitano, *Modern Quantum Mechanics*. 09 2020.

[145] B. Erler and R. Roth, "Collective excitations in deformed sd-shell nuclei from realistic interactions," *arXiv preprint arXiv:1409.0826*, 2014.

[146] A. Edmonds, *Angular momentum in quantum mechanics*. Princeton university press, 1996.

[147] B. Erler, "Mean-Field Approach to Collective Excitations in Deformed sd-Shell Nuclei using Realistic Interactions," 2012.

[148] C. Federschmidt and P. Ring, "Symmetry-conserving random phase approximation," *Nuclear Physics A*, vol. 435, no. 1, pp. 110–124, 1985.

[149] J. Dukelsky and P. Schuck, "Towards a variational theory for RPA-like correlations and fluctuations," *Nuclear Physics A*, vol. 512, no. 3, pp. 466–482, 1990.

[150] A. Bohr and B. Mottelson, *Nuclear Structure (in 2 volumes)*. World Scientific Publishing Company, 1998.

[151] D. Thouless, "Vibrational states of nuclei in the random phase approximation," *Nuclear Physics*, vol. 22, no. 1, pp. 78–95, 1961.

[152] A. Lane and J. Martorell, "The Random Phase Approximation: Its role in restoring symmetries lacking in the Hartree-Fock approximation," *Annals of Physics*, vol. 129, no. 2, pp. 273–302, 1980.

[153] A. Faessler and R. Nojarov, "Purely collective versus RPA rotational vibrations," *Physics Letters B*, vol. 215, no. 3, pp. 439–443, 1988.

[154] D. Gambacurta, G. Colò, and A. Pastore, "Nuclear incompressibility from spherical and deformed nuclei," in *Journal of Physics: Conference Series*, vol. 1643, p. 012129, IOP Publishing, 2020.

[155] R. Machleidt and D. Entem, "Chiral effective field theory and nuclear forces," *Physics Reports*, vol. 503, no. 1, pp. 1–75, 2011.

[156] A. Ekström, G. Jansen, K. Wendt, G. Hagen, T. Papenbrock, B. Carlsson, C. Forssen, M. Hjorth-Jensen, P. Navratil, and W. Nazarewicz, "Accurate nuclear radii and binding energies from a chiral interaction," *Physical Review C*, vol. 91, no. 5, p. 051301, 2015.

[157] A. Nogga, S. Bogner, and A. Schwenk, "Low-momentum interaction in few-nucleon systems," *Physical Review C*, vol. 70, no. 6, p. 061002, 2004.

[158] K. Hebeler, S. Bogner, R. Furnstahl, A. Nogga, and A. Schwenk, "Improved nuclear matter calculations from chiral low-momentum interactions," *Physical Review C*, vol. 83, no. 3, p. 031301, 2011.

[159] S. Stroberg, J. Holt, A. Schwenk, and J. Simonis, "Ab initio limits of atomic nuclei," *Physical Review Letters*, vol. 126, no. 2, p. 022501, 2021.

[160] M. Frosini, T. Duguet, B. Bally, Y. Beaujeault-Taudière, J.-P. Ebran, and V. Somà, "In-medium k-body reduction of n-body operators: A flexible symmetry-conserving approach based on the sole one-body density matrix," *The European Physical Journal A*, vol. 57, no. 4, p. 151, 2021.

[161] J. Cameron, M. Bentley, A. Bruce, R. Cunningham, W. Gelletly, H. Price, J. Simpson, D. Warner, and A. James, "High-spin gamma spectroscopy of recoil-separated sup 49 Cr, sup 49 V, and sup 46 Ti," *Physical Review, C (Nuclear Physics);(United States)*, vol. 44, no. 5, 1991.

[162] Y. Tokimoto, Y.-W. Lui, H. Clark, B. John, X. Chen, and D. Youngblood, "Giant resonances in Ti 46,48," *Physical Review C*, vol. 74, no. 4, p. 044308, 2006.

[163] V. Lapoux, V. Somà, C. Barbieri, H. Hergert, J. Holt, and S. Stroberg, "Radii and binding energies in oxygen isotopes: a challenge for nuclear forces," *Physical Review Letters*, vol. 117, no. 5, p. 052501, 2016.

[164] J. Martínez-Larraz and T. Rodríguez, "Optimization of the number of intrinsic states included in the discrete generator coordinate method," *Physical Review C*, vol. 106, no. 5, p. 054301, 2022.

[165] S. Nishizaki and K. Andō, "A fluiddynamical description of isoscalar giant resonances in deformed nuclei," *Progress of Theoretical Physics*, vol. 73, no. 4, pp. 889–904, 1985.

[166] J. Darai, J. Cseh, and D. Jenkins, "Shape isomers and clusterization in the ^{28}Si nucleus," *Physical Review C*, vol. 86, no. 6, p. 064309, 2012.

[167] G. Kelly, N. Clarke, M. Freer, B. Fulton, S. Hoad, R. Le Marechal, and R. Ward, "Search for highly deformed shape isomers in ^{28}Si, ^{24}Mg and ^{20}Ne linked by successive alpha decays," *Nuclear Physics, A*, vol. 628, 1998.

[168] D. Jenkins, C. Lister, M. Carpenter, P. Chowdury, N. Hammond, R. Janssens, T. L. Khoo, T. Lauritsen, D. Seweryniak, T. Davinson, *et al.*, "Candidate superdeformed band in ^{28}Si," *Physical Review C*, vol. 86, no. 6, p. 064308, 2012.

[169] D. Youngblood, Y.-W. Lui, and H. Clark, "Isoscalar giant resonance strength in ^{28}Si," *Physical Review C*, vol. 76, no. 2, p. 027304, 2007.

[170] T. Peach, U. Garg, Y. Gupta, J. Hoffman, J. Matta, D. Patel, P. M. Rao, K. Yoshida, M. Itoh, M. Fujiwara, *et al.*, "Effect of ground-state deformation on isoscalar giant resonances in ^{28}Si," *Physical Review C*, vol. 93, no. 6, p. 064325, 2016.

[171] A. Bahini, V. Nesterenko, I. Usman, P. von Neumann-Cosel, R. Neveling, J. Carter, J. Kvasil, A. Repko, P. Adsley, N. Botha, *et al.*, "Isoscalar giant monopole resonance in ^{24}Mg and ^{28}Si: Effect of coupling between the isoscalar monopole and quadrupole strength," *Physical Review C*, vol. 105, no. 2, p. 024311, 2022.

[172] C. Beck, P. Papka, A. S. i Zafra, S. Thummerer, F. Azaiez, P. Bednarczyk, S. Courtin, D. Curien, O. Dorvaux, D. Lebhertz, *et al.*, "Binary reaction decays from ^{24}Mg + ^{12}C," *Physical Review C*, vol. 80, no. 3, p. 034604, 2009.

[173] Y. Gupta, U. Garg, J. Matta, D. Patel, T. Peach, J. Hoffman, K. Yoshida, M. Itoh, M. Fujiwara, K. Hara, *et al.*, "Splitting of ISGMR strength in the light-mass nucleus ^{24}Mg due to ground-state deformation," *Physics Letters B*, vol. 748, pp. 343–346, 2015.

[174] Y. Gupta, U. Garg, J. Hoffman, J. Matta, P. M. Rao, D. Patel, T. Peach, K. Yoshida, M. Itoh, M. Fujiwara, *et al.*, "Deformation effects on isoscalar giant resonances in ^{24}Mg," *Physical Review C*, vol. 93, no. 4, p. 044324, 2016.

[175] T. Kawabata, "Search for Alpha Condensed State in ^{24}Mg," *Few-Body Systems*, vol. 54, no. 7-10, pp. 1457–1460, 2013.

[176] J. Zamora, C. Sullivan, R. Zegers, N. Aoi, L. Batail, D. Bazin, M. Carpenter, J. Carroll, Y. Fang, H. Fujita, *et al.*, "Investigation of the isoscalar response of ^{24}Mg to ^{6}Li scattering," *Physical Review C*, vol. 104, no. 1, p. 014607, 2021.

[177] D. Youngblood, Y.-W. Lui, X. Chen, and H. Clark, "Isoscalar giant resonance strength in ^{24}Mg," *Physical Review C*, vol. 80, no. 6, p. 064318, 2009.

[178] T. Nakatsukasa, T. Inakura, and K. Yabana, "Finite amplitude method for the solution of the random-phase approximation," *Physical Review C*, vol. 76, no. 2, p. 024318, 2007.

[179] P. Avogadro and T. Nakatsukasa, "Finite amplitude method for the quasiparticle random-phase approximation," *Physical Review C*, vol. 84, no. 1, p. 014314, 2011.

[180] N. Hinohara, M. Kortelainen, W. Nazarewicz, and E. Olsen, "Complex-energy approach to sum rules within nuclear density functional theory," *Physical Review C*, vol. 91, no. 4, p. 044323, 2015.

[181] L. Capelli, G. Coló, and J. Li, "Dielectric theorem within the Hartree-Fock-Bogoliubov framework," *Physical Review C*, vol. 79, no. 5, p. 054329, 2009.

[182] R. Stroberg, "Isospin Breaking in the IMSRG," *Progress in Ab Initio Nuclear Theory, TRIUMF, February 28 - March 3 2023, TRIUMF, Vancouver BC*, meetings.triumf.ca/event/349/contributions/4257/attachments/3155/4035/StrobergPAINT2023.pdf.

[183] G. Fricke, C. Bernhardt, K. Heilig, L. Schaller, L. Schellenberg, E. Shera, and C. Dejager, "Nuclear Ground State Charge Radii from Electromagnetic Interactions," *Atomic Data and Nuclear Data Tables*, vol. 60, no. 2, pp. 177–285, 1995.

[184] M. Bender, G. Bertsch, and P.-H. Heenen, "Global study of quadrupole correlation effects," *Physical Review C*, vol. 73, no. 3, p. 034322, 2006.

[185] V. Somà, P. Navrátil, F. Raimondi, C. Barbieri, and T. Duguet, "Novel chiral Hamiltonian and observables in light and medium-mass nuclei," *Phys. Rev. C*, vol. 101, p. 014318, Jan 2020.

[186] P. Chomaz and N. Frascaria, "Multiple phonon excitation in nuclei: experimental results and theoretical descriptions," *Physics Reports*, vol. 252, no. 5-6, pp. 275–405, 1995.

[187] T. Aumann, P. Bortignon, and H. Emling, "Multiphonon giant resonances in nuclei," *Annual Review of Nuclear and Particle Science*, vol. 48, no. 1, pp. 351–399, 1998.

[188] J. Scarpaci, Y. Blumenfeld, P. Chomaz, N. Frascaria, J. Garron, M. Lamehi-Rachti, I. Lhenry, J. Roynette, T. Suomijärvi, D. Beaumel, *et al.*, "Signature of a two-phonon state through its proton decay pattern," *Physical review letters*, vol. 71, no. 23, p. 3766, 1993.

[189] M. Fallot, J. Scarpaci, N. Frascaria, Y. Blumenfeld, A. Chbihi, P. Chomaz, P. Désesquelles, J. Frankland, E. Khan, J. Laville, *et al.*, "Evidence for a Three-Phonon Giant Resonance State in ^{40}Ca Nuclei," *Physical review letters*, vol. 97, no. 24, p. 242502, 2006.

[190] J. Bartel, P. Quentin, M. Brack, C. Guet, and H.-B. Håkansson, "Towards a better parametrisation of Skyrme-like effective forces: A critical study of the SkM force," *Nuclear Physics A*, vol. 386, no. 1, pp. 79–100, 1982.

[191] M. Stoitsov, J. Dobaczewski, W. Nazarewicz, and P. Ring, "Axially deformed solution of the Skyrme–Hartree–Fock–Bogolyubov equations using the transformed harmonic oscillator basis. The program HFBTHO (v1. 66p)," *Computer physics communications*, vol. 167, no. 1, pp. 43–63, 2005.

[192] F. Mercier, A. Bjelčić, T. Nikšić, J.-P. Ebran, E. Khan, and D. Vretenar, "Low-energy cluster modes in N= Z nuclei," *Physical Review C*, vol. 103, no. 2, p. 024303, 2021.

[193] P. Ellis, "RPA ground state correlations from perturbation theory," *Nuclear Physics A*, vol. 155, no. 2, pp. 625–643, 1970.

[194] D. Rowe, "Methods for calculating ground-state correlations of vibrational nuclei," *Physical Review*, vol. 175, no. 4, p. 1283, 1968.

[195] F. Catara, N. D. Dang, and M. Sambataro, "Ground-state correlations beyond RPA," *Nuclear Physics A*, vol. 579, no. 1-2, pp. 1–12, 1994.

[196] H. Lenske and J. Wambach, "RPA ground state correlations in nuclei," *Physics Letters B*, vol. 249, no. 3-4, pp. 377–380, 1990.

[197] D. Pena Arteaga and P. Ring, "Relativistic random-phase approximation in axial symmetry," *Physical Review C*, vol. 77, no. 3, p. 034317, 2008.

[198] A. Ekström, C. Forssén, G. Hagen, G. Jansen, W. Jiang, and T. Papenbrock, "What is ab initio in nuclear theory?," *Frontiers in Physics*, vol. 11, p. 125, 2023.

[199] C. Hebborn, F. Nunes, G. Potel, W. Dickhoff, J. Holt, M. Atkinson, R. Baker, C. Barbieri, G. Blanchon, M. Burrows, *et al.*, "Optical potentials for the rare-isotope beam era," *arXiv preprint arXiv:2210.07293*, 2022.

[200] T. Marumori, A. Hayashi, T. Tomoda, A. Kuriyama, and T. Maskawa, "Concept of a Collective Subspace Associated with the Invariance Principle of the Schrödinger Equation: A Microscopic Theory of the Large Amplitude Collective Motion of Soft Nuclei," *Progress of Theoretical Physics*, vol. 63, no. 5, pp. 1576–1598, 1980.

[201] T. Marumori, T. Maskawa, F. Sakata, and A. Kuriyama, "Self-consistent collective-coordinate method for the large-amplitude nuclear collective motion," *Progress of Theoretical Physics*, vol. 64, no. 4, pp. 1294–1314, 1980.

[202] M. Matsuo, "Treatment of Nucleon-Number Conservation in the Selfconsistent Collective-Coordinate Method: —Coupling between Large-Amplitude Collective Motion and Pairing Rotation—," *Progress of Theoretical Physics*, vol. 76, no. 2, pp. 372–386, 1986.

[203] K. Goeke and P.-G. Reinhard, "The generator-coordinate-method with conjugate parameters and the unification of microscopic theories for large amplitude collective motion," *Annals of Physics*, vol. 124, no. 2, pp. 249–289, 1980.

[204] P.-G. Reinhard and K. Goeke, "The generator coordinate method and quantised collective motion in nuclear systems," *Reports on Progress in Physics*, vol. 50, no. 1, p. 1, 1987.

[205] N. Hizawa, K. Hagino, and K. Yoshida, "Generator coordinate method with a conjugate momentum: Application to particle number projection," *Physical Review C*, vol. 103, no. 3, p. 034313, 2021.

[206] N. Hizawa, K. Hagino, and K. Yoshida, "Applications of the dynamical generator coordinate method to quadrupole excitations," *Physical Review C*, vol. 105, no. 6, p. 064302, 2022.

[207] D. Frame, R. He, I. Ipsen, D. Lee, D. Lee, and E. Rrapaj, "Eigenvector continuation with subspace learning," *Physical review letters*, vol. 121, no. 3, p. 032501, 2018.

[208] A. Ekström and G. Hagen, "Global sensitivity analysis of bulk properties of an atomic nucleus," *Physical Review Letters*, vol. 123, no. 25, p. 252501, 2019.

[209] S. König, A. Ekström, K. Hebeler, D. Lee, and A. Schwenk, "Eigenvector continuation as an efficient and accurate emulator for uncertainty quantification," *Physics Letters B*, vol. 810, p. 135814, 2020.

[210] T. Tsuchimochi and T. Van Voorhis, "Time-dependent projected Hartree-Fock," *The Journal of Chemical Physics*, vol. 142, no. 12, p. 124103, 2015.

[211] G. Wick, "The Evaluation of the Collision Matrix," *Physical Review*, vol. 80, pp. 268–272, Oct. 1950.

[212] J. Ripoche, A. Tichai, and T. Duguet, "Normal-ordered k-body approximation in particle-number-breaking theories," *Eur. Phys. J. A*, vol. 56, no. 2, 2020.

[213] S. Lang, *Linear algebra*. Springer Berlin, 1987.

[214] C. Jiménez-Hoyos, T. Henderson, T. Tsuchimochi, and G. Scuseria, "Projected Hartree–Fock theory," *The Journal of chemical physics*, vol. 136, no. 16, p. 164109, 2012.

[215] C. Bender and T. Wu, "Anharmonic oscillator," *Physical Review*, vol. 184, no. 5, p. 1231, 1969.

[216] T. Banks, C. Bender, and T. Wu, "Coupled anharmonic oscillators. I. Equal-mass case," *Physical Review D*, vol. 8, no. 10, p. 3346, 1973.

[217] C. Bender and T. Wu, "Anharmonic oscillator. II. A study of perturbation theory in large order," *Physical Review D*, vol. 7, no. 6, p. 1620, 1973.